$\pi^o\pi^o$, η and η' photoproduction off the deuteron or The search for missing resonances

Inauguraldissertation

zur
Erlangung der Würde eines Doktors der Philosophie
vorgelegt der
Philosophish-Naturwissenschaftlichen Fakultät
der Universität Basel

von

Igal JAEGLÉ

aus Earth

Basel, 2009

Genehmigt von der Philosopish-Naturwissenschaftlichen Fakultät
auf Antrag von
Prof. Dr. Bernd Krusche und Prof. Dr. Herbert Loehner

Basel, den 19 Dezember 2007
(Datum der Fakultätssitzung)

Prof. Dr. Hans-Peter Hauri
Dekan

Contents

Introduction

The main topic of this thesis are the cross sections, angular distributions and Dalitz plot measurements of the photoproduction of $\pi^o\pi^o$, η and $\eta^{'}$ - mesons off the deuteron. These measurements were done in order to study nucleon resonance, of mass locations between 1.2 GeV and 2.5 GeV, that couples strongly to the neutron.

The study of the nucleon structure is one of the primary interests in strong interaction physics and has been the subject of experimental and theoretical studies for several decades. One of the primary manifestations of the complex internal structure of the nucleon is the existence of its excited states, i.e. baryon resonances (see Figure 1.1). These play an important role in intermediate energy phenomenon and understanding their nature is a necessarily step to reach a comprehansive picture of strong interaction physics. The excited states of the nucleon were first observed in πN scattering in which their contribution was clearly evident as bumps in the total cross section. These measurements allowed a first classification of the excitation spectrum of the nucleon, providing measurement of the masses, widths, quantum numbers, and branching ratios of many baryon resonances [1]. In spite of the large amount of information collected by these experiments, the number of states that were identified was less than that predicted by the standard quark model [2]. A possible explanation is that such "missing" states may decouple from the πN channel, making them undetectable in experiments with pion beams. Other explanations come from theoretical models that are able to predict a smaller number of states based on a reduced set of degrees of freedom [3].

Unraveling this problem requires measurements with probe other than pion

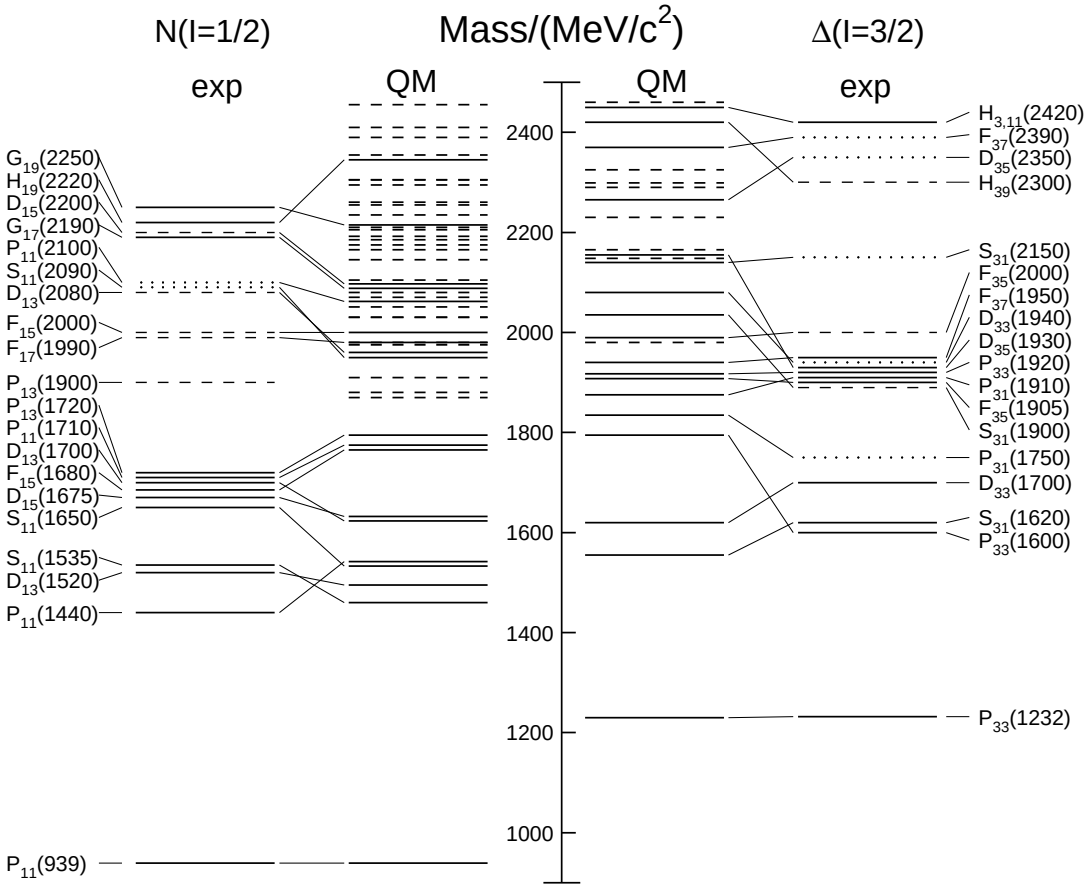

Figure 1.1: *Excitation spectrum of the nucleon. Compared are the positions of the excited states identified in experiment, to those predicted by a modern quark model calculation. Left hand side: isospin I = 1/2 N-states, right hand side: isospin I = 3/2 Δ-states. Experimental: (column labeled 'exp'), three and four star states are indicated by full lines (two-star dashed lines, one-star dotted lines). At the very left and right of the Figure the spectroscopic notation of these states is given. Quark model [4]: (columns labeled 'QM'), all states for the N=1,2 bands, low lying states for the N=3,4,5 bands. Full lines: at least tentative assignment to observed states, dashed lines: so far no observed counterparts. Many of the assignments between predicted and observed states are highly tentative.*

beams. The construction of high intensity and high duty cycle electron and photon facilities, two decades ago, opened new possibilities for the study of baryon resonances using electromagnetic probes. These provide information on the resonance and nucleon wavefunctions through the measurement of the helicity amplitudes, i.e. the electromagnetic couplings between nucleon ground state and initial states. In addition electroproduction also allows us to explore baryon structure for different distance scales by varying the photon virtuality. Nowadays electroexcitation processes are a fundamental tool

to pursue these studies. However due to the complexity of the baryon spectrum, the proximity and overlapping nature of the various excited states, the measurement of a single channel is not sufficient to complete this research program. On the contrary a thorough study of resonance properties requires the measurement of cross sections, angular distributions, Dalitz plots, as well as polarization observables for different final states. Figure 1.2 illustrates the problems, a possible and partial solution by looking at specific meson(s) photoproduction that can tag specific resonances !

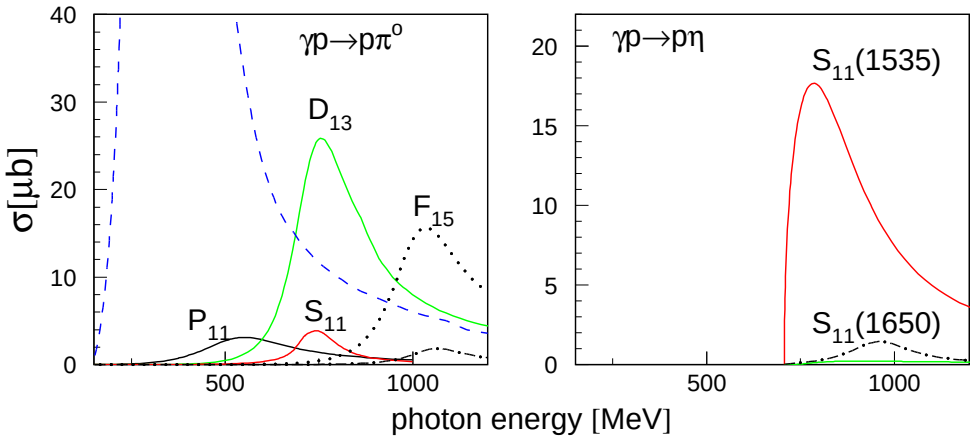

Figure 1.2: *Contribution of resonances to π^o and η photoproduction (not quantitative). Full curves labeled P_{11}, D_{13} and S_{11} correspond to the $P_{11}(1440)$, the $D_{13}(1520)$, and the $S_{11}(1535)$ resonances. The dashed curve corresponds to the Δ, the dash-dotted curves to the $S_{11}(1650)$, and the dotted curve to the $F_{15}(1680)$.*

A broad experimental program for the study of nucleon resonances was setup in 2001 and is still in progress in Bonn by the CB-ELSA/TAPS collaboration. During the measurement campaign different settings were used for the electron beam (2.6 GeV, 2.8 GeV, 3.2 GeV and 3.5 GeV electron beam of the ELSA accelerator) and different target types (liquid hydrogen, liquid deuterium and solid targets : C, Ca, Nb and Pb).

For the meson (s) photoproduction off the deuteron, a tagged photon beam has been produced by bremsstrahlung with two different settings: 2.6 GeV and 3.2 GeV electron beam of the ELSA accelerator. The target was a liquid deuterium target of 5 cm. An almost 4π detection system was used, centered around the target. It was composed of: Crystal Barrel (CB) and Travel Around Photon Spectrometer (TAPS) wall, and their respective Charge Particle Counters (CPC), the inner detector and the veto wall. The deuterium data was taken between January and August 2003.

1.1 Structure of this thesis

This thesis is divided into 7 parts :

- Chapter 1 : Theory and hadron models are introduced by explaining that the quarks and gluons constitute the elementary degrees of freedom of hadrons, yet in a nontrivial manner. This chapter also stresses that experimental measurements are necessarily to understand the effective degrees of freedom.
- Chapter 2 : The link between experimental measurements and theory is not direct, an additional step must be introduced to extract the properties of nucleon states. This chapter is a short overview of the different reaction models that extract these properties.
- Chapter 3 : This chapter is a classic description of all the different components of the setup.
- Chapter 4 : discusses the calibrations, which are fundamental to understand the detector signals.
- Chapter 5 : emphasizes the key points of the data selections.
- Chapter 6 : presentation of the results and discussion.
- Chapter 7 : concludes and presents an overview of the future experiments.

Quarks (spin 1/2; color = red (R), green (G), blue (B))						
Flavor	M	Flavor	M	Flavor	M	Q
u	0.003	c	1.3	t	175	2/3
d	0.006	s	0.1	b	4.3	-1/3

Leptons (spin = 1/2)						
Flavor	M	Flavor	M	Flavor	M	Q
e	0.000511	μ	0.106	τ	1.7771	-1
ν_e	$< 1 \times 10^{-8}$	ν_μ	< 0.0002	ν_τ	< 0.02	0

Table 1.1: Standard Model particles, charges Q and approximate masses M (in GeV). The particles which make up matter are called quarks and leptons.

1.2 The Standard Model of particle physics

A "Standard Model" (SM) is a theoretical framework built from observation that predicts and correlates new data. The Mendeleyev table of elements was an early example in chemistry; from the periodic table one could predict the properties of many hitherto unstudied elements and compounds.

A very brief description of the SM of particle physics is presented in this section. Only the important points for the nucleon resonance study are emphasized.

1.2.1 Fundamental particles and fields

For the SM, matter is composed of 12 fermions (quarks and leptons) along with their anti-particles and 5 vector bosons.

- fermions (spin $\frac{1}{2}$ particles)
  1) quarks: three doublets of quarks : (u, d), (c, s) and (t, b)
  2) leptons: three doublets of leptons: (e, ν_e), (μ, ν_μ) and (τ, ν_τ)

- bosons (spin 1 particles)
  Five force carrying gauge bosons : γ, $W^{\pm}$, Z^o and g (gluon)

These types of matter are considered structureless and treated as interacting fields appearing in Lagrangians that describe the dynamics of their interactions. Table 1.1 and Table 1.2 summarize the quantum numbers of these particles (fields). The known particles are excitations of these fields, in particular hadrons (baryons and mesons) have a finite size ($\sim 1\ fm$) and can not be considered elementary. Hadrons are composed of groups of fundamental particles, the quarks.

Bosons (spin 1)					
Force	Strong	Electromagnetic	Weak		
Carrier	g	γ	W^-	W^+	Z^o
M [GeV]	0	0	80.4	80.4	91.2
Q	0	0	-1	+1	0
Range [m]	10^{-15}	∞		10^{-18}	
Strength	α_S	α		α_W	
Gauge Group	$SU(3)$	$U(1)$		$SU(2)$	

Table 1.2: Fundamental interactions and their carriers (Gauge Bosons). The particles which carry the interaction are called bosons. The boson which carries the electromagnetic force is the photon (γ). The weak force is carried by $W^{\pm}$ and Z bosons, while the strong force is mediated by gluons (g). For each particle an anti-particle with the same mass and the opposite charge exists.

1.2.2 The Quark Model and Quantum Chromodynamics

In 1964, Gell-Mann [5] and Zweig [6] postulated the existence of the quarks. They proposed a quark model for the internal structure of the strongly interacting particles. In the quark model, the hadrons are described by combinations of quarks. There are two types of hadrons: mesons, which are made of quark-antiquark pairs ($q\bar{q}$), and baryons, which are made of three quarks (qqq). The quantum numbers of hadrons are obtained from their quark content, as shown in Table 1.1. The baryon number is conserved i.e. a single quark can neither be created nor destroyed. However, a $q\bar{q}$ pair (or meson) can be created or annihilated.

Apart from the electric charge, the quarks carry also a new kind of charge : the color charge (as shown in table 1.1, it will be described below). The ordinary matter observed in every day life is made of the lightest quarks (u and d), which form protons (uud) and neutrons (udd) in the atomic nucleus, and electrons, which orbit around the nucleus. Protons and neutrons are the most common baryons. Protons are stable particles, while neutrons live in average for 15 minutes before decaying, when they are not captured inside a nucleus. The u and d quarks are members of an isospin doublet, while the s quark is a singlet, as illustrated by 1.3. The isospin splitting of the hadron masses is due to the mass difference of the u and d quarks and the electromagnetic interactions between them [7, 8].

The discovery of strange particles [9, 10] extended the $SU(2)$ flavor symmetry to $SU(3)$ symmetry. The $SU(3)$ symmetry is not exact. The s quark is much heavier than both u and d quarks. In $SU(3)$, each quark flavor belongs to

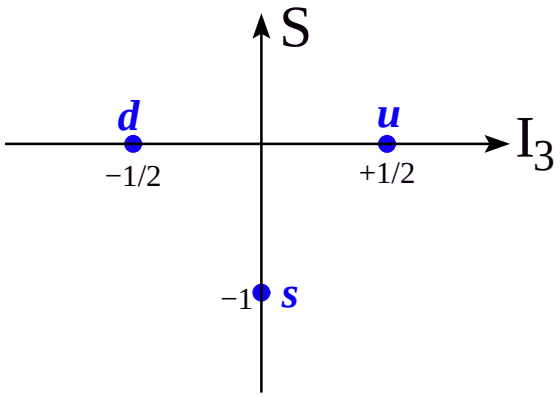

Figure 1.3: *The three quark flavors used in flavor $SU(3)$ to reproduce the hadrons in Figures 1.4 and 1.5. S is the strangeness. I_3 is the $z-$component of the isospin.*

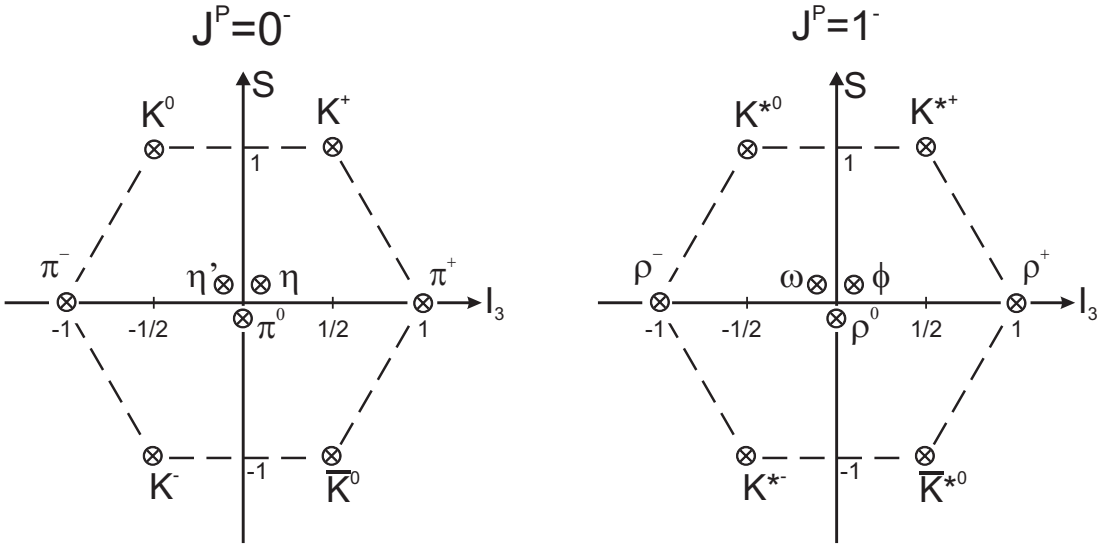

Figure 1.4: *The nonets of pseudoscalar (left) and vector mesons (right).*

the fundamental representations (3) and contains a triplet of quark fields. The antiquark field belongs to the complex conjugate representations (3^*) which also contains a triplet fields. Therefore $SU(3)$ classifies the hadron spectrum as follows :

- mesons, the nine states (nonet) of the $SU(3) \otimes SU(3)$ can be decomposed into two representations of light mesons ($q\bar{q}$) :
  $3 \otimes 3^* = 8 \oplus 1$

The flavor wave functions of the three pions and the octet and singlet

states of the η-meson are given by:

$$\begin{aligned}
|\pi^+\rangle &= |u\bar{d}\rangle \\
|\pi^-\rangle &= |d\bar{u}\rangle \\
|\pi^o\rangle &= \frac{1}{\sqrt{2}}|u\bar{u} - d\bar{d}\rangle \\
|\eta\rangle_8 &= \frac{1}{\sqrt{6}}|u\bar{u} + d\bar{d} - 2s\bar{s}\rangle \\
|\eta\rangle_1 &= \frac{1}{\sqrt{3}}|u\bar{u} + d\bar{d} + s\bar{s}\rangle \quad .
\end{aligned}$$

As $|\eta_1>$ and $|\eta_8>$ have the same quantum numbers, $|\eta_1>$ and $|\eta_8>$ can mix ($SU(3)$ breaking [11]) in order to form the physical η-mesons and $\eta^{'}-$mesons [12]:

$$\begin{aligned}
|\eta\rangle &= cos(\Theta)|\eta\rangle_8 \; - \; sin(\Theta)|\eta\rangle_1 \\
|\eta'\rangle &= sin(\Theta)|\eta\rangle_8 \; + \; cos(\Theta)|\eta\rangle_1
\end{aligned}$$

where Θ is the mixing angle. The mixing angle is not well known, but most estimates are in the range -23^o – -10^o [11]. This means that the η-meson is the dominant octet while the η' is the dominant singlet.

Table 1.3: *Properties of pseudoscalar mesons [13] . E_{thr} is the threshold energy for photoproduction from the proton.*

	I^G	J^{PC}	**mass [MeV]**	**E$_{thr}$ [MeV]**	**life time [s]**	**decays [%]**	
$\pi^{\pm}$	1^-	0^-	139.57	149.95	2.6×10^{-8}	$\mu^{\pm}\nu_{\mu}$	100.0
π^o	1^-	0^{-+}	134.98	144.69	8.4×10^{-17}	$\gamma\gamma$	98.8
						γe^+e^-	1.2
η	0^+	0^{-+}	547.45	707.2	5.5×10^{-19}	$\gamma\gamma$	38.8
						$\pi^o\pi^o\pi^o$	31.9
						$\pi^+\pi^-\pi^o$	23.6
						$\pi^+\pi^-\gamma$	4.9
η'	0^+	0^{-+}	957.8	1446.7	3.1×10^{-21}	$\pi^+\pi^-\eta$	43.7
						$\rho^o\gamma$	30.2
						$\pi^o\pi^o\eta$	20.8

The most important properties of the non strange members of the meson multiplet are summarized in table 1.3.

- baryons, the three quark states make up 27 combinations and therefore the $SU(3)$ decomposes into :
  $3 \otimes 3 \otimes 3 = 10 \oplus 8 \oplus 8 \oplus 1$
  For ground state baryons (l=0), combinations of the decomposition of both the $SU(3)$ flavor with the $SU(2)$ spin produces the ground states shown in Figure 1.5. The most common baryons, as already mentioned, are the isospin partners (of the $SU(2)$ isospin symmetry), the proton and the neutron : $p|uud>$ and $n|udd>$.

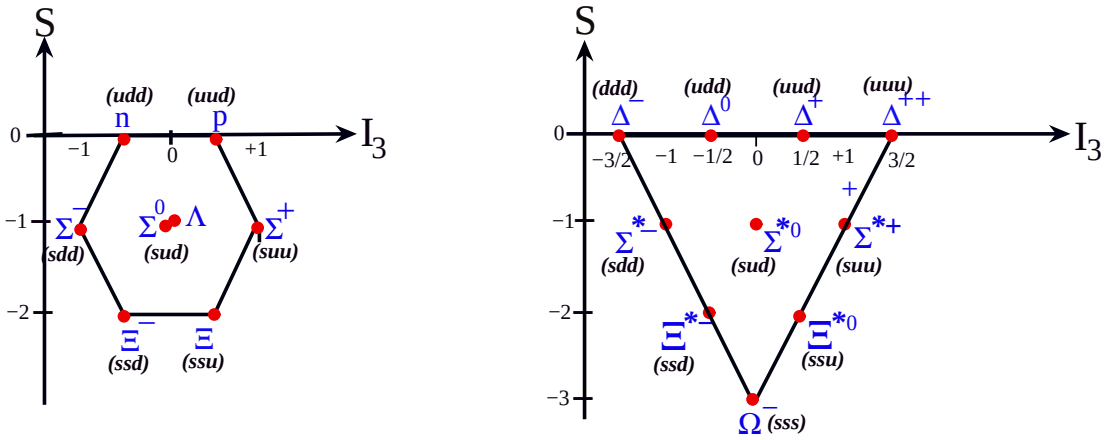

Figure 1.5: *Baryon ground states in the quark model. Left : the baryon octet ($J = 1/2$ baryons). Right : the baryon decouplet ($J = 3/2$ baryons).*

The three baryons, at the corners of the triangle of Figure 1.5, have three identical quarks each, which violates Pauli exclusion principle (only if $S = 3/2$ and $l = 0$). This problem was solved by assigning a new quantum number to the quarks : the color charge. The color charge represents the strong force's strength. The theory that describes the strong interaction of colored quarks and gluons is the Quantum Chromodynamics (QCD). The QCD is a non-Abelian gauge field theory based on the $SU_c(3)$ group, where the subscript c stands for color. The gluon couples to the color charge, and the coupling constant for strong interaction is denoted by α_S in analogy with the fine structure constant α of the electromagnetic interaction. The major difference between QCD and Quantum Electrodynamics (QED) arises from the non-Abelian nature of the former gauge group, $SU(3)$. This means that unlike electric charge, the color charge can take three possible directions in an abstract space, i.e. a quark's color can take three values: red, green and blue; and that of an anti-quark can take on three anti-colors: anti-red, anti-green and anti-blue. As the quarks come in three colors, they belong to the fundamental representation of the group $SU_c(3)$. The cancellation of the color charges of quarks ensures that strongly interacting particles (hadrons) composed of color singlet combi-

nations of quarks, antiquarks and gluons are colorless.

Thus, the colored quarks interact through exchanging gluons, which also carry color charge. The (3 colors $\otimes$ 3 anti-colors) combinations produce eight gluons which belong to the adjoint representation (8) of the color group.

$3 \otimes 3$ would be one octet of 8 and one singlet.

$$\begin{array}{lll} R\bar{R}, & R\bar{B}, & R\bar{G} \\ G\bar{G}, & G\bar{R}, & G\bar{B} \\ B\bar{B}, & B\bar{R}, & B\bar{G} \end{array}$$

Real gluons are orthogonal linear combinations of the above states, the state combination in the first column, $\frac{1}{\sqrt{3}}(R\bar{R} + G\bar{G} + B\bar{B})$, is colorless and does not contribute to the strong interaction. Thus gluons form an octet field.

The non-Abelian nature of the QCD results in an important feature of this theory : the gluon self-interaction which results in a constant force. That is, at large distances, the $q - q$ potential increases linearly with the distance, $V_S = \alpha_S r$. The quarks are confined within hadrons as it would need an infinite amount of energy to split them apart. On the other hand, the isotropic distribution of the electric lines of force results in a force decreasing like $1/r^2$, i.e. $V_E = \alpha/r$.

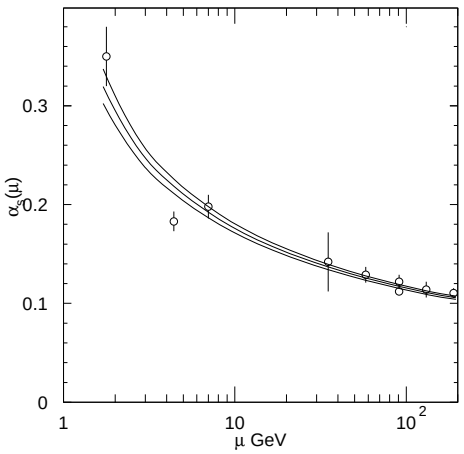

Figure 1.6: *Evolution of the effective coupling constant $\alpha_S = g^2/4\pi$ with the energy scale μ [14]*

It is impossible to solve QCD exactly because of the complexity of the phenomena described. As for QED, one can try to make a perturbative expansion of the theory in terms of the coupling constant α. Figure 1.6 which represents the evolution of the QCD coupling constant with the energy scale suggests that QCD has two distinct energy regimes. At high energy, where the coupling constant is small, leading to the asymptotic freedom, one can apply a perturbative approach and then explain the high energy behavior for the production and the interaction of hadrons. In the low energy regime, as is typical for baryon spectroscopy, such a perturbative method does not work. Some non-perturbative approaches have been developed to solve the problem. One can cite for example the computational approach of lattice QCD. However, its application to baryon spectroscopy needs an improvement of the calculation methods and of the capacity of computers. Another way to extend QCD to nucleons is to construct phenomenologic models inspired by QCD.

1.2.3 Particle interactions (Gauge Bosons)

For the SM, there are four basic forces among the elementary particles : the strong force, which affects only the hadrons, and the electromagnetic and weak forces as well as gravity. In the field theory, each force is governed by exchanging field particles (quanta) which are themselves elementary particles of integer spin (bosons). Apart from gravitation, which is too weak to affect their interaction, the other three are all gauge interactions. They are all mediated via spin 1 gauge bosons, whose interactions are completely specified by the corresponding gauge group.

- Electromagnetic interactions (EM):
  In electromagnetism the photon feels the electric charge but does not carry it. There is no photon self-interaction in this Abelian gauge theory.

- Weak interactions: For the electroweak interaction, the carriers are the three W bosons for the $SU(2)_L$ sector, universally coupled with strength α, and the neutral boson B^o for the $U(1)$ sector, with coupling α_W.

- Strong force : In chromodynamics on the other hand, the gluon feels the color charge and carries it. It is an octet tensor of color. This property of a non-Abelian gauge theory leads, in the case of chromodynamics, to confinement and asymptotic freedom.

1.2.4 Resonances

Combining the lightest three quarks produces a list of possible states corresponding to the ground state mesons and baryons. Each of these ground states can be excited into higher energy states, "resonances". These "resonances" decay strongly and therefore live for a very short period of time (10^{-24} s) so they cannot be observed directly. However they can be observed by the detection of their decay products.

There are two types of resonances :

- meson resonances : e.g. $\rho(775)$, $\omega(784)$, ...
- baryon resonances : N (nucleon resonance), Λ, Σ, ...

The nucleon resonances are divided into two families, namely : the I=1/2 N^* and the I=3/2 Δ resonances (see Figure 1.7).

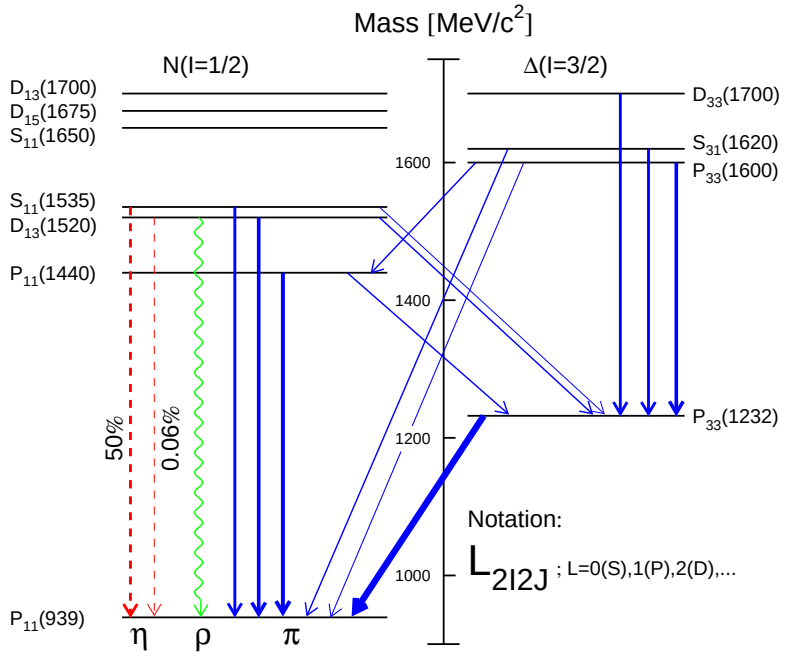

Figure 1.7: *The low lying excitation spectrum of the nucleon. The arrows indicate the observed transitions between the excited states. Only the most prominent transitions are shown.*

The nucleon resonances are labeled according to their decay mode into pion and nucleon: S_{11}, P_{11}, P_{13}, D_{13}, ... the letter gives the angular momentum value with respect to the pion-nucleon system. The letters, S, P, D, F correspond to $L = 0, 1, 2, 3, ...$ The first index gives $2 \times I$, I is the resonance isospin and the second index is $2 \times J$, J is the resonance spin.

Once the proton (neutron) is in an excited state, this excited state $N^*(\Delta)$ decays by strong interaction (Figure 1.7 according to rules specified in section 2.2.1) :

1. directly to the nucleon ground state by emitting a meson and a proton (neutron)

2. sequentially to a lower lying resonance (this resonance could be a N^* or Δ) which could again decay by emitting a meson and a proton (neutron) or going to a lower lying resonance

In the second resonance region, the branching ratios for the $\pi N-$channel is on the order on $50\ \%$ for all nucleon states. Only the $S_{11}(1535)$ has a branching ratio for ηN pretty large $\approx 50\ \%$. The $\eta-$ and $\eta^{'}-$ mesons work as isospin filter, due to isospin conservation : only N^* resonances contribute to $N\eta$ and $N\eta^{'}$ final states while resonances in $\Delta\eta$ and $\Delta\eta^{'}$ belong to the Δ^* series. Hence, the choice of Fig. 1.2 presented in the very beginning. Hence, the choice of looking for $\eta-$ and $\eta^{'}-$mesons. With these two mesons, a reduced numbers of resonances can be tagged as the resonances tagged are all N^*. The $\eta(\eta^{'})-$meson has isospin $I = 0$ and the nucleon at ground state (proton or neutron) has isospin $I = 1/2$, consequently, contributions from Δ^* resonances are excluded.

1.2.5 The missing resonances

The "missing resonances" problem is linked to the effective degrees of freedom. For example, in the quark model approach the effective degrees of freedom are constituent quarks. Various QCD-based models disagree about the nature of the short-range, tensor and spin-orbit interaction between quarks. There are now three competing models for the short-range interaction between light quarks in baryon:

- one-gluon exchange
- instanton-induced forces
- Goldston-boson exchange (recently supplemented by scalar- and vector-meson exchange)

With the present knowledge, all of these models can explain the data to some degree of accuracy. If our knowledge of the baryon spectrum could be improved by finding a few more excited states in selected partial waves, along with detailed decay properties, a much clearer picture of the quark-quark interactions in baryons would surface. In standard potential models such quarks are treated symmetrically, unlike those in quark-diquark and collective models. All symmetric quark models predict too many excited states relative to

what has been observed until now.

Diquark models predict fewer states by investing binding energy into a tightly bound isoscalar-scalar diquark which may push some positive-parity excitations higher in mass, leading to a deficit of positive-parity states at intermediate (1.7 - 2 GeV) energies.

QCD does not forbid the existence of colorless objects which have a quark configuration different from $q\bar{q}$ and qqq. These object are known as exotic hadrons (glue-balls, hybrid mesons) and strange hadrons ($q\bar{q}q\bar{q}$, $qqqq\bar{q}$ and ...).

1.3 Scope of the present experiment

Most of the data available comes from meson photoproduction off the proton, for the simple reason there are no free neutron targets. However, the study of neutron excited states is of some interest.

What are the expected differences between a proton resonance and a neutron resonance ?

- Intuitively, from quantum mechanical considerations
  the neutron / proton cross section ratio σ_n/σ_p should be equal to the sum squared of their electric charge contents :

$$\sigma_n/\sigma_p = \frac{Q_u^2 + Q_d^2 + Q_d^2}{Q_u^2 + Q_u^2 + Q_d^2} = \frac{4/9 + 1/9 + 1/9}{4/9 + 4/9 + 1/9} = 2/3 \tag{1.1}$$

  A 2/3 ratio would not necessarily mean that this hypothesis is correct. But any deviation from this hypothesis would mean a more complex internal structure of the nucleon.

- Isospin composition of the nucleon resonances : isospin conservation implies that the isospin must be conserved at the hadronic vertex. Thus for η ($\eta^{'}$) photoproduction only N^* resonances are allowed, while for pion photoproduction it is N^* or/and Δ resonances which are allowed. But, the electromagnetic interactions violate isospin conservation. Indeed, the production vertex involves the presence of isoscalar ($\Delta I = 0$) and isovector ($\Delta I = \pm 1$ for $I_3 = 0$ and $\Delta I = 0, \pm 1$ for $I_3 \neq 0$) components of the electromagnetic current. The $I = 1/2$ N^* nucleon resonances can take two isospin independent amplitudes : isoscalar and isovector, and the $I = 3/2$ Δ nucleon resonances involves a third amplitude : a second isovector amplitude. In the case of $\eta(\eta^{'})$ photoproduction for a given

excited state reached by a γ coupling to a neutron or a proton :

$$\sigma_p \sim |A^{IS}_{1/2} + A^{IV}_{1/2}|^2 = |A^{p}_{1/2}|^2 \tag{1.2}$$

$$\sigma_n \sim |A^{IS}_{1/2} - A^{IV}_{1/2}|^2 = |A^{n}_{1/2}|^2 \tag{1.3}$$

where $A^{IS}_{1/2}$ denotes the isoscalar and $A^{IV}_{1/2}$ the isovector part of the helicity amplitude. The sign difference comes from the $z-$component of the isospin $I_3 = 1/2$ for a proton $-1/2$ for a neutron.

From equations 1.1, 1.2 and 1.3 $A^{n}_{1/2} = \pm\sqrt{2/3}A^{p}_{1/2}$.

Figure 1.8 shows the total cross section for photoabsorption on the proton and on the neutron. The electromagnetic coupling could be very different for the proton and neutron. It is known from πN scattering studies [1], that some resonances couple very weakly to a proton, while they couple strongly to a neutron and vice-versa, i.e. most of the time $A^{n}_{1/2} \neq \pm\sqrt{2/3}A^{p}_{1/2}$!

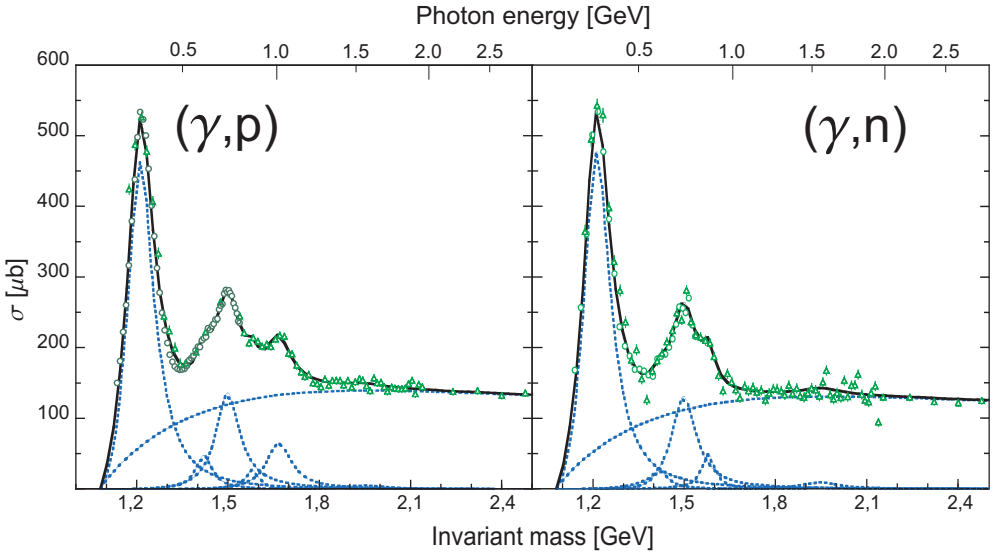

Figure 1.8: *Total photoabsorption cross section on the proton and on the neutron [15]. The non-resonant pionic background and different resonance contributions are shown (dashed lines). From left to right :* $P_{33}(1232)$, $P_{11}(1440)$, $D_{13}(1520)$, $S_{11}(1535)$, $F_{15}(1680)$ *(proton only) and* $F_{37}(1950)$.

1.3.1 The measurements

The non-existence of free neutron targets is solved by using a deuteron target. The difficulty with using deuterium as a target to learn about neutrons, however, is that the kinematics are "altered", when it is bound inside a deuterium nucleus, by Fermi motion and other nuclear effects.

The reaction of interest is

$$\gamma(k) + d(p_i) \rightarrow$$

where :
$k = (E_\gamma, \vec{k})$ is the four-momentum of the incoming photon γ,
$p_i = (E_d^i, \vec{p_d}^i)$ is the four-momentum of the nucleus d (deuterium),

The deuterium is composed of a proton and a neutron. The proton and the neutron are bound inside the nuclei. There are two possible production mechanisms (as the deuteron does not have excited states).

- Coherent production :

$$\gamma(k) + d(p_i) \rightarrow \quad m(q) + d(p_f) \tag{1.4}$$

- Quasi-free production :

$$\gamma(k) + d(p_i) \rightarrow \quad m(q) + N^{recoil}(p_f^1) + N^{spectator}(p_f^2) \tag{1.5}$$

where :
$q = (E_m, \vec{p_m})$ is the four-momentum of the meson (s) $m = (\pi^o\pi^o$ or η or $\eta^{'})$;
in the case of double π^o photoproduction $m(q) = m_1(q_1) + m_2(q_2)$,
$p_f = (E_d^f, \vec{p_d}^f)$ is the four-momentum of the recoil nucleus,
$p_f^1 = (E_{N_1}^f, \vec{p_{N_1}}^f)$ is the four-momentum of the recoil nucleon (proton or neutron),
$p_f^2 = (E_{N_2}^f, \vec{p_{N_2}}^f)$ is the four-momentum of the spectator nucleon (neutron or proton).

The coherent production leaves the nucleus intact. The nucleus remains in its ground state. The meson (s) four-momenta is (are) fixed for a four-momentum of an incoming photon. The coherent production mechanism is negligible for the three reactions of interest.

The quasi-free production is the dominant process. Contrary to the previous process the meson (s) is (are) produced off one of the target nucleons, the

Threshold	free proton [MeV]	free neutron [MeV]	coherent [MeV]
$E^{\pi^o\pi^o}_{\gamma,thres}$	308.59	308.53	289.18
$E^{\eta}_{\gamma,thres}$	706.92	706.7	627.05
$E^{\eta^{'}}_{\gamma,thres}$	1446.63	1445.95	1202.04

Table 1.4: The threshold energy for $\pi^o\pi^o$, η and $\eta^{'}$ photoproduction for a free nucleon target and for the deuterium target.

other nucleon does not participate in the reaction. The participating nucleon is knocked out of the nucleus due to the momentum transfer. Thus, in the final state, there are three (four) particles : the meson (s), the participant nucleon (or the recoil nucleon) and the spectator nucleon. Most of the time, the spectator nucleon does not have enough energy to leave the deuterium target. The Fermi motion of the nucleons inside the nucleus strongly influences the relation between the meson (s) four-momenta and the four-momenta of the incoming photon (see section 2.3.2).

The total center of momentum energy is $\sqrt{s}$ (for coherent and free productions):

$$\sqrt{s} = \sqrt{(k + p_i)^2} = \sqrt{2E_\gamma m_N + m_N^2} \tag{1.6}$$

where:
E_γ is the photon energy,
m_m is the mass of the meson (for η $m_\eta = 547.3$ MeV, for $\eta^{'}$ $m_{\eta'}$= 957.78 MeV),
m_N is the mass of the nucleus (for deuterium target $m_d = 1877.84$ MeV, for free proton target m_p= 938.27 MeV, for free neutron target m_n= 939.56 MeV).

The center of momentum energy has to be higher than the sum of the masses of the outgoing particles:

$$\sqrt{s} \geq m_m + m_N \tag{1.7}$$

After calculation, the threshold energy for meson photoproduction is:

$$E^m_{\gamma,thresh} = m_m + \frac{m_m^2}{2m_N} \tag{1.8}$$

The table 1.4 summarizes the threshold energy production for the free and the coherent productions.

The quasi-free production energy threshold is slightly higher than the coherent production energy threshold as one has to take into account the separation

energy of the participating (and knocked out) nucleon.

With a deuteron target four different measurements are possible : the meson (s) is (are) detected alone (inclusive measurement) or in coincidence with the recoil deuteron (exclusive coherent measurement) or in coincidence with the (participant) recoil nucleon (exclusive measurement).

$$\mathcal{M}^{inclusive} = \mathcal{M}^{deuteron} + \mathcal{M}^{proton} + \mathcal{M}^{neutron} \tag{1.9}$$

The exclusive coherent contribution is negligible ($\mathcal{M}^{deuteron} \ll 1$ for the three channels considered). So, the reaction on the neutron is measurable in two different ways :

1. directly : $\mathcal{M}_1^{neutron}$
2. indirectly : $\mathcal{M}_2^{neutron} = \mathcal{M}^{inclusive} - \mathcal{M}^{proton}$

where $\mathcal{M}$ is a measurable quantity, a differential cross section or a total cross section.

$\mathcal{M}^{proton}$ could be extracted from the free proton target as well, knowing the nuclear effects occurring in a light target nucleus or assuming approximations (e.g. impulse approximation).

1.3.2 The study of known resonances

Among the known resonances, as table 1.3.2 shows, not all of them are well explored, but even among well established resonances the very nature of some of these established resonances as an excited nucleon gives rise to questions , e.g. Roper $P_{11}(1440)$ [16, 17], $S_{11}(1535)$ [18] and more recently $P_{11}(1710)$ [19].

One of the primary interests of the study of meson photoproduction off the deuteron is that it is the only possibility to disentangle the isospin structure of the electromagnetic resonance excitations. The extraction of the isospin structure of the helicity amplitude is not straight forward. The extraction requires the knowledge of the relative phase between the proton and the neutron amplitude. To gain this knowledge the coherent meson (s) photoproduction off light nuclei should be studied in addition.

Octet	N		Σ	Λ	Ξ	
Decuplet		Δ	Σ		Ξ	Ω
Singlet				Λ		
****	11	7	6	9	2	1
***	3	3	4	5	4	1
**	6	6	8	1	2	2
*	2	6	8	3	3	0
No J	-	-	5	-	8	4
Total	22	22	26	18	11	4

Table 1.5: Status of baryon resonances according to The Particle Data Group. The number of stars reflects how well a resonance is known.

NB : the reaction models mentioned below will be shortly described in the next chapter.

$\pi^o\pi^o$ photoproduction off the deuteron

For the $N2\pi-$channels, there are three possible reactions on the proton and three on the neutron :

$$\begin{array}{llll} (a) & \gamma p \rightarrow \pi^+\pi^- p & (d) & \gamma n \rightarrow \pi^+\pi^- n \\ (b) & \gamma p \rightarrow \pi^+\pi^0 n & (e) & \gamma n \rightarrow \pi^-\pi^0 p \\ (c) & \gamma p \rightarrow \pi^0\pi^0 p & (f) & \gamma n \rightarrow \pi^0\pi^0 n \end{array} \tag{1.10}$$

All these reactions have been studied experimentally at different levels of sophistication from threshold up to $\sim$ 0.9 GeV. Only the reactions (a) and (c) have been extensively studied over a wide incident photon beam range (see Fig. 1.9).

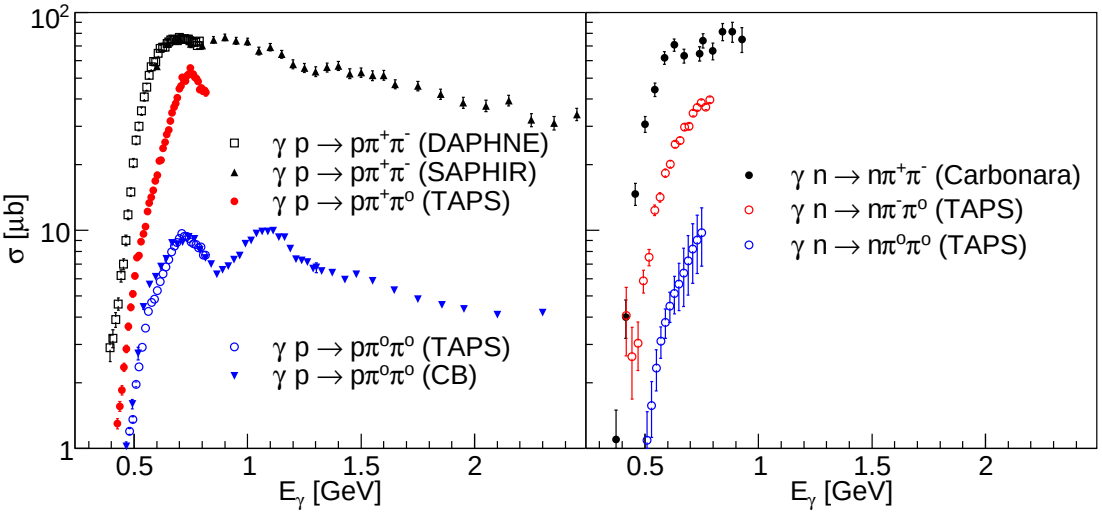

Figure 1.9: $2\pi-$*photoproduction cross section for different isospin channels :*
Left: of the proton. The data shown stems from different experiments, the $\gamma p \rightarrow p\pi^+\pi^--$*data from DAPHNE [20] and ABBHHM [21], the* $\gamma p \rightarrow n\pi^+\pi^o-$*data from TAPS [22] and the* $\gamma p \rightarrow p\pi^o\pi^o-$*data from TAPS [23] (empty circles at lower energies) and from CB-ELSA [24]. Right: of the neutron. The data shown stems from different experiments, the* $\gamma n \rightarrow n\pi^+\pi^--$*data from [25], the* $\gamma n \rightarrow p\pi^-\pi^o-$*data from [25] and the* $\gamma n \rightarrow n\pi^o\pi^o-$*data from TAPS [26]*

The photoproduction of two neutral pions off the nucleon is the best suited among the different $N2\pi-$channels to investigate the $\Delta\pi$ and $N^*\pi$ decays of baryon resonances (while channels which include charged pions are best suited to investigate $N\rho$ decay baryon resonances). The non-resonant terms (see section 2.1), which are important or dominant in charged pion channels, do not contribute to $N2\pi^o-$channels. Among the non-resonant terms, which contribute to the signal, Born terms and $t-$channel processes are strongly re-

duced.

Double π^o photoproduction from the proton has been studied in detail [24, 27, 28, 29, 23, 30]. Figure 1.10 shows the TAPS [23] and CB [24] data along with the $\pi\pi-$`MAID` [31] calculation that described the different contributions [31].

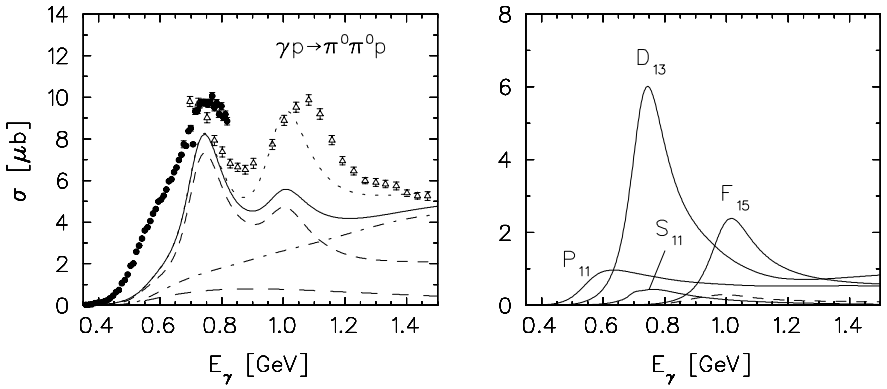

Figure 1.10: *An Effective Lagrangian Approach [31] is used to find the different contributions. Left : dash-dotted : contribution of $N\Delta$ $s-$ and $u-$channels (Figure 2.7 - diagrams (12)); long-dashed : contribution of the Z-graph (Figure 2.7 - diagram (17)); dotted : calculation with positive sign of the $F_{15}(1680) \rightarrow \pi\Delta$ as predicted [4]. Experimental data from Ref. [23] (circles) and Ref. [24] (empty triangles). Right : solid : contributions of $P_{11}(1440)$, $D_{13}(1520)$, $F_{15}(1680)$ and $S_{11}(1535)$; dotted : contribution of $D_{33}(1700)$; dashed : combined contribution of the $S_{31}(1620)$, $P_{13}(1720)$ and $D_{15}(1675)$.*

The two peak-like structures observed are not well understood. The Bonn-Gatchina model [32] interprets the two peak-like structures as the constructive and destructive interference between $D_{13}(1520)$ and $D_{33}(1700)$ resonances, while in the $\pi\pi-$`MAID` calculation (see Figure 1.10) the $D_{33}(1700)$ resonance contribution is not visible (for more details read Ref. [31] and Ref [32]). The study of the $n(\gamma, 2\pi^o)n$ reaction will certainly not solve alone this problem, but it will give additional constrains to the different models.

$\pi^o\pi^o$ photoproduction off the deuteron was already studied, by the TAPS collaboration in Mainz, from threshold up to 0.82 GeV in incident photon energy [26, 33]. The TAPS collaboration setup covered $\sim 40\%$ of the full solid angle, which has two consequences : holes in the acceptance and a strong background coming from single$-\eta$ photoproduction. Therefore they were only able to measure the inclusive Dalitz plots and total cross section, and deduced the neutron total cross section indirectly (as explained above).

However, they found that the data are in good agreement with model predic-

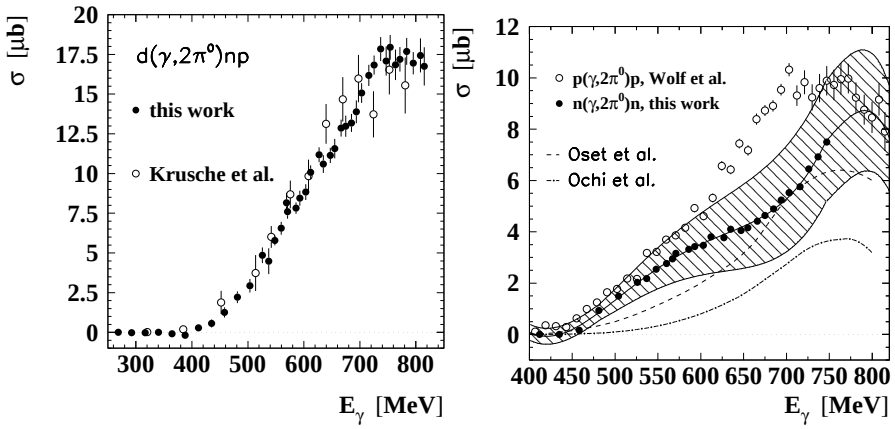

Figure 1.11: *Left : Cross section of double$-\pi^o$ photoproduction from the deuteron as a function of the incident photon energy. The filled circles symbolize the cross section obtained in [26]. The open circles represent the results of [33].*
Right : Cross section of the double $-\pi^o$ photoproduction from the free neutron as a function of the incident photon energy (black curve). The error band (hatched area) is obtained taking into account the statistical and systematic uncertainties of the cross-section from the deuteron and the proton uncertainties due to the analysis method. The open circles are the elementary cross-section from the proton [29]. Also shown are the predictions of the models Oset et al [34] (dashed line) and Ochi et al. [35] (dashed-dotted line).

tions of a dominant contribution of the sequential $N^* \rightarrow \pi^o\Delta \rightarrow \pi^o\pi^o N$ decays from the $D_{13}(1520)-$resonance [34]. It should be noted that the free proton data has been interpreted with the Laget model [36] and Valencia model [34], resulting in very different interpretations. In the Valencia-model which is limited to the low energy region, the $D_{13}(1520)$ decaying into $\Delta(1232)\pi$ dominates the lower energy peak, while in the Laget-model the $P_{11}(1440)$ decaying into σp is clearly the dominant contribution.

In this thesis, inclusive and exclusive differential and total cross sections and Dalitz plots were measured from threshold up to 2 GeV in incident photon beam.

$\eta-$meson photoproduction off the deuteron

The $\eta-$meson photoproduction off the hadron (and off the nuclei in general) is a good channel to test the validity of existing models. The resonant terms are dominant (the background terms are pretty low) and it involves less than 12 resonances below 2.5 GeV (in invariant mass) that create bump-like and dip-like structures.

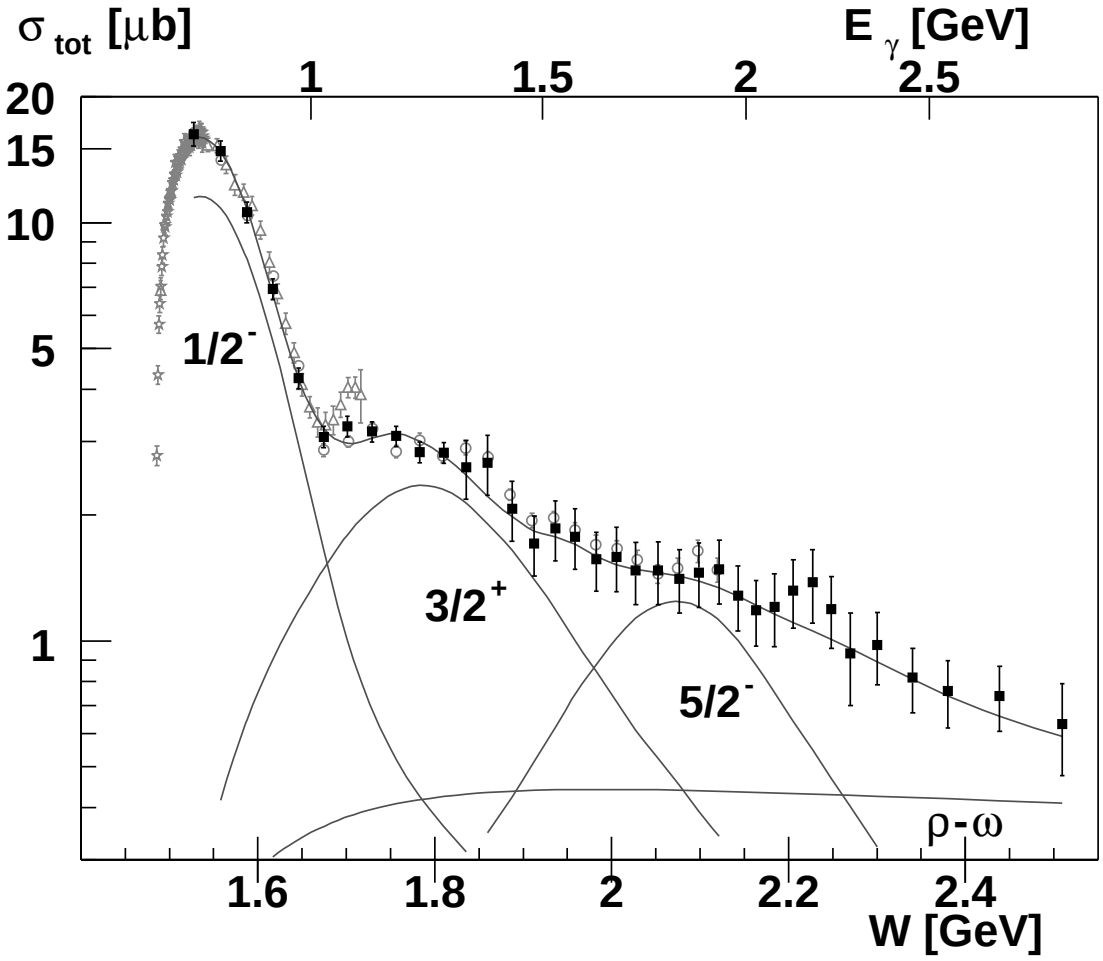

Figure 1.12: *Total cross section (logarithmic scale) for the reaction $\gamma p \to p\eta$; CB-ELSA (black squares) [37],TAPS [38],GRAAL [39] and CLAS [40] data (in light gray). the solid line represents the result of the* BnGa *calculation (for further details see [37]) and the contributions according to this calculation of the two S_{11} resonances, of the $P_{13}(1720)$, of the $D_{15}(2070)$ and the background amplitudes mainly $\rho - \omega$ exchange.*

Figure 1.12 shows the total cross section for the reaction $\gamma p \to p\eta$. From threshold up to 1.9 GeV in invariant mass, there are 2 clear structures : a "big bump" and a "small bump", which can be seen by following the Bonn-

Gatchina (BnGa) calculation [37]. The 2 structures correspond, in broad outline, to the contributions of the two S_{11}'s (for the "big bump") and a $P-$wave resonance (for the "small bump"), the $S_{11}(1535)-$resonance which is dominant and the second $S_{11}(1650)$ which interfers with the first $S_{11}(1535)$, but also with - the $P_{11}(1710)$ (according to the eta-MAID [41] and the Giessen [42] calculations) - or - the $P_{13}(1720)$ (according to BnGa calculation [37]). Therefore the different quantum numbers, sign and magnitude of the N^* decay parameters involved and interferences between the different resonances can explain the signal.

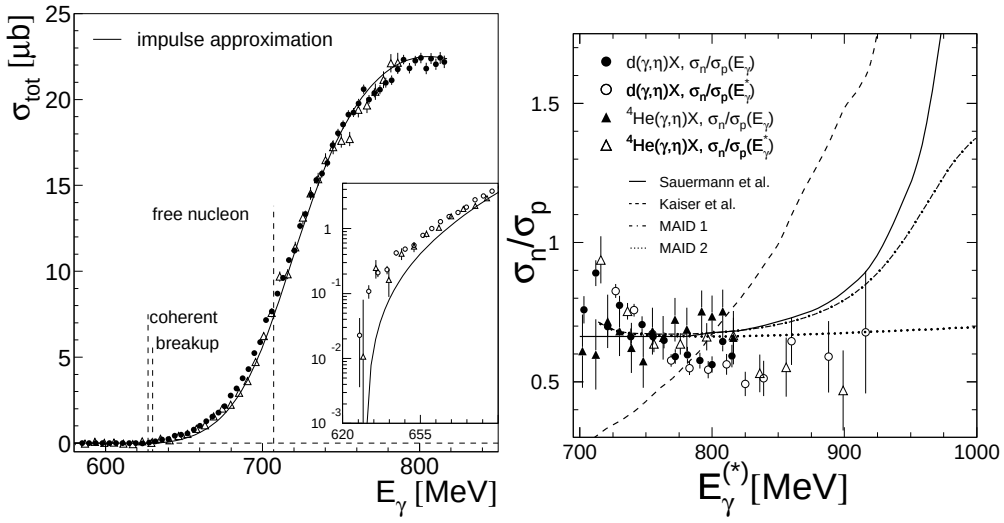

Figure 1.13: *Left : Inclusive η photoproduction from the deuteron. Circles : ref [43], triangles : ref [44]. The dashed lines indicate the coherent, the breakup and the free nucleon production thresholds. The solid curves are the result of the impulse approximation model under the assumption of a constant $\sigma_n/\sigma_p = 2/3$ ratio. Inserts : threshold region.*
Right : Ratio of exclusive neutron - proton cross sections for the deuteron and for ^4He [43, 44]. Dashed curve: prediction from the $K\Sigma$ model of the S_{11} (1535) (Kaiser et al. [18, 45]). The curves labeled eta-MAID *are the predictions from the* eta-MAID *model [41] for the full model (*eta-MAID 1*), the $S_{11}(1535)-$resonance, Born terms and vector meson exchange (*eta-MAID 2*), and for the $S_{11}(1535)$ alone (*eta-MAID 3*).*

Most models agree on the dominant role of the $S_{11}(1535)$ and on the interference between the first $S_{11}(1535)$ and the second $S_{11}(1650)$ which reduces the magnitude of the cross section as the interference between the two S_{11} is destructive. As already mentioned, the branching ratio $S_{11} \rightarrow \eta N$ decay mode is of ≈ 50 %, whereas the $S_{11}(1650) \rightarrow \eta N$ decay mode has a branching ratio of ≈ 5 %. This difference puts questions onto the nature of the resonance $S_{11}(1535)$ as baryonic resonance i.e. a three quark resonance [18]. In [18] Kaiser, Siegel and Weise proposed that the $S_{11}(1535)$ is a quasi-bound $K\Sigma$ state i.e. a

five quark state.

In this context, the TAPS collaboration measured the $\eta-$meson photoproduction off light nuclei (^2H, ^3He and ^4He) from threshold up to 820 MeV at different levels of sophistication (for more details see ref [43, 44, 46, 47, 48, 49, 50]). As previously mentioned, the TAPS collaboration experiment setup covered $\sim$ 40 % of the full solid angle. The TAPS collaboration were able to measure the inclusive angular distribution and the cross section, whereas the exclusive angular distribution and cross section could not be measured, due to holes in the acceptance. However, by assuming that in the $S_{11}(1535)$ energy region, the angular distribution is flat, the TAPS collaboration extracted the neutron - proton cross section ratio. The TAPS collaboration reported that at threshold the neutron - proton cross section ratio was constant and equal to $2/3$ for different light nuclei (^2H,^4He), Figure 1.13 illustrates it. A constant ratio implies that a resonance is dominating. The data clearly disfavors the interpretation of the resonance as a $K\Sigma$ bound state.

Different models predicted that the neutron - proton cross section should increase due to higher lying resonances., e.g. for the `eta-MAID` model, this sharp rise should be due mainly to the $D_{15}(1675)$. The resonance $D_{15}(1675)$ is known to strongly couple to the neutron.

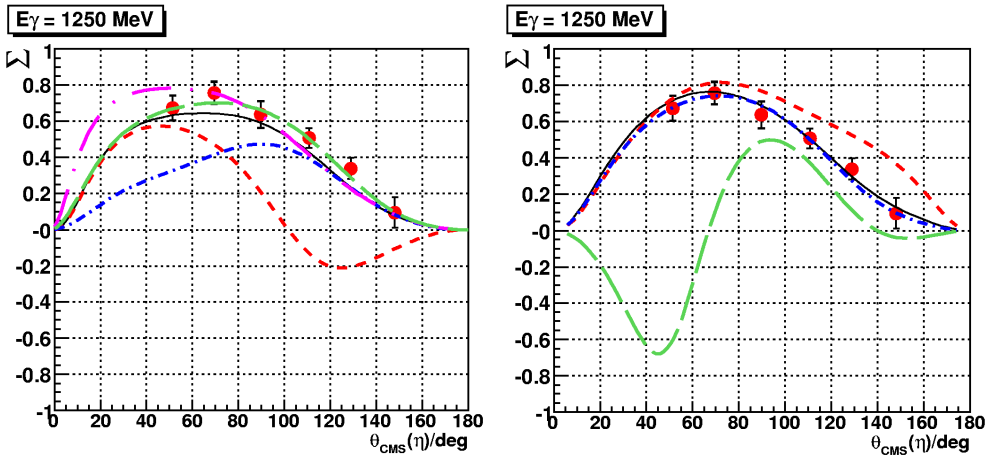

Figure 1.14: *Measured photon beam asymmetry* Σ.
Left the `eta-MAID` *result [41] is shown, right the* `BnGa` *analysis [52]. The full lines represent the respective full calculations. The broken curves illustrate the impact of "turning off" individual resonances: Long dashed without* $P_{13}(1720)$*, long dashed-dotted without* $P_{11}(1710)$ *(no difference to full calculation in* `BnGa` *analysis), short dashed without* $D_{13}(1520)$*, and short dashed-dotted without* $D_{15}(1675)$.

The second structure, the "small bump", noticed on Figure 1.12 at $\sim$ 1710 MeV mass location, is discussed in more details in ref [51]. Figure 1.14 [51] shows the measured photon beam asymmetry and the sensivity of the `eta-MAID` [41] and `BnGa` [37] calculations to different resonance contributions in the energy bin E_γ= (1250 $\pm$ 50) MeV.

In addition, the `BnGa` calculation [37] found a new resonance $D_{15}(2070)$ with (M, Γ) = (2068 $\pm$ 22,295 $\pm$ 40) MeV, but no evidence of a third S_{11}. Whereas a third S_{11} resonance is claimed at masses of 1780 MeV in [53] and 1846 MeV in [54]. These two resonances are predicted by the quark model and reported as "missing". According to [4] the $N\eta$ channel should have appreciable couplings to these two states.

In this thesis, inclusive and exclusive, angular distributions and total cross sections were measured from threshold up to 2.5 GeV in incident photon beam. These measurements give new informations on the resonances that contribute to the $\eta-$meson photoproduction.

$\eta^{'}-$meson photoproduction off the deuteron

The study of the $\eta^{'}-$meson photoproduction off the deuteron is the first study of this kind. Very little is known about the $\eta^{'}-$meson photoproduction mechanisms in general. Depending on the model the production mechanism is dominant due to either background terms or resonance terms. Furthermore, all resonances that could contribute to $\eta^{'}-$meson photoproduction are far from being well established.

Another interest in $\eta^{'}-$meson photoproduction is the possibility to impose a more stringent constraint on its poorly known coupling strength to the nucleon. This interest is related to the so-called "nucleon-spin crisis" in polarized deep inelastic lepton scattering [55]. The EMC collaboration [55] measured a surprising small value of the flavor-singlet axial charge $G_A \approx 0.20 \pm 0.35$. The $NN\eta^{'}$ coupling constant $g_{NN\eta'}$ is related to the quark contribution to the "spin" of the nucleon [56, 57, 58, 59, 60]. The flavor singlet Goldberger-Treiman relation in the zero squared momentum ($q^2 = 0$) limit (Eq. 1.11) links $g_{NN\eta'}$ and G_A:

$$\begin{array}{lcccc} 2m_N G_A(0) & = & F g_{NN\eta'}(0) & + & \frac{F^2}{2N_F} m^2_{\eta'} g_{NNG}(0) \\ & & \underset{\substack{quark\ contribution \\ to\ the\ \text{“}spin\text{”}\ of\ the\ nucleon}}{} & & \underset{gluon\ contribution}{} \end{array} \quad (1.11)$$

where F is a renormalization group invariant decay constant defined in Ref. [57],
N_F is the number of flavors,
m_N is the nucleon mass,
$m_{\eta'}$ is the $\eta^{'}$ mass and
g_{NNG} is the coupling of the nucleon to the gluons emanating from the contributions violating the Okubo-Zweig-Iuzuka (OZI) rule [61].

The OZI rule "roughly" requires some of the initial quark content of the decaying particle to survive in the decaying products. This rule is used to tag the meson flavor created in J/ψ decays when one of the two mesons has a known flavor content. This study was done for the $\eta-$ and $\eta^{'}-$mesons, their flavor structure and the pseudoscalar mixing angle were estimated (as discussed in section 1.2.2 [11]).

Once $g_{NN\eta'}$ for $q^2 = 0$ is known, g_{NNG} for $q^2 = 0$ can be extracted by using Eq. 1.11. But, the reaction models would only be able to extract $g_{NN\eta'}$ for $q^2 = m^2_{\eta'}$ i.e. at the on shell kinematic point. However, by assuming that the hadronic form factors for off shell mesons decreases for $q^2 < m^2$ (which is the normal

behavior), only an upper limit could be determined. Reaction processes where the $\eta^{'}-$meson is produced directly off a proton and off a neutron can offer a unique opportunity to approach this coupling constant.

In this thesis, inclusive and exclusive : angular distributions and total cross sections were measured from threshold up to 2.5 GeV in incident photn beam.

1.3.3 The exotic resonances

In addition to the as yet unidentified qqq states, confinement models using flux tubes predict the lightest qqq hybrid baryons with $P_{11}, P_{13}, P_{31}, P_{31}$ and F_{35} quantum numbers [62]. In addition there are states such as the Roper resonance which are hard to explain as pure qqq excitations, and so may be mixed with hybrid baryons. All hybrid baryons have conventional quantum numbers, so to find them, a surplus of states above those required by qqq potential models must be found. The predicted anomalous decay properties of this surplus of states must also be extracted. In fact, the same method was applied in case of the glueball and scalar-isoscalar mesons, where lower exotic quantum numbers may occur.

Thus to establish the existence of hybrid baryons all qqq states in the energy range between 1.7 and 2.2 GeV must be extracted.

1.3.4 The strange resonances

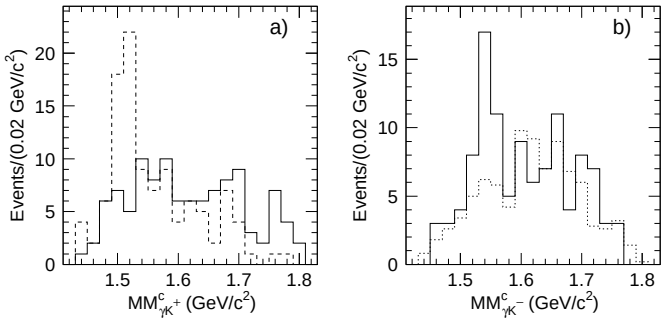

Figure 1.15: *The LEPS experiment, corrected missing mass distributions for K^+K^- production. a, $MM^c_{\gamma K^+}$ for data on H_2 (dashed) showing the $\Lambda(1520)$ and on Carbon with a detected proton (solid). b, $MM^c_{\gamma K^-}$ from H_2 (dashed) and on Carbon (solid). The latter peak is assigned to reaction $\gamma n \rightarrow \Theta^+ K^-$; $\Theta^+ \rightarrow nK^+$ [63].*

The controversial Θ^+ [63] (Fig. 1.15), a pentaquark state whose existence or non-existence is not yet established, sheds a new light on the reaction $\gamma n \rightarrow \eta n$. The Chiral Quark Soliton Model [64] (CQSM) predicted the mass and the small

width of the Θ^+ and identified the $S = 0$ baryons of the antidecuplet (Fig. 1.16) with the nucleon resonance $N^*(1710)$, with $N^* = P_{11}$. According to this model the $P_{11}(1710) \to \eta n$ decay mode should be strong while the $P_{11}(1710) \to \eta p$ decay mode should be small and this resonance should have a width below 20 MeV.

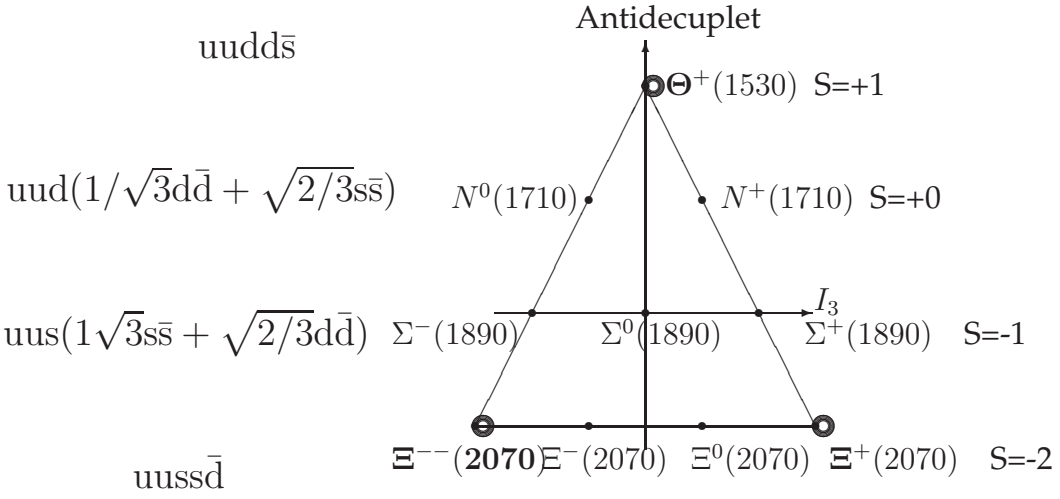

Figure 1.16: The antidecuplet and its quark model decomposition. The antidecuplet predicted by the chiral soliton model describes nucleons in terms of the pion field and not by the number of quarks [63]

The CQSM is an effective theory dominated by pseudoscalar mesons, the Goldstone modes of QCD. These allow topologically stable soliton solutions. In the CQSM, baryons are interpreted as different rotational states of the same physical object. The first two rotational states correspond to the octet and decuplet of the observed baryon mass spectrum (Fig.1.5). Using symmetry considerations it relates the characteristics of the members of the octet and the decuplet.

A great success of the CQSM is the Guadanini formula which relates the mass splitting inside the decuplet with that inside the octet,

$$8(m_{\Xi^+} + M_S) + 3m_\Sigma = 11m_\Lambda + 8m_{\Xi^+} \tag{1.12}$$

This formula is experimentally verified within $1\ \%$ accuracy. The $\Theta^+(1540)$ is the lightest member of the antidecuplet corresponding to the third rotational state of the CQSM. The members with an exotic quark configuration are only those on the corners of the antidecuplet. From symmetry considerations, the

value of the mass splitting in the antidecuplet can be obtained,

$$\Delta m = 180\ MeV \tag{1.13}$$

The absolute value of the mass depends on the moment of inertia of the rotating object and is model dependent. Therefore, Diakonov et al. fixed the mass by identifying one of the members of the multiplet with the $P_{11}(1710)$. The narrow width of the $\Theta^+(1540)$ and of $P_{11}(1710)$ comes from the cancellation of the coupling constant in the LO, NLO and NNLO of the perturbative expansion in the numbers of quark colors (N_C).

The GRAAL collaboration [65] was the first to show their result for the reaction $\gamma + n \rightarrow \eta + n$. The GRAAL collaboration measured the $M(\eta, n)$ spectrum i.e. the Fermi smearing is eliminated (for more details read section 6.3.7).

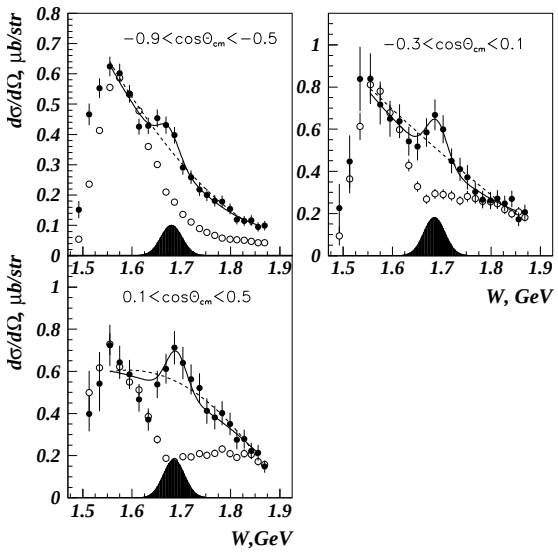

Figure 1.17: *$\gamma n \rightarrow \eta n$ cross sections (after the elimination of the Fermi smearing) for different $cos\theta_{cm}$ bin. θ_{cm} is the η $\theta-$angle in the center of mass. Polynomial-plus-narrow-state fit of $\gamma n \rightarrow \eta n$ cross sections. Black circles are $\gamma n \rightarrow \eta n$ data. Open circles correspond to $\gamma p \rightarrow \eta p$ cross section normalized on the cross section on the neutron in the maximum of the $S_{11}(1535)$ resonance. Dashed areas show simulated contribution of the narrow state. Solid lines are the result of the fit. Dashed lines show the fit by 3-order polynomial only.*

Figure 1.17 [65] shows a clear bump for the neutron cross section which is not seen for the proton cross section. This bump is at $\approx$ 1680 MeV mass location with an unusual narrow width $\approx$ 40 MeV, which is at the limit of the detector energy resolution. The resonance that creates this bump was presented as a possible candidate for the non-strange member of the anti-decuplet [66].

The LNS collaboration also reported a "bump-like" structure in the $\gamma n \rightarrow \eta n$ cross section in their preliminary analysis using the second method described in section 1.3.1.

The resonance region may include on the order of 100 resonances, but has only two distinct "bumps" above the first resonance region (fig. 1.8). The discovery of an additional "bump" to the first S_{11} in the reaction $\gamma n \rightarrow \eta n$ drives new attention to the $\eta-$meson channel. At least 3 new experiments are underway in GRAAL, Bonn and Mainz to study this channel.

In this thesis, inclusive and exclusive angular distributions and total cross sections were measured from threshold up to 2.5 GeV. The results shown, presented in this thesis are similar to those obtained by the GRAAL collaboration.

2 Reaction models

In the last chapter, we saw that studying the baryon spectrum provides one avenue to learn more about "strong" QCD since the location and properties of excited states reflects dynamics and the relevant degrees of freedom within hadrons. Ideally, one would like to study the nucleon resonance structure by analyzing the meson-baryon reaction data completely within QCD. This however is far from our reach. To make progress, the data analyses are being performed in two steps. First, reaction models (RM) or partial wave analyses (PWA) are developed to extract nucleon resonance parameters from the data. The next step is to develop interpretations of the extracted nucleon resonance parameters in terms of effective degrees of freedom. Figure 2.1 summarizes the multi-step processes analysis. This chapter is a very short qualitative overview

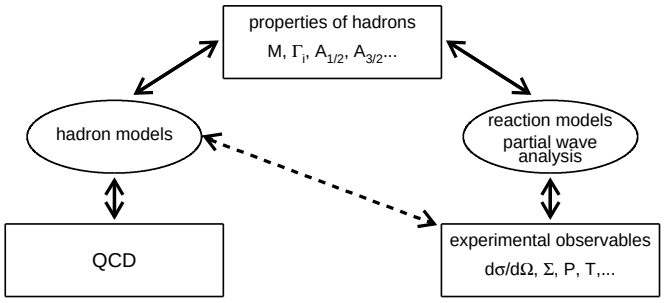

Figure 2.1: *Schematic representation of the relation between experimental observables, baryon properties, and QCD via reaction and hadron models.*

of the different models and partial wave analysis with which the data are compared.

2.1 The model descriptions

The most important processes that enter in the meson (s) photoproduction off the free nucleon are :

- the direct production (non-resonant terms or Born terms) in $u-$channel and $s-$channel (Fig. 2.2- (a) (b)),
- the vector meson exchange terms in $t-$channel, it corresponds to the exchange of a ρ, ω or ϕ vector meson (Fig. 2.2- (c)),
- the passage through a resonance (resonant terms) in $s-$channel (Fig. 2.2- (e)),
- meson (π, $\eta(\eta^{'})$ in our cases) rescattering (FSI),
- Primakoff effect : there is an exchange of a γ between the hadron vertex and the electromagnetic vertex. This effect is only present at high incident energy.

In order to understand the production mechanisms and determine which processes contribute to what and with which percentage, different approaches were developed by the theorists.

The first step is to draw the tree level diagrams, Figure 2.2, contributing to the meson (s) photoproduction from the nucleon.

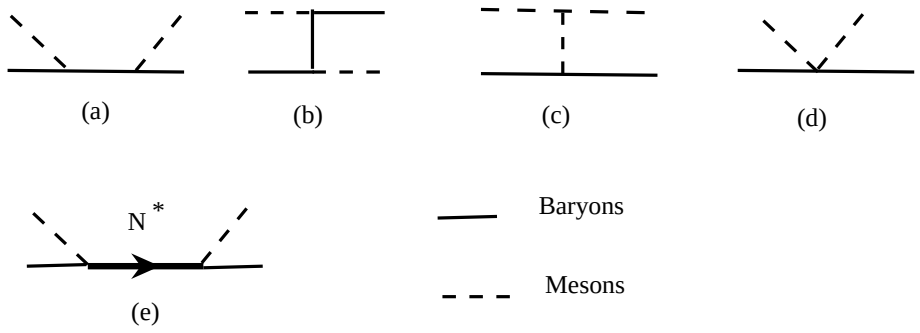

Figure 2.2: Tree-diagram mechanisms of meson-baryon interactions.
(a) and (b) non-resonant terms (Born terms) : $s-$channel and $u-$channel.
(c) vector meson exchange terms : $t-$channel
(d) non-resonant terms : $u-$channel.
(e) resonant terms : $s-$channel.

In Figure 2.2, to each vertex a coupling constant is associated which describes the interaction of particles at his vertices. Unfortunately, the coupling

constants can not be calculated.

To overcome this problem, the obersvables are adapt to the theoretical values by keeping the coupling constants as free parameters. By doing so the coupling constant are the values extracted. The extraction of the coupling constant for the different mechanisms involved in the meson (s) production requires a so-called "complete" experiment. However, with the existing data base, the coupling constants were determined with an accuracy of 10 $\%$.

The different approaches arise from the fact, that one could treat a specific reaction alone or in broad context by including different channels, which is the so-called coupled-channel approach; and could write for each vertex the effective Lagrangian, which is the so-called effective Lagrangian approach or apply other approaches in order to simplify the RM or the PWA. Depending of the approaches there will be more or less free parameters to calculate for RM or to fit for PWA.

2.1.1 General formalism

With the equations presented in this section, one can derive the models and PWA that are used to analyze the data.

The coupled-channel equation is the starting point for all the models discussed [67] :

$$T_{a,b}(E) = V_{a,b} + \sum_{c} V_{a,c} g_c(E) T_{c,b}(E)\,, \tag{2.1}$$

where :

a, b, c = γN, πN, ηN, ωN, KY, $\pi\Delta$, ρN σN, $\cdots$.
$V_{a,b}$ is the interaction term
$V_{a,b} =< a|V|b >$, with V a potential.

The potential V can be divided into two parts :

$$V = v^{bg} + v^{R}\,. \tag{2.2}$$

where :

v^{bg} are the non-resonant terms (i.e. the backgrounds).
v^R are the resonant terms (i.e. the nucleon resonances).

The resonant and non-resonant terms are :

The tree diagrams illustrated in Figure 2.2 summarizes the different terms. In most models, the resonant terms are included by the Breit-Wigner ansatz and can be written as :

$$v^R(E) = \sum_{N_i^*} \frac{\Gamma_i^\dagger \Gamma_i}{E - M_i^0}\,, \tag{2.3}$$

where :

Γ_i is the decay of the i-th nucleon resonances into meson-baryon states.
M_i^0 is the mass (resonance position).

In (2.1), $g_c(E)$ is the meson-baryon propagator :

$$g_c(E) = < c \mid g(E) \mid c >\,,$$

with

$$\begin{aligned} g(E) &= \frac{1}{E - H_0 + i\epsilon} \\ &= g^P(E) - i\pi\delta(E - H_0)\,, \end{aligned} \tag{2.4}$$

where :

H_0 is the free Hamiltonian
$g^P(E)$ can be written as :

$$g^P(E) = \frac{P}{E - H_0}\,. \tag{2.5}$$

P stands for the principal-value part of any integration over the propagator.

By replacing $g(E)$ by $g^P(E)$ and $T_{a,b}(E)$ by $K_{a,b}(E)$, (2.1) then defines the K-matrix which is linked to the T-matrix by

$$T_{a,b}(E) = K_{a,b}(E) - \sum_c T_{a,c}(E)[i\pi\delta(E - H_0)]_c K_{c,b}(E)\,. \tag{2.6}$$

By introducing the two potentials (2.2), one can write (2.1) into

$$T_{a,b}(E) \;=\; t^{bg}_{a,b}(E) + t^{R}_{a,b}(E) \tag{2.7}$$

with

$$+t^{R}_{a,b}(E) \;=\; \sum_{N^*_i, N^*_j} \bar{\Gamma}^{\dagger}_{N^*_i,a}(E)[G(E)]_{i,j}\bar{\Gamma}_{N^*_j,b}(E)\,. \tag{2.8}$$

$t^{bg}_{a,b}(E)$, in (2.7), is only a function of the non-resonant interaction

$$t^{bg}_{a,b}(E) = v^{bg}_{a,b} + \sum_{c} v^{bg}_{a,c} g_c(E) t^{bg}_{c,b}(E)\,. \tag{2.9}$$

$t^{R}_{a,b}(E)$, the resonant amplitude in (2.8), is determined by the dressed vertex

$$\bar{\Gamma}_{N^*,a}(E) \;=\; \Gamma_{N^*,a} + \sum_{b} \Gamma_{N^*,b} g_b(E) t^{bg}_{b,a}(E)\,, \tag{2.10}$$

and the dressed propagator

$$[G(E)^{-1}]_{i,j}(E) = (E - M^0_i)\delta_{i,j} - \Sigma_{i,j}(E)\,. \tag{2.11}$$

The mass-shift term can be written as :

$$\Sigma_{i,j}(E) = \sum_{a} \Gamma^{\dagger}_{N^*,a} g_a(E) \bar{\Gamma}_{N^*_j,a}(E)\,. \tag{2.12}$$

For the double pion production, the meson-baryon propagator $g_a(E)$ must be modified to include a width in order to take into account the sequential decay.

2.1.2 Unitary isobar approach

The Unitary Isobar approach (UIA) is used to analyze the $\eta-$ and $\eta^{'}-$meson photoproduction off the deuteron.

The UIA was developed [68] by the Mainz group, the so-called MAID calculations. MAID is not a model as in this approach partial wave analysis of the data are done. It is the most accessible approach available and it is making a good starting point for the discussion.

MAID is based on the on-shell relation (2.6). By including only one hadronic channel, ηN, (2.6) leads to :

$$T_{\eta N,\gamma N} = e^{i\delta_{\eta N}} cos\delta_{\eta N} K_{\eta N,\gamma N} \,, \tag{2.13}$$

where :

$\delta_{\eta N}$ is the η-nucleon scattering phase shift.

Assuming that $K \rightarrow V = v^{bg} + v^{R}$, (2.13) becomes :

$$T_{\eta N,\gamma N}(UIA) = e^{\delta_{\eta N}} cos\delta_{\eta N}[v^{bg}_{\eta N,\gamma N}] + \sum_{N^*_i} T^{N^*_i}_{\eta N,\gamma N}(E) \,. \tag{2.14}$$

v^{bg}, the non-resonant term in (2.14), is calculated from the standard Born terms but with an energy-dependent mixture of pseudo-vector (PV) and pseudo-scalar (PS) ηNN coupling. For the resonant term in (2.14), MAID uses the Breit-Wigner ansatz with the parameterization defined by Walker [69]

$$T^{N^*_i}_{\eta N,\gamma N}(E) = f^i_{\eta N}(E) \frac{\Gamma_{tot} M_i e^{i\Phi}}{M_i^2 - E^2 - iM_i\Gamma^{tot}} f^i_{\gamma N}(E) \bar{A}^i \,, \tag{2.15}$$

where :
$f^i_{\eta N}(E)$ and $f^i_{\gamma N}(E)$ are the form factors describing the decays of the nucleon resonances.
Γ^{tot} is the total decay width.
$\bar{A}^i$ is the $\gamma N \rightarrow N^*$ excitation strength.
Φ, the phase, is set by the unitarity condition and is determined by an assumption that relates the phase of the total photoproduction amplitude to the ηN scattering phase shift.

Since both η and $\eta^{'}$ have the same quantum numbers, one can expect that an extension of the UIA to the $\eta^{'}$ photoproduction should be straightforward. However, this is not the case. The reason for this problem turned out to be the much higher threshold for $\eta^{'}$ compared to η production. The UIA is intended for the resonance region at about W$\leq$ 2 GeV. Therefore, the UIA has to be modified as the energy increases.

It is well known that Regge theory is successful in describing various re-

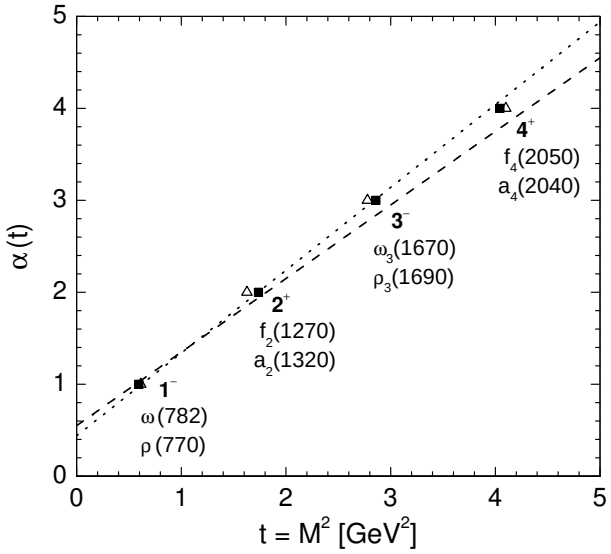

Figure 2.3: *Regge trajectories of the ρ and ω mesons shown by the dashed and dotted lines, respectively. Meson belonging to the $\bigtriangleup$ ω trajectories $\bullet$ and ρ trajectories.*

actions at high energy and low momentum transfer. In ref. [70], the Regge trajectories in the $t-$channel have been applied to pion and kaon photoproduction at high energies with success. The Regge trajectories take the form $\alpha(t) = \alpha_o + \alpha^{'} t$, where t is the Mandelstam variable, and shown in Fig 2.3 for ρ and ω trajectories.

The Reggeized approach [71] also developed by Mainz, is very similar to MAID. The main difference is that this model uses the Regge parameterization to define the amplitudes at high energies. The non-resonant amplitude is written as $[Background] = [e^{\delta_{\eta N}} cos\delta_{\eta N} v^{bg}]$ of (2.14) as

$$[Background] = [Born + \rho + \omega]_{UIA} \quad at \quad s < s_0 \tag{2.16}$$

$$= [Born + \rho + \omega]_{UIA} \frac{1}{1 + (s - s_0)^2} + [Regge - Poles] \frac{(s - s_0)^2}{1 + (s - s_0)^2} \quad at \ s > s_0 \tag{2.17}$$

where $s_0 \sim 1.2$ GeV was determined phenomenologically in fitting the pion photoproduction data.

2.1.3 K-matrix coupled-channel approach

The K-matrix coupled-channel approach is used to analyze the $\eta-$meson photoproduction off the deuteron.

The Giessen group works on a K-matrix coupled-channel approach [72, 73, 74, 75]. The K-matrix can be obtained from (2.6) by taking the approximation $K = V$. A matrix equation is deduced which involved only the on-shell matrix elements of V

$$T_{a,b}(E) \rightarrow \sum_c [(1 + iV(E))^{-1}]_{a,c} V_{c,b}(E) \,. \tag{2.18}$$

The interaction $V = v^{bg} + v^R$ is calculated from tree diagrams such as those illustrated in Figure 2.2.

2.1.4 Dynamical approach

The Dynamical approach is used to analyze all the three channels. The Bonn-Gatchina group [76] works on a Dynamical approach (DA). A meson-baryon reactions DA take into account the off-shell scattering dynamics by the integral equations employed, i.e. (2.1) or their equivalence (2.7)- (2.12). The off-shell dynamics are linked to the meson-baryon scattering wavefunctions in the short-range region where the nucleon resonance structures can be studied. The DA is a step forward into interpreting the extracted nucleon resonance parameters as the DA tries to take into account in a realistic way the interplay of various production channels, the interference among resonant and non-resonant parts of the scattering amplitudes. The Bonn-Gatchina DA varies from the exact formulation based on (2.1) or (2.7)- (2.12) by employing the Breit-Wigner Ansatz 2.15 to describe the resonant amplitude. The non-resonant amplitude definition is different from equation 2.9 : $t^{bg}_{c,b}$ on the right-hand side of equation 2.9 is replaced by the full amplitude $T_{c,b}$. The Bonn-Gatchina group also follows MAID to calculate the non-resonant interaction $v^{bg}_{\eta N,\gamma N}$ from an energy-dependent mixture of PS and PV Born terms.

2.2 The resonance identifications

The resonance identification is based on a choice of formalism. This formalism is defined by the number of independent variables on which depends the final state studied.

2.2.1 For two body decays

Consider the reaction :

$$\gamma(k) + N(p_i) \rightarrow \eta(q) + N^{'}(p_f) \tag{2.19}$$

where N (N=p or N=n) has spin $\frac{1}{2}$ and $\eta(\eta^{'})$, a pseudo-scaler meson, has spin 0. Figure 2.4 resumes the convention used.

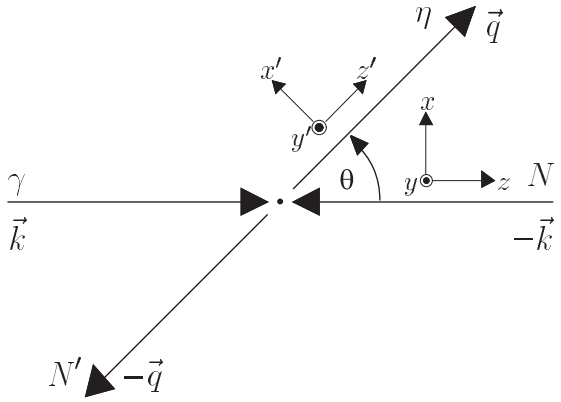

Figure 2.4: *Frames for polarization vectors in $\eta(\eta^{'})$ photoproduction in the c.m. system.*

The transition matrix between the initial state γN and the final state $\eta N^{'}(\eta^{'} N^{'})$ is :

$$< q m_{s'} | T | k m_s \lambda > \tag{2.20}$$

The photon has two polarization states $\lambda = \pm 1$. The nucleon N, at rest, has two spin states $m_s = \pm 1$. The recoil nucleon $N^{'}$ has also two spin states $m_{s'} = \pm 1$. This gives 8 elements to the matrix T. From the 8 elements, 4 stay independents after the conservation laws are applied. There are then 8 real numbers. Therefore the complete reaction requires the determination of 8 independent real quantities at every photon energy and for each meson emission angle. The question of the so-called "complete" experiment is widely discussed in literature (see e.g. [77, 78, 79, 80]). A complete experiment requires single and double polarization observables. There is also an extension of this idea to vector meson production which needs substantially more observables [81]. It is difficult however to obtain this "complete" set of measurements. Therefore different reaction models must be used. In reality it is possible to reduce the number of observables needed by applying basic considerations like analycity and unitarity of the amplitude; photoproduction close to threshold allows one to exploit the fact that only a few partial waves contribute, see e.g. [82].

In the center-of-mass system, the amplitude F of photoproduction of a pseudoscalar meson on a nucleon reads [83, 84, 85]

$$< qm_{s'}|T|km_s\lambda >= F = \sum_{1}^{4} if_k F_k \tag{2.21}$$

where f_k are the Chew-Goldberg-Low-Nambu (CGLN) -amplitudes [83]. Eq. 2.21 leads to :

$$F = iF_1 \cdot \vec{\sigma} \cdot \vec{\epsilon} + F_2 \vec{\sigma} \cdot \hat{q}(\hat{k} \times \vec{\epsilon}) + iF_3 \vec{\sigma} \cdot \hat{k}\hat{q} \cdot \vec{\epsilon} + iF_4 \vec{\sigma} \cdot \hat{q}\hat{q} \cdot \vec{\epsilon} \tag{2.22}$$

where $\vec{\sigma}$ are Pauli matrices, representing the nucleon spin operator; $\hat{k} = \vec{k}/k$ and $\hat{q} = \vec{q}/q$ with $\vec{k}$ and $\vec{q}$ being the photon and the meson (η or $\eta^{'}$) c.m. momenta, and the unit vector $\vec{\epsilon}$ determines the photon polarization. The four values F_i are functions of the total energy W and the meson c.m. angle θ_{cm}.

In the angular momentum representation, the F's are expressed in terms of electric $E_{l\pm}$ and magnetic $M_{l\pm}$ multipole amplitudes [83, 86]. l stands for the meson angular momentum,

$$\begin{aligned}
F_1 &= \sum_{l=0}^{\infty} [lM_{l+} + E_{l+}]P'_{l+1}(x) + [(l+1)M_{l-} + E_{l-}]P'_{l-1}(x) \\
F_2 &= \sum_{l=0}^{\infty} [(l+1)M_{l+} + lM_{l-}]P'_{l}(x) \\
F_3 &= \sum_{l=0}^{\infty} [E_{l+} - M_{l+}]P''_{l+1}(x) + [E_{l-} - M_{l-}]P''_{l-1}(x) \\
F_4 &= \sum_{l=0}^{\infty} [M_{l+} - E_{l+} - M_{l-} - E_{l-}]P''_{l-1}(x)
\end{aligned} \tag{2.23}$$

and $P_l(x) = P_l(cos\theta_{cm})$ are Legendre polynomials. The observables of process 2.19 can be expressed in terms of the amplitudes F_i as follows. Differential cross section:

$$\begin{aligned}
\frac{k}{q}\frac{d\sigma}{d\Omega} &= [|F_1|^2 + |F_2|^2 + \frac{1}{2}|F_3|^2 + \frac{1}{2}|F_4|^2 + Re(F_1F_3^\star)] \\
&+[Re(F_3F_4^\star) - 2Re(F_1F_2^\star)]cos(\theta_{cm}) \\
&-[\frac{1}{2}|F_3|^2 + \frac{1}{2}|F_4|^2 + Re(F_1F_4^\star) + Re(F_2F_3^\star)]cos^2(\theta_{cm}) \\
&-[Re(F_3F_4^\star)]cos^3(\theta_{cm})
\end{aligned} \tag{2.24}$$

Final state	Initial state	Amplitude
ηN	γN	$J_\gamma = L_\gamma$ Magnetic $J_\gamma = L_\gamma \pm 1$ Electric
$J = L_\eta + \frac{1}{2}$	$J_\gamma = J - \frac{1}{2} = L_\eta$	Magnetic $M_{L_p^+}$
$J = L_\eta + \frac{1}{2}$	$J_\gamma = J + \frac{1}{2} = L_\eta + 1$	Electric $E_{L_p^+}$
$J = L_\eta - \frac{1}{2}$	$J_\gamma = J - \frac{1}{2} = L_\eta - 1$	Electric $E_{L_p^-}$
$\Delta(J, L_\eta, \frac{1}{2})$	$\Delta(J, J_\gamma, \frac{1}{2})$ $\Delta(J, J_\gamma, 1)$	Parity $= -(-1)^{L_\eta}$ Parity $= -(-1)^{L_\eta}$

Table 2.1: States and quantum numbers for the η photoproduction.

The electromagnetic multipoles

In the eq. 2.19, we have $J^\pi = 0^-$ for an η and $\frac{1}{2}^+$ for the proton. The total angular momentum J for the ηp system can have two values $L_\eta + \frac{1}{2}$ and $L_\eta - \frac{1}{2}$. The ηp system parity is $(-1)^{L_\eta}\pi_\eta\pi_p = -(-1)^{L_\eta}$. The total angular momentum in the initial system γp is the addition of the proton spin $\frac{1}{2}$vector and of the γ angular momentum J_γ vector. The system parity γp is $-(-1)^{L_\gamma}$.
One has $J_\gamma = L_\gamma$ for magnetic multipoles of the order L and $J_\gamma = L_\gamma \pm 1$ for electric multipoles of the order L. Thus, when the ηp system angular momentum is $J = L_\eta + \frac{1}{2}$, we will have for the initial state system $J = J_\gamma + \frac{1}{2}$ or $J_\gamma - \frac{1}{2}$. According to table 2.1, it gives respectively:

- when $J_\gamma = J - \frac{1}{2} = L_\eta$, the conservation laws for the angular momentum and the parity are fulfilled for $J_\gamma = L_\gamma = L_\eta$. For this case, there is a magnetic multipole of the order $L = L_\eta$.

- when $J_\gamma = J + \frac{1}{2}$, $L_\gamma = L_\eta$, the conservation laws for the angular momentum and the parity are fulfilled for $J_\gamma = L_\gamma + 1$, $L_\gamma = L_\eta$. There is then an electric multipole of the order $L = L_\eta$.

The decay rules

Figure 2.5 sketches schematically the process 2.19 via the excitation of a N^* resonance. The photon with momentum L_γ and parity P_γ couples electromagnetically to the nucleon with $J_N^{P_N}$ to produce a resonance
with $P_{N^\star} = P_\gamma \cdot P_N$ and $|L_\gamma - J_N| \leq J_{N^\star} \leq L_\gamma + J_N$. The resonance subsequently decays by strong interaction to the nucleon ground state via emission of the meson where again $P_{N^\star} = P_\eta \cdot P_N = (-1)(-1)^{L_\eta} \cdot P_N$ and
$|L_\eta - J_N| \leq J_{N^\star} \leq L_\eta + J_N$ must hold due to momentum and parity conservation (as explained just before).

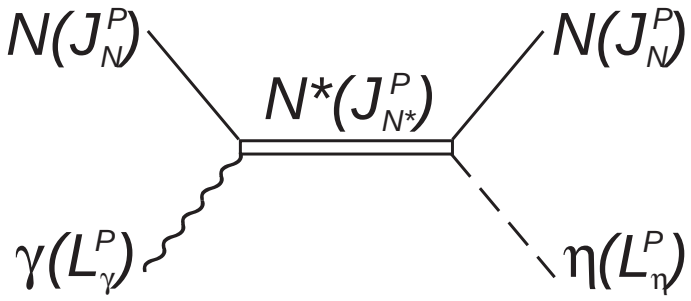

Figure 2.5: *Photoproduction of mesons via excitation of nucleon resonances.*

If the order multipoles $l = 0, 1, 2$ are inserted in equation 2.23 then the eq. 2.23 gives the well known form of the differential cross section:

$$\frac{k^\star}{q^\star}\frac{d\sigma}{d\Omega} = a \; + \; b\,cos(\theta_{cm}) \; + \; c\,cos^2(\theta_{cm}) \; + \; d\,cos^3(\theta_{cm}) \tag{2.25}$$

where the coefficients a, b, c and d are given in terms of the multipole amplitudes.

2.2.2 For three body decays

A three body decays, for a given incident photon beam, has :

$$\begin{aligned} 3\,particles \cdot 4 - vectors &= 12\,dof \\ -3\,identified\,masses &= 9\,dof \\ -\,energy\,and\,momentum\,conservations &= 5\,dof \end{aligned} \tag{2.26}$$

(dof = degrees-of-freedom)

Therefore the complete reaction requires the determination of 12 independent real quantities at every photon energy and for each meson (s) emission angle. As before, the number of obervables needed can be reduced, here to 5 independent real quantities by applying basic considerations like mass constrain and conservation laws.

Thus the multipole decomposition is not adapted here, since its application to reactions with three or more particles in the final states is not straight forward.

Usually a three body decays is studied via Dalitz plots which allows the resonances contributions. Two variables are needed to identify the kinematics of

a three-body decay. In the Daltiz plot, the axes of the plot are the squares of the invariant masses of two pairs of the decay products.

Consider the reaction :

$$\gamma(k) + N(p_i) \rightarrow \pi^o(q_1) + \pi^o(q_2) + N^{'}(p_f) \tag{2.27}$$

The Dalitz plot for this decay is : $m^2_{\pi^o\pi^o}$ on the x-axis and $m^2_{\pi^o N'}$ on the y-axis. If the decay is a true three-body decay, with the particle decaying directly into the 3 decay products, then the distribution of the Dalitz plot will be uniform. However, the double π^o photoproduction is dominated by resonant processes, in which the particle decays into two decay products, with one of those decay products immediately decaying into two additional decay products. In this case, the Dalitz plot will show a non-uniform distribution, with a peak around the mass of the resonant decay. In this way, the Dalitz plot provides an excellent tool for studying the dynamics of three-body decays.

2.3 Meson (s) photoproduction off the deuteron

2.3.1 "Nuclear effects"

The theoretical approaches are usually focused on the experimentally favorable case where the target is a proton, whereas the results on the neutron depend on model assumptions used for extracting the data from measurements with the deuteron target. The model assumptions concern the "nuclear effects", e.g., Fermi motion, final state interaction (FSI), and two-nucleon production contributions. This assumptions prevent a model independent study of the neutron amplitude. Whereas the Fermi motion is naturally included in the spectator - participant approach (or impulse approximation - see next section), the interaction between the final particles requires considerably more calculational efforts. However, it is considered that FSI and other higher order processes have negligible influence. In particular, the validity of the spectator - participant approach was shown in [26, 38] for the extraction of the $\gamma n \rightarrow \pi^o\pi^o n$ and $\gamma n \rightarrow \eta n$ cross section. This approach is validated for example by the observed missing mass spectra (for more details see the Chapter 6 - "The reaction identification").

2.3.2 Impulse approximation

The goal of this section is to describe the installation of the impulse ap-

proximation (IA), which was extensively used in this thesis. The MAID and the Giessen models provide us with calculations done for the free nucleon case. Therefore, we have total cross section $\sigma(E_\gamma)$ or a differential cross section $d\sigma/d\Omega(E_\gamma, \theta_{cm})$ where we have to fold in the Fermi motion. We did also fold the Fermi motion into the measurements done with a free proton target. And the impulse approximation is also used in the event generator of the Monte-Carlo simulation.

Let's take the case where we have the differential cross section $d\sigma/d\Omega(E_\gamma, \theta_{cm})$ for the $\eta-$meson photoproduction off the free proton in which we want to fold the Fermi motion. The IA is an approximation for studying the collision of an incident particle with a bound target particle by taking into account the momentum distributions of the bound particles. The momentum distribution or the Fermi motion distribution $\vec{p_f}$, can take the form of the Paris [87] or another wave function [88] or in the most simple approximation ignoring the high moementum tail as a normalized Gaussian distribution with proper σ. The form chosen, in this study, is a Paris wave function calculated for a deuteron nucleus as illustrates by Figure 2.6.

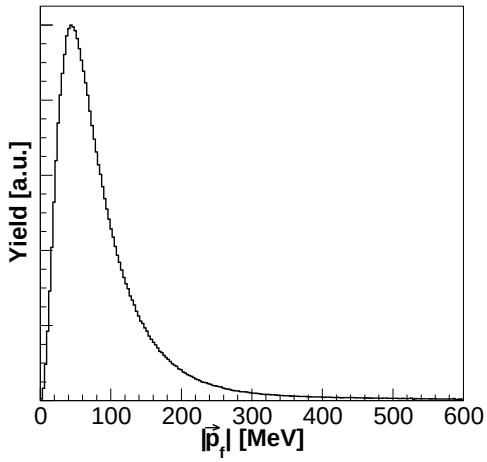

Figure 2.6: Fermi momentum $|\vec{p_f}|$ distribution generated from a Paris wave function calculated for a deuteron nuclei. The most probable momentum is $\sim$ 40 MeV.

In the spectator - participant approach a participant nucleon with momentum $\vec{p_f}$ corresponds to a spectator with $-\vec{p_f}$ which becomes on shell in the γd reaction. Then by following [89], the kinematical variables follow from the

momentum and the energy conservation :

$$E_{(S)} = \sqrt{m_{(S)}^2 + P_{(S)}^2} \quad (2.28)$$

$$E_{(P)} = m_d - \sqrt{m_{(S)}^2 + P_{(P)}^2} \quad (2.29)$$

$$s = t + 2E_\gamma(\sqrt{P_{(P)}^2 + t} - P_{(P)z}) \quad (2.30)$$

$$t = (m_d - m_{(S)})^2 - 2m_d(E_{(S)} - m_{(S)}) \quad (2.31)$$

where $E_{(S)}$ is the energy of the spectator nucleon,
$E_{(P)}$ is the energy of the participant nucleon,
s is the square of the effective mass of the final $\eta N-$system,
t is the square of the off-shell mass of the participant nucleon,
the indices (P) and (S) refer to participant and spectator nucleon, respectively;
and $P_{(P)} = \vec{p_f}$ and $P_{(S)} = -\vec{p_f}$.

The on-shell cross section measured in the experiment has to be linked to the off-shell cross section of the interacting particle, but the off-shell cross section depends on s and t [90]. Therefore the following approximations of the off-shell behavior is made [91] :

$$\frac{d\sigma}{d\Omega}(s(E_\gamma, P_{(P)}, t), t, \theta_{cm}^{exp.}) \approx \frac{d\sigma}{d\Omega}(s(E_\gamma, P_{(P)}, m_{(P)}^2), m_{(P)}^2, \theta_{cm}^{exp.}) \quad (2.32)$$

with $d\sigma/d\Omega(s(E_\gamma, P_{(P)}, t), t, \theta_{cm}^{exp.}) = 0$ for $\sqrt{s(E_\gamma, P_{(P)}, t)} < m_{(P)} + m_\eta$, where $\theta_{cm}^{exp.}$ is the "experimental" η angle in the "experimental" cm system. In this approach the differential cross section is evaluated at the on-shell $\sqrt{s}$ value and the "true" η angle in the reaction or "true" cm system (θ_{cm}). The θ_{cm}^{exp} is a measured quantity and is defined below.

The on-shell $s = s^{on}$ and the off-shell $s = s^{off}$ are :

$$s^{on} = (k + P_{(S)})^2 = 2E_\gamma(E_{(S)} - P_{(S)z}) + (E_{(S)})^2 - P_{(S)}^2 \quad (2.33)$$

$$s^{off} = (k + P_{(P)})^2 = 2E_\gamma(E_{(P)} - P_{(P)z}) + (E_{(P)})^2 - P_{(P)}^2 \quad (2.34)$$

with $k = (E_\gamma, 0, 0, E_\gamma)$ (the incident photon beam).

Then in the reaction or "true" cm system (the system corresponds to Figure 2.4), the η energy ($E_{\eta,cm}$) and momentum ($P_{\eta,cm}$) is:

$$E_{\eta,cm} = \frac{s_{off} - m^2_{(P)} + m^2_\eta}{2\sqrt{s_{off}}} \tag{2.35}$$

$$|P_{\eta,cm}| = \sqrt{E^2_{\eta,cm} - m^2_\eta} \tag{2.36}$$

$$P_{\eta,cm,x} = |P_{\eta,cm}| sin(\theta_{cm}) cos(\phi_{cm}) \tag{2.37}$$

$$P_{\eta,cm,y} = |P_{\eta,cm}| sin(\theta_{cm}) sin(\phi_{cm}) \tag{2.38}$$

$$P_{\eta,cm,z} = |P_{\eta,cm}| cos(\theta_{cm}) \tag{2.39}$$

where θ_{cm} corresponds to the "true" η angle in the reaction or "true" system.

To find the "experimental" η angle in the "experimental" cm system, we have first to calculate the η 4-vector in the laboratory system and then boost from the laboratory system to the "experimental" cm system the same η 4-vectors. But, it should not be forgotten that the N^*-system is different from the $\gamma N-$system as pictured in Figure 2.4 (in our case the system is $\gamma N_{(P)}$). Therefore, the Lorentz transformation must be done from the N^*-system to the laboratory system.

As the spectator is not at rest (in the "experimental" system the nucleon is at rest), the reaction cm system is "moving" as function of :

$$P_{cm,x} = p_{f,x} \tag{2.40}$$

$$P_{cm,y} = 0 \tag{2.41}$$

$$P_{cm,z} = p_{f,z} + E_\gamma \tag{2.42}$$

$$P_{cm} = \sqrt{P^2_{cm,x} + P^2_{cm,y} + P^2_{cm,z}} \tag{2.43}$$

$$\tag{2.44}$$

with $\vec{p_f} = (p_{f,x}, f_{f,y}, p_{f,z})$. $P_{cm,y}$ is set to 0 as the differential cross section is $\phi-$symmetric. Then, only the x-component and the z-component have to be changed:

$$P_{\eta,cm,N^*,x} = \frac{P_{cm,z}}{P_{cm}} \cdot P_{\eta,cm,x} + \frac{P_{cm,x}}{P_{cm}} \cdot P_{\eta,cm,z} \tag{2.45}$$

$$P_{\eta,cm,N^*,z} = -\frac{P_{cm,x}}{P_{cm}} \cdot P_{\eta,cm,x} + \frac{P_{cm,z}}{P_{cm}} \cdot P_{\eta,cm,z} \tag{2.46}$$

The participant (or recoil nucleon) has then the following energy ($E_{(P),cm}$)

and momentum ($P_{(P),cm}$)

$$
\begin{aligned}
E_{(P),cm} &= \frac{s_{off} + m_{(P)}^2 - m_\eta^2}{2\sqrt{s_{off}}} && (2.47)\\
P_{(P),cm,x} &= -P_{\eta,cm,N^*,x} && (2.48)\\
P_{(P),cm,y} &= -P_{\eta,cm,y} && (2.49)\\
P_{(P),cm,z} &= -P_{\eta,cm,N^*,z} && (2.50)
\end{aligned}
$$

Now, the η 4-vectors can be calculated in the laboratory frame, note that only the z-component needs to be transformed :

$$
\begin{aligned}
E_{\eta,lab.} &= \gamma_f(E_{\eta,cm} + \beta_{f,z} \cdot P_{\eta,cm,N^*,z}) && (2.51)\\
P_{\eta,lab.,x} &= P_{\eta,cm,N^*,x} && (2.52)\\
P_{\eta,lab.,y} &= P_{\eta,cm,y} && (2.53)\\
P_{\eta,lab.,z} &= \gamma_f(P_{\eta,cm,N^*,z} + \beta_{f,z} \cdot E_{\eta,cm}) && (2.54)
\end{aligned}
$$

with $\gamma_f = \frac{1}{\sqrt{1-(\vec{\beta_f})^2}}$ and $\vec{\beta}_f = (\frac{p_{f,x}}{E_\gamma + E_{(P)}}, 0, \frac{p_{f,z}+E_\gamma}{E_\gamma + E_{(P)}})$

And, finally be boosted into the "experimental" cm system along the z-axis only :

$$
\begin{aligned}
E_{\eta,cm}^{exp.} &= \gamma(E_{\eta,lab.} - \beta_z \cdot P_{\eta,lab.,z}) && (2.55)\\
|P_{\eta,cm}^{exp.}| &= \sqrt{(E_{\eta,cm}^{exp.})^2 - m_\eta^2} && (2.56)\\
P_{\eta,cm,z}^{exp.} &= \gamma(P_{\eta,lab.,z} - \beta_z \cdot E_{\eta,lab.}) && (2.57)\\
\theta_{cm}^{exp.} &= \frac{P_{\eta,cm,z}^{exp.}}{|P_{\eta,cm}^{exp.}|} && (2.58)
\end{aligned}
$$

with $\gamma = \frac{1}{\sqrt{1-(\vec{\beta})^2}}$ and $\vec{\beta} = (0, 0, \frac{E_\gamma}{E_\gamma + m_{(P)}})$

Thus, the differential cross section folded corresponds to $(E_\gamma, \theta_{cm}^{exp.})$ with a weight evaluating on $d\sigma/d\Omega(s^{on}, \theta_{cm})$.

2.3.3 $\pi^o\pi^o-$meson photoproduction off the deuteron

The theoretical models for double-pion photoproduction are based on the coupling of the photons and pions to nucleons and resonances using effective Lagrangians which yield a set of Feynman diagrams at the tree level. The general idea of these models are described in Figure 2.7 where the Feynman diagrams (1) to (17) are referred to as the Born terms or non-resonant terms and (18) to (20) to as resonance terms.

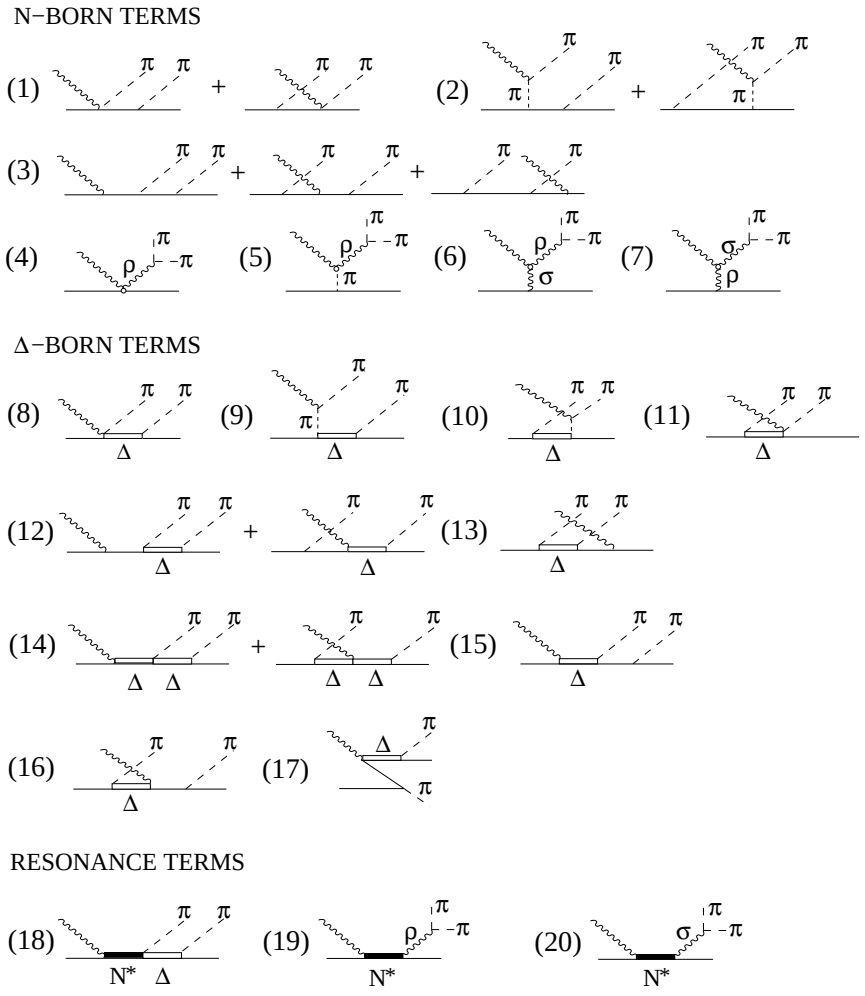

Figure 2.7: *Diagrams for the reaction $\gamma \rightarrow \pi\pi N$ used in the $\pi\pi-$`MAID` [31] calculation.*

For the charged channel, the contributions from the non-resonant term (especially contact term - Figure 2.7 diagram (1)) dominate the cross section. In the case of the neutral channel, however, since the photon cannot couple directly to the neutral pion in the t-channel, the contact term cannot contribute to the

cross section. When gauge invariance is applied, the contributions from the remaining non-resonant terms is significantly reduced. The reduction of these non-resonant background terms implies that the contribution to the cross section must then to a large extent be due to direct resonance production. This makes the neutral pion channel an ideal candidate for the investigation of nucleon resonances. For the two neutral pions channel most models assume a two step process, so that the three particle final state is reached by two successive two body reactions. The two particle subsystems are also decomposed into partial waves and in this way, estimates are made of the decay branching ratios of all N^* resonances into channels like $\Delta\pi$ and $N\rho$. Generally, information on the γN couplings of the N^* and Δ resonances are determined from others channels (e.g. single-pion photoproduction). With the two step process hypothesis and the information on the γN couplings, the models can estimate the contributions of various N^* and Δ resonances. Three models have done calculations for the reaction $\gamma + n \rightarrow \pi^o\pi^o + n$: the Valencia model [34], the Laget model [36] and the $\pi\pi-$`MAID` [31] calculation. All three models include a large numbers of diagrams as pictured in Figure 2.7, but disagree on the main features of the reaction.

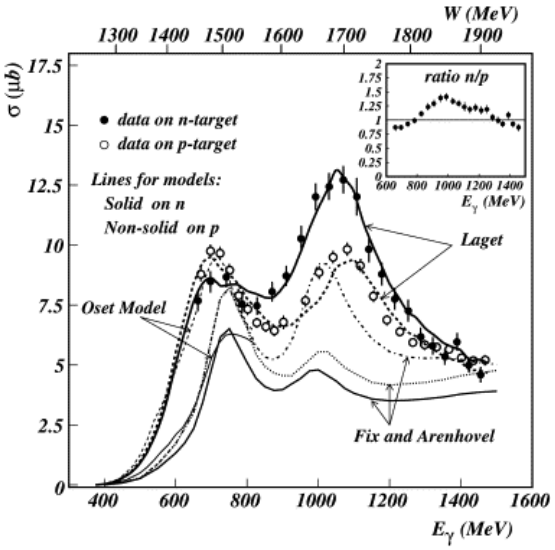

Figure 2.8: *Total cross section for double π^o photoproduction on the nucleon as function of the beam energy. In dots, are the GRAAL collaboration result [92] for $\gamma n \rightarrow n\pi^o\pi^o$ on "free neutron". In circles, the GRAAL collaboration result for the free proton [29]. The lines show the results models, the solid lines being on neutron and the non-solid ones on proton. The dotted and dashed lines of $\pi\pi-$`MAID` calculation are for positive and negative sign of $F_{15}\pi\Delta$ coupling respectively. In the insert, on the upper right side, the quasi-free neutron to quasi-free proton cross section ratio.*

Figure 2.8 shows the GRAAL result [92] for the $\gamma n \rightarrow n\pi^o\pi^o$ reaction compared to the $\gamma p \rightarrow p\pi^o\pi^o$ reaction and to the three models. For the Valencia model (as already mentioned), the dominant mechanism for the $p\pi^o\pi^o-$ and for the $n\pi^o\pi^o-$channels is $N^* \rightarrow \pi^o\Delta \rightarrow \pi^o\pi^o N$ for $E_\gamma < 0.8$ GeV. For the Laget model, which was fitted to the GRAAL data, the double-bump structure for the $p\pi^o\pi^o-$ and for the $n\pi^o\pi^o-$channel are due to the interference between the direct emission of the σ meson and the decay of the P_{11} (first bump - $P_{11}(1440)$ and second bump- $P_{11}(1710)$) resonances into the σN channel.

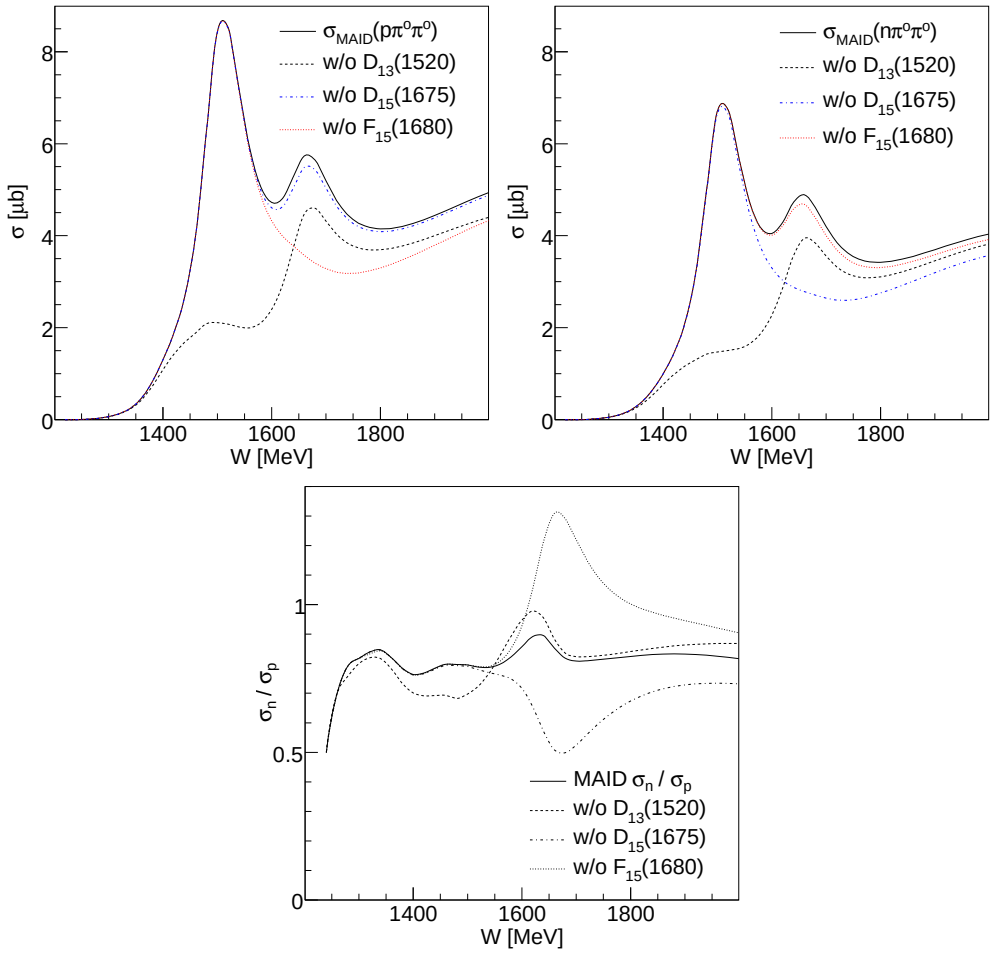

Figure 2.9: *$\pi\pi$-MAID calculation for the total cross section for the $\pi^o\pi^o$ photoproduction off the nucleon as function of the invariant mass. The $D_{13}(1520)$, $F_{15}(1680)$ and $D_{15}(1675)$ roles in $\pi\pi$-MAID calculation are underlined. Top left : for the reaction $\gamma p \rightarrow \pi^o\pi^o p$. Top right : for the reaction $\gamma n \rightarrow \pi^o\pi^o n$. Bottom : The neutron - proton cross section as function of the invariant mass.*

The $\pi\pi-$MAID calculation gives the same interpretation as the Valencia model

for the origin of the first bump. The second bump is due in this model for the $p\pi^o\pi^o-$channel to the $F_{15}(1680)$, whereas for the $n\pi^o\pi^o-$channel it is due to the $D_{15}(1675)$. Figure 2.9 shows the $\pi\pi$-MAID calculation for the total cross section (top-left for the proton and top-right for the neutron) and the neutron - proton cross section (bottom) as function of the invariant mass. The different roles of the $D_{13}(1520)$, $F_{15}(1680)$ and $D_{15}(1675)$ are underlined. The $D_{15}(1675)$ couples mainly to the neutron and the $F_{15}(1680)$ couples mainly to the proton. This can be seen when one looks at the helicity couplings $A_{1/2}$ and $A_{3/2}$ in Table 2.3.4. Both resonances are very close, so the total cross section seems "similar" in shape.

2.3.4 $\eta-$meson photoproduction off the deuteron

The data measured in this work will be compared to three different calculations : the eta-MAID calculation [41], the Giessen model [42] and the BnGa calculation [37]. The eta-MAID calculation was done before the data was taken, by using the measurement on the free proton target and the data taken on the deuteron by the TAPS collaboration (which covers incident photon beam energies from the coherent threshold production to 820 MeV).

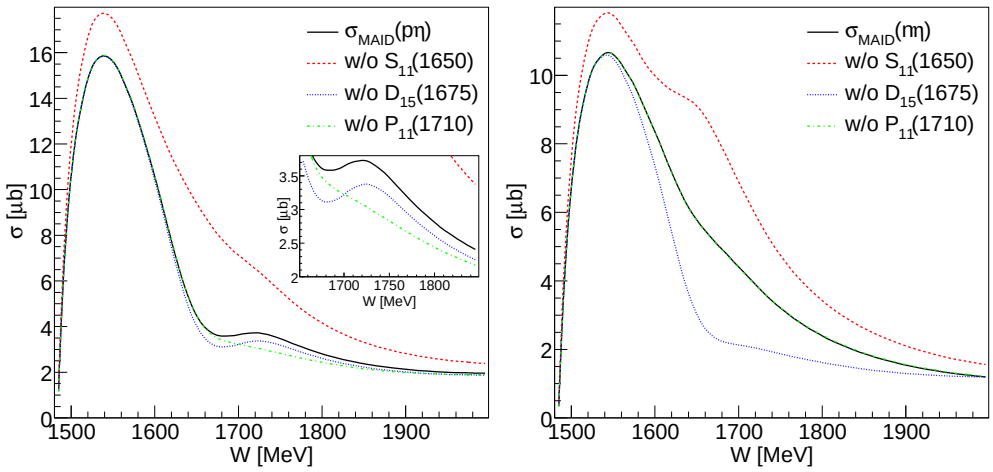

Figure 2.10: *eta-MAID calculation for the total cross section for the $\eta-$meson photoproduction off the free nucleon as function of the invariant mass. The $S_{11}(1650)$, $D_{15}(1675)$, $P_{11}(1710)$ roles in the eta-MAID calculation are underlined. Left : for the reaction $\gamma p \rightarrow \eta p$ in the insert the $P_{11}(1710)$ role is shown. Right : for the reaction $\gamma n \rightarrow \eta n$.*

The resonances used in the eta-MAID calculation are the same as the resonances used in the Giessen model (see Table 2.3.4). The differences between

the two calculations is that in the `eta-MAID` calculation certain resonances had fixed parameters while others were fitted. The `eta-MAID` calculation fitted the proton data and the $S_{11}(1535)$ energy region for the neutron. At higher energy, the calculations for the neutron are done by simply taking into account the neutron helicity couplings. Figure 2.10 shows the `eta-MAID` prediction of the total cross section for the proton (left) and for the neutron (right). The roles of the dominant resonances are underlined. In particular, the role of the second $S_{11}(1650)$ which interferes destructively with the first $S_{11}(1535)$. The $P_{11}(1710)$ plays an important role in the $p\eta-$channel, it creates a small bump around 1710 MeV mass location. For the $n\eta-$channel, the $P_{11}(1710)$ alone has no role, but the interference between the $P_{11}(1710)$ and the second S_{11} has an influence on the shape of the angular distribution. The $D_{15}(1675)$ has a dominant role in the $n\eta-$channel. It is the same resonance that creates in the $\pi\pi-$`MAID` calculation the second bump. In the $n\eta-$channel this resonance is enhancing the total cross section in such a way that the neutron - proton cross section ratio increased (see Figure 2.12-right).

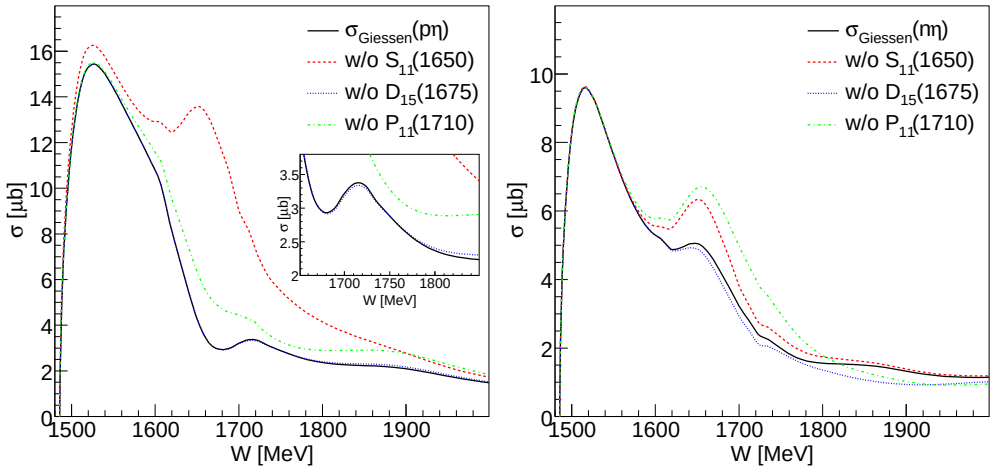

Figure 2.11: *Giessen model for the total cross section for the $\eta-$meson photoproduction off the free nucleon as function of the invariant mass. The $S_{11}(1650)$, $D_{15}(1675)$, $P_{11}(1710)$ roles in the Giessen model are underlined. Left : for the reaction $\gamma p \rightarrow \eta p$ in the insert the $P_{11}(1710)$ role is shown. Right : for the reaction $\gamma n \rightarrow \eta n$.*

The Giessen model studied the $\eta-$meson photoproduction off the free nucleon within an unitary coupled-channel effective Lagrangian approach. This model was developed for the simultaneous analysis of the pion- and photon-induced reactions up to 2 GeV. The different channels used in this model are : $\pi N \rightarrow \pi N, 2\pi N, \eta N, \omega N, K\Lambda, K\Sigma$ and $\gamma N \rightarrow \gamma N, \pi N, \eta N, \omega N, K\Lambda, K\Sigma$ reactions at energies from the threshold up to 2 GeV.

N^*	mass	Γ_{tot}	$\Gamma_{\pi N}$	$\Gamma_{\eta N}$	$A^p_{1/2}$	$A^n_{1/2}$	$A^p_{\frac{3}{2}}$	$A^n_{\frac{3}{2}}$
S_{11} (1535)	1526	136	34.4	$56.2[+]$	95	-74		—
	1526	136	34.4	$56.1[+]$	92	-13		—
	1535 (10)	150 (25)	45 (10)	53 (7)	90 (30)	-46 (27)		—
S_{11} (1650)	1664	133	71.9	$2.5[-]$	57	-9		—
	1664	131	72.4	$1.4[-]$	57	-25		—
	1655 (15)	165 (20)	72 (22)	6 (3)	53 (16)	-15 (21)		—
P_{11} (1440)	1517	608	56.0	—	-84	138		—
	1517	608	56.0	—	-84	138		—
	1440 (30)	325 (125)	65 (10)	—	-65 (4)	40 (10)		—
P_{11} (1710)	1723	397	1.7	$41.5[+]$	-50	24		—
	1723	408	1.7	$43.0[+]$	-50	68		—
	1710 (10)	150 (100)	15 (5)	6 (1)	9 (22)	-2 (14)		—
P_{13} (1720)	1700	152	17.1	0.1[+]	-65	3	35	-1
	1700	152	17.1	0.2[+]	-65	1	35	-4
	1725 (25)	225 (75)	15 (5)	4 (1)	18 (30)	1 (15)	-19 (20)	-29 (61)
P_{13} (1900)	1998	369	24.5	5.4[-]	-8	12	0	23
	1998	404	22.2	2.5[-]	-8	-19	0	6
	1900	NG	26 (6)	14 (5)	-17	-16	31	2
D_{13} (1520)	1505	100	56.5	1.2[+]	-15	-64	146	-136
	1505	100	56.6	1.2[+]	-13	-70	145	-141
	1520 (5)	112 (12)	60 (5)	0.2 (0.04)	-24 (9)	-59 (9)	166 (5)	-139 (11)
D_{13} (1950)	1934	855	10.5	0.1[-]	11	26	26	-55
	1934	859	10.5	0.5[-]	11	40	26	-33
	2080	NG	NG	4 (4)	-20 (8)	7 (13)	17 (11)	-53 (34)
D_{15} (1675)	1666	148	41.1	0.1[+]	9	-56	21	-84
	1666	148	41.1	0.3[+]	9	-56	21	-84
	1675 (5)	146 (16)	40 (5)	0 (1)	19 (8)	-43 (12)	15 (9)	-58 (13)
F_{15} (1680)	1676	115	68.3	0.0[+]	3	30	116	-48
	1676	115	68.3	0.0[+]	3	30	116	-48
	1685 (5)	130 (10)	68 (3)	0 (1)	-15 (6)	29 (10)	133 (12)	-33 (9)
F_{15} (2000)	1946	198	9.9	2.0[-]	11	9	25	-3
	1946	198	9.9	2.0[-]	11	9	25	-3
	2000	490 (130)	8 (5)	NG				

Table 2.2: Parameters of resonances considered in the Giessen calculations. First line: parameters obtained from [42]. Second line: parameters are taken from [93]. In square brackets the sign of the ηNN^* coupling relative to the πNN^* coupling is given. Third line: values from PDG; in brackets estimated errors are given. NG - no average value in PDG is given. Helicity amplitudes are given in units of $10^{-3}\ GeV^{-\frac{1}{2}}$.

The Giessen model and the eta-MAID calculation have similar results for the $p\eta-$channel i.e. the total cross section and the angular distribution can be explained by similar mechanisms. The total cross section of the $p\eta-$channel as function of the invariant mass is shown in Figure 2.11-left. The roles of the $S_{11}(1650)$, $D_{15}(1675)$ and $P_{11}(1710)$ are underlined. The only difference with the eta-MAID calculation is the cusp effect observed by the Giessen model : the bump structure seen in the S_{11} partial wave between 1.61 GeV and 1.72 GeV in W in Figure 2.11-left (red dashed line). These threshold effects are coming from the opening of $K\Lambda$ and ωN channels.

The Giessen model did use the preliminary $n\eta-$channel result of this work above W=1.6 GeV. Starting from their best solution to the pion- and photon-induced reactions they perform an additional fit varying only the helicity decay amplitudes and ηNN^*-couplings of the isospin-$1/2$ resonances keeping all other parameters fixed. The obtained parameters are shown in Table 2.3.4 in comparison with the results from[93]. Figure 2.11 (right) shows the neutron total cross section as function of the invariant mass given by the Giessen model. The $S_{11}(1650)$, $D_{15}(1675)$ and $P_{11}(1710)$ roles are underlined as well. In this model, the bump observed for the neutron is due to two effects : a destructive interference between the second $S_{11}(1650)$ and the $P_{11}(1710)$ resonances and the threshold effects coming from the opening of $K\Lambda$ and ωN channels. The Giessen model also shows that the amplitude of the bump can be changed by the value of the neutron helicity couplings of the $S_{11}(1650)$ and $P_{11}(1710)$ resonances.

The BnGa calculation did perform a fit for the final results of this work, therefore the results of this calculation will be discussed in the discussion of the results in section 6.3.7.

To compare the `eta-MAID` calculation and the Giessen model with the data, we did fold into their calculations the Fermi motion as explained in section 2.3.2. Figures 2.12 and 2.13 show the results.

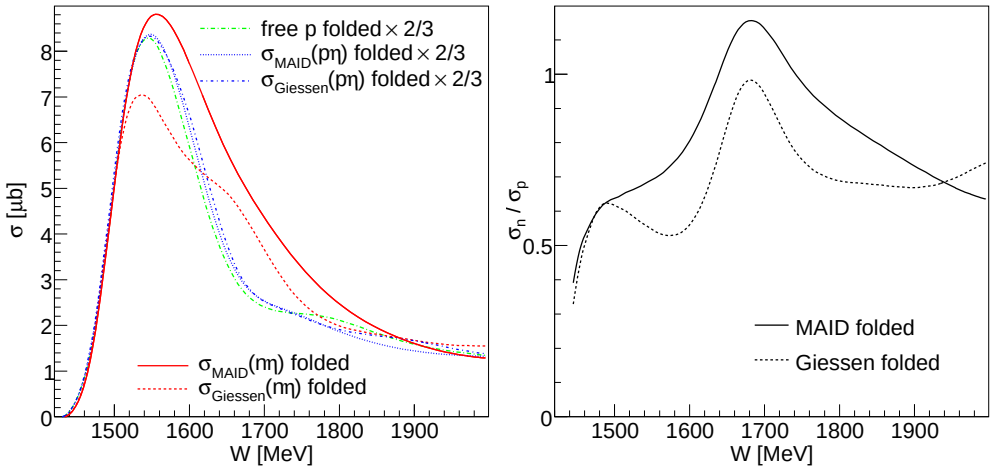

Figure 2.12: *Left : Quasi-free nucleon total cross section as function of the invariant mass for the* `eta-MAID` *calculation and the Giessen model. The quasi-free proton prediction has been downscaled by a factor 2/3 and is compared to the measured proton folded. Right : the neutron - proton cross section ratio as function of the invariant mass for two models.*

The structure for the neutron, which is not observed for the proton, does not disappear. Above 1.3 GeV incident photon beam energy, the t and u channel exchanges become more important in the data (see the green dashed-doted line in Figure 2.13), the `eta-MAID` calculation and the Giessen model have some difficulty to describe properly the proton data.

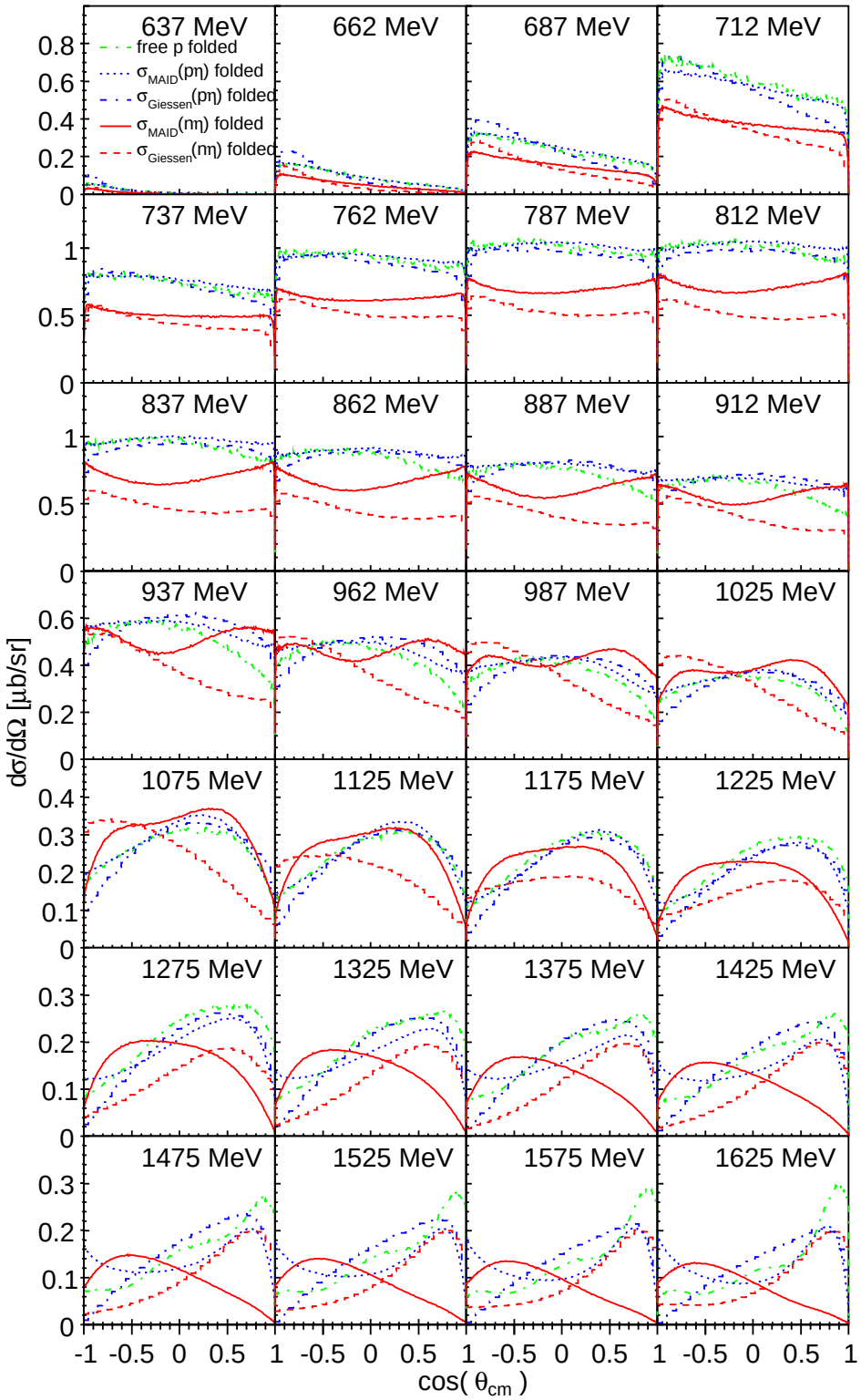

Figure 2.13: *Quasi-free nucleon angular distribution as function of the η angle in the cm system for different incident photon beam ranges for the* `eta-MAID` *calculation and the Giessen model. The quasi-free proton prediction can be compared to the measured angular distributions folded.*

2.3.5 $\eta^{'}-$meson photoproduction off the deuteron

There are no models available at the moment for the $n\eta^{'}-$channel mostly because until now there were no data. However, the $p\eta^{'}-$channel was extensively studied in the last 5 years. Unlike the $\eta-$meson photoproduction off the free proton with an almost constant differential cross section in the threshold region, the $\eta^{'}-$meson photoproduction off the free proton exhibits a sizeable $P-$wave contribution from threshold to the maximum energy. Figure 2.14 shows the most recent data published by the CLAS collaboration [94] for the free proton target.

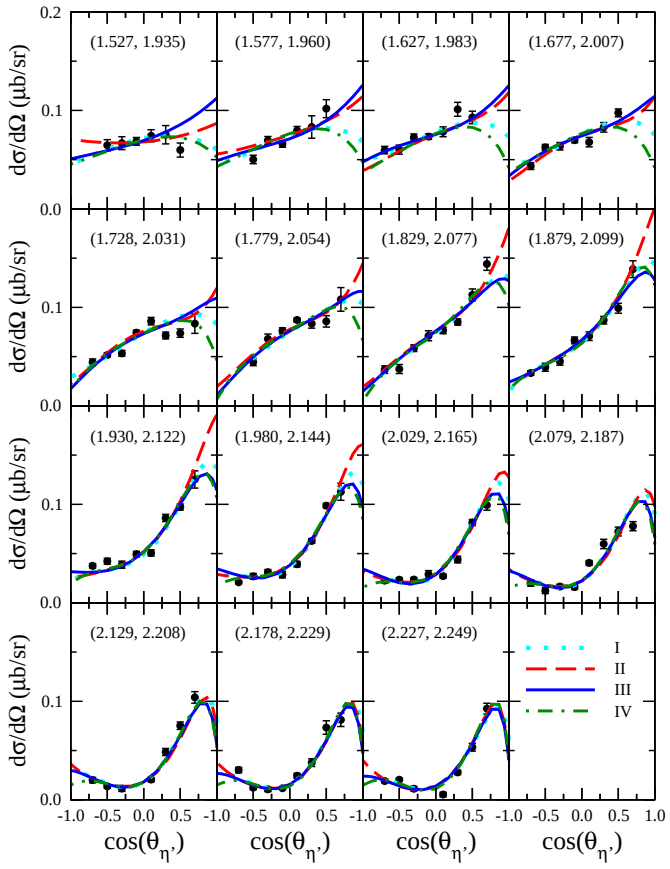

Figure 2.14: *Differential cross section for $\gamma p \rightarrow p\eta^{'}$ as function of the $\eta^{'}$ emission angle $\theta_{\eta'}$ in the cm system. The lines correspond to different fit made by the Athens-Washington model. The numbers (E_γ, W) in parentheses are the incident photon energy E_γ and the corresponding invariant mass in GeV.*

The CLAS data were fitted by the Athens-Washington model [95] which is

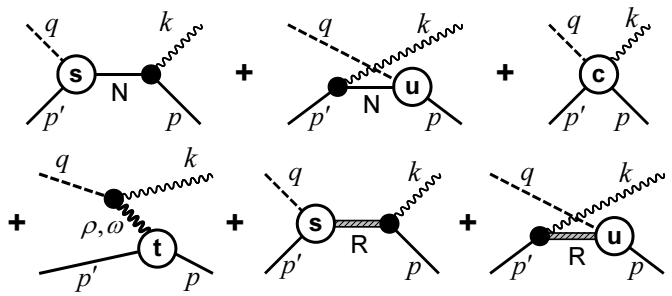

Figure 2.15: Diagrams contributing to $\gamma p \to \eta' p$. The intermediate baryon states are denoted N for the nucleon, and R for the nucleon resonances. The total current is made gauge-invariant by an appropriate choice of the contact current depicted in the top-right diagram. The nucleonic current (nuc) referred to in the text corresponds to the top line of diagrams; the mesonic current (mec) and resonance current contributions correspond, respectively, to the leftmost diagram and the two diagrams on the right of the bottom line of diagrams.

at the moment the most up-to-date model. The diagrams contributing to the $\gamma p \to \eta^{'} p$ are shown in Figure 2.15. This model chooses an approach based on a relativistic meson-exchange model of hadronic interactions.

The results of the Athens-Washington model [95] is that the mesonic as well as the spin$1/2$ and $3/2$ resonance currents play an important role and that the angular distributions are due to the interference between the different currents involved. No new resonances were found. However, the model predicts a bump in the total cross section at W $\approx$ 2.09 GeV (E_γ = 1.85 GeV) which should be due to the $D_{13}(2080)$ and/or $P_{11}(2100)$ resonances.

3 Setup

The experiment was conducted at the Elektronen-Stretcher-Anlage (ELSA) in Bonn, Nordrhein-Westfalen, Germany, which is operating since 1987. The setup can be divided in five parts:

- the accelerator which provides an e^-−beam of a fixed energy,

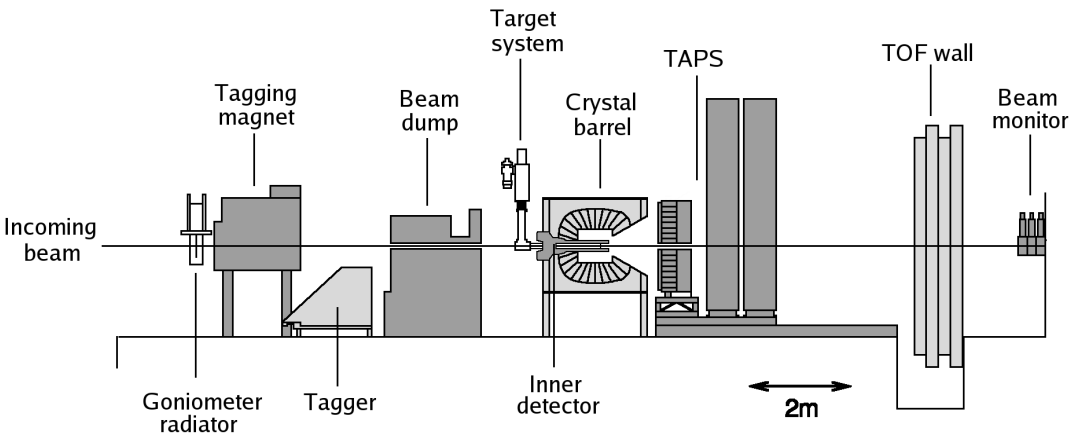

Figure 3.1: Layout of the beam line of the CBELSA / TAPS experiment.

- the tagged γ−beam, which is produced by Bremsstrahlung, and that hits the liquid deuterium target,

- the liquid deuterium target in which the hadronic reactions occurs,
- the detector system that detects the final products of the hadronic reactions and
- the $\gamma-$veto which is in the end of the beam line, that measured the photon numbers that hit the deuterium target.

Two others "components" are essential for the setup : the electronics and the trigger condition. Each detector of the setup has its own electronics for read-out of the measured values for each event. A trigger condition must be applied in order to filter the interesting events.

3.1 The accelerator

3.1.1 The description

The ELSA accelerator is an accelerator chain of different type (Figure 3.2) : a source, a LINAC, a synchrotron and a storage ring. The ELSA accelerator can provide electron beams up to 1 nA current and 3.5 GeV.

3.1.2 The e^--beam

The electrons are accelerated in four different stages. First the electrons are produced in an ionic generator namely the electron gun from energies varying between an eV and keV. Then the electrons are injected into the second stage, the LINAC 1 (in this experiment) where they are accelerated up to 20 MeV. Then, the electrons are injected into the third stage, the booster synchrotron, where they are accelerated up to 1.2 GeV. And finally the electrons are injected into the ELSA stretcher ring.

Different operating modes exist for the ring. For the measurement, the electrons were accelerated up to 2.6 GeV for two beam times and up to 3.2 GeV for two other beam times. It took 2 s to rich 1 nA current (the maximum current). The stored electron extraction took 8 s. A feedback loop was built in order to have a constant beam intensity by monitoring the count rate at the experiment and by controlling the extraction. A fully detailed description of the accelerator is given in [96].

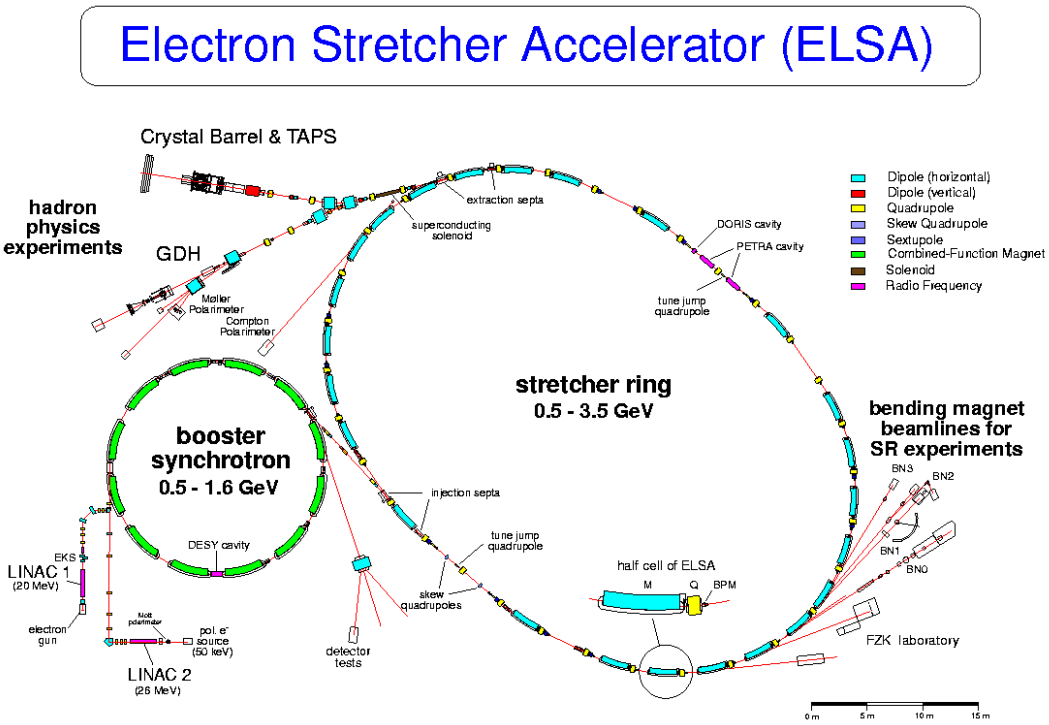

Figure 3.2: Layout of the ELSA electron accelerator.

3.2 The $\gamma-$beam

The photon beam is made by directing the electron beam on a copper foil (called radiator), where it produces photons by the bremsstrahlung process.

3.2.1 The Bremsstrahlung

In first approximation, the energy spectrum of the emitted photons is given by ([97]) :

$$\Phi \sim \frac{1}{E_\gamma} \tag{3.1}$$

The emitted photon and the half-angle of the incoming electron (in rad) can be written for relativistic energies by ([98],[99]) :

$$< \theta^2 >^{\frac{1}{2}} = \frac{1}{\gamma} = \frac{m_e c^2}{E} \tag{3.2}$$

According to the formula (3.2), a 1 GeV photon has a 0.5 mrad half-angle, which means the photon is emitted in a very narrow cone along the incoming

electron beam direction.

In this experiment unpolarized bremsstrahlung was used for one beam time, but for the three other beam times, linearly polarized bremsstrahlung was used. Linearly polarized bremsstrahlung photon is obtained by using a crystalline radiator (i.e. a synthetic diamond for more details read [100]) to produce coherent bremsstrahlung. With a diamond radiator the $\frac{1}{E_\gamma}$ intensity shape is changed and an enhancement is observed at the diamond reciprocal lattice vector energies. This energy is choosen by orientating the crystal.

The bremsstrahlung recoil electrons are then deflected downwards by a uniform dipole magnetic field onto the tagging system focal plane, where energy and timing informations are extracted.

3.2.2 The tagging system

See Figure 3.3 for a schematic of the tagging system. A detailed discussion can be found in [101].

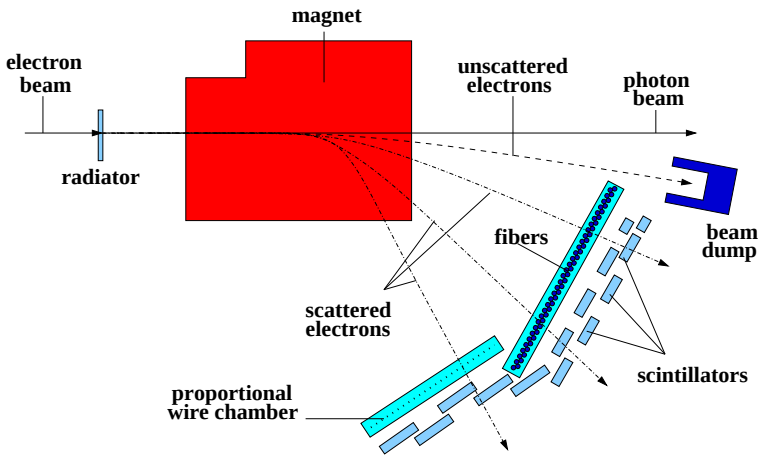

Figure 3.3: Layout of the tagging system.

The bremsstrahlung photons are nearly collinear with the incident electron beam and pass through a hole in the magnet yoke, after which they are collimated, and then impinge on the deuterium target which sits in the center of the CB-TAPS detectors.

The core of the tagging system are the 14 overlapping plastic scintillator bars which have each a photomultiplier on both ends. To obtain a higher energy resolution, a second layer is added : a scintillating fiber and a proportional

wire chamber (which was not used). The scintillating fiber consists of two layers of 2 $\times$ 240 plastic scintillator fibers arranged in such a way that each fiber partly covers two fibers in the other layer. The photon energy covered by the bars lies between 22 $\%$ and 92 $\%$ of the incoming electron beam energy, and the scintillating fibers covered a range between 18 $\%$ and 80 $\%$.

3.3 The target

The target had a cylindrical form with a radius of 1.5 cm and a length of 5.275 cm aligned along the beam axis. The target consisted of liquid deuterium (but could be also filled with liquid hydrogen for LH_2 runs) in a cell made of kapton foil of 0.625 mm. The target was placed inside of the aluminum beam-pipe (1 mm thick and 17 cm length). For more details read [102].

3.4 The CB-TAPS detectors

The aim of the CB-TAPS detectors is to acquire informations of the particles that emerge from the interaction between the incident photon beam and the nucleon ("located" inside the deuterium target). The informations are the 4-vectors of all the relevant particles, the photons coming from the decay of the neutral mesons and the recoil nucleon (proton or/and neutron).

The parameters directly measured by the setup are :

- the particle detection time (with respect to a time reference),
- the particle position and
- the particle energy.

From this three parameters, measured simultaneously in different parts of the setup, it is possible to deduce which particle was detected and to determine its momentum and energy. The physical principals which are the basis of all detectors rely on the electromagnetic interactions of this particles with the matter i.e. ionization processes. These interactions are characterized by the particle type.

- the hadrons, in our case p, n and $\pi^{\pm}$ with life time long enough to reach the detector, interact with the atoms of the matter they are passing through and are loosing their energy in elastic or inelastic collisions which may

produce secondary hadrons. The Bethe-Bloch formula describes the energy-loss by ionization of swift charged particles (protons, charged pions, but not electrons) traversing matter.

- the photon and the electrons are loosing their energy in electromagnetic showers : alternating Bremsstrahlung and pair production.

- the muons much more heavier than the electron, are loosing much less efficient their energy (only due to Bethe-Bloch) and can pass trough a lot of material without being stopped.

Once the decay products (e.g. photons) are identified it is possible to reconstruct the decaying particles (e.g. π^o, η and $\eta^{'}$ mesons) with invariant mass analyses. If m and p represent the mass and the 4-vector of the initial instable particle and p_1 and p_2 the 4-vectors of the two final particles (m_1, m_2 their masses, E_1, E_2 their total energies and $\vec{p_1}, \vec{p_2}$ their momenta), then

$$\begin{aligned} m^2 &= p^2 \\ &= (p_1 + p_2)^2 \\ &= m_1^2 + m_2^2 - 2\vec{p_1}\vec{p_2} + 2E_1E_2 \end{aligned} \tag{3.3}$$

A very important point for the success of the experiment is the reconstruction of neutral π and η which have a large branching ratio into two photons.

3.4.1 The Crystal Barrel (CB)

The CB was built to detect photons with high efficiency and good energy and spatial resolution over an energy range between 20 MeV and 2 GeV. The energy resolution is :

$$\frac{\sigma_E}{E} = \frac{2 - 3\%}{\sqrt[4]{\frac{E}{GeV}}} \tag{3.4}$$

The CB covers angles between 30^o and 168^o, in a barrel shape, because all crystal modules are arranged in a vertex-pointing geometry [103]. The CB is made of 1290 CsI (Tl) crystals, the Tl (a dopend) is used to improve the light output. The Figure 3.4 shows a cross section of the CB calorimeter. The crystals are ordered in 23 rings of 60 crystals. Each crystal (Figure 3.5) is mounted in a titanium case for mechanical stability and is wrapped in kapton foil for electrical isolation. The crystals are equipped with photo-diodes because the CB at the LEAR experiment was operating in a magnetic field. Between the photodiode and the crystal there is a 3 mm Plexiglas wave length shifter in order to improve the mismatch between the light emitting area of a crystal

and the sensitive area of a photodiode. A preamplifier is directly positioned on the crystal module in order to reduce the background noise. The stability of the gain of each CsI (Tl) was monitored by a light pulser system. The light pulser system consists of a connection between the wave length shifter and a xenon flash-lamp operating at a repetition rate of 4 Hz.

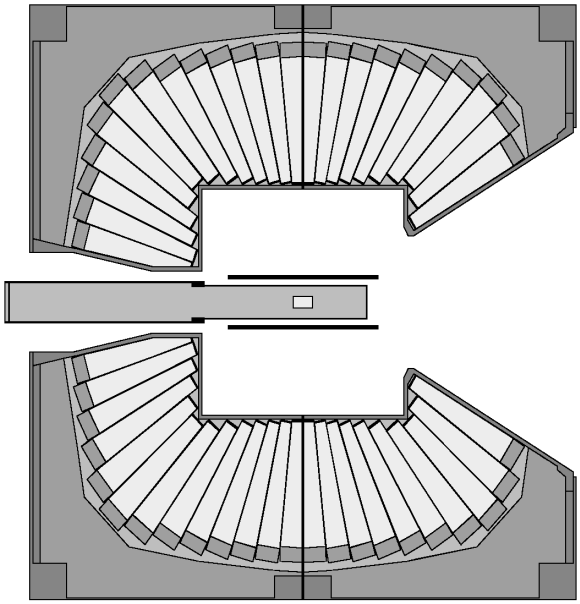

Figure 3.4: Cross section of the Crystal Barrel calorimeter.

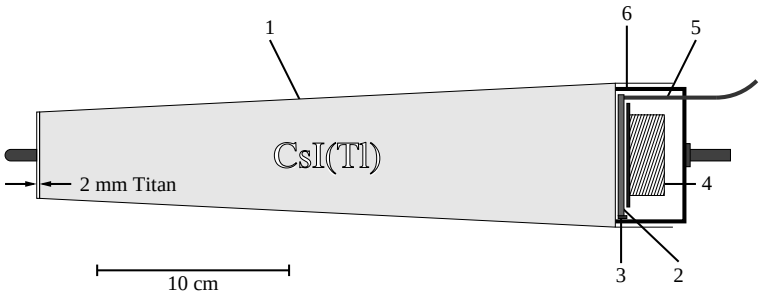

Figure 3.5: Cross section of a CsI (Tl) module. (1) 0.1 mm titanium can. (2) wavelength shifter. (3) photodiode. (4) preamplifier. (5) light fiber.

For more details read [104].

3.4.2 The Inner detector

The inner detector, which is inside the CB, is used in order to distinguish between charged and neutral particles [105]. The inner detector consists of three layers of scintillating fibers (Figure 3.6).

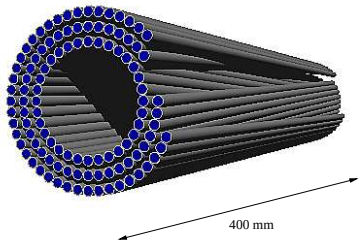

Figure 3.6: The scintillating fiber inner detector used for charged-particle identification. The differing orientation of the three separate layers enables to extract the three spatial coordinates of each hit.

The inner detector has a cylindrical shape and a length of 40 cm. It is covering the angles between 28^o and 172^o. The outer layer (191 fibers, diameter of 128 mm) runs parallel to the z-axis. The middle layer (165 fibers, diameter of 122 mm) is bent anticlockwise with also an angle of 25^o with respect to the z-axis. The fibers of the inner layer (157 fibers, diameter of 116 mm) are bent clockwise with an angle of 25^o with respect to the z-axis. Each fiber has a diameter of 2 mm. The orientation of the three layers allows the reconstruction of the spatial coordinates of the intersection point of the charged particle trajectory with the detector.

3.4.3 The Travel Around Photon Spectrometer (TAPS)

The TAPS detector was designed as electromagnetic calorimeter which is optimized for the detection of photons over a wide range of energies (few MeV to few GeV). It has, however, also capabilities for the detection of charged mesons ($\pi^{\pm}$) and recoil nucleons (proton and neutron). In the setup discussed here, the TAPS detector consisted of 528 modules assembled in a hexagonal wall. The TAPS wall is shown in Figure 3.7. This arrangement makes it possible to reconstruct the position of the detected particles with a resolution smaller of the module size (since the electromagnetic shower spread over a cluster of mod-

ules) and a good energy resolution described by :

$$\frac{\sigma_E}{E} = \frac{3\%}{\sqrt[4]{\frac{E}{GeV}}} \tag{3.5}$$

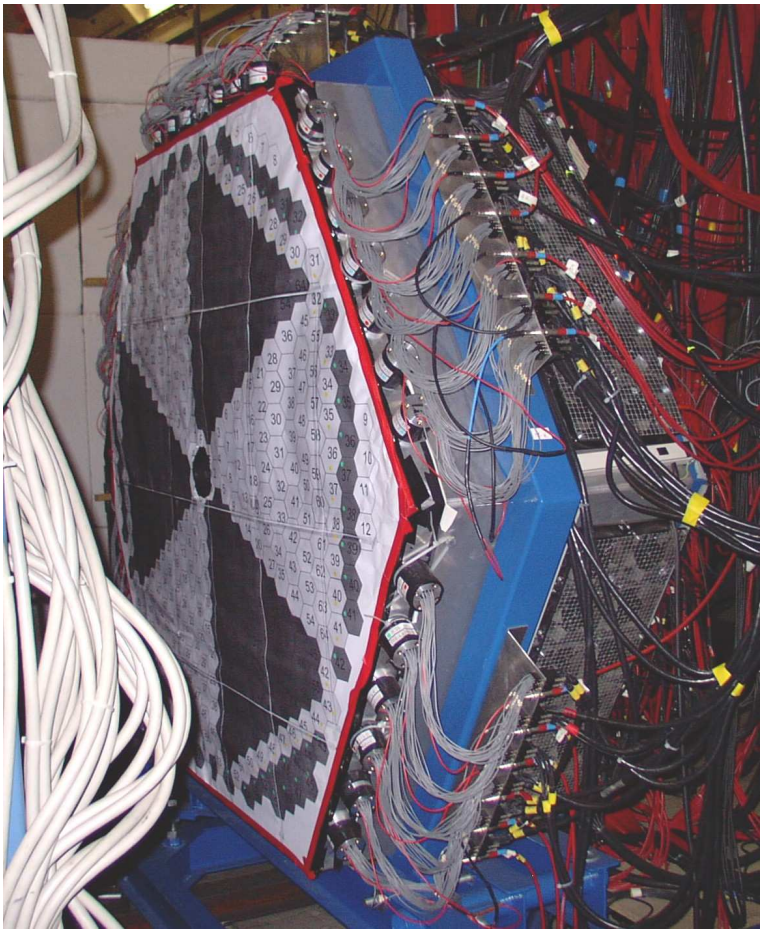

Figure 3.7: A picture of the TAPS wall.

The modules, Figure 3.8, are composed of two parts, an inorganic scintillator (BaF_2) and a plastic scintillator as Charged Particle Counter (veto) [106]. The BaF_2 crystals are composed of two parts : one hexogonally shaped with an inscribed diameter of 59 mm and a length of 250 mm (12 radiation lengths) and a cylindric crystal part to make the connection to the photomultiplier. The BaF_2 has three scintillation components, two fast ones with a decay time of 0.6 ns at 195 and 210 nm, and a slow one with a decay time of 620 ns at 310 nm. The scintillation light depends on the ionization density and, therefore, allows particle discriminations. The scintillation light that emerged from the crystals

is converted to charge and amplified by a photomultiplier (Hamamatsu R2059-01) mounted on the back of the crystal.

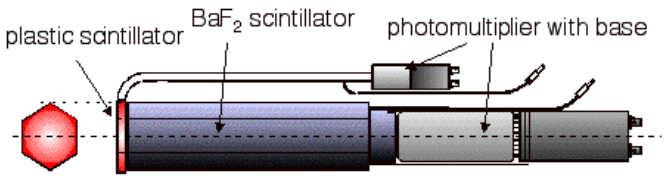

Figure 3.8: A single module of the TAPS detector.

The TAPS-wall was placed 1.2 m from the target in order to fill the 30^o opening angle of the CB Figure 3.1.

3.4.4 The veto

The vetos [107] are made of 5 mm thick plastic scintillator (NE102A) which respond to charged particles but not to neutral particles. The plastic slices are hexagonally shaped and have an inscribed diameter of 59 mm. Fiber light-guides links the veto and the photomultiplier mounted at the side of the TAPS wall (in Figure 3.7 they are visible).

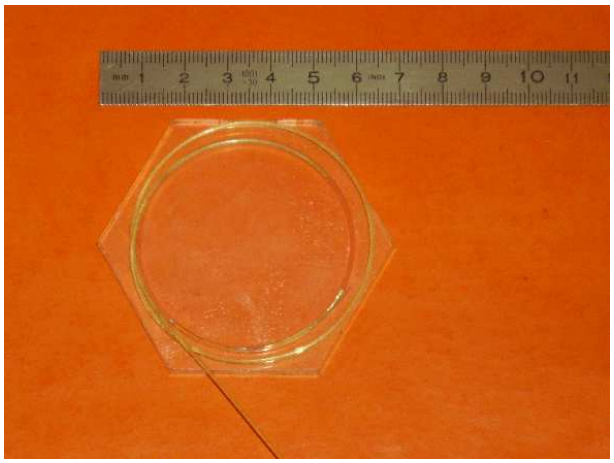

Figure 3.9: A picture of the veto detector. The hexagonal 5 mm plastic scintillator and its fiber guide.

3.5 The $\gamma-$veto

The use of the collimator in defining the photon beam spot on the deuterium target has the consequence that not all the bremsstrahlung photons "seen" by the tagging system (by detection of the associated electron) reached the deuterium target. In addition, the tagging system will also register "accidental" hits not correlated to bremsstrahlung photons at all. Indeed, the electron numbers detected by the tagging system do not necessarily correspond one-to-one to the incident photon number that reached the deuterium target. Thus the efficiency of the tagging system must be determined in order to correctly estimate the flux on the target.

There is a device put at the end of the beam line, the $\gamma-$veto, that is used for this purpose. The $\gamma-$veto consists of 9 lead glass crystals. It measured those bremsstrahlung photons that passed through the target without creating a hadronic reaction (the bremsstrahlung photons that underwent a hadronic reaction are negligible). The ratio between the bremsstrahlung photons "seen" by the $\gamma-$veto with the bremsstrahlung photons "seen" by the tagging system gives the tagging efficiency.

3.6 DATA acquisition and DATA reading

3.6.1 The tagging system

The electronics of the tagging system record for each event the time (and the energy deposited in the bar scintillator) of all modules. Each of the 480 fibers of the scintillating fiber detector are connected to CFDs (Constant-Fraction Discriminator) close to the detector. From there the resulting logic signals are taken outside the experimental hall through delay lines and passed through a passive splitter. Then the signals go from the splitter to a multi-hit TDC (64 ps/ch) and a scaler. A photoreaction product is signaled by a coincidence between an electron in the tagging spectrometer and a trigger from the CB-TAPS detectors. The TDCs (Time to Digital Converters) are used in common stop mode, where the trigger from the CB-TAPS detectors gives the stop signal. If this coincidence condition is satisfied, the TDC is read. The time is needed to determine whether or not a real coincidence has occurred between TAPS and the electron or if it was a random coincidence. The TDCs and the scaler are mounted on top of CATCH boards. The CATCH boards are readout via the VME interface by a similar VMIC event-builder as is used for the two CB halves. The signals from the tagger bars (two for each bar, left and right) are linked through delay lines to normal TDCs, QDCs and scalers.

3.6.2 The CB

The CB electronics records for each event the energy deposited in all modules. The signals coming from the CB photodiodes are passed via shapers to the Charge to Digital Converters (QDC), which integrate the total charge present in the signal in low energy ranges. The QDCs contain two different capacitors and the incoming signal is split in a ratio of 1 to 8 between them. The internal logic then decides which charge will be digitized. If the signal is small the charge on the capacitor with the highest charge will be integrated, if the signal is large the other capacitor will be used. In this way each QDC covers two different ranges, up to 200 MeV, and up to 2 GeV. Each range is digitized into 12 bits and an additional bit is set to specify the used range. The pedestal of each channel is monitored before each run and tracked roughly every 10 minutes. The QDCs are read-out by a VMIC compatible board running Linux. The interface to the VME backplane is accomplished via a Tundra Universe PCI-VME interface. Two such modules collect the digitized data from the QDCs where one module is responsible for the upstream and one for the downstream CB half. The two VMIC computers each build their sub-event and send this via TCP/IP to a central event builder. More details can be found

in [108].

3.6.3 The Inner detector

The Inner detector electronics records for each event the time of all modules. The signals from the Inner detector are read using photomultipliers, which are connected to trigger electronics inside the experimental area which is able to determine how many of the three layers detected a hit. The signals for all individual fibers are taken outside the hall and connected to TDCs.

3.6.4 The TAPS wall

The TAPS electronics records for each event the deposited energy and the time of all modules. A scheme of the electronics is given in Figure 3.10.

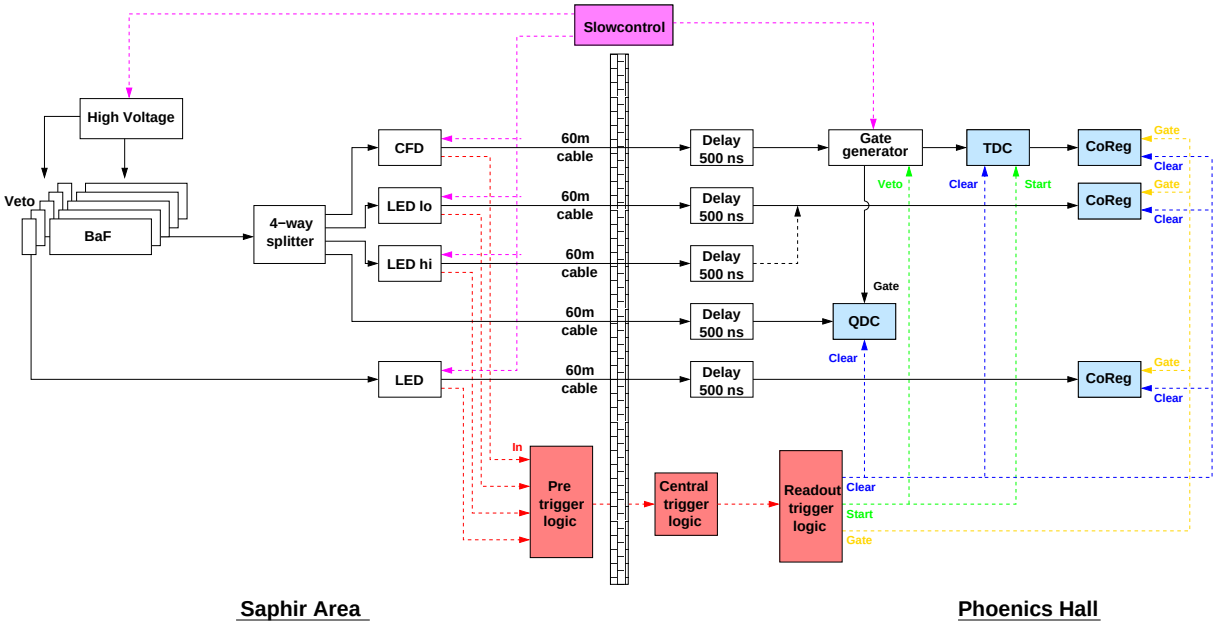

Figure 3.10: Diagram of the TAPS read-out electronics

The BaF_2 signals are split 4-fold by active splitters located close to the TAPS-wall. Three signals are used to generate a three level-discriminating logic signal., one CFD and two Leading-Edge Discriminator signals (LED Low, LED High). The fourth output presents the analogue signal to the QDC. The CFDs have been set to a threshold of 20 mV. It was found during the offline analysis that this corresponds to an energy threshold of about 15 MeV. The LED Low and LED High discrimination levels were set per rings. The calibration of the

LEDS was achieved by observing for each ring where the discriminators cut the calibrated energy spectrum. It was found that the LED discrimination level could be accurately set to their designated value with a spread of 5 MeV. The analogue BaF_2-signals are integrated by QDCs. The integration over a short and a long time gate allows one to separate the response from the fast and slow scintillation components. These time gates are individually generated for each module by gate-generators (Retard de Dureé Variable RDV) which are started by the CFD signal of the module. The voltage on the photomultipliers were chosen such that the QDCs cover a dynamic range up to 2400 MeV. The intrinsic resolution is then 0.6 MeV/channel (the range and the intrinsic resolution values are based on the cosmic calibration). The time of the BaF_2 signal is measured by TDCs. The TDC start signal is generated by the trigger. The TDCs are stopped by the CFD signal of the individuals modules. In this way, the time-of-flight from the target to crystal is recorded. The TDCs have an intrinsic resolution of 40 ps/channel, far better than the resolution needed to separate nucleons from photons on the basis of the difference in time-of-flight which is in the order of 3 to 10 ns. In addition to the energy, pulse shape and time-of-flight information, the logic signals CFD and LED High of each module are recorded in bit-patterns units (BPUs). More details can be found in [109].

3.6.5 The veto wall

The veto detectors provide two output signals, from the photomultiplier anode and one from the last dynode. The anode signal was not used. The dynode signal was used to generate a LED logic signal. The level of the LEDs was set such that it was above the noise level. The veto is said to have "fired" if the resulting logical output signal is above this threshold and this was recorded by feeding the LED outputs to a pattern unit.

3.7 The trigger

The huge amount of data can not be completely recorded and stored. Thus a quick and reliable trigger system was needed. Furthermore, in order to investigate particular channels, it was necessary to enrich the data sample with these particular channels during the data taking periods. There were three main triggers for the read-out, corresponding each to a specific measurement (for more details read [109].).

3.7.1 Cosmic trigger

A cosmic ray calibration run was necessary for the TAPS detectors. This trigger requires one single hit in TAPS and is used before and after the measurement to allow an energy calibration of the TAPS detectors (for details cp. section).

3.7.2 Experiment trigger

The experiment trigger was determined by two factors : the speed of the decision and the channels we wanted to measure. The trigger system for the CB-TAPS experiment was built in two consecutive stages.

The first level trigger

The first level trigger should be as fast as possible. Indeed the first decision made is whether the measurement is good enough to start the digitization of all measured values. Furthermore, the logic decision has to be made before the analog signals reach the readout electronics through appropriate delay lines.

The slow signal rise time, 2 μs, of the CB (which is due of the CB'photodiodes) excluded the use of the CB in the first level trigger, because the analog signals from TAPS pass through a delay line of 300 ns. Thus the logic decision has to be made and passed to the readout electronics within 300 ns. The first-level trigger is entirely done by TAPS, which is equipped with fast photomultiplier tubes. The informations coming from the LED was used to make the trigger. As mentioned, two different LED threshold voltages have been applied in our experiment : LED-low and LED-high. The TAPS-wall was subdivided in different segments.

Three different first-level triggers or "pre-trigger" have been used :

- LED-low mutl 2 : two hits in the TAPS detectors above the LED-low threshold were required. Figure 3.11 shows the 8 segments of the TAPS-wall.

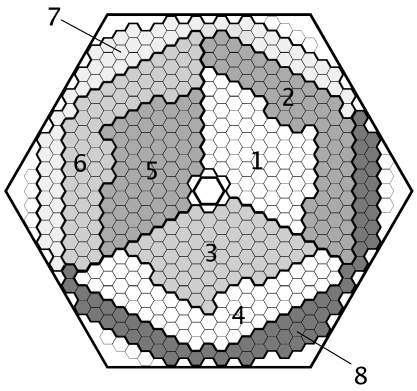

Figure 3.11: Segmentation [109] of the TAPS detector for the LED low multiplicity 2 pre-trigger.

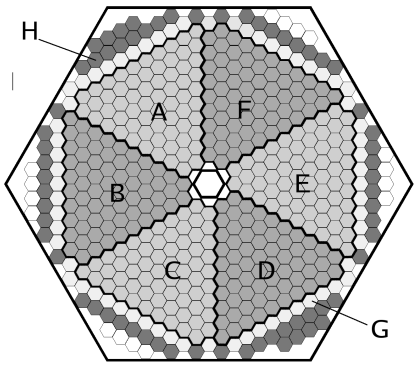

Figure 3.12: Segmentation [109] of the TAPS detector for the LED high multiplicity 1 pre-trigger.

- LED-low OR : one hit in TAPS. This trigger was downscaled.
- LED-high OR : one hit in TAPS. For the LED-high a different segmentation was used see Figure 3.12.

Figures 3.13 and 3.14 illustrate the electronic sketch of the LED-low and LED-high.

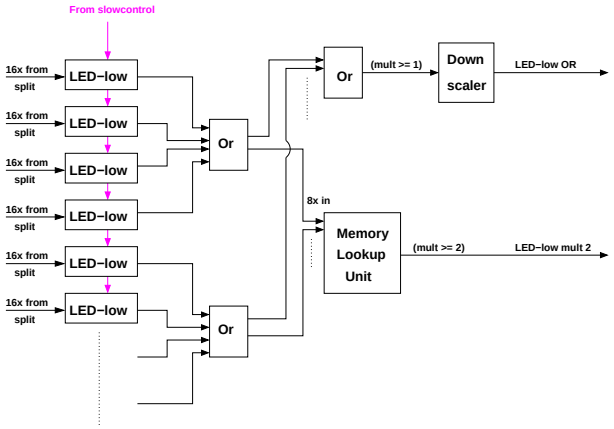

Figure 3.13: Diagram [109] of the two LED-low pre-triggers. Each LED module is connected to 16 detectors. In the first step each block of 64 detectors is OR'ed. The eight block outputs are connected to the input of a Memory Lookup Unit (MLU) which is programmed to select multiplicities of 2 and higher. The resulting signal is used as the LED-low mult 2 pre-trigger. For the minimum bias trigger the eight block outputs are OR'ed together to form an OR of the entire signal. This signal is scaled down and is used as the LED-low OR pre-trigger. The slow-control is responsible for setting the threshold values for the LED's.

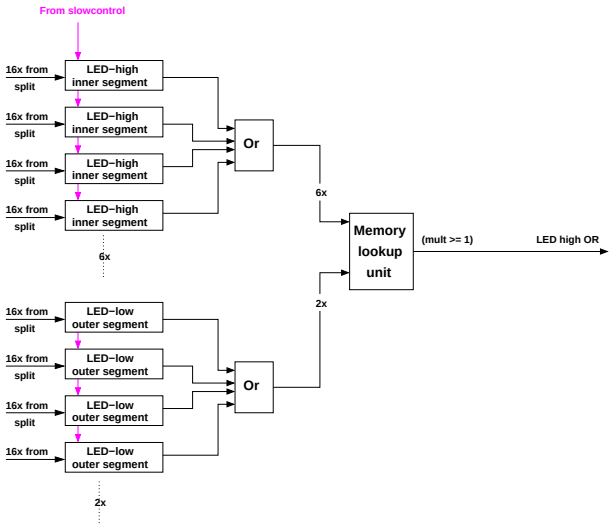

Figure 3.14: Diagram [109] of the LED-high OR pre-trigger. The logic is arranged similar to the logic for the LED-low pre-triggers in figure 3.13. For this trigger the Memory Lookup Unit (MLU) is programmed to select multiplicities of 1 and higher. The slow-control is again responsible for setting the threshold values for the LED's.

The second level trigger

The second stage of the trigger is used to determine whether the digitized signals will be read out for further processing. As the digitization takes ~ 1 ms, the CB signals are used.

The number of clusters found in the FAst Cluster Encoder (FACE) is used in the second level trigger. The cluster procedure finding can take up to 10 μs, which is slow compared to required timescale of the first-level trigger. It was required that the number of the clusters should be equal to 2 or higher.

In summary, the trigger was (LED-low mult 2) OR (FACE mult 2 AND LED-high mult 1).

3.7.3 Tagger trigger

To find the photon number that reached the target, the so-called tagging efficiency has to be measured. This was done several times during the experiment in separate runs with normal beam intensity and very low beam intensity (for more details see section 6.1.2). The trigger signal for this measurement was an OR between the scintillation bars of the tagging system.

4 Calibrations

The calibration procedures map the raw-data as presented by the data-acquisition system to values which have physical units : energy [MeV] and time [ns]. The calibration procedures are in principle simple. Indeed, this was more or less the case for the tagging system and the CB detectors, but not for the TAPS detectors. The cooling system was not powerful enough to compensate completely the temperature changes in the experimental hall. Furthermore, some electronic modules caused problems due to aging effects (the entire electronic system of the detector was replaced by a new, highly compact system after this experiment). In order to solve these complications, a daily calibration was necessary and a strict data selection was applied which will be explained later.

4.1 The tagging system

For the tagging system two quantities needed to be calibrated : the time and the energy.

4.1.1 Energy calibration

The energy calibration of the tagging system was performed by colleagues of the Universities of Bonn and Groningen. The calibration is based on the measurement of the energy of the recoil electron. The energy of the recoil electron corresponds to the hit position. The hit position depends on the electron momentum (p) :

$$E_{e^-} = pc = q_{e^-} B \rho c \tag{4.1}$$

where B is the magnetic field and ρ is the radius. If these two quantities are known, then the energy of the electron can be determined and also the energy of the bremsstrahlung photon.

$$E_\gamma = E^o_{e^-} - E_{e^-} \tag{4.2}$$

where $E^o_{e^-}$ is know from the accelerator.

In this experiment two different $E^o_{e^-}$ were used : 2.6 GeV and 3.2 GeV. The magnetic field has been adjusted in such a way, that the part of the beam that did not undergo any bremsstrahlung always describes the same trajectory. Thus :

$$E_\gamma^{2.6\ GeV} = \frac{E_{e^-}^{2.6\ GeV}}{E_{e^-}^{3.2\ GeV}} E_\gamma^{3.2\ GeV} \tag{4.3}$$

A detailed description of the energy calibration can be found in [110].

4.1.2 Time calibration

The time-zero signal of the reaction was made by the trigger, i.e. by the start detector which is one of the 528 BaF_2 detectors.

The reference time choosen was 0 for the recoil electron that hit the tagger scintillator fibers and the photons coming from the hadronic reaction detected in TAPS.

The tagger scintillator fiber TDC (tagger TDC) is started by the detection of an electron and stopped by the trigger, so :

$$Tagger\,TDC \;=\; trigger \;-\; electron \tag{4.4}$$

The time calibration of the tagging system was done after the TAPS time calibration was finished for the event sample corresponding to photons detected in TAPS. The tagger TDC spectra were aligned by examining the difference between the time signals from each individual tagger TDC and the time from all the TAPS channels. This is because the TAPS TDC is started by the trigger and stopped by the CFD of the TAPS elements, then :

$$TAPS\ TDC \;=\; photon \;-\; trigger \tag{4.5}$$

Adding equation 4.4 and 4.5 gives :

$$Tagger\,TDC + TAPS\ TDC \;=\; photon \;-\; electron = alignment\,offset \tag{4.6}$$

The tagger TDC gain was 0.05 ns/TDC-channel (taken from the constructor).

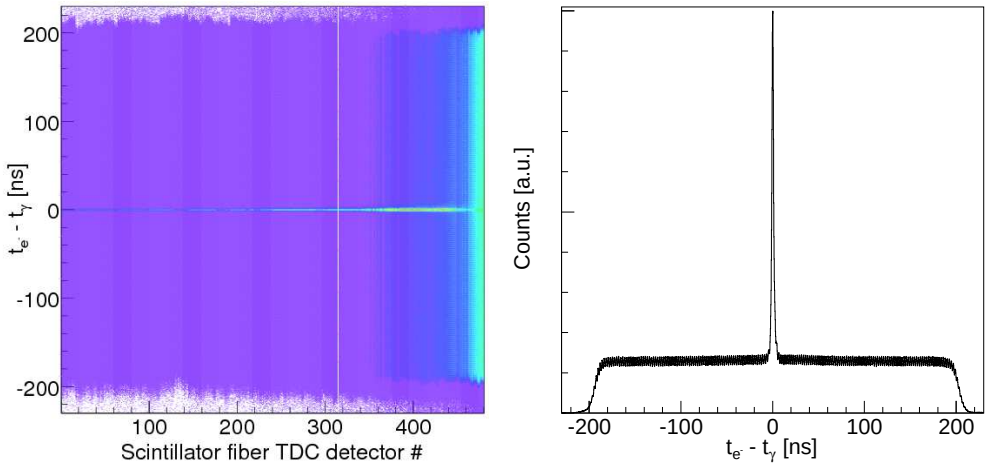

Figure 4.1: *Right: The time difference between the detection of a photon in TAPS and an electron in the tagging system summed over all tagger fibers. Left: .The same time difference plotted versus the number of the tagger fiber channel.*

Figure 4.1 (left) shows the timing of each tagger fiber after the alignment. Figure 4.1 (right) shows the sum over all detectors. The FHMW of the TAPS-tagger timing is 1.6 ns.

4.2 The CB

For the CB, only one quantity needed to be calibrated : the energy.

4.2.1 Energy calibration

The energy calibration of the CB detector was partly done by colleagues of the University of Bonn. Earlier work with the CB detector (and the TAPS detector) established that the response of the Cs (Tl)-modules (and BaF_2-modules) to photons is linear. Then, the raw data conversion can be written as following :

$$energy = \ gain \ \times (channel - \ pedestal) \tag{4.7}$$

The two parameters, the gain and the pedestal (or offset), depend on the specific conditions of the experiment like ambient temperature. For the CB detectors : the gain and the pedestal did not change much between two experiments.

The pedestals are determined and subtracted online. The CB QDCs have two ranges. For the low range, the gain is determined with the π^o invariant mass method (for more details see TAPS energy calibration). For the high range, the gain is determined by injecting laser light of different known energies into the crystals.

Figure 4.2 shows the two-photon invariant mass distribution over all CB detectors. After the calibration, the π^o and η peaks are at the correct position $\pm$ 1 %, respectively 135.9 MeV and 547.6 MeV. A detailed description of the

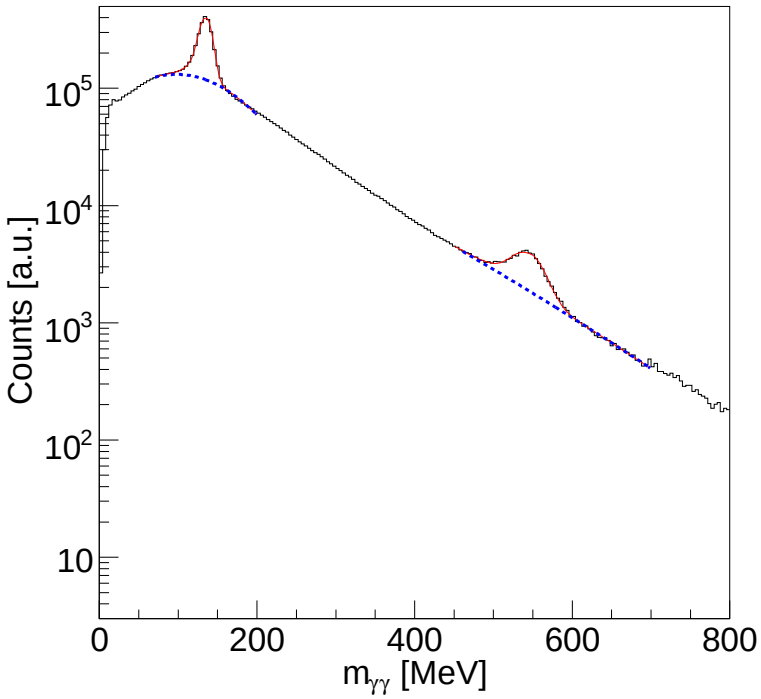

Figure 4.2: *The two-photon invariant mass spectrum for photons detected in CB showing the π^o and the η peak. The peaks are at 135.9 MeV and 545.6 MeV, respectively.*

energy calibration can be found in [111].

4.3 The Inner detector

For the Inner detector, only one quantity needed to be calibrated : the time. The TDC outputs for the Inner detector channels were aligned with each other. This was performed during the experiment. In the offline analysis a gate is put on the TDC spectrum around the prompt peak to determine if a fiber was hit.

4.4 The TAPS

For the TAPS detectors two quantities needed to be calibrated : the time and the energy.

4.4.1 Energy calibration

The TAPS energy calibration is done in three stages : in the first stage the cosmic muons are used to do a rough calibration, in the second stage an absolute calibration is done using the $\pi^o \rightarrow 2\gamma$ invariant mass and in the third stage the non-linearity in the energy response of the detector is corrected by the $\eta \rightarrow 2\gamma$ invariant masses.

For the TAPS detectors, the gain and pedestal (of equation 4.7) strongly depend on the high voltage on the photomultipliers and ambient temperature. In Figure 4.3 an example of a raw-data spectrum for one BaF_2-module is shown.

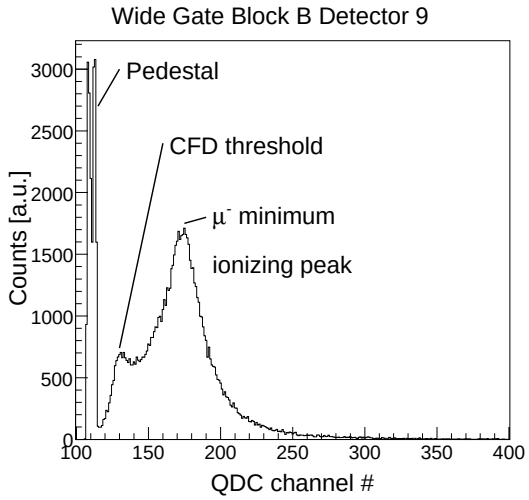

Figure 4.3: *A TAPS cosmic ray energy deposition spectrum showing the pedestal (or offset) at* $0\ MeV$ *and the cosmic muon peak at* $38.5\ MeV$.

The pedestal is determined as the QDC-channel which is returned by the QDC if it did an integration without any signal at all. To determine this offset the data with the pedestal-trigger has been analyzed. The pedestal trigger is a pulser which causes all CFDs to fire. Then all the QDCs are forced to integrate over the short and the long gate, without receiving an input signal from the photomultipliers.

The gain is determined by using the peak of the distribution of energies deposited by minimum ionizing muons of cosmic origin (see Figure 4.3). The energy deposition is proportional to the track length through the detector. For horizontally positioned crystals, the average energy deposition is 38.5 MeV. This calibration is only valid for particles that lose their energy generating an electromagnetic shower. To obtain the final absolute calibration two effects must be corrected:

1. there is a difference in the detector response to cosmic rays as compared to photons, protons and neutrons due to a difference in the efficiency to produce scintillation light in the BaF_2 and

2. part of the photon shower is leaking away at the back, at the front, between the detectors and through the sides of the TAPS wall (this effect introduces a small energy dependence which is not observed for the CB).

Because of these two effects, a second stage and a third stage in the energy calibration is needed. As the pedestal was already determined in the first stage, only the gain needs corrections to obtain the absolute calibration for photons. These corrections are confirmed by observing that the peak in the two photon invariant mass squared distribution in Figure 4.5 (left) is shifted. In the second stage, where the first effect is corrected, a correction factor is applied in order to shift the π^o peak at the correct position. This correction factor was established for each TAPS module.

The invariant mass is given by :

$$m_{\gamma 1,\gamma 2} = \sqrt{2E_{\gamma 1}E_{\gamma 2}(1 - cos\theta_{1,2})} \tag{4.8}$$

where :
$E_{\gamma 1}$ and $E_{\gamma 2}$ are the measured photon energies
($E_\gamma = \sum E_{deposited} = E_{central\ detector} + \sum E_{neighbour}$) and
$\theta_{1,2}$ is the opening angle between the two measured photons.

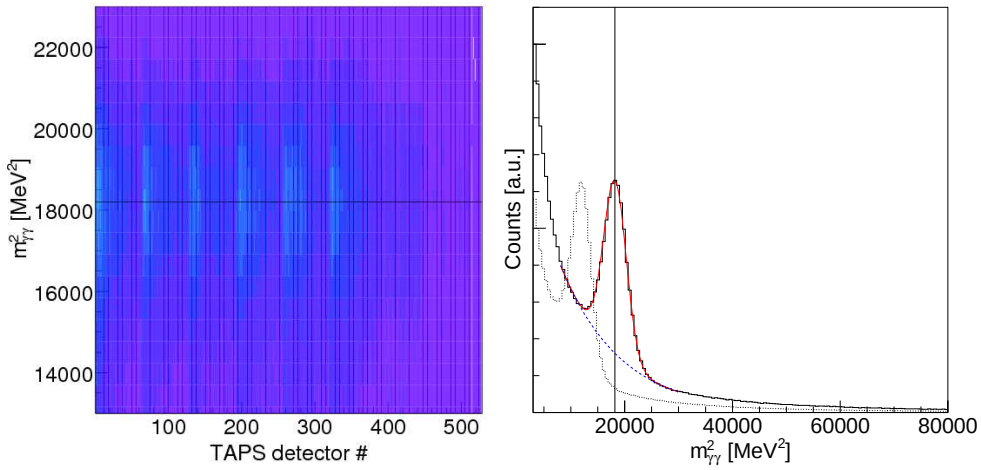

Figure 4.4: *Left: The two-photon invariant mass squared for photons detected in TAPS summed over all TAPS QDC channels before (dotted line) and after the second stage correction. Right: The same invariant mass squared plotted versus the number of the TAPS QDC channel.*

This factor f_E is then :

$$f_E^2 = \frac{m_{\pi^o}^2}{m_{\gamma 1,\gamma 2}^2} \tag{4.9}$$

where m_{π^o} is the π^o mass.

By inserting equation 4.8 into 4.9 and considering that the $\theta_{1,2}-$angle is correct, it gives :

$$f_E^2 = \frac{E_{\gamma 1}^o E_{\gamma 2}^o}{E_{\gamma 1} E_{\gamma 2}} \tag{4.10}$$

where $E_{\gamma 1}^o$ and $E_{\gamma 2}^o$ would be the correct photon energies.

By inserting equation 4.7 into 4.10 and considering that most of the energy is deposited into the central detector of the cluster and that the channels and the pedestals are correct, it gives, :

$$f_E^2 = \frac{gain_{\gamma 1}^o \times gain_{\gamma 2}^o}{gain_{\gamma 1} \times gain_{\gamma 2}} \tag{4.11}$$

where $gain_{\gamma 1}^o$ and $gain_{\gamma 2}^o$ would be the correct gains.

Let's introduce G_i as :

$$G_i = \frac{gain_{\gamma i}^o}{gain_{\gamma i}} \tag{4.12}$$

For a fixed central detector of a cluster and by looping over all the other

clusters equation 4.11 becomes

$$f_E^2 = \frac{1}{N} \sum_{k\ is\ fixed} G_k G_i = \frac{G_k}{N} \sum_{k\ is\ fixed} G_i \approx G_k \times 1 \tag{4.13}$$

As G_k is fixed, it can be brought outside of the sum and
$lim_{i\to\infty} \sum G_i = N$

Finally the correct gain, $gain^o$, is :

$$gain^o = gain \times \frac{m_{\pi^o}^2}{m_{\gamma 1,\gamma 2}^2} \tag{4.14}$$

Figure 4.4 (left) shows the two-photon invariant mass squared distribution for photons detected in TAPS for each TAPS detector. Figure 4.4 (right) shows the sum over all detectors before (dotted line) and after the second stage correction.

In the third and last stage of the energy calibration, the second effect is corrected. Figure 4.5 (doted line) shows that the $\eta-$peak is not at the correct position. The peak position is $\sim 3\ \%$ to high. Due to a lack of statistics, this correction was not possible for the individual detectors. It was done for the sum spectrum of all modules. The energy dependence was corrected in the following way :

$$E_\gamma^o = a + b \cdot E_\gamma + c \cdot E_\gamma^2 \tag{4.15}$$

where :
a is equal to 0 as 0 MeV corresponds to the pedestal and should not move,
b and c are the correction factors which we are looking for.

By assuming that the two photons have roughly equal energies and using the π^o and the η signals, equation 4.10 becomes :

$$\frac{m_{\pi^o}}{m_{\pi^o}^{measured}} = \frac{E_{\gamma\ from\ \pi^o}^o}{E_{\gamma\ from\ \pi^o}} \tag{4.16}$$

$$\frac{m_{\eta}}{m_{\eta}^{measured}} = \frac{E_{\gamma\ from\ \eta}^o}{E_{\gamma\ from\ \eta}} \tag{4.17}$$

By inserting equation 4.15 into 4.16 and 4.17, c and b are :

$$c = \frac{\frac{m_{\pi^o}}{m_{\pi^o}^{measured}} - \frac{m_{\eta}}{m_{\eta}^{measured}}}{E_{\gamma\ from\ \pi^o} - E_{\gamma\ from\ \eta}} \tag{4.18}$$

$$b = \frac{m_{\pi^o}}{m_{\pi^o}^{measured}} - c.E_{\gamma\ from\ \pi^o} \tag{4.19}$$

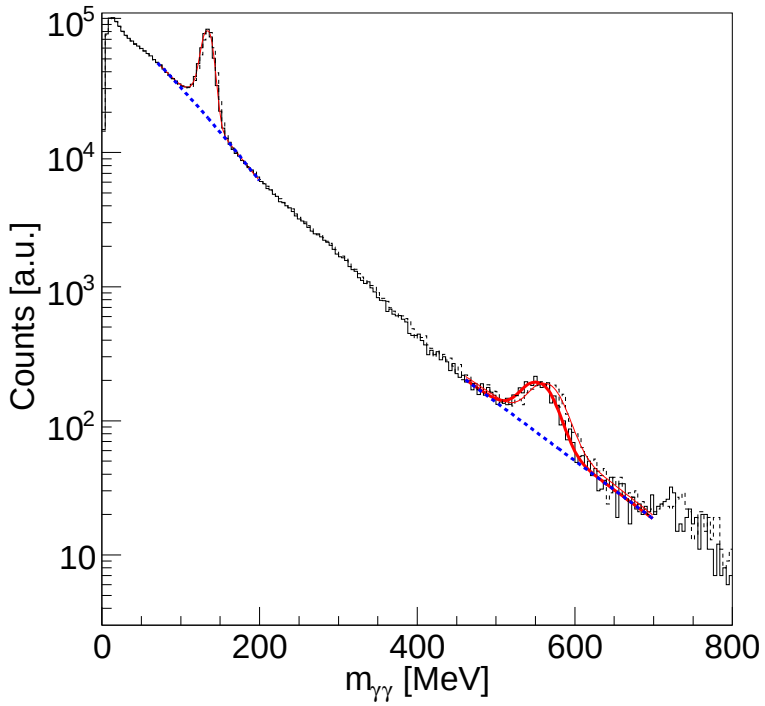

Figure 4.5: *The two-photon invariant mass spectra for photons detected in TAPS showing the π^o and the η peak before and after the energy dependence correction. Before, the peaks are at 134.7 MeV and 566 MeV, respectively (dotted line). After correction they are at 134.75 MeV and 553 MeV.*

Due to the approximations made above, several iteration for the stage two and three were necessary in order to have the peak positions for the π^o and η at the correct position $\pm$ 1 %.

4.4.2 Pulse Shape Analysis (PSA)

The fact that the intensity of the two different components in the scintillation light produced by BaF_2 depends on the ionization density and therefore on the type of the particle can be exploited in order to discriminate particles. With minimum electronic effort pulse-shape discrimination is performed by integrating the anode charge of the BaF_2 photomultiplier during two time gates within 50 ns and 2 μs resulting in the measured energies E_{narrow} and E_{wide} respectively.

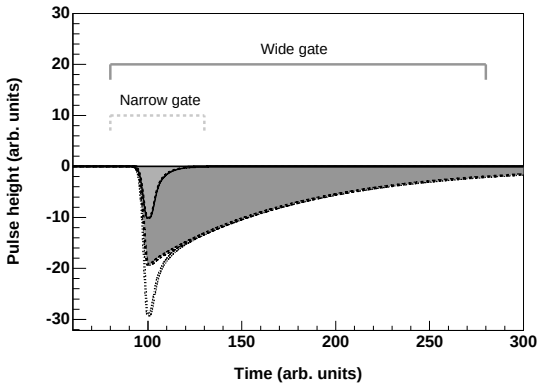

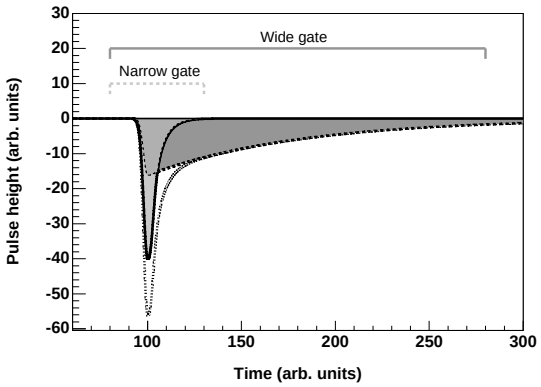

Figure 4.6: Left: A schematic drawing of the pulse shape [109] for protons in TAPS. Right: A schematic drawing of the pulse shape for photons in TAPS. The larger long component makes it possible to differentiate protons from photons.

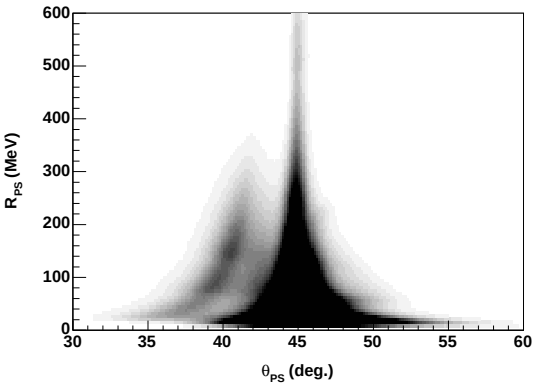

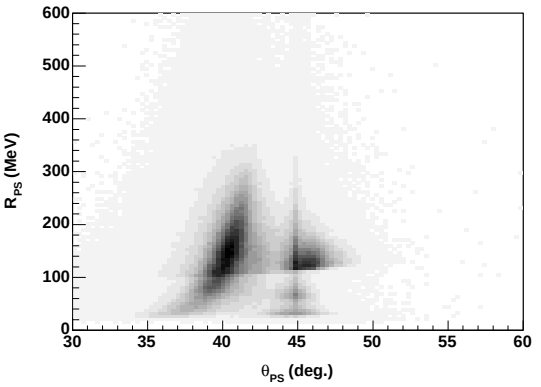

Figure 4.7: Left: The pulse-shape spectrum [109] in polar coordinates after calibration. The band at 45° are photons, the band to the left are protons. Right: The pulse-shape spectrum of protons. The band on the left is still visible, but the higher energy protons that have punched through the detector appear on the position of the photon band making a complete separation impossible.

Each event can be described by polar coordinates (for more details read [109]) as illustrated in Figure 4.7 (left), where :

$$\theta_{PS} = arctan(\frac{E_{narrow}}{E_{wide}}) \quad (4.20)$$

$$R_{PS} = \sqrt{E^2_{narrow} + E^2_{wide}} \quad (4.21)$$

The pulse shape calibration is to align the photon band at 45^o by recalculating the pedestal and the gain of the narrow gate. Once, the alignment was done, a cut based on the photon band can be established. Due to electronic problems, the pulse shape calibration was only possible for $\sim 75\ \%$ of the 528 BaF_2. Therefore, the PSA was not used at all in this experiment.

4.4.3 Time calibration

The raw data conversion can be written as following :

$$time = \ gain \ \times (channel - \ offset) \tag{4.22}$$

The gain was measured using a 20 ns pulse fed to the TDCs via the pedestal pulser input of the splitters. Figure 4.8 shows the pattern of sharp peaks , from which the gain is calculated, obtained for one detector.

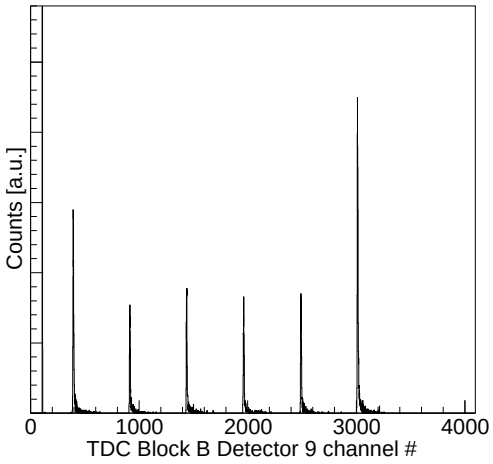

Figure 4.8: *Sharp peaks pattern. The distance between each peaks is 20 ns.*

The events selected for the offset determination for each channel were two or more photons detected in TAPS. The photons were identified by means of the charged-particle veto detectors and by a cut on the π^o mass. The time of the central cluster was used.

Subtracting equation 4.5 of 4.5 for two different photons, we obtained :

$$TAPSTDC_1 - TAPSTDC_2 = photon_1 - photon_2 \tag{4.23}$$

As already mentioned, the time reference choosen was 0 for photons detected in TAPS. Thus the offset was choosen in order to have a time difference between two photons detected in TAPS equal to 0. 17 $\%$ of all detectors did not

have a correct time signal (hence Figure 4.9 (left) empty channels).

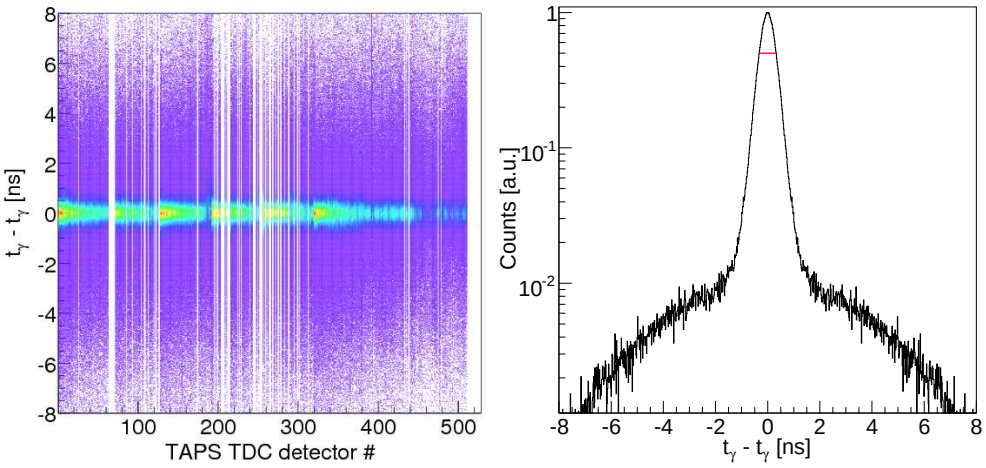

Figure 4.9: *Left: The time difference between two photons detected in TAPS summed over all tagger fibers. Right: .The same time difference plotted versus the number of the TAPS detector.*

Figure 4.9 (left) shows the timing of each TAPS channel after the alignment. Figure 4.9 (right) shows the sum over all detectors. The FHMW of the TAPS-TAPS timing is 650 ps. The alignment procedure does not only correct for the different cable length that linked the detector to the TDC, but also for the different flight path.

4.4.4 Threshold calibration

The information of the LED modules are essential for the hardware trigger (as explained in section 3.7.2). Furthermore, to be able to compare the simulation results to the data, the trigger condition must be included in the simulations.

The LED Low were calibrated before the beam time using the cosmic rays spectra. The LED high were calibrated during the first hours of beam time using the products of the hadronic reactions. At this stage, the energy calibration used was the one found with the cosmic ray. For LED Low and High, the calibration procedure was the same, we took three measurements : at the desired values, 40 % lower and 40 % higher. From this three points the linear dependence between MeV and mV was found.

As mentioned earlier the cosmic calibration is “relative” for photons. Then the LED calibration is also “relative”. During the offline analysis, the absolute threshold was found for each type of particle which was allowed to trigger. In

our measurements as we want to compare the reaction on the proton and the reaction on the neutron, only photons were allowed to trigger.

Figure 4.10 illustrates the LED Low and High photon thresholds. The LED threshold calibration was done per ring of detector modules in the TAPS wall.

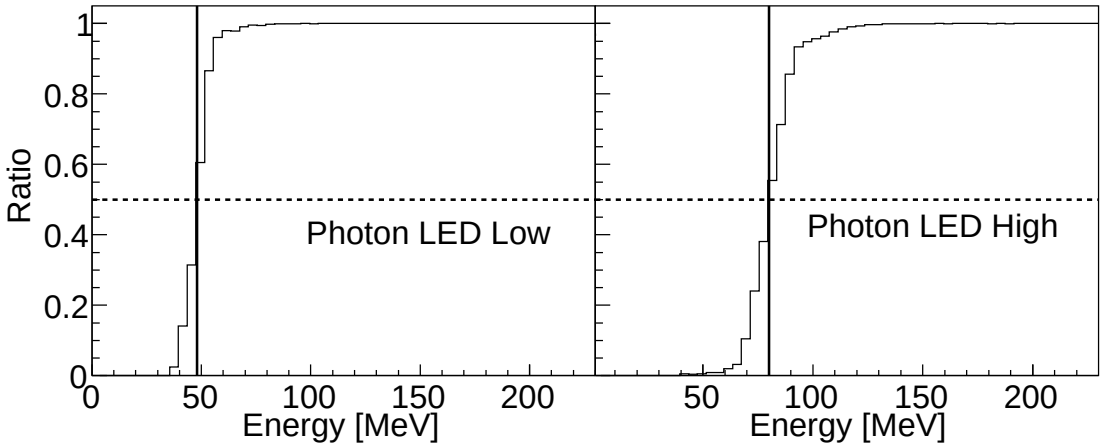

Figure 4.10: *Photon threshold for ring 7. Left : The threshold for the LED Low. Right : The threshold for the LED high. The ratio represents the fraction of hits that fire their LED i.e. the energy spectra with the LED condition and the energy spectra without LED condition ratio.*

It was checked that the individual LED thresholds of the ring were equal or lower than the ring threshold. The threshold values were monitored on a daily basis (during the offline analysis). The values choosen were the highest values found.

4.5 The veto

The veto did not require any calibrations. All the LEDs were fixed to 20 mV. During the offline analysis it was found that the threshold in MeV was 0.04 MeV in average (for more details read section 5.6.3).

5 Data analysis

This chapter details the different steps leading to the four-vector construction of : the incident photon energy, the mesons ($\pi^o\pi^o$, η and $\eta^{'}$) and the recoil nucleon (proton and neutron). The recoil nucleon identification and detection efficiency will be also discussed in this chapter.

An important point should be noted : the particles detected in the CB-TAPS detector are divided in two families : "neutral" hit and "charged" hit. Normally, the particles detected in the TAPS detector can be divided in three families : photon, neutron and "charged" hit; but because the PSA was not used the photon and the neutron can not be distinguished as it is the case in the CB detector. However, by the analysis, i.e. by reconstructing the meson we will see that the photon and the neutron can be separated and identified.

5.1 The tagged incident photon beam

The 1 nA intensity electron beam results in a large number of photons produced in the radiator. The left hand side of Figure 5.1 shows the tagger hit multiplicity. In average, there are 20 solutions for the incident photon energy. The time difference between the electron linked to a reaction in the target and the reaction products detected in TAPS is used for the identification of the electron related to a reaction in the target. The right hand side of Figure 5.1 illustrates this time difference. There are two event types : the coincidence events and the accidental coincidence events. The two inserted pictures (of the right Figure 5.1) show this two events types. The coincidence events show up in the prompt peak centered at 0. The accidental coincidence events are

randomly distributed. Bellow the coincidence peak (area A in red), there are accidental coincidence (area B in blue), which have to be subtracted. This is done by estimating the accidental coincidence outside of the prompt peak area (areas C and D), then B can be estimated as following :

$$B = (C + D) \times \frac{6ns}{220ns} \tag{5.1}$$

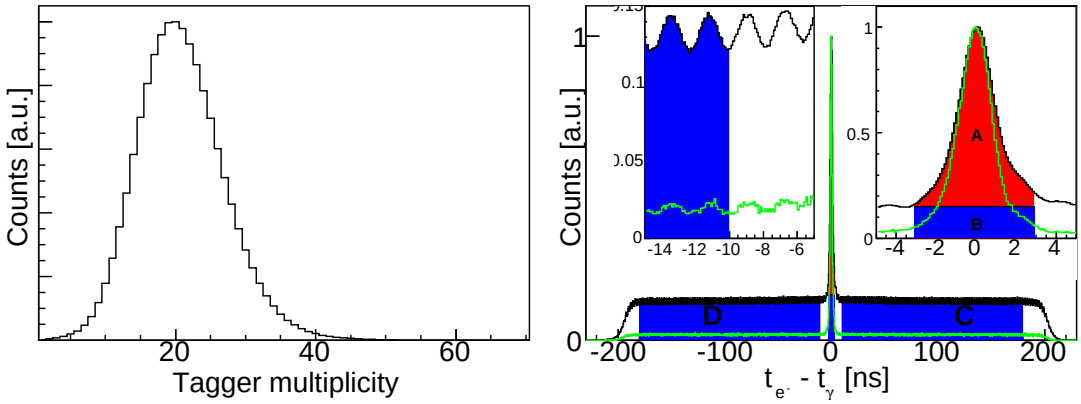

Figure 5.1: *Left : Electron multiplicity in the tagger within a 460 ns time range. Right : relative timing of a photon detected in TAPS and an electron detected in the tagging system (black line all photons, green line photons coming from a η). The blue marked regions correspond to the accidental coincidence. The red marked region corresponds to the coincidence. Inserted pictures. Left : zoom on the accidental coincidence. The 2 ns clock of the beam time structure is visible. Right : zoom on the coincident peak.*

The green line, in Figure 5.1, corresponds to the time difference between an electron and the photons coming from a $\eta-$decay detected in TAPS. B is a factor of magnitude lower than before.

5.2 The four-vector

If a particle is detected in CB-TAPS, its energy in general is distributed over more than one detector module. For a physic analysis and a better energy resolution the information of each of these modules must be combined to determine the type of particle that is detected, its energy and its position.

5.2.1 The clustering

The clustering routine, which finds all modules in CB and in TAPS that contain the energy deposited by one particle, is the most important part of the offline analysis code. These modules form a cluster if they are neighboring

detectors and have an energy deposition of at least 10 MeV in a TAPS detector and of at least 1 MeV in CB. The total energy of a cluster is calculated by summing the energy deposited in each member of that cluster. The cluster energy should be at least 25 MeV in TAPS and 20 MeV in CB in order to reduce split-offs.

The lower granularity of the CB detectors implies a second step in the cluster recognition in order to separate two overlapping clusters. This is done by looking at the local maxima. These maxima are defined as the centers of the electromagnetic showers. The central detector energy of each local maximum should be at least 13 MeV. The different sub-clusters are called Particle Energy Deposits (PED). For more details read [109] and [112] for TAPS and [111] for CB.

5.2.2 The position reconstruction

The position of the particle is reconstructed by taking the average of the positions of all modules in the cluster or PED (r_i), logarithmically weighted by their energy E_i.

$$\vec{r} = \frac{\sum_i W_i \vec{r_i}}{\sum_i W_i} \tag{5.2}$$

where,

$$W_i = \text{MAX}\left\{0, \left[W_0 + \ln \frac{E_i}{\sum_i E_i}\right]\right\} \tag{5.3}$$

It was found in [113] and [111] , that for TAPS W_o= 4 MeV and for CB W_o= 4.25 MeV.

This method of position determination works well if the cluster consists out of a large number of members. However, the cluster-sizes in TAPS were small : 2-3 modules in average. To avoid introducing artificial structure in the spectra due to binning effects, the position of each module in the cluster is randomized over the surface of the BaF_2-modules as described in [114].

5.3 The particle identification

The first discrimination done is between neutral particles and charged particles using the Inner detector and the veto detectors.

5.3.1 The proton

A proton candidate is defined as following :

A proton candidate in CB

A PED is identified as a charged hit if two or three layers of the Inner-detector have responded and match the hit in the CB, an example is given in Figure 5.2 (left). A "match" is defined by a cut on the difference between the azimuthal angles ($|\phi_{PED} - \phi_{Inner}| \leq 10\ ^o$) as illustrated in Figure 5.2 (right).

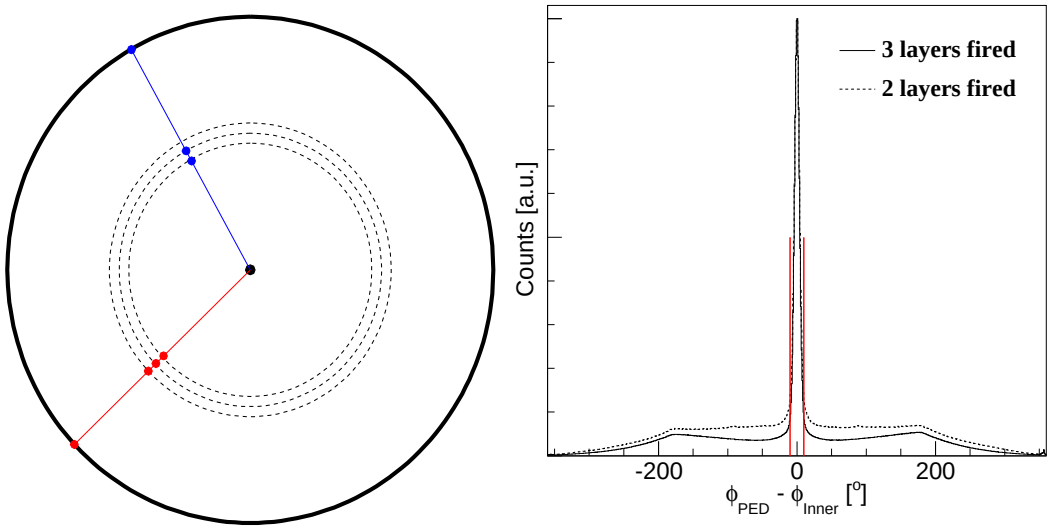

Figure 5.2: *Left : Schematic drawing of the CB (black line) and the Inner-detector (dotted line). In blue hits in two layers match a hit in CB. In red hits in three layers match a hit in CB. Right : Difference between the azimuthal angles (full line three layers fire, dotted line two layers fire). The prompt peak corresponds to a hit detected in coincidence in the Inner detector and the CB. The red lines shows* $\pm 10\ ^o$ *cut that define a "match".*

A missing mass analysis must be done to clearly identify a proton in CB (see section 5.6.1).

A proton candidate in TAPS

A cluster is identified as a charged particle if at least one veto in the cluster fired or a veto corresponding to a neighbor of the central detector of the cluster fired. Figure 5.3 (left) illustrates two cases. Case one (gree line) the veto in front of the BaF_2 module fire. Case two (violet line) the veto belonging to a neighbor detector did fire. The PSA can not be used to identify charged particles, in Figure 4.7 (right - section 4.4.2), the charged particles (mostly p and $\pi^{\pm}$) that have punched through the detector appear on the position of the photon band making a complete separation impossible.

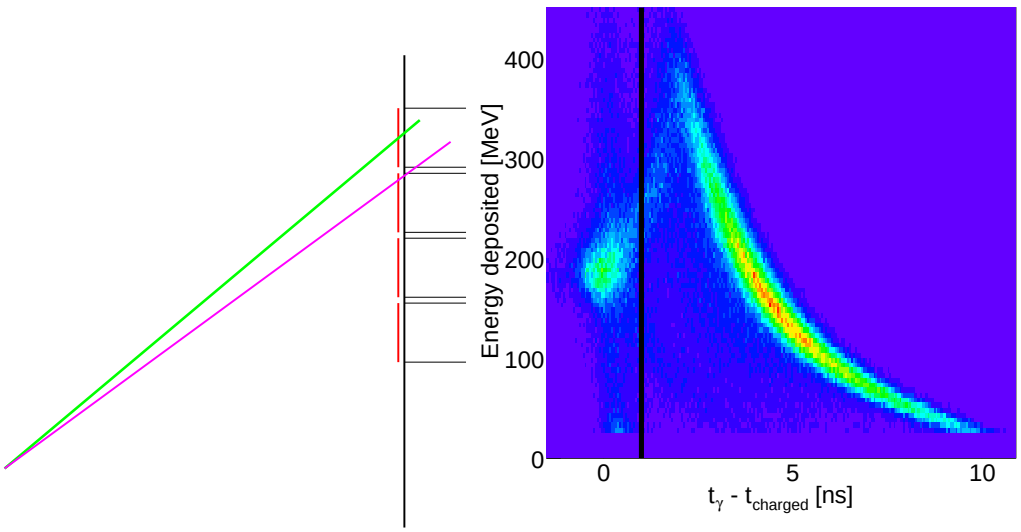

Figure 5.3: *Left : Schematic drawing of TAPS wall and BaF_2−scintillator (black line) and the veto detector (red line). Case one (green line) the veto in front of the BaF_2 fired. Case two (violet line) the veto belonging to a neighbor detector did fire. Right : Time difference between a photon detected in TAPS and a charged particle detected in TAPS versus the energy deposited. The typical "banana" trace can be observed. The "banana" trace stops at the maximum ionizing energy (2.5 ns,400 MeV). The spot at (0 ns,200 MeV) is the minimum ionizing energy. As the PSA was not used to identify the photons, the photons can be seen at the right of the black line.*

The TAPS timing allows to visualize the charged particle (mostly p and $\pi^{\pm}$) time-of-flight versus the energy deposited (Figure 5.3-right). There are three different areas : 0 - 1 ns (which corresponds to the minimum ionizing energy), 1 - 2.5 ns (between the minimum and maximum ionizing energy) and 2.5 - 10 ns (below the maximum ionizing energy). The charged particle timing is based on the photon prompt peak which calibration is relative. Therefore the charged particle timing is not directly usable. Because of the short radiation length of BaF_2 (X_o= 2.05 cm) the finite length of the detector modules plays a similar role for the timing of charged particles as it does for the timing of photons. In both cases, light production essentially starts at the front end of the detector. Thus, there is a relation between the energy deposited and the time-of-flight, hence the "banana" trace; and the kinetic energy can be directly provided by the calculated energy $T_{kin.}$ as obtained from the time-of-flight information (for more details see section 5.6.2), with the energy resolution being determined by the time resolution of the detector. This relation is only valid below the maximum ionizing energy i.e. for 2.5 ns and energy deposited below 400 MeV. Above the maximum ionizing energy, only the time-of-flight can be used to determine the kinetic energy of the charged particle. With the incident photon energy available in ELSA, we can have charged particles that reach the minimum ionizing energy : the spot at 0 ns and 200 MeV. At the

minimum ionizing energy, the charged particles are not anymore stopped in the TAPS detector, but they punched through the detector and always deposit the same energy.

5.3.2 The photon

A this level a $\gamma-$candidate corresponds to the "anti-"identification of a charged particle i.e. :

A γ candidate in CB

None of the layers of the Inner-detector fired or there is no "match" between a hit in CB and a hit in the Inner detector.

A γ candidate in TAPS

No veto belonging to a detector of the cluster fired and no veto belonging to a neighbor of the central detector of the cluster fired.

Figure 5.10 shows that the PSA could be used in order to clearly identify the photons in TAPS. However, it was not used in this analysis (for reasons that will be explained later).

5.3.3 The neutron

A neutron candidate in CB

A PED is identified as a possible neutron candidate if no layers of the Inner-detector fired. To clearly identify a neutron, we have to rely on the Inner-detector efficiency (see section 5.6.5), an invariant mass analysis (see section 5.5) and a missing mass analysis (see section 5.6.1).

A neutron candidate in TAPS

The same conditions on the veto as for the photon candidate was required for the neutron candidate. The PSA was not used to separate the neutron from the photon.

The TAPS timing allows to visualize the neutron candidate time-of-flight versus the energy deposited (Figure 5.4).

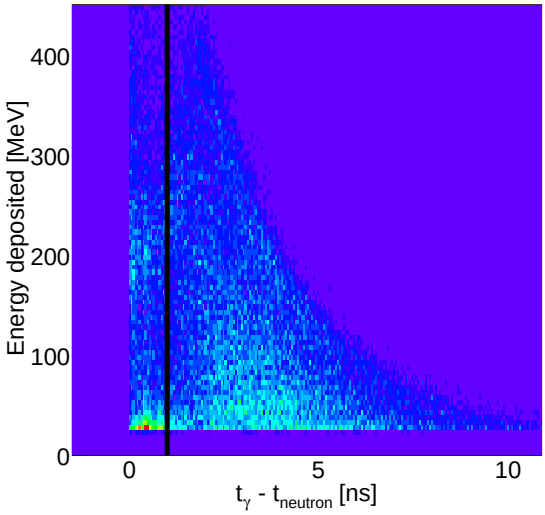

Figure 5.4: *Relative neutron time-of-flight versus the energy deposited. There is no relation between the energy deposited and the time-of-flight. Hence, the typical no trace picture for the neutron.*

The situation for the neutrons is different than the situation for the proton. There is no band-like structure. We do not see a banana trace because the neutrons always deposit only small fractions of their energy. Indeed, the actual interaction point of the neutron varies along the length l of the detector, whereas the interaction point of the proton is most of the time at the front end of the detector. Therefore, there is an additional contribution to the uncertainty in the time-of-flight information apart from the intrinsic detector resolution : the uncertainty Δl.

5.4 The software trigger

The hardware trigger is (see section)

$$(two\ LED\ low)\ OR\ (FACE\ 2\ and\ one\ LED\ high) \tag{5.4}$$

As we want to compare the reaction on the neutron and the reaction on the proton, this comparison is fair only if the photons make the trigger. Thus a software trigger was applied which reduced the total number of events. Then the hardware becomes :

$$(two\,photons\ LED\ low)\ OR\ (2\,photons\ FACE\ and\ one\,photon\ LED\ high) \tag{5.5}$$

Ring number	LED-low	LED-high
1	2000	2000
2	300	400
3	150	210
4	90	150
5	60	140
6	60	120
7	60	80
8	60	80
9	60	80
10	60	-
11	60	-
12	60	-

Table 5.1: The threshold values determined per ring of the TAPS detector, for photons and for LED-low and LED-high. All values are in MeV. The LED values for the innermost ring have been put as high as possible to reject background from e^+e^--pairs created when the incoming photons convert.

There are two important points to note : only the photons coming from the meson (s) studied are allowed to trigger and all detectors with broken QDCs or/and broken TDC are excluded from the trigger. This implies that the CB-TAPS detector response signal is not at all $\phi-$symmetric. Therefore, the linear asymmetry measurement was not analysed.

5.5 The meson (s) reconstruction

Reminder of the mesons that are reconstructed :

- $\pi^o\pi^o \rightarrow \gamma\gamma\gamma\gamma$
- $\eta \rightarrow \pi^o\pi^o\pi^o \rightarrow \gamma\gamma\gamma\gamma\gamma\gamma$
- $\eta^{'} \rightarrow \eta\pi^o\pi^o \rightarrow \gamma\gamma\gamma\gamma\gamma\gamma$
- $\eta^{'} \rightarrow \eta\pi^o\pi^o \rightarrow \pi^o\pi^o\pi^o\gamma\gamma\gamma\gamma \rightarrow \gamma\gamma\gamma\gamma\gamma\gamma\gamma\gamma\gamma\gamma$

Thus, all events which have between 4 and 11 neutral PEDs (or/and clusters) are studied. The term "neutral PED" refers to photon and neutron. The distinction between photon and neutron is not possible in CB (by "hardware"). Thus the neutron is "included" in the meson construction or the meson construction will leave out one particle that is a neutron candidate. In the first stage the neutron and the photon were not separated in TAPS by using prior to the meson construction the PSA or/and TOF in order to study the reliability to find the meson (s) and a neutron candidate in this way. It turned out be the easiest way not to use PSA or/and TOF to discriminate between neutron and photons because of the high number of detectors in TAPS which did not have PSA or/and TOF. Only after, the meson is reconstructed, if there is a neutron candidate, we do check if indeed this candidate is a neutron (for more details see section 5.6).

For a given meson and a given neutral PED number, all the possible combinations are tested.

$X(= 4, 5, 6, 7, 8, 9, 10, 11)$ neutral PEDs can be combined into $n_{\gamma\gamma}$, number of $\gamma\gamma$ pair's, in :

$$N = \frac{n_\gamma!}{2^{n_{\gamma\gamma}} n_{\gamma\gamma}!} \tag{5.6}$$

distinct ways (if the $\gamma\gamma$ pair's always correspond to the same meson i.e. $\pi^o \rightarrow \gamma\gamma$ or $\eta \rightarrow \gamma\gamma$).

If the $\gamma\gamma$ pair are not the same then :

$$N' = N \times C_j^i \tag{5.7}$$

where :
$C_j^i = \frac{i!}{j!(i-j)!}$ is the probability to find i in the ensemble j (if $i > j$).

To find the correct combination of $\gamma\gamma$ pair's a χ^2 test is done.

5.5.1 The χ^2-test

The χ^2-test is based on the test of the $\gamma\gamma$ pair's mass (equation 5.8). For each combination, the χ^2 was calculated. The best combination corresponds to the lowest χ^2.

$$\chi^2 = \sum_{i=1}^{n_{\gamma\gamma}} \left(\frac{m_{\gamma\gamma}^{th} - m_{\gamma\gamma,i}^{exp}}{\Delta m_{\gamma\gamma,i}^{exp}} \right)^2 \tag{5.8}$$

where :
$m_{\gamma\gamma}^{th}$ corresponds to the π^o-meson or/and $\eta-$meson mass.
$m_{\gamma\gamma}^{exp} = \sqrt{2E_1E_2 \cdot (1 - \cos\psi_{12})}$
$\Delta m_{\gamma\gamma}^{exp} = \frac{1}{2} m_{\gamma\gamma}^{exp} (\frac{\Delta E_1}{E_1} + \frac{\Delta E_2}{E_2} - \frac{\Delta cos\psi_{12}}{1-cos\psi_{12}})$
$\Delta cos\psi_{12} = sin(\theta_1)cos(\theta_2)(cos(\phi_1 - \phi_2) - 1)\Delta\theta_1 + cos(\theta_1)sin(\theta_2)(cos(\phi_1 - \phi_2) - 1)\Delta\theta_2 - sin(\theta_1)sin(\theta_2)sin(\phi_1 - \phi_2)(\Delta\phi_1 - \Delta\phi_2) - sin(\theta_1 - \theta_2)(\Delta\theta_1 - \Delta\theta_2)$

Once, the best combination is selected, the $\gamma\gamma$ pair mass is constrained to its theoretical value.

Example : $\eta' \to \eta\pi^o\pi^o \to \gamma\gamma\gamma\gamma\gamma\gamma$, the equation 5.8 becomes

$$\chi^2 = \left(\frac{m_{\eta}^{th} - m_{\eta}^{exp}}{\Delta m_{\eta}^{exp}} \right)^2 + \left(\frac{m_{\pi^o}^{th} - m_{\pi^o,1}^{exp}}{\Delta m_{\pi^o,1}^{exp}} \right)^2 + \left(\frac{m_{\pi^o}^{th} - m_{\pi^o,2}^{exp}}{\Delta m_{\pi^o,2}^{exp}} \right)^2 \tag{5.9}$$

Figure 5.5 (right) shows the χ^2 distribution for data and MC events.

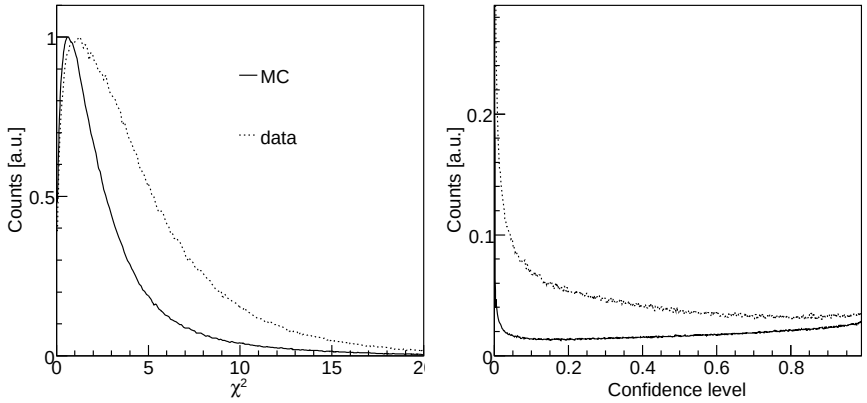

Figure 5.5: *Left : χ^2 distribution for 3 degrees of freedom (black line data, dotted line MC). Right : Confidence-level distributions (black line data, dotted line MC). If the errors are known the distribution should be flat.*

The confidence level (CL) :

$$CL = 1 - \left(\int_0^{\chi^2} f_{st}(\chi^2) d\chi^2 \right) \tag{5.10}$$

can also be calculated if the number of the degrees-of-freedom is known. In the case of the $\eta^{'}$, it is 3 for each constrain : one is the η mass and two are the two π^o masses, the results can be seen in Figure 5.5 (left). The difference between MC and data is coming from the fact, that in the data the errors are overestimated (because the confidence-level distribution decreases at higher confidence-level values) while in MC they are underestimated (because the confidence-level distribution shows a rise at higher confidence-level values). If the errors of the measurement would have been exactly known, the confidence-level distribution would have been flat (for more details read [109]).

5.5.2 $\pi^o\pi^o$ reconstruction

Events with four or five neutral hits are selected. The invariant mass of all photon pairs is built (Table 5.2).

Hit number	4	5
N	3	15

Table 5.2: Number of possible combinations.

A cut on the π^o mass is applied between 110 MeV and 160 MeV. The best combination of 4γ to $2\pi^o$ is selected by the χ^2-test. Figure 5.6 shows the best $\gamma\gamma$ - $\gamma\gamma$ invariant mass spectrum before the cuts on the π^o (which is removing part of the combinational background). The reactions $\gamma + d \rightarrow \pi^o\pi^o X$ and $\gamma + d \rightarrow \eta\pi^o X$ are clearly visible.

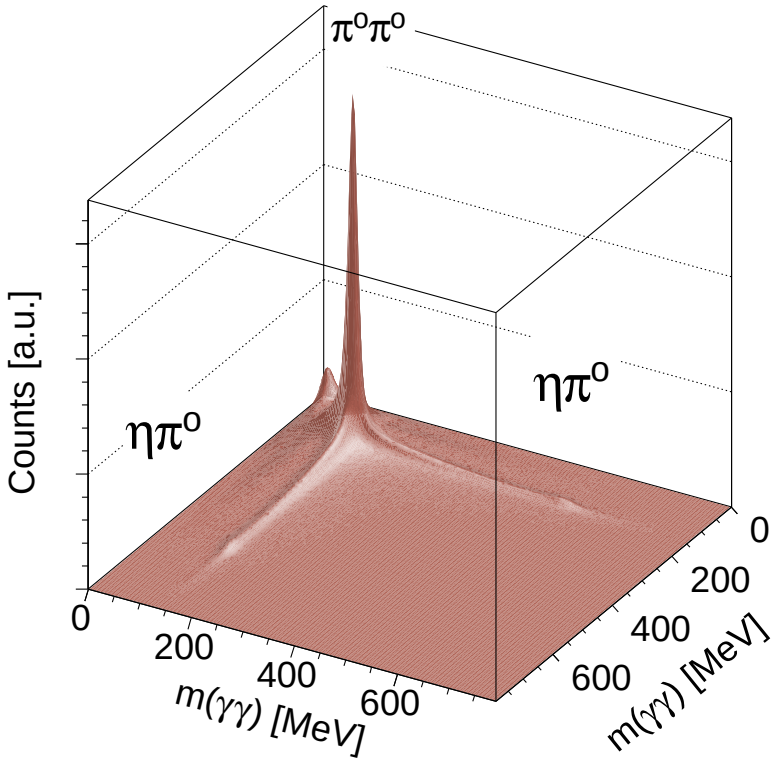

Figure 5.6: *Best $\gamma\gamma$ - $\gamma\gamma$ invariant mass spectrum. The reactions $\gamma + d \rightarrow \pi^o\pi^o X$ and $\gamma + d \rightarrow \eta\pi^o X$ are clearly visible.*

5.5.3 η reconstruction

Events with six to eleven neutral hits are selected. The invariant mass of all photon pairs is built (Table 5.3).

Hit number	6	7	8	9	10	11
N	15	105	105	945	945	10395
C_j^i	-	-	C_3^4	C_3^4	C_3^5	C_3^5
N'	-	-	420	3780	9450	103950

Table 5.3: Number of possible combinations.

A cut on the π^o mass is applied between 110 MeV and 160 MeV. The best combination of 6γ to $3\pi^o$ is selected by the χ^2-test. In order to improve the mass resolution the π^o mass is used as a constrain.

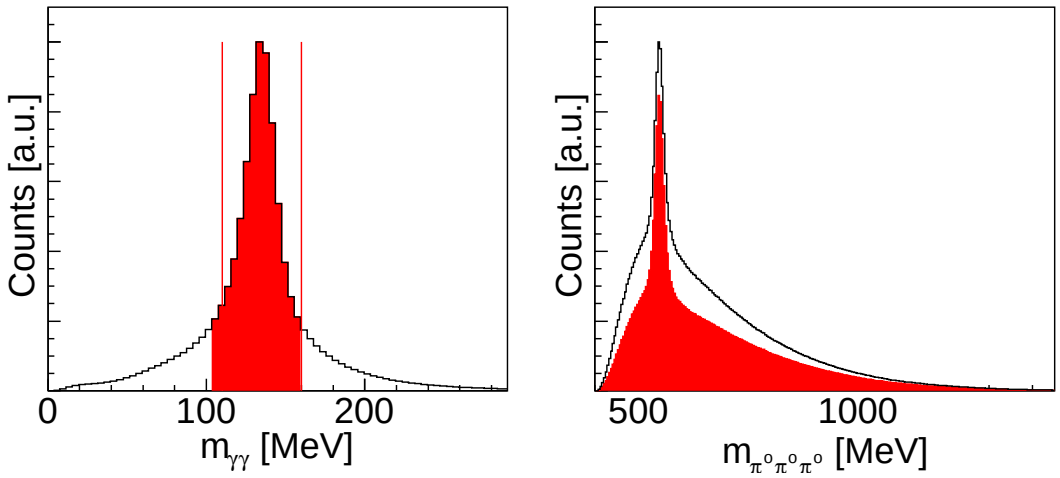

Figure 5.7: *Left : $\gamma\gamma$ invariant mass spectrum of the $3\pi^o$ selected by the χ^2-test. Right : The resulting $3\pi^o$ invariant mass spectrum. The red area shows the influence of the cut on the π^o mass. The combinational background is reduced.*

Figure 5.7 shows the $\gamma\gamma$ invariant mass spectrum of the $3\pi^o$ selected by the χ^2-test and the influence of the π^o mass cut on the $3\pi^o$ invariant mass spectrum. This picture was produced for 6 neutral hits. Figure 5.8 shows the $3\pi^o$ invariant mass spectrum reconstructed from six to eleven neutral hits. As expected the signal-to-background ratio increased with the number of hits as the background coming from $3\pi^o$ which did not originate from a η increased.

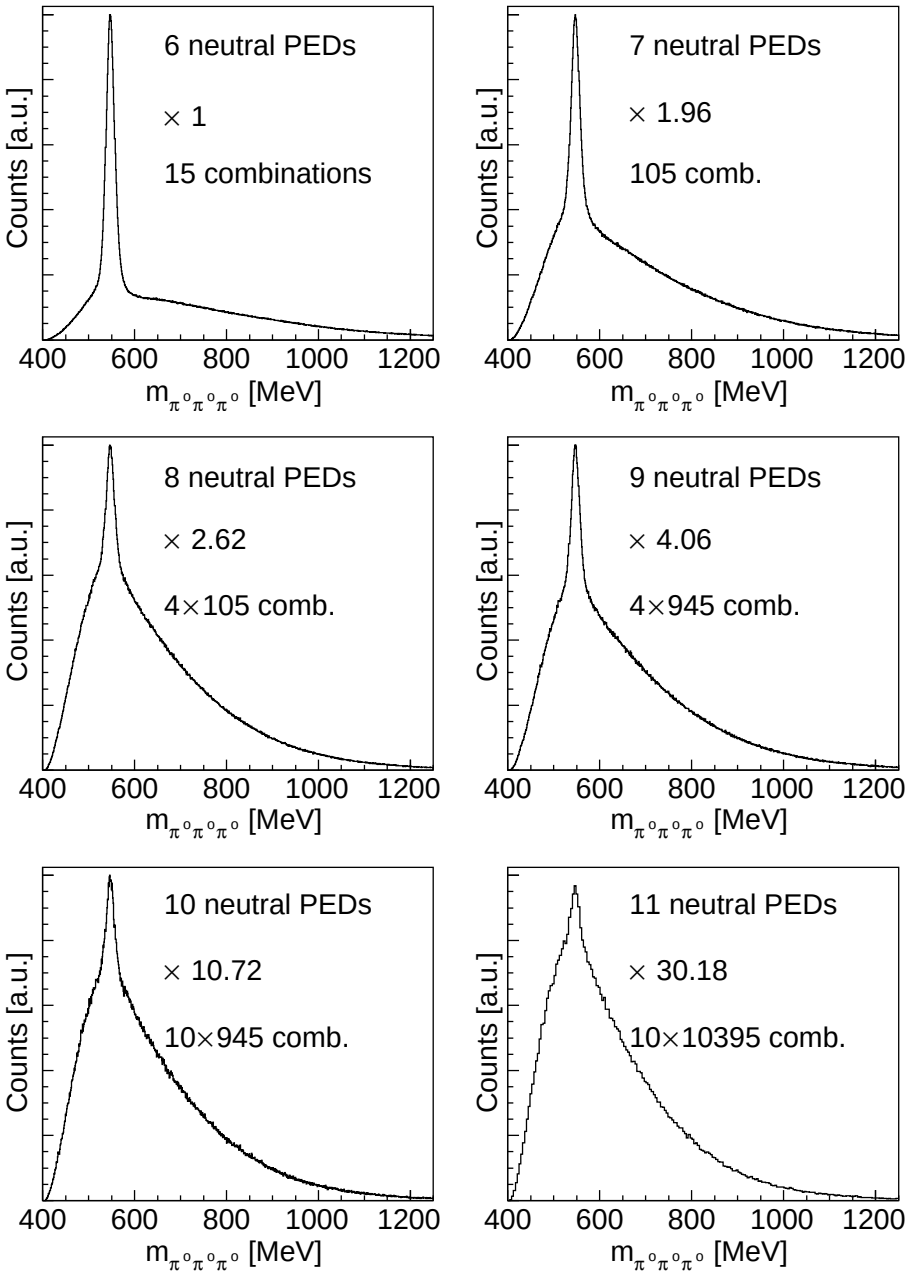

Figure 5.8: $3\pi^o$ *invariant mass spectrum reconstructed from six to eleven neutral hits (the* $\times$ *and a number are the scale).*

5.5.4 $\eta^{'}$ reconstruction

Events with six or seven and ten or eleven neutral hits are selected. The invariant mass of all photon pairs is built (Table 5.4).

Hit number	6	7	10	11
N	15	105	945	10395
C_j^i	C_1^3	C_1^3	C_3^5	C_3^5
$N^{'}$	45	315	9450	103950

Table 5.4: Number of possible combinations.

For six or seven neutral hits, a cut on the π^o mass is applied between 110 MeV and 160 MeV and on the η mass between 500 MeV and 600 MeV. For ten or eleven neutral hits, a cut on the π^o mass is applied between 115 MeV and 150 MeV and on the η mass between 530 MeV and 565 MeV. The best combination of 6γ or 10γ to $2\pi^o\eta$ is seletect by the χ^2-test. The π^o and the η masses were used as constrains. Figure 5.9 shows the principle stages of the $\eta^{'}$ construction. The background to signal ratio is important (see Figure 5.9-bottom), which is coming from $2\pi^o$ and an uncorrelated η. For eleven neutral hits, we basically do not see a $\eta^{'}$, because of the trigger conditions, indeed
the ratio $(\eta^{'}(\rightarrow 10\gamma)+n)/\eta^{'}(\rightarrow 10\gamma)$ $\sim$10 $\%$, while
the ratio $(\eta^{'}(\rightarrow 6\gamma)+n)/\eta^{'}(\rightarrow 6\gamma)$ $\sim$40 $\%$.

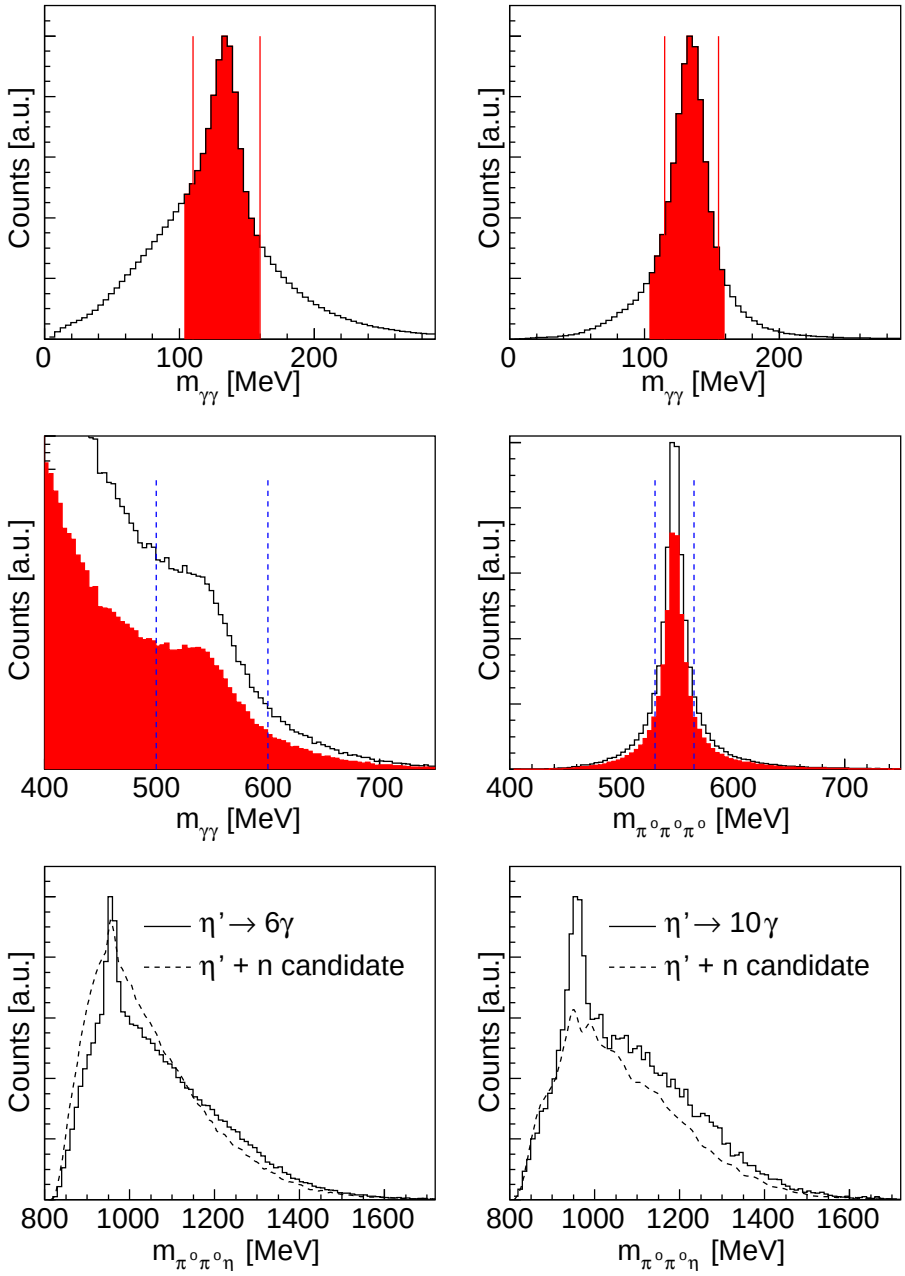

Figure 5.9: *Left column six or seven neutral hits selected : Top and middle best $\gamma\gamma$ invariant mass spectrum of the $2\pi^o$ and of the η selected. Bottom : The resulting $2\pi^o\eta$ mass spectrum (black line six neutral hits, dotted line seven neutral hits). Right column ten or eleven hits : Top and middle best $\gamma\gamma$ invariant mass spectrum of the $2\pi^o$ and of the $3\pi^o$ (corresponding to a η) selected. Bottom : The resulting $2\pi^o\eta$ mass spectrum (black line ten neutral hits, dotted line eleven neutral hits). The red area shows the influence of the cuts on the π^o and η masses.*

5.6 The recoil nucleon

At this level of the analysis, after the reconstruction of the meson (s), we can check if the charged hit is a proton and the neutron candidate a neutron. Only when the recoil nucleon is going into TAPS, we can clearly say if the charged hit is a proton and the neutron candidate (given by the meson (s) reconstruction) is a neutron by using the veto and the time-of-flight. We can also crosscheck with the PSA, if the neutrons have been separated from the photons (only for 75 % of the TAPS detectors which have a PSA). Figure 5.10 shows the pulse-shape spectrum in polar coordinates for the photons (left) and for the neutrons (right). The photons and the neutrons are separated.

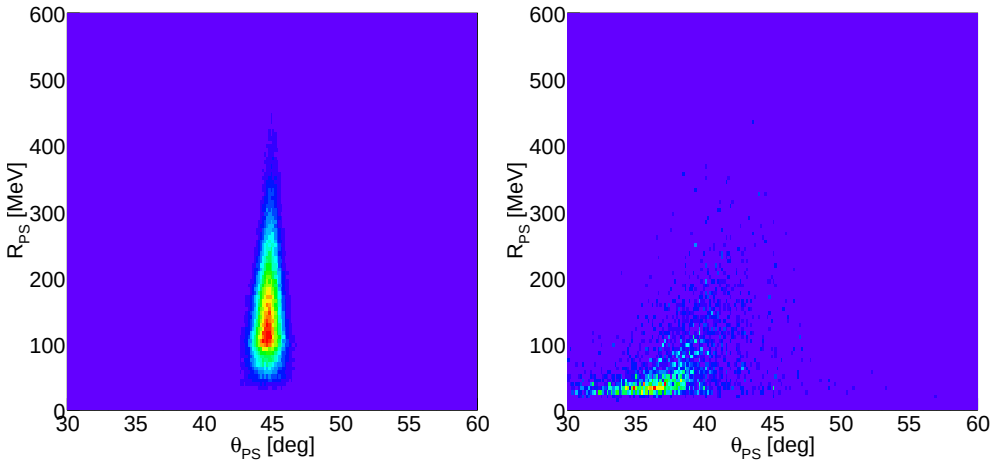

Figure 5.10: *The pulse-shape spectrum in polar coordinates. Left : for photons identified via invariant mass analysis and "anti-veto" conditions. Right : for neutrons identified via invariant mass analysis, "anti-veto" conditions, time-of-flight analysis.*

When the recoil nucleon is going into CB, we have to use the missing mass analysis to confirm that the charged hit is a proton and the neutron candidate is truly a neutron.

Another key feature of this experiment is the measurement, when it is possible and an approximation when it is not possible, of the four-vector of the recoil nucleon. Both detectors CB and TAPS provide the θ and the ϕ laboratory angles. The energy of the recoil proton can be measured also in both detectors by the energy deposited. However, this is only possible for a narrow range of kinetic energies as after the maximum ionizing energy ($\sim$ 280 MeV for CB and $\sim$ 400 MeV for TAPS) the energy deposited is no more related to the kinetic energy; and we want to measure the kinetic energy of the recoil nucleon up to 1 GeV. Furthermore the energy deposited cannot be used for the neutrons (see

section 5.3.3). Thus the proton and the neutron kinetic energies can be measured only in TAPS (with the time-of-flight) and approximated in CB (with the missing mass analysis).

5.6.1 The missing mass analysis

The missing mass analysis is used for three different purposes :

- to separate the production we are looking for from competing channel (s) (see the results Chapter - "The reaction identification"),
- to check that there is indeed a recoil nucleon detected in coincidence and
- to approximate the kinetic energy of the recoil nucleon detected in the CB.

The missing mass four-vector is calculated from the incident photon beam and the reconstructed meson (s) as follows :

$$(E_N, \vec{p}_N) = (E_\gamma, \vec{p}_\gamma) - (E_m, \vec{p}_m) \tag{5.11}$$

where :
E_N, E_γ and E_m are, respectively, the missing nucleon energy, the incident photon beam energy and the meson (s) energy and
$\vec{p}_N$, $\vec{p}_\gamma$ and $\vec{p}_m$ are, respectively, the missing nucleon momentum, the incident photon beam momentum and the meson (s) momentum.

The missing nucleon energy and momentum is computed as follows :

$$E_N = E_\gamma + m_N - E_m \tag{5.12}$$
$$\vec{p}_N = \vec{p}_\gamma - \vec{p}_m \tag{5.13}$$

The missing nucleon mass is :

$$m_N = \sqrt{(E_\gamma + m_N - E_m)^2 - (\vec{p}_\gamma - \vec{p}_m)^2} \tag{5.14}$$

The kinetic energy of the recoil nucleon returned by the missing mass analysis ranges between 0.025 GeV and 1 GeV.

5.6.2 The time-of-flight (TOF)

The time-of-flight (TOF) is the time that it takes a particle to travel from within the target to the TAPS detector. Between these two points, the particle might loose energy, and slow down, in the different materials that are lying in its flight path.

In section 5.3.1 , we saw that the massive particle time t_m is relative to the time of the photon, the absolute TOF normalized to one meter is then calculated as follows :

$$TOF = \frac{t_m - t_\gamma}{d} + t_{\gamma,1m} \tag{5.15}$$

where :
d is the particle (proton, neutron, $\pi^{\pm}$, deuteron, ...) flight path and
$t_{\gamma,1m} = \frac{1.10^9}{c} = 3.33564\ ns$ is the time-of-flight for a photon that travels one meter (c is the speed of light in vacuum).

From the TOF, the velocity β on one meter flight path is deduced :

$$\beta = \frac{1}{c \cdot TOF} \tag{5.16}$$

where :
the number "1" refers to one meter.

Then the measured kinetic energy, $T_{kinetic}$, is :

$$T_{kinetic} = m(\gamma - 1) \tag{5.17}$$

where :
m is the mass of the particle and
$\gamma = \frac{1}{\sqrt{1-\beta^2}}$

The kinetic energy of the recoil nucleon measured with the time-of-flight ranges between 0.025 GeV and 1 GeV.

In Figure 5.11 the TOF versus the energy deposited is plotted for protons (5.11-left) and for neutrons (5.11-right).

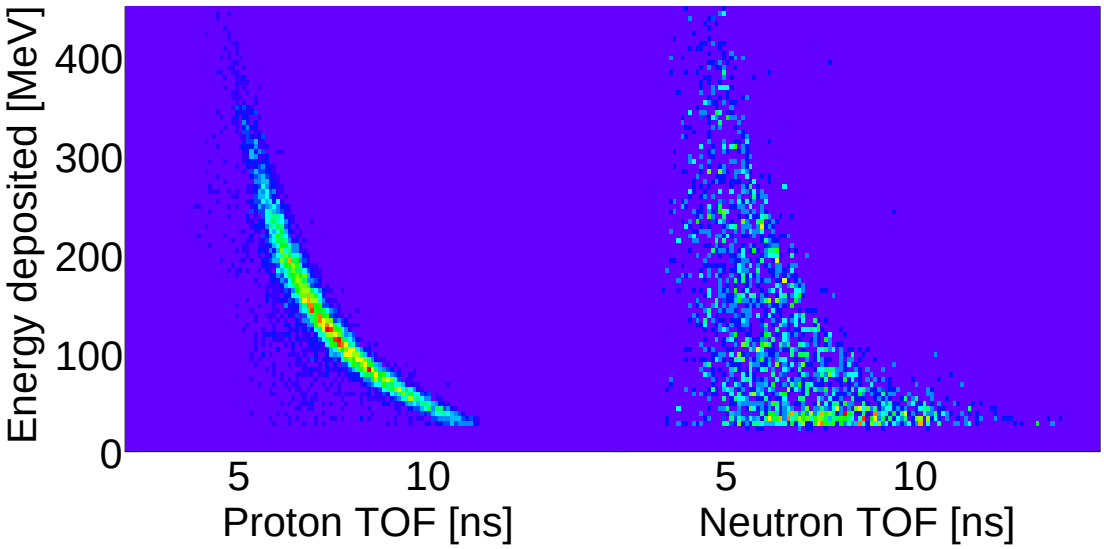

Figure 5.11: *Time-of-flight versus energy deposited of the recoil nucleon. Left : for protons. Right : for the neutrons. The banana-trace for the protons is observed.*

To the measured kinetic energy two corrections should be applied which are the energy loss (E_{loss}) which occurred during the flight path of the particle and for the variation of the interaction point ($T_{\Delta l}$) of the neutron and the proton (fast one, $T_{kinetic} > 300\ MeV$). The corrected kinetic energy, $T_{kinetic}^{corrected}$, is then :

$$T_{kinetic}^{corrected} = T_{kinetic}^{measure} + E_{loss} + T_{\Delta l} \tag{5.18}$$

The energy loss and the variation of the interaction point were determined together with the Monte-Carlo simulation package GEANT including the complete setup of the real measurement [115].

The corrections are done as following, the measured nucleon kinetic energy (by the setup simulated) is plotted against the generated nucleon kinetic energy, Figures 5.12 (left column) and 5.13 (left colum). The variations are traced and parameterized in two polynomial functions of degree three and eight. The results are plotted in Figures 5.12 (right column) and 5.13 (right colum).

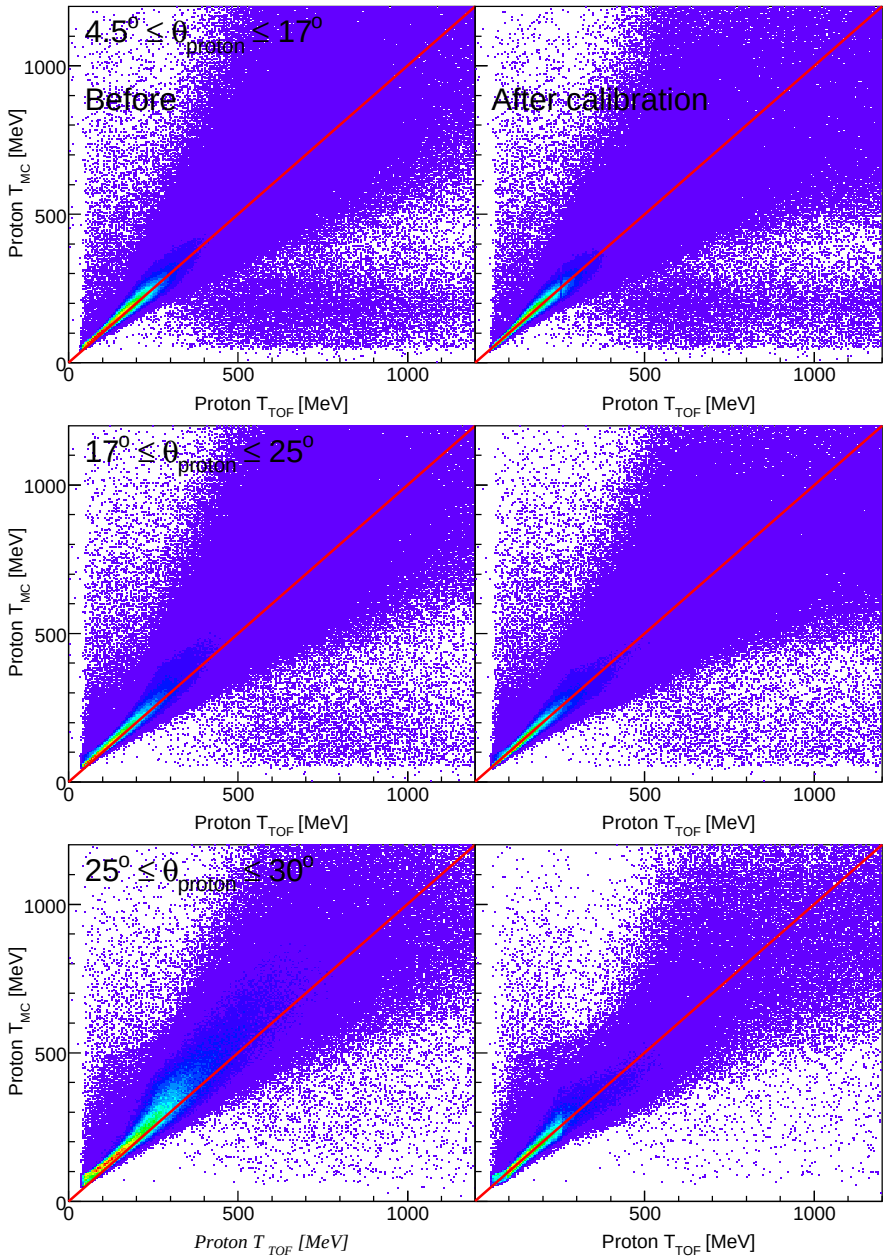

Figure 5.12: *Proton measured kinetic energy versus the proton generated kinetic energy. Left column : before calibration. Right column : after calibration. Top : first flight path, middle second flight path and bottom third flight path.*

Three sets of functions were determined corresponding to three different flight paths. Meaning that the materials were "different" for each flight path. The target is inside a kapton cylinder which is surrounded by a beam-pipe made of aluminum which is sealed by a kapton window. The first flight path (between 4.5^o and 17^o) corresponds to nucleons that are passing the kapton

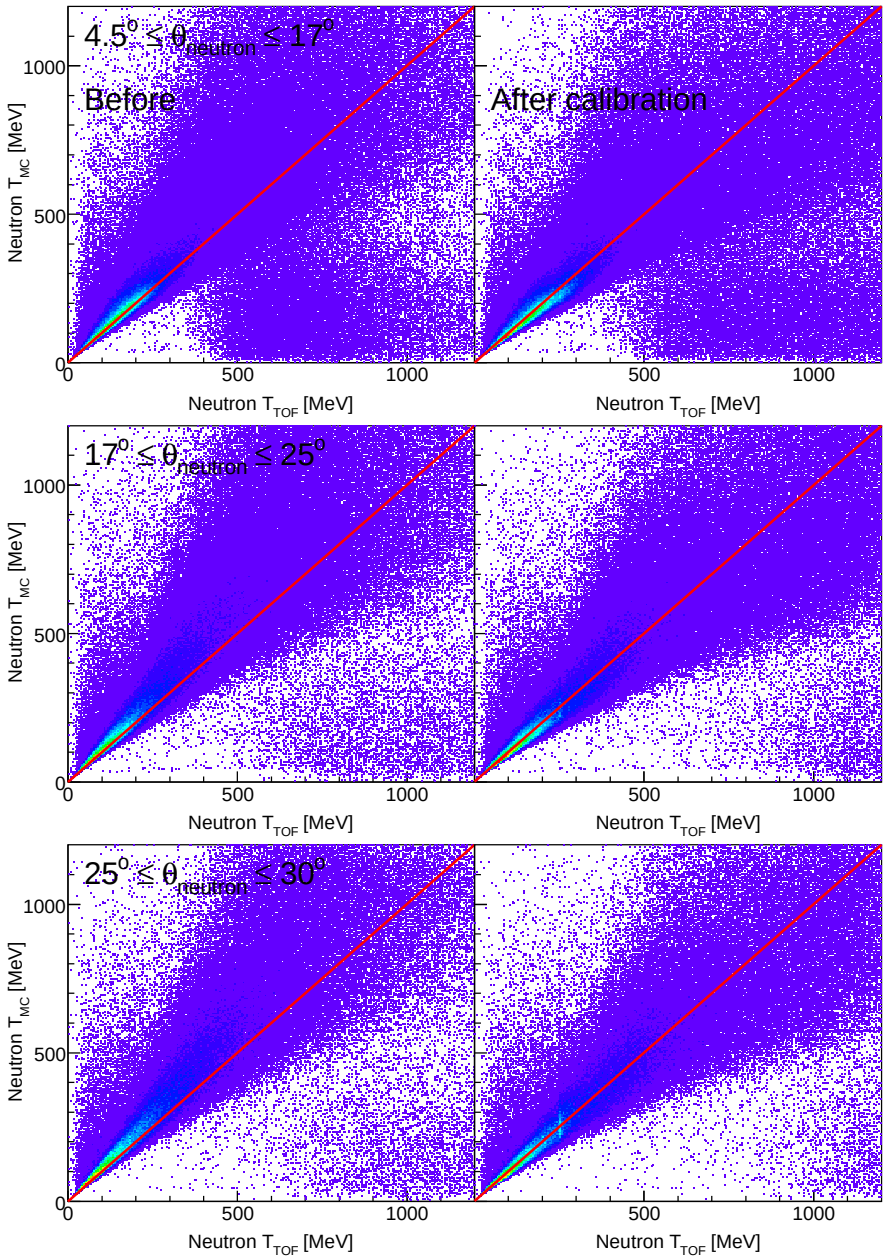

Figure 5.13: *Neutron measured kinetic energy versus the neutron generated kinetic energy. Left column : before calibration. Right column : after calibration. Top : first flight path, middle second flight path and bottom third flight path. The variation of the interaction point is more important for the neutron. The corrections for fast neutrons are more important.*

window. The second flight path (between 17^o and 25^o) corresponds to nucleons that are passing between the edge of the kapton window and the Inner detector. The third flight path (between 25^o and 30^o) corresponds to nucleons that are passing through the Inner-detector.

The uncertainties of the measured kinetic energy is dominated by the TOF resolution of the detector, but the variation of the interaction point also plays a role, then $\Delta T_{kinetic}/T_{kinetic}$ can be written as :

$$\frac{\Delta T_{kinetic}}{T_{kinetic}} = \sqrt{(\frac{\Delta l}{l})^2 + (\frac{\beta^3\gamma^3}{\gamma - 1}\frac{\Delta TOF}{TOF})^2} \tag{5.19}$$

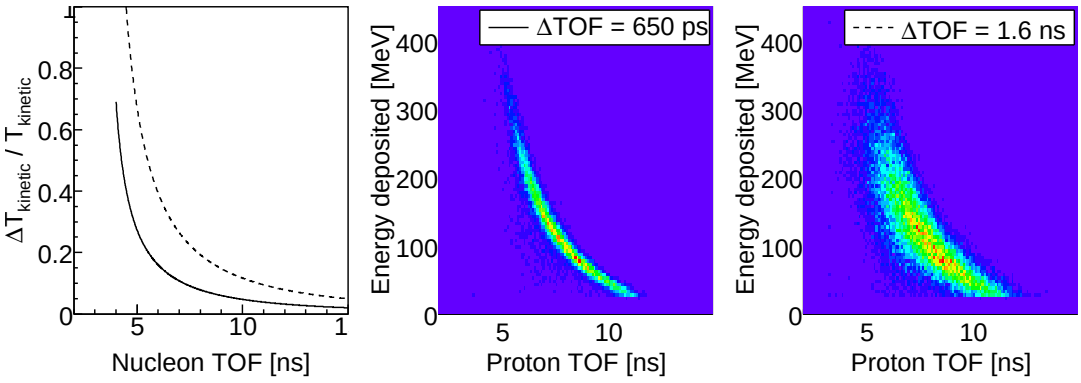

Figure 5.14: *Left: Evolution of the recoil nucleon kinetic energy resolution for different time resolution (in this picture $\frac{\Delta l}{l}$ is not considered). Middle : Proton TOF by using the TAPS resolution of 650 ps. Right : Proton TOF by using the tagging system resolution of 1.6 ns.*

The influence of the time resolution is illustrated in Figure 5.14. The TOF versus the energy deposited is plotted for two time resolutions, the TAPS resolution Figure 5.14 (middle) of 650 ps and the tagging system resolution Figure 5.14 (right) of 1.6 ns. Figure 5.14 (left) shows the calculated kinetic energy resolution from equation 5.19 ($\Delta l/l$ is set to 0) evolution against the TOF.

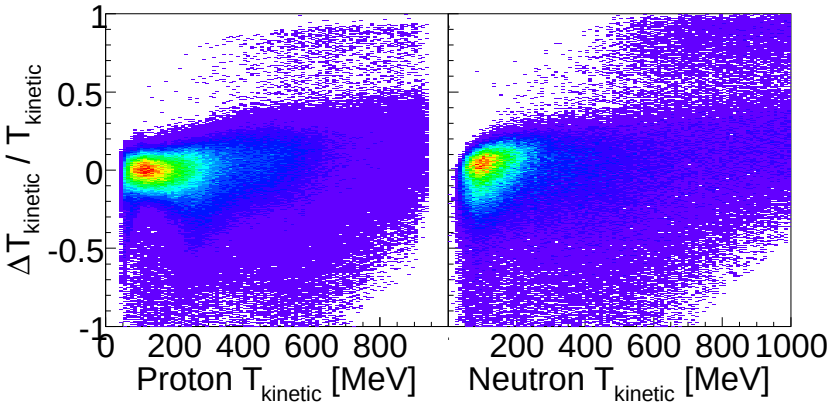

Figure 5.15: *$\Delta T_{kinetic}/T_{kinetic}$ evolution with the $T_{kinetic}$. Left : For proton. Right : For neutron. The resolution gets worst for high energetic nucleons as expected.*

The $\Delta T_{kinetic}/T_{kinetic}$ behavior was checked with MC simulations (see Figure 5.15). The detector responses seem to be treated correctly by the MC simulation. In [116], the $\Delta T_{kinetic}/T_{kinetic}$ due to the variation of the interaction point was estimated between 2 $\%$ and 15 $\%$ for neutron energies between 100 MeV and 1.5 GeV.

5.6.3 The proton detection efficiency

The proton detection efficiency is determined with the data using a missing mass analysis technique.

Two channels, measured with a LH_2 target, were analyzed for this purposes:

- $\gamma + p \rightarrow p + \pi^o\pi^o$ and
- $\gamma + p \rightarrow p + \eta$.

These two reactions have relatively large cross sections so that it yields two different high statistics samples. Furthermore, since there are more than two particles in the final state, the proton kinetic energy and the proton θ-angle in the laboratory vary over a wide range. The proton detection efficiency is for example for the $\gamma + p \rightarrow p + \pi^o\pi^o$, the ratio of events observed in five-hits to the sum of events in five- or four-hits data. In the five-hits sample, we search for two π^o (as explained in section 5.5.2) and a proton (as explained in section 5.3.1). The proton is treated as a missing particle. A missing mass analysis is performed. The missing mass analysis (as explained in section 5.6.1) returns the direction (the $\theta-$angle) and the kinetic energy ($T_{kin.}$) of the "missing" proton. If the calculated missing mass corresponds to the proton mass, we take into account this event. Naturally, the missing mass analysis does return a finite mass as it can be seen in Figure 5.16 (colored lines). In Figure 5.16, Δm is $\Delta m = m_N - m_p$ where m_N corresponds to equation 5.14 and m_p is the proton mass. Therefore, the events selected are between -3σ and $+1\sigma$ around the peak.

In the four-hits sample, we search for two π^o. A missing mass analysis is again performed and returns the direction and the kinetic energy of the missing proton (truly missing this time). The Δm distributions obtained can be seen in Figure 5.16 (black line), again the events selected are between -3σ and $+1\sigma$ around the peak. For both channels a cut on the proton time-of-flight was applied $TOF > 4$ ns in order to remove the photons and the charged pions. For the $2\pi^o-$channel in addition a cut on the π^o mass was applied between 110 MeV and 160 MeV. For the $\eta-$channel also an additional cut was applied on the η mass between 515 MeV and 580 MeV.

The proton detection efficiency is for the $\pi^o\pi^o-$meson channel :

$$\epsilon_{LH_2}^{DATA}(p\pi^o\pi^o) = \frac{5\ hits}{4\ hits + 5\ hits} \tag{5.20}$$

where: $4\ hits$ is $(\pi^o\pi^o)$-events and $5\ hits$ is $(\pi^o\pi^o + p)$-events.

Figure 5.16 shows examples of missing mass distributions for $4\ hits$ and $5\ hits$ events. The events selected are between -3σ and $+1\sigma$ around the peak.

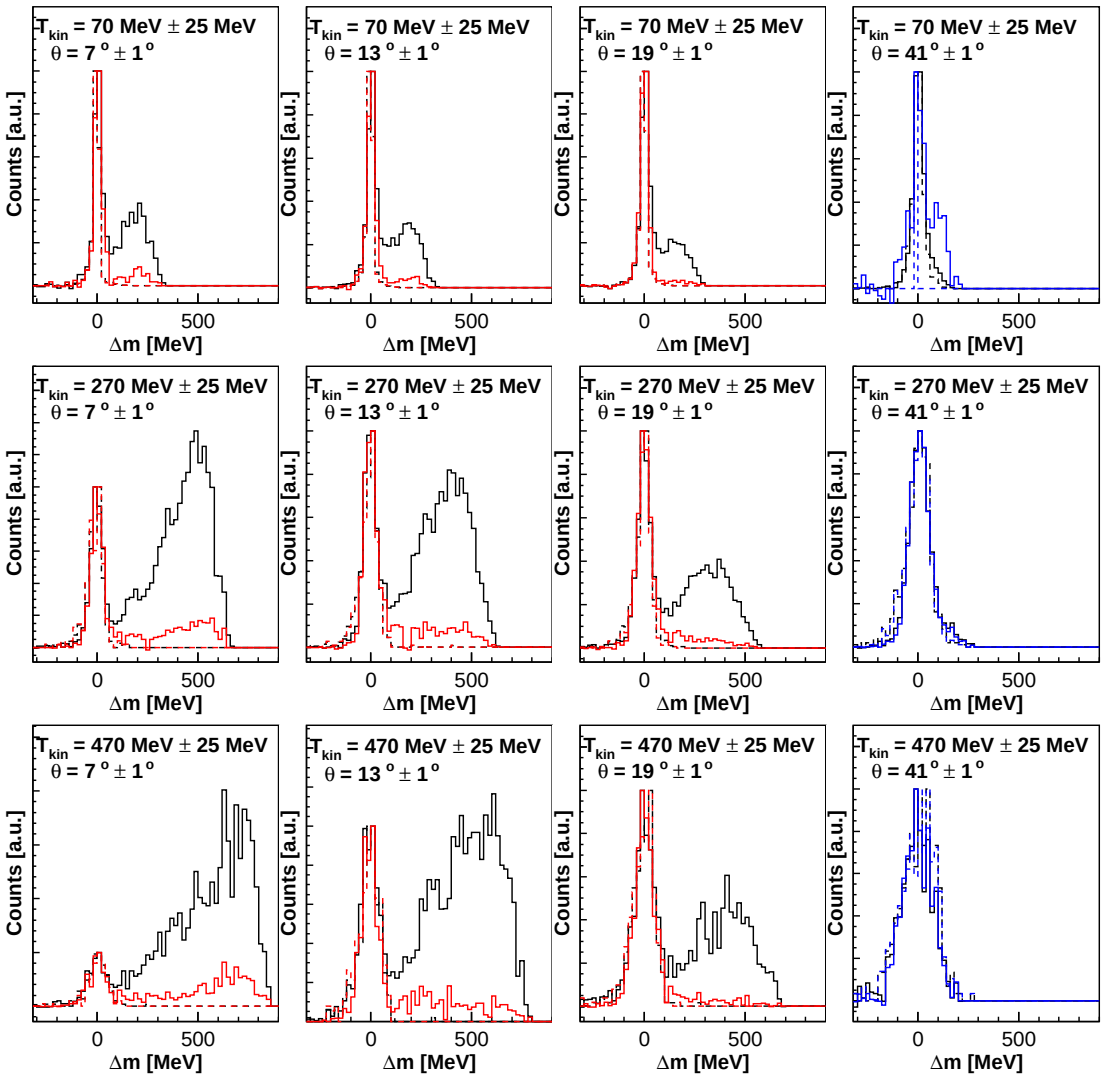

Figure 5.16: *Missing mass distributions for different kinetic energy bin T_{kin} and $\theta-$angle bin of the "missing" proton. The missing mass calculation includes the measured kinematic values of the $\pi^o\pi^o$ and the incident photon beam. The invariant mass $m_{\gamma\gamma}$ of the two π^o is requested between 110 MeV and 160 MeV (4 $hits$ black line, 5 $hits$ colored lines in red for a proton in TAPS in blue for a proton in CB). The distributions have been normalized to each other.*

The proton detection efficiency is for the $\eta-$meson channel :

$$\epsilon_{LH_2}^{DATA}(p\eta) = \frac{7\ hits}{6\ hits + 7\ hits} \tag{5.21}$$

where: $6\ hits$ is $(\pi^o\pi^o\pi^o)$-events and $7\ hits$ is $(\pi^o\pi^o\pi^o + p)$-events.

Figure 5.17 shows examples of missing mass distributions for $6\ hits$ and $7\ hits$ events. The events selected are between -3σ and $+1\sigma$ around the peak.

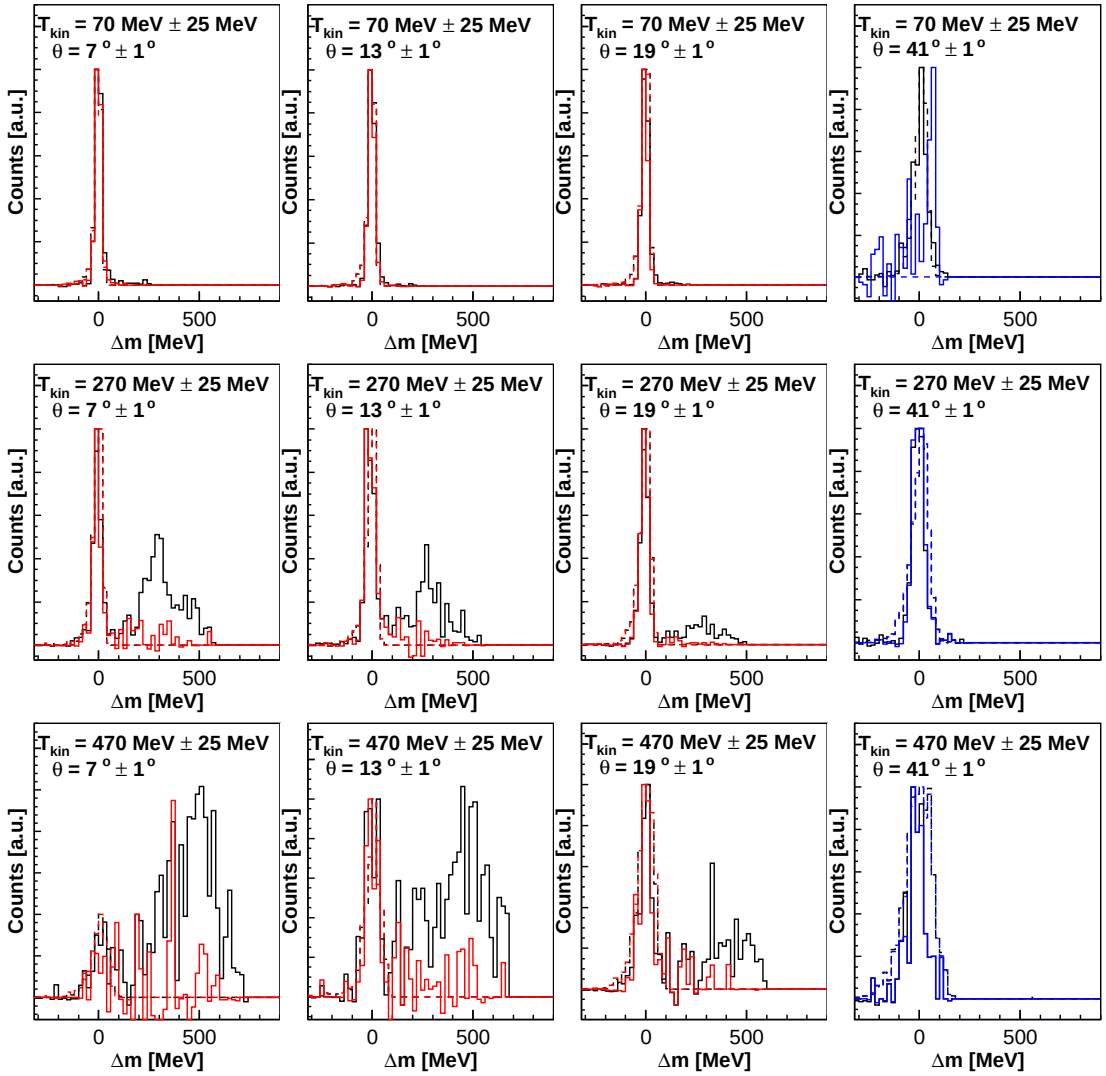

Figure 5.17: *Missing mass distributions for different kinetic energy bin T_{kin} and $\theta-$angle bin of the "missing" proton. The missing mass calculation includes the measured kinematic values of the η and the incident photon beam. The invariant mass $m_{\pi^o\pi^o\pi^o}$ of the three π^o is requested between $515\ MeV$ and $585\ MeV$ ($6\ hits$ black line, $7\ hits$ colored lines in red for a proton in TAPS in blue for a proton in CB). The distributions have been normalized to each other.*

The agreement between data and Monte Carlo simulations was also checked. It is important to correctly estimate the reliability of the Monte Carlo simulations. Indeed, the efficiency determination for the $\pi^o\pi^o-$meson photoproduction off the deuteron relies only on the Monte Carlo simulations as well as the neutron detection efficiency and the signal loss in order to isolate the single-η (and $\eta^{'}$) photoproduction.

The setup behavior (in particular the Inner-detector) is very well established and implemented in Monte Carlo, but not the veto detectors. There were no electronics for readout of the energy deposited in the veto. Thus the energy threshold of the veto is not known. The threshold value has to be approximated with the help of Monte Carlo simulations.

In a first step, the veto inefficiency was used i.e. the fact that photons or electron from the electromagnetic shower produced by the photons fire the veto. This is done by counting the number of π^o detected in TAPS with requesting two neutral hits (i.e. no veto did fire) and with requesting two unidentified hits (i.e. no veto used). Figure 5.18 summarizes the results for the DATA Figure 5.18 (left) and for Monte Carlo simulations Figure 5.18 (right). With the simulations one can play with the threshold of the veto.

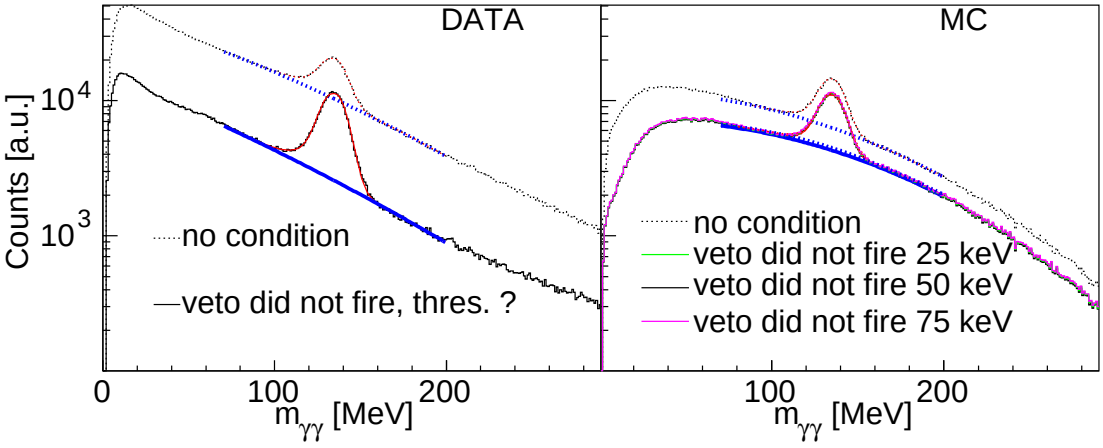

Figure 5.18: *The 2γ invariant mass spectrum for two unidentified hits and for two neutral hits (as defined in section 5.3.2) detected in TAPS. Left : Data (black line veto not used, dotted line veto did not fire). Right : Monte Carlo simulation (black line veto did not fire with a threshold set to 50 keV, green line veto did not fire with a threshold set to 25 keV, violet line veto did not fire with a threshold for to 75 keV, dotted black line veto not used).*

Table 5.5 shows the different results. 14 % of the π^o are lost in data by requesting that no veto did fire. It was decided to set the veto threshold to 50 keV for the MC simulations (the minimum ionizing energy is $\sim$ 1 MeV for the veto).

LED threshold	?	25 keV	50 keV	75 keV
Portion of π^o lost in MC [%]	-	12.4	14.7	21
Portion of π^o lost in DATA [%]	14.27			

Table 5.5: Portion of π^o lost in DATA and MC by requesting that no veto did fire.

In a second step, three channels were simulated with a LD_2 target (the Fermi motion effect was switched off):

- $\gamma + p \rightarrow p + \pi^o\pi^o$,
- $\gamma + p \rightarrow p + \eta$ and
- $\gamma + p \rightarrow p + \eta^{'}$.

The proton detection efficiency is for the $\eta^{'}-$meson channel :

$$\epsilon^{MC}_{LD_2}(p\eta^{'}) = \frac{7\ hits}{6\ hits + 7\ hits} \tag{5.22}$$

where: $6\ hits$ is ($\eta\pi^o\pi^o$)-events and $7\ hits$ is ($\eta\pi^o\pi^o + p$)-events.

In addition, another simulation has been done where the protons have been launched isotropically into the detectors. In that case :

$$\epsilon^{MC}_{LD_2}(p) = \frac{N_{detected}}{N_{started}} \tag{5.23}$$

The Figures 5.19, 5.21, 5.20, 5.21 and 5.22 summarize the results.

Figures 5.19 and 5.20 summarize the proton detection efficiency in TAPS. In Figure 5.19 are plotted the efficiencies $\epsilon^{MC}_{LD_2}(p)$, $\epsilon^{MC}_{LD_2}(p\pi^o\pi^o)$, $\epsilon^{DATA}_{LH_2}(p\pi^o\pi^o)$, $\epsilon^{DATA}_{LH_2}(p\pi^o\pi^o + p\eta)$ versus the proton kinetic energy for different $\theta-$angle bins. In Figure 5.20 are plotted the systematic differences between the measured efficiencies : $\epsilon^{DATA}_{LH_2}(p\eta)/\epsilon^{DATA}_{LH_2}(p\pi^o\pi^o)$, the systematic difference between Monte Carlo and data : $\epsilon^{DATA}_{LH_2}(p\eta)/\epsilon^{MC}_{LD_2}(p\eta)$ and $\epsilon^{DATA}_{LH_2}(p\pi^o\pi^o)/\epsilon^{MC}_{LD_2}(p\pi^o\pi^o)$ and the systematic difference between $\epsilon^{MC}_{LD_2}(p\pi^o\pi^o)/\epsilon^{MC}_{LD_2}(p)$. The measurements from channels $\gamma + p \rightarrow p + \pi^o\pi^o$ and $\gamma + p \rightarrow p + \eta$ give the same results within $\pm$ 10 % (Fig. 5.20). The comparison with the same simulated channels are similar within $\pm$ 10 % for protons with kinetic energies below 600 MeV. For protons with kinetic energies above 600 MeV, data and Monte Carlo do not match anymore. The cut on the proton time-of-flight of 4 ns corresponds to protons with a kinetic energy of ≈710 MeV, but as the resolution is changing with the proton velocity (worst for the fastest protons) also some protons with energies larger

than 710 MeV are included. Thus there might be three reasons for this mismatch : the time resolution, hardware or physics. There is also a small angle dependence that might come from the target position. The simulations were done with the target at the center of the setup, but in the measurement the LH_2 target was displaced by z= -7 cm (the LD_2 target was also displaced for one measurement, but for the three other measurements the LD_2 target was at the center of the setup).

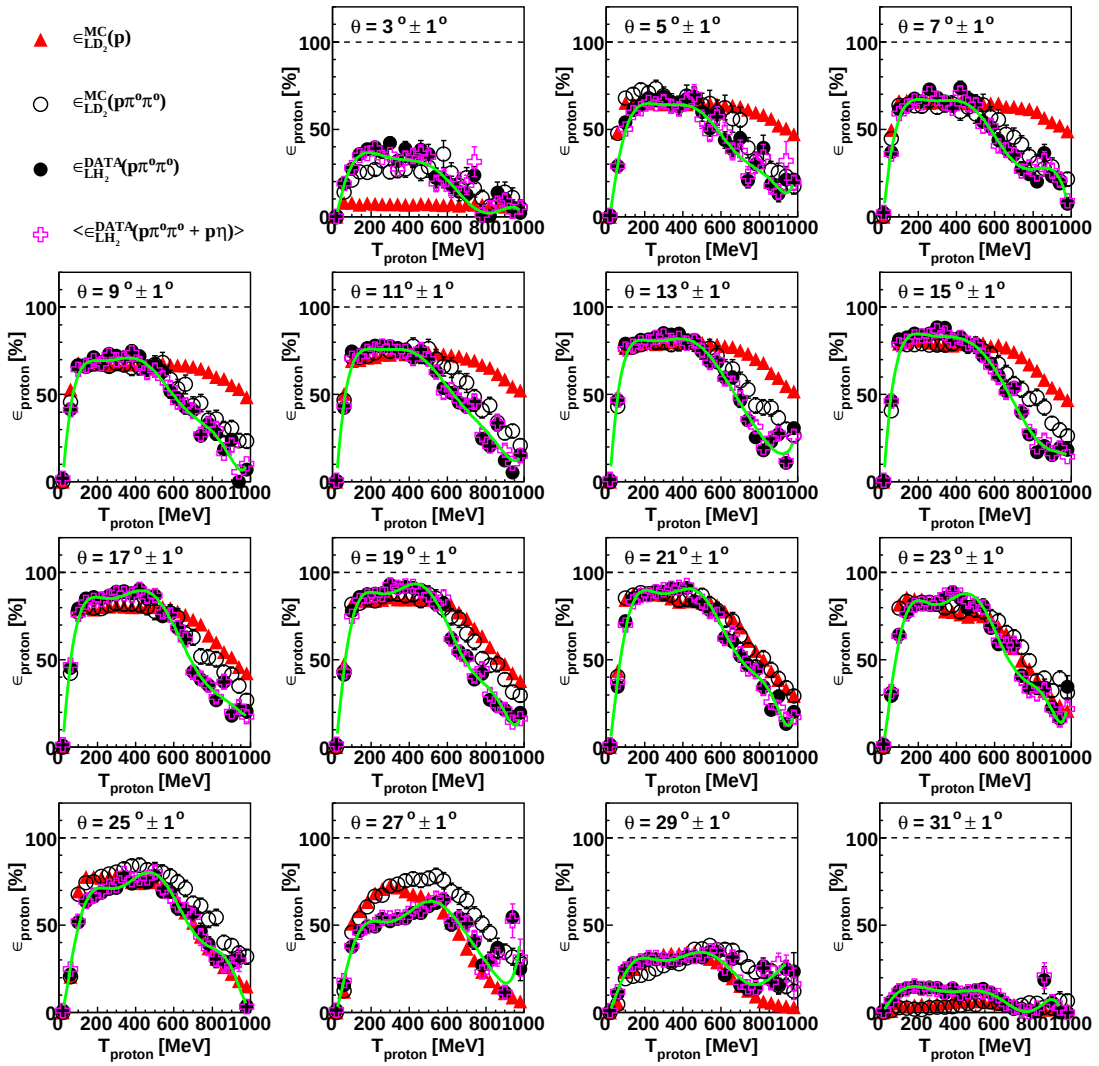

Figure 5.19: *The proton detection efficiency in TAPS for different θ−angle bin. ($\epsilon^{DATA}_{LH_2}(p\pi^o\pi^o)$ black points, $\epsilon^{DATA}_{LH_2}(p\pi^o\pi^o + p\eta)$ violet cross which is the average of $\epsilon^{DATA}_{LH_2}(p\pi^o\pi^o)$ and $\epsilon^{DATA}_{LH_2}(p\eta)$, $\epsilon^{MC}_{LD_2}(p\pi^o\pi^o)$ open black circle and $\epsilon^{MC}_{LD_2}(p)$ red triangle). The green line is a fit (by a polynom of 8th order) of the $\epsilon^{DATA}_{LH_2}(p\pi^o\pi^o + p\eta)$.*

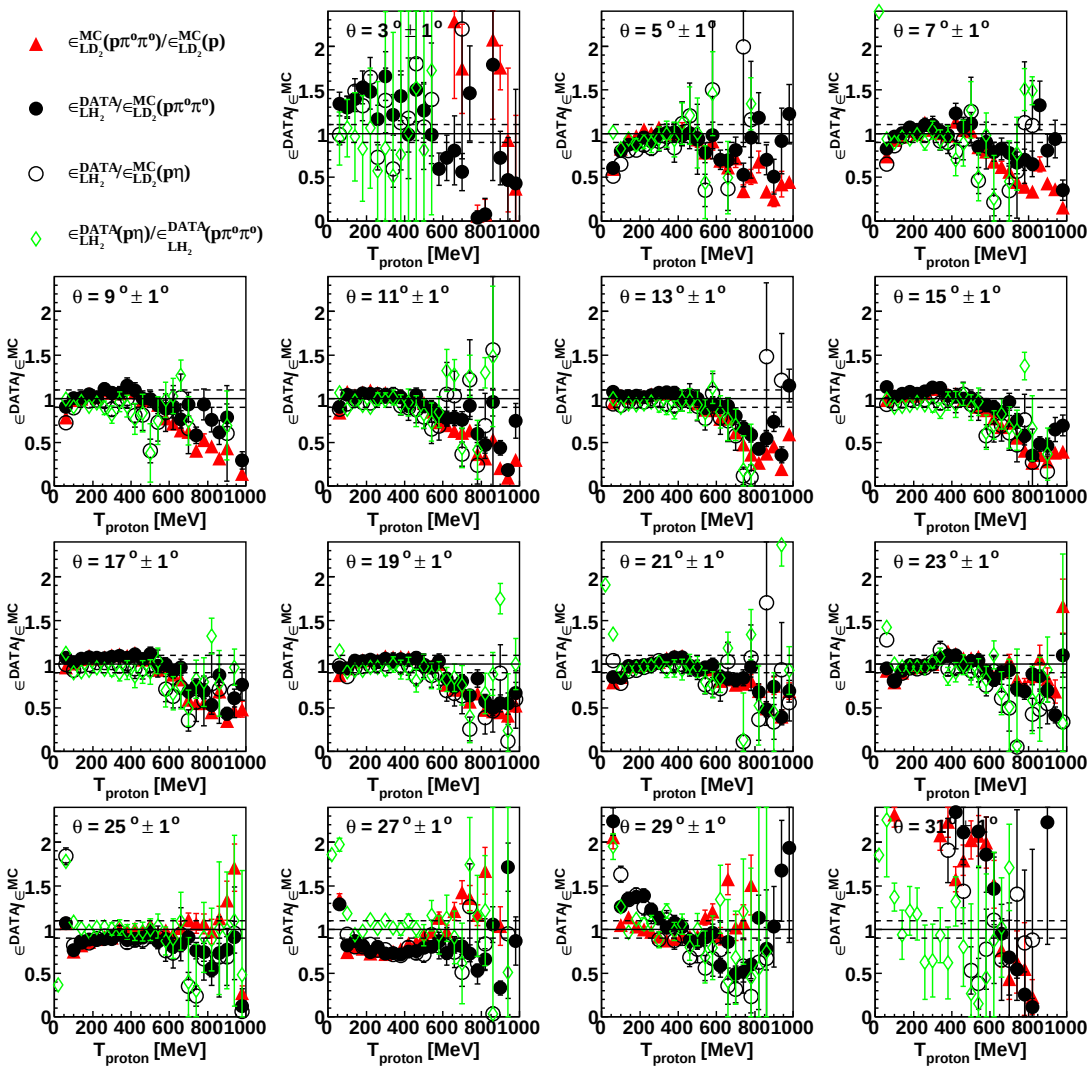

Figure 5.20: *The proton detection efficiency systematic difference in TAPS between data and between data and Monte Carlo for different $\theta-$angle bin. ($\epsilon^{MC}_{LD_2}(p\pi^o\pi^o)/\epsilon^{MC}_{LD_2}(p)$ red triangle, $\epsilon^{DATA}_{LH_2}(p\pi^o\pi^o)/\epsilon^{MC}_{LD_2}(p\pi^o\pi^o)$ black point, $\epsilon^{DATA}_{LH_2}(p\eta)/\epsilon^{MC}_{LD_2}(p\eta)$ open black circle and $\epsilon^{DATA}_{LH_2}(p\eta)/\epsilon^{DATA}_{LH_2}(p\pi^o\pi^o)$ open green diamond.)*

Figures 5.21 and 5.22 concerned the proton detection efficiency in CB. Figures 5.21 shows that there is no angle dependence.

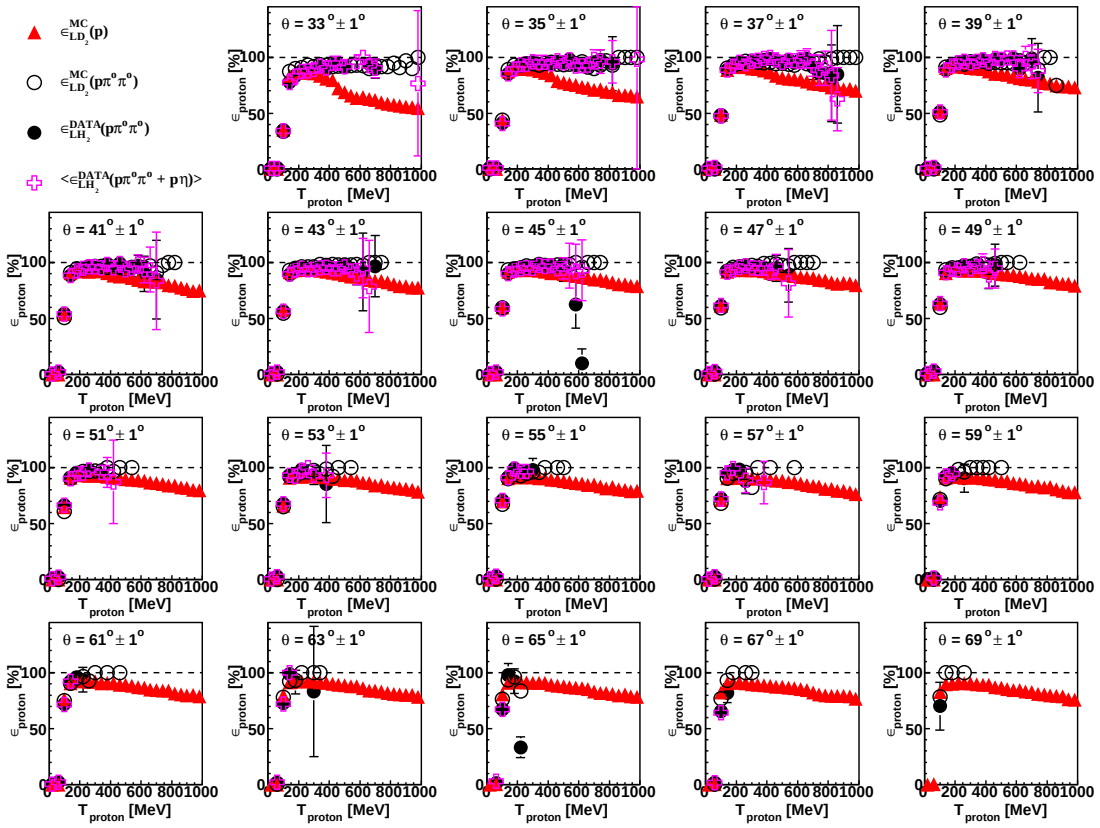

Figure 5.21: *The proton detection efficiency in CB for different $\theta-$angle bin. ($\epsilon^{DATA}_{LH_2}(p\pi^o\pi^o)$ black points, $\epsilon^{DATA}_{LH_2}(p\pi^o\pi^o + p\eta)$ violet cross which is the average of $\epsilon^{DATA}_{LH_2}(p\pi^o\pi^o)$ and $\epsilon^{DATA}_{LH_2}(p\eta)$, $\epsilon^{MC}_{LD_2}(p\pi^o\pi^o)$ open black circle and $\epsilon^{MC}_{LD_2}(p)$ red triangle). There are no angular dependences as expected.*

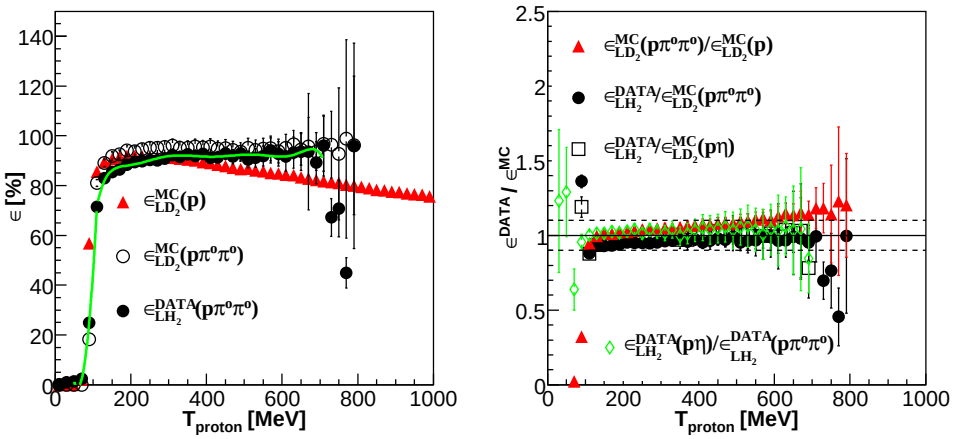

Figure 5.22: *Left : The proton detection efficiency in CB. ($\epsilon^{DATA}_{LH_2}$ $(p\pi^o\pi^o)$ black points, $\epsilon^{MC}_{LD_2}$ $(p\pi^o\pi^o)$ open black circle and $\epsilon^{MC}_{LD_2}(p)$ red triangle). Right : The proton detection efficiency systematic difference in CB between data and between data and Monte Carlo. ($\epsilon^{MC}_{LD_2}(p\pi^o\pi^o)/\epsilon^{MC}_{LD_2}(p)$ red triangle, $\epsilon^{DATA}_{LH_2}(p\pi^o\pi^o)/\epsilon^{MC}_{LD_2}(p\pi^o\pi^o)$ black point, $\epsilon^{DATA}_{LH_2}(p\eta)/\epsilon^{MC}_{LD_2}(p\eta)$ open black circle and $\epsilon^{DATA}_{LH_2}(p\eta)/\epsilon^{DATA}_{LH_2}(p\pi^o\pi^o)$ open green diamond). The green line is a fit (by a polynom of 8th order) of the $\epsilon^{DATA}_{LH_2}(p\pi^o\pi^o + p\eta)$.*

Figure 5.22 (left) shows the proton detection efficiency in CB. There is a good agreement between DATA and the Monte Carlo simulations ± 10 % (see Figure 5.22-right).

5.6.4 The neutron detection efficiency

For this experiment, there was no possibility to measure from the data the neutron detection efficiency. Therefore we have to rely on the Monte Carlo simulation to determine the neutron detection efficiency.

There was also no applicable neutron detection efficiency from past measurements. The previously measured neutron detection efficiency in TAPS [117] was biased by the poor efficiency of the old veto system (was replaced before this experiment) and the CFD threshold was at 1 MeV instead of 10 MeV for this experiment. For the experiment CB-LEAR at CERN, the neutron detection efficiency was measured [118] but the thresholds for the cluster and the hits were different. However, we could use this measurement to test our Monte Carlo simulations by setting the threshold and the cluster threshold as they were supposed to be.

For the most realistic simulations the GCALOR program package was installed [119]. The GCALOR simulates hadronic interactions from 1 MeV to several GeV. It is a compilation of different programs that calculate the reaction mechanisms of the neutron with matter depending on the energy region. The neutron looses its energy by nuclear processes : elastic and inelastic scattering off nuclei, radiative capture (n, γ) or reaction of the type (n, p), (n, d). All this reactions (except for the elastic scattering) produce secondary particles which are measured. This is why the interaction point of the neutron along the length of the detector can vary.

The neutron detection efficiency was deduced from the following simulated channels :

- isotropic n,
- $\gamma + n \rightarrow n + \pi^o\pi^o$,
- $\gamma + n \rightarrow n + \eta$ and
- $\gamma + n \rightarrow n + \eta^{'}$.

The neutron detection efficiency was also deduced from a missing mass analysis technique. The same cuts as for the protons were applied. The neutron in CB and in TAPS was selected by the χ^2-test. Thus it is important to check if the efficiency remains the same or changes for the different channels studied.

Figure 5.23, 5.24 and 5.25 summarizes the results. The neutron detection efficiency is on average 15 $\%$ in TAPS and 25 $\%$ in CB. The three channels

have similar neutron detection efficiencies (see the systematic differences of Figure 5.24 and 5.25). The neutron detection efficiency was however deduced for each channel.

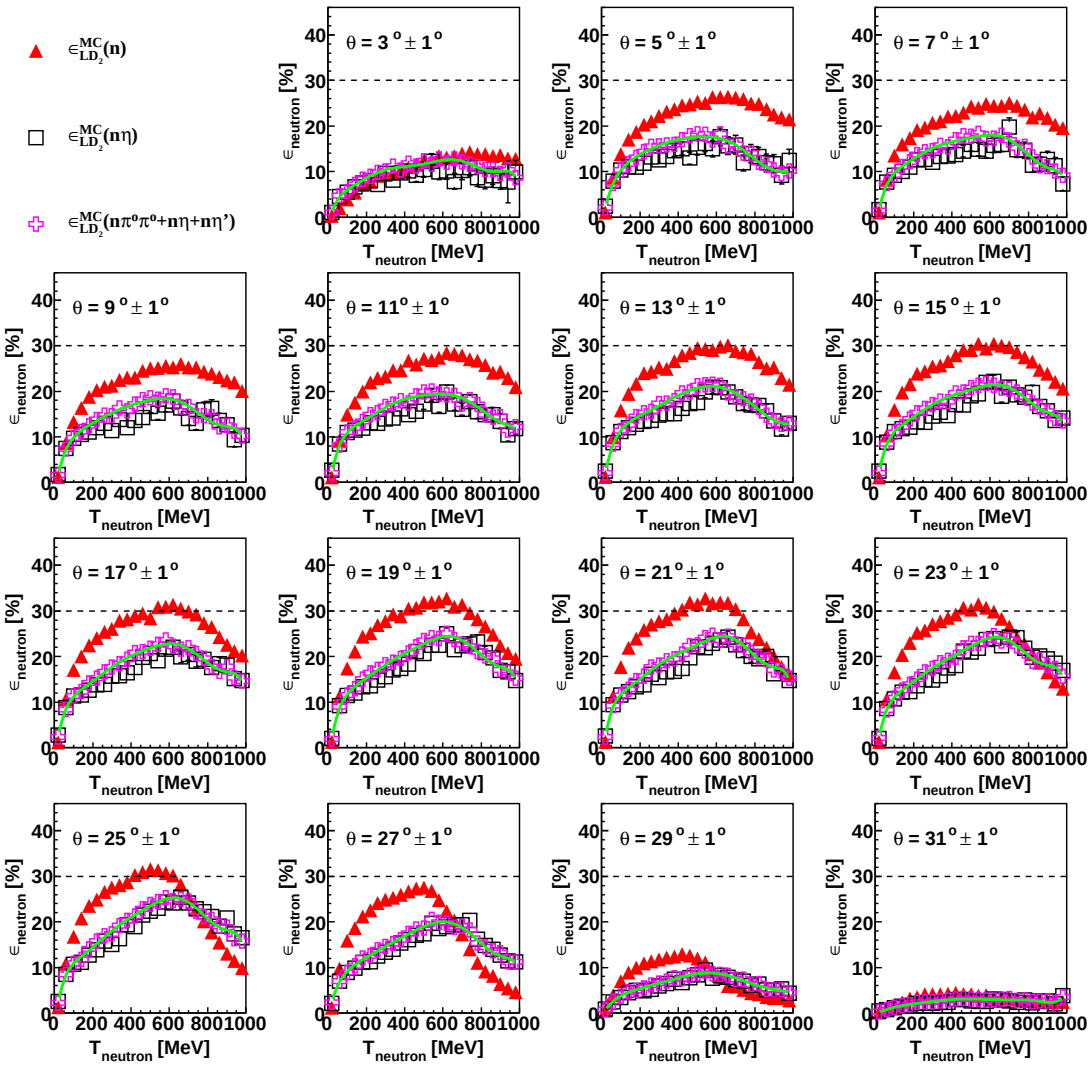

Figure 5.23: *The neutron detection efficiency in TAPS for different θ−angle bin. ($\epsilon^{MC}_{LD_2}(n\pi^o\pi^o + n\eta + n\eta^{'})$ violet cross which is the average of $\epsilon^{MC}_{LD_2}$ $(n\pi^o\pi^o)$, $\epsilon^{MC}_{LD_2}(n\eta)$ and $\epsilon^{MC}_{LD_2}(n\eta^{'})$, $\epsilon^{MC}_{LD_2}(n\eta)$ open black squared and $\epsilon^{MC}_{LD_2}(n)$ red triangle). The green line is a fit (by a polynom of 8th order) of the $\epsilon^{MC}_{LD_2}(n\pi^o\pi^o + n\eta + n\eta^{'})$.*

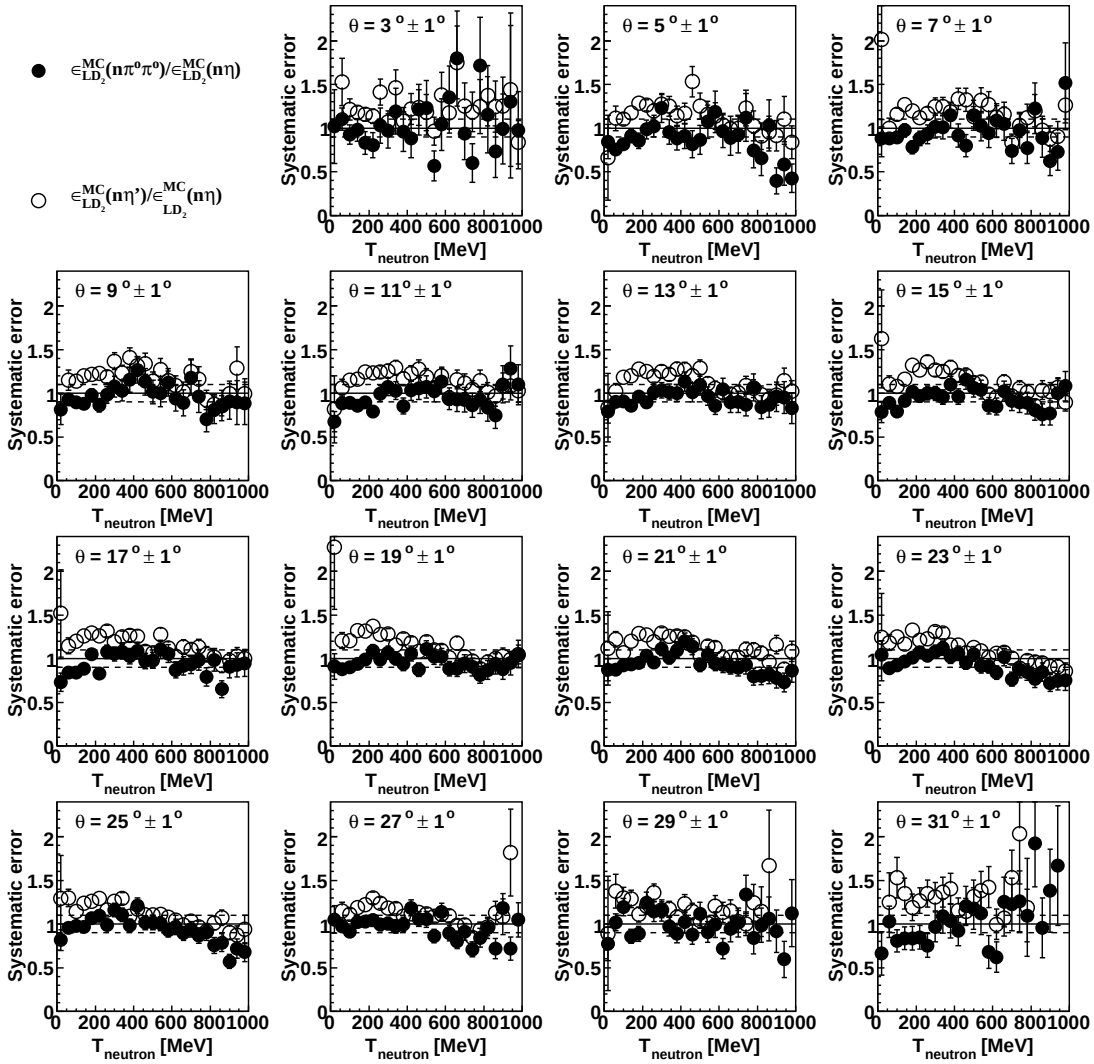

Figure 5.24: *The neutron detection efficiency systematic difference in TAPS between the different channels for different $\theta-$angle bin. ($\epsilon^{MC}_{LD_2}(n\pi^o\pi^o)/\epsilon^{MC}_{LD_2}(n\eta)$ black point, $\epsilon^{MC}_{LD_2}(n\eta)/\epsilon^{MC}_{LD_2}(n\eta^{'})$ open black circle).*

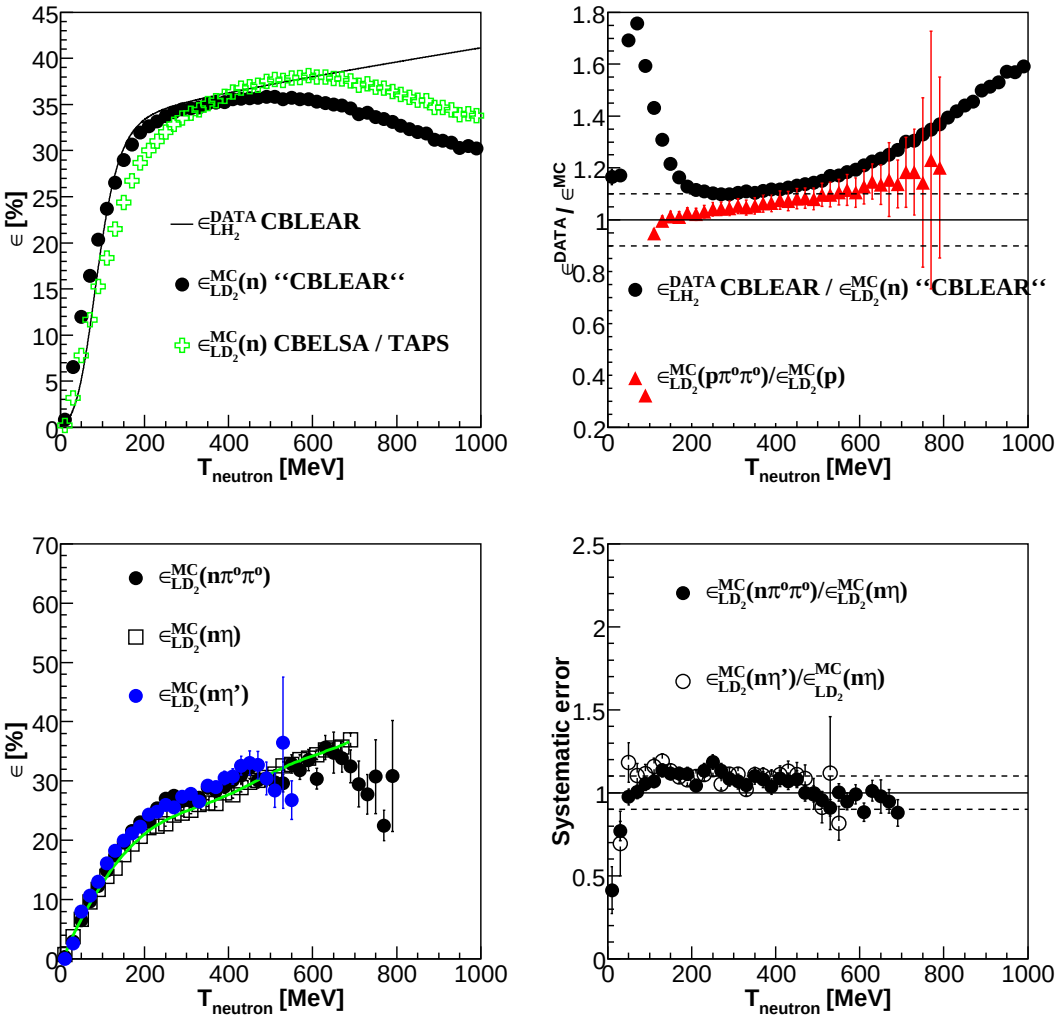

Figure 5.25: *Top left : The neutron detection efficiency in CB for LEAR experiment in CERN. (black line $\epsilon^{DATA}_{LH_2}$ parametrization of the measured neutron detection efficiency in CBLEAR experiment at CERN, black points $\epsilon^{MC}_{LD_2}(n)$ simulated "CBLEAR" conditions and open black circle $\epsilon^{MC}_{LD_2}(n)$ simulated CBELSA/TAPS). Top right : The neutron detection efficiency systematic difference in CB between data and Monte Carlo. ($\epsilon^{DATA}_{LH_2} CBLEAR/\epsilon^{MC}_{LD_2}$"$CBLEAR$" black points and $epsilon^{MC}_{LD_2}(p\pi^o\pi^o)/\epsilon^{MC}_{LD_2}(p)$ red triangle). Bottom left : The neutron detection efficiency in CB for this experiment simulated. ($\epsilon^{MC}_{LD_2}(n\pi^o\pi^o)$ black points, $epsilon^{MC}_{LD_2}(n\eta)$ open black squared and $\epsilon^{MC}_{LD_2}(n\eta^{'})$ blue circle). The green line is a fit (by a polynom of 8th order) of the $\epsilon^{MC}_{LD_2}(n\pi^o\pi^o + n\eta + n\eta^{'})$. Bottom right : The neutron detection efficiency systematic difference between the different channels simulated. ($\epsilon^{MC}_{LD_2}(n\pi^o\pi^o)/\epsilon^{MC}_{LD_2}(n\eta)$ black point, $\epsilon^{MC}_{LD_2}(n\eta^{'}/\epsilon^{MC}_{LD_2}(n\eta))$ open black circle).*

5.6.5 The Inner- and the veto detectors detection efficiencies

In order to estimate the fraction of protons that are mis-identified as neutrons, the Innner-detector and the veto detectors efficiencies were deduced from Monte Carlo simulations. Figure 5.26 shows the results. The proton contamination is on average 4 % in TAPS and 2.5 % in CB.

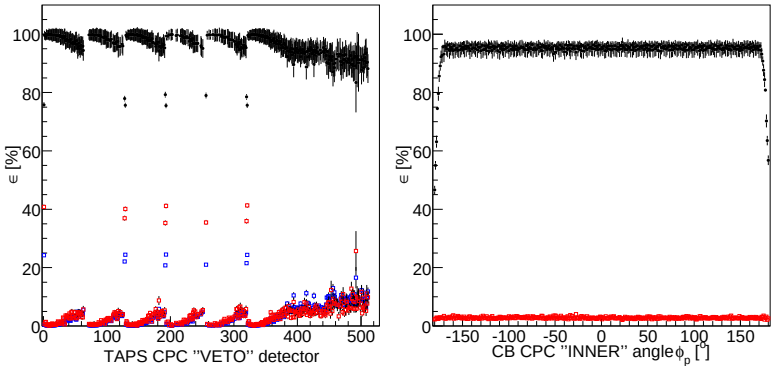

Figure 5.26: *The charged particle counter detectors efficiencies. Left : for the veto detectors. (the black point is the efficiency for protons, the colored points are the fraction of protons that are mis-identified as neutrons). Right : for the Inner detector. (the black point is the efficiency for proton, the colored point is the fraction of protons that are mis-identified as neutrons)*

The fraction of protons that are mis-identified can be also approximated from the data via the time-of-flight - versus - energy analysis (Figure 5.11). To be fair, it should be done for reactions clearly identified with the same cuts. In this case, it was : $\gamma + d \rightarrow \eta + p(n)$ for the proton TOF and $\gamma + d \rightarrow \eta + n(p)$ for the neutron TOF.

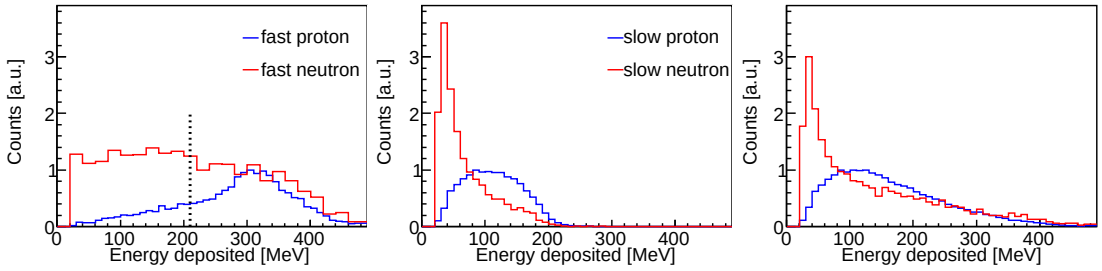

Figure 5.27: *The TOF projection on the y-axis. Left : for the fast recoil nucleon with* $4\ ns \leq TOF \leq 5\ ns$. *Middle : for slow recoil nucleon with* $6\ ns \leq TOF \leq 10\ ns$. *Right : for recoil nucleon* $2\ ns \leq TOF \leq 10\ ns$. *(red line neutron, blue line proton). No clear signs of proton contamination.*

For different time bins a projection on the y-axis is done. The neutron is normalized to the proton banana which served as reference point. The results

are shown in Figure 5.27. There are no clear signs of proton contamination. One would expect to see for example in Figure 5.27 (left) also a peak around 310 MeV for the neutron. But the red histograms is almost flat from 25 MeV to 310 MeV. Nevertheless if we considered Figure 5.27 (left) as correct, for TOF between 4 ns and 5 ns and an energy deposited below 210 MeV (dashed line vertical in Figure 5.27-left), the contamination is estimated to $\sim 12\ \%$ and without any cut on the energy deposited the contamination is $\sim 40\ \%$. These values were obtained by making the ratio between the integration of the blue histogram (proton) and the integration of the red histogram (neutron). For slow proton, Figure 5.27 (middle), the proton contamination is considered negligible. As $\sim 30\ \%$ of the neutrons are between 4 ns and 5 ns, the overall proton contamination is estimated for neutrons between 4 ns and 15 ns to $\sim 1.35\ \%$. However to be on the safe side, cuts on the TOF - versus - energy were applied.

5.6.6 The TOF cuts

For all the measurements performed : only protons with a TOF $>$ 4 ns were taken into account (Figure 5.28-left) and only neutrons that are on the right side of the black lines show in Figure 5.28-right are taken into account. The

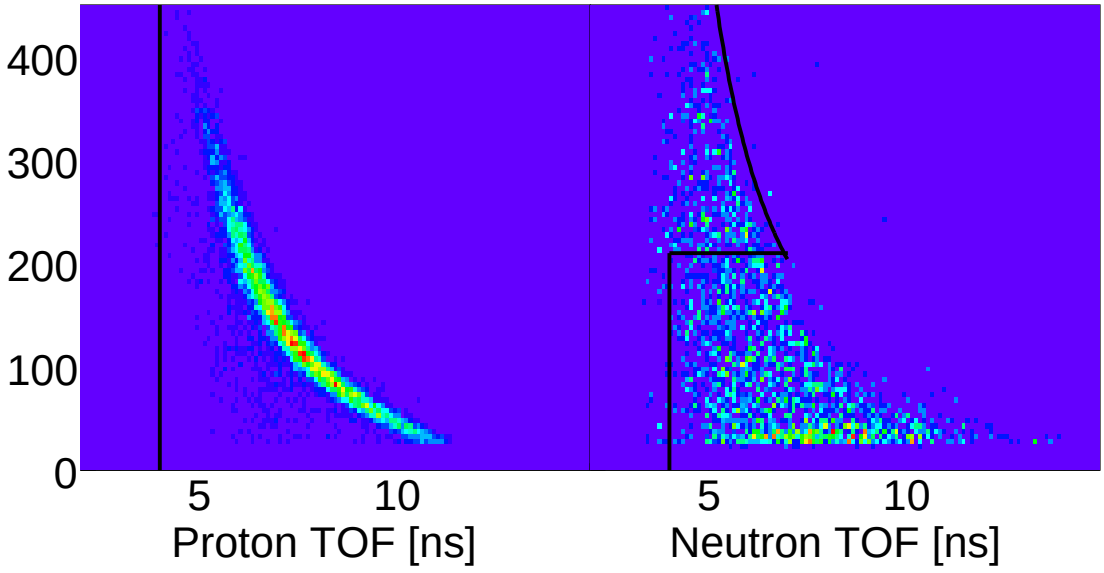

Figure 5.28: *Time-of-flight versus energy deposited of the recoil nucleon with the TOF cuts applied. Left : for protons of the reaction $\gamma + d \rightarrow \eta + p(n)$. Right : for the neutrons for the reaction $\gamma + d \rightarrow \eta + n(p)$. The black lines show the cuts applied.*

effect by the neutron TOF cuts, on the proton contamination, can be seen in 5.26 (left), red points TOF $>$ 4 ns and blue points neutron TOF cuts.

Results

This chapter presents the results of

- $\gamma + d \rightarrow\ meson(s)\ + NNX$, the full inclusive reaction,
- $\gamma + d \rightarrow\ meson(s)\ + (pn)$, the quasi-free inclusive reaction,
- $\gamma + d \rightarrow\ meson(s)\ + p(n)$, the quasi-free proton exclusive reaction and
- $\gamma + d \rightarrow\ meson(s)\ + n(p)$, the quasi-free neutron exclusive reaction.

(where $meson(s) = \pi^o\pi^o\ or\ \eta\ or\ \eta^{'}$)

For each channel, the procedure was the same. First, the channel is identified as well as the sources of background by a missing mass analysis. Then, the signal and the background is reproduced by Monte-Carlo simulations. The cuts are defined so that the signal-to-background ratio is optimal. Secondly, the efficiencies are determined. Finally, the observables are extracted. The observables extracted are the differential and total cross sections.

6.1 The Differential and Total Cross Sections

6.1.1 The formula

$$\frac{d\sigma}{d\Omega}(E_\gamma,\theta) = \frac{N(E_\gamma,\theta)}{\epsilon_\gamma(E_\gamma)\rho N_{scaler}(E_\gamma)\Omega\Gamma_m\epsilon_r(E_\gamma,\theta)} \tag{6.1}$$

where :

- N is the event number detected of the desired reaction in that E_γ and θ cell (θ is angle in the center-of-mass of the incident photon beam frame),
- ϵ_γ is the tagging efficiency for that E_γ,
- ρ is the target density [$nuclei/cm^2$]

$$\rho = \frac{N_A.\rho_{LD_2}.l_{target}}{A_d} \tag{6.2}$$

  where:
  N_A is the Avogadro number ($N_A = 6.022136.10^{23}$ mol^{-1}),
  ρ_{LD_2} is the liquid deuterium density (ρ_{LD_2} =0.169 g/cm^3),
  l_{target} is the target length (l =5.3 cm) and,
  A_d is the atomic weight (A_d = 2.0141 g/mol).
- N_{scaler} is the number of tagger scaler counts,
- Ω is the solid angle of the angular bin [sr],
- Γ_m is the branching ratio of the decay and
- ϵ_r is the reaction detection efficiency in that E_γ and θ cell.
  ϵ_r is obtained by comparing the initial number, $N^{started}$, created in the simulation with the number of detected events, $N^{detected}$,after the analysis:

$$\epsilon_r = \frac{N^{detected}}{N^{started}} \tag{6.3}$$

The total cross section can be obtained directly or by integrating the differential cross section. In practice this was done by summing over the angle bins.

$$\sigma = \frac{N(E_\gamma)}{\epsilon_\gamma(E_\gamma)\rho N_{scaler}(E_\gamma)\Gamma_m\epsilon_r(E_\gamma)} \tag{6.4}$$

$$\sigma = \int \frac{d\sigma}{d\Omega}(E_\gamma,\theta)d\Omega \sim 2\pi \sum_{\theta\ bin} \frac{d\sigma}{d\Omega}(E_\gamma,\theta)sin\theta.\Delta\theta \tag{6.5}$$

6.1.2 The photon flux

The photon flux, ϕ, is the photon number per second that reaches the liquid deuterium target and is proportional to $\frac{1}{E_\gamma}$ (section 3.2.1).

The tagging system provides the tagged photon number (section 3.2.2 : $N^{e^-}_{scaler}$). Due to the beam dispersion not all the photons can reach the liquid deuterium target. Furthermore just after the copper target, the photons are collimated in order to be aligned with the target. Thus :

$$\phi(E_\gamma) = \frac{N^{e^-}_{scaler}(E_\gamma) \times \epsilon_\gamma(E_\gamma)}{\Delta E_\gamma . \Delta t} \tag{6.6}$$

where:
ΔE_γ is the incident photon beam step and
Δt is the number of hours of beam time.

The scalers : $N^{e^-}_{scaler}(E_\gamma)$

The scalers are counted over the spill time, whereas the data acquisition is recorded over the life time. Thus, the scalers have to be corrected for dead time effects. Figure 6.1 shows a typical scaler spectrum (left) and the ratio between life time and spill time (right).

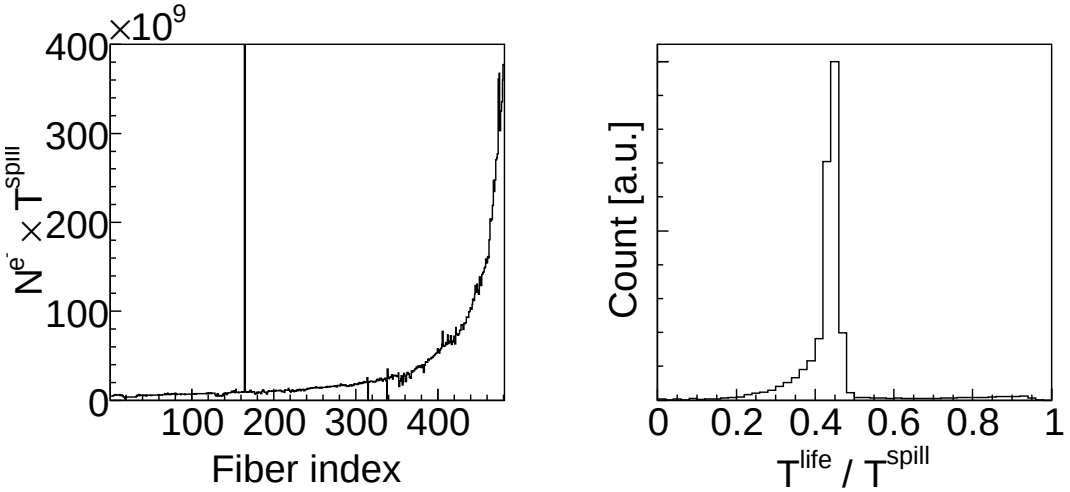

Figure 6.1: *Left : Scaler spectra. Right : Ratio between life time and spill time. The dead time is* $\approx 40\ \%$.

In addition, the scaler modules suffered from a defect. In principle, every

second the scalers were recorded onto tape and initialized to 0. But due to a hardware problem from time to time they were initialized between two scaler events. This random initialization was tracked and the badly recorded scaler events were removed from the analysis.

The tagging efficiency : $\epsilon_\gamma(E_\gamma)$

The tagging efficiency is the probability that a tagged photon reaches the liquid deuterium target. For this purpose, one has to record the number of the tagged photons $N^{e^-}_{scaler}$ recorded by the scalers, and the number of the photons, $N^{\gamma}_{\gamma-veto}$, that are passing through the collimator and reach the liquid deuterium target (99.99 $\%$ of the photons are passing through the target without interacting with the nucleons).

In order to enhance these events a special trigger was used for this measurement : an "OR" between the 14 tagger scintillator bars.

Then, the tagging efficiency is :

$$\epsilon_\gamma = \frac{N^{\gamma}_{\gamma-veto}}{N^{e^-}_{scaler}} \tag{6.7}$$

As the trigger was not derived from the scintillator fibers and we want to know the tagging efficency per fiber, the first step is to determine the time base i.e. the time over which the scintillator fiber and the $\gamma-$veto are counting in parallel (for more details read the internal report [Daniel]).

The time base could only be determined when the bar scintillator TDC was equal to zero because the start and the stop can only be seen in the scintillator fiber TDCs in the underflow of the bar scintillator TDCs. Figure 6.2 shows the scintillator fiber TDC and the $\gamma-$veto TDC spectra when the bar scintillator TDC was equal to zero. The two peaks in the fiber scintillator TDC spectra correspond to the start and the stop. There is no underflow with multi-hit TDCs. These two peaks determine the time base (Figure 6.2-top red part), which is then used for the γ-veto (Figure 6.2-bottom red part).

The tagging efficiency measurement was performed at low (0.3 MHz) and high (20 MHz) rates. The advantage, to measure the tagging efficiency at low rates, is that there is no problem of multi-hits in the tagging system.

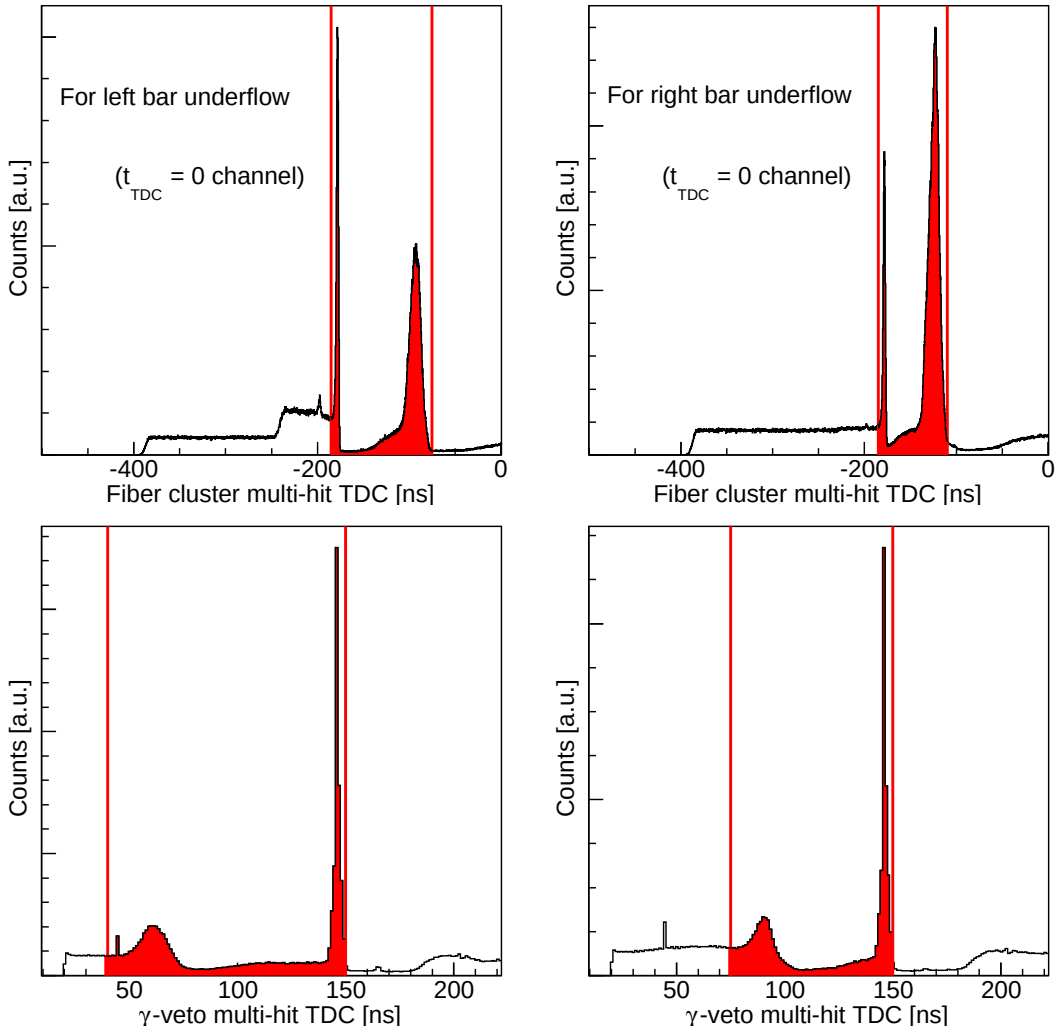

Figure 6.2: *Top left : for bar scintillator left TDC = 0, the fiber scintillator TDC spectrum. Top right : for bar scintillator right TDC = 0, the fiber scintillator spectrum. Bottom the same for the $\gamma-$veto spectra. The time base for the left bars, it is $\approx$ 100 ns; and the right bars, it is $\approx$ 80 ns.*

The tagging efficiency was measured every four to eight hours (see Figure 6.3). The data were taken in four beam times. The table below summarizes the characteristics of each beam time.

Caracteristcs	Beam A	Beam B	Beam C	Beam D
$E_b\ [GeV]$	2.6	2.6	3.2	3.2
$E_{polarization}\ [GeV]$	1.05	1.05	non	1.6
Total scaler time $[h]$	294	35	300	109
Corrected scaler time $[h]$	138	18	189	51
$\phi_o \times 10^7\ [e^-/s]$	1.75	1.6	1.6	2.8

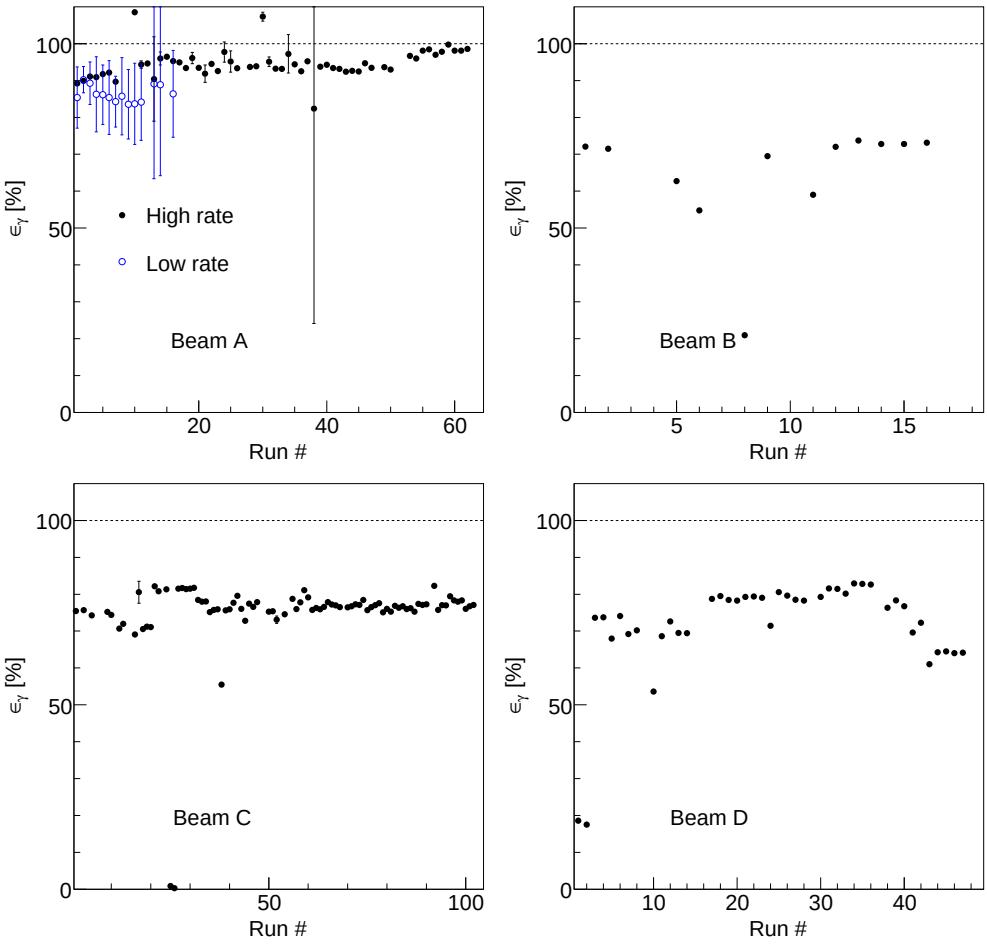

Figure 6.3: *The tagging efficiency evolution for the different beam times (black point high rate, ≈20 MHz, blue open circle low rate ≈0.3 MHz). The runs were taken every 4 hrs.*

The tagging efficiency, for beam A and beam C, remains constant within ± 10 % (see Figure 6.3). The tagging efficiency for beam B and beam D is varying a lot. Beam B and beam D were among the first polarized beam times. At this

time, the orientation of the diamond was not optimized.

The tagging efficiency for each scintillator fiber is plotted in Figure 6.4. For the unpolarized beam time (Figure 6.4-bottom right), the tagging efficiency is constant ± 5 %. The polarized beam times have non-constant tagging efficiency, which is an expected effect from the polarization.

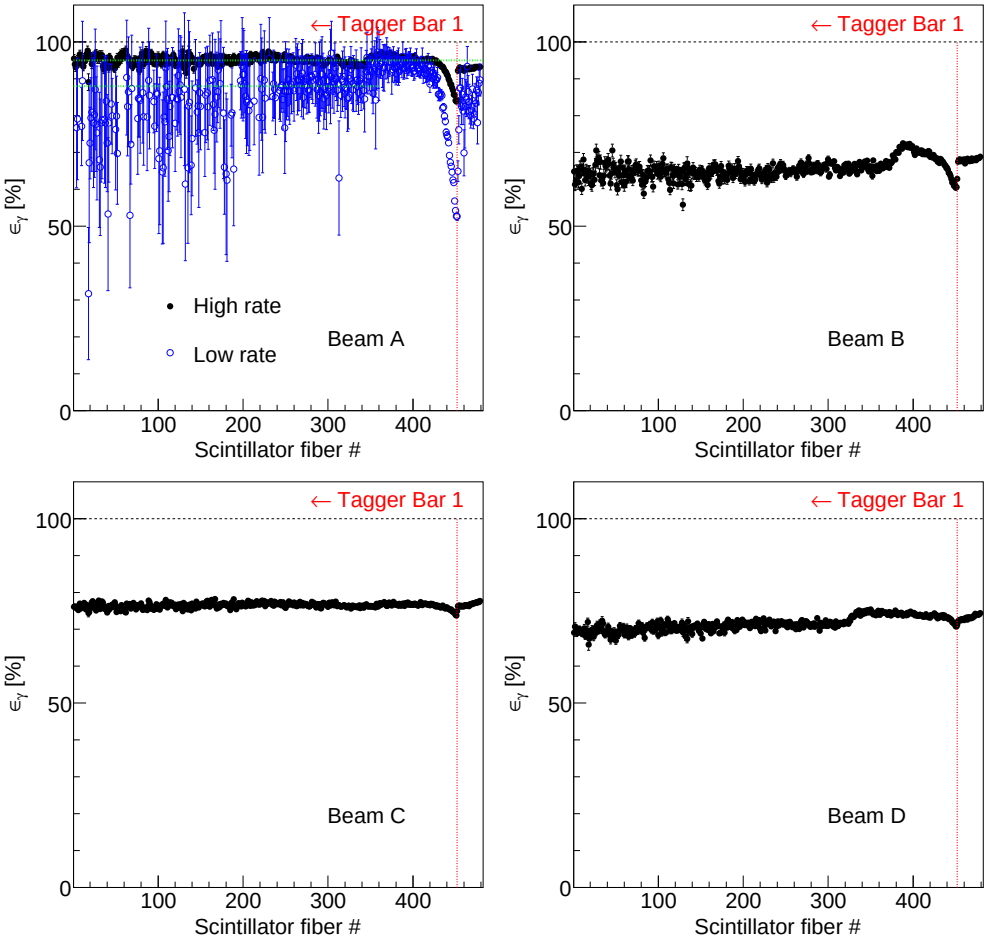

Figure 6.4: *The tagging efficiency for each scintillator fiber for the different beam times (black point high rate, ≈20 MHz, blue open circle low rate ≈0.3 MHz).*

Now, we can calculate the flux from equation 6.7, the results are plotted in Figure 6.5. Earlier, we mentioned that the flux should have a $1/E_\gamma$ behavior. This is a first order approximation, corrections can be applied to this approximation to match the experimental behavior (for details read [120]).

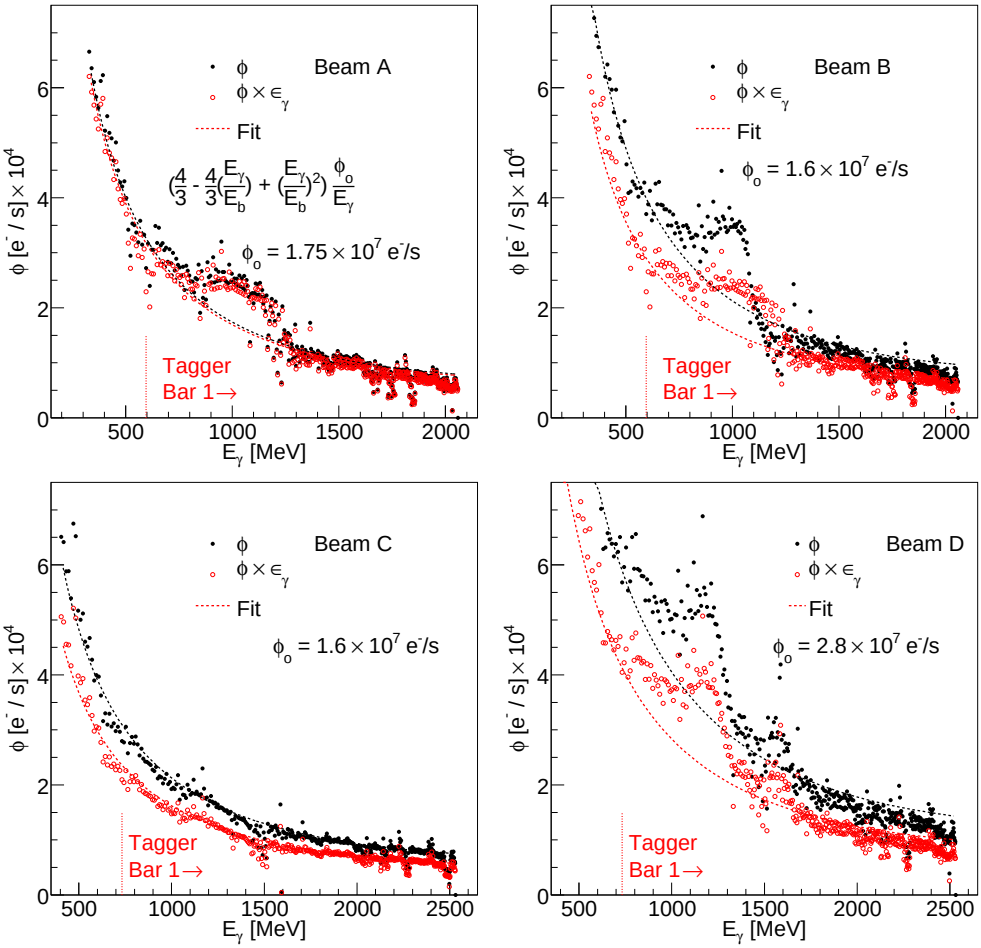

Figure 6.5: *The photon flux for the different beam times (black points the flux before the collimator, red points after the collimater, dashed line a fit corresponding to a* $\frac{1}{E_\gamma}$ *function slightly modified by a polynomial).*

The flux $\phi(E_\gamma)$ can be written as following :

$$\phi(E_\gamma) = (\frac{4}{3} - \frac{4}{3}\frac{E_\gamma}{E_b} + (\frac{E_\gamma}{E_b})^2)\frac{\phi_0}{E_\gamma} \tag{6.8}$$

Equation 6.8 was used to fit the measured flux (Figure 6.5 red and black lines). The flux for the linearly polarized beam does of course not follow the $1/E_\gamma$ behavior in the region of the polarization peak (see [121] for details). The absolute normalization was possible only for two beam times : beam A and beam C as the correct number of scalers were found for these two beam times only.

6.2 The $\pi^o\pi^o$ photoproduction off the deuteron

Three channels were studied :

- $\gamma + d \rightarrow \ \pi^o\pi^o \ + (pn)$ (quasi-free inclusive),
- $\gamma + d \rightarrow \ \pi^o\pi^o \ + p(n)$ (quasi-free proton) and
- $\gamma + d \rightarrow \ \pi^o\pi^o \ + n(p)$ (quasi-free neutron).

The reaction $\gamma + d \rightarrow \ \pi^o\pi^o \ + NNX$ was not studied. The results presented here are preliminary.

6.2.1 The reaction identification

Once two π^o have been detected in coincidence with or without a recoil nucleon (proton or neutron) a missing mass analysis is performed.

The expected competing channels are :

- $\gamma + d \rightarrow \ \eta \ + p(n)$,
- $\gamma + d \rightarrow \ \eta \ + n(p)$ and
- $\gamma + d \rightarrow \ \eta \ + NNX$,

Figure 6.6 summarizes the analysis for the quasi-free inclusive (left column), the quasi-free proton (middle column) and the quasi-free neutron (right column). The proton (neutron) has been detected in coincidence with the two π^o but is treated as a missing particle. Just above the threshold a strong background is observed at the negative part of Δm for the quasi-free inclusive and quasi-free neutron. Near production threshold most of the recoil nucleons are going in to TAPS. The missing mass for the quasi-free inclusive case for incident photon beam energies ranging between 330 MeV - 450 MeV is plotted in Figure 6.7. The red histogram is obtained by plotting the missing mass for $\theta-$angles in the laboratory of the missing nucleon below 30 degrees (i.e. for missing nucleons pointing to TAPS). Most of the background is removed. Therefore, this background is not coming from a competing channel but from a mis-identified neutron in the CB.

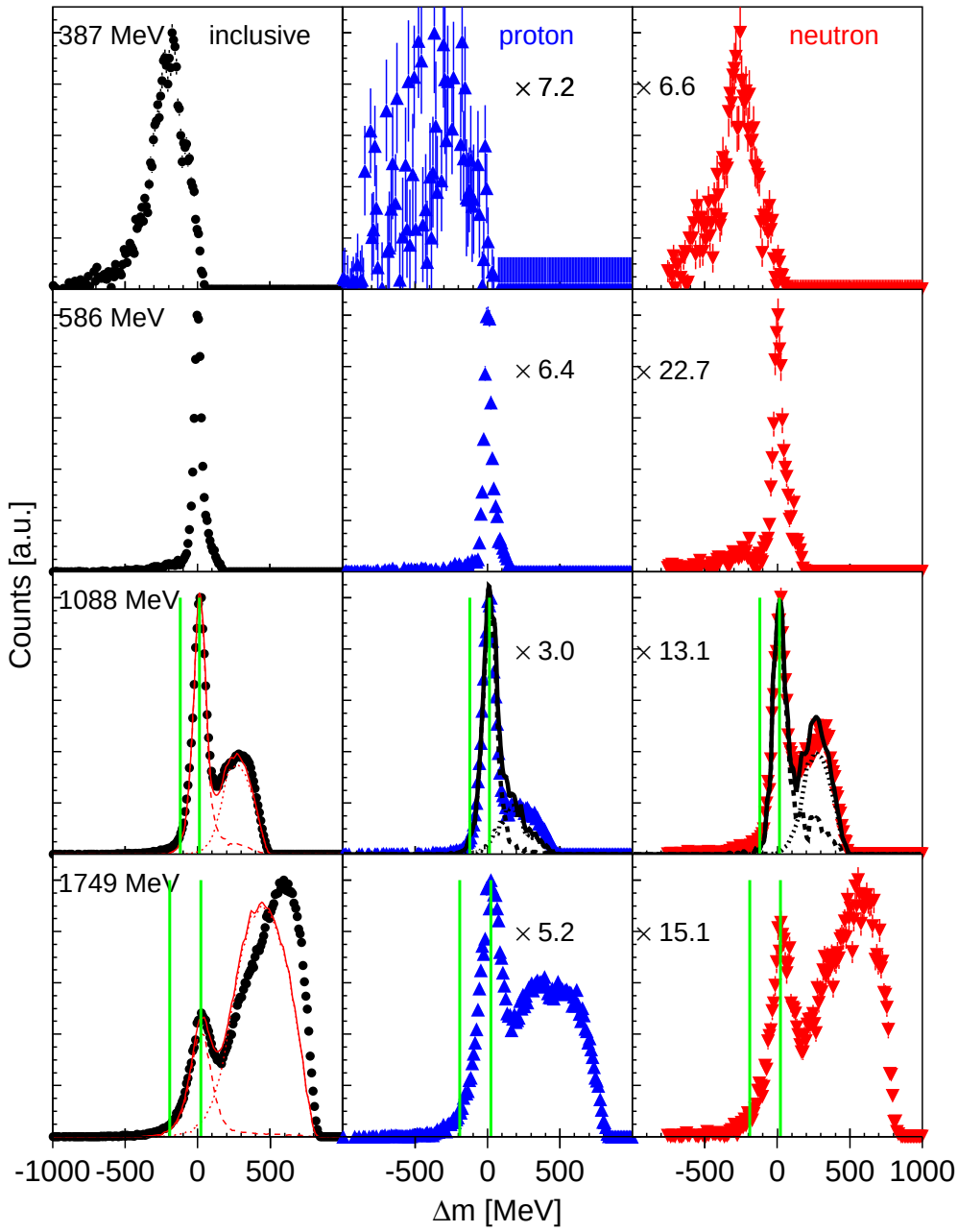

Figure 6.6: *Missing mass spectra for double π^o photoproduction off the deuterium. Left column : quasi-free inclusive (black points). Middle column : quasi-free proton (blue points). Right column : quasi-free neutron (red points). The proton and the neutron are detected but are treated as a missing particle. Top row : incident photon energy range 375 MeV - 400 MeV (below η threshold). Second row from top : range 575 MeV - 600 MeV (below η threshold). Second row from bottom : range 1075 MeV - 1100 MeV (above η threshold and $\eta\pi$). Bottom row : range 1700 MeV - 1800 MeV (above η threshold and $\eta\pi$) at this energy range the $\eta\pi$ becomes dominant. Black closed circles, blue triangle up and red triangle down are experiment. Lines are simulations : dashed $2\pi^o$ photoproduction, dotted η photoproduction and the solid line is the sum of both. The green lines are the cuts applied to remove the background coming from competing channels (The scale is relative to the quasi-free inclusive).*

Just below the η threshold the missing mass is clean (Figure 6.6 second row from the top). The background (coming from competing channels) starts to appear above the η threshold ($E_\gamma > 627\ MeV$). At high energies the background coming from $\eta\pi$ is dominant ($\eta\pi$ threshold $E_\gamma = 807\ MeV$).

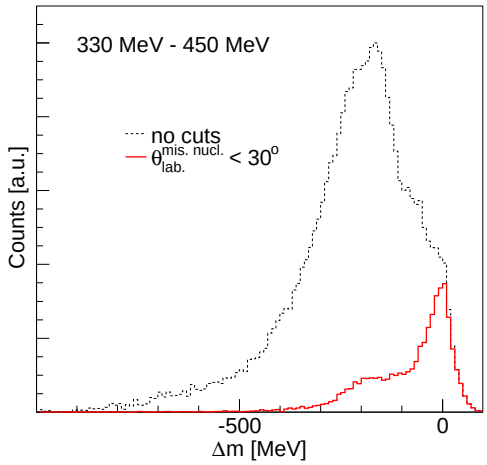

Figure 6.7: *Missing mass spectra for quasi-free inclusive. The incident photon energies range between 330 MeV - 450 MeV. Dotted black line no cuts applied. Red line a cut on the $\theta-$angle of the missing nucleon is applied ($\theta^{mis.}_{lab.} < 30^o$). Most of the background is removed.*

The missing mass line shape was reproduced by simulations at 1 GeV (Figure 6.6-second from the bottom) . The reactions simulated are :

- $\gamma + p(n) \rightarrow \pi^o\pi^o + p(n)$
- $\gamma + n(p) \rightarrow \pi^o\pi^o + n(p)$
- $\gamma + p(n) \rightarrow \eta + p(n)$ (competing channel)
- $\gamma + n(p) \rightarrow \eta + n(p)$ (competing channel)

At 1.7 GeV, the missing mass line shape was not reproduced. The single$-\eta$ photoproduction is no longer dominant. At this energy range the $\eta\pi$ production is five times bigger than the η production (see η photoproduction off the deuteron).

From the missing mass analysis, a cut was applied to remove the competing background channel (which is illustrated by the vertical green line in Figure 6.6). The simulated missing mass was fitted : the peak and the width were extracted for each tagged incident photon beam. Figure 6.8-right show the results. The remaining background was removed by fitting the 2γ invariant mass distribution (when the cuts on the missing mass are applied, Figure 6.8-top-right show an example) by a function that takes the line shape into account

([122]) plus a polynomial function for the background.

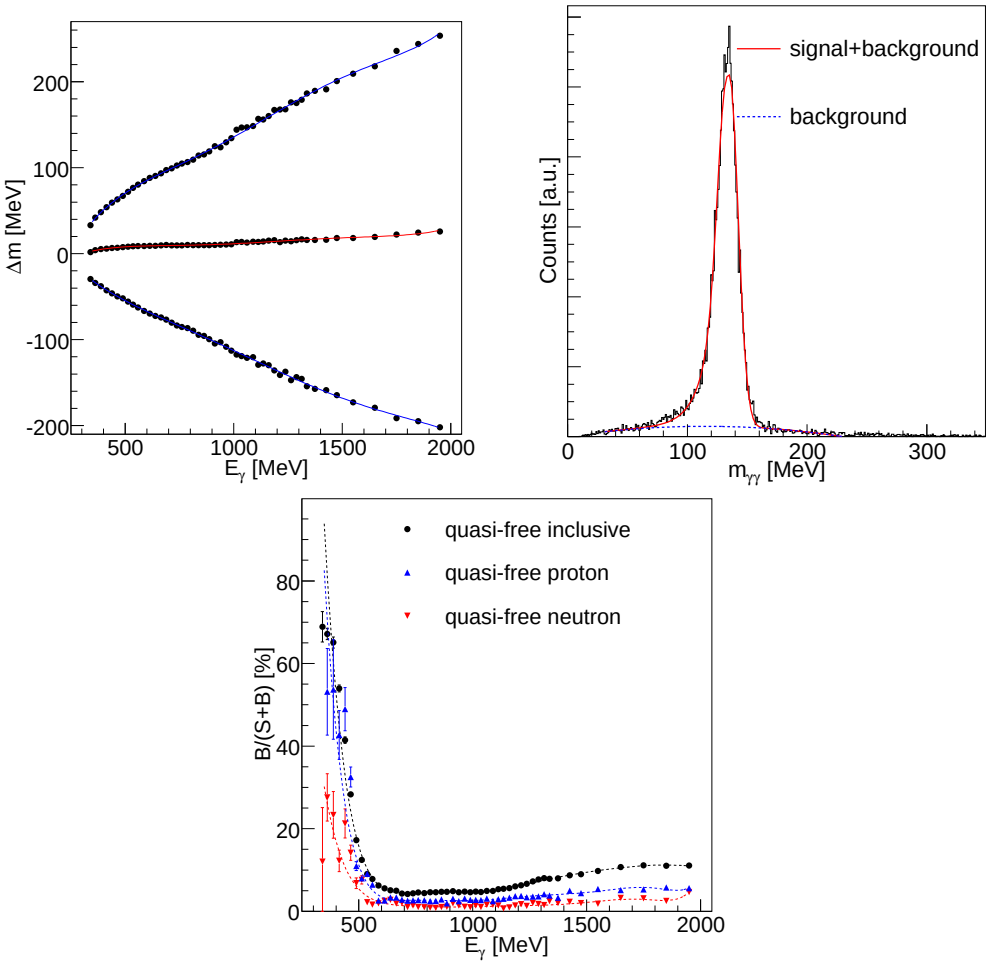

Figure 6.8: *Top left : Simulated Δm peak position and peak position $\pm 3 \times \sigma$ as function of the incident photon beam. Lines polynomial fit of fifth order. The cut used is between $-3 \times \sigma$ and the peak position. Top right : typical two-photon invariant mass spectrum. Bottom : Background evolution as function of the incident photon beam for all reactions.*

The function is :

$$\begin{aligned} y = & \quad NG & \text{for } E \leq E_{peak}, \\ y = & \quad N\left(G + exp\left\{\frac{E-E_{peak}}{\lambda}\right\} \cdot (1-G)\right) & \text{for } E \geq E_{peak}, \\ \text{with:} & \quad G = exp\left(-\frac{4 \cdot ln(2) \cdot (E-E_{peak})^2}{\Gamma^2}\right) \end{aligned} \tag{6.9}$$

The remaining background is approximately 5 % for all reactions (Figure 6.8-bottom - B/ (S+B) as function of the incident photon beam). The background

was estimated only as function of the incident photon beam. Therefore, in the differential cross section, the background was not removed (which might explain some discrepencies observed).

6.2.2 The determination of the detection efficiency

As already mentioned, two reactions were simulated:

- $\gamma + p(n) \rightarrow \pi^o\pi^o + p(n)$
- $\gamma + n(p) \rightarrow \pi^o\pi^o + n(p)$

The $2\pi^o$ and the recoil nucleon have been generated according to phase space distributions in quasi-free kinematics taking into account the Fermi motion of the nucleons derived from the deuteron wave function (all others effect such as FSI have not been taken into account).

This assumption is justified by the good description of the reaction kinematics as demonstrated in Figure 6.6. But the invariant mass distributions in the $2\pi^o-$system and in the $N\pi^o-$system will show that this assumption is an approximation with large systematic uncertainty. Indeed a reaction on a free proton target with three particles in the final state depends on five independent variables, instead of one with two particles in the final state. With a deuteron target, an additional independent variable must be added : the Fermi motion. The acceptance calculation of a reaction with three particles in the final state in only one dimension implies an integration over the other five variables. Thus, if the acceptance in at least one of these five variables changes strongly, the acceptance calculation for one dimensional acceptance will give incorrect results if the reaction physics is not properly included in the MC simulation.

The data and the simulation were analyzed with the same program . At the exception of the incident photon beam (which was not simulated), all the others steps leading to the $2\pi^o$, the proton or the neutron constructions were exactly the same as described in chapter five. The cuts applied to clean the data and to identify the reaction were the same. Below a short summary:

- neutral hits and charged hits are identified by the setup (the CFD, cluster/PED thresholds included in MC as well)
- events with four or five neutral hits are selected (no limitation on the number of charged hits)
- all possible combinations of photon pairs are tested
- χ^2-test that gives the best solution for $2\pi^o$ (in the case of four neutral hits) or $2\pi^o$ and a neutron candidate (in the case of five neutral hits)

- cut on the π^o mass between 110 MeV and 160 MeV
- π^o mass constrain
- events with $2\pi^o$ or $2\pi^o$ and a charged hit or $2\pi^o$ and a neutron candidate are selected
- cut on the missing mass
- application of the software trigger on the 4γs.

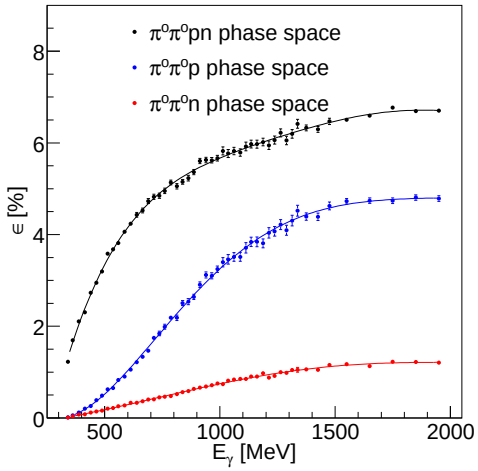

Figure 6.9: *Detection efficiency as a function of the incident photon energy for the quasi-free inclusive (black points), for the quasi-free proton (blue points) and for the quasi-free neutron (red points).*

The efficiency has been determined for the total cross section as a function of the incident photon beam (Figure 6.9) and for the invariant mass distribution in the $2\pi^o-$system (Figure 6.10) and in the $N\pi^o-$system (Figure 6.11). The quasi-free inclusive was not simulated. The efficiency shown for the quasi-free inclusive corresponds to the average of the efficiencies obtained from the quasi-free proton and the quasi-free neutron reactions analysis.

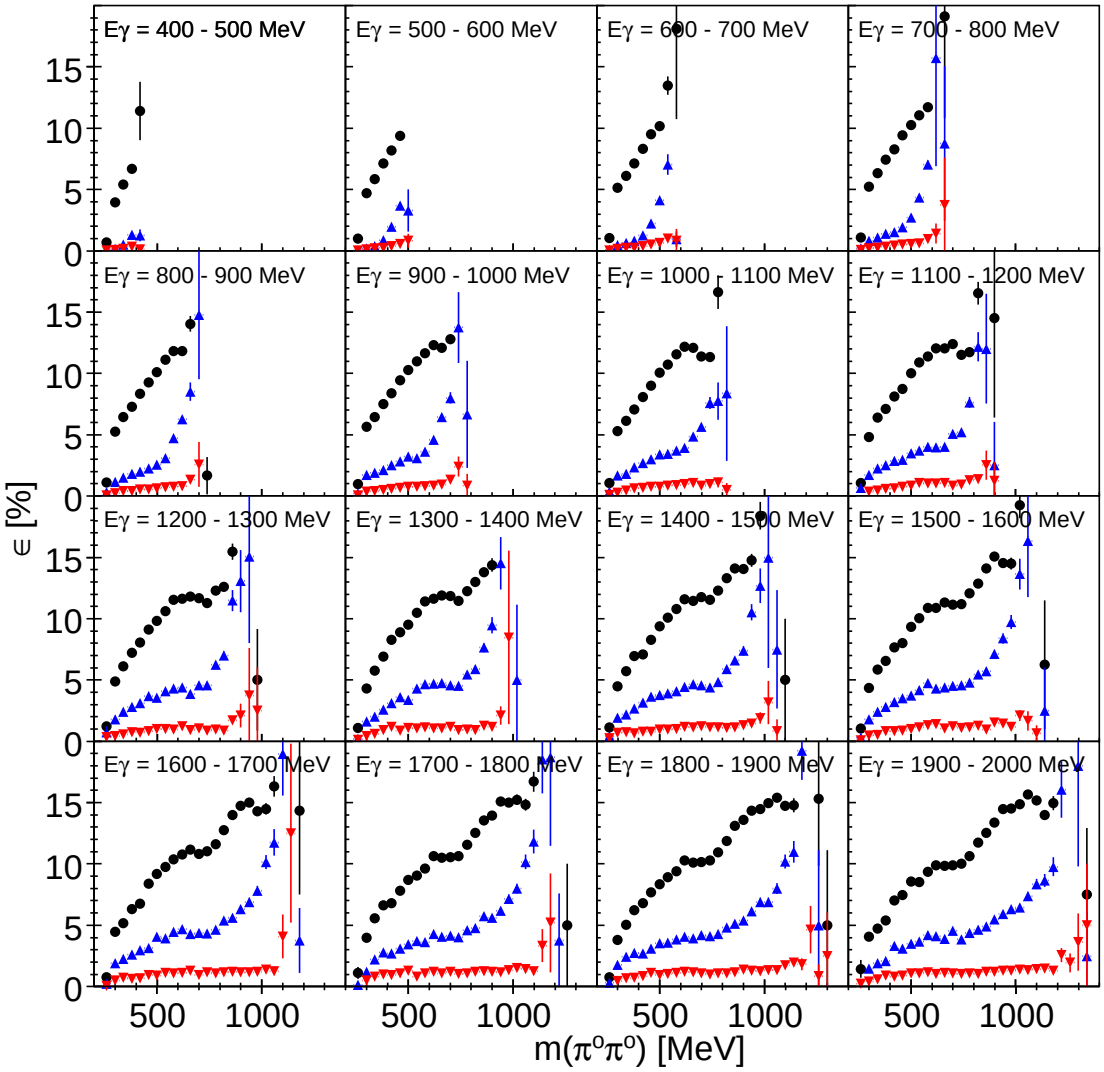

Figure 6.10: *Detection efficiency as a function of the two neutral pions mass for different incident photon energy ranges. For the quasi-free inclusive black points. For the quasi-free proton blue triangle up. For the quasi-free neutron red triangle down.*

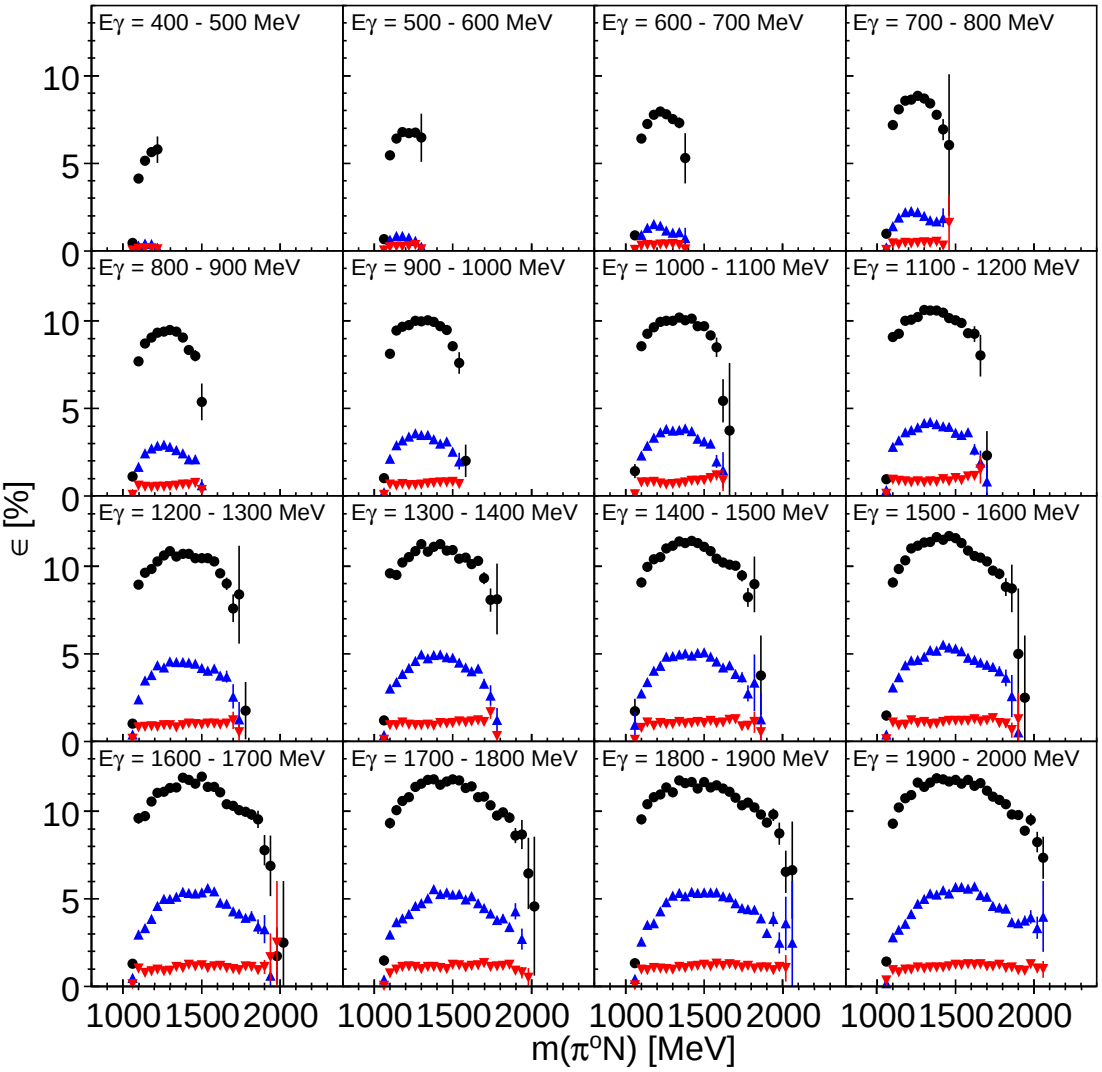

Figure 6.11: *Detection efficiency as a function of the neutral pion and the nucleon mass for different incident photon energy ranges. For the quasi-free inclusive black points. For the quasi-free proton blue triangle up. For the quasi-free neutron red triangle down.*

6.2.3 Dalitz plot

An example of a Dalitz plot is shown in Figure 6.12 for the reaction $\gamma + d \rightarrow \pi^o\pi^o + pn$.

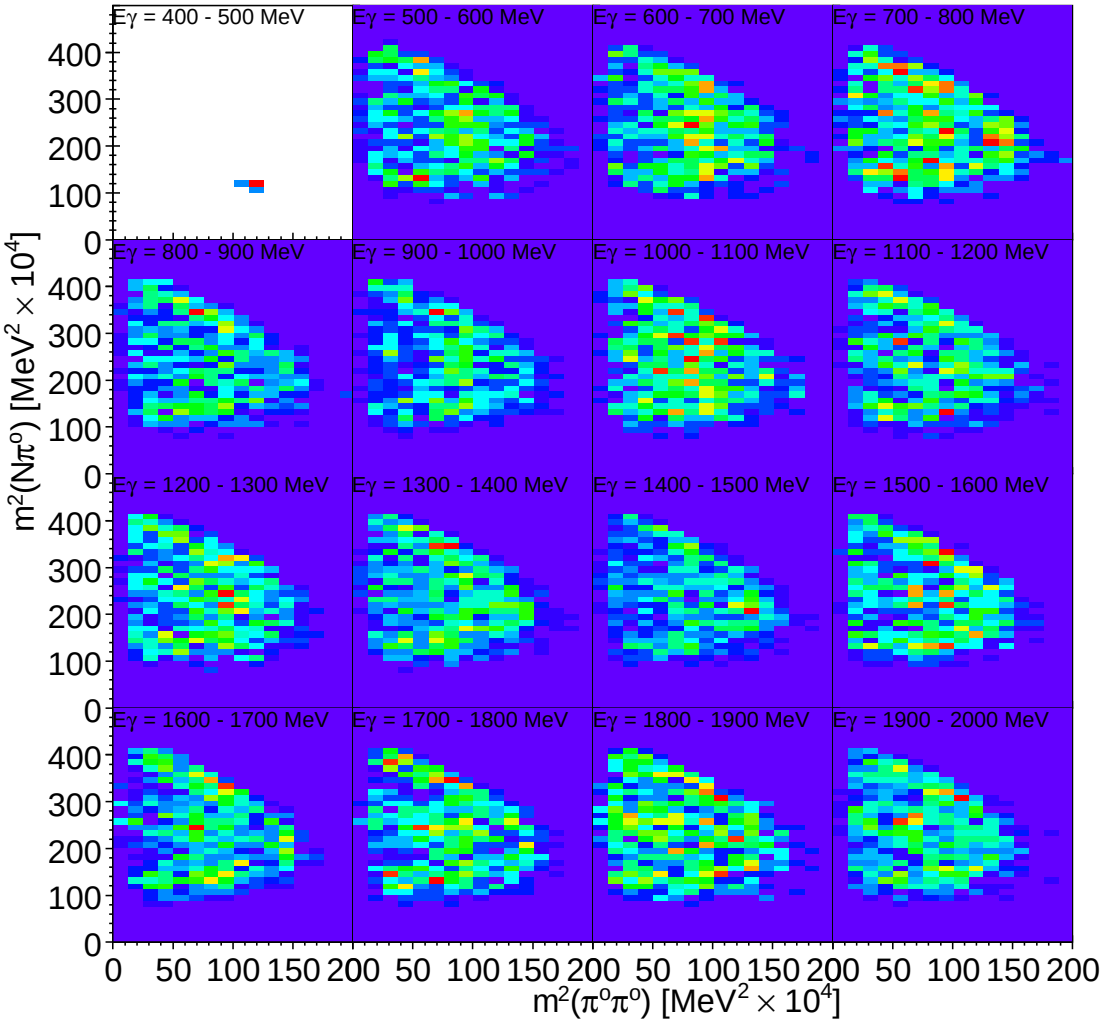

Figure 6.12: *Dalitz plot : $m^2(\pi^o\pi^o)$ as function of $m^2(N\pi^o)$ for the quasi-free inclusive for different incident photon beam ranges.*

The dynamic of the reaction is more obvious in the mass distributions as it is shown below.

6.2.4 The differential cross sections

Replacing θ by m in equation 6.1 gives :

$$\frac{d\sigma}{dm}(E_\gamma, m) = \frac{N(E_\gamma, m)}{\epsilon_\gamma(E_\gamma)\rho N_{scaler}(E_\gamma)\Gamma_m \epsilon_r(E_\gamma, m)}, \quad \Gamma_m = BR(\pi^o \to 2\gamma)^2 \qquad (6.10)$$

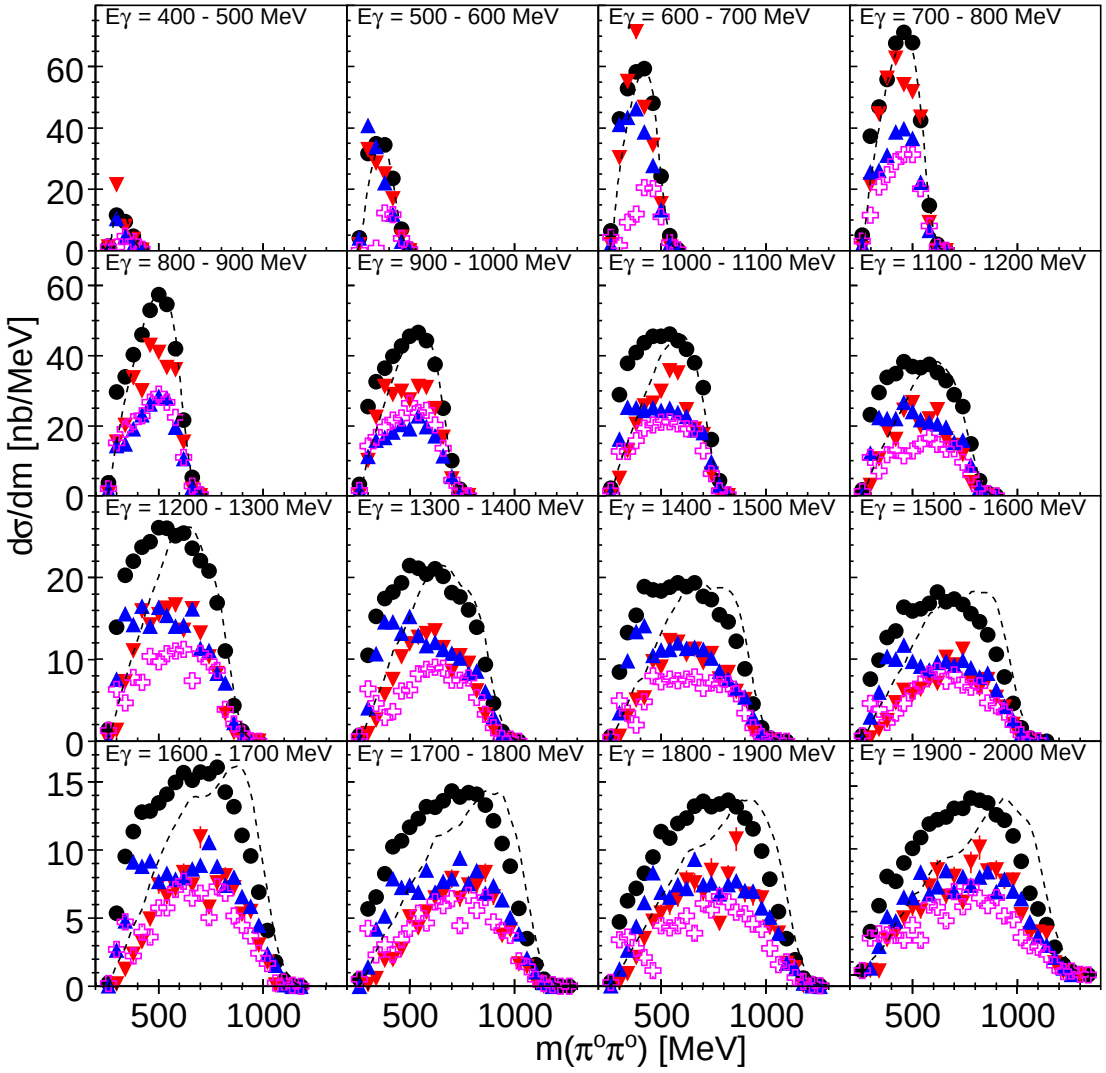

Figure 6.13: *$\pi^o\pi^o$ mass distribution for different incident photon energy ranges. For quasi-free inclusive black points. For quasi-free proton blue triangle up. For quasi-free neutron red triangle down. $\frac{d\sigma}{dm}(pn\pi^o\pi^o) - \frac{d\sigma}{dm}(p\pi^o\pi^o)$ indirect measurements of the quasi-free neutron violet cross. Black dashed line in phase space distribution for the quasi-free inclusive case. The remain background below the π^o peak has not been subtracted.*

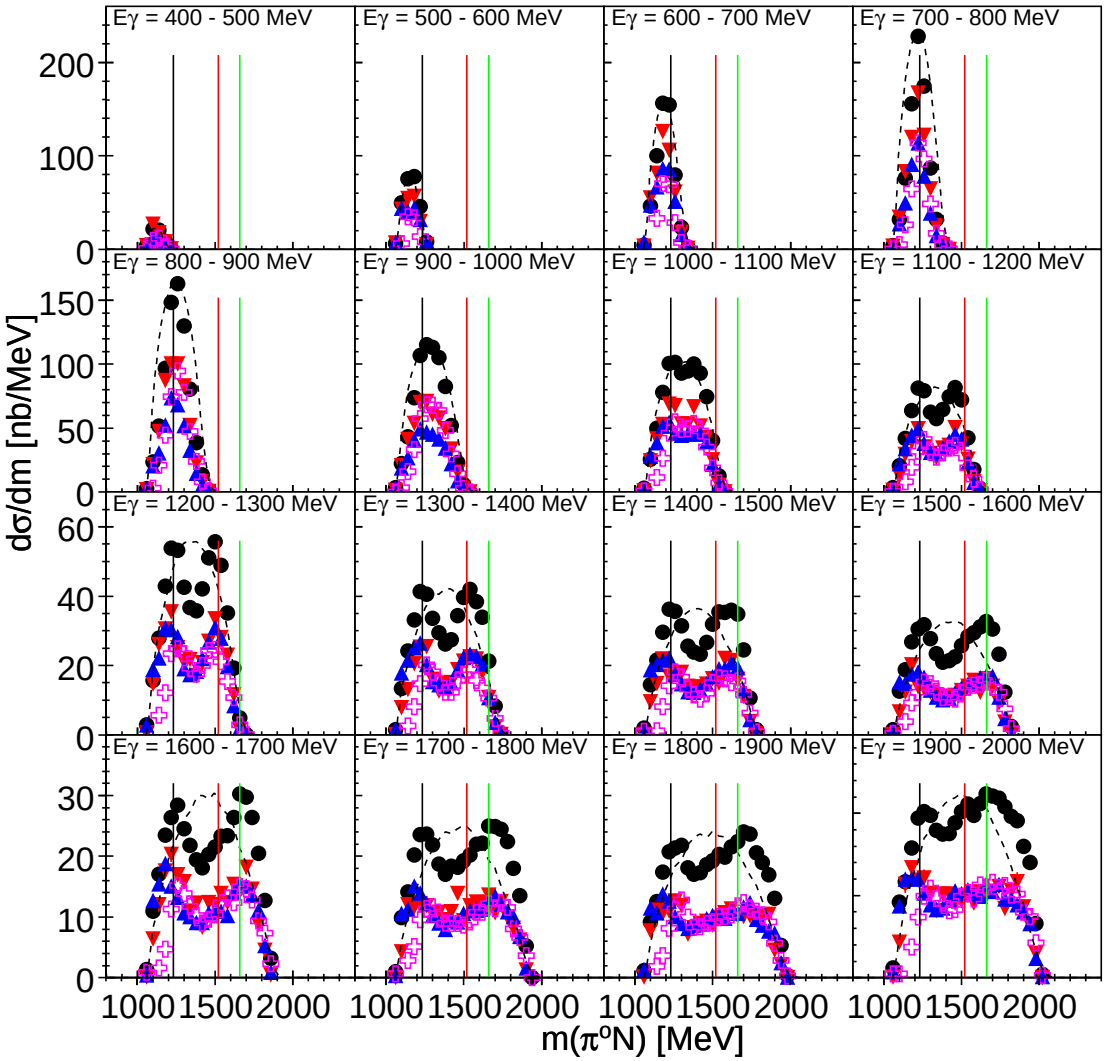

Figure 6.14: *$N\pi^o$ mass distribution for different incident photon energy ranges. For quasi-free inclusive black points. For quasi-free proton blue triangle up. For quasi-free neutron red triangle down. $\frac{d\sigma}{dm}(N\pi^o) - \frac{d\sigma}{dm}(p\pi^o)$ indirect measurements of the quasi-free neutron violet cross. Black dashed line in phase space distribution for the quasi-free inclusive case. The remain background below the π^o peak has not been subtracted. Vertical lines : 1232 MeV (black), 1520 MeV (red) and 1660 MeV (green).*

The extraction of the mass distributions was obtained by applying equation 6.10. The mass distributions for the $2\pi^o-$system and the $N\pi^o-$system can be seen in Figure 6.13 and 6.14, respectively, for different incident photon energy ranges. The quasi-free inclusive mass distributions are compared to quasi-free inclusive MC phase space distribution. There is good agreement between data and MC phase space distribution up to 800 MeV. Above 800 MeV, the two distributions clearly differ as the reaction is dominated by $\gamma + d \rightarrow X \rightarrow \Delta(1232)\pi^o$ (this is also the case for the quasi-free proton and

quasi-free neutron reactions). With increasing energy a shoulder appears in Figure 6.14 (E_γ = 1.2 - 1.3GeV) and can be identified as $D_{13}(1520)$. With even higher energies an indication for an additional resonance at 1660 MeV mass location can be observed in Figure 6.14 (E_γ = 1.5 - 1.6 GeV). The mass distributions in the $2\pi^o-$system do not exhibit any clear structures.

6.2.5 The total cross sections

The preliminary total cross sections, shown in Figure 6.15, were not obtained from the integration of the mass distributions, but by counting directly the number of events per incident photon beam bins.

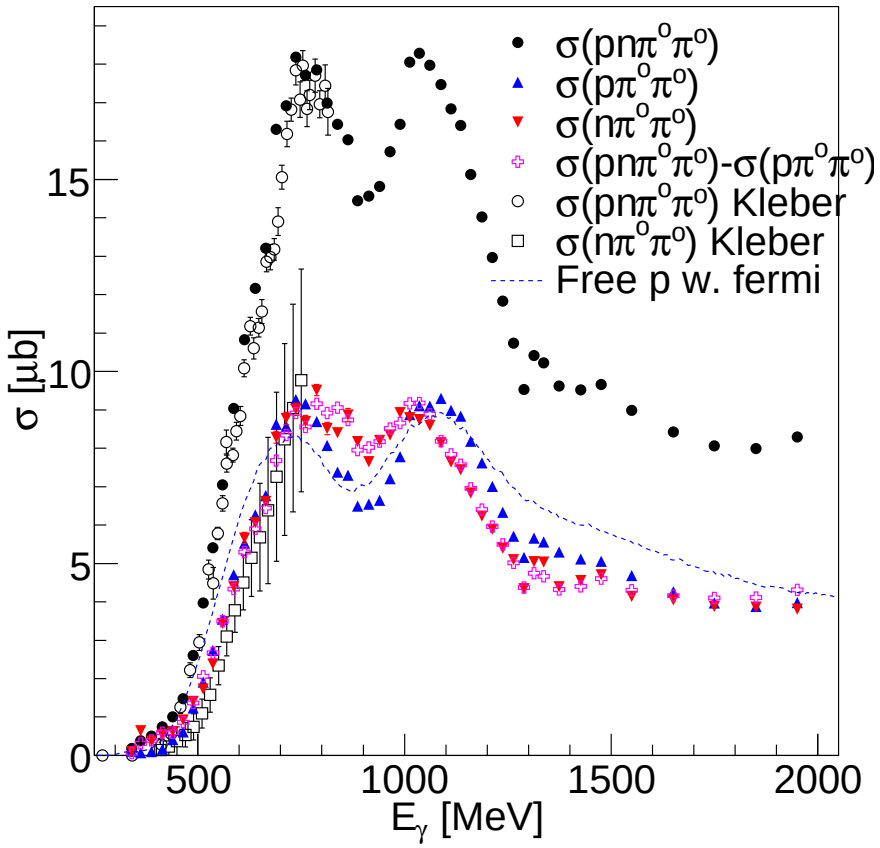

Figure 6.15: *Total cross section as a function of the incident photon energy for the quasi-free inclusive (black points), for the quasi-free proton blue triangle up) and for the quasi-free neutron (red triangle down) reactions. $\sigma(pn\pi^o\pi^o) - \sigma(p\pi^o\pi^o)$ indirect measurement of the quasi-neutron reaction (violet cross). The quasi-free inclusive and the quasi-free neutron are compared to Kleber et al. [26] and the quasi-free proton to the free proton folded with Fermi motion [24].*

From threshold to 800 MeV, the quasi-free inclusive and the quasi-free neu-

tron are in good agreement with previous measurements from [26] (Kleber et al. did use the same phase space MC distributions as this work). The statistics for the quasi-free neutron have been improved by two orders of magnitude at least. The measurements were extended up to 2 GeV. The quasi-free neutron was measured in two different ways : directly by measuring the $2\pi^o$ and the recoil neutron in coincidence and indirectly from the difference of the inclusive cross section and in coincidence with the recoil proton. The two different measurements are in good agreement. The proton cross section is compared to the free proton cross section folded with Fermi motion. They are somewhat different. This difference is understood as the acceptance correction for the free proton [24] was closer to the reality. The MC events for the free proton were modified by using a Partial Wave Analysis (PWA) to calculate a weight factor for each of the phase space generated MC events. This difference gives an indication of the acceptance correction uncertainty (see Figure 6.16), which is on the order of 10 % to 20 % between 800 MeV and 2000 MeV. Between threshold to 800 MeV, other effects (like FSI, than wrong acceptance correction) might explain the difference.

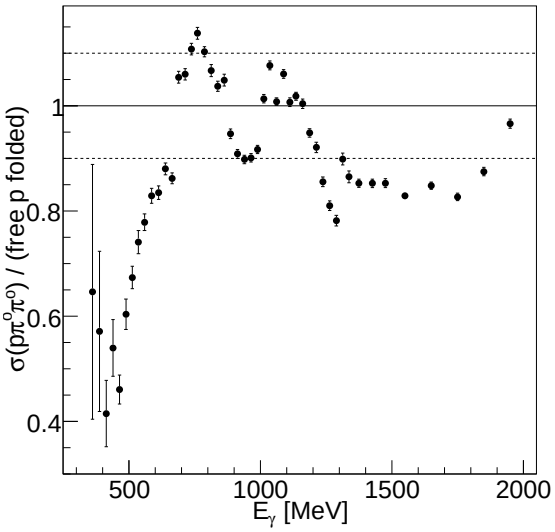

Figure 6.16: *Quasi-free proton - free proton folded with Fermi motion ratio.*

The first peak, at $E_\gamma \sim 750$ MeV (or W$\sim$ 1500 MeV), observed for the three reactions studied is understood as coming from the $D_{13}(1520)-$resonance contribution. The origin of the second peak, at $E_\gamma \sim 1200$ MeV (or W$\sim$ 1700 MeV), observed also for the three reactions; is not yet understood. The second peak was first observed in $p\pi^+\pi^-$ electroproduction from CLAS [123]. They find that for increasing Q^2 the second peak observed gets more prominent. A possible explanation given by the BnGa calculations [124] is that the structure of

the two peaks might be due to constructive and destructure interference of $D_{13}(1520) + D_{33}(1700)$. The neutron and the proton helicity couplings of the $D_{13}(1520)-$ and $D_{33}(1700)$ have the same strength in PDG, therefore this explanation might be also valid for the neutron. Another explanation is proposed by the $\pi\pi-$`MAID` calculations [31]. These calculations proposed that a resonance creates the second bump, the $F_{15}(1680)$ for the proton and the $D_{15}(1675)$ for the neutron. Indeed, we do observe a resonance around 1660 MeV mass location for both channels in the Figure 6.14. Thus, even if the quasi-free neutron and the quasi-free proton seem to have the same overall behavior, some differences might come from the different electromagnetic couplings of the neutron and the proton. These differences can be studied by looking at the neutron - proton cross section ratio.

6.2.6 The neutron - proton cross section ratio

The neutron - proton cross section ratio was calculated for the two neutron measurements as shown in Figure 6.17. There is a good agreement.

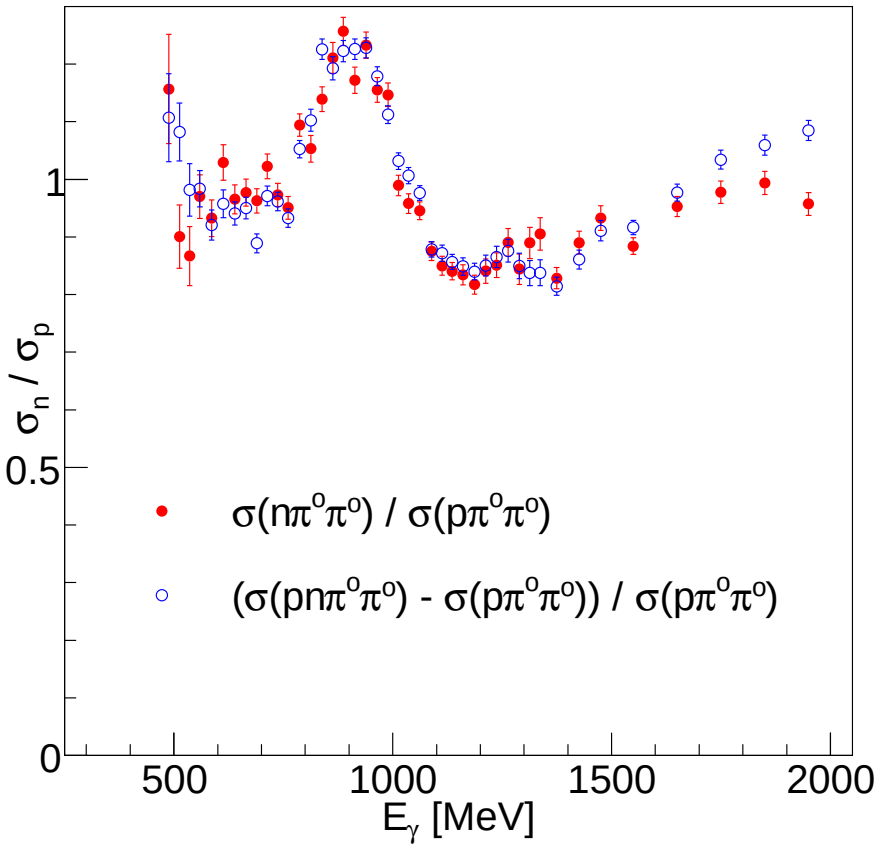

Figure 6.17: *The neutron - proton cross section ratio for the two neutron measurements.*

In the $D_{13}(1520)$ energy region the ratio is close to one. Between the two peaks ($E_\gamma \sim 900\ MeV$), a broad peak appears in the ratio. At $E_\gamma \sim 1300$ MeV, there is a small structure. Above E_γ= 1500 MeV, the ratio rises. The neutron

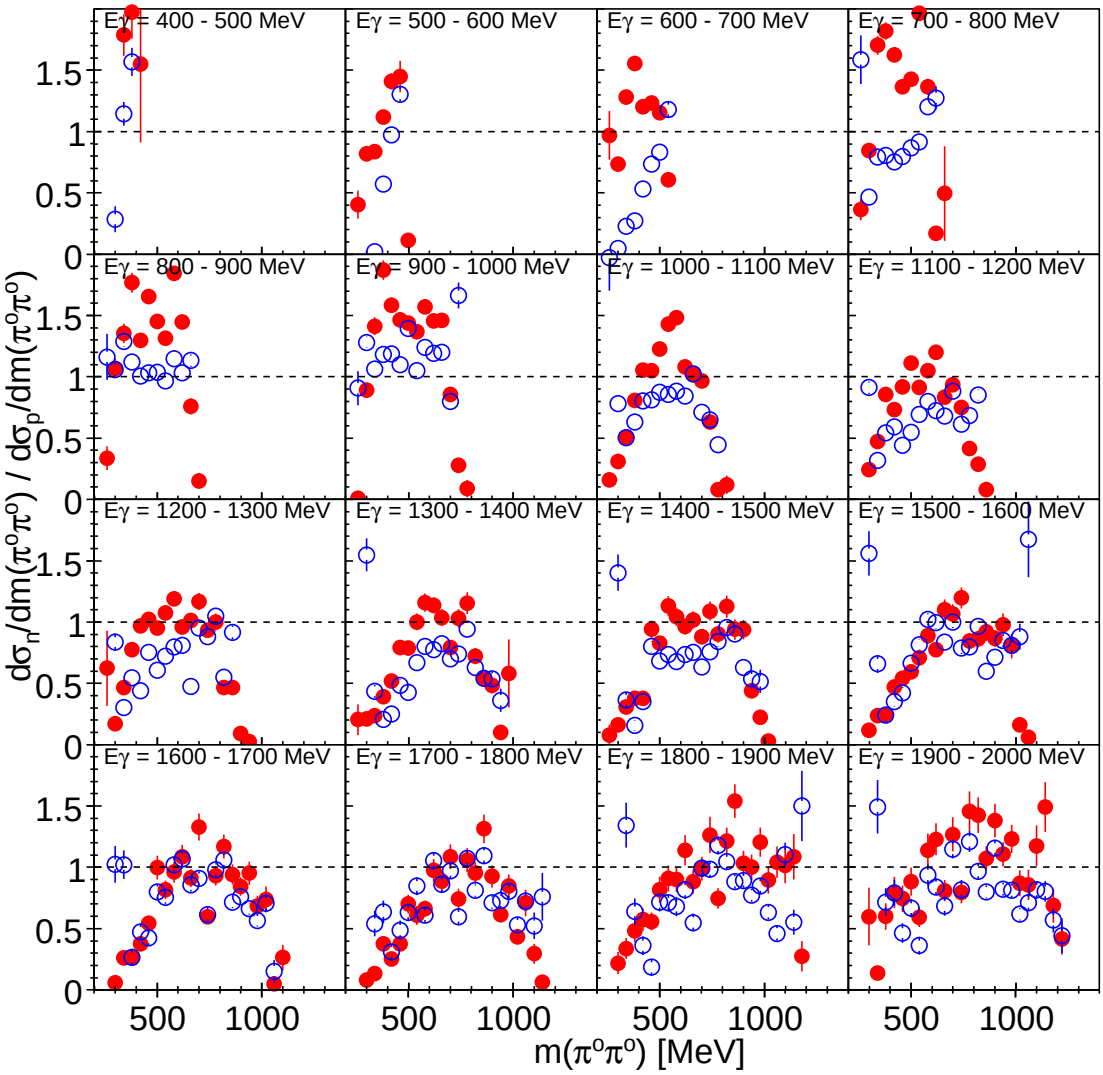

Figure 6.18: *neutron - proton $\pi^o\pi^o$ mass distribution ratio for different incident photon energy ranges. For $m_n(\pi^o\pi^o)/m_p(\pi^o\pi^o)$ red points. For $(m_{pn}(\pi^o\pi^o) - m_p(\pi^o\pi^o))/m_p(\pi^o\pi^o)$ blue open circle.*

- proton differential cross section ratio was also calculated : Figures 6.18 in $\pi^o\pi^o-$system and 6.19 in $N\pi^o-$system. For each system, the ratio was calculated from the two neutron measurements. The ratio seems to be equal one, except for the edge of the phase space distribution and for E_γ = 400 - 1100 MeV.

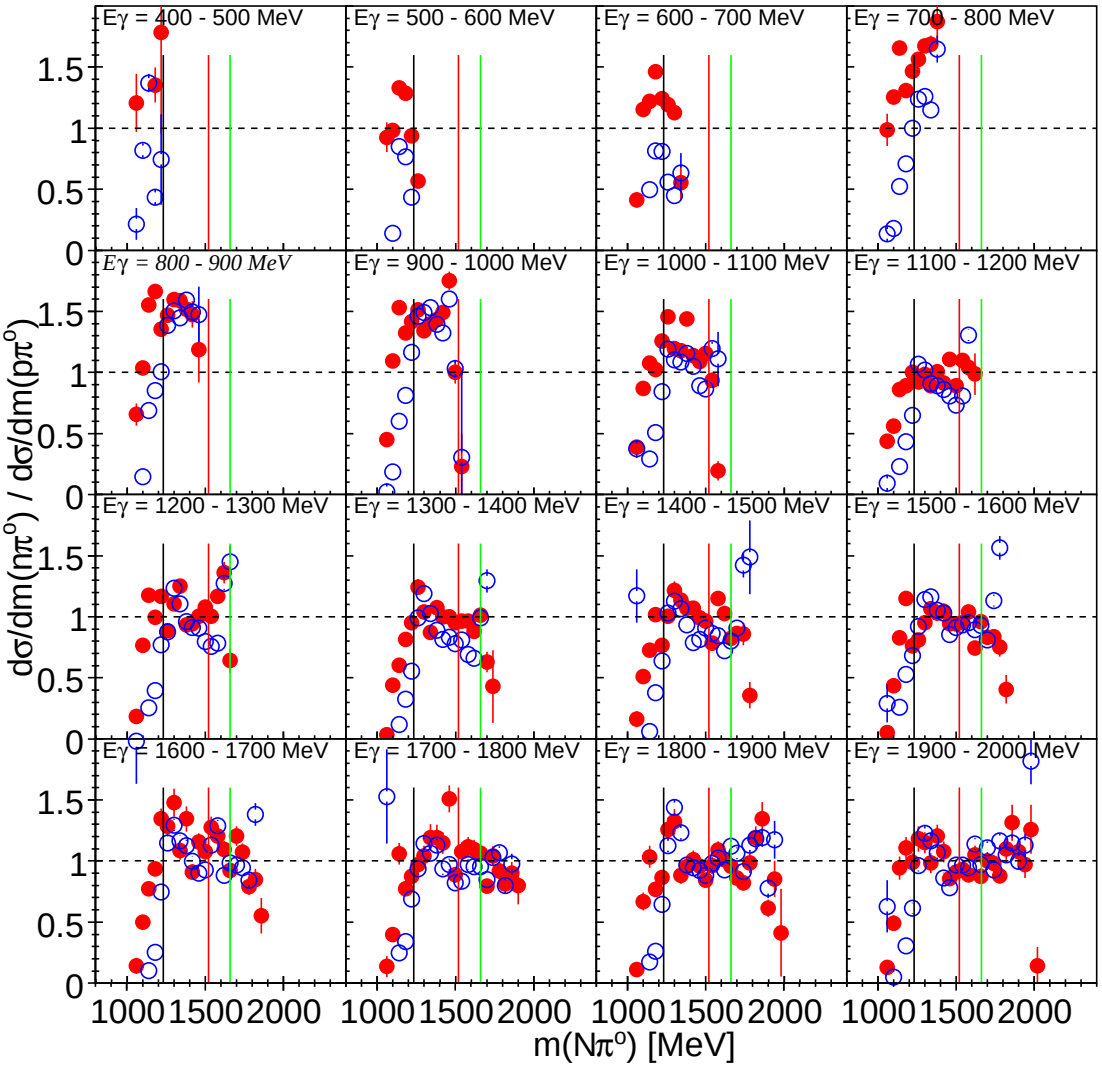

Figure 6.19: $m(n\pi^o)\,/\,m(p\pi^o)$ *mass distribution for different incident photon energy ranges. For* $m(n\pi^o)/m(p\pi^o)$ *red points. For* $(m(N\pi^o) - m(p\pi^o))/m(p\pi^o)$ *blue open circle. Vertical lines : 1232 MeV (black), 1520 MeV (red) and 1660 MeV (green).*

6.2.7 The discussions

Most of the discussion was already done. The behavior of the observable extracted seems to be similar to what was observed for the free proton target. The two peaks observed in the total cross section on the free proton target [24] are also seen in the three reactions studied. The baryon cascade is clearly observed for the three reactions studied :

- $\gamma N \rightarrow N^*/\Delta^* \rightarrow \Delta\pi$
- $\gamma N \rightarrow N^*/\Delta^* \rightarrow D_{13}(1520)\pi$
- $\gamma N \rightarrow N^*/\Delta^* \rightarrow N^*/\Delta^*(\sim 1660)\pi$

There are differences between the quasi-free proton and the quasi-free neutron, which seems to be most likely due to the different electromagnetic couplings for the proton and the neutron as the general tendency is very similar for protons and for neutrons. The total cross section of $\gamma + n(p) \rightarrow 2\pi^o + n(p)$ measured at GRAAL [92] is similar to this work in the first bump area, but is different in the second bump area. This difference could be explained if the background coming from the competing channels is included in the measurement. Indeed, in [92], there is no missing mass analysis performed as it was done in this work (see section 6.2.1). Figure 6.20 shows the total cross sections obtained in this work if the competing channels are included. The second bump is higher !

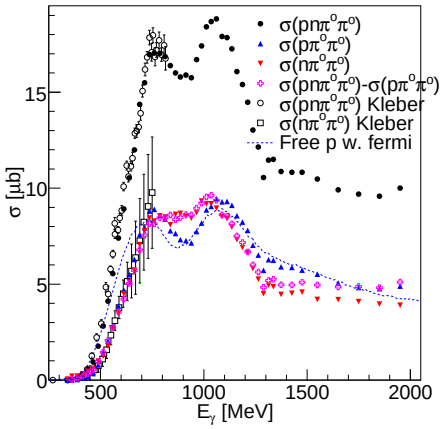

Figure 6.20: *Total cross section (by including the signal coming from the competing channels) as a function of the incident photon energy for the quasi-free inclusive (black points), for the quasi-free proton blue triangle up) and for the quasi-free neutron (red triangle down) reactions. $\sigma(pn\pi^o\pi^o) - \sigma(p\pi^o\pi^o)$ indirect measurement of the quasi-neutron reaction (violet cross). The quasi-free inclusive and the quasi-free neutron are compared to Kleber et al. [26] and the quasi-free proton to the free proton folded with Fermi motion [24].*

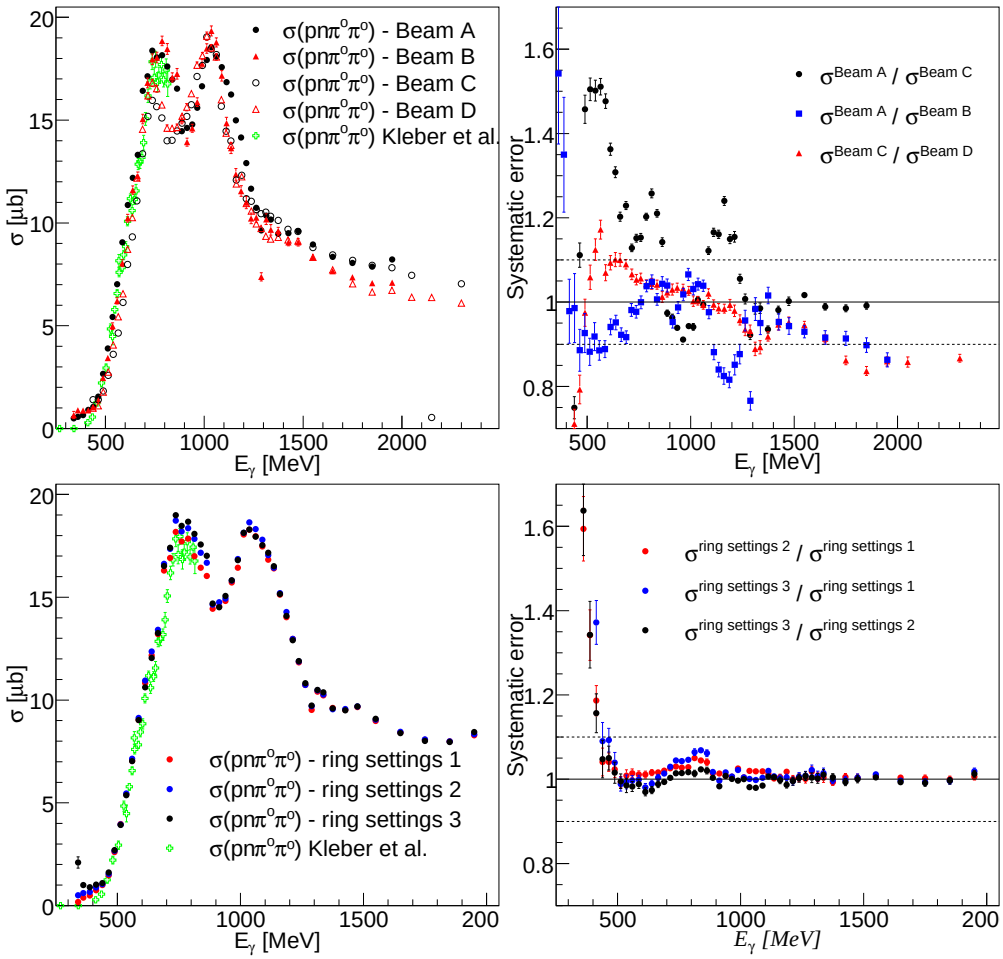

Figure 6.21: *Top left : The quasi-free inclusive total cross section for different beam time. Top right : The systematic difference between the different beam times. Bottom left : The quasi-free inclusive total cross section for different ring settings (Table 6.1). Bottom right : The systematic difference between the different ring settings.*

The results presented here are only $1/3$ of the full statistics. In Figure 6.21 (top-left), the results for the four beam times (as defined in table 6.1.2) are shown. The absolute normalization was only possible for beam A and beam C. Thus, beam B and beam D are normalized respectively to beam A and beam C. The first peak region is different for beam A and beam C (or beam D), but is the same with beam B. Whereas, the second peak region is similar for all beam times. Figure 6.21 (top-right) illustrates the systematic difference between the different beam times.

With higher electron beam energy, the probability that an unscattered electron was not stopped by the beam dump, but did backscatter, increased. It is believed that these backscattered electrons are detected by the fiber scintilla-

Ring #	low (set. 1)	high	low (set. 2)	high	low (set. 3)	high
1	2000	2000	2000	2000	3000	3000
2	300	400	200	260	450	600
3	150	210	150	210	225	315
4	90	150	90	150	135	225
5	60	140	75	140	90	210
6	60	120	75	120	90	180
7	60	80	75	100	90	120
8	60	80	75	100	90	120
9	60	80	75	100	90	120
10	60	-	75	-	90	-
11	60	-	75	-	90	-
12	60	-	75	-	90	-

Table 6.1: The different LED settings used to find the systematic error coming from the LEDs determination.

tors close to the beam dump. Thus, they are counted by the scalers which then consequevtly decrease the total cross section in the first peak energy region.

The systematic uncertainty linked to the LED threshold determination was also studied with the help of the $2\pi^o-$channel. Figure 6.21 (bottom-left) shows the quasi-free inclusive total cross section for different ring settings (see table 6.1). The systemic difference between the different settings are plotted as function of the incident photon beam in Figure 6.21 (bottom-right). The threshold determination induced a systematic error of the order of 5 $\%$.

6.3 The η photoproduction off the deuteron

Four channels were studied :

- $\gamma + d \rightarrow \ \eta \ + X$ (fully inclusive),
- $\gamma + d \rightarrow \ \eta \ + (pn)$ (quasi-free inclusive),
- $\gamma + d \rightarrow \ \eta \ + p(n)$ (quasi-free proton) and
- $\gamma + d \rightarrow \ \eta \ + n(p)$ (quasi-free neutron).

The main goal of this work was the extraction of the angular distributions and of the total cross sections for the η photoproduction off the deuteron. Certain points discussed previously will be again emphasized in this section ($\eta-$meson, proton and neutron four-vector constructions) and other points developed in more details (absolute normalization, weighted average of the different beam times).

6.3.1 The reaction identification

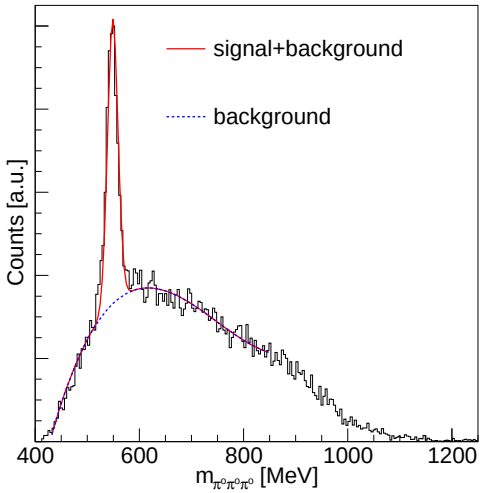

Figure 6.22: *Typical $3\pi^o$ invariant mass spectrum fitted by a combined fit : signal + background. The signal is fitted by a Gaussian function which has the peak position and the width fixed, respectively to 547.3 MeV and 10 MeV. The background is fitted by a polynomial function of third order. The $\eta-$meson was reconstructed from 7 neutral hits for incident photon between 1400 MeV and 1600 MeV.*

For all reactions, the η-meson is identified by its $3\pi^o$ invariant mass distribution (see Figures 6.22 and section 5.5.3). The $3\pi^o$ invariant mass distribution shows a peak at $\sim$ 547.3 MeV (the $\eta-$mass) of σ = 10 MeV (due to

the experimental energy resolution) typical for the $\eta-$signal signature. The η invariant mass spectrum is not background free (see Figures of section 5.5.3 and the $3\pi^o$ invariant mass spectra that are shown in this section). The background below the $\eta-$signal is due to the combinational background coming from three uncorrelated π^o (i.e. this background could go below the $\eta-$peak) like $\gamma + d \rightarrow \pi^o\pi^o\pi^o + X$. This background can be easily treated by an appropriate fit of the $\eta-$signal line shape. The $\eta-$signal line shape is fitted by an usual combined fit : signal (S) + background (B), as illustrated in Figure 6.22. The $\eta-$signal is fitted by a Gaussian which has the peak position and the width fixed, respectively to 547.3 MeV and 10 MeV. The background is fitted by a polynomial function of third order.

For all reactions and all extracted observables the number of $\eta-$meson, N_η, corresponds to :

$$N_\eta^{detected} = \frac{S}{S+B} \cdot N^{detected} \tag{6.11}$$

where :
$N^{detected} = \sum_{m_{\pi^o\pi^o\pi^o}=515\ MeV}^{580\ MeV} N_{m_{\pi^o\pi^o\pi^o}}^{detected}$ is the sum of the (signal + background) events detected for 515 MeV $\leq m_{\pi^o\pi^o\pi^o} \leq$ 580 MeV and
$\frac{S}{S+B}$ is extracted for all reactions studied (with the same fit function).

Among the reactions that can produce $\gamma + d \rightarrow \pi^o\pi^o\pi^o + X$, there are the reactions :

- $\gamma + p \rightarrow \ \eta \ + \pi^o \ + p$
- $\gamma + n \rightarrow \ \eta \ + \pi^o \ + n$

where one the of π^o of the η is not detected. That also means : there is the possibility that the $\eta-$meson coming from one of these two reactions can be detected alone or in coincidence with a nucleon while the remaining π^o is not detected.

But in fact for the $N\eta\pi-$channels there are two reactions on the proton and two reactions on the neutron. Indeed not only this two reactions can give a fake quasi-free reaction signature, but also two additional reactions :

- $\gamma + p \rightarrow \ \eta \ + \pi^+ \ + n$
- $\gamma + n \rightarrow \ \eta \ + \pi^- \ + p$

The production threshold of the $N\eta\pi-$channels is $\sim$ 806 MeV.

Thus from all these reactions a $\eta-$meson can be detected alone or in coincidence with a nucleon while the remaining $\pi^{o,\pm}$ is not detected as shown in Figure 6.23.

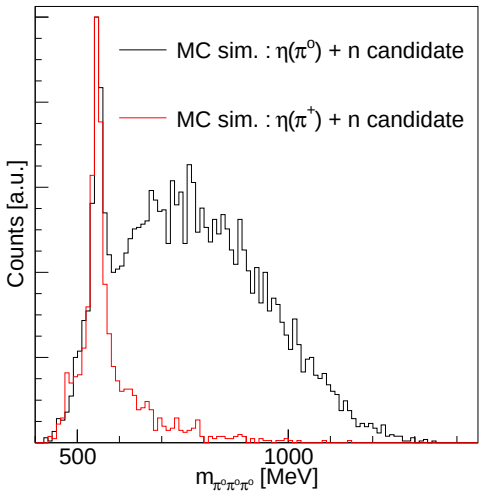

Figure 6.23: *Simulated $3\pi^o$ invariant mass distribution for E_γ = 1400 - 1600 MeV coming from the $\eta\pi-$channels. 7 hits were requested. After the $\Delta m \leq 0$ missing mass cut, this histogram is empty. The combinational background is mainly coming from $\eta\pi^o+$channels.*

In Figure 6.23, the reactions $\gamma + d \rightarrow \eta + \pi^o + n$ and $\gamma + d \rightarrow \eta + \pi^+ + n$ have been simulated. The $\eta-$meson was reconstructed from seven neutral hits. As expected, there is a large combinational background in the $\eta\pi^o-$channel. Thus, in the data, these ηs are going into the $\eta-$peak of the $3\pi^o$ invariant mass distribution. This is not a problem for the study of the fully inclusive reaction as we are looking for such events, but for the quasi-free reactions (or single$-\eta$ photoproduction) study it is a problem. For the quasi-free reactions, the $\eta-$meson is detected alone (for the quasi-free inclusive reaction) or in coincidence with the recoil nucleon (for the quasi-free proton and the quasi-free neutron reactions). Therefore, the $\eta-$meson identication alone is not sufficient for the identification of the quasi-free reactions. A missing mass analysis is necessary to disentangle the single$-\eta-$meson photoproduction from the $N\eta\pi-$channels.

Before giving an example of a missing mass analysis for the identification of the reaction $\gamma + d \rightarrow \eta + n(p)$, a few words should be spent on the kinematical limits for a two body reaction.

For a two body reaction, the kinematical limits of the reaction are easily calculated for a free nucleon target, as well as the kinematical limits of the reaction altered by the Fermi momenta, i.e. for a quasi-free nucleon target. For a quasi-free nucleon target, the kinematical limits are dependent on the reaction kinematics. The calculation gives a hint of the alterations that could occur. Figure 6.24 shows the kinematical limits.

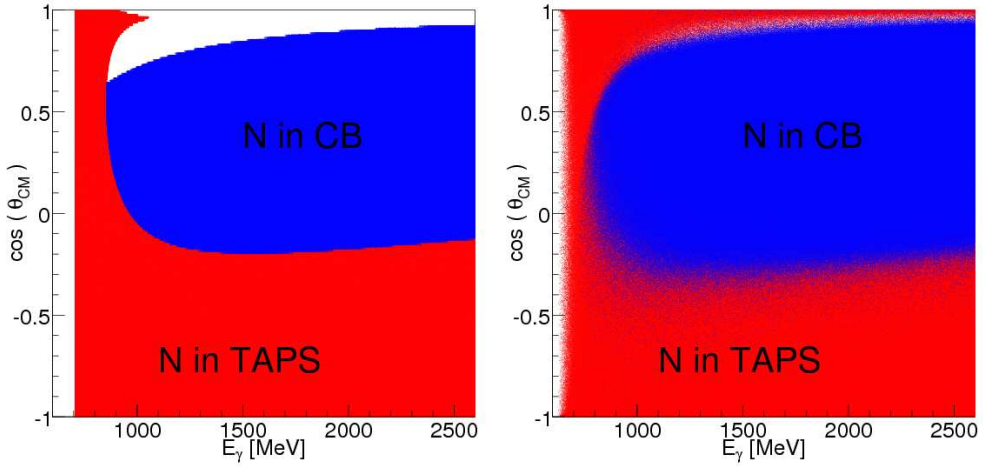

Figure 6.24: *Kinematical limits as a function of incident photon beam and $cos(\theta_{CM})$ of the η-meson in the center-of-mass. Left : for a free nucleon target. Right: for a quasi-free nucleon target. Red area the nucleon is detected in TAPS. Blue area the nucleon is detected in CB. White area : the nucleon is not detected.*

The kinematical limits show, in which part of the detector the recoil nucleon should appear depending on the energy of the incident photon and the polar center-of-mass-angle of the produced $\eta-$meson. On the free proton target, there is a hole in the acceptance (see Figure 6.24-left white area above the $\eta-$meson threshold production), because protons that are detected in the CB should have at least a kinetic energy above $\sim$ 70 MeV. The protons are loosing most of their energy in the Inner detector ($\sim$ 20 MeV / layer). For quasi-free nucleons the kinematics is smeared out by Fermi motion, so that even for mesons at extreme backward angle nucleons may be detected (as shown in Figure 6.24-right). However, systematical uncertainties for this kinematical region are high.

The identification of the reaction $\gamma + d \rightarrow \ \eta \ + n(p)$

Only events with seven neutral hits are considered. The $\eta-$meson is constructed from these seven neutral hits. The neutron candidate is identified by the χ^2-test.

The kinematical limits can also be used to check if the neutron candidate, given by the χ^2-test (see section 5.3.3), and suposedly detected in CB, is a realistic solution or not. The CB detectors can only measure the neutron laboratory angles (θ and ϕ). Therefore, Figure 6.25 shows the kinematical limits as function of the neutron laboratory angle and of the incident photon beam.

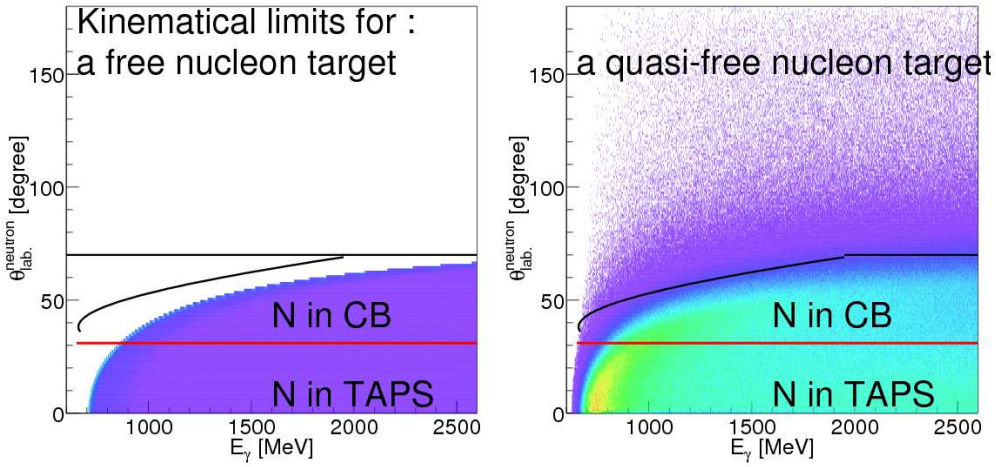

Figure 6.25: *Kinematical limits as a function of incident photon beam and the neutron laboratory angle. Left : for a free nucleon target. Right: for a quasi-free nucleon target. The red line represents the separation between the TAPS and CB detectors. The neutron candidates below the black line are accepted in the analysis.*

The solutions, below the black line in Figure 6.25, are accepted in the analysis. It was checked with the protons that this cut does not remove good events. Indeed with this cut, a big part of the background coming from misidentified neutrons, is removed (this kind of cut can not remove the same type of background in the $2\pi^o-$channel, see Figure 6.6). It should be noted that events which are only allowed by the contribution of the Fermi momenta should not contribute much to the signal except if they correspond to an area which is an "acceptance hole" for the free nucleon target case.

The neutrons in TAPS detectors should fulfill the neutron TOF cuts (as defined in section 5.6.6).

A missing mass analysis is performed not only to disentangle the single $\eta-$meson photoproduction reaction from the competing reactions, but also to confirm that the setup has seen a recoil nucleon in coincidence, and to approximate the kinetic energy of the recoil nucleon detected in CB.

From the missing mass analysis and the reproduction of the missing mass line shape by the MC simulation, a cut is established to remove the background coming from the competing channels. In a first step, the $3\pi^o$ invariant mass distribution is plotted for different incident photon beam ranges. The neutron candidates fulfill the conditions described above. Figure 6.27 (-left column) shows the invariant mass spectra below the production threshold of the $N\eta\pi-$channels, at E_γ = 950 - 1000 MeV, where the resonance that couple strongly to the neutron should be observed, and at E_γ = 1400 - 1600 MeV where the $N\eta\pi$ production should be at its maximum. The combinational background increases with the incident photon energy because the contribution of the $N\eta\pi^o-$channel increases as well. To have a feeling for the contribution of the $N\eta\pi^o-$channel, in Figure 6.26 the total cross section for $\gamma p \rightarrow p\eta\pi^o$ [Igor] is compared to the total cross section for $\gamma p \rightarrow p\eta$. The $N\eta\pi^\pm-$channels should have bigger total cross sections (considering the Clebsch-Gordon coefficients), however, they are somewhat suppressed by the condition that only neutral hits have been detected. Nevertheless, the number of η events coming from those channels is not negligible.

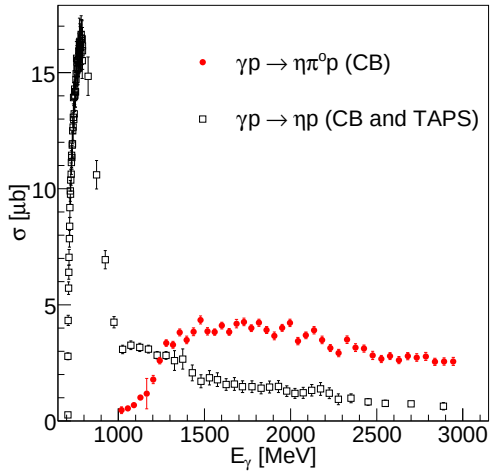

Figure 6.26: *Total cross section for $\gamma p \rightarrow p\eta\pi^o$ [125] (red points) compared to the total cross section for $\gamma p \rightarrow p\eta$ [37] (black open squared).*

If we apply a cut on the invariant mass around the $\eta-$peak (illustrated by the vertical dashed line in Figure 6.27-left-column) and treat the detected neu-

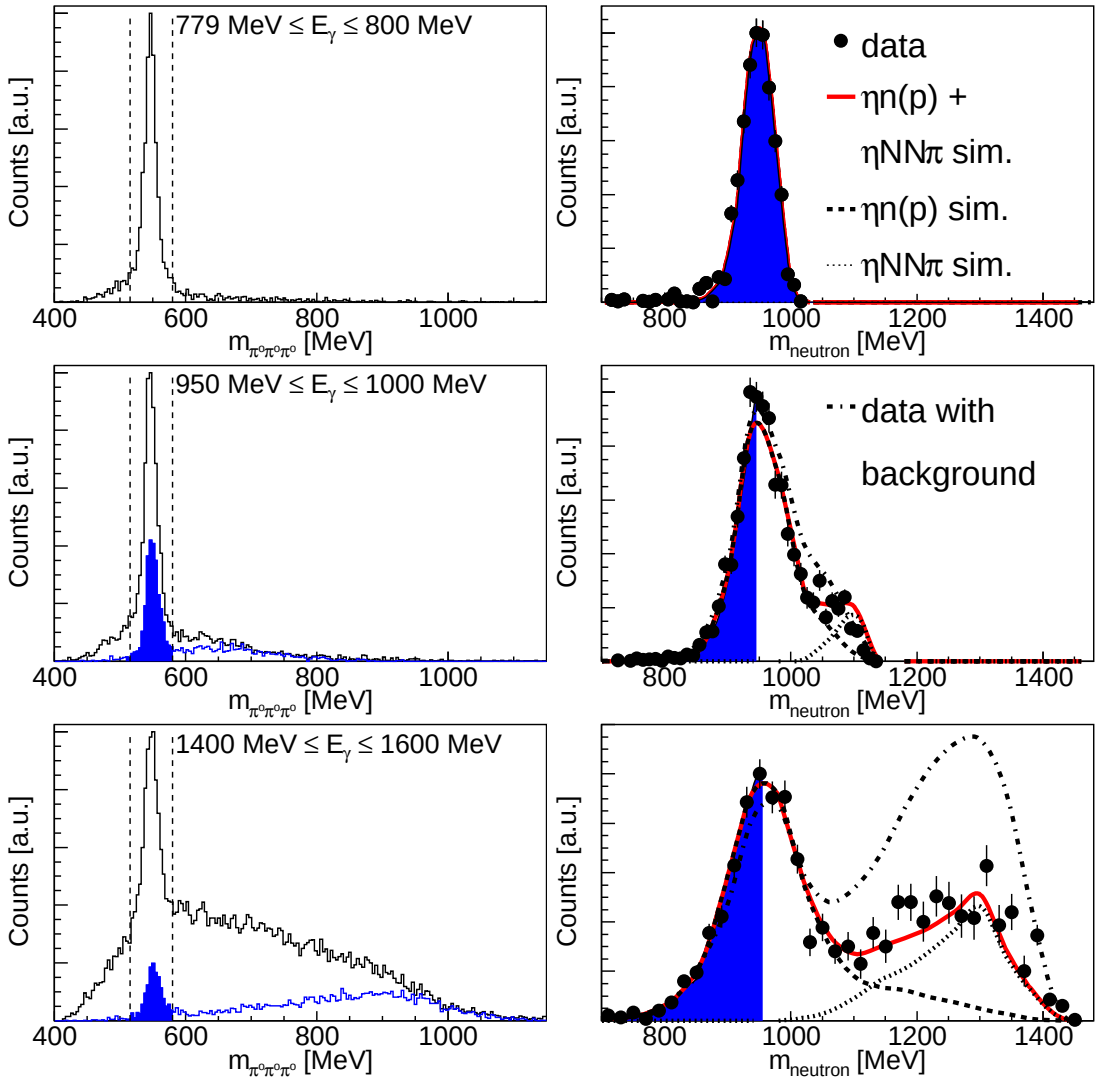

Figure 6.27: *Left column : $3\pi^o$ invariant mass distribution for three different incident photon beam ranges (black line full projection of the two dimensional histogram of Figure 6.28, blue line projection of the two dimensional histogram for the blue area of the missing mass distribution). Right column : Missing mass distribution for the same photon beam ranges (for $515\ MeV\ \leq m_{\pi^o\pi^o\pi^o} \leq 580\ MeV$−dashed vertical lines). The blue area corresponds to the cut applied in the missing mass to remove the $\eta\pi$ background.*

tron as a missing particle, we obtain the corresponding missing mass which is shown in Figure 6.27 (right-column) as dashed-dotted line.

The comparison to MC simulation is simplified if the combinational background is removed. This is done by extracting the $\frac{S}{S+B}$ ratio for the invariant mass spectrum for all bins of the missing mass histograms. After the evaluation of the number of η's that contribute to missing mass spectra correspond-

ing to the peak-over-background signal in invariant mass are plotted as data points with error bars.

Figure 6.28 summarizes this evaluation. For example, in the bottom row of Figure 6.28, a two dimensional histogram is plotted : the missing mass ($m_{neutron}$) versus the $3\pi^o$ invariant mass ($m_{\pi^o\pi^o\pi^o}$) for the incident photon beam range E_γ = 1400 - 1600 MeV. The coincidence peak corresponding to the $\eta-$meson detected in coincidence with the recoil neutron is barely seen due to the background coming from the competing channels (and low statistics). By comparison for lower incident photon beam ranges, Figure 6.28 (left-top-row and left-middle-row), the coincidence peak is clearly seen for $m_{neutron} \sim$ 939.56533 MeV and for $m_{\pi^o\pi^o\pi^o} \sim$ 547.3 MeV. For different missing mass values (as shown in Figure 6.28-middle and -left column), the η number is estimated. For $m_{neutron}$ values close to the neutron mass (Figure 6.28-middle column) the combinational background is low. But for higher $m_{neutron}$ values, the combinational background is pretty high (Figure 6.28-bottom left column). In addition to the competing channels, the $\eta-$meson photoproduction off the neutron was simulated : $\gamma + n(p) \rightarrow \eta + n(p)$. All the channels simulated have been generated according to phase space distributions in quasi-free kinematics taking into account the Fermi motion of the nucleons derived from the deuteron wave function (exactly as for the $2\pi^o-$channel simulations). The simulated missing mass distributions are shown in Figure 6.27 (-right colum) for the single $\eta-$channel (dotted line) and for the $\eta\pi^\pm-$channels (dashed line). The two distributions have been adjusted to the data distribution in such a way that the sum of the two simulated distributions (red line) matches the data distribution.

A very conservative cut is applied, above the $\eta\pi$ production threshold, to remove the $N\eta\pi$ background. It is represented by the blue area in the missing mass distribution. The result of this cut can be seen in the invariant mass distribution (blue line). The statistics is drasticaly reduced. Some background is still remaining. This background is coming from three uncorrelated π^o i.e. $\gamma + d \rightarrow \pi^o\pi^o\pi^o + X$.

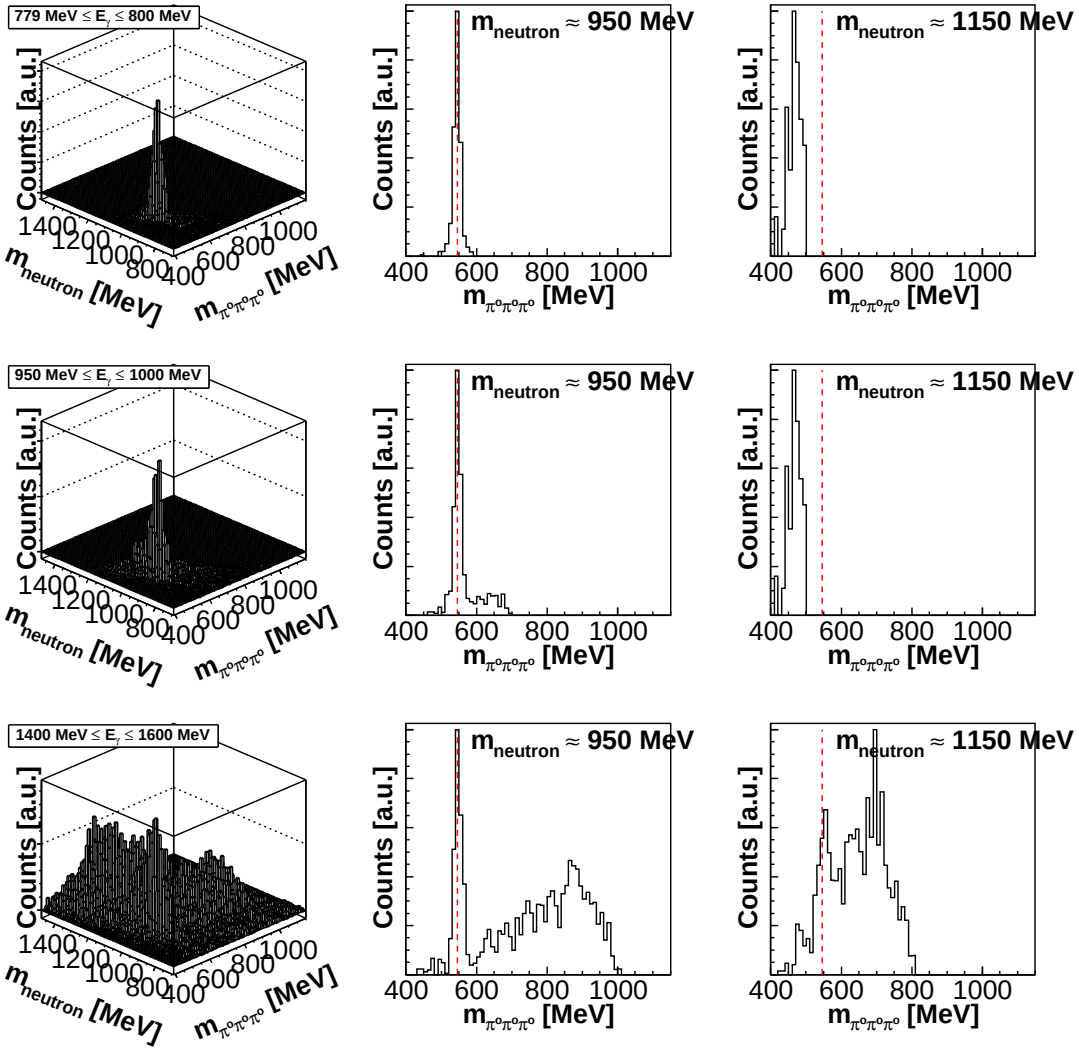

Figure 6.28: *Left column : Missing mass $m_{neutron}$ vs. the $3\pi^o$ invariant mass $m_{\pi^o\pi^o\pi^o}$ for three different incident photon beam ranges. Top row : E_γ = 779 - 800 MeV. Middle row: E_γ = 950 - 1000 MeV. Bottom row : E_γ = 1400 - 1600 MeV. Middle and right column : projection on the $m_{\pi^o\pi^o\pi^o}-$axis respectively for $m_{neutron}$ = 950 MeV $\pm$ 50 MeV and for $m_{neutron}$ = 1150 MeV $\pm$ 50 MeV. Red dashed line corresponds to the $\eta-$mass, 547.3 MeV.*

Figure 6.29 (left) shows the peak position and the peak position $\pm 3 \times \sigma$ of the simulated missing mass distribution (when the nucleon mass is subtracted) as a function of the incident photon beam energy (for the quasi-free inclusive reaction).

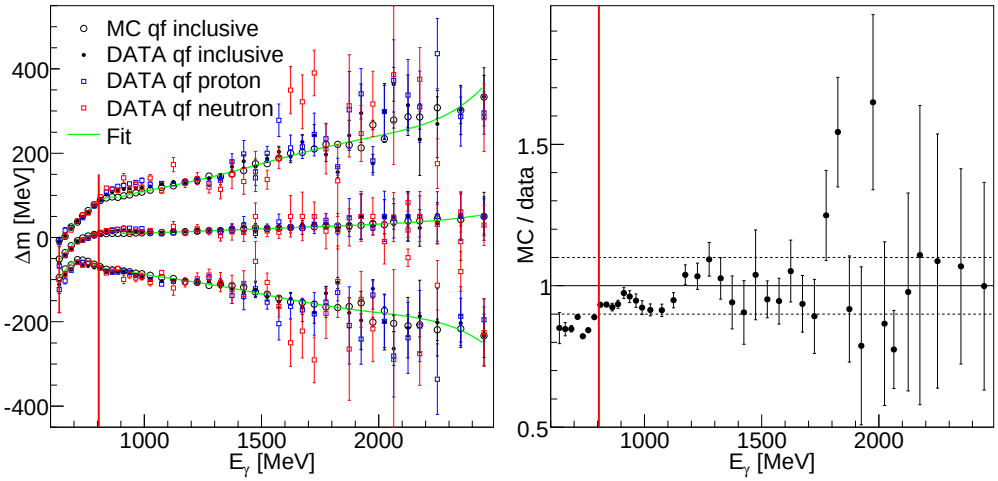

Figure 6.29: *Left : The peak position and the peak position* $\pm 3 \times \sigma$ *of the simulated missing mass distribution (when the nucleon mass is subtracted) as a function of the incident photon beam. Right : (MC: peak position* $-3 \times \sigma$*) / (data: peak position* $-3 \times \sigma$*) for the quasi-free inclusive reaction. The vertical red line represents the* $\eta\pi$ *threshold production,* $E_\gamma \sim 806$ *MeV.*

The MC missing mass peak position and the peak position $\pm 3 \times \sigma$ are compared to the data missing mass peak position and the peak position$\pm 3 \times \sigma$ (data : quasi-free inclusive, proton and neutron reactions). Above the $\eta\pi$ production threshold, where the cut on the missing mass is applied, the systematic difference between data and MC ranges from $\pm$ 10 $\%$ to below $\pm$ 5 $\%$. Figure 6.29 (right) shows the systematic difference between data and MC for the quasi-free inclusive reaction. Plotted is the ratio $\frac{MC\text{: }peak\ postion-3\times\sigma}{data\text{: }peak\ postion-3\times\sigma}$ as a function of the incident photon beam. The small difference can be attribute to approximations in the MC simulation. Below the $\eta\pi$ production threshold no missing mass cut is applied. Above the $\eta\pi$ production threshold, a missing mass cut is applied. This cut is the same for the three quasi-free reactions (inclusive, proton and neutron) studied. Events that are between the missing mass peak position and peak position $-3 \times \sigma$ are allowed. This cut is parametrised by a fit (green line) in Figure 6.29 (left) and will be called in the rest of this thesis : cut for $\Delta m \leq 0$. Cut for Δm would be : events that are between the missing mass peak position $+3 \times \sigma$ and peak position $-3 \times \sigma$ are allowed.

In summary, the reaction identification of $\gamma + d \rightarrow \eta + n(p)$ is based on the

identification of the $\eta-$meson, the recoil neutron and the missing mass analysis.

Before explaining the determination of the efficiencies, the key points of the reaction identification for the other channels of interest will be described.

The identification of the reaction $\gamma + d \rightarrow \ \eta \ + X$

Events from six to eleven neutral hits are considered (there is no limitation on the number of charged hits). The $\eta-$meson is constructed from this six to eleven neutral hits (as described in section 5.5.3). The reaction identification is only based on the identification of the $\eta-$signal.

The identification of the reaction $\gamma + d \rightarrow \ \eta \ + (pn)$

Events from six to seven hits are considered, i.e. six neutral hits only or six neutral hits and one charged hit or seven neutral hits only. The $\eta-$meson is constructed from this six or seven neutral hits. Some constraints are applied on the 7th hit (charged or neutral). If, the 7th hit is in the TAPS detector, it should have a TOF $>$ 4 ns. If the 7th hit is in the CB detector and is neutral, it should have a laboratory $\theta-$angle below 70 degrees. Above the $\eta\pi$ production threshold a $\Delta m \leq 0$ cut is applied. The reaction identification is based on the identification of the $\eta-$meson and of the single$-\eta-$meson production.

The identification of the reaction $\gamma + d \rightarrow \ \eta \ + p(n)$

Events with six neutral hits and one charged hit are considered. The $\eta-$meson is constructed from this six neutral hits. If the charged hit is in TAPS detectors, it should have a TOF $>$ 4 ns. The TOF is used to construct the four-vector of this particle. If the charged hit is in the CB detector, the missing mass analysis is used to approximate the kinetic energy of this particle. Above the $\eta\pi$ production threshold a $\Delta m \leq 0$ cut is applied. Below the $\eta\pi$ production threshold all the charged hits are considered as protons, above the $\eta\pi$ production threshold, the charged hit is considered as a proton if the event passes the $\Delta m \leq 0$ cut. The reaction identification is based on the identification of the $\eta-$meson, the recoil proton and of the single$-\eta-$meson production.

Once, the reactions are identified, the number of events corresponding to each reaction can be counted. To do so as shown by equation 6.11, the S / (S+B) (or B / (S+B)) ratio has to be extracted.

The extraction of B / (S+B)

The background, B / (S+B), was found for each reaction studied, and for each $E_\gamma-$cell for the total cross section, and for each $(E_\gamma, cos(\theta_{cm}))-$cell for the differential cross section. For the background estimation the four beam times have been added. The extraction of B / (S+B) is based on the fit of the $3\pi^o$ invariant mass spectrum. The fit function is a Gaussian of fixed parameters (peak and width) plus a polynomial of third order (as explained earlier). The error matrix of the fit was used to estimate the uncertainty of B / (S + B) by taking into account the effects of the correlation of the errors which are only dependent (as the Gaussian parameters are fixed) of the polynomial function. This is important to mention as this error should be included in the statistical error. Then the statistical error should be :

$$\sqrt{\left(\frac{\Delta N_\eta^{detected}}{N_\eta^{detected}}\right)^2 + \left(\frac{\Delta\left(\frac{B}{S+B}\right)}{\frac{B}{S+B}}\right)^2} \tag{6.12}$$

with

$$\Delta\left(\frac{B}{S+B}\right) = 1\cdot\epsilon_{11} + x^2\cdot\epsilon_{22} + x^4\cdot\epsilon_{33} + 2(x\cdot\epsilon_{12} + x^2\cdot\epsilon_{13} + x^3\cdot\epsilon_{23}) \tag{6.13}$$

where ϵ_{ij}'s are the covariant terms in the symmetric error matrix.

Figure 6.30 shows the evolution of the background as a function of the incident photon beam. The background behavior has been parameterized by a fit.

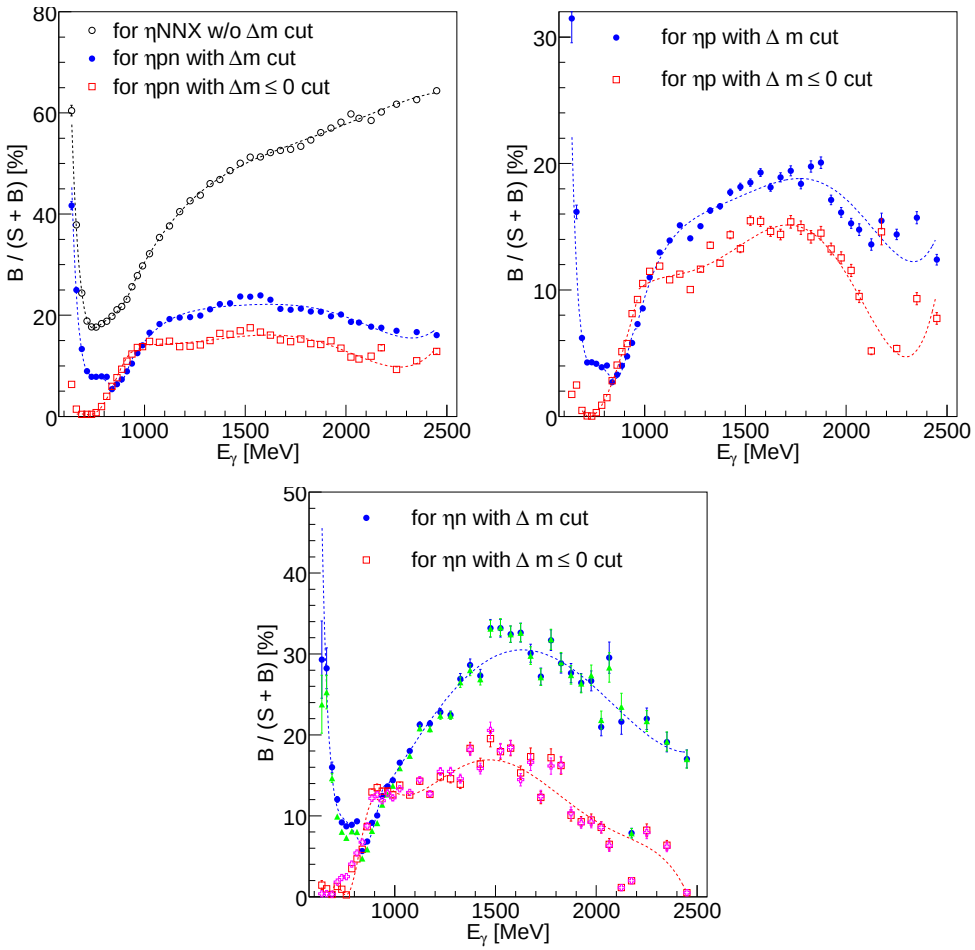

Figure 6.30: *Background evolution as a function of the incident photon beam. Top left : for the fully and the quasi-free inclusive reactions. Top Right : for the quasi-free proton reaction. Bottom : for the quasi-free neutron. (Δm cut blue squared, $\Delta m \leq 0$ cut red open squared, for the quasi-free neutron in addition Δm cut green sqaredand $\Delta m \leq 0$ cut violet open squared for neutron TOF $>$ 4 ns). The lines correspond to the fit of the background evolution.*

Figure 6.31 shows the evolution of the background as a function of $cos(\theta_{cm})$ of the $\eta-$meson in the center-of-mass for different incident photon beam ranges for the quasi-free neutron case. The background behavior is again parameterized by a fit.

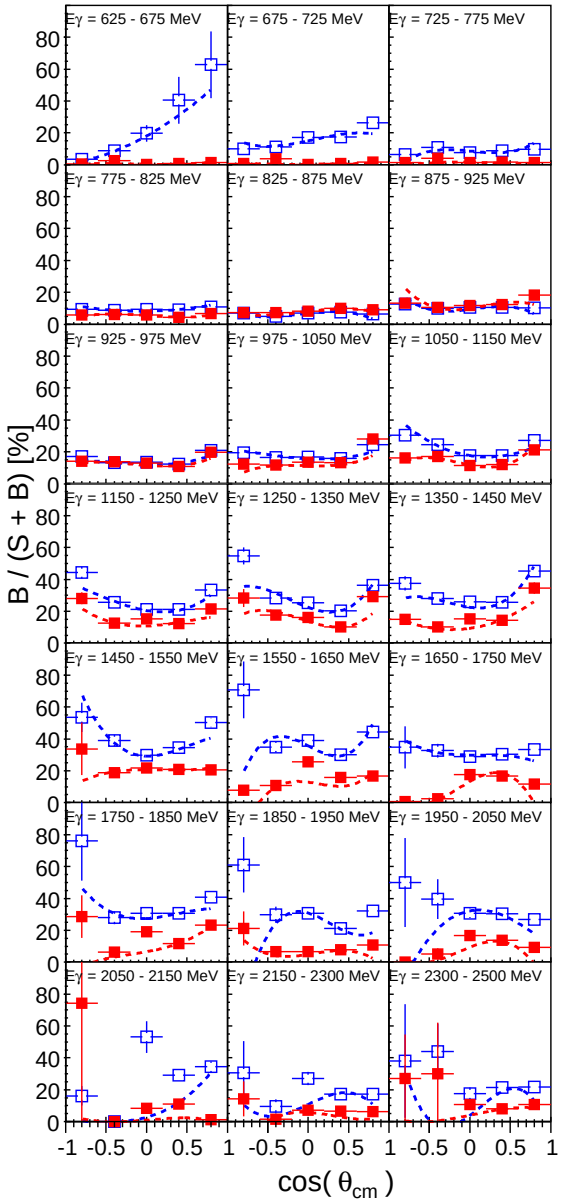

Figure 6.31: *Background evolution as a function of $cos(\theta_{cm})$ of the $\eta-$meson in the center-of-mass for different incident photon beam ranges for the quasi-free reaction (blue open squared Δm cut, red squared $\Delta m \leq 0$ cut).*

6.3.2 The determination of the detection efficiency

The acceptance correction for the reaction $\gamma + d \rightarrow \ \eta \ + X$: $\epsilon(NN\eta X)$

The fully inclusive reaction identification is based on the identification of the $\eta-$meson. Therefore the simulation must also be based on the simulation of the $\eta-$meson (hence the software trigger choice - section 5.4). The η-meson detection efficiency depends on the correlation between the kinetic energy ($T_{\eta,lab.}$) and polar angle ($\theta_{\eta,lab.}$) of the mesons. The detection efficiency was simulated as function of $T_{\eta,lab.}, \theta_{\eta,lab.}$. This efficiency was corrected event-by-event using the measured $T_{\eta,lab.}, \theta_{\eta,lab.}$ of the mesons. It is therefore independent on any assumptions about the kinematical distributions of the $\eta-$mesons.

For the quasi-free reactions, strong kinematical constraints have been applied to identify the channel of interest (invariant mass cut, missing mass cut for $\Delta m \leq 0$ and kinematical cuts for the quasi-free neutron as explained in section 6.3.1) in order to have an optimal signal-to-background ratio. All these constraints make require the MC simulation for the reactions :

- $\gamma + p(n) \rightarrow \eta + p(n)$ and
- $\gamma + n(p) \rightarrow \eta + n(p)$.

in order to estimate the signal loss by these cuts.

The first approach would be to rely entirely on MC simulation of the two channels above to find the effiencies. The above channels were (as already mentioned) generated according to phase space distributions in quasi-free kinematics taking into account the Fermi motion of the nucleons derived from the deuteron wave function. Such a phase space simulation is accurate enough to determine the signal loss due to the dufferent cuts apllied. However, it is not necessarily precise enough for the absolute detection efficiency of the $\eta-$meson. For the $2\pi^o$ photoproduction off the deuteron (see section 6.2.5), we clearly saw that the acceptance correction uncertainty due to the phase space simulation choice was not negligible (see Figure 6.16). In order to minimize the acceptance correction uncertainty an alternate acceptance correction was chosen.

The acceptance correction for the reaction $\gamma + d \rightarrow \ \eta \ + (pn)$: $\epsilon(pn\eta)$

The quasi-free reaction identification is based on the identification of the $\eta-$meson and on the single$-\eta-$meson production. The acceptance correction can also be decomposed into two parts : one correction for the $\eta-$meson (which is a correction similar to the one done for the fully inclusive) and one

correction for the single$-\eta-$meson production (i.e. the correction for the signal loss due to the cuts in order to identify the reaction).

The acceptance correction for the reaction $\gamma + d \rightarrow \ \eta \ + p(n)$: $\epsilon(p\eta)$

The quasi-free proton reaction identification is based on the identification of the $\eta-$meson, the recoil proton and of the single$-\eta-$meson production. The acceptance correction can also be decomposed into three parts : one correction for the $\eta-$meson, one correction for the recoil proton (as for the $\eta-$meson, the proton detection efficiency is corrected event-by-event) and one correction for the single$-\eta-$meson production.

The acceptance correction for the reaction $\gamma + d \rightarrow \ \eta \ + n(p)$: $\epsilon(n\eta)$

The quasi-free neutron reaction identification is based on the identification of the $\eta-$meson, the recoil neutron and of the single$-\eta-$meson production. The acceptance correction can also be decomposed into three parts : one correction for the $\eta-$meson, one correction for the recoil neutron (as for the $\eta-$meson, the neutron detection efficiency is corrected event-by-event) and one correction for the single$-\eta-$meson production.

The different efficiencies could be factorized as following :

$$\epsilon(NN\eta X) = \epsilon_{\eta}^{'} \tag{6.14}$$
$$\epsilon(pn\eta) = \epsilon_{\eta} \cdot \epsilon^{loss}(pn\eta) \tag{6.15}$$
$$\epsilon(p\eta) = \epsilon_{\eta} \cdot \epsilon_{proton} \cdot \epsilon^{loss}(p\eta) \tag{6.16}$$
$$\epsilon(n\eta) = \epsilon_{\eta} \cdot \epsilon_{neutron} \cdot \epsilon^{loss}(n\eta) \tag{6.17}$$

$\epsilon_{\eta}^{'}$ and ϵ_{η} are different (the difference is explained later in the summary on the key points of the $\eta-$meson efficiency determination).

To be clear, the $\eta-$meson and the recoil nucleon (if detected) are corrected event-by-event using the measured $T_{\eta,lab.}, \theta_{\eta,lab.}$ and $T_{nucleon,lab.}, \theta_{nucleon,lab.}$. The signal loss (which is reaction dependent) was corrected depending on the $\eta-$meson center-of-mass angle and incident photon energy with the phase space simulation.

The proton and the neutron detection efficiencies were already determined (see sections 5.6.3 and 5.6.4). Remains to find the $\eta-$meson detection efficiency. Since the actual distribution of $\eta-$angle and kinetic energy is not known an assumption must be made for the start distribution in the MC simulation.

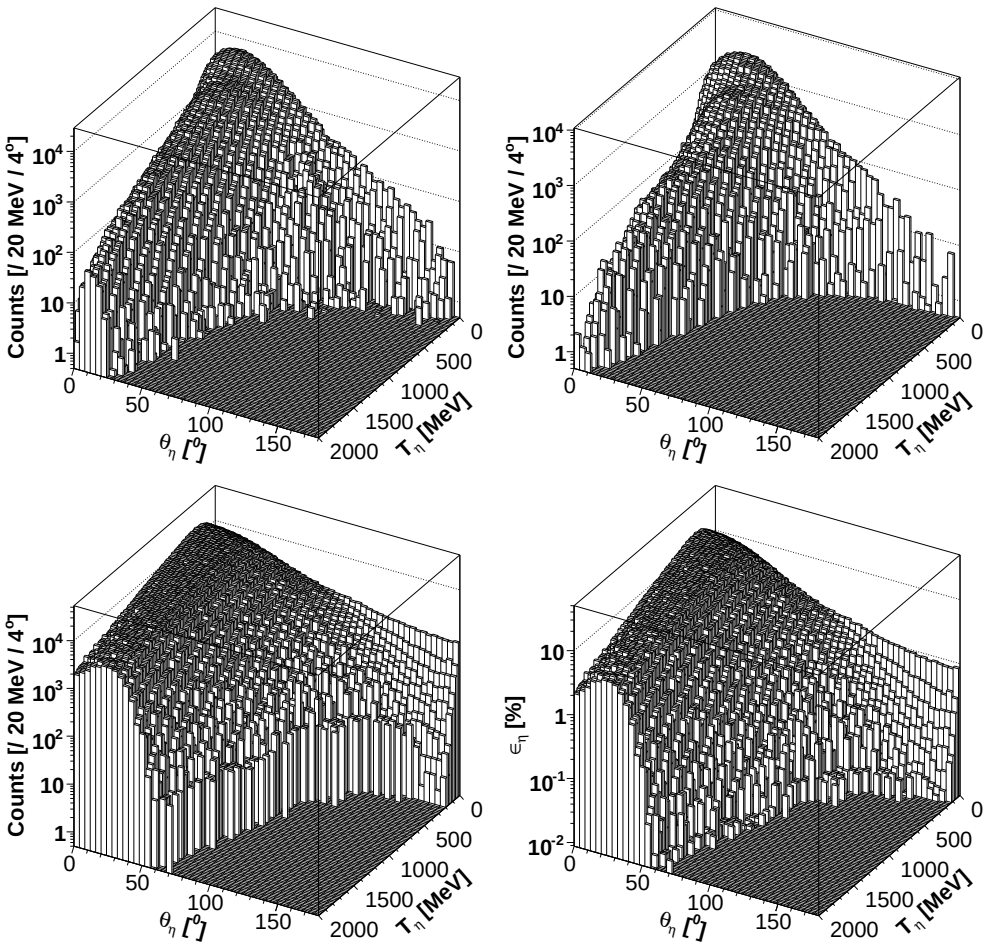

Figure 6.32: *Upper left : Distribution of the reconstructed events for the measured data that includes all channels with a η decay. Upper right : Distribution of the reconstructed events for the measured data in the case of single $\eta-$meson photoproduction (i.e. a missing mass cut was done $\Delta m \leq 0$). Lower left : Distribution of the reconstructed events for the Monte Carlo simulation when the start distribution is isotropic. Lower right : The $\eta-$meson detection efficiency for six neutral hits.*

The start distribution chosen for the $\eta-$meson was isotropic. If the start distribution chosen was truly correct the distribution of the reconstructed events for the measured data and the Monte Carlo simulation should be the same. However, even if the distributions are not identical, the event-by-event correction is still correct. It was shown in [126] that the distribution is only influenced by limited resolution which could be iterated but has in fact only small influence. Figure 6.32 shows the distribution of the data as function of the T_η and θ_η (upper row for the fully inclusive left and the quasi-free inclusive right) and the simulated distribution reconstructed and the simulated detection efficiency (lower row). The important point is, that the limit of non-vanishing

detection efficiency is much more extended than the region where due to the reaction kinematics data is observed, so that no systematic bias occurs due to acceptance holes.

Two $\eta-$meson detection efficiencies were determined : one for the fully inclusive and one for the quasi-free reactions.

Below a short summary on the key points of the $\eta-$meson efficiency determination:

- $\eta \rightarrow \pi^o\pi^o\pi^o \rightarrow 6\gamma$ isotropically launched through the setup
- neutral hits are identified by the setup (the CFD, cluster/PED thresholds included in MC)
- events with six to eleven neutral hits are selected (event that has between seven and eleven neutral hits are split-offs)
- all possible combinations of photon pairs are tested
- χ^2-test that gives the best solution for $3\pi^o$
- cut on the π^o mass between 110 MeV and 160 MeV
- π^o mass constrain
- application of the software trigger on the 6γs of the $3\pi^o$.
- a $\eta-$meson is defined has been seen if the $m_{\pi^o\pi^o\pi^o}$ is between 515 MeV and 580 MeV (the invariant mass is fitted by a combined fit : signal + background)
- Number of $\eta-$mesons corresponding to six neutral hits,$N_{6hits}^{detected}$, is counted and
- the corresponding efficiency is deduced $\epsilon_\eta = \frac{N_{6hits}^{detected}}{N^{started}}$,
- Number of $\eta-$mesons corresponding to six to eleven neutral hits,$N_{6\rightarrow 11hits}^{detected}$ is counted and
- the corresponding efficiency is deduced $\epsilon_\eta^{'} = \frac{N_{6\rightarrow 11hits}^{detected}}{N^{started}}$.

For the fully inclusive, the efficiency determination in principle is done once the η-meson detection efficiency has been determined. However, an additional step can be introduced. The event-by-event correction of the detection efficiency using the histogram from Figure 6.32 introduces additional statistical fluctuations since the efficiency cannot be simulated with arbitraryly good statistical quality (requires too much computer power). Therefore, as function of

any observable (incident photon beam energy, cm-angle, etc ...) the detection efficiency can be re-calculated from the ratio of the observed counts and the efficiency corrected counts. Since the efficiencies are smooth fractions, they can be fitted by polynomials and then this smoothed efficiency curves are used to correct the data. The efficiencies that can be re-calculated are : $\epsilon_{\eta}^{'}$, ϵ_{η}, the product $\epsilon_{\eta} \cdot \epsilon_{proton}$ and the product $\epsilon_{\eta} \cdot \epsilon_{neutron}$.

The efficiency re-calculated, ϵ^{grid} is :

$$\epsilon^{grid} = \frac{N^{detected}}{N^{detected}_{corrected}} \tag{6.18}$$

where $N^{detected}$ is the number of detected counts (S+B) and $N^{detected}_{corrected}$ is corresponding to the counts corrected by the event-by-event efficiency.

These efficiencies were re-calculated for the phase-space MC simulations of the quasi-free reactions (inclusive, proton and neutron) and the MC simulations based on the actual distribution of the data (which we will call "MC-data" simulations). Before showing the results, an example of the recalculation for the quasi-free neutron reaction should be given :

The ϵ^{grid} as function of $cos(\theta_{cm})$ is :

$$\epsilon^{grid}(cos(\theta_{cm})) = \frac{N^{detected}(cos(\theta_{cm}))}{N^{detected}_{corrected}(cos(\theta_{cm}))} \tag{6.19}$$

For a quasi-free neutron reaction, $N^{detected}_{corrected}$ is:

$$N^{detected}_{corrected} = \sum_{event\ i=1}^{event\ n} \frac{N_i^{detected}(T^i_{\eta,lab.}, \theta^i_{\eta,lab.}, T^i_{n,lab.}, \theta^i_{n,lab.})}{\epsilon_{\eta}(T^i_{\eta,lab.}, \theta^i_{\eta,lab.}) \cdot \epsilon_{neutron}(T^i_{n,lab.}, \theta^i_{n,lab.})} \tag{6.20}$$

Figure 6.33 shows the $N^{detected}$ distribution, the $N^{detected}_{corrected}$ distribution and the deduced efficiency (from eq. 6.19) as function of the $cos(\theta_{cm})$ for the MC-data and for the MC simulation for different incident photon energies for the quasi-free neutron reaction. The re-calculated efficiency from the MC-data and the phase-space MC simulations is very similar (for all incident photon beam ranges as it will be seen in Figure 6.38). Therefore, the MC simulation, based on phase-space that takes into account the Fermi motion of the nucleons derived from the deuteron wave function, is a realistic simulation. But, only the efficiency as function of the $cos(\theta_{cm})$ is calculated correctly by a phase-space MC simulation. In Figure 6.33, it can be seen that the data $N^{detected}$ and the MC-data $N^{detected}_{corrected}$ distributions are different above $E_{\gamma} = 1$ GeV from the phase-space MC $N^{detected}$ and $N^{detected}_{corrected}$ distributions.

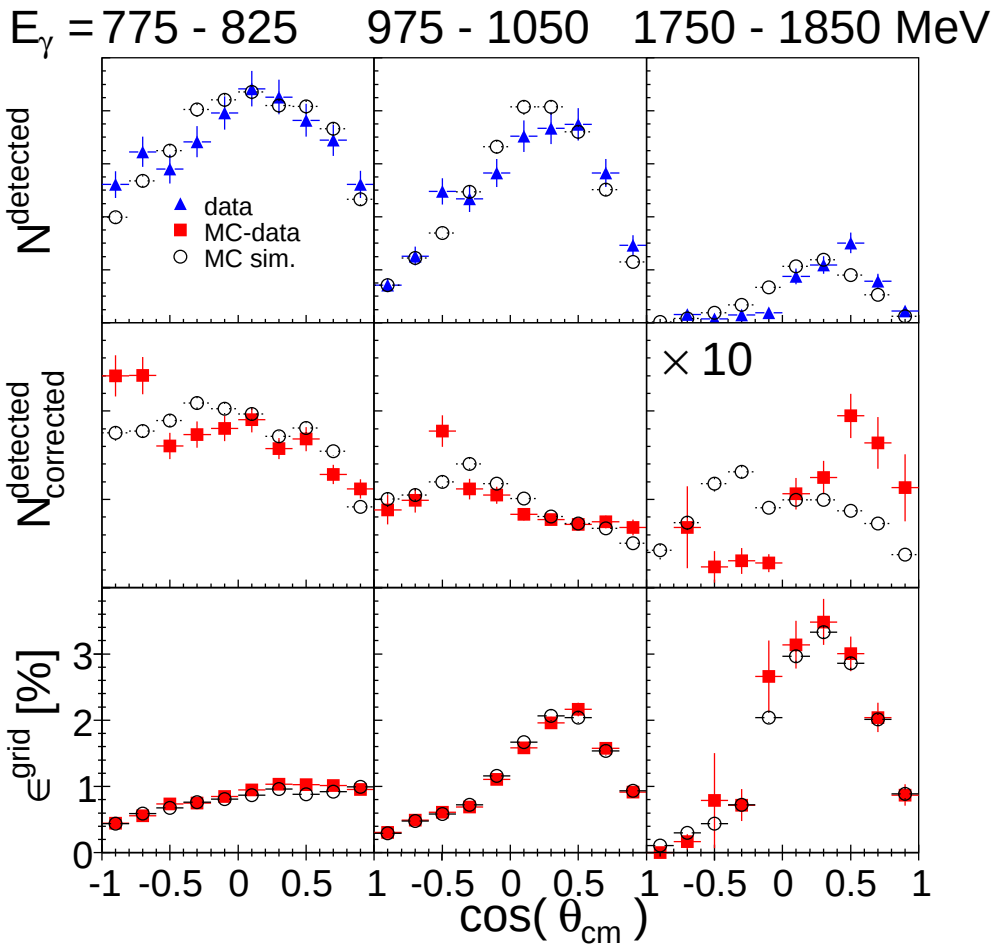

Figure 6.33: *The $N^{detected}$ (top row) distribution, the $N^{detected}_{corrected}$ (middle row) distribution and the deduced efficiency (bottom row) as function of the $cos(\theta_{cm})$ for the quasi-free neutron reaction for three different incident photon beam ranges. The phase-space MC simulation $N^{detected}$ and $N^{detected}_{corrected}$ distributions are "normalized" to the data and MC-data distributions. The MC-data and phase-space MC simulation $N^{detected}_{corrected}$ distributions for E_γ = 1750 - 1850 MeV are enhanced by a factor of magnitude.*

The ϵ^{grid} as function of the incident photon energy is :

$$\epsilon^{grid}(E_\gamma) = \frac{\sum(N^{detected}_{corrected}(cos(\theta_{cm})) \cdot \epsilon^{grid}(cos(\theta_{cm})))}{\sum N^{detected}_{corrected}(cos(\theta_{cm}))} \tag{6.21}$$

From equation 6.21, it is clear that if the $N^{detected}_{corrected}$ distribution is different for the MC-data and the phase-space MC simulation, then the re-calculated efficiency would be also different for the MC-data and the phase-space MC simulation. Figure 6.34 shows the re-calculated efficiencies for all reactions

as function of the incident photon beam (left column) and the systematic difference between the re-calculated efficiency from the MC-data and the phase-space MC simulation i.e. $\epsilon^{grid}_{MC-data}/\epsilon^{grid}_{MC}$ (for the quasi-free reactions only).

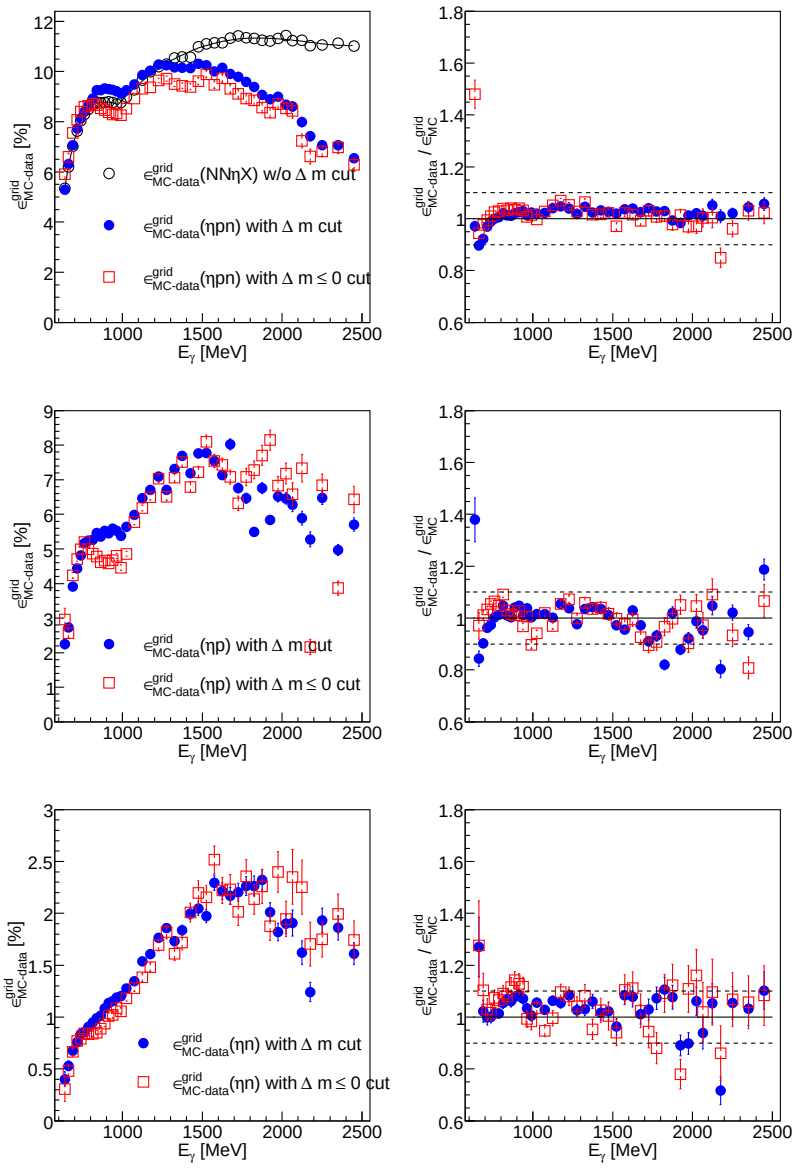

Figure 6.34: *Left column : The re-calculated efficiency as a function of the incident photon beam energy. Right column : The systematic difference between MC-data and MC simulation. From top to bottom respectively for the fully and quasi-free inclusive, for the quasi-free proton and the quasi-free neutron. The MC-data $N^{detected}_{corrected}$ distribution should be used to recalculate the efficiency from MC simulation.*

For the quasi-free inclusive, the data and phase-space MC simulation distributions as function of $T_{\eta,lab.}, \theta_{\eta,lab.}$ were also compared. Figure 6.35 shows that

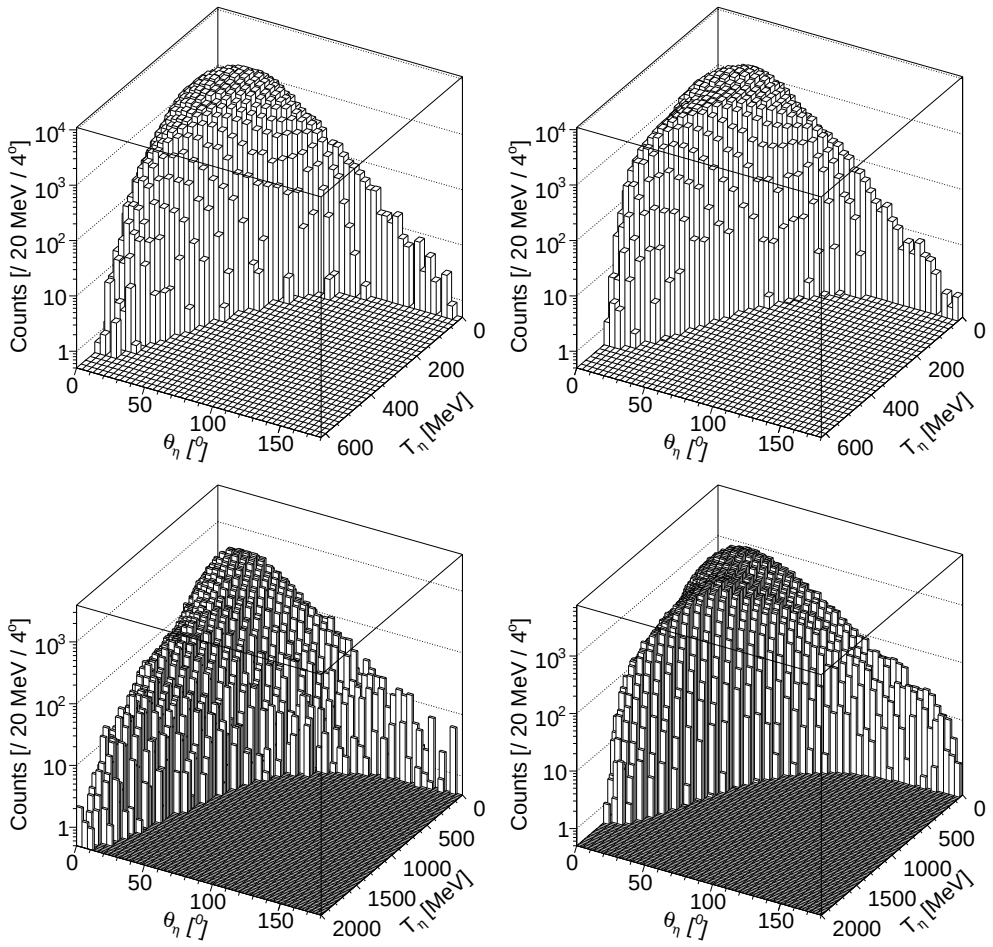

Figure 6.35: *Upper left : Distribution of the reconstructed events for the measured data for the quasi-free inclusive reaction below 1 GeV. Upper right : Distribution of the reconstructed events for the simulation for the quasi-free inclusive reaction below 1 GeV. Lower left : Distribution of the reconstructed events for the measured data for the quasi-free inclusive reaction above 1 GeV. Lower right : Distribution of the reconstructed events for the simulation for the quasi-free inclusive reaction above 1 GeV.*

below E_γ = 1 GeV (top row), the data and phase-space MC simulation distributions look similar, whereas they are different above E_γ = 1 GeV. Therefore, to re-calculate the efficiency as function of E_γ, the actual distribution of the data must be taken into account (in section 6.3.3, it will be explained why we need to re-caculate the efficiency as funcion of the incident photon beam energy).

It remains now to determine the signal loss for the different quasi-free reactions due to all the different cuts applied. The signal loss is the number of phase space MC simulation events detected corrected divided by the initial number of events simulated.

$$\epsilon^{loss} = \frac{N^{detected}_{corrected}}{N^{started}} \tag{6.22}$$

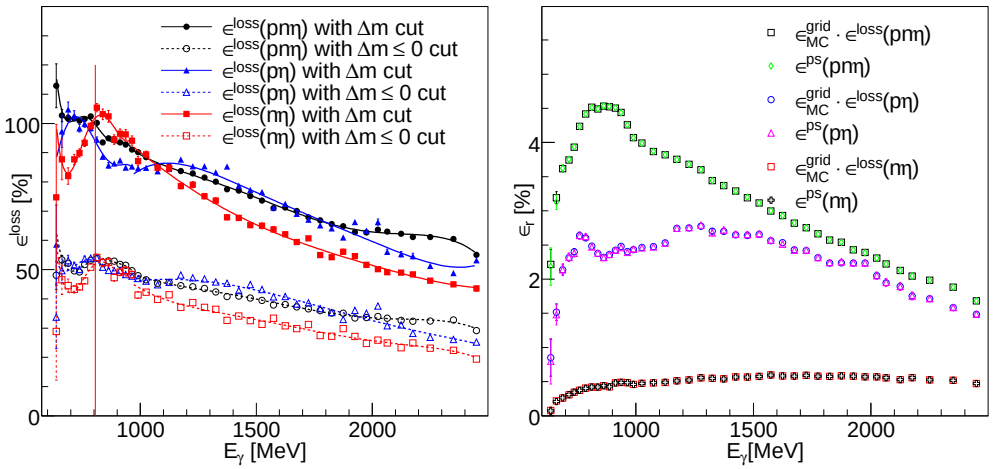

Figure 6.36: *Left : Simulated signal loss as function of the incident photon beam. Right : Simulated efficiency as function of the incident photon beam calculated directly and by using the $\eta-$meson, the proton and the neutron detection efficiencies and the signal loss due to the $\Delta m \leq 0$ cut (and the additional cuts to get a better signal-to-background ratio).*

Figure 6.91 (left) shows the signal loss for all quasi-free reactions. As internal consistency check that the $\eta-$meson, the proton and the neutron detection efficiencies are correct, the reaction efficiency ϵ_r determined from phase space MC simulation of the reactions (ϵ^{ps}) or from the grid efficiencies and the signal loss should be equal i.e. $\epsilon_r = \epsilon^{ps}(= \frac{N^{detected}}{N^{started}}) = \epsilon^{grid} \cdot \epsilon^{loss}$ (for the check purposes ϵ^{grid}_{MC} was calculated by using the phase-space MC simulation $N^{detected}_{corrected}$ distribution). Figure 6.91 (right) shows the perfect agreement between $\epsilon^{grid}_{MC} \cdot \epsilon^{loss}$ and ϵ^{ps} and tells that the grid method is working perfectly, and is independent of the input for the start distributions for the simulated quasi-free reactions.

Now, the different reaction efficiencies can be calculated. Figure 6.37 shows the efficiencies as function of the incident photon beam.

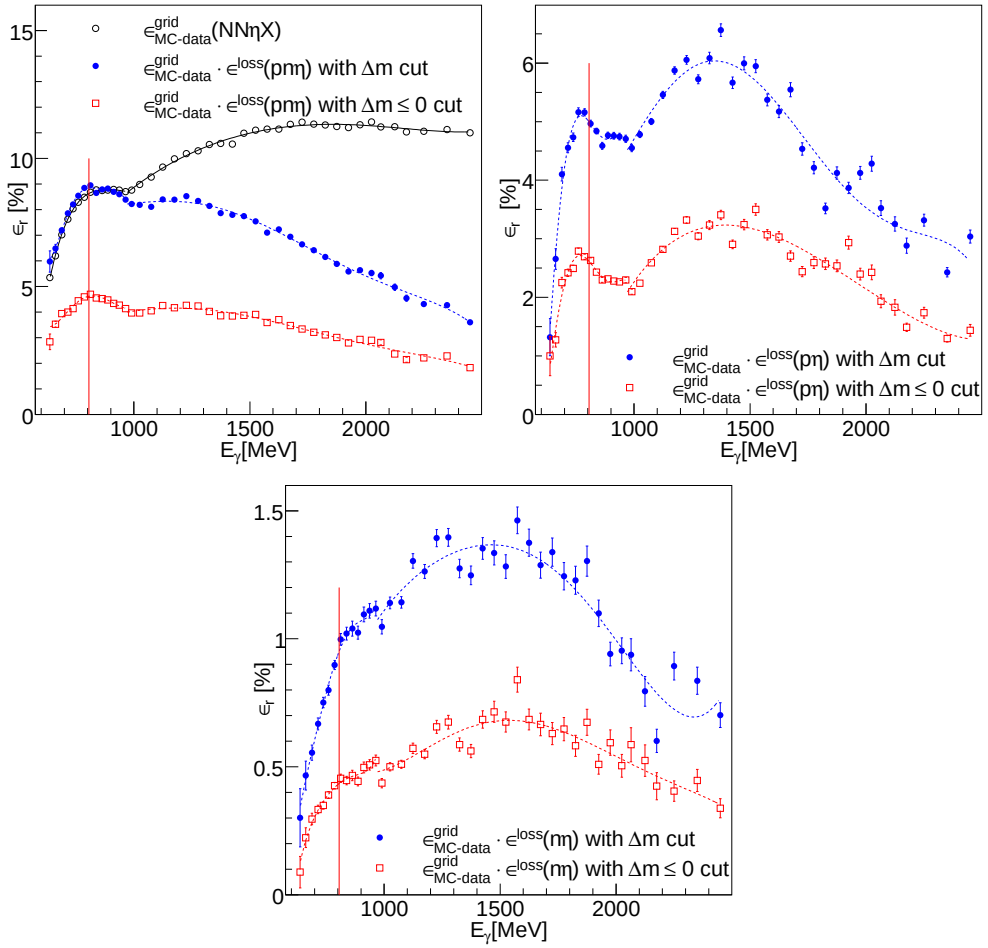

Figure 6.37: *Reaction efficiency as a function of the incident photon beam. Top left : for the fully and the quasi-free inclusive reactions. Top Right : for the quasi-free proton reaction. Bottom : for the quasi-free neutron. (only the Δm cut and the $\Delta m \leq 0$ cut are mentioned in the legends as the additional cuts are the same for both missing mass cut). The lines correspond to the fit of the efficiency evolution. The red vertical line represents the threshold of the $N\eta\pi-$channels.*

The dip visible around E_γ = 0.8 GeV for the quasi-free proton efficiency (Figure 6.37-top-right) corresponds to the energy area where the protons start to be detected in the CB detector (see Figure 6.24). This dip is due to the different proton detection thresholds in the TAPS and the CB detectors: $\sim$ 40 MeV and $\sim$ 70 MeV, respectively. There is no dip around E_γ = 0.8 GeV for the quasi-free neutrons as the neutron detection threshold is the same for the CB and TAPS

detectors : $\sim$ 25 MeV.

The efficiencies as a function of $cos(\theta_{cm})$ for different incident photon beam ranges and for each reaction studied were also determined. Figure 6.38 shows the results for the quasi-free neutron reaction.

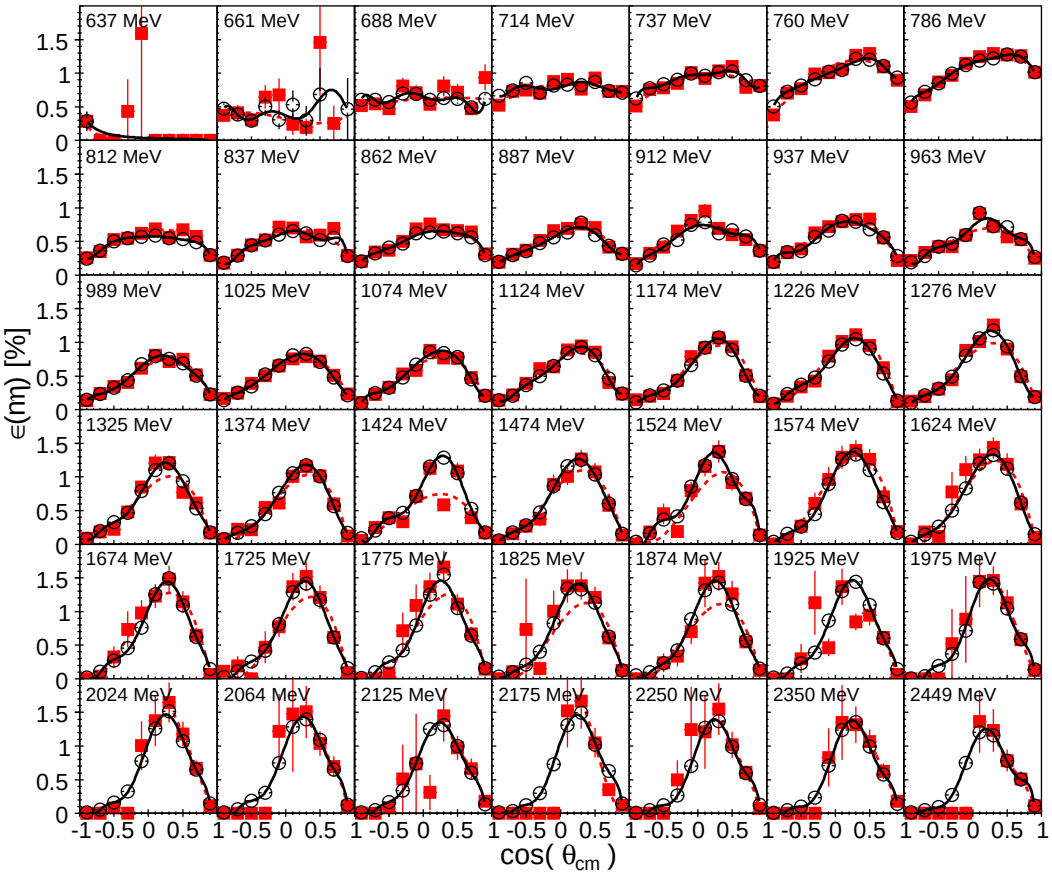

Figure 6.38: *Angular efficiency for the quasi-free neutron reaction for different incident photon beam ranges. (red squared $\epsilon_{data}^{grid} \cdot \epsilon^{loss}$ and open black circle ϵ^{ps}). The lines are the fit.*

The fact, that the data and the phase space MC simulation efficiency as function of the $cos(\theta_{cm})$, is similar, was used to correct $cos(\theta_{cm})-$bin with very low statistics mostly at backward angles and for incident photon energies above 1.5 GeV.

Figure 6.39 shows the angular efficiency for the quasi-free proton reaction.

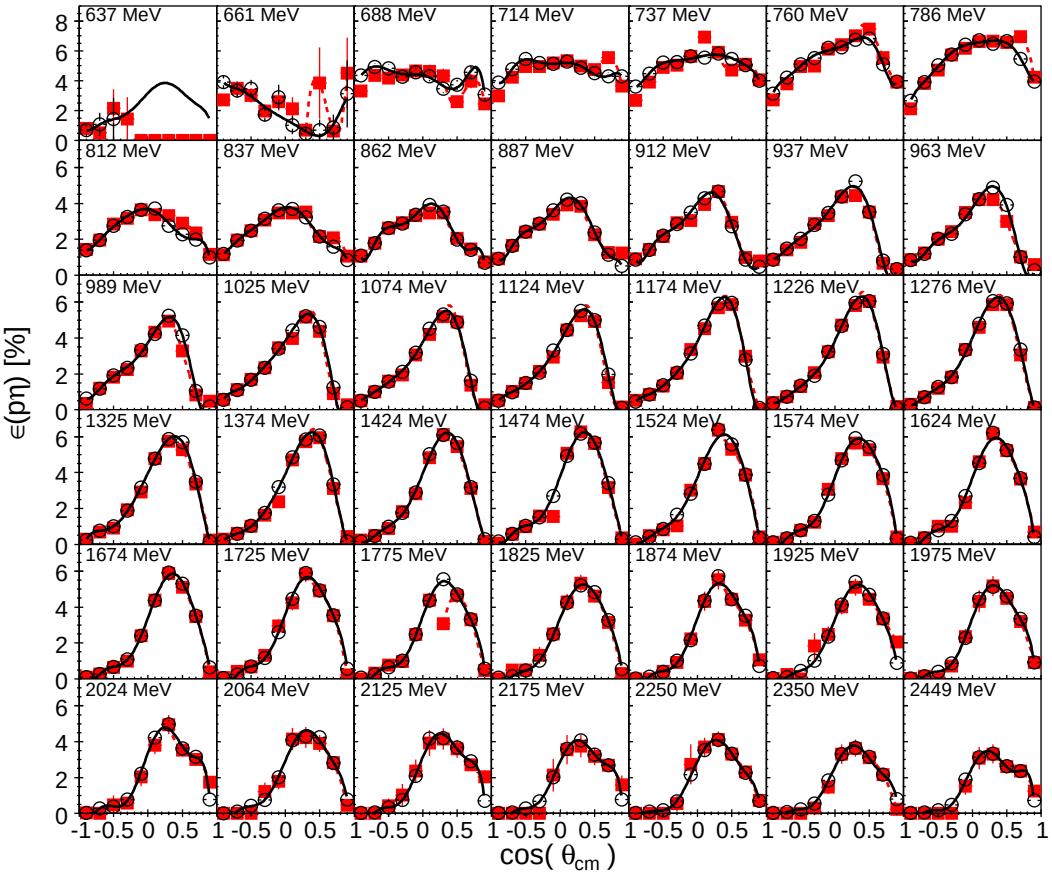

Figure 6.39: *Angular efficiency for the quasi-free proton reaction for different incident photon beam ranges. (red squared $\epsilon^{grid}_{MC-data} \cdot \epsilon^{loss}$ and open black circle ϵ^{ps}). The lines are the fit.*

Again, the phase space MC simulation ($\epsilon^{ps} = \frac{N^{detected}}{N^{started}}$) reproduces pretty well the efficiency deduced from the MC-data simulation corrected by the signal loss ($\epsilon^{grid}_{MC-data} \cdot \epsilon^{loss}$), except for the $cos(\theta_{cm})-$bin that corresponds to the acceptance hole for the free proton target ($cos(\theta_{cm})$ $\leq$0.8 for E_γ $\geq$800 MeV, see Figure 6.24-left white area above the $\eta-$meson photoproduction threshold). This discrepancy is more obvious by comparing the two angular distributions obtained from phase space MC simulation and from $\epsilon^{grid}_{MC-data} \cdot \epsilon^{loss}$ (see Figure 6.44).

Figure 6.40 shows the angular efficiency for the quasi-free inclusive reaction.

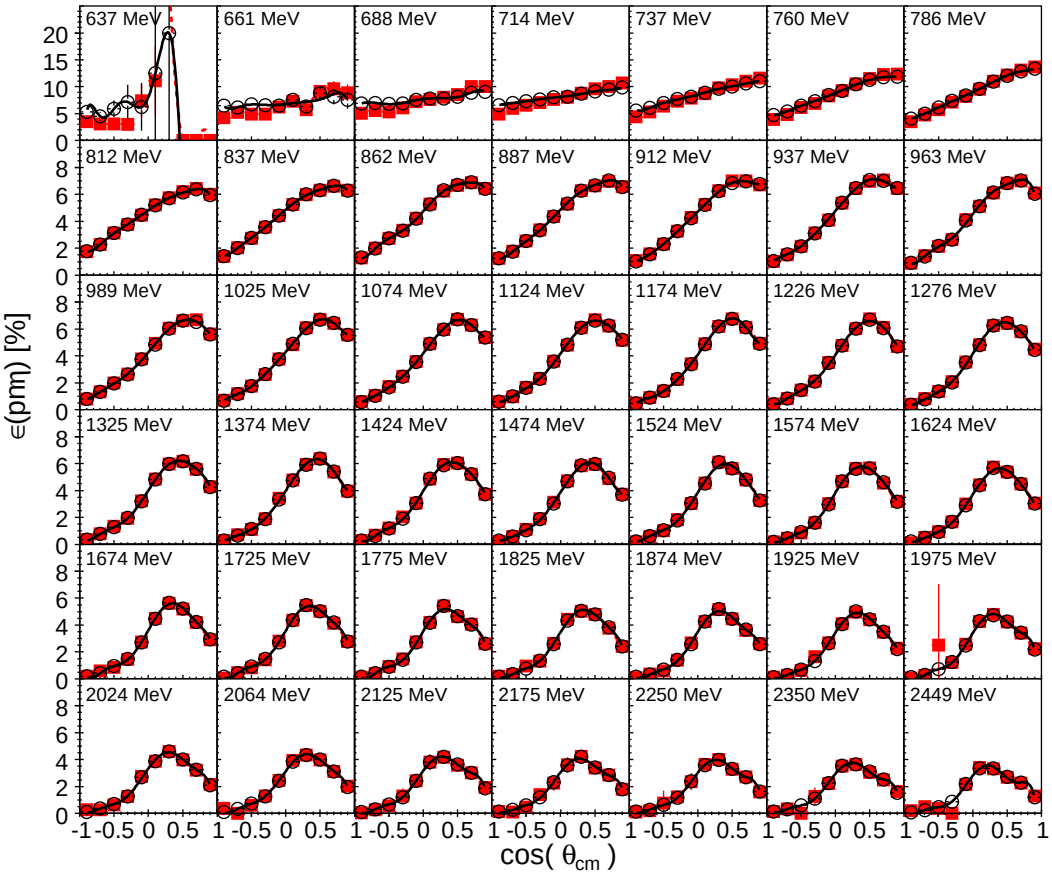

Figure 6.40: *Angular efficiency for the quasi-free inclusive reaction for different incident photon beam ranges. (red squared $\epsilon^{grid}_{data} \cdot \epsilon^{loss}$ and open black circle ϵ^{ps}). The lines are the fit.*

The quasi-free inclusive phase-space MC efficiency and the signal loss correspond to the simulated reaction, $\gamma + p(n) \rightarrow \eta + p(n)$, analyzed in a quasi-free inclusive manner.

The angular efficiency behavior (for all reactions), backward to forward peaking, is explained by the trigger conditions. Approximately two third of the $\eta-$meson are lost because of this trigger i.e. all the η-meson (going backward), which decay products (i.e. photons) go into the CB detectors, are lost.

Figure 6.41 shows the angular efficiency for the fully inclusive reaction.

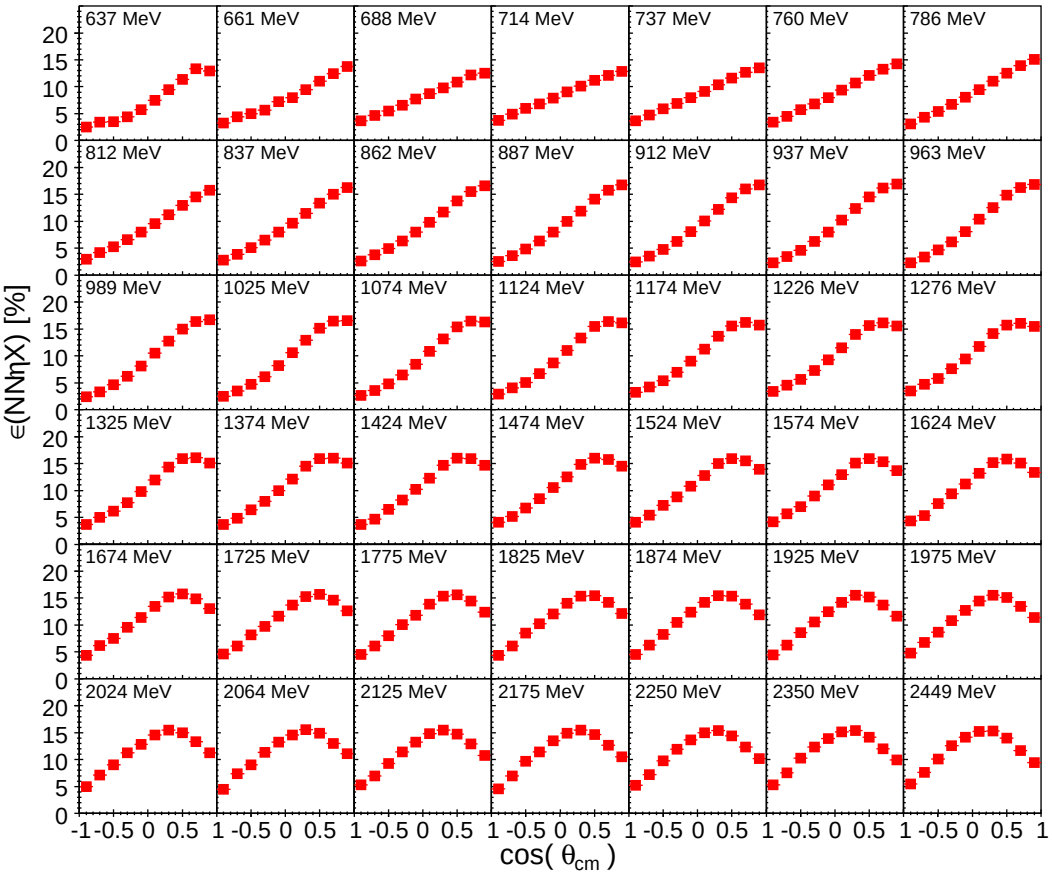

Figure 6.41: *Angular efficiency for the fully inclusive reaction for different incident photon beam ranges. (red squared ϵ_{data}^{grid}). The lines are the fit.*

All the efficiencies as function of $cos(\theta_{cm})$ and as function of E_γ for all reactions studied were parameterized by a fit. This parameterization was used for the acceptance correction.

6.3.3 The fabrication recipe for the observable and the systematic uncertainties

The binning in E_γ for the total cross section and in $(E_\gamma, cos(\theta_{cm}))$ for the angular distributions has been chosen according to the available statistics of the data. As already mentioned, quantities like the relative background contribution (see e.g. Figure 6.30) and the detection efficiencies (see e.g. Figure 6.37) have been parametrized by polynomial fits as functions of E_γ or E_γ and $cos(\theta_{cm})$. The total cross sections can be obtained either from equation 6.4 using the fitted integrated detection efficiency $\epsilon_r(E_\gamma)$ or from equation 6.5 by integration of the angular distributions constructed from the differential efficiencies fitted as functions of E_γ and θ_{cm}. These two results may slightly differ due to the fitting procedures. It has been checked, that such deviations are within statistical fluctuations and for most of the energy range are within ± 10 $\%$. For this purpose the total cross sections have been determined in three different ways using three different acceptance corrections, ϵ_r :

1. $\epsilon_r(E_\gamma, cos(\theta_{cm}))$ of equation 6.5 can be equal to $\epsilon^{grid}_{MC}(E_\gamma, cos(\theta_{cm})) \cdot \epsilon^{loss}(E_\gamma, cos(\theta_{cm}))$

2. $\epsilon_r(E_\gamma, cos(\theta_{cm}))$ of equation 6.5 can be equal to $\epsilon^{grid}_{MC-data}(E_\gamma, cos(\theta_{cm})) \cdot \epsilon^{loss}(E_\gamma, cos(\theta_{cm}))$

3. $\epsilon_r(E_\gamma)$ of equation 6.4 can be equal to $\epsilon^{grid}_{MC-data}(E_\gamma) \cdot \epsilon^{loss}(E_\gamma)$

Figure 6.42 shows the comparison between the total cross section obtained by using ϵ_r from 3 and 1 (top) and from 3 and 2 (bottom) for beam time A (left column) and beam time C (right column). For the final results of the total cross sections method 3, which is least prone to strong fluctuations related to single events with very small detection efficiencies has been used. The deviations shown in Figure 6.42 estimate systematical uncertainities introduced by this procedure. Some larger deviations, in particular for the neutron channel at high incident photon energies are due to a few events at extreme backward angles which are connected with very low detection efficiency and have only small statistical weight, they are ignored for further analysis.

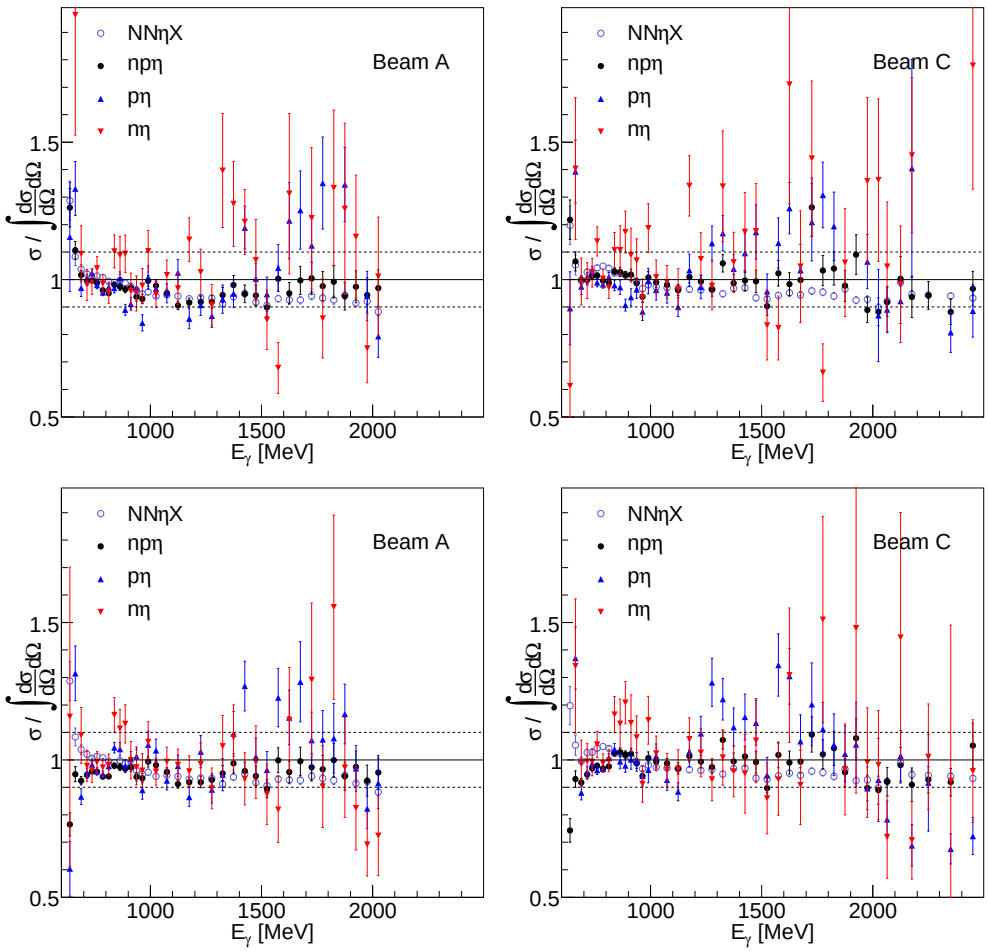

Figure 6.42: *Systematic difference of the total cross section obtained from equation 6.4 and from equation 6.5 for all reactions studied for beam time A (left column) and beam time C (right column). Top : the total cross section obtained by using ϵ_r from 3 and 1. Bottom : from 3 and 2.*

The angular distributions have been determined from $\epsilon^{grid}_{MC}(E_\gamma, cos(\theta_{cm})) \cdot \epsilon^{loss}(E_\gamma, cos(\theta_{cm}))$ and from $\epsilon^{grid}_{MC-data}(E_\gamma, cos(\theta_{cm})) \cdot \epsilon^{loss}(E_\gamma, cos(\theta_{cm}))$ and have been compared as internal consistency check. The comparison is shown for the quasi-free neutron reaction in Figure 6.43.

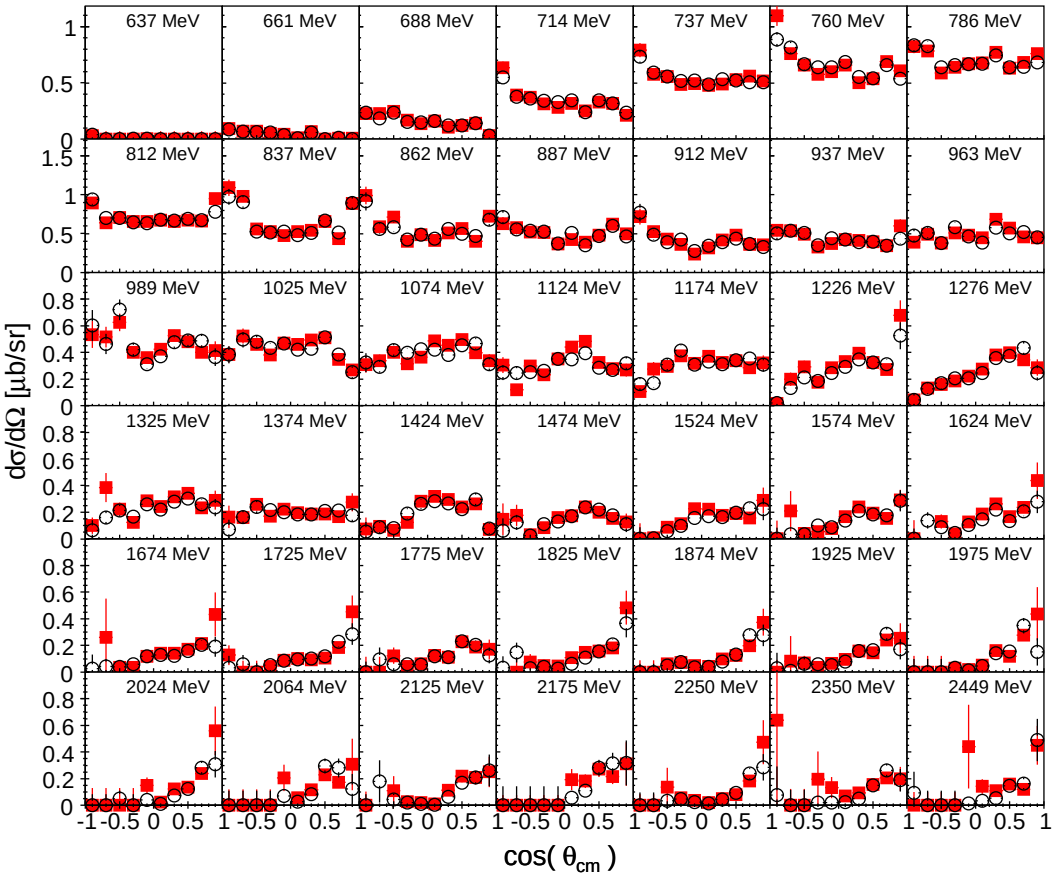

Figure 6.43: *Angular distribution for the quasi-free neutron reaction for different incident photon beam ranges. (red squared the* $\epsilon^{grid}_{MC-data} \cdot \epsilon^{loss}$ *was used and open black circle* $\epsilon^{ps} = \frac{N^{detected}}{N^{started}}$ *(ps stands for phase-space) was used.*

The two sets of angular distributions show no systematic deviations. A few points determined with the efficiency calculated with MC-data simulation (in particular at very forward or backward angles) show large deviations. This can happen if e.g. rare background events appear in kinematical regions associated with very small detection efficiencies. Those points have been ignored.

Figure 6.44 shows the quasi-free proton angular distributions determined from ϵ^{ps} and $\epsilon^{grid}_{MC-data} \cdot \epsilon^{loss}$ acceptance corrections.

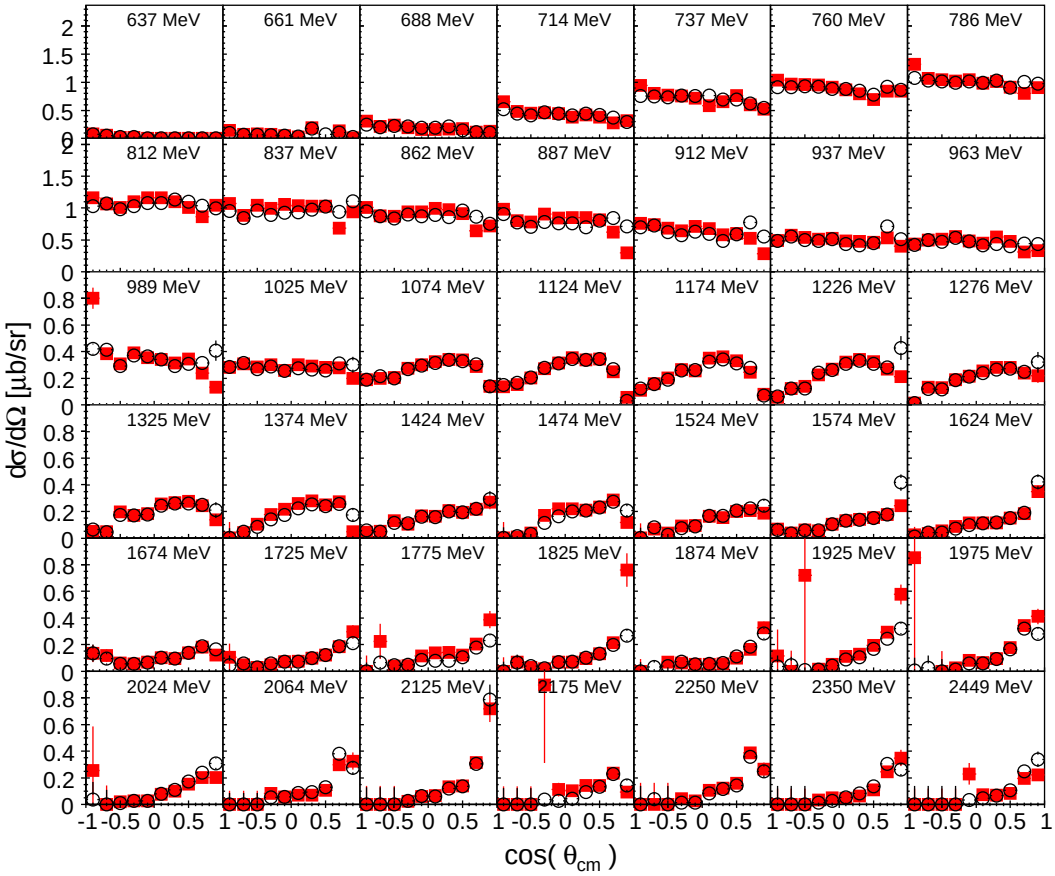

Figure 6.44: *Angular distribution for the quasi-free proton reaction for different incident photon beam ranges. (red squared the* $\epsilon^{grid}_{MC-data} \cdot \epsilon^{loss}$ *was used and open black circle* $\epsilon^{ps} = \frac{N^{detected}}{N^{started}}$ *was used.*

Figure 6.45 shows the quasi-free inclusive angular distributions determined from $\epsilon^{ps} = \frac{N^{detected}}{N^{started}}$ (ps stans for phase-space) and $\epsilon^{grid}_{MC-data} \cdot \epsilon^{loss}$ acceptance corrections.

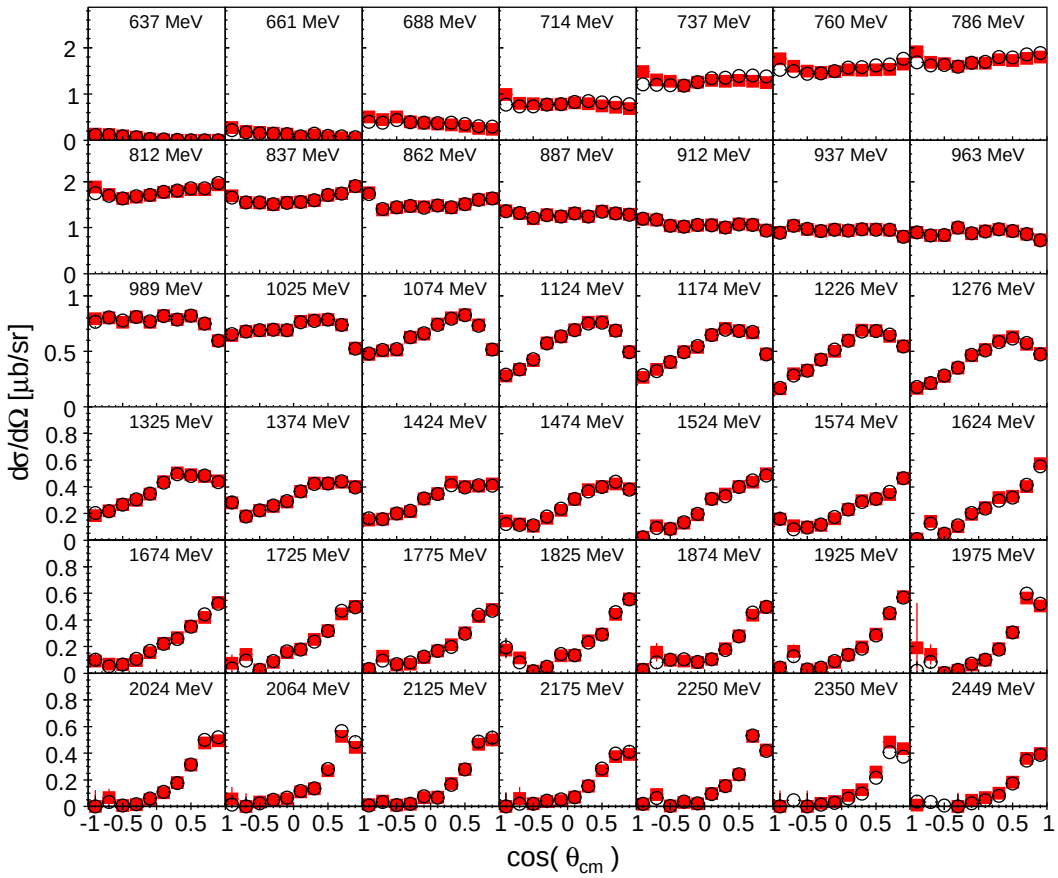

Figure 6.45: *Angular distribution for the quasi-free inclusive reaction for different incident photon beam ranges. (red squared the $\epsilon^{grid}_{MC-data} \cdot \epsilon^{loss}$ was used and open black circle ϵ^{ps} was used.)*

The angular distributions shown in Figure 6.43, 6.44 and 6.45 correspond to the full statistics (i.e. data are not restricted to correct scalers) and the weighted average of three beam times : beam A, beam C and beam D. The absolute normalization was possible only for two beam times : beam A and beam C as the correct number of scalers was found for these two beam time only. Figure 6.46 (top-left) shows the fully inclusive total cross section for the four different beam times. The maximum height agrees for beam A and C : 24.26 μb and 23.07 μb. If we used the entire data available, i.e. the data with the scalers correctly registered and the data without scalers, the maximum height

for beam A and beam C : 35.09 μb and 28.19 μb, respectively. From these values, two coefficients were deduced to be able to use the full statistics $\frac{24.26}{35.09}$ and $\frac{23.07}{28.1}$. It was checked that these factors are consistent with the $N2\pi^o-$channels. These coefficients were used for all studied channels. The fully inclusive total cross section was used to normalize beam B and beam D. The normalization factor as function of the incident photon beam is shown in Figure 6.46 (top-right). The normalization factor for beam B and beam D is respectively : $\sigma(NN\eta X)^{beam\ A}/\sigma(NN\eta X)^{beam\ B}$ and $\sigma(NN\eta X)^{beam\ C}/\sigma(NN\eta X)^{beam\ D}$.

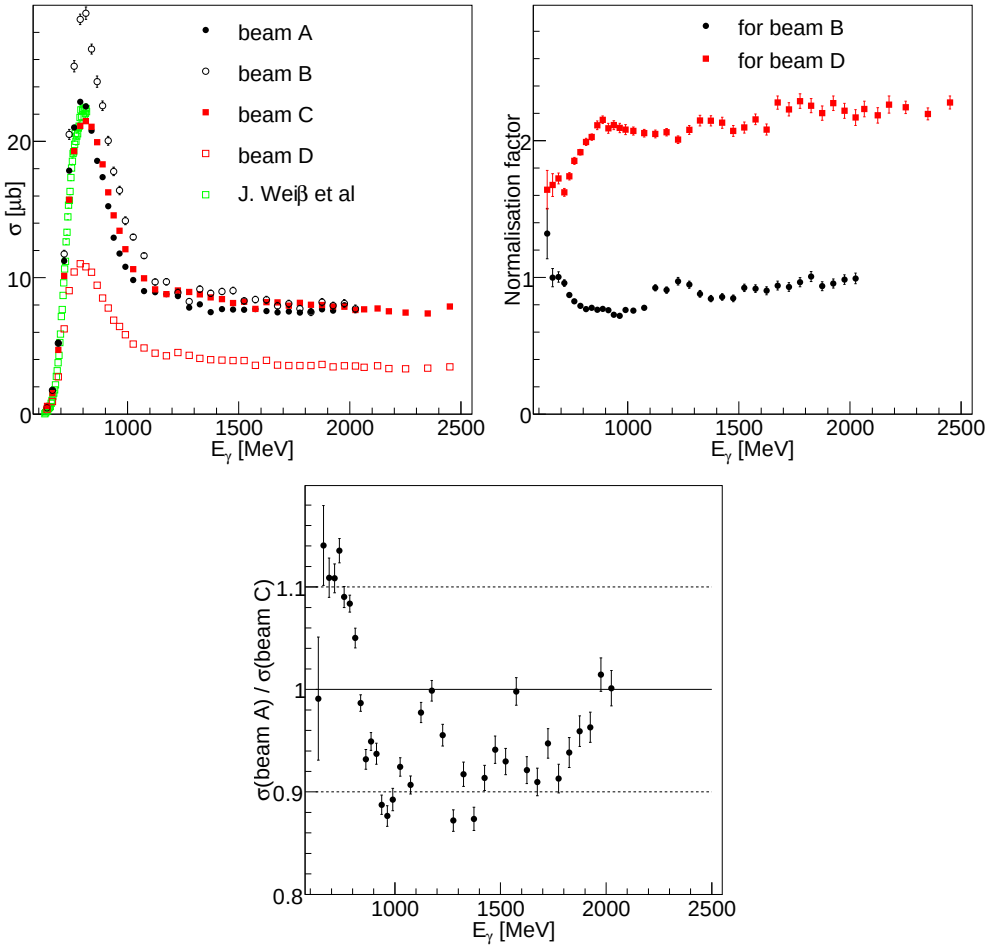

Figure 6.46: *Top left: Fully inclusive total cross section as function of the incident photon beam for the four different beam times. The Weiβ measurement [43] is also shown. Top Right: Normalization values for beam B and beam D. Bottom : Systematic difference between beam A and beam C.*

The systematic difference between beam A and beam C is plotted in Figure 6.46 (bottom). The systematic difference is of the order of $\pm$ 10 %. At threshold the systematic difference is more important than at higher energies

(for the same reasons as explained in section 6.2.7). Nevertheless, it can be considered as acceptable. This systematic difference gives also the systematic error on the absolute normalization i.e. on the product : scalers $\times$ the tagging efficiency. The other systematics (see Figure 6.47), ΔS, are coming from the efficiency and from the signal loss and are equal to :

$$\Delta S = \sqrt{\frac{(\Delta\epsilon^{grid})^2}{(\epsilon^{grid})^2} + \frac{(\Delta\epsilon^{loss})^2}{(\epsilon^{loss})^2}} \tag{6.23}$$

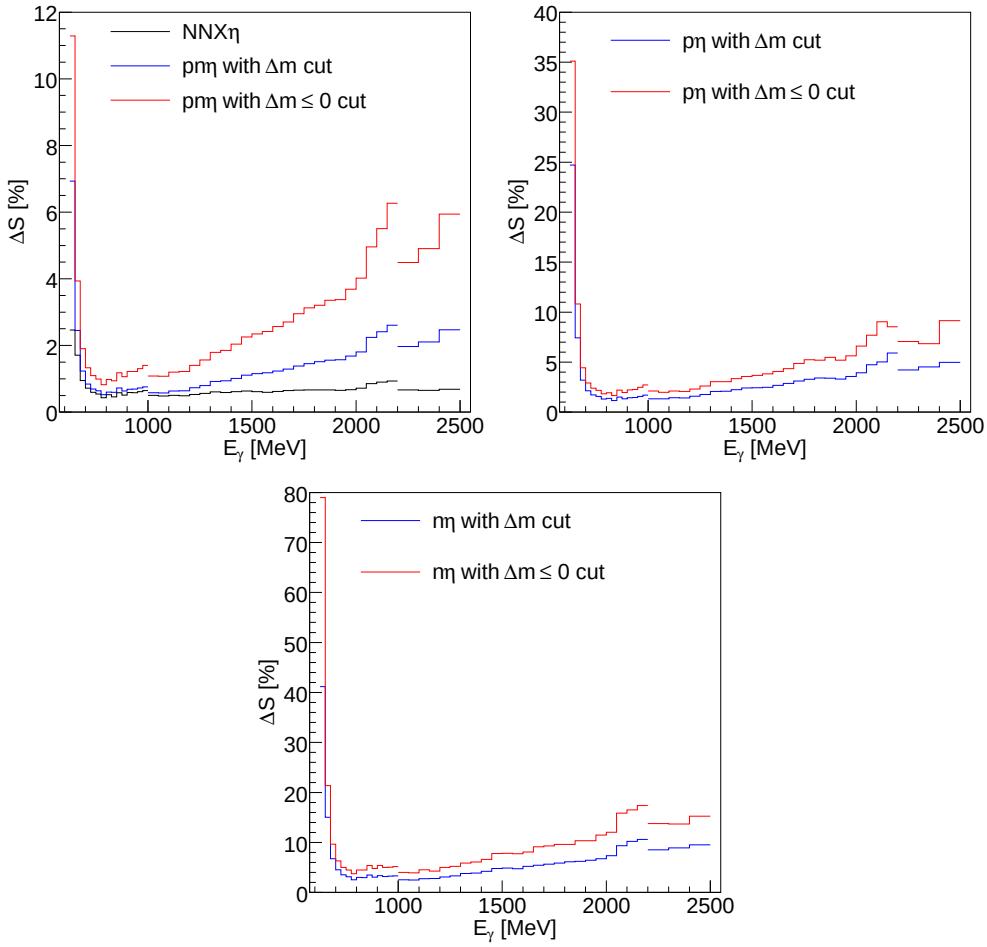

Figure 6.47: *Systematic errors of the measurements - ΔS - as function of the incident photon beam (the systematic error on the absolute normalization is not included). Top left : for the fully inclusive and the quasi-free inclusive reactions. Top right : for the quasi-free proton reaction. Bottom : for the quasi-free neutron reaction. The jumps are due to different E_γ ranges: 25 MeV (for E_γ= 625 - 1000 MeV), 50 MeV (for E_γ= 1000 - 2200 MeV) and 100 MeV (for E_γ= 2200 - 2500 MeV).*

Below E_γ = 1 GeV, the systematic error for the neutron measurements is 5 %, between E_γ = 1 - 2 GeV, it is 10 %, above it is 15 %.

6.3.4 The differential cross sections

The differential cross sections of the reactions : $d(\gamma,\eta)X$ (Figures 6.48 and 6.51), $d(\gamma,\eta)pn$ (Figures 6.52 and 6.54), $d(\gamma,\eta)p(n)$ (Figures 6.55 and 6.57), $d(\gamma,\eta)n(p)$ (Figures 6.58 and 6.60) have been extracted and plotted in two different ways as function of $cos(\theta_{cm})$ for different incident photon beam ranges and as function of the incident photon beam for different $cos(\theta_{cm})$ ranges.

The angular distributions have been fitted using the equation 2.25 in terms of associated Legendre polynomials $P_l^n(cos(\theta_{cm}))$ which is :

$$\frac{d\sigma}{d\Omega} = \sum_{l=0}^{3} A_l P_l^0(cos(\theta_{cm})) \tag{6.24}$$

The four polynomials are (with $x = cos(\theta_{cm})$) :

$$\begin{aligned} P_0^0(x) &= 1 \\ P_1^0(x) &= x \\ P_2^0(x) &= \frac{1}{2}(3x^2-1) \\ P_3^0(x) &= \frac{1}{2}(5x^3-3x) \end{aligned}$$

Then the coefficients A_l as function of the coefficients a,b,c and d of equation 2.25 become :

$$\begin{aligned} A_0 &= \frac{q_\eta^*}{k^*}(a+\frac{1}{3}c) \\ A_1 &= \frac{q_\eta^*}{k^*}(b+\frac{3}{5}d) \\ A_2 &= \frac{q_\eta^*}{k^*}(\frac{2}{3}c) \\ A_3 &= \frac{q_\eta^*}{k^*}(\frac{2}{5}d) \end{aligned}$$

Figures 6.50, 6.53, 6.56 and 6.59 show the coefficients A_0, A_1, A_2 and A_3 of the angular distributions for the different reactions studied.

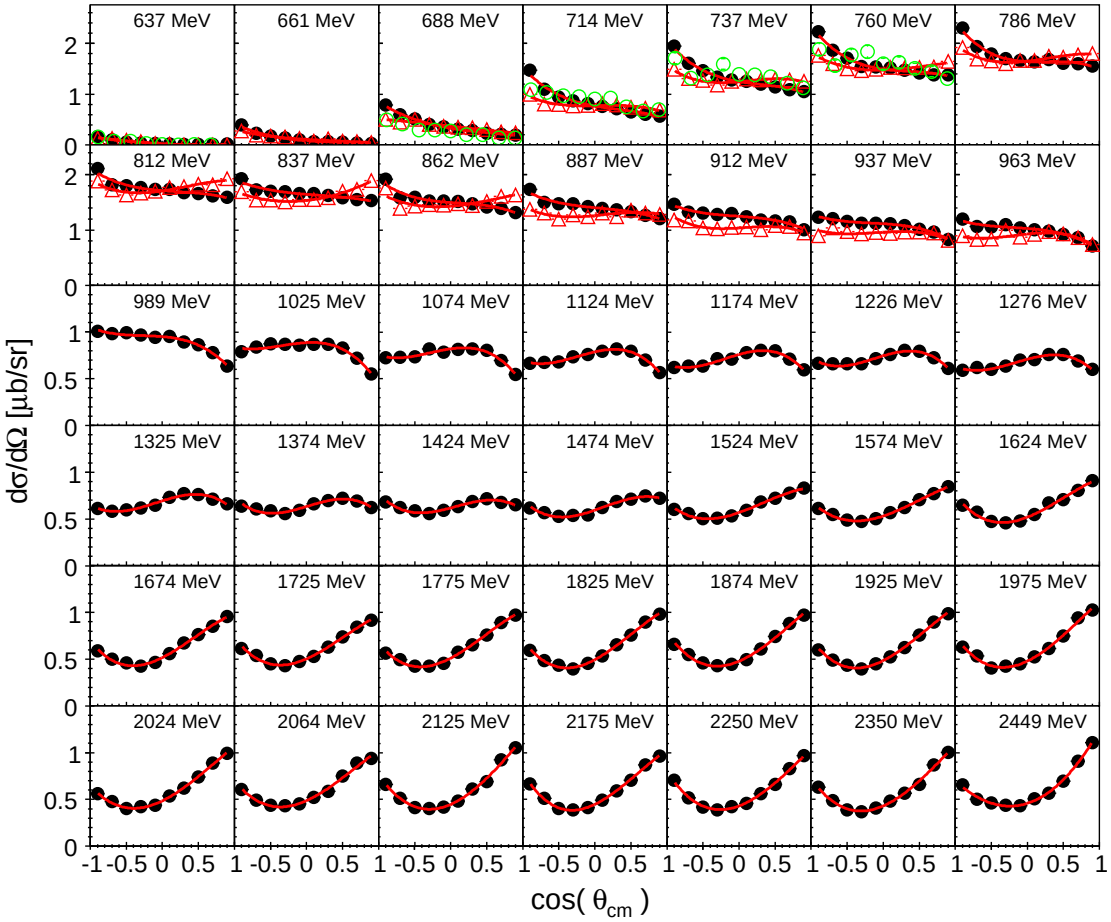

Figure 6.48: *The fully inclusive angular distributions for different incident photon beam ranges (black dots this work, red open triangle up the quasi-free inclusive, open green circle [43]). The red lines is the fit.*

This work is in quite good agreement with the previous measurement done by Weiβ et al [43]. (open green circle), the largest deviation is found for extreme backward angles.

The angular distributions show three different types of distribution : from threshold to E_γ = 1 GeV, the angular distributions show a slight backward to forward peaking behavior. Above E_γ = 1 GeV, there is a change in the angular distribution probably related to the contribution of different resonances. Then, above E_γ = 1.3 GeV, the angular distributions change again, with a $t-$channel behavior that gets more and more pronounced with increasing incident photon

beam energy and of course above the $\eta\pi$ threshold production, this reaction is dominated by the $\eta\pi$ final state. Figure 6.49 shows above the $\eta\pi$ threshold the difference of the fully inclusive and the quasi-free inclusive angular distributions associated with the $\eta\pi$ final state.

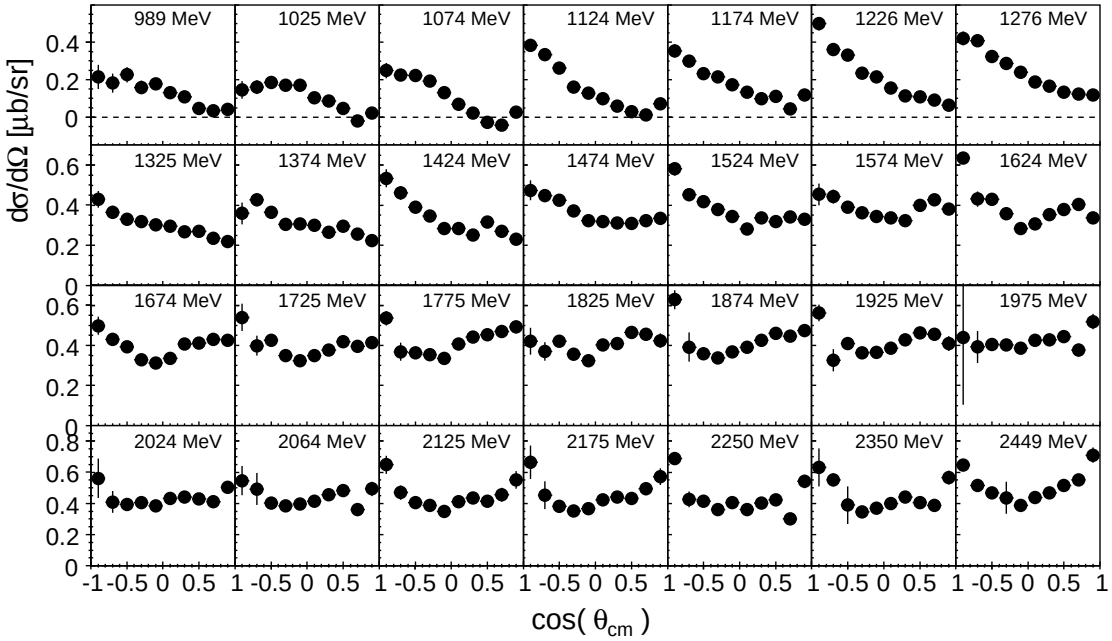

Figure 6.49: *The angular distributions of the difference of the fully inclusive and the quasi-free inclusive angular distribution for different incident photon beam ranges.*

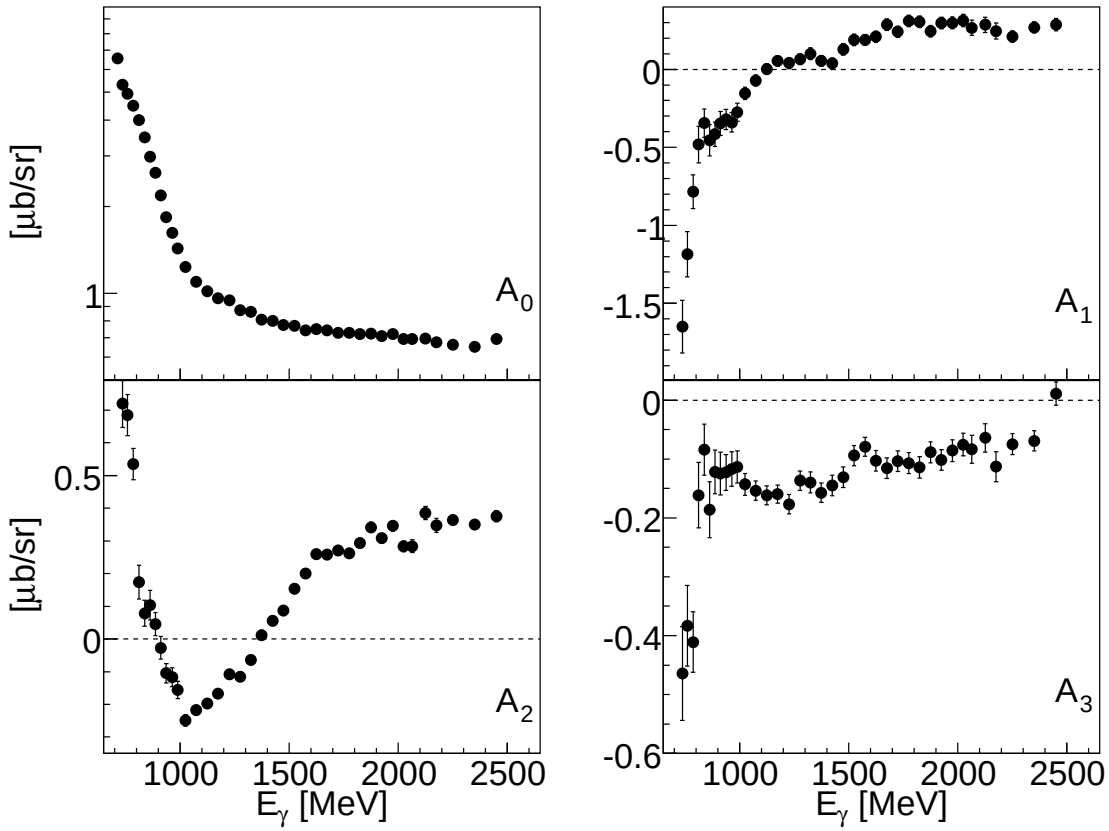

Figure 6.50: *Coefficients A_0, A_1, A_2 and A_3 of the angular distributions for the fully inclusive.*

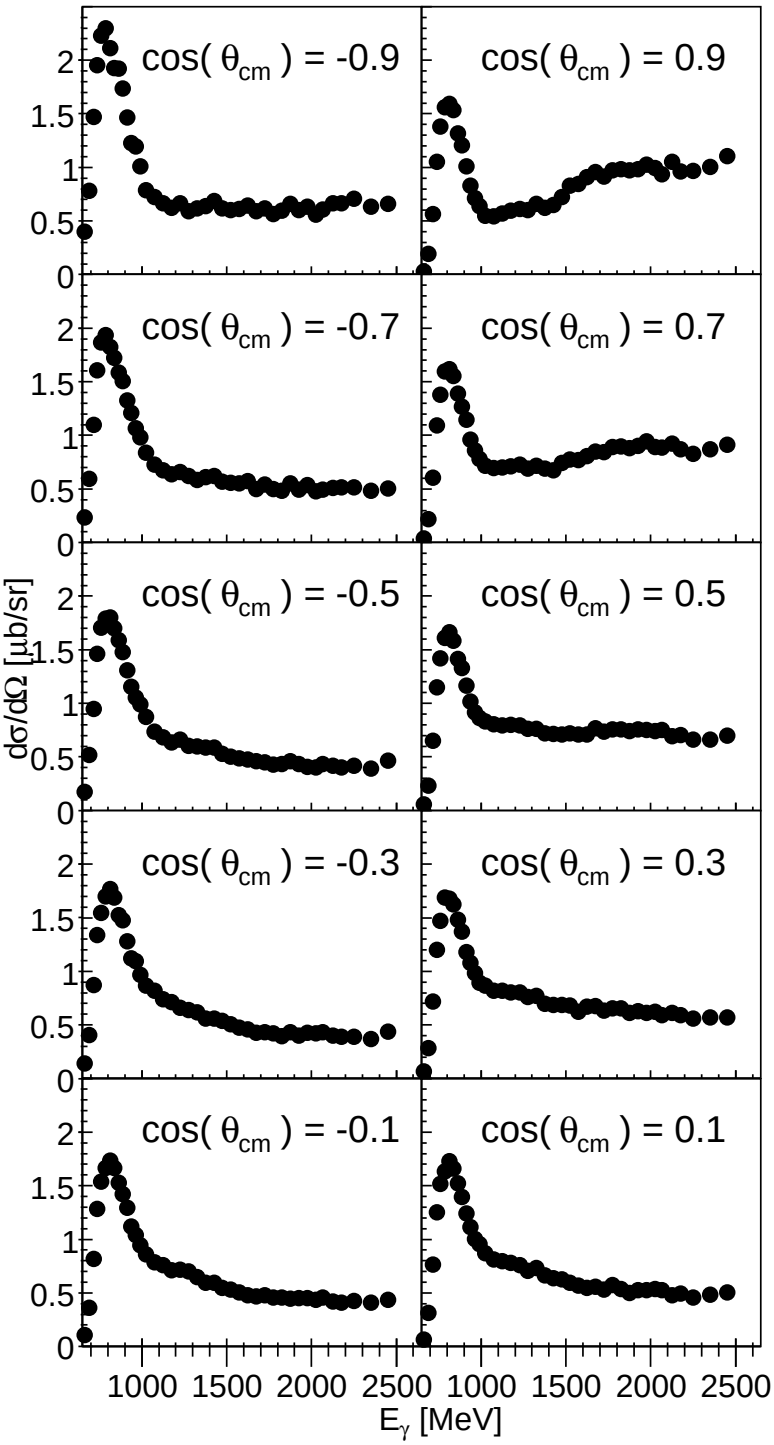

Figure 6.51: *Fully inclusive cross sections for different $cos(\theta_{cm})$ bins.*

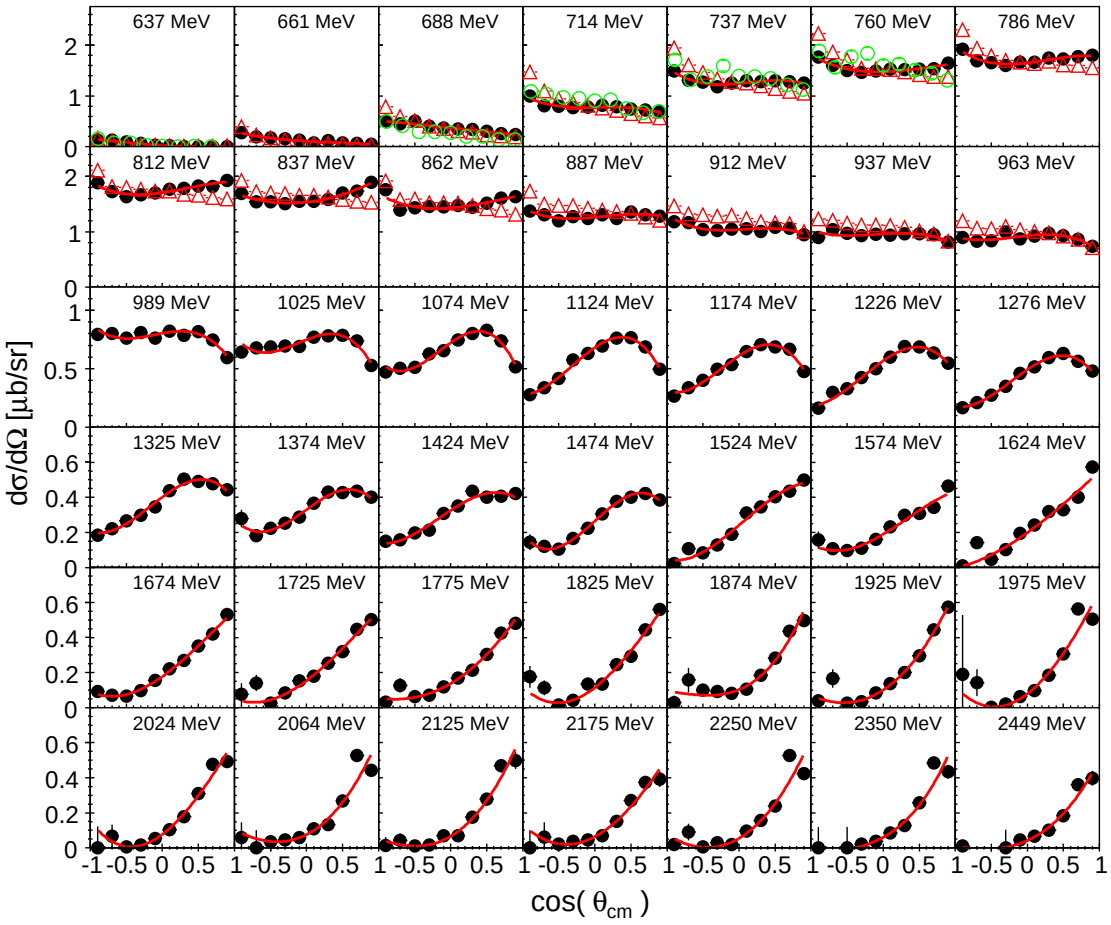

Figure 6.52: *The quasi-free inclusive angular distributions for different incident photon beam ranges (black dots this work, red open triangle up the quasi-free inclusive, open green circle [43]). The red lines is the fit.*

The quasi-free inclusive is in even better agreement with the Weiβ et al. measurements [43] (open green circle). Below the $N\eta\pi-$channels threshold, there is small systematic difference between the fully inclusive and the quasi-free inclusive. The quasi-free inclusive is rather "flat" and the fully inclusive shows some backward to forward peaking behavior. This difference can be explained if reactions with nucleon spectator knock-out from the target is non-negligible. Indeed, in the discussion we will see that it is the case. The angular distribution remains "flat" up to E_γ = 1 GeV. Then around E_γ = 1 GeV, the angular distribution changes, because of the interference between the $S_{11}-$resonance (s) and a $P-$wave resonance. Then, above E_γ = 1.3 GeV, the $t-$channel contri-

bution gets more and more important with increasing incident photon beam energy.

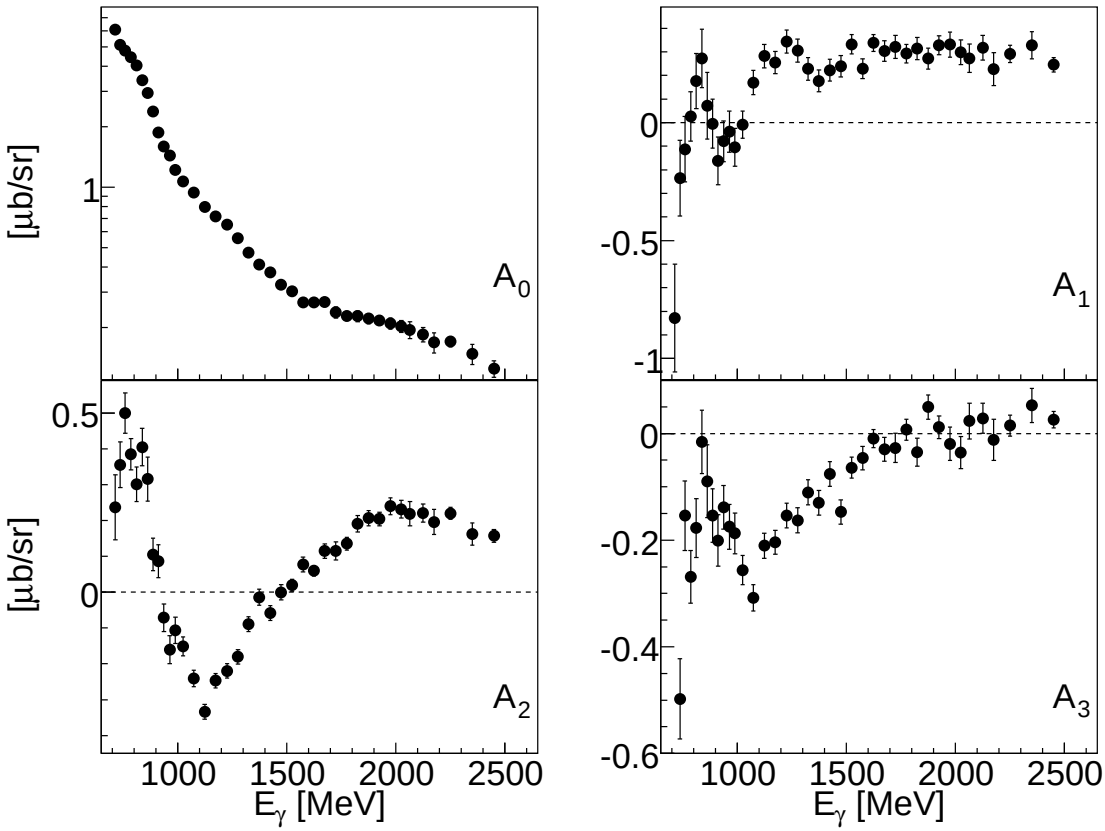

Figure 6.53: *Coefficients A_0, A_1, A_2 and A_3 of the angular distributions for the quasi-free inclusive.*

The interference between the $S_{11}-$resonance and $P-$wave creates a structure which is $cos(\theta_{cm})$ dependant and is visible around E_γ = 1 GeV in Figure 6.54. In the discusion we will see that the ratio A_1/A_0 also shows an evidence of the interference between the $S_{11}-$resonance and $P-$wave.

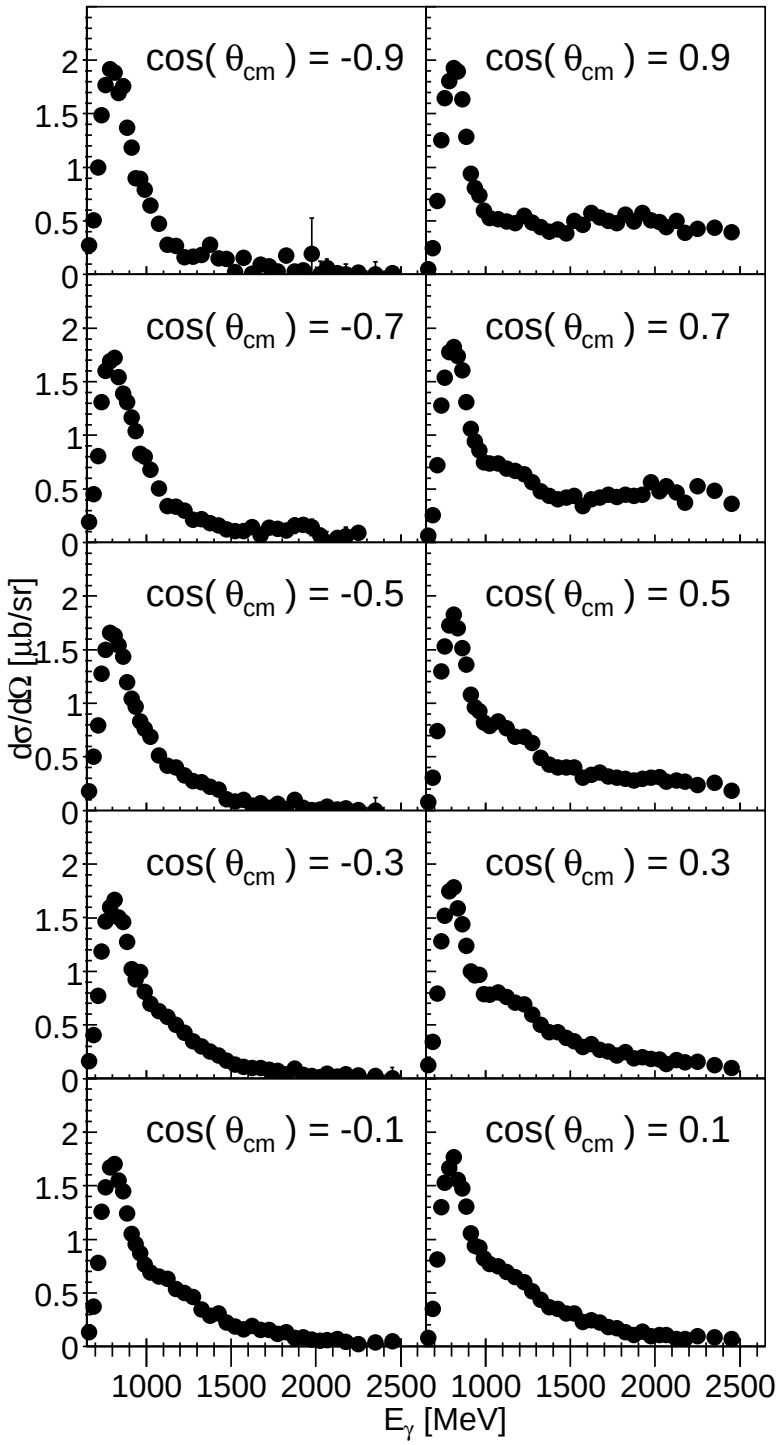

Figure 6.54: *Quasi-free inclusive cross sections for different* $cos(\theta_{cm})$ *bins.*

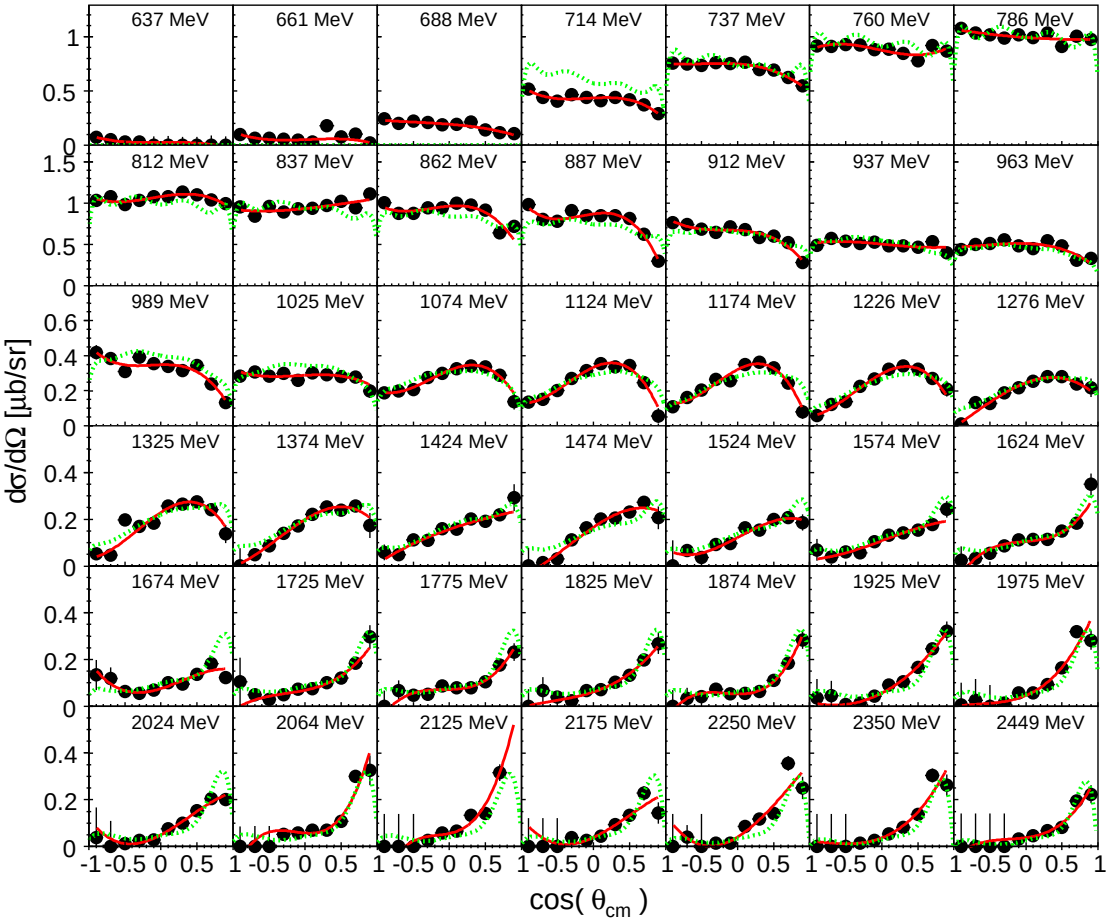

Figure 6.55: *The quasi-free proton angular distributions for different incident photon beam ranges (black dots this work, green line free proton folded [37]). The red lines is the fit of the black dots.*

This work and the free proton folded [37] with the momentum distribution of the bound protons are in good agreement.

Again, for the quasi-free proton, there are three different types of angular distributions exactly as for the quasi-free inclusive. The interference between the $S_{11}-$resonance (s) and a $P-$wave resonance is more pronounced than for the quasi-free inclusive in Figure 6.57 and as well in the ratio A_1/A_0 as we will see in the discussion.

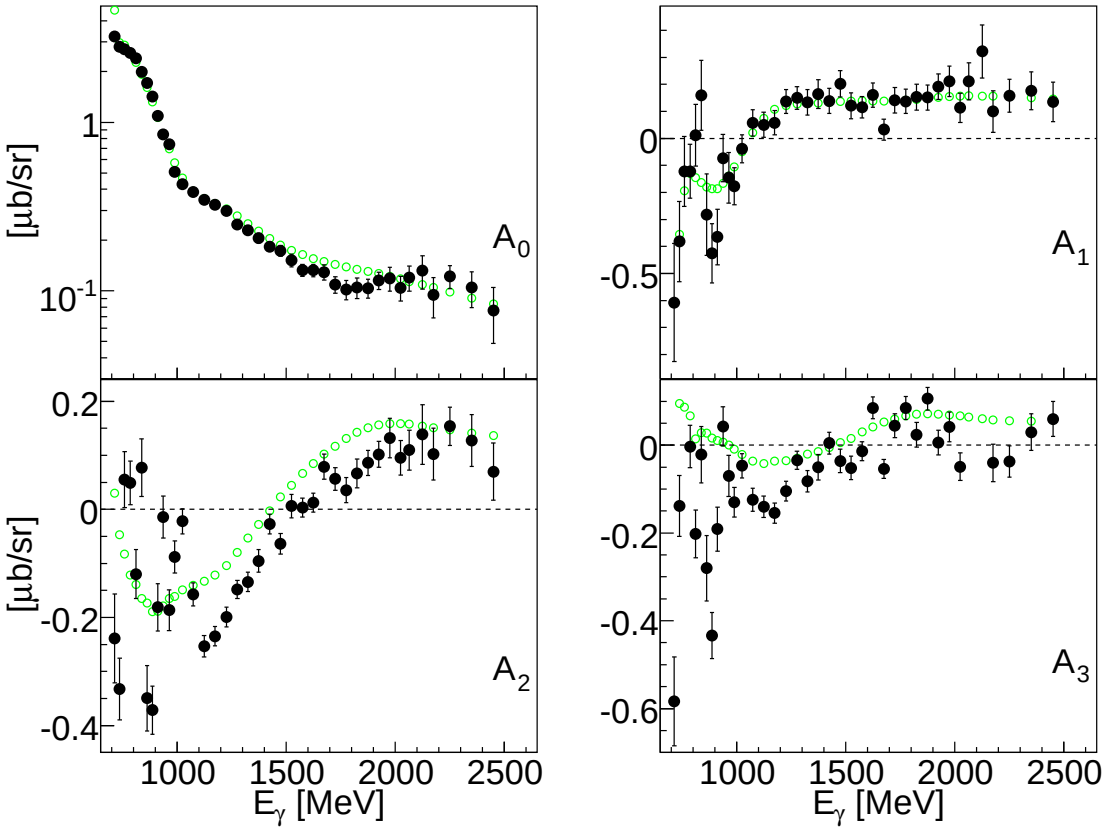

Figure 6.56: *Coefficients A_0, A_1, A_2 and A_3 of the angular distributions for the quasi-free proton (black dots this work, open green circle free proton folded).*

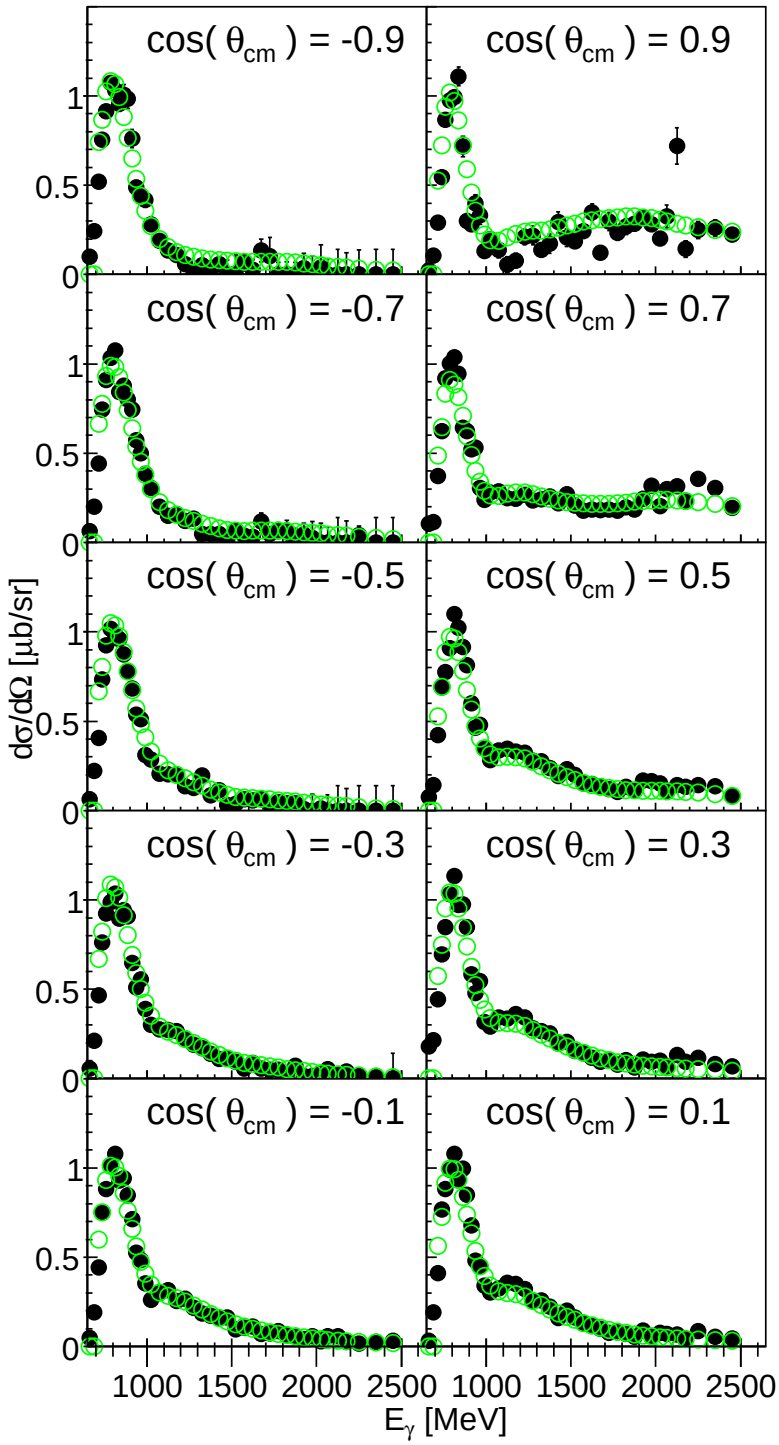

Figure 6.57: *Quasi-free proton cross sections for different $cos(\theta_{cm})$ bin (black dots this work, open green circle free proton folded).*

The quasi-free neutron angular distributions

There are three different ways to get the quasi-free neutron angular distributions: the direct measurement (black dots), from the difference between the quasi-free inclusive and the quasi-free proton (open violet circle) or from the difference of the quasi-free inclusive and the free proton cross section folded with the momentum distribution (open green triangle up). The last is of course most prone to systematic erros partly due to the folding procedure partly because systematic uncertainties like flux normalisation do not cancel. It is therefore only extracted as an additional cross check.

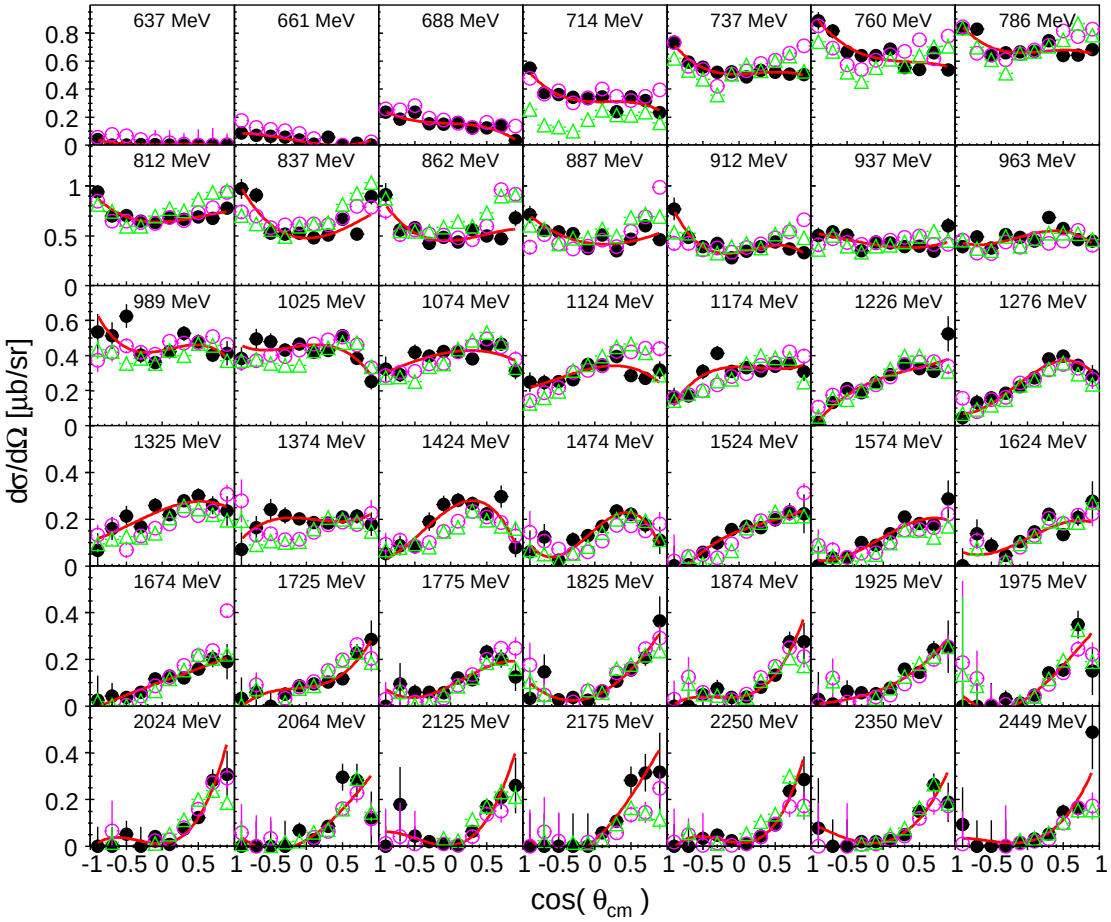

Figure 6.58: *The quasi-free neutron angular distributions for different incident photon beam ranges (black dots direct measurement, open violet circle difference between quasi-free inclusive and quasi-free proton and open green triangle up difference between quasi-free inclusive and the free proton folded). The red lines is the fit of the black dots.*

The three different measurements, which correspond to three different systematics, of the quasi-free neutron cross section are consistent with each other.

The angular distribution for the quasi-free neutron cross section is appreciably different from the quasi-free proton cross section up to E_γ = 1.3 GeV. Then the two angular distributions seems to have a similar behavior.

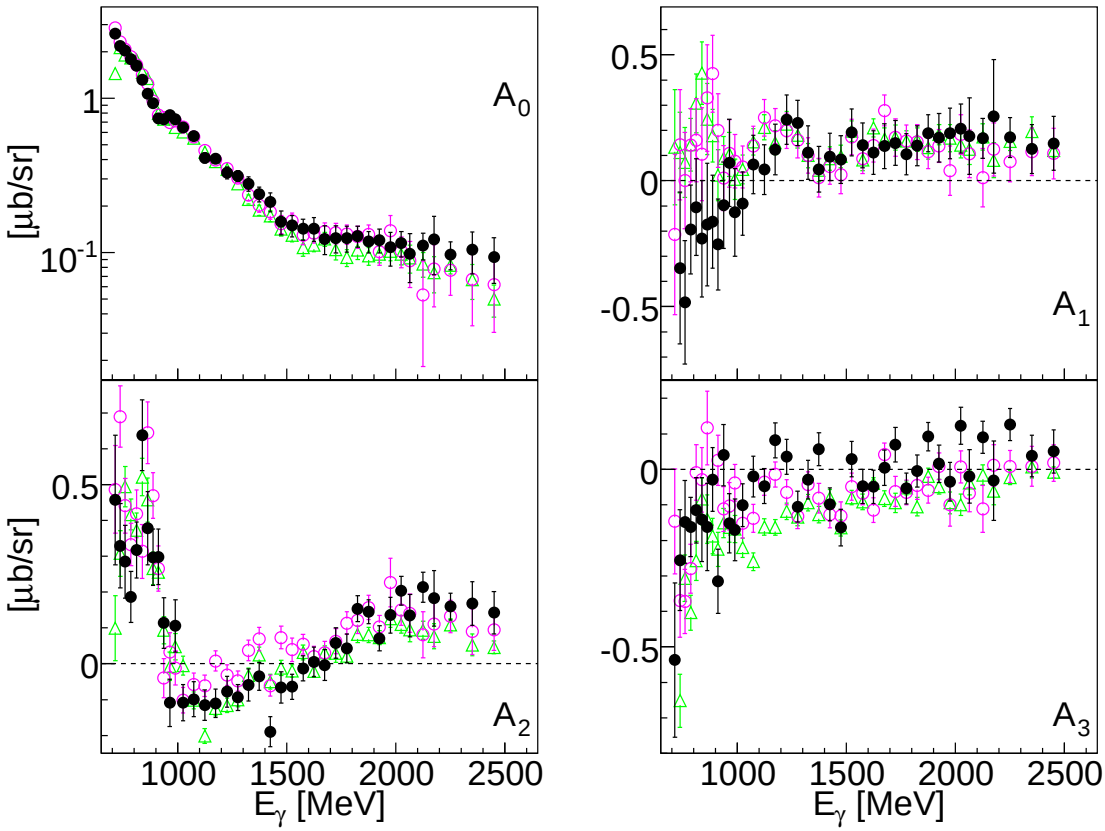

Figure 6.59: *Coefficients A_0, A_1, A_2 and A_3 of the angular distributions for the quasi-neutron (black dots direct measurement, open violet circle difference between quasi-free inclusive and quasi-free proton and open green triangle up difference between quasi-free inclusive and the free proton folded).*

The differences in the behavior is more obvious for the coefficients A_0, A_1, A_2 and A_3 of the angular distributions, Figure 6.59 and in the differential cross section as function of the incident photon beam for different $cos(\theta_{cm})-$bins, Figure 6.60. The large difference in the A_2-coefficient at low incident photon energies is due to the known interference between the $S_{11}(1535)$ and the $D_{13}(1520)$ which has different sign for neutron and proton [43].

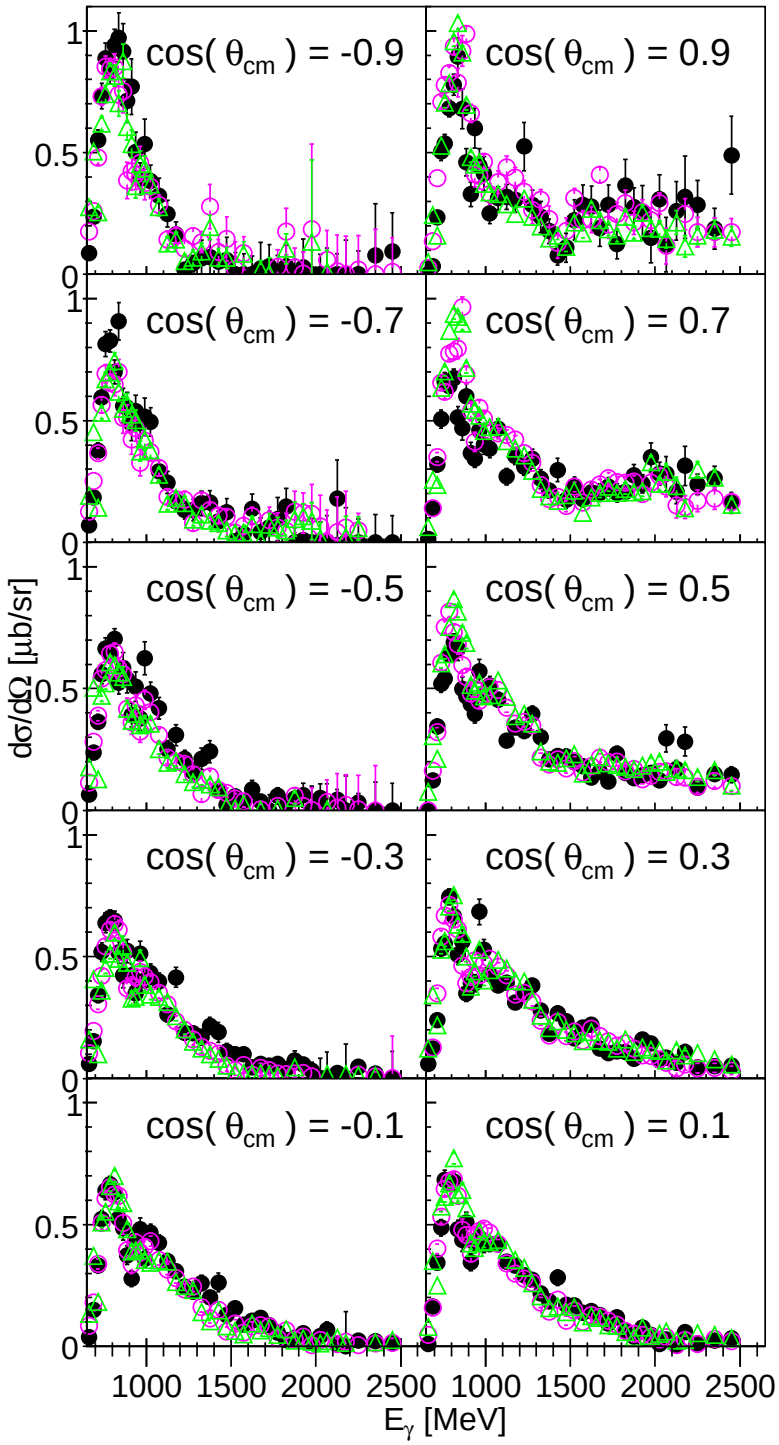

Figure 6.60: *Quasi-free neutron cross sections as function of the incident photon beam for different $cos(\theta_{cm})$ bin (black dots direct measurement, open violet circle difference between quasi-free inclusive and quasi-free proton and open green triangle up difference between quasi-free inclusive and the free proton folded).*

6.3.5 The total cross sections

The fully inclusive and the quasi-free inclusive total cross sections

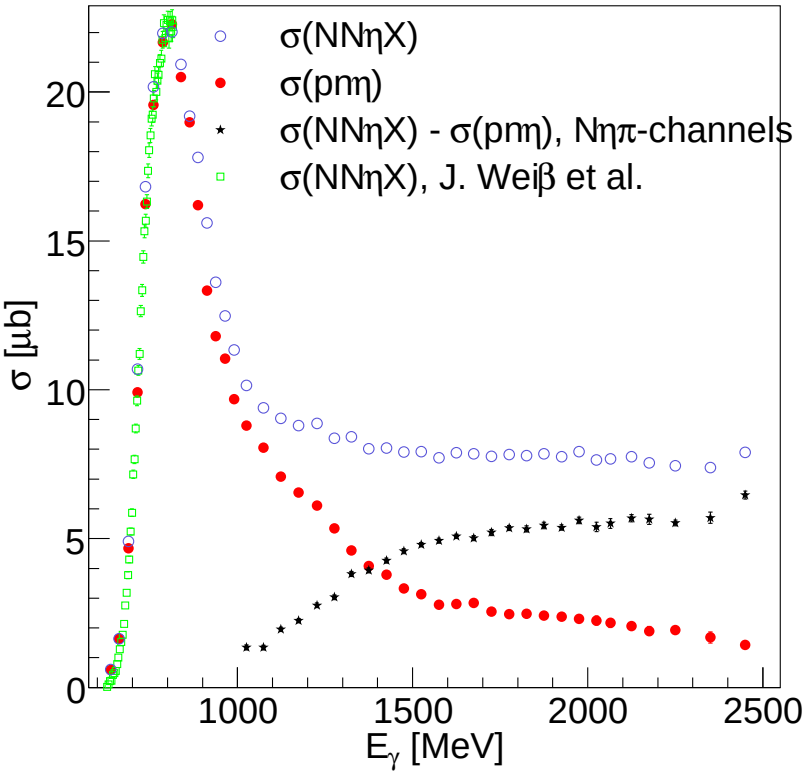

Figure 6.61: *Total cross sections for the fully inclusive ($\sigma(NN\eta X)$) and the quasi-free inclusive ($\sigma(pn\eta)$) compared to Weiβ et al. measurement (open green square), the difference between the fully inclusive and the quasi-free inclusive is also plotted (black star).*

From the $\eta-$meson threshold production to E_γ = 800 MeV, the fully inclusive and the quasi-free inclusive total cross sections reproduce the Weiβ et al. measurement. In this energy region, there is a systematic difference between the fully inclusive and the quasi-free inclusive : the fully inclusive total cross section is systematically slightly higher. Above the $N\eta\pi-$channels production threshold, i.e. E_γ = 806 MeV, the fully inclusive and the quasi-free inclusive total cross sections differ due to the opening of the $N\eta\pi-$channels. The fraction due to $\eta\pi-$final states is estimated (black star in Figure 6.61), it is the difference between the fully inclusive total cross section and the quasi-free inclusive total cross section.

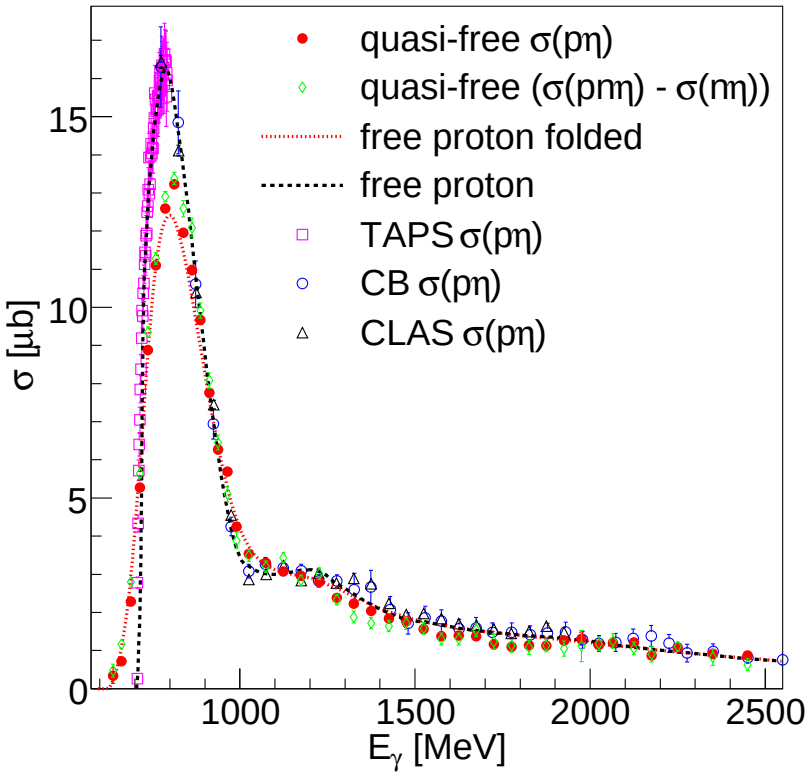

Figure 6.62: *Quasi-free proton total cross section as function of the incident photon beam energy compared to the free proton folded and to the free proton total cross sections from TAPS [38], CB [37] and CLAS [40]. The quasi-free proton is measured in two different ways : directly (red dot) and by making the difference between the quasi-free inclusive and the quasi-free neutron (green open diamond).*

The quasi-free proton total cross section was measured. There is a very good agreement between the quasi-free proton total cross sections (red dot) and the free proton folded (dashed red line) up to E_γ = 1.3 GeV. The systematic difference between the two (quasi-free proton and free proton folded) as function of the incident photon beam can be seen in Figure 6.63. Between E_γ = 1.3 and E_γ = 2 GeV, the systematic difference ranges from $\pm$ 10 % to $\pm$ 20 %. In order to understand the systematic difference the quasi-free proton was measured in a different way, from the difference between the quasi-free inclusive total cross section and the quasi-free neutron total cross section (green open diamond).

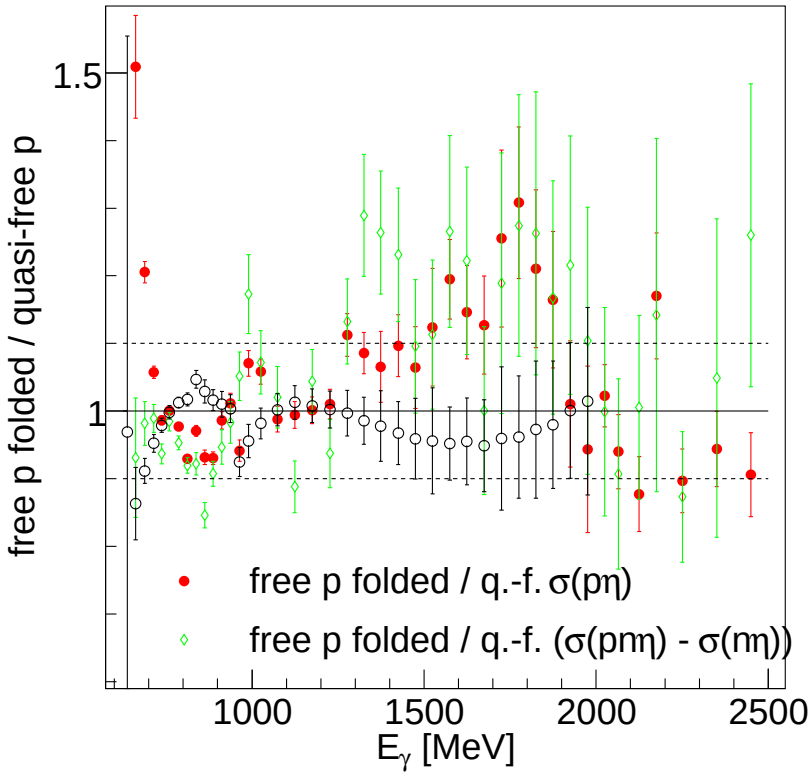

Figure 6.63: *Systematic difference of the quasi-free proton total cross section (measured in two different ways) and the free proton folded. Black open circle systematic difference of the quasi-free proton with the kinetic energy of the recoil proton measured in TAPS and the quasi-free proton with the kinetic energy of the recoil proton approximated in TAPS (as in CB) by using the missing mass analysis (see section 5.6.1).*

This systematic difference between E_γ = 1.3 and E_γ = 2 GeV, is also observed for the indirect measurement of the quasi-free proton total cross section (see Figure 6.63 open green diamond). The direct and the indirect measurements have different systematics, which indicates that the systematic difference to the free proton folded is due to the absolute normalizations like the flux measurements. The systematic difference due to the approximation of the kinetic energy of the recoil proton detected in CB by using the missing mass analysis was also checked. The systematic difference of the quasi-free proton with the kinetic energy of the recoil proton measured in TAPS and the quasi-free proton with the kinetic energy of the recoil proton approximated in TAPS (as in CB) by using the missing mass analysis (see section 5.6.1) is also plotted in Figure 6.63 (black open circle). The approximation of the kinetic energy by the missing mass analysis is correct within $\pm$ 5 %.

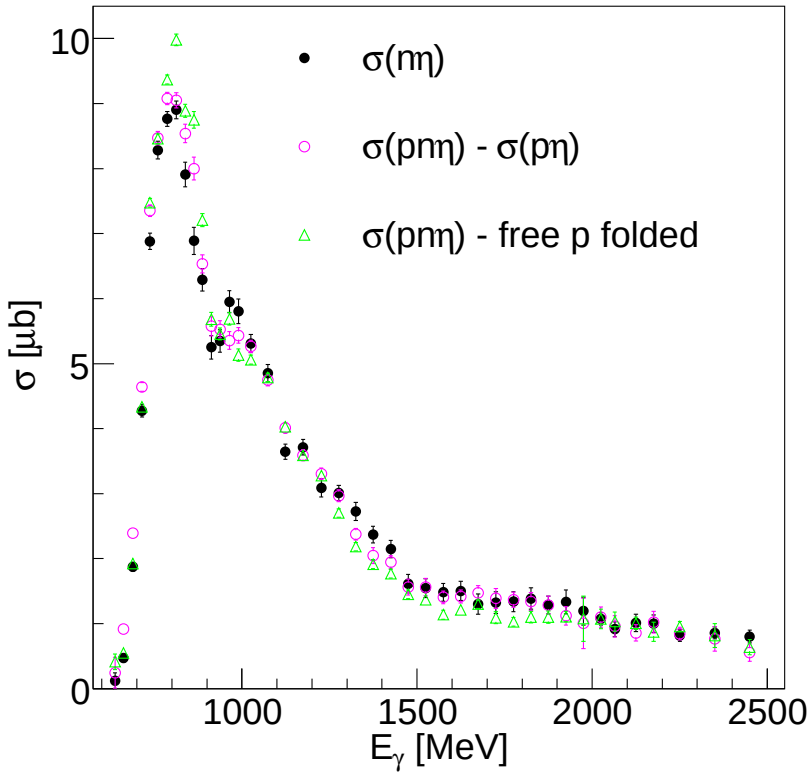

Figure 6.64: *Quasi-free neutron total cross section as function of the incident photon beam measured in three different ways : directly (black dot), by making the difference between the quasi-free inclusive and the quasi-free proton (violet open circle) or the free proton folded (green open triangle up).*

The quasi-free neutron total cross section can be measured in three different ways : directly, by making the difference between the quasi-free inclusive total cross section and the quasi-free proton total cross section or the free proton folded as illustrated in Figure 6.64.

Figure 6.65 shows the systematic difference between the different measurements. The direct measurement and the indirect measurement deduced from the difference between the quasi-free inclusive and the quasi-free proton give similar results (within $\pm$ 10 %) through the entire incident photon beam range. Furthermore the quasi-free neutron deduced from the quasi-free inclusive and the free proton folded give also similar results from the production threshold to E_γ = 1.3 GeV.

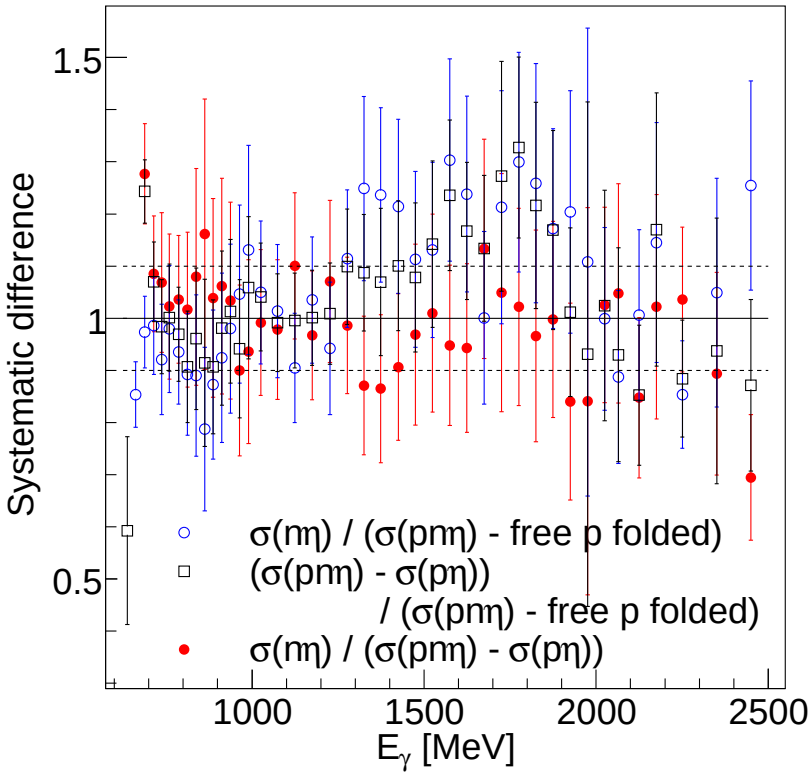

Figure 6.65: *Systematic difference as function of the incident photon beam between the three different ways to measure the quasi-free neutron total cross section.*

Above E_γ = 1.3 GeV as for the quasi-free proton, there is of course a systematic difference between ($\sigma(pn\eta)$ - free p folded) and the two others measurements that might come from from the uncertainty in the tagging efficiency determination. Around E_γ = 1 GeV, all three measurements show a bump structure which is not observed on the quasi-free proton. The final neutron measurement presented in the discussion is the average of the direct measurement and the difference between the quasi-free inclusive and quasi-free proton measurements.

6.3.6 The neutron - proton cross section ratio

The neutron - proton cross section was calculated for the three neutron measurements as shown in Figure 6.66. There is good agreement up to E_γ = 1.3 GeV.

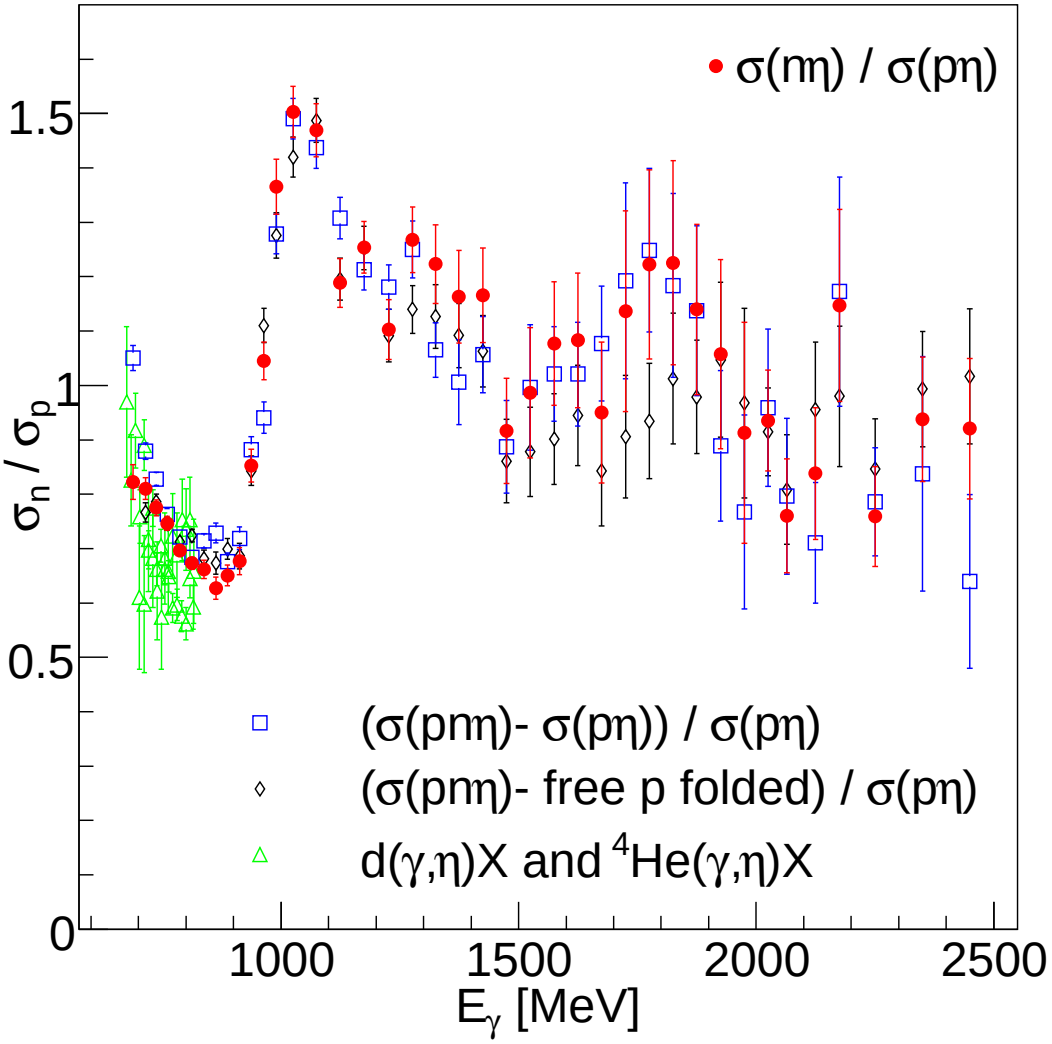

Figure 6.66: *The neutron - proton cross section ratio for the three neutron measurements compared to the different measurements made in Mainz by the TAPS collaboration [43, 44].*

The neutron - proton cross section ratio reflects the different mechanisms at work. There are two interesting structures around E_γ = 1 GeV and around E_γ = 1.8 GeV. First, in the $S_{11}(1535)$ energy region, a constant $2/3$ ratio is measured consistent with earlier results obtained by TAPS collaboration [43, 44]. Then above E_γ = 800 MeV, the ratio starts to increase due to higher lying resonances. The nature of these resonances will be discussed in the discussions part.

6.3.7 The discussions

Before discussing the details of the different results, a short compilation of the relevant results should be done. Figure 6.67 (left) shows the total cross section as function of the incident photon beam energy for all the reaction studied :

- the fully inclusive and the quasi-free inclusive compared to the Weiβ et al. measurement and an estimate of the background coming from the $N\eta\pi-$channels (i.e. the difference between the fully inclusive total cross section and the quasi-free inclusive total cross section)
- the quasi-free proton and the two different neutron measurements for the quasi-free neutron.

Figure 6.67 (right) compares the average of the two measurements for the quasi-free neutron to the quasi-free proton measurement (the black bar chart is the mean difference between the two measurements). In the insert the neutron - proton cross section ratio is plotted as function of the incident photon beam, compared to the Weiβ et al. measurement.

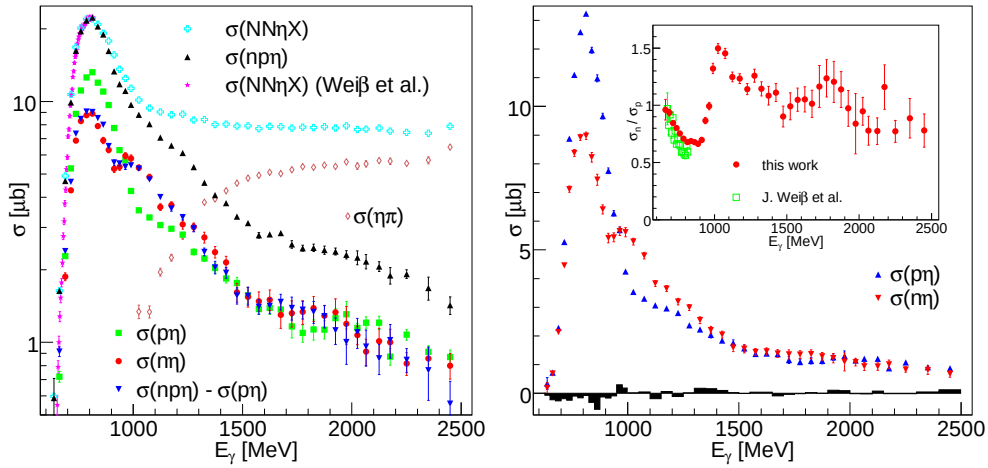

Figure 6.67: *Total cross sections as function of the incident photon beam. Left : for all reactions studied. Right : for the exclusive reactions and in insert the neutron - proton cross section ratio. The black bar charts are the mean difference between the two neutron measurements.*

In the neutron - proton cross section ratio as function of the incident photon beam, three distinct energy areas can be distinguished : the $S_{11}(1535)$ energy region. above the $S_{11}(1535)$ energy region to E_γ = 1.5 GeV and above E_γ = 1.5 GeV.

This three energy areas corresponds to three different angular distributions for the proton and the neutron as one one can see in Figure 6.68. Moreover,

the angular distributions of the proton and of the neutron are different and are starting to be similar above E_γ = 2 GeV.

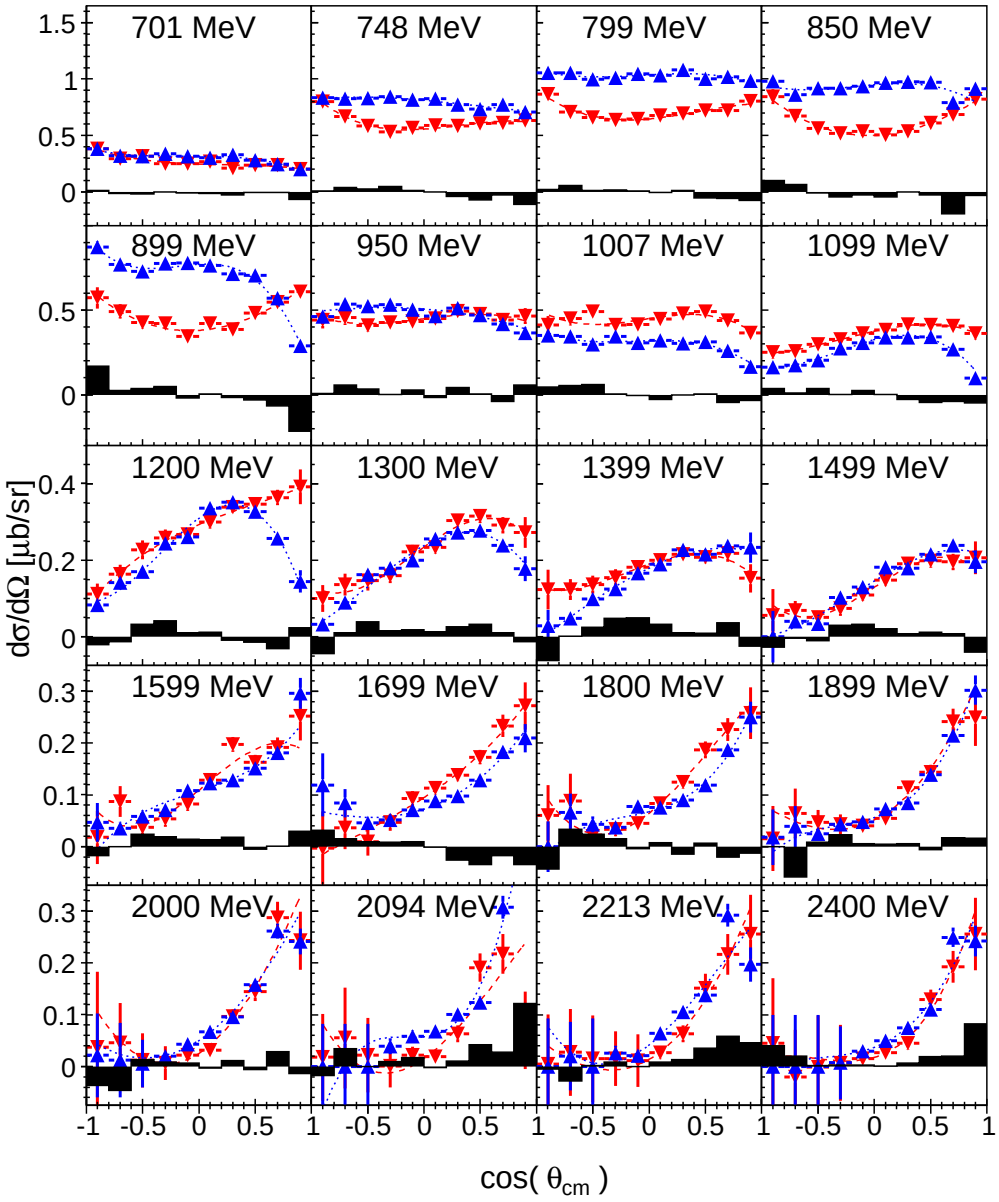

Figure 6.68: *Angular distributions for the quasi-free proton and for the quasi-free neutron. The black bar charts is the mean difference between the two neutron measurements.*

The difference between the proton and the neutron angular distributions is translated into different coefficients A_0, A_1, A_2 and A_3 as shown in Figure 6.69.

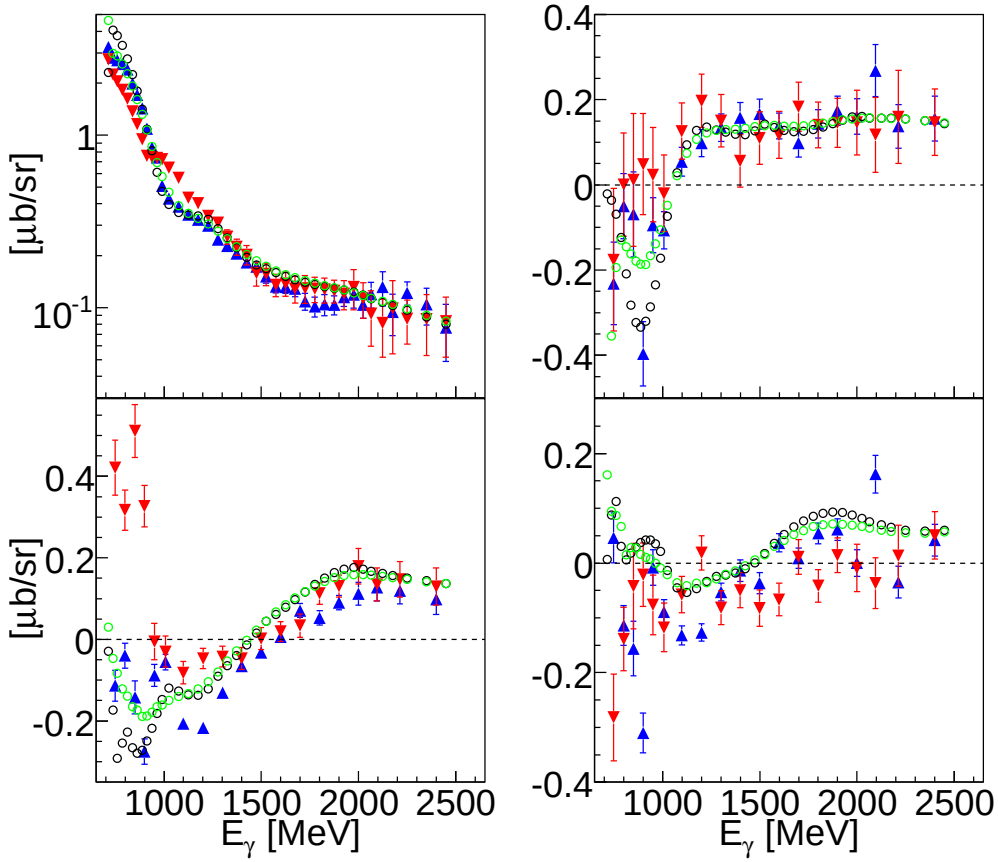

Figure 6.69: *Coefficients A_0, A_1, A_2 and A_3 of the angular distributions for the quasi-free neutron (red triangle down) and the quasi-free proton (blue triangle up). The coefficients are compared to the free proton (black open circle) and to the free proton folded (green open circle).*

The discussion itself is divided into four parts : in the first part the near threshold photoproduction of the $\eta-$meson off the deuteron is revisited, in the second part the data is compared to the different models available and to a preliminary fit of the data up to E_γ = 1.5 GeV. In the third part, the unfolding of the Fermi motion is discussed. In the last part, the smaller bump observed in the neutron - proton cross section ratio is discussed.

With this work, the "Near threshold photoproduction of η-mesons from the deuteron"[46] and the "Exclusive measurement of quasi-free η-photoproduction from deuterium"[43] papers can be revisited.

Near threshold photoproduction of the inclusive $\eta-$meson off the deuterium

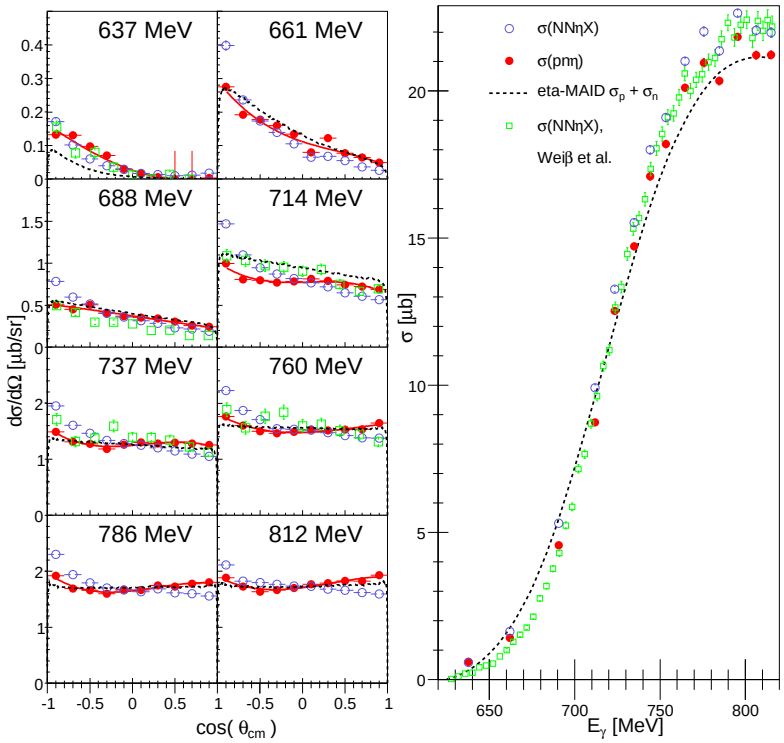

Figure 6.70: *Left : Angular distributions as function of the η cm angle for the $d(\gamma,\eta)X$ (of this work and Weiβ et al.) and $d(\gamma,\eta)pn$ reactions from threshold up to E_γ = 820 MeV, compared to the* `eta-MAID` *calculation folded. Right : Inclusive η photoproduction cross section for $d(\gamma,\eta)X$ and $d(\gamma,\eta)pn$ reactions compared to the* `eta-MAID` *calculation folded and Weiβ et al. measurement.*

Figure 6.70 shows the angular distributions (left) and the total cross sections (right) near threshold for the fully inclusive and the quasi-free inclusive reactions compared to the fully inclusive measurements of Weiβ et al. and to the quasi-free inclusive `eta-MAID` calculation folded.

There is some difference between the fully inclusive and the quasi-free inclusive measurements of this work at backward angles. Above the free production threshold, the observed angular distributions for the quasi-free inclusive reaction is rather flat, whereas the fully inclusive angular distributions show a forward - backward asymmetry. This asymmetry is more important below

the free production threshold and is also observed for the quasi-free inclusive. The asymmetry in the angular distributions is due to the fact that Fermi motion contributes asymmetrically. Below the threshold, a reaction is more likely when the momenta of the incident photon beam and the bound nucleon are opposed than when the two momenta point in the same direction. Therefore the cm-system is different on average. Note, that this asymmetry is reproduced by the `eta-MAID` calculations folded with the momentum of the bound nucleon.

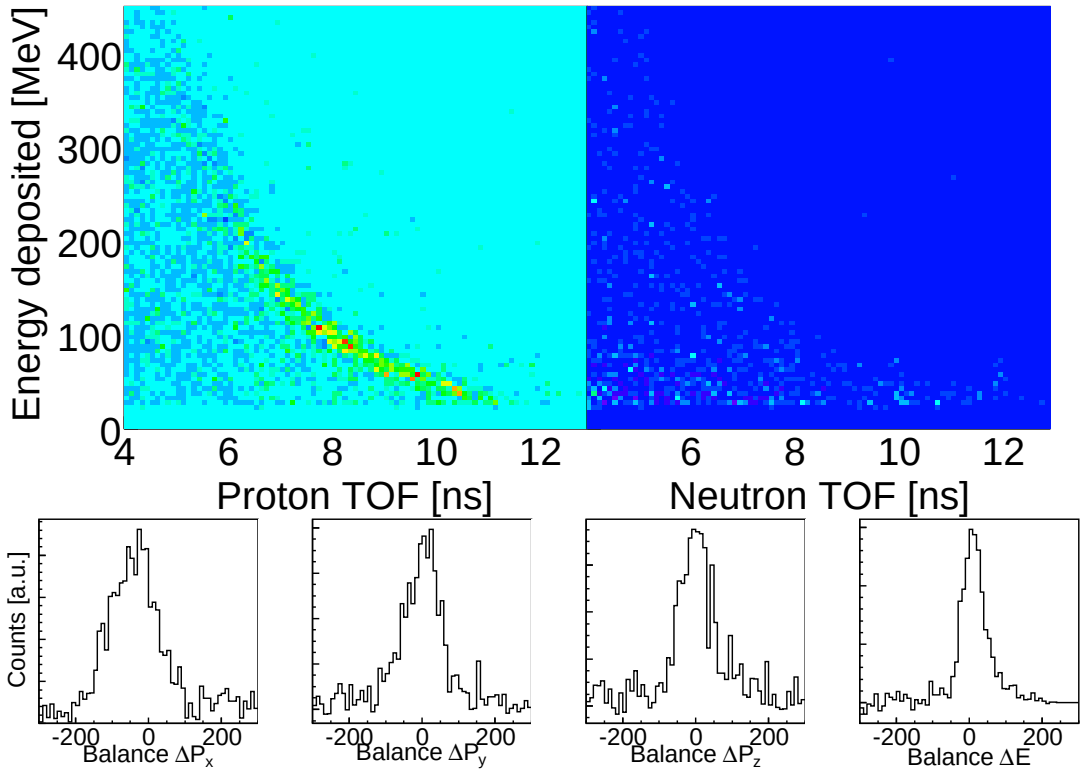

Figure 6.71: *Top : The proton and the neutron time-of-flight detected in coincidence with the $\eta-$meson for incident photon beam below 820 MeV. Bottom : Momenta balance and energy balance (the mass of the deuteron is subtracted) of the reaction $\gamma + d \rightarrow \eta + p + n$.*

Figure 6.71 intends to show that a $\eta-$meson is detected in coincidence with the participant nucleon and the spectator nucleon. In Figure 6.71 (top), the proton and the neutron time-of-flight as function of the energy deposited are shown when the two are detected in coincidence with the $\eta-$meson for E_γ = 710 - 820 MeV. With the help of the time-of-flight, the four-vector of the neutron and of the proton were reconstructed. Figure 6.71 (bottom) shows the momenta and the energy balances (see equations 6.25, 6.26, 6.27 and 6.28) of the reaction $\gamma + d \rightarrow \eta + p + n$.

$$0 = \Delta E = E_\gamma + m_d - (E_{(S)} + E_{(P)} + E_\eta) \quad (6.25)$$
$$0 = \Delta P_x = 0 - (P_{(S),x} + P_{(P),x} + P_{\eta,x}) \quad (6.26)$$
$$0 = \Delta P_y = 0 - (P_{(S),y} + P_{(P),y} + P_{\eta,y}) \quad (6.27)$$
$$0 = \Delta P_z = E_\gamma - (P_{(S),z} + P_{(P),z} + P_{\eta,z}) \quad (6.28)$$

The distributions around 0 MeV (Figure 6.71-bottom) show that the equations 6.25, 6.26, 6.27 and 6.28 hold. The fully inclusive reaction includes event where a $\eta-$meson is detected in coincidence with the participant nucleon and the spectator nucleon. When the participant and the spectator nucleons are detected in TAPS, the $\eta-$meson should move in the opposite direction, thus these events show up in the angular distrutions at backward angles. Above, the production threshold, apart the extreme backward angles, the angular distributions of the fully inclusive and the quasi-free inclusive are similar. Therefore, there is no reason to expect that the spectator-participant approach should not be valid above the threshold production.

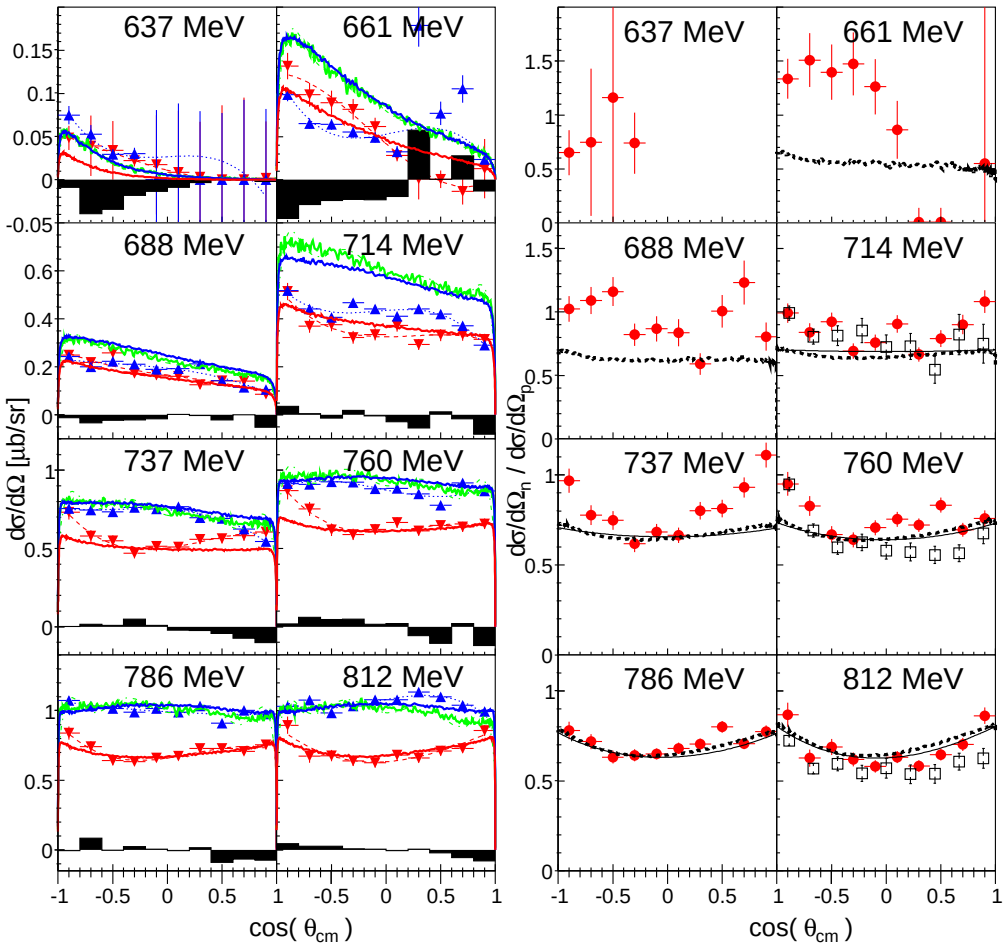

Figure 6.72: *Left : Angular distributions for the $d(\gamma,\eta)p(n)$ (blue triangle up) and $d(\gamma,\eta)n(p)$ (red triangle down) reactions in the cm system from threshold up to E_γ = 820 MeV, compared to the* `eta-MAID` *calculation folded: red line $n\eta$ and blue line $p\eta$; and the free proton folded (green line). The black charts is the mean difference between the two neutron measurements. Right : Neutron - proton cross section ratio as function of the η cm angle. The red dot is this work, the open black squared is Weiβ et al., the black line the* `eta-MAID` *calculation [41] and the dotted line is the* `eta-MAID` *calculation folded.*

Figure 6.72 (left) shows the angular distributions for the quasi-free neutron and quasi-free proton compared to the `eta-MAID` calculation folded and the free proton folded. The neutron - proton cross section as function of the η cm angle is plotted in Figure 6.72 (right) and is compared to the Weiβ et al. measurement.

The total cross section as function of the incident photon energy for the coincident measurement of $\eta-$meson and nucleon is plotted in Figure 6.73 (left) and the neutron - proton cross section ratio as function of the incident photon beam energy in Figure 6.73 (right).

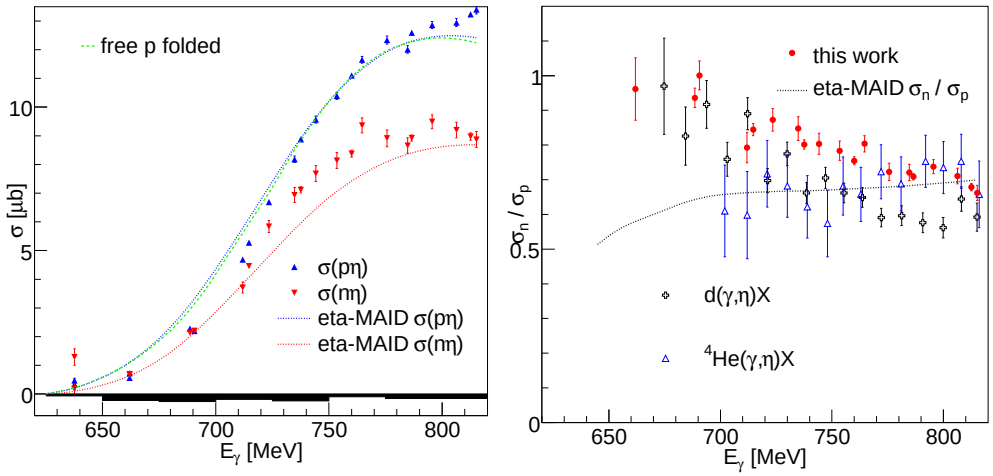

Figure 6.73: *Left : Quasi-free proton and neutron total cross section as function of the incident photon beam compared to the* `eta-MAID` *calculation folded. Right : Neutron - proton cross section ratio as function of the incident photon beam compared to [43, 44] and* `eta-MAID` *calculation folded.*

The total cross sections are compared to the `eta-MAID` calculations folded (for the neutron and the proton) and to the free proton folded. The cross section ratio is compared to previous measurements and the folded `eta-MAID` calculation.

The `eta-MAID` calculation for the folded proton reproduces quite well the data, except for the energy region between the quasi-free production threshold and E_γ = 750 MeV. In this energy range, the neutron - proton cross section ratio as function of the η cm angle (Figure 6.72-right) and as function of the incident photon beam energy (Figure 6.73-right) are close to one. This certainly means that the participant nucleon and the spectator nucleon can not be distinguished. It is known that below the free production threshold, the simple participant - spectator approach is supposed to be no more valid. Above E_γ = 750 MeV, the measured proton angular distributions and total cross section start to behave as expected i.e. it is similar to the free proton folded. Above E_γ = 750 MeV, the measured neutron angular distributions and total cross section are close to the neutron `eta-MAID` calculation folded, therefore the neutron - proton cross section as well. However, the neutron - proton cross section ratio

is closer to [he4] than the Weiβ et al. measurement. Now, if we consider that the spectator - participant approach starts to be realistic above incident photon energies higher than 750 MeV, we can extract some numbers and compare them to previous measurements.

The average ratio from E_γ = 0.75 GeV to E_γ = 0.82 GeV is 0.714 ± 0.006 (statistical error) and 0.66 ± 0.10 for the Weiβ et al. measurement. From this ratio, the neutron - proton helicity amplitude $|A^n_{1/2}/A^p_{1/2}|$ ratio of the $S_{11}(1535)-$resonance can be deduced from :

$$|A^n_{1/2}/A^p_{1/2}| = \sqrt{\sigma_n/\sigma_p} \tag{6.29}$$

and is

$$|A^n_{1/2}/A^p_{1/2}| = 0.845 \pm 0.078 \tag{6.30}$$

The isovector part - isoscalar part ratio can also be calculated and is obtained from :

$$\left(\frac{A^{IV}_{1/2}}{A^{IS}_{1/2}}\right)^{\pm 1} = \frac{1+\sqrt{\sigma_n/\sigma_p}}{1-\sqrt{\sigma_n/\sigma_p}} = 11.9 \pm 1.55 \tag{6.31}$$

where the exponents depends on the relative sign of $A^p_{1/2}$ and $A^n_{1/2}$. That means, that either the isoscalar part or the isovector part of the $S_{11}(1535)-$resonance is dominant.

Normally, only the coherent $\eta-$meson photoduction studies can determine which one is the dominating part. But, in Weiβ et al. another method to determine the relative sign was discussed : the use of the interference between the $D_{13}(1520)-$ and $S_{11}(1535)-$resonances. If only the $D_{13}(1520)-$ and $S_{11}(1535)-$resonances contribute to the signal, the angular distributions can be approximated by :

$$\left(\frac{d\sigma}{d\Omega}\right)_N \propto (A^N_{1/2}(S_{11}))^2 + \mathcal{G}(E_\gamma) A^N_{1/2}(S_{11}) A^N_{1/2}(D_{13})(3cos^2(\theta_{cm}) - 1) \tag{6.32}$$

where $A^N_{1/2}$ is the helicity $1/2$ couplings for the resonance excitations on proton ($N = p$) and on neutron (N=n). $\mathcal{G}(E_\gamma)$ is a function which is the sane for proton and neutron. The $D_{13}(1520)-$resonance parameters are well know from previous experiments. The Particle Data Group gives : $A^p_{1/2}(D_{13}) = (-24 \pm 9)$ and $A^n_{1/2}(D_{13}) = (-59 \pm 9)$. The observed proton angular distributions around E_γ = 800 MeV have a maximum at 90^o, whereas the observed neutron angular distributions have a minimum at 90^o (see Figure 6.72-left). As the helicity couplings for the D_{13} are both negative, the $A^p_{1/2}(S_{11})$ is positive and the $A^n_{1/2}(S_{11})$ is negative.

The relative sign of $A^p_{1/2}$ and $A^n_{1/2}$ is even more obvious for the coefficient A^N_1 (see Figure 6.56 and 6.59) and can be approximated around E_γ = 800 MeV by :

$$A^N_1 \propto \mathcal{G}(E_\gamma) A^N_{1/2}(S_{11}) A^N_{1/2}(D_{13}) \tag{6.33}$$

for the proton A^p_1 is negative and for the neutron A^n_1 is positive. Therefore, because of $A^p_{1/2} = A^{IS} + A^{IV} > 0$ and $A^n_{1/2} = A^{IS} - A^{IV} < 0$, the isovector part, A^{IV}, is dominant.

Behavior above the $S_{11}(1535)$ energy region upto E_γ = 1.5 GeV

In Figure 6.74, the measured total cross section is compared to three different calculations : the `BnGa` calculations [127], the `eta-MAID` calculations [41] and the Giessen calculations [42]. All three models folded describe pretty well the proton total cross section (Figure 6.74-right). To be able to compare the proton to the neutron, the proton total cross section has been down scaled by a factor $2/3$ (the calculations as well).

For the proton, two resonances are dominating the total cross section from production threshold upto E_γ = 1.5 GeV : for the `BnGa` calculations : the $S_{11}(1535)-$ and the $P_{13}(1720)-$resonances. Whereas for the `eta-MAID` and the Giessen calculations, it is the $S_{11}(1535)-$ and the $P_{11}(1710)-$resonances (see also section 2.3.4). The origin of the bump observed only for the neutron gives place to different explanations. The `eta-MAID` calculation should be distinguished from the Giessen and the `BnGa` calculations. The `eta-MAID` calculation is deduced from the different resonances that contribute to the free proton by simply taking into account the neutron helicity couplings of these same resonances. A third resonance, the $D_{15}(1675)$ that couples strongly to the neutron and very weakly to the proton should enhance the neutron signal (Figure 6.74-middle and section 2.3.4). For the Giessen calculations, it is a combination of two phenomena, either the $S_{11}(1650)-$ and/or the $P_{11}(1710)-$resonances (by changing the helicity couplings of these two resonances, the amplitude of the bump can change) and the opening of the $K\Lambda$ and ωN channels (Figure 6.74-bottom and section 2.3.4) can produce an enhancement of the neutron signal.

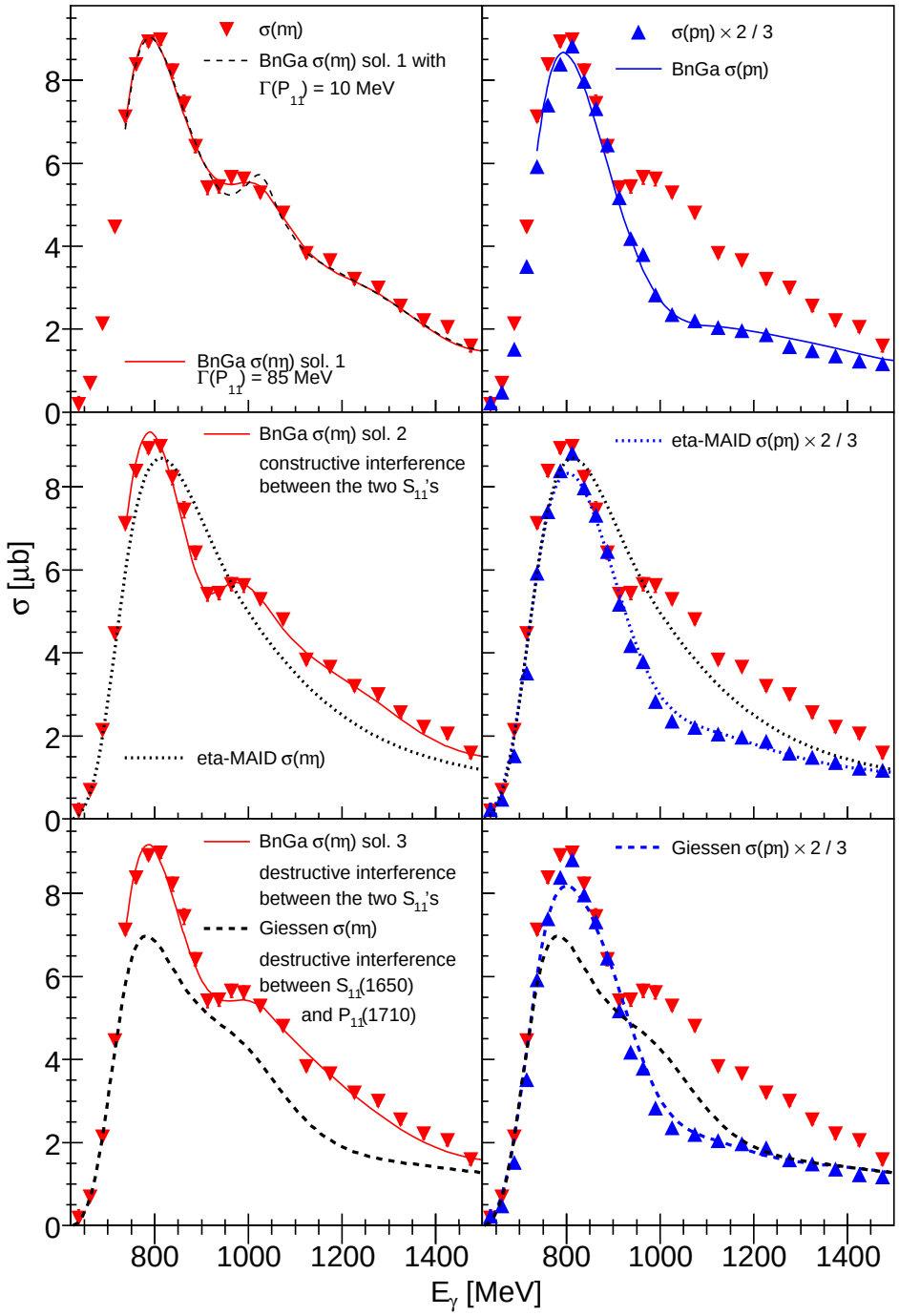

Figure 6.74: *Exclusive total cross sections as function of the incident photon beam energy. Left column : for the quasi-free neutron compared to the different solutions of the* `BnGa` *(solution one - top, solution two - middle and solution three - bottom), the* `eta-MAID` *(middle) and Giessen (bottom) calculations. Right column : for the quasi-free neutron and the quasi-free proton down scaled by a factor 2/3. The quasi-free proton is compared to the* `BnGa` *(top), the* `eta-MAID` *(middle) and Giessen (bottom) calculations.*

The BnGa calculations try different solutions to fit the bump structure : first solution (Figure 6.74-top-left), a narrow P_{11}, around 1660 MeV mass location, is introduced; second solution (Figure 6.74-middle-left) by a constructive interference between the $S_{11}(1535)$ and the $S_{11}(1650)$ and cusp effects; and third solution (Figure 6.74-bottom-left) by a destructive interference between the two S_{11}'s and a contribution from $D_{13}(1720)$. The differences between the different solutions are more obvious in the neutron - proton cross section ratio as function of the incident photon beam energy as plotted in Figure 6.75. The wave function used for the Fermi motion was a Paris wave function.

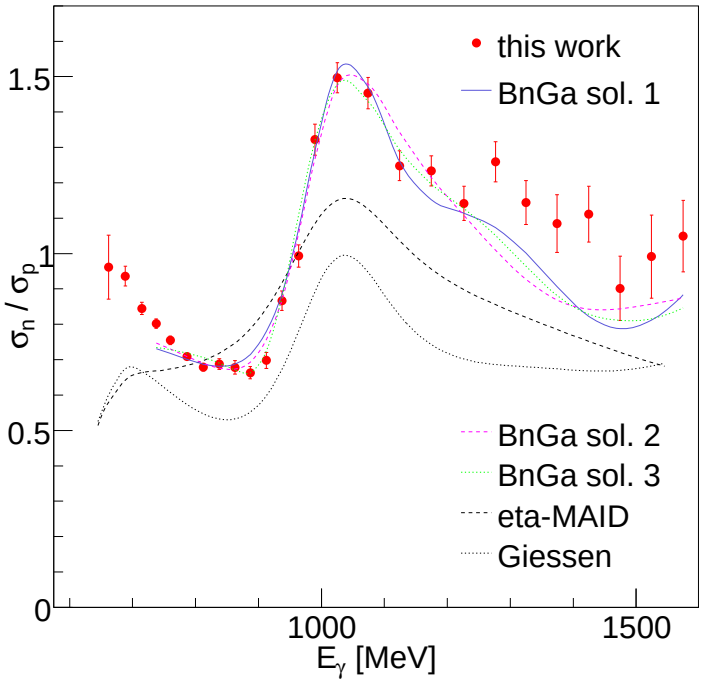

Figure 6.75: *Neutron - proton cross section ratio as function of the incident photon beam compared to the different calculations.*

The first solution gives a width of 85 $\pm$ 15 MeV for the P_{11} introduced. The resonance mass is 1668 $\pm$ 6 MeV. Moreover with a P_{11} of fixed width of 10 MeV, the bump structure is not fitted well (Figure 6.74-top-left). To obtain the second solution, a non-resonant $P-$vector couplings was introduced. The cusp effects of the reaction $\gamma n \rightarrow K\Lambda$ and $\gamma n \rightarrow K\Sigma$ have little influence. The third solution requires a small destructive interference between the $S_{11}(1535)-$ and the $S_{11}(1650)-$resonances, thus a very small γn coupling but requires a notable contribution from $D_{13}(1720)$. The preliminary fit of the data by the BnGa calculations does not favor any solution. The cross section as function of the incident photon beam for different $cos(\theta_{cm})$ bin is plotted in Figure 6.77,

the cross section is compared to the Giessen calculations and the solution one of the BnGa calculations. If only the $S_{11}(1650)-$ and the $P_{11}(1710)-$resonances contribute to the signal, equation 2.24 becomes:

$$\frac{k^*}{q^*}\frac{d\sigma}{d\Omega} = |E_{o+}|^2 + |M_{1-}|^2 - 2cos(\theta_{cm})Re(E^*_{o+}M_{1-}) \tag{6.34}$$

Then, the ratio A_1/A_0 corresponds to the following expression:

$$\frac{A_1}{A_0} = \frac{-2Re(E^*_{o+}M_{1-})}{|E_{o+}|^2 + |M_{1-}|^2} \tag{6.35}$$

Figure 6.76 shows the evolution of this ratio as function of the incident photon beam energy for the quasi-free nucleon reaction. This ratio is compared to the free proton, the free proton folded and the eta-MAID calculations. For the eta-MAID calculations, only three resonances were taken into account the two S_{11}'s and the $P_{11}(1710)$.

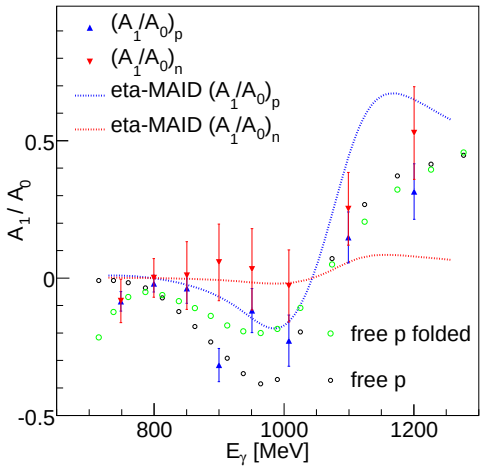

Figure 6.76: A_1/A_0 *as function of the incident photon beam.*

A $A_0 + A_1 cos(\theta_{cm})$ behavior is clearly seen in the data in both channels: in Figure 6.77 (left) the bump changes with the $cos(\theta_{cm})$ bin and in Figure 6.77 (right) the left arm also changes with $cos(\theta_{cm})$ bin. The A_1/A_0 changes rapidly for the neutron and the proton for incident photon beam energies higher than 1 GeV (see Figure 6.76). For both channels, the behavior of the data can be interpreted by an interference of this type. The eta-MAID calculations of the proton multipoles show also this tendency but not the eta-MAID calculations for the neutron. It should be noted that an interference between the two S_{11}'s and the $P_{13}(1720)$ could also explain the A_1/A_0 behaviour.

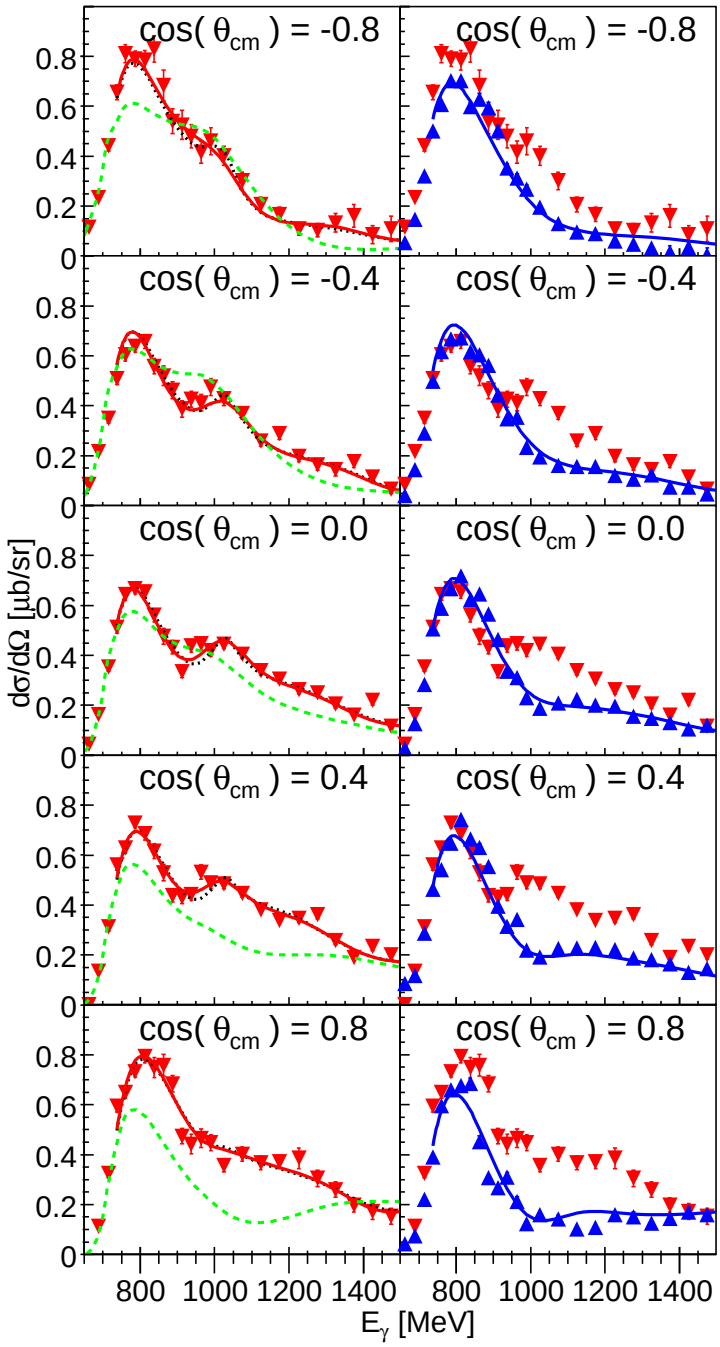

Figure 6.77: *Quasi-free nucleon cross sections as function of the incident photon beam for different $cos(\theta_{cm})$ bin. Left : compared to different model. Right : compared to the quasi-free proton downscaled by a factor 2/3. (red triangle down quasi-free neutron compared to the solution one of* BnGa *calculations - red line : $\Gamma(P_{11})$ =80 MeV - and - black dotted line $\Gamma(P_{11}) = 10$ MeV and to Giessen calculation - green dashed line, blue triangle up quasi-free proton down scaled by a factor $2/3$ compared to* BnGa *calculations).*

Thus, there are different possibilities to explain the bump-structure observed for the neutron. A possible way to disentangle the different solution, it is to unfold the Fermi motion from the measurements.

Unfolding the Fermi motion

The only rigorous way to unfold the Fermi motion is to find event-by-event the true total cm energy of the participant nucleon - η system from:

$$s = (E_\eta + E_p)^2 - (p_\eta + p_p)^2 \tag{6.36}$$

This is only possible when the recoil nucleon is detected in the TAPS detector (see Figure 6.24) i.e. for $cos(\theta_{cm}) \leq -0.1$. Only the TAPS detector can measure the kinetic energy of the recoil nucleon by using the time-of-flight (see section 5.6.2). Then, the effective incident photon energy E^*_γ is calculated from:

$$E^*_\gamma = \frac{s - m_N^2}{2m_N} \tag{6.37}$$

Figure 6.78 shows the cross sections as function of the effective incident photon energy compared to the cross sections as function of the incident photon beam for the proton case (left) and for the neutron case (right).

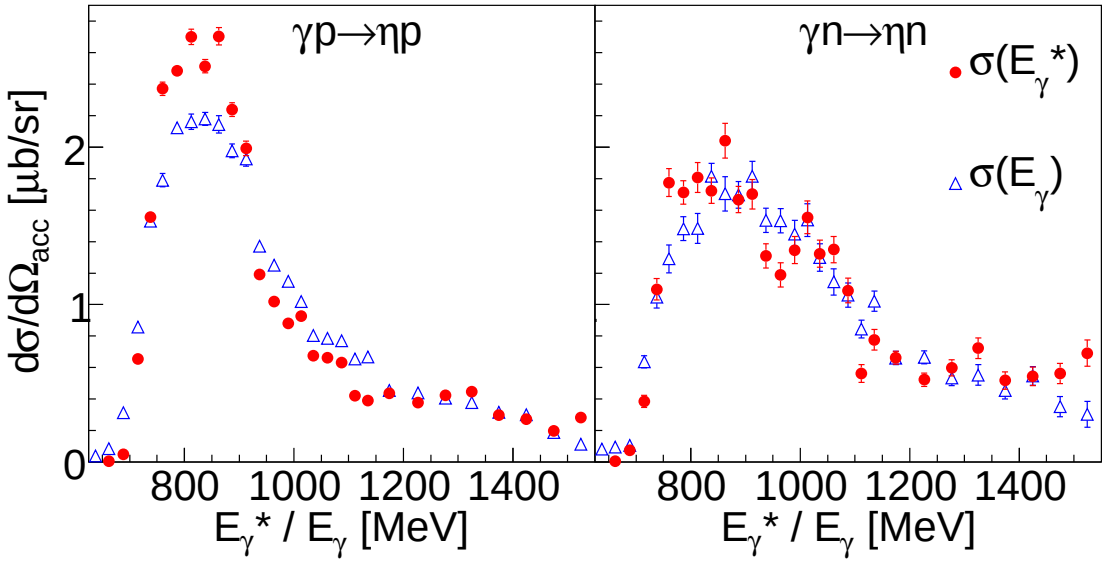

Figure 6.78: *Cross sections as function of the effective incident photon energy (red dot) and of the incident photon beam (blue open triangle up) for* $cos(\theta_{cm}) \leq -0.1$. *Left : for proton case. Right : for the neutron case. A very strong coplanarity cut was applied :* $170^o \leq |\phi_N^{lab.} - \phi_\eta^{lab.}| \leq 190^o$ *(which was not corrected, no missing mass cut was applied).*

To extract these cross sections, a coplanarity cut was applied i.e. $170^o \leq |\phi_N^{lab.} - \phi_\eta^{lab.}| \leq 190^o$. With this cut, the background coming from the competing channels is removed, thus no missing mass cut was applied. The coplanarity cut was not corrected.

In the proton case, the $S_{11}(1535)-$resonance gets narrower and the amplitude increases in the expected way as illustrates by Figure 6.79. For the neutron, this is as well the case but due to the statistic fluctuation it is not so obvious. But the bump around E_γ = 1 GeV clearly gets narrower and is slightly shifted to higher incident photon energy.

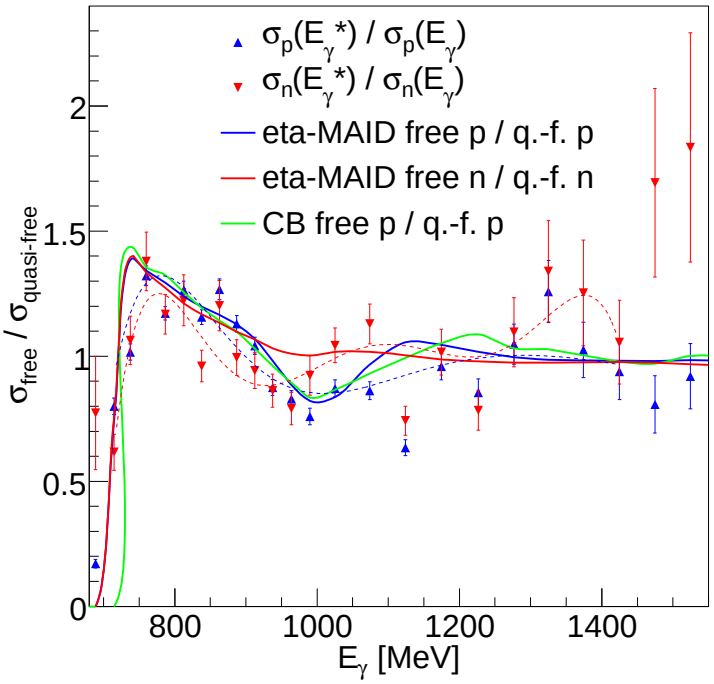

Figure 6.79: *Measured free nucleon - bound nucleon cross section ratio as function of the incident photon beam compared to the ratios determined from free proton measurenent and* `eta-MAID` *calculations and a Paris wave function. The dashed lines are the fit of the measured ratios.*

Figure 6.79 shows the free nucleon - bound nucleon cross section ratio as function of the incident photon beam energies for the proton and the neutron (it is the ratio of the cross sections of Figure 6.78). The measured ratio of the proton is similar to the ratios obtained from the `eta-MAID` calculations - `eta-MAID` calculations folded and the free proton - free proton folded, specially in the $S_{11}(1535)$ energy region. The measured ratio of the neutron is similar to the measured ratio of the proton from threshold upto E_γ = 0.9 GeV, above this energy they start to differ.

The free nucleon - bound nucleon cross section ratio, R_C, determined from the data can be used to eliminate approximately the Fermi smearing by assuming its validity for all $cos(\theta_{cm})$ bin. These ratios (for the proton and for the neutron) were parameterized by a polynom of fifth order. Then, the free nucleon cross section is obtained from :

$$\sigma_{free} = R_c \cdot \sigma_{quasi-free} \tag{6.38}$$

The results can be seen in Figure 6.80 (left). The results for the de-folded proton cross section, which is compared to the free proton measurements, are not convincing (see Table 6.3.7). The result is more convincing with $R_c^{\texttt{eta-MAID}}$ (determined from `eta-MAID` calculations and a Paris wave function - see Table 6.3.7)), see Figure 6.80 (right). The corrected neutron cross section by R_c

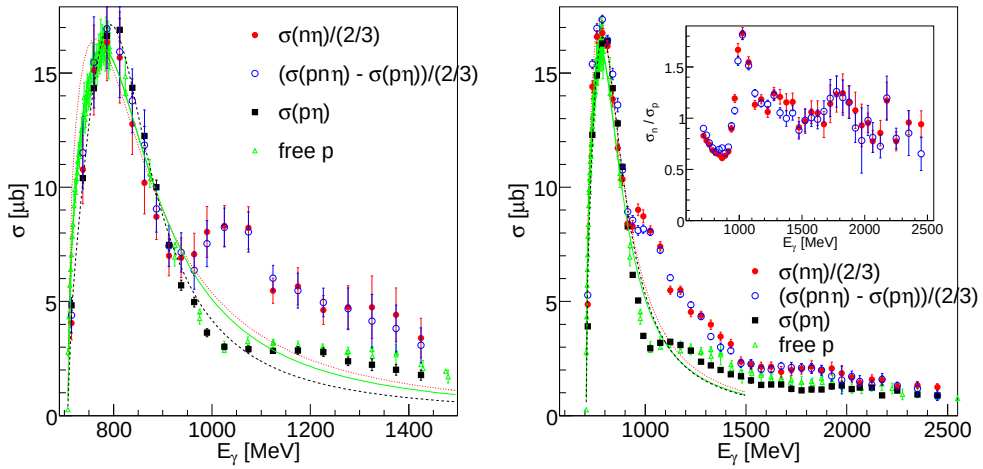

Figure 6.80: *Free nucleon total cross sections as function of the incident photon beam. Left : corrected by the free nucleon - bound nucleon ratio determined from the data. Right : corrected by the free nucleon - bound nucleon ratio derived from* `eta-MAID` *and the Paris wave function and in insert the neutron - proton cross section ratio. The neutron was scaled by a factor* $3/2$*. The lines are the Breit-Wigner fit.*

and $R_c^{\texttt{eta-MAID}}$ are similar in the $S_{11}(1535)$ energy region and also very similar to the shape of the free proton measurements. To demonstrate the similarity of the neutron and proton shape in the $S_{11}(1535)$ energy region, this shape was fitted.

To fit the total cross section a Breit-Wigner fit was used :

$$\sigma(W) = \frac{q_\eta^*}{q_{\eta R}^*} \frac{k_R^*}{k^*} \frac{2m_N (A_{1/2}^N)^2 b_\eta M_R \Gamma_R}{(M_R^2 - W^2)^2 + M_R^2 \Gamma_R^2 x^2} \tag{6.39}$$

Parameters	free p
M_R [MeV]	1535.97 $\pm$ 0.5
Γ_R [MeV]	156 $\pm$ 3.2
$A^N_{1/2}$ [$10^-3(GeV)^{-1/2}$]	102.3 $\pm$ 0.85

Table 6.2: Resonance position M_R, the width Γ_R and the photon coupling $A^N_{1/2}$ extracted.

Parameters	p (with R_c^{data})	n (with R_c^{data})
M_R [MeV]	1544.26 $\pm$ 0.2	1534.63 $\pm$ 1.5
Γ_R [MeV]	120.7 $\pm$ 1	166.44 $\pm$ 4.57
$A^N_{1/2}$ [$10^-3(GeV)^{-1/2}$]	93 $\pm$ 0.31	86.67 $\pm$ 1.34

Table 6.3: Resonance position M_R, the width Γ_R and the photon coupling $A^N_{1/2}$ extracted.

Parameters	p (with $R_c^{\texttt{eta-MAID}}$)	n (with $R_c^{\texttt{eta-MAID}}$)
M_R [MeV]	1542.85 $\pm$ 0.3	1534.85 $\pm$ 0.8
Γ_R [MeV]	150.55 $\pm$ 1.77	160 $\pm$ 5
$A^N_{1/2}$ [$10^-3(GeV)^{-1/2}$]	102.25 $\pm$ 0.5	88 $\pm$ 1.4

Table 6.4: Resonance position M_R, the width Γ_R and the photon coupling $A^N_{1/2}$ extracted.

where

$$x = b_\eta \frac{q^*_\eta}{q^*_{\eta R}} + b_\pi \frac{q^*_\pi}{q^*_{\pi R}} + b_{\pi\pi} \tag{6.40}$$

the notation used is the same as in [Bernd28].

The free parameters were the resonance position M_R, the width Γ_R and the photon coupling $A^N_{1/2}$ ($N = p$ or $N = n$). The decay branching ratios of the resonance were fixed : b_η = 0.5, b_π = 0.4 and $b_{\pi\pi}$ = 0.1.

The values of the fits are summarized in Tables 6.3.7, 6.3.7 and 6.3.7. The errors are coming from the fit. The mass and the width extracted for the free proton measurements and the neutron corrected are comparable. The helicity coupling ratio $|A^n_{1/2}/A^p_{1/2}| = 0.86 \pm 0.018$ is comparable with the one obtained from the neutron - proton cross section ratio (equation 6.30).

As in [65], the bump observed at $\sim$ 1685 MeV (in W) in the differential cross section (Figure 6.78-right) and the total cross section (Figure 6.80-left) can be fitted with a Polynomial-plus-Breit-Wigner (see Figure 6.81).

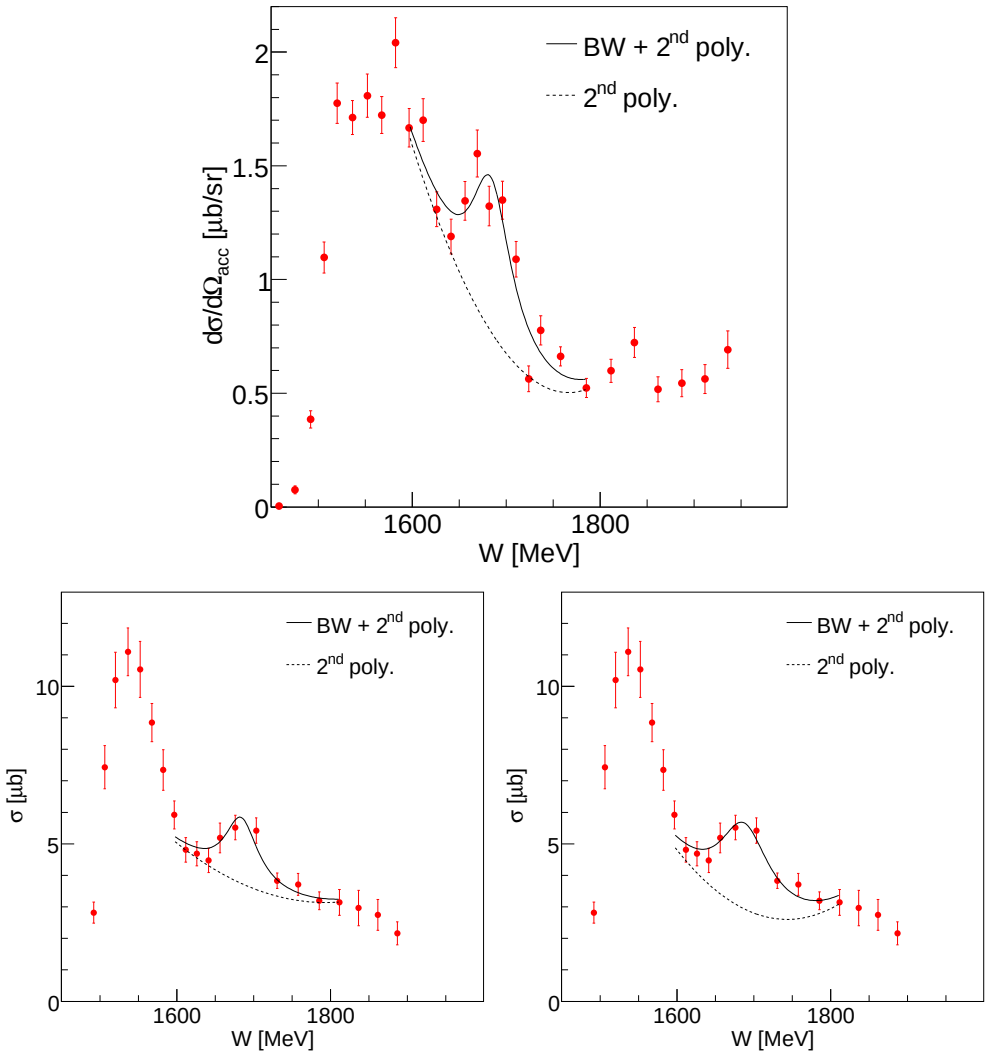

Figure 6.81: *Top : $\gamma + n \rightarrow \eta + n$ differential cross section as function of the true W for $cos(\theta_{cm}) \leq -1$ of the η in the CM (i.e. after the elimination of the Fermi motion). Black line Polynomial-plus-Breit-Wigner fit of $\gamma + n \rightarrow \eta + n$ differential cross section. Bottom : $\gamma + n \rightarrow \eta + n$ total cross section as function of the true W (i.e. after the elimination of the Fermi motion with R_c^{data}). Bottom left : Polynomial-plus-Breit-Wigner fit obtained with the mass and the width of the Breit-Wigner function fixed to the values given by the fit of the differential cross section. Bottom right : Polynomial-plus-Breit-Wigner fit obtained with requesting that the width of the Breit-Wigner function is larger than 80 MeV.*

The fit of the differential cross section gives a mass of 1685 MeV and a width of 53 MeV (Figure 6.81-top). If the mass and the width are fixed to 1685 MeV and 53 MeV, respectively, the fit of the total cross section gives Figure 6.81 (bottom-left). If we require that the width should be at least 80 MeV, the fit of the total cross section gives Figure 6.81 (bottom-right). The bump area could be fitted correctly with a width of 180 MeV. Therefore, the width of the bump depends on the contribution of the other resonance-terms and the background-terms.

Thus, after the elimination of the Fermi smearing, the bump structure is more pronounced. The peak in the neutron - proton cross section ratio around E_γ = 1 GeV gets sharper (see Figure 6.80-right in insert). At E_γ = 1.8 GeV, the difference between the proton and the neutron is more visible.

Above E_γ = 1.5 GeV

Above E_γ = 1.5 GeV, an interesting structure appears for the neutron (Figures 6.80 and 6.67-right) and in the neutron - proton cross section ratio (Figures 6.80right in insert and 6.67-right in insert), precisely around E_γ = 1.8 GeV. At this energy range, the new resonance $D_{15}(2070)$ was proposed from the analysis of the free proton data, which is according to the `BnGa` calculations the third resonance that contributes most to the $\eta-$meson photoproduction.

In conclusion, we can compare the free neutron total cross section calculated from R_c^{data} with the different models (Figure 6.82) upto E_γ = 1.6 GeV.

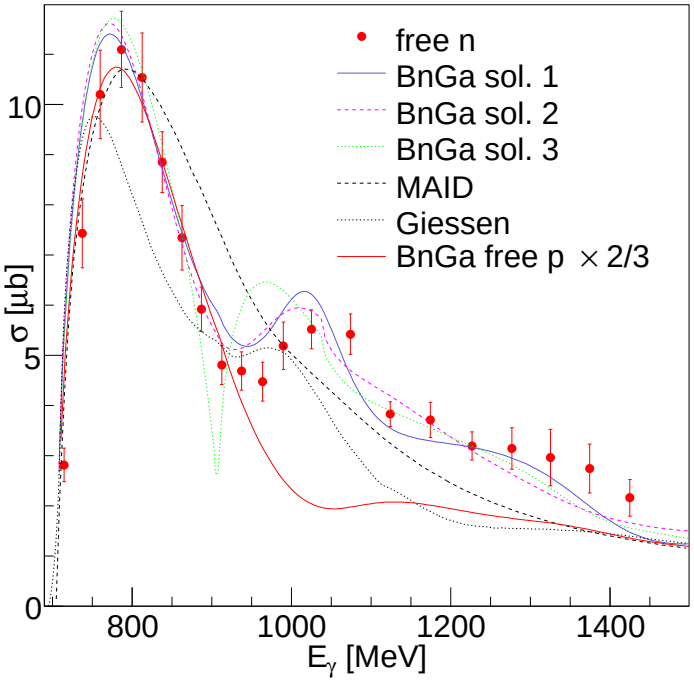

Figure 6.82: *Free neutron total cross section as function of the incident photon beam compared to the different models.*

Even if the use of R_c^{data} is correct, the determination of R_c^{data} is however limited by the detector energy resolution.

6.4 The $\eta^{'}$ photoproduction off the deuteron

Four channels were studied :

- $\gamma + d \rightarrow \eta^{'} + X$ (fully inclusive),
- $\gamma + d \rightarrow \eta^{'} + (pn)$ (quasi-free inclusive),
- $\gamma + d \rightarrow \eta^{'} + p(n)$ (quasi-free proton) and
- $\gamma + d \rightarrow \eta^{'} + n(p)$ (quasi-free neutron).

with $\eta^{'} \rightarrow \pi^o\pi^o\eta \rightarrow 6\gamma$.

The reaction identification, the determination of the detection efficiency and the calculation of the total cross section and of the differential cross section follow point-by-point the methodology used for the η photoproduction off the deuteron study. Therefore, the points similar to the η photoproduction off the deuteron study will not be developped again. The results presented here are preliminary.

6.4.1 The reaction identification

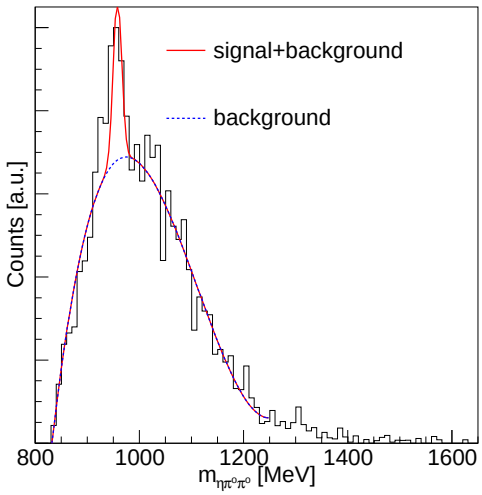

Figure 6.83: *Typical $\eta\pi^o\pi^o$ invariant mass spectrum fitted by a combined fit : signal + background. The signal is fitted by a Gaussian function which has the peak position and the width fixed, respectively to 957.43 MeV and 10 MeV. The background is fitted by a polynomial function of third order. The $\eta^{'}-$meson was reconstructed from 7 neutral hits for incident photon between 1700 MeV and 1800 MeV.*

The reaction identification is based on the identification of the $\eta^{'}-$signal by an invariant mass analysis and moreover for the quasi-free inclusive, proton and neutron reactions on the identification of the single$-\eta^{'}-$meson production by a missing mass analysis. Figure 6.83 shows a typical $\eta\pi^o\pi^o$ invariant mass spectrum. For all reactions, the $\eta^{'}-$meson is identified by its $\eta 2\pi^o$ invariant mass distribution (see Figures 6.83 and section 5.5.4). The background has two sources : combinational background coming from $2\pi^o$ and an uncorrelated η and also competing channels that can create a fake single$-\eta^{'}-$meson production signal. The competing channels were not study, but are considered to be:

- $\gamma + p \rightarrow \ \eta \ + \pi^o \ + p$
- $\gamma + n \rightarrow \ \eta \ + \pi^- \ + p$
- $\gamma + n \rightarrow \ \eta \ + \pi^o \ + n$
- $\gamma + p \rightarrow \ \eta \ + \pi^+ \ + n$

The production threshold of the $N\eta^{'}\pi-$channels is $\sim$ 1410 MeV.

The missing mass analysis was partially performed. Figure 6.84 (left-column) shows the $\eta\pi^o\pi^o$ invariant mass spectrum for seven neutral hits and for three different incident photon energy ranges. If we apply a cut on the invariant mass around the $\eta^{'}-$peak (illustrated by the vertical dashed line in Figure 6.84 (left-column) and treat the detected neutron as a missing particle, we obtain the corresponding missing mass (after removing the combinational background) which is shown in Figure 6.84 (right-column) as black dots. The simulated missing mass distributions are shown in Figure 6.84 (right-column) for the $\gamma + n(p) \rightarrow \eta^{'} + n(p)$ reaction.

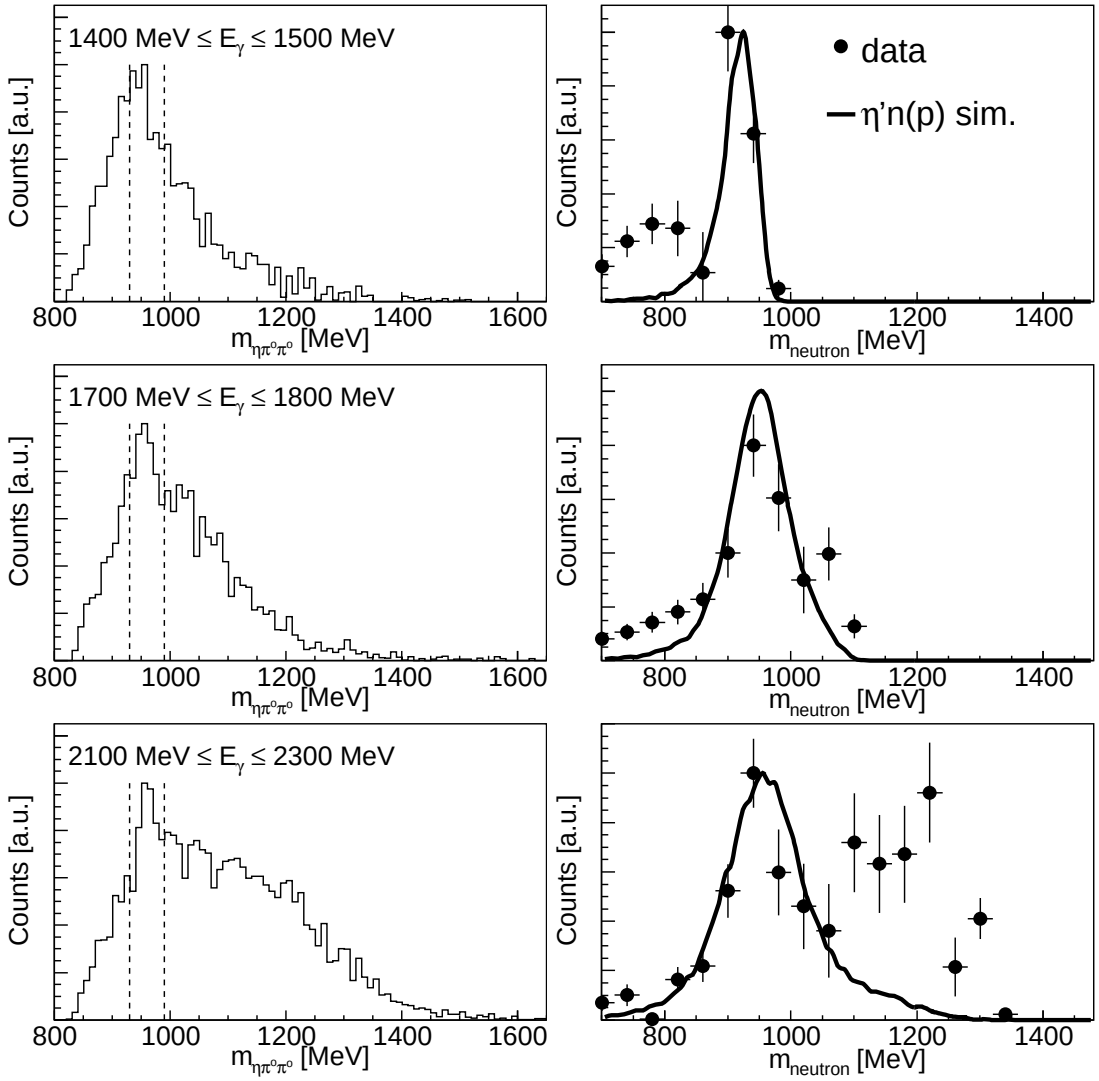

Figure 6.84: *Left column : $3\pi^o$ invariant mass distribution for three different incident photon beam ranges. Right column : Missing mass distribution for the same photon beam ranges (for* $930\ MeV\ \leq m_{\eta\pi^o\pi^o} \leq 990\ MeV-$*dashed vertical lines).*

A very conservation cut is applied, above the $\eta^{'}\pi$ threshold production to remove the $N\eta^{'}\pi-$channels backgound even if the background seems to appear at higher incident photon energies as we will see later. Figure 6.85 shows the peak postion and the peak position $\pm$ 3 $\times\sigma$ of the simulated missing mass distribution (when the nucleon mass is substracted) as function of the incident photon beam (for the quasi-free inclusive reaction).

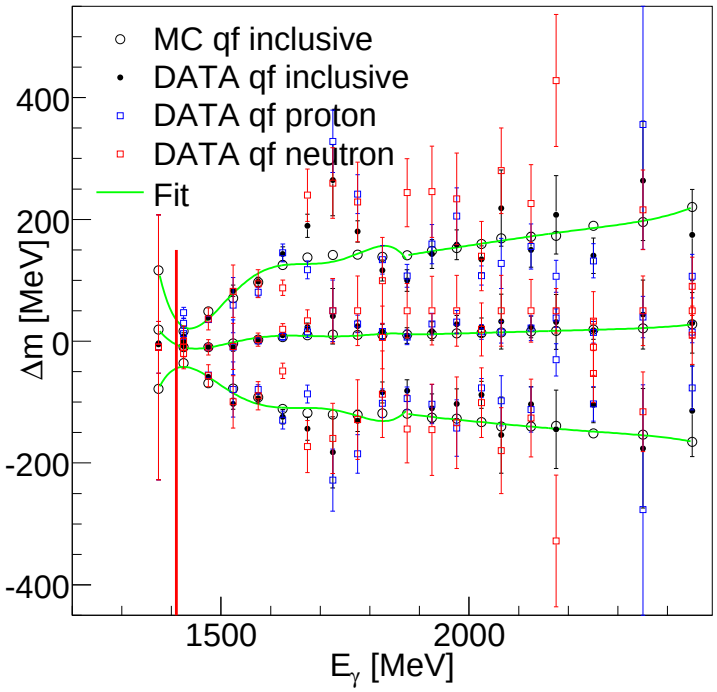

Figure 6.85: *The peak position and the peak position $\pm 3 \times \sigma$ of the simulated missing mass distribution (when the nucleon mass is subtracted) as a function of the incident photon beam. The vertical red line represents the $\eta^{'}\pi$ threshold production, $E_{\gamma} \sim$ 1410 MeV.*

The kinematical limits were also studied, but no cuts based on the kinematical limits in the results presented here were applied. Figure 6.86 shows the kinematical limits as a function of incident photon beam and $cos(\theta_{CM})$ of the $\eta^{'}$-meson in the center-of-mass for a free nucleon target (left) and for a quasi-free nucleon target (right).

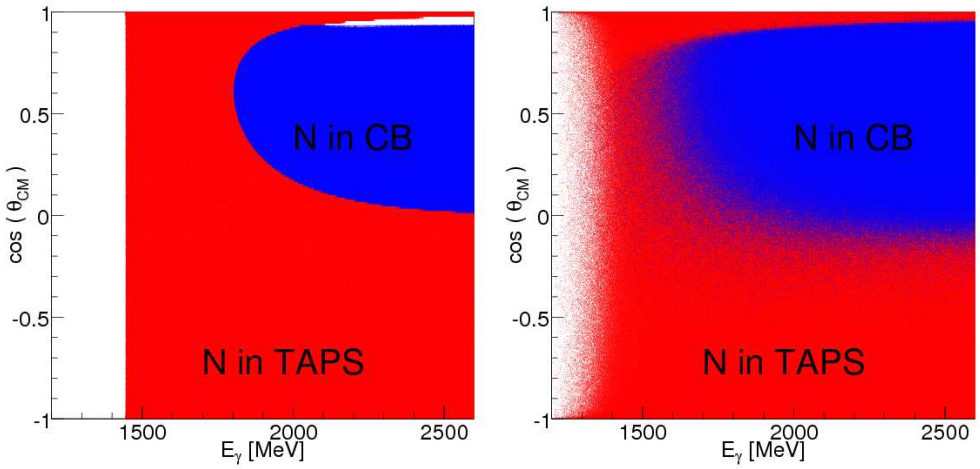

Figure 6.86: *Kinematical limits as a function of incident photon beam energy and* $cos(\theta_{CM})$ *of the* $\eta^{'}$*-meson in the center-of-mass. Left : for a free nucleon target. Right: for a quasi-free nucleon target. Red area the nucleon is detected in TAPS. Blue area the nucleon is detected in CB. White area : the nucleon is not detected.*

Compared to the η photoproduction off the deuteron, there are much more recoil nucleons which are going into the TAPS detector. Figure 6.87 shows the kinematical limits as a function of incident photon beam energy and the neutron laboratory angle.

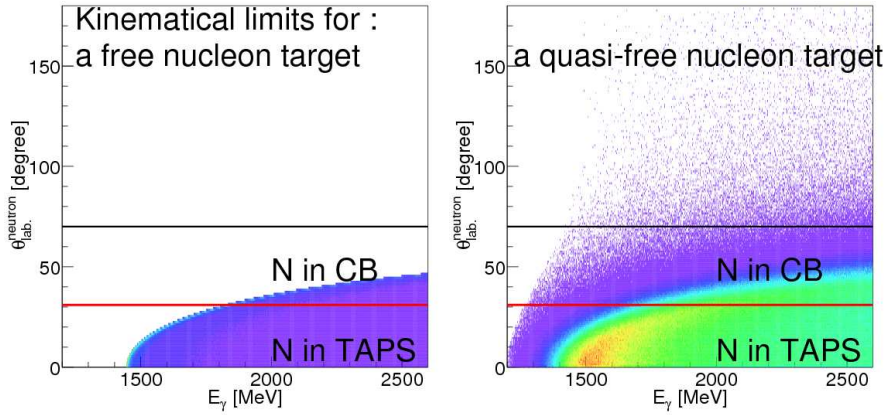

Figure 6.87: *Kinematical limits as a function of incident photon beam and the neutron laboratory angle. Left : for a free nucleon target. Right: for a quasi-free nucleon target. The red line represents the separation between the TAPS and CB detectors.*

In summary,

The identification of the reaction $\gamma + d \rightarrow \ \eta^{'} \ + X$

Events with six or seven neutral hits are considered (there is no limitation on the number of charged hits). The $\eta^{'}-$meson is constructed from these six or seven neutral hits (as described in section 5.5.4). The reaction identification is only based on the identification of the $\eta^{'}-$signal.

The identification of the reaction $\gamma + d \rightarrow \ \eta^{'} \ + (pn)$

Events from six to seven hits are considered, i.e. six neutral hits only or six neutral hits and one charged hit or seven neutral hits only. The $\eta^{'}-$meson is constructed from this six or seven neutral hits. Some constraints are applied on the 7th hit (charged or neutral). If, the 7th hit is in the TAPS detector, it should have a TOF $>$ 4 ns. If, the 7th hit is in the CB detector and is neutral, it should have a laboratory $\theta-$angle below 70 degrees. Above the $\eta^{'}\pi$ production threshold a $\Delta m \leq 0$ cut is applied. The reaction identification is based on the identification of the $\eta^{'}-$meson and of the single$-\eta^{'}-$meson production.

The identification of the reaction $\gamma + d \rightarrow \ \eta^{'} \ + p(n)$

Events with six neutral hits and one charged hit are considered. The $\eta-$meson is constructed from these six neutral hits. If the charged hit is in TAPS detectors, it should have a TOF $>$ 4 ns. The TOF is used to construct the four-vector of this particle. If the charged hit is in CB detectors, the missing mass analysis is used to approximate the kinetic energy of this particle. Above the $\eta^{'}\pi$ production threshold a $\Delta m \leq 0$ cut is applied. The reaction identification is based on the identification of the $\eta^{'}-$meson, the recoil proton and of the single$-\eta^{'}-$meson production.

The identification of the reaction $\gamma + d \rightarrow \ \eta^{'} \ + n(p)$

Events with seven neutral hits are considered. The $\eta-$meson is constructed from this seven neutral hits. If, the 7th hit is in the TAPS detector, it should fullfiled the neutron TOF cut. The TOF is used to construct the four-vector of this particle. If the 7th neutral hit is in CB detectors, the missing mass analysis is used to approximate the kinetic energy of this particle. If the 7th hit is in the CB detector, it should have a laboratory $\theta-$angle below 70 degrees. Above the $\eta^{'}\pi$ production threshold a $\Delta m \leq 0$ cut is applied. The reaction identification is based on the identification of the $\eta^{'}-$meson and of the single$-\eta^{'}-$meson production.

The extraction of B / (S+B)

Once, the reactions are identified, the number of events corresponding to each reaction can be counted. To do so the B / (S+B) ratio has to be extracted for each reaction studied, and for each $E_\gamma-$cell for the total cross section (e.g. Figure 6.88), and for each $(E_\gamma, cos(\theta_{cm}))-$cell for the differential cross section.

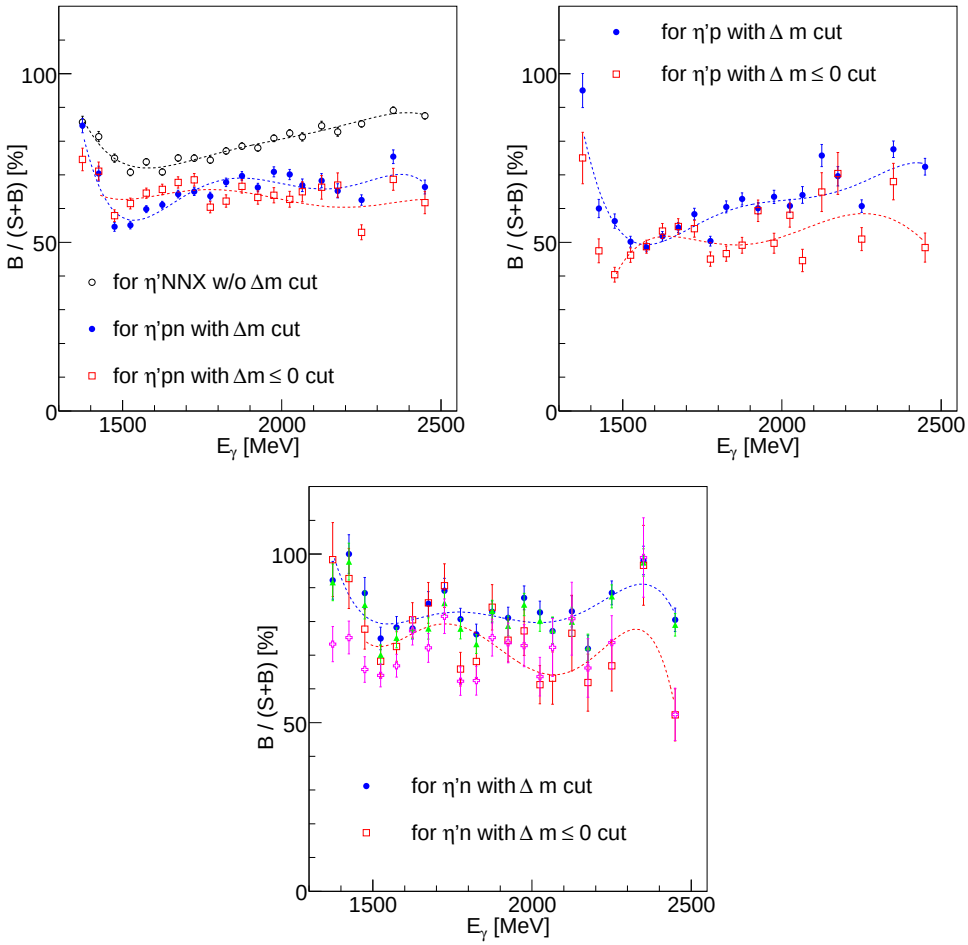

Figure 6.88: *Background evolution as a function of the incident photon beam. Top left : for the fully and the quasi-free inclusive reactions. Top Right : for the quasi-free proton reaction. Bottom : for the quasi-free neutron. (Δm cut blue squared, $\Delta m \leq 0$ cut red open squared, for the quasi-free neutron in addition Δm cut green sqaredand $\Delta m \leq 0$ cut violet open squared for neutron TOF $>$ 4 ns). The lines correspond to the fit of the background evolution.*

6.4.2 The determination of the detection efficiency

The main difference with the η photoproduction off the deuteron is that the data distibutions are similar to phase-space distributions in quasi-free kinematics taking into account the Fermi motion of the nucleons derived from the deuteron wave function (e.g. see Figure 6.90). Therefore, a phase-space MC simulation is a realistic simulation.

The following channels were simulated :

- $\eta^{'} \rightarrow \eta\pi^{o}\pi^{o}$ isotropically launched through the setup
- $\gamma + p(n) \rightarrow \eta^{'} + p(n)$
- $\gamma + n(p) \rightarrow \eta^{'} + n(p)$

The efficiency of the quasi-free reactions was determined again in two different ways, directly from the phase-space MC simulation (ϵ_{r}^{ps}) and by factorizing the efficiency i.e. $\epsilon_{r} = \epsilon_{MC-data}^{grid} \cdot \epsilon^{loss}$, with $\epsilon_{MC-data}^{grid} = \epsilon_{\eta'} \cdot \epsilon_{N}$. The $\epsilon_{MC-data}^{grid}$ was calculated in four steps (for the quasi-free proton and neutron):

1. the $\eta^{'}-$meson detection efficiency is calculated (Figure 6.89),
2. the nucleon detection efficiency is also calculated (see sections 5.6.3 and 5.6.4),
3. the $\epsilon_{\eta'}$ and the ϵ_{N} are applied to the data event-by-event and
4. the $\epsilon_{MC-data}^{grid}$ is re-calculated as function of the variables of interest.

For the fully inclusive and the quasi-free inclusive reactions, the $\epsilon_{MC-data}^{grid}$ was calculated in three steps since there is no condition on the recoil nucleons. The ϵ^{grid} - ϵ_{MC}^{grid} - was also re-calculated for the phase-space MC simulation in order to check the validity of the factorization of the efficiency.

Figure 6.89 shows the distribution of the data as function of the $T_{\eta'}$ and $\theta_{\eta'}$ (upper row for the fully inclusive left and the quasi-free inclusive right) and the simulated distribution reconstructed and the simulated detection efficiency (lower row).

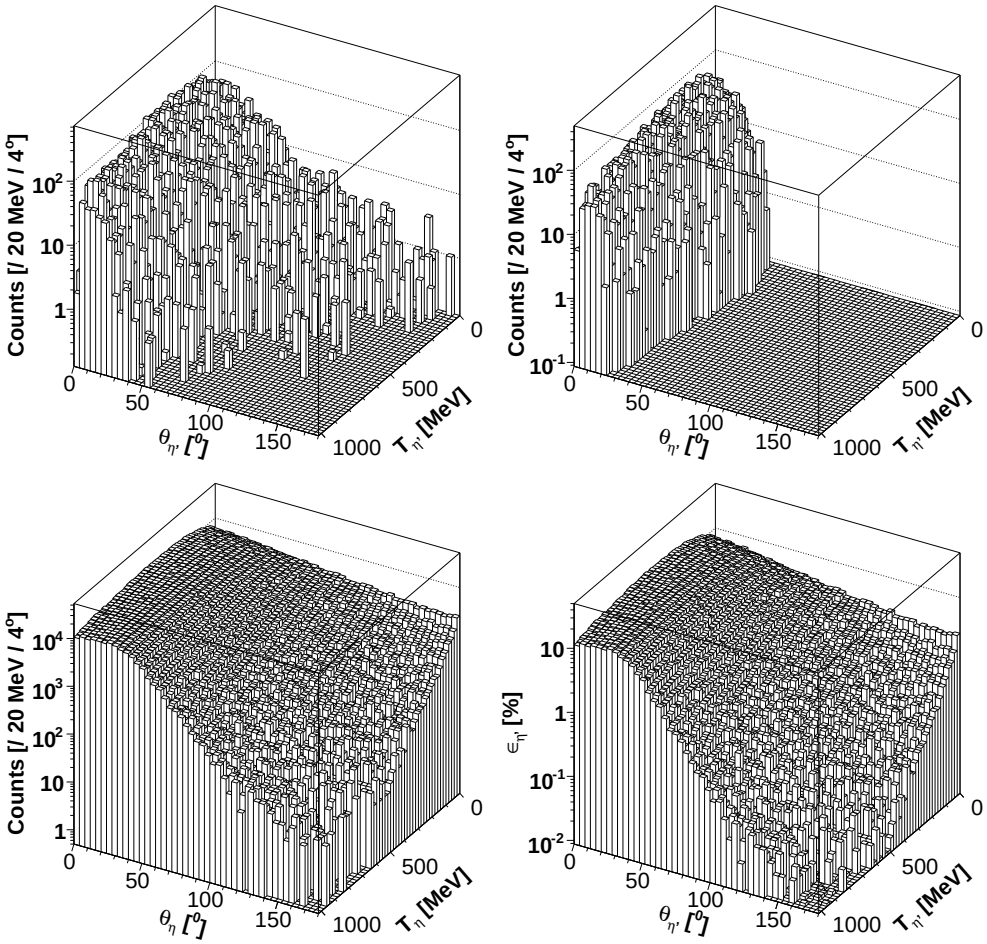

Figure 6.89: *Upper left : Distribution of the reconstructed events for the measured data that includes all channels with a η' decay. Upper right : Distribution of the reconstructed events for the measured data in the case of single $\eta'-$meson photoproduction (i.e. a missing mass cut was done $\Delta m \leq 0$). Lower left : Distribution of the reconstructed events for the Monte Carlo simulation when the start distribution is isotropic. Lower right : The $\eta'-$meson detection efficiency for six neutral hits.*

Figure 6.90 shows the re-calculated efficiencies for all reactions as function of the incident photon beam energy (left column) and the systematic difference between the re-calculated efficiency from the MC-data and the phase-space MC simulation (for the quasi-free reactions only).

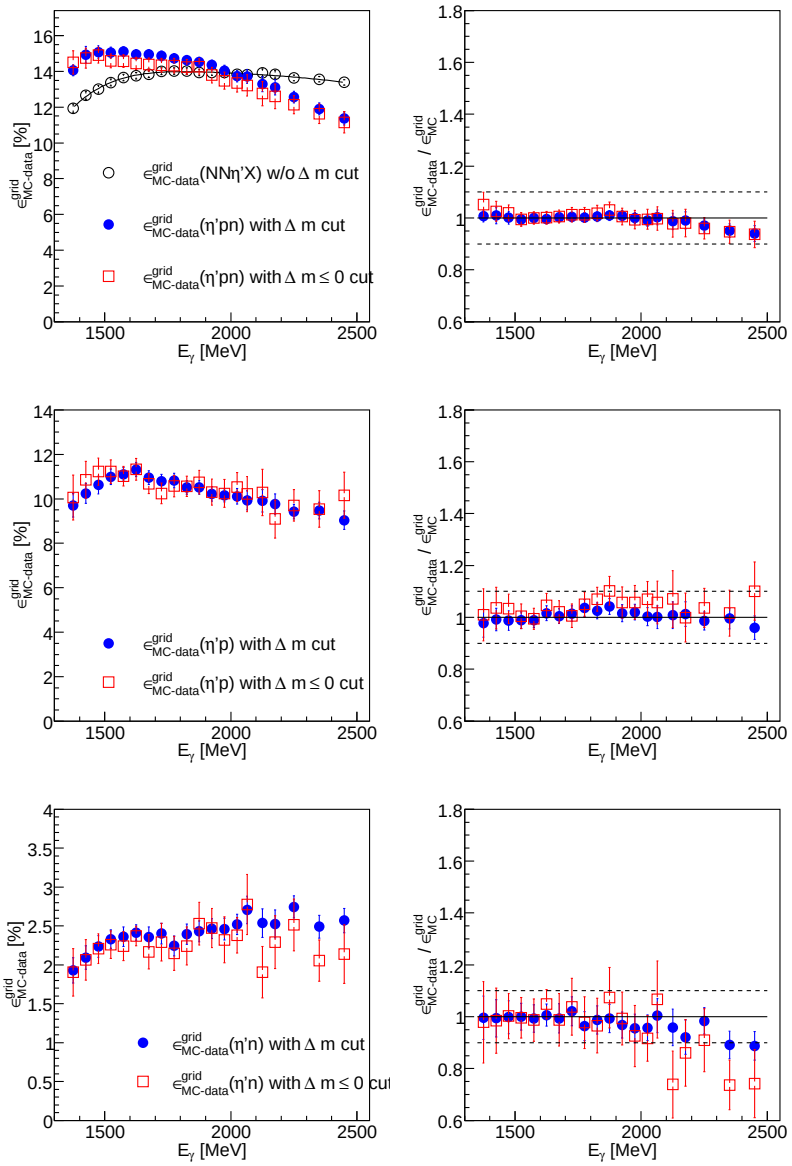

Figure 6.90: *Left column : The re-calculated efficiency as a function of the incident photon beam energy. Right column : The systematic difference between MC-data and MC simulation. From top to bottom respectively for the fully and quasi-free inclusive, for the quasi-free proton and the quasi-free neutron. The MC-data or the phase-space MC* $N^{detected}_{corrected}$ *distributions can be used to recalculate the efficiency from MC simulation.*

Figure 6.91 (left) shows the signal loss as function of the incident photon beam energy. The validity of the "grid" was also checked, Figure 6.91 (right).

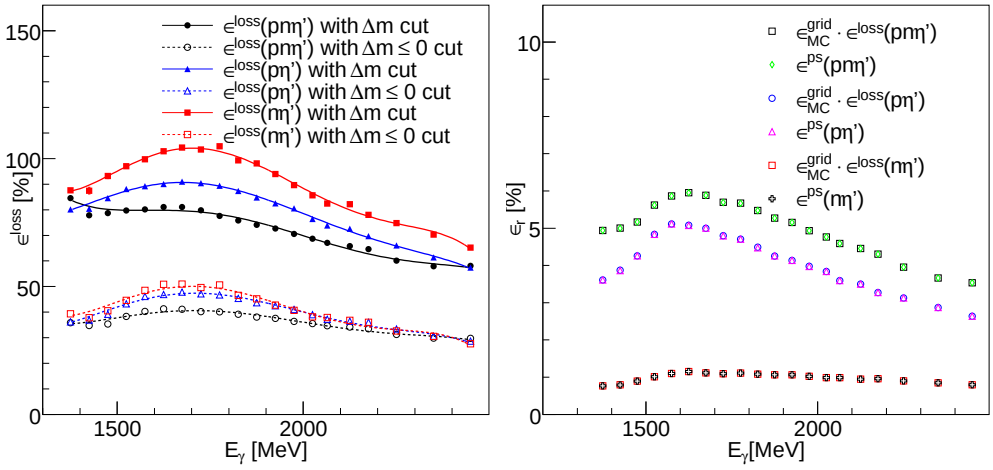

Figure 6.91: *Left : Simulated signal loss as function of the incident photon beam. Right : Simulated efficiency as function of the incident photon beam calculated directly and by using the η'−meson, the proton and the neutron detection efficiencies and the signal loss due to the $\Delta m \leq 0$ cut (and the additional cuts to get a better signal-to-background ratio).*

Figure 6.92 shows the reaction efficiencies as function of the incident photon beam energy.

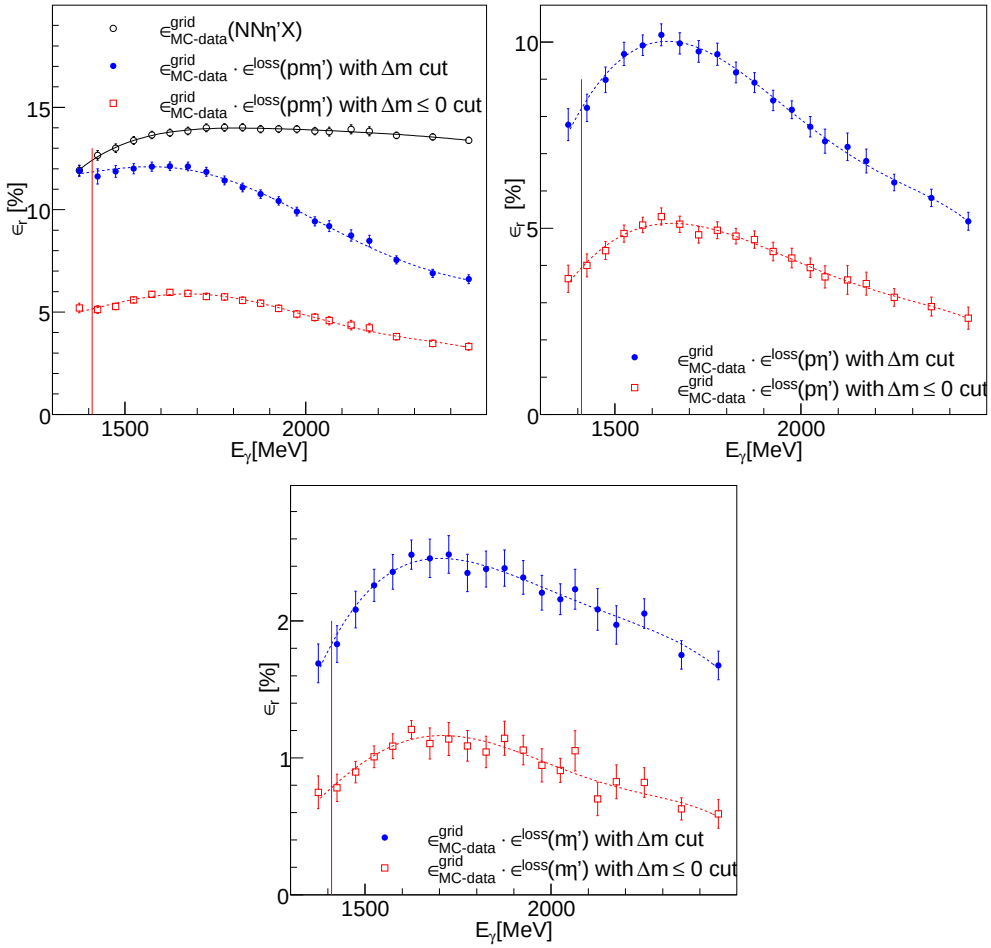

Figure 6.92: *Reaction efficiency as a function of the incident photon beam. Top left : for the fully and the quasi-free inclusive reactions. Top Right : for the quasi-free proton reaction. Bottom : for the quasi-free neutron. (only the Δm cut and the $\Delta m \leq 0$ cut are mentioned in the legends as the additional cuts are the same for both missing mass cut). The lines correspond to the fit of the efficiency evolution. The red vertical line represents the threshold of the $N\eta'\pi-$channel.*

The efficiencies as a function of $cos(\theta_{cm})$ for different incident photon beam ranges and for each reaction studied were also determined. Figure 6.93 shows the results for the quasi-free neutron reaction.

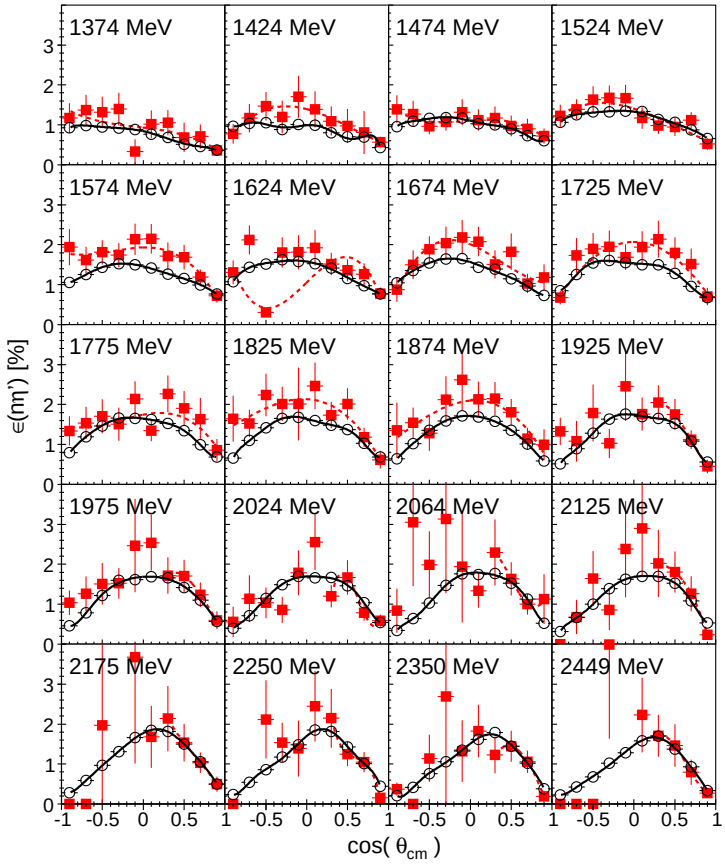

Figure 6.93: *Angular efficiency for the quasi-free neutron reaction for different incident photon beam ranges. (red squared $\epsilon^{grid}_{data} \cdot \epsilon^{loss}$ and open black circle ϵ^{ps}). The lines are the fit.*

Figure 6.94 shows the angular efficiency for the quasi-free proton reaction.

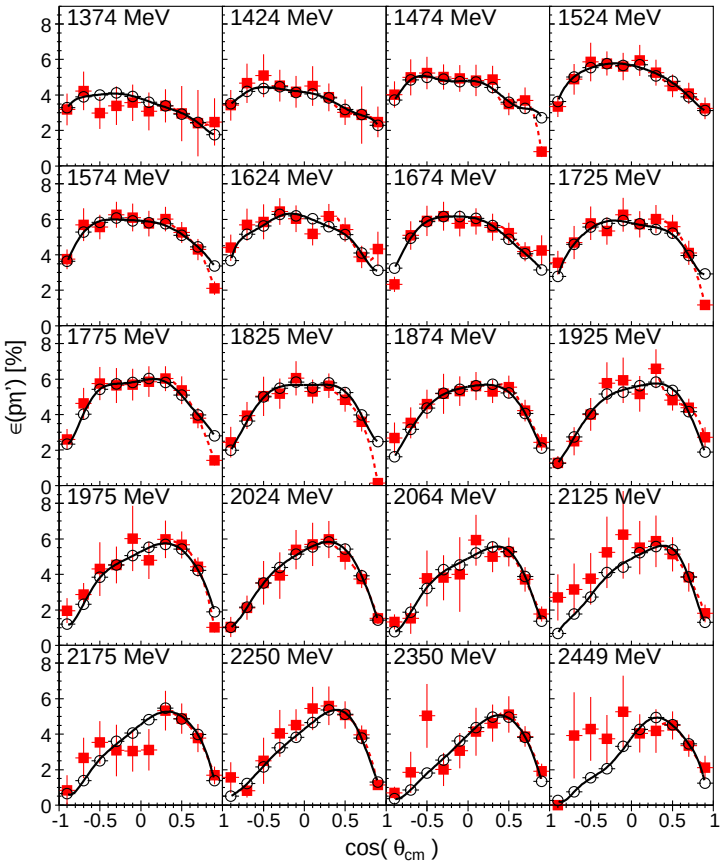

Figure 6.94: *Angular efficiency for the quasi-free proton reaction for different incident photon beam ranges. (red squared $\epsilon^{grid}_{MC-data} \cdot \epsilon^{loss}$ and open black circle ϵ^{ps}). The lines are the fit.*

Figure 6.95 shows the angular efficiency for the quasi-free inclusive reaction.

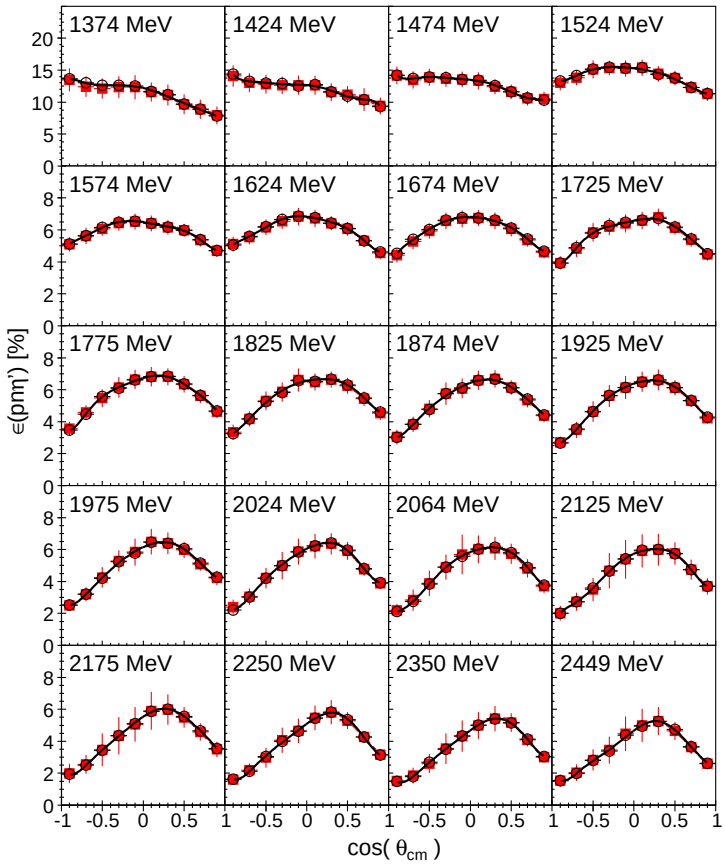

Figure 6.95: *Angular efficiency for the quasi-free inclusive reaction for different incident photon beam ranges. (red squared $\epsilon^{grid}_{MC-data} \cdot \epsilon^{loss}$ and open black circle ϵ^{ps}). The lines are the fit.*

Figure 6.96 shows the angular efficiency for the fully inclusive reaction.

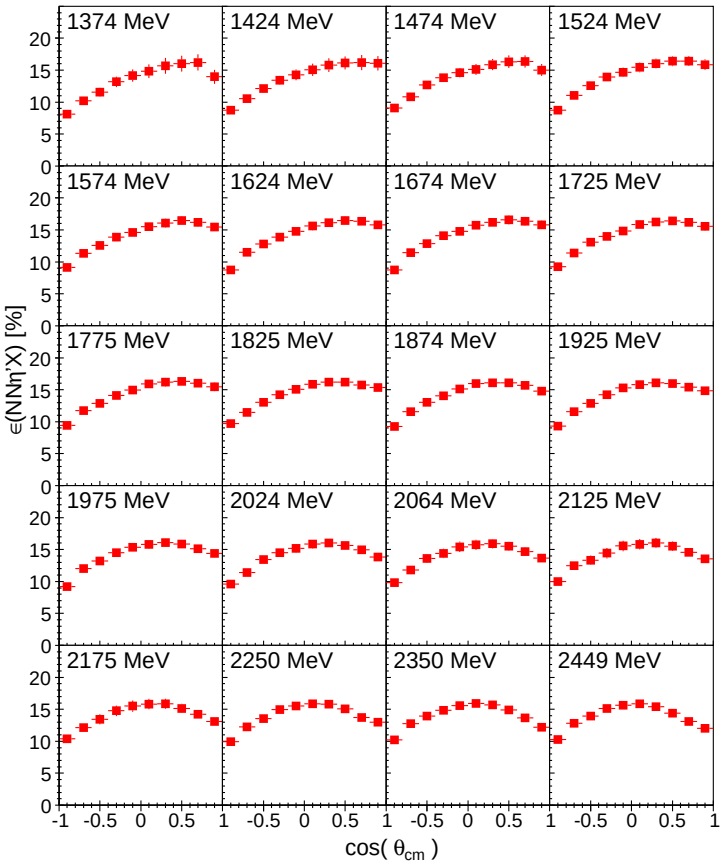

Figure 6.96: *Angular efficiency for the fully inclusive reaction for different incident photon beam ranges. (red squared ϵ_{data}^{grid}). The lines are the fit.*

All the efficiencies as function of $cos(\theta_{cm})$ and as function of E_γ for all reactions studied were parameterized by a fit. This parameterization was used for the acceptance correction.

6.4.3 The differential cross sections

The differential cross sections of the reactions : $d(\gamma,\eta^{'})X$ (Figures 6.97), $d(\gamma,\eta^{'})pn$ (Figures 6.97), $d(\gamma,\eta^{'})p(n)$ (Figures 6.100), $d(\gamma,\eta^{'})n(p)$ (Figures 6.102) have been extracted and plotted as function of $cos(\theta_{cm})$ for different incident photon beam ranges.

Figures 6.98, 6.99, 6.101 and 6.103 show the coefficients A_0, A_1, A_2 and A_3 of the angular distributions for the different reactions studied.

The fully and the quasi-free inclusive angular distributions

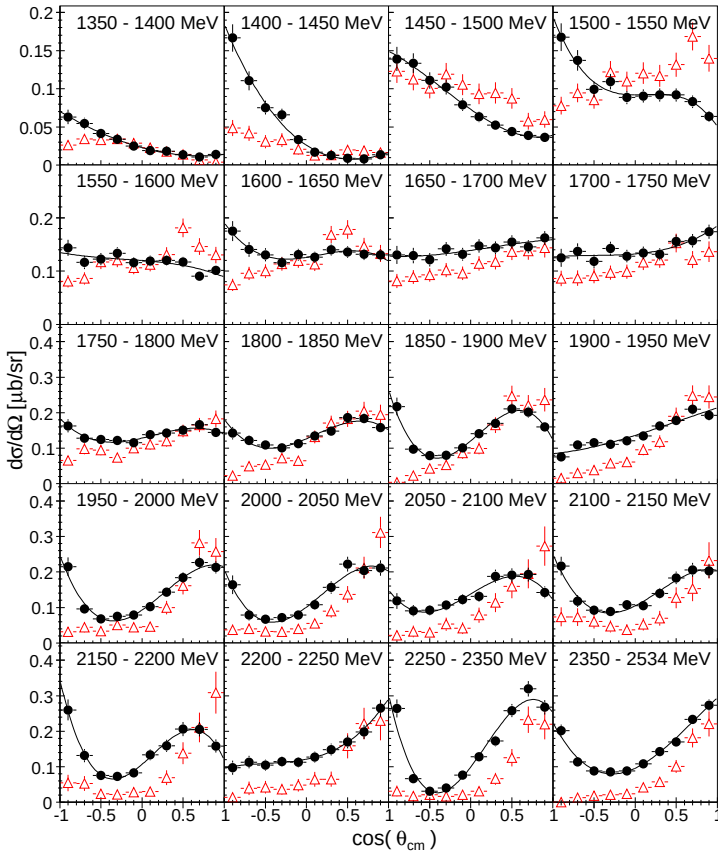

Figure 6.97: *The fully and the quasi-free inclusive angular distributions for different incident photon beam ranges (black dots the fully inclusive, red open triangle up the quasi-free inclusive). The lines are the fit.*

As expected, below the free production threshold the angular distributions show a backward - forward asymmetry (because the incident photon beam

and Fermi momenta are opposed). Above the free production threshold the angular distributions are "flat" up to E_γ= 1.7 GeV. Moreover the fully inclusive and the quasi-free inclusve distributions are similar up to E_γ=1.7 GeV. Above, E_γ=1.7 GeV, both angular distributions change again, with a $t-$channel behavior that gets more and more pronounced with increasing incident photon energy. Of course, in addition for the fully inclusive reaction, the $\eta^{'}\pi$ final state gets more and more dominant. The fact, that the $N\eta^{'}\pi-$channels start to appear at higher incident photon beam energy than expected, does not rule out their contribution, but on the contrary gives a hint on their reaction mechanisms i.e. a sequential decay. Possible sequential decay are $\gamma N \rightarrow \Delta\eta^{'}$ with a production threshold is around E_γ= 1600 MeV.

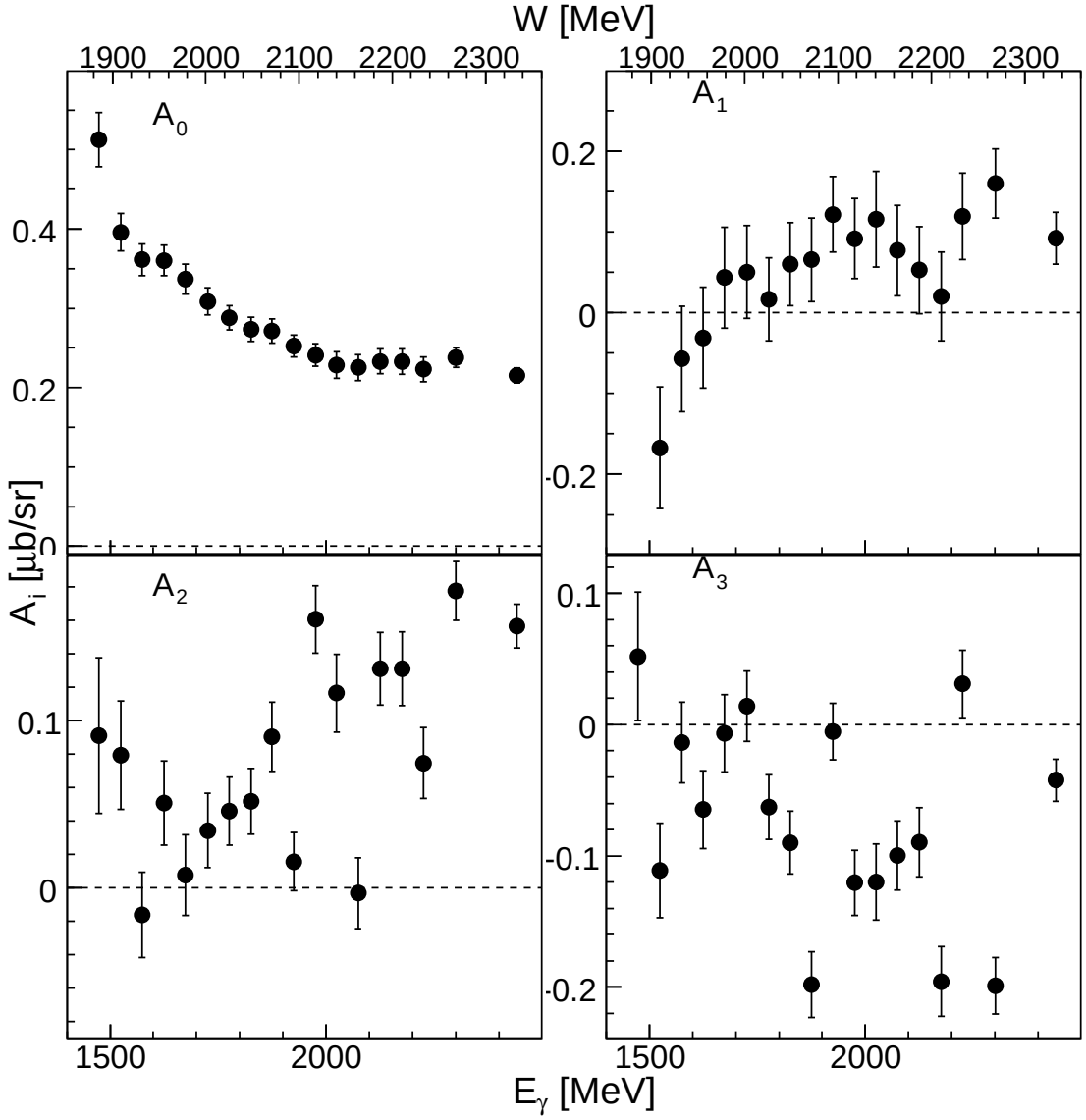

Figure 6.98: *Coefficients A_0, A_1, A_2 and A_3 of the angular distributions for the fully inclusive.*

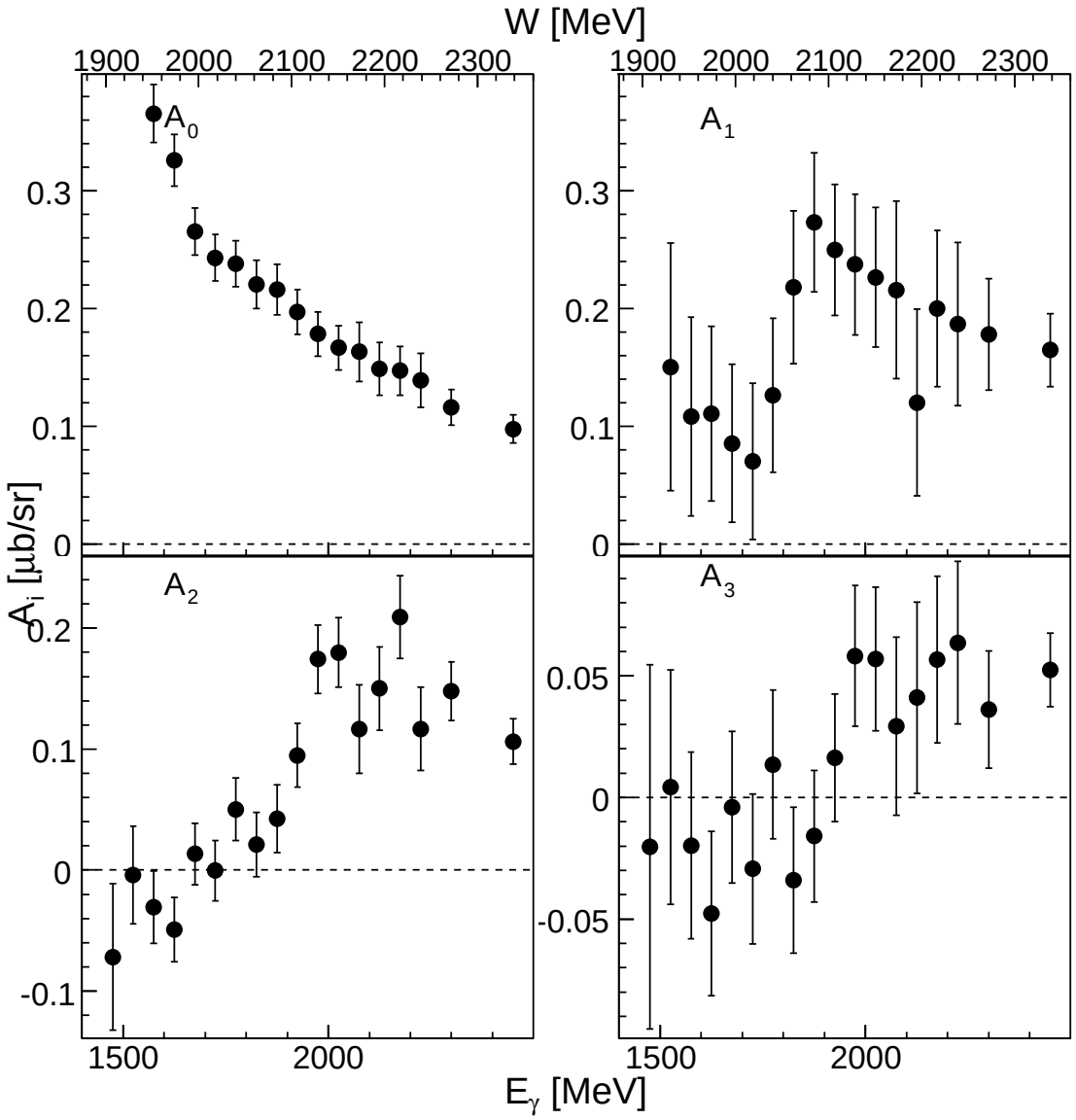

Figure 6.99: *Coefficients A_0, A_1, A_2 and A_3 of the angular distributions for the quasi-free inclusive.*

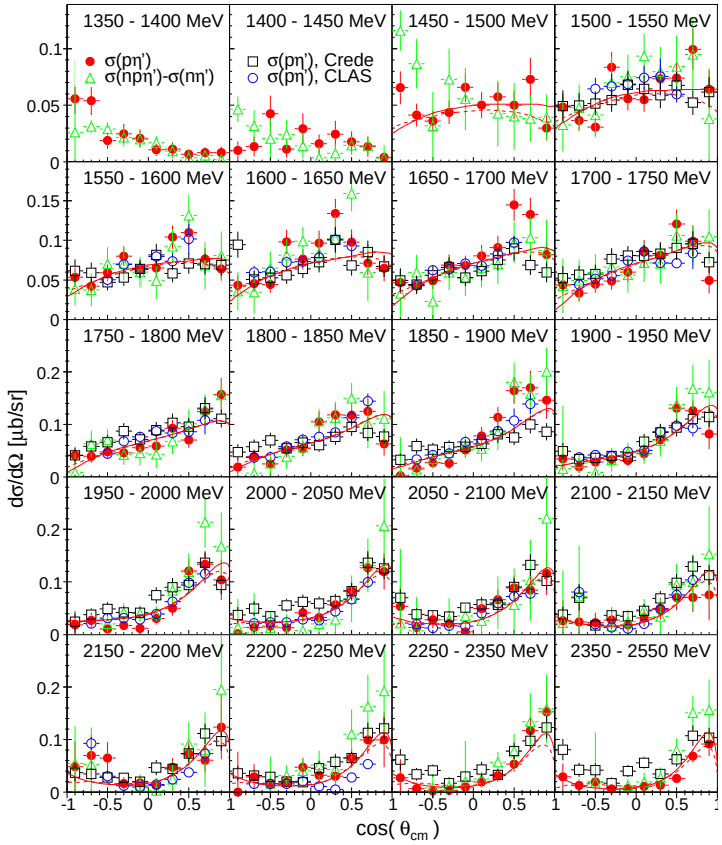

Figure 6.100: *The quasi-free proton angular distributions for different incident photon beam ranges (red dots this work, green open triangle up the difference between the quasifree inclusive and neutron angular distributions, open black square free proton [128] and open blue circle CLAS [94]). The red lines is the fit of the black dots.*

The quasi-free proton angular distributions (black dot) are compared to the free proton measurements [128] and [94] (open black square and open blue circle). The two measurements are in good agreement. Furthermore, the indirect measurement of the quasi-free proton (i.e. the difference between the quasi-free inclusive and the neutron) and the direct measurement are also in good agreement.

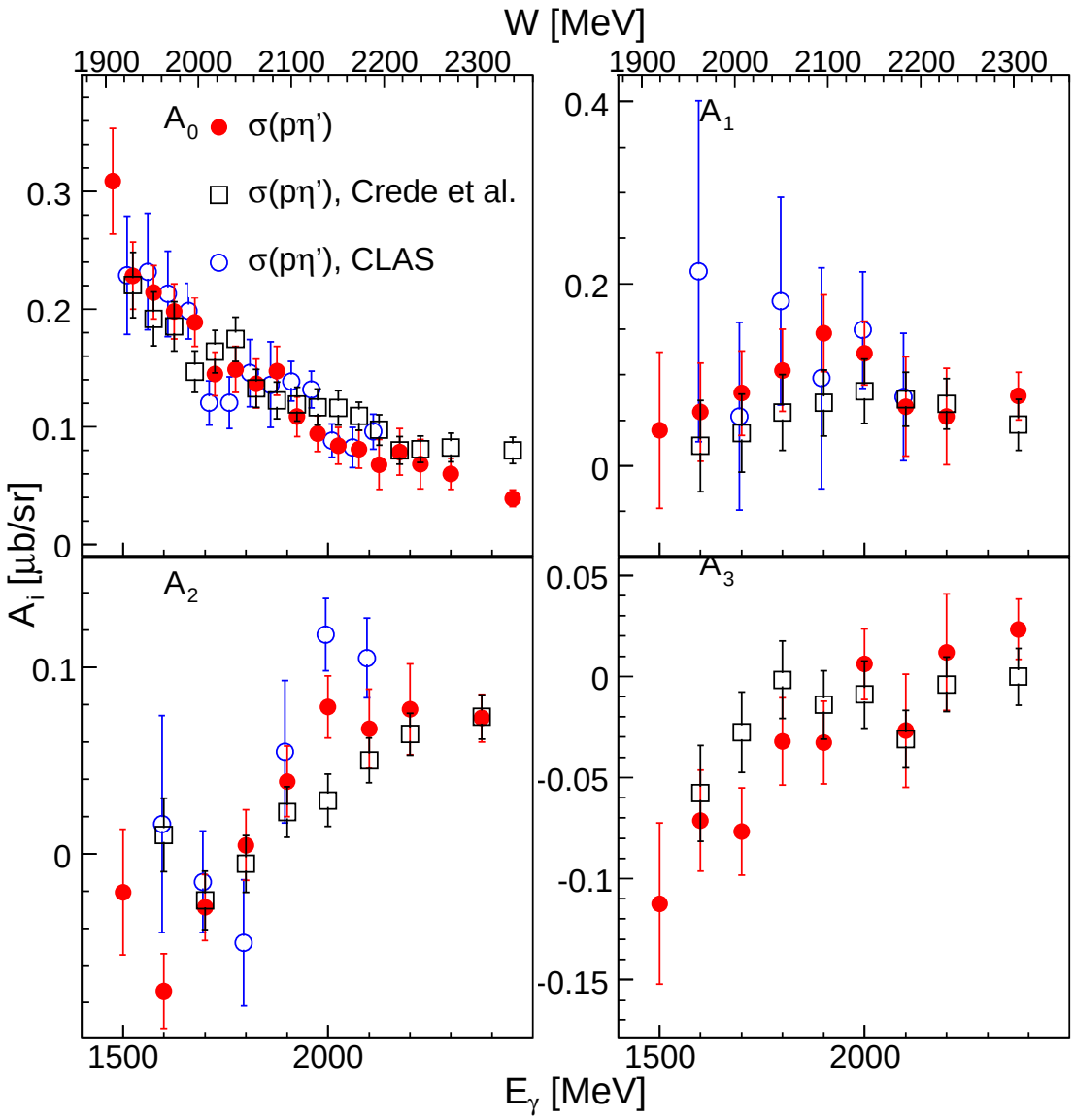

Figure 6.101: *Coefficients A_0, A_1, A_2 and A_3 of the angular distributions for the quasi-free proton (red dots this work and the free proton - open blue circle [94] and open black square [128]).*

The quasi-free neutron angular distributions

The quasi-free neutron angular distributions were measured in two different ways : directly (black dot) and from the difference of the quasi-free inclusive and the quasi-free proton (violet open circle).

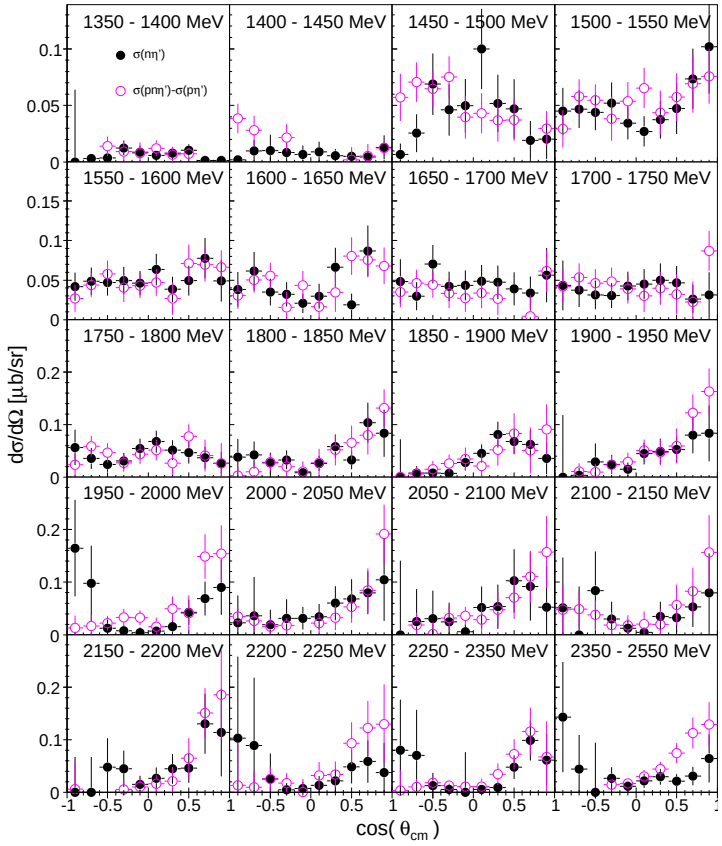

Figure 6.102: *The quasi-free neutron angular distributions for different incident photon beam ranges (black dots direct measurement, open violet circle difference between quasi-free inclusive and quasi-free proton).*

The two different measurements, which correspond to two different systematics, of the quasi-free neutron cross section are consistent with each other.

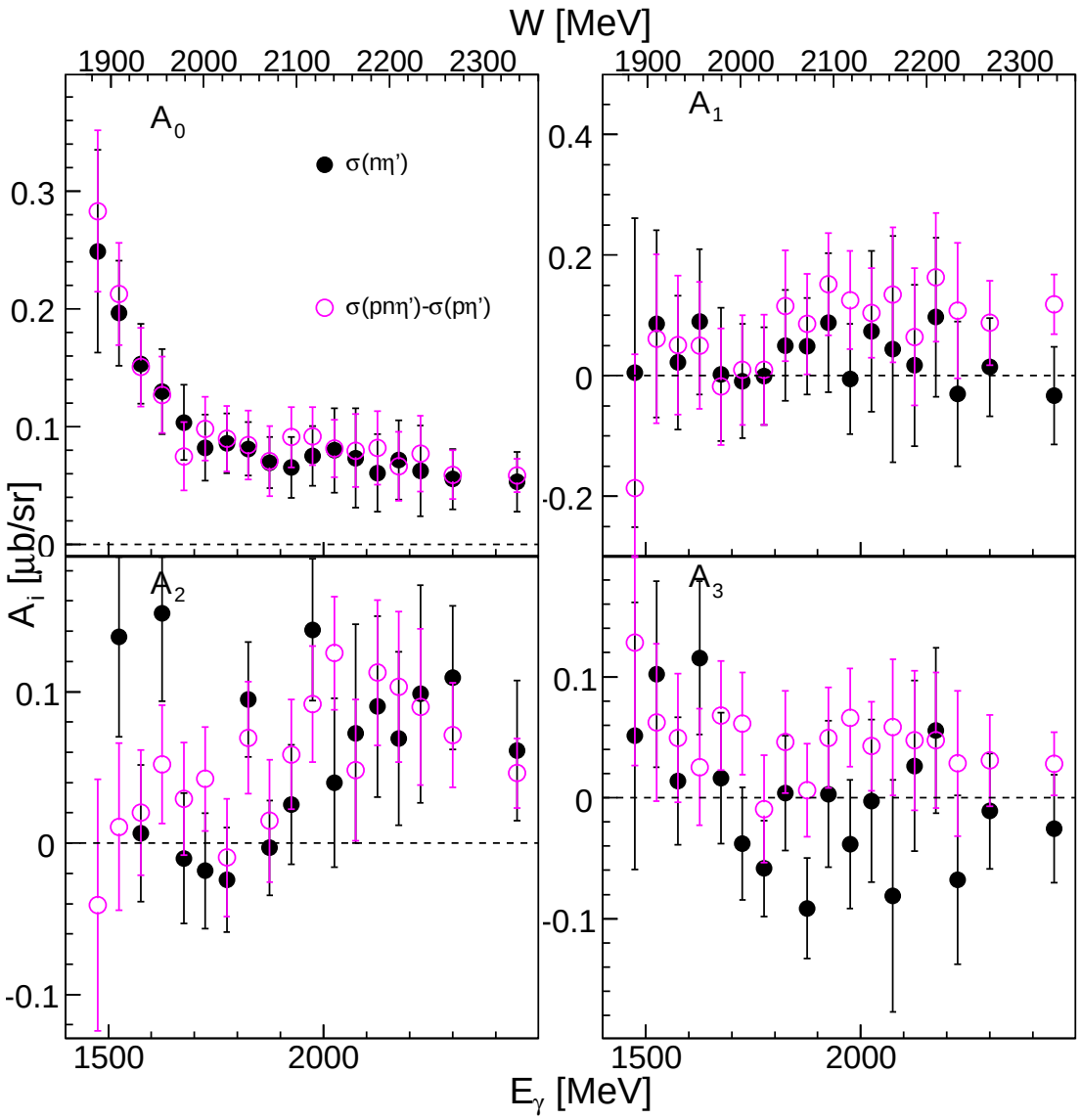

Figure 6.103: *Coefficients A_0, A_1, A_2 and A_3 of the angular distributions for the quasi-neutron proton (black dots direct measurement, open violet circle difference between quasi-free inclusive and quasi-free proton).*

6.4.4 The total cross sections

Figure 6.104 shows the total cross sections for all the reactions studied. The differences between the quasi-free proton and the quasi-free neutron total cross sections can be been observed.

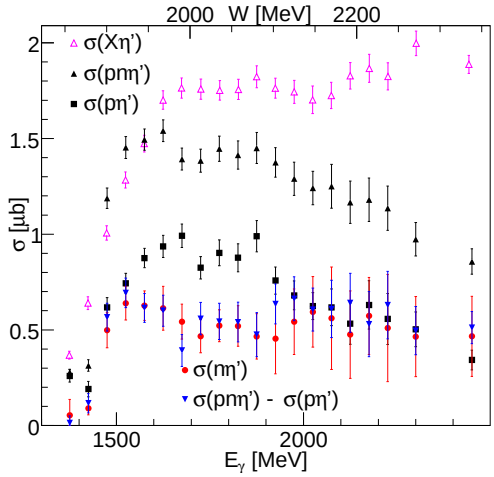

Figure 6.104: *Total cross sections as function of the incident photon beam : for all reactions studied.*

The fully inclusive and the quasi-free inclusive start to differ above E_γ= 1600 MeV, which is the production threshold of the reaction $\gamma + d \rightarrow \Delta\eta^{'}$. At E_γ = 1.8 GeV, the quasi-free neutron total cross section differs from the quasi-free proton total cross section. The Athens-Washington model [95] predicts a bump at this mass location for the proton cross section due to the $D_{13}(2080)$ and/or the $P_{11}(2100)$ resonances. Unfortunately, there are no available neutron helicity couplings for these two resonances. Above E_γ = 2 GeV, the quasi-free proton and the quasi-neutron total cross sections are similar.

6.4.5 The neutron - proton cross section ratio

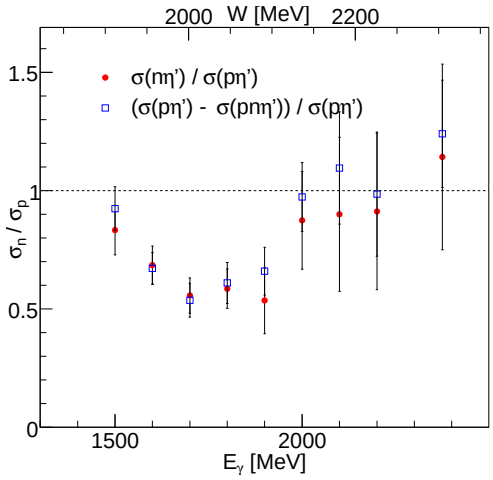

Figure 6.105: *Neutron - proton cross section ratio as function of the incident photon beam.*

At E_γ = 1.8 GeV, the neutron - proton cross section is constante and approximatly equal to 2/3.

6.4.6 The discussions

In summary, we did measure the differential cross section (Figure 6.106). The neutron and the proton angular distributions exhibit different behavior up to E_γ= 2 GeV. The proton, angular distribution shows a $P-$wave behavior whereas the neutron angular distributions are rather flat. Above E_γ= 2 GeV, the neutron and the proton angular distribution are similar.

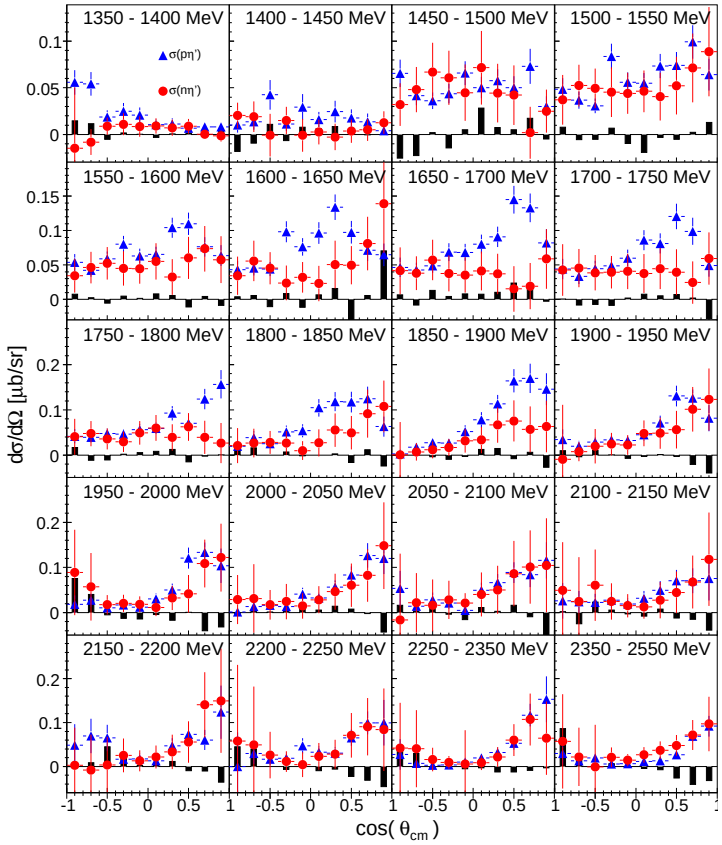

Figure 6.106: *Angular distributions for the quasi-free proton and for the quasi-free neutron. The black bar charts is the mean difference between the two neutron measurements.*

The difference between the proton and the neutron angular distributions is translated to different coefficients A_0, A_1, A_2 and A_3 as shown in Figure 6.107.

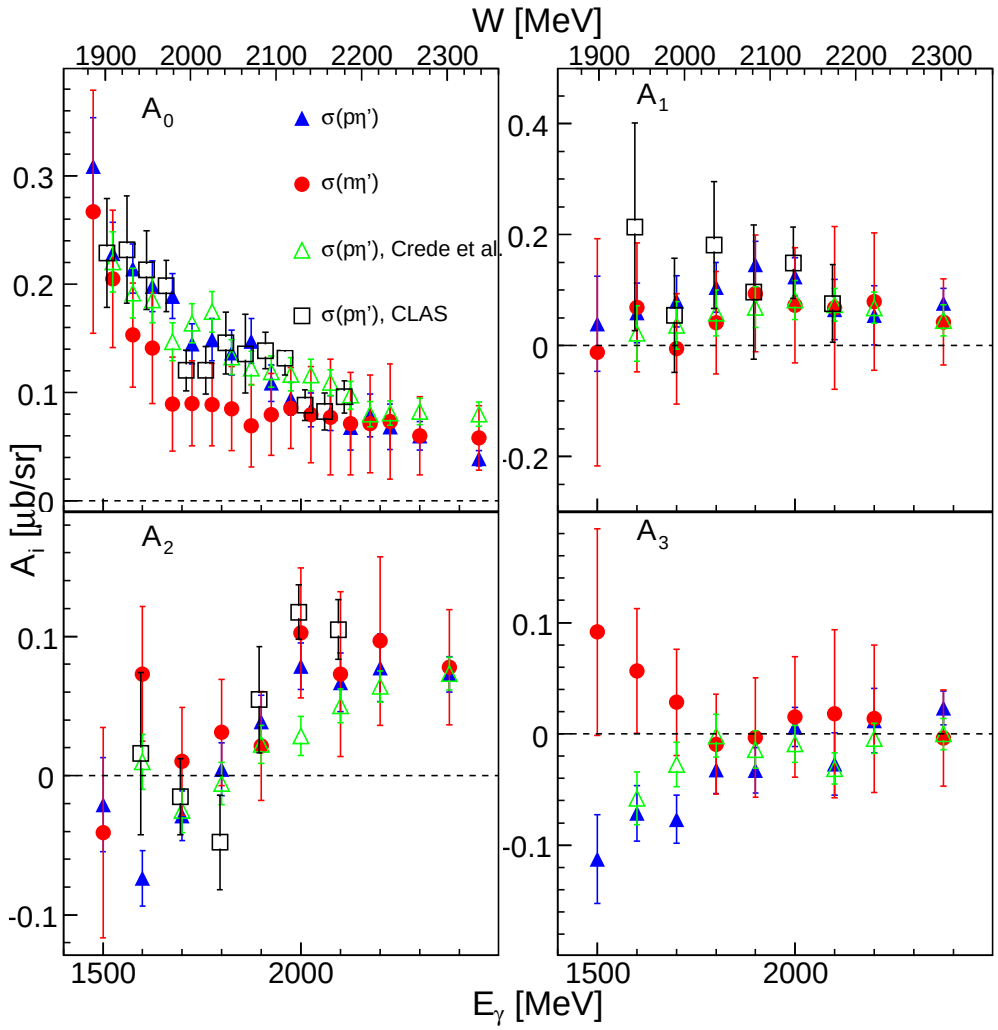

Figure 6.107: *Coefficients A_0, A_1, A_2 and A_3 of the angular distributions for the quasi-free neutron (red triangle down) and the quasi-free proton (blue triangle up). The coefficients are compared to the free proton (green open triangle [94] and black open square [128]).*

For the proton the coefficient A_o decreases with increasing incident photon beam and the coeffecient A_1 increases with the incident photon beam. For the neutron, the coefficient A_o seems to be constant, but the coefficient A_1 increases slightly with the incident photon beam. The coefficient A_2, at E_γ= 1.6 GeV, is "positive" for the neutron and is clearly negative for the proton.

Figure 6.108 shows the evolution of A_1/A_0 ratio as function of the incident photon beam energy for the quasi-free nucleon reactions. This ratio is compared to the free proton.

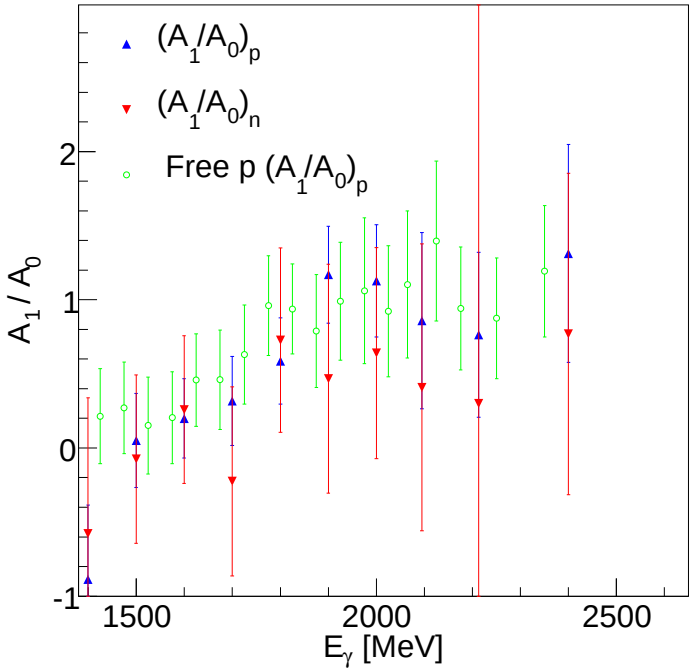

Figure 6.108: *A_1/A_0 as function of the incident photon beam.*

It seems, that the proton A_1/A_0 ratio increases with the incident photon beam, whereas the neutron A_1/A_0 ratio seems flat or increases very slowly compared to the proton A_1/A_0 ratio.

Conclusion

The photoproduction of $\pi^o\pi^o$, η and $\eta^{'}$ mesons off the deuteron has been measured. In particular, the reactions from the neutron have been measured in two different ways : directly and from the difference of the quasi-free inclusive and the quasi-free proton. Both measurements, which have different systematic errors, gave similar resutls within ± 10 %.

7.1 $\pi^o\pi^o$ photoproduction off the deuteron

The invariant mass distributions and the total cross sections have been measured from threshold to 2 GeV in incident photon beam energy for the quasi-free inclusive ($d(\gamma, 2\pi^o)N_{(P)}(N_{(S)})$), the quasi-free proton ($d(\gamma, 2\pi^o)p(n)$) and the quasi-free neutron ($d(\gamma, 2\pi^o)n(p)$) reactions. This work reproduces a previous measurement [26] which did stop at E_γ=0.82 GeV, but is different from the GRAAL collaboration [92] results which did stop at E_γ=1.4 GeV (specially in the second bump area). The invariant mass distributions and the total cross sections of the $d(\gamma, 2\pi^o)n(p)$ and $d(\gamma, 2\pi^o)p(n)$ show the same patterns i.e. the baryon cascade is clearly observed for both reactions studied:
$\gamma N \rightarrow N^*/\Delta^* \rightarrow \Delta\pi$,
$\gamma N \rightarrow N^*/\Delta^* \rightarrow D_{13}(1520)\pi$ (first bump) and
$\gamma N \rightarrow N^*/\Delta^* \rightarrow N^*/\Delta^*(\sim 1660)\pi$ (second bump);
which translated in the total cross section as two bumps. The origin of the first bump is more or less established, but not the origin of the second bump.

There are three different calculations that could be tested with the new data. The `BnGa` calculations [24] which did interpret the two bumps observed in

the $p(\gamma, 2\pi^o)p$ reaction as the constructive and the destructive interference between the $D_{13}(1520)$ and the $D_{33}(1700)$, could be applied as well to the neutron case. Indeed, both resonances couple strongly to the neutron. The $\pi\pi-$MAID calculations [31]: in this calculation, the $D_{15}(1675)$ couples mainly to the neutron and the $F_{15}(1680)$ couples mainly to the proton. Therefore, the second bump is due to the D_{15} for the neutron and to the F_{15} for the proton. The Laget model [36]: in this model the two bumps are due for the neutron and proton to the interference between the direct emission of the σ meson and the decay of the P_{11} (first bump - $P_{11}(1440)$ and second bump-$P_{11}(1710)$) resonances into the σN channel.

7.2 η photoproduction off the deuteron

The angular distributions and the total cross sections have been measured from threshold to 2.5 GeV in incident photon beam energy for the fully inclusive ($d(\gamma,\eta)X$)), the quasi-free inclusive ($d(\gamma,\eta)N_{(P)}(N_{(S)})$), the quasi-free proton ($d(\gamma,\eta)p(n)$) and the quasi-free neutron ($d(\gamma,\eta)n(p)$) reactions. This work reproduces the previous measurement [43] which did stop at E_γ= 0.82 GeV and is similar to the GRAAL collaboration results [65] which did stop at E_γ=1.4 GeV. Moreover, the quasi-free proton reaction measurement is similar to the free proton measurement folded with Fermi motion.

The $S_{11}(1535)$ energy region was first studied. This work shows that the S_{11} line shape is the same for proton and neutron and that from the total cross section the mass, the width and the helicity couplings of the $S_{11}(1535)-$resonance could be extracetd by a Breit-Wigner fit. For the first time, the angular distributions of the ($d(\gamma,\eta)n(p)$) reaction were measured. The proton and neutron angular distributions reveal as expected the interference between the $D_{13}(1520)-$ and the $S_{11}(1535)-$resonances.

Above the $S_{11}(1535)$ energy region, at E_γ= 1 GeV a bump is observed for the neutron which is not seen for the proton. This bump can be explained by a narrow $P_{11}(1675)$ resonance [64, 66] or in terms of photoexcitation and interference of the $S_{11}(1650)$ and $P_{11}(1710)$ [42] or $S_{11}(1535)$ and $S_{11}(1610)$ resonances [127]. The smearing effect of the Fermi motion make the analysis of the results difficult. Therefore, an attempt was made to remove the smearing effect of the Fermi motion. The result obtained is similar to the result of GRAAL collaboration, the bump was fitted by a Breit-Wigner function plus a second-order polynomial, the extracted width varies from 53 MeV to 180 MeV and the mass location extracted is $\sim$ 1685 MeV.

Above E_γ = 1.4 GeV, a small bump is observed at E_γ= 1.8 GeV for the neu-

tron which is not seen for the proton. This is corresponding to the mass location of the new $D_{15}(2080)$ resonance found by the BnGa analysis of the proton data [37].

7.3 $\eta^{'}$ photoproduction off the deuteron

The angular distributions and the total cross sections have been measured from threshold to 2.5 GeV in incident photon beam energy for the fully inclusive ($d(\gamma,\eta)X$)), the quasi-free inclusive ($d(\gamma,\eta)N_{(P)}(N_{(S)})$), the quasi-free proton ($d(\gamma,\eta)p(n)$) and the quasi-free neutron ($d(\gamma,\eta)n(p)$) reactions. The quasi-free proton reaction measurement is similar to the free proton measurement [128].

This is the first attempt to study the $\eta^{'}$ photoproduction off the bound nucleon. At 2100 MeV mass location, where the Athens-Washington model [95] predicts a bump on the proton, a dip is observed on the neutron.

7.4 Next experiments

More statistics are needed for the η and $\eta^{'}$ photoproduction off the deuteron. Indeed, new data will be taken at Mami (see Figure 7.2) and at ELSA (see Figure 7.3) with setups similar to this work. In addition to improved statistics, these experiments will also measure the photon asymmetry Σ and the double polarization observables G and E. The measurements of these three observables plus the angular distribution measurements should allow to determine the contribution of the different partial waves.

Figure 7.1 shows the predicted sensivity of the Σ, G and E observables for the reaction $\gamma + n \rightarrow \eta + n$ by the eta-MAID calculation, in particular the large sensivity to the $D_{15}(1675)$. However, the preliminary measurement of the photon asymmetry Σ at GRAAL [129] seems to rule out the contribution of the $D_{15}(1675)$. The modified eta-MAID calculation with a narrow P_{11} [66] predicts a weak sensivity to the photon asymmetry Σ and to the double polarization observables E and G.

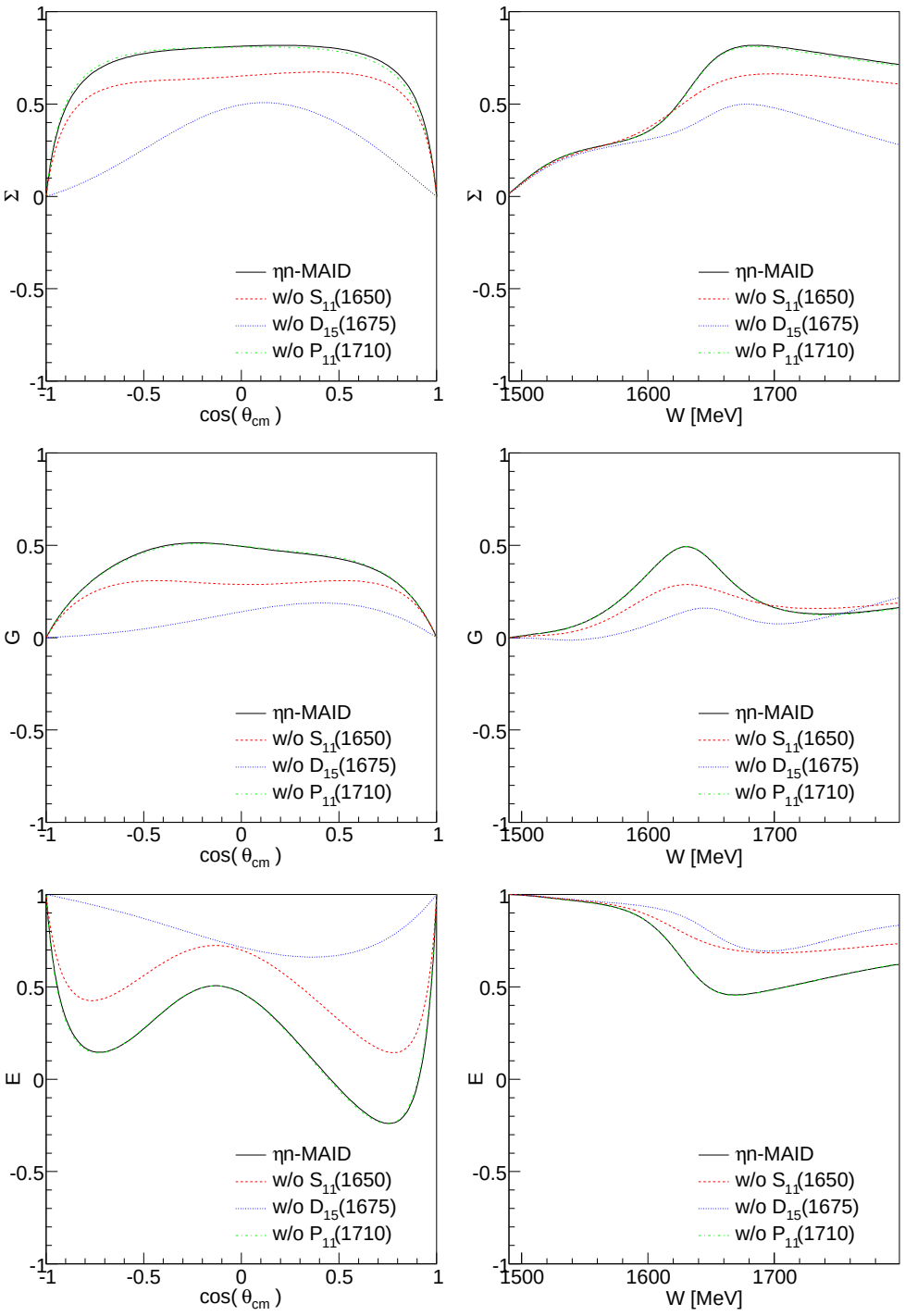

Figure 7.1: *Sentivity of the photon beam asymmetry Σ, the double polarization obervables G and E as function of $cos(\theta_{cm})$ at W = 1675 MeV (for Σ and E) and at W = 1630 MeV (for G) (left-colum) and as function of W at θ_{cm} = 90^o (right-column) to resonance contributions in the* `eta-MAID` *calculation.*

The main difference between the Bonn setup and the Mainz setup is that the Crystal Ball can be included in the trigger, whereas the Crystal Barrel cannot be included (see section 3.7).

7.4.1 Crystal Ball - TAPS at Mami

The Mami accelerator can provide an electron beam of 1.5 GeV with an intensity of 100 nA. The tagging system has a resolution of $\approx$ 2 MeV. With the intensity available at Mami and the "4π" trigger, the η photoproduction off the deuteron measurements can be re-do with a statistic at least 40 times higher than this work. Therefore, high precision angular distributions and total cross sections will be extracted. Moreover, the correction of the Fermi smearing can be done for much finer $cos(\theta_{cm})-$ (but for $cos(\theta_{cm}) \leq$ -0.2) and effective E^*_γ-bins. The measurement of the double polarization observable E, circularly polarized beam on frozen-spin target (deuteron butanol), will also be done. The near threshold photoproduction of $\eta^{'}-$mesons from the deuteron can also be studied at Mami.

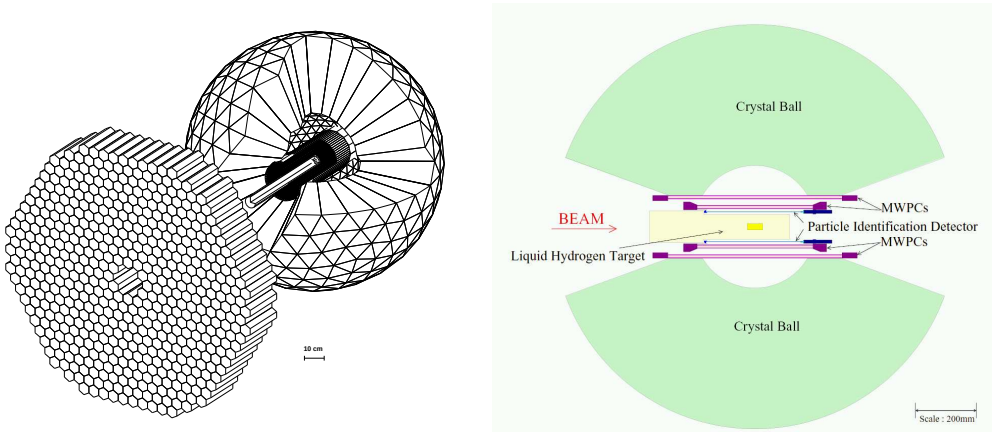

Figure 7.2: *The Crystal Ball - TAPS at Mami setup.*

7.4.2 Crystal Barrel - TAPS at ELSA

The ELSA accelerator was upgrate and can provide an electron beam of 3.5 GeV with an intensity of 5 nA. The resolution of the tagged photon beam is $\approx$ 25 MeV. The measurement of the asymmetry Σ and the double polarization observable G (linearly polarized beam on a frozen-spin target deuterated butanol) will be done for the η photoproduction off the deuteron and the η' photoproduction off the deuteron.

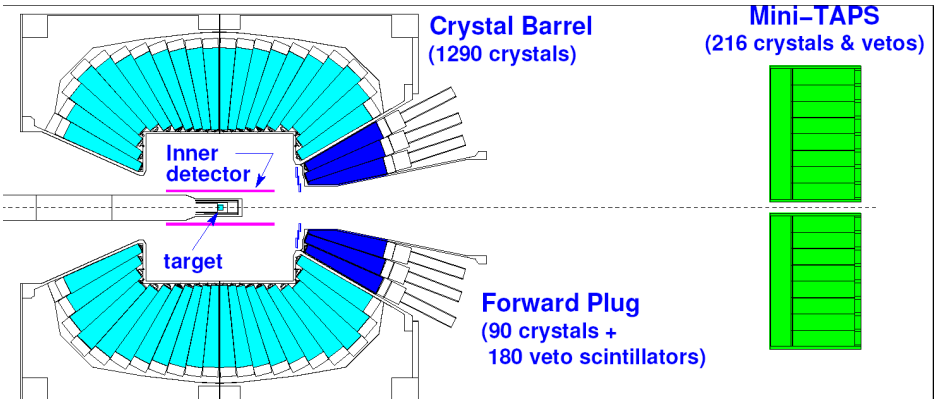

Figure 7.3: *The Crystal Barrel - TAPS at ELSA setup.*

Acknowledgements

I would like to thank Prof. Bernd Krusche for offering valuable advice and support, and to allow me to learn more about physics. I would like also to thanks the “Postdocs”, Johan Messchendorp, Susan Schadmand, Martin Kotulla and Harald von Pee, for the help they provided during the experiment and the analysis. Many thanks to my fellow TAPSseurs Ralph Castelijns, Sugat Shende, Thierry Mertens, David Trnka and Mariana Nanova for their works and the fun we have together. Many thanks also to the CB-ELSA/TAPS collaboration, Ulrike, Daniel, Frank , Andre, Michael, Joerg, ... for the collective efforts provided throughout the experiment which contributed to the fruition of this work. Many thanks also to the Basel team past and new members, Cédric, Fred, Kristoff, Thierry, Béné, Alan, Fabien, Yasser, Francis and Giuseppe for the coffe break, aperos, the food parties we did. Thanks also to all those I did forget.

Bibliography

[1] D. E. Groom et al., Eur. Phys. J C 15, 1 (2000).

[2] M. Kirchbach, Mod. Phys. Lett. A12 3177 (1997).

[3] B. Mecking et al., Nucl. Instr. and Meth. 94, 262 (2003).

[4] S. Capstick et al., Phys. Rev. D49 4570 (1994) ; ibid. D57, (1998) 4301; ibid. D58, 074011 (1998).

[5] M.Gell-Mann, Phys.Lett. 8 214 (1964).

[6] G.Zweig,CERN-8181-TH-401, CERN-8419-TH-412(1964).

[7] N. Isgur, Phys. Rev. D21 779 (1980).

[8] S. Capstick, Phys. Rev. D36 2800 (1987).

[9] W.D. Waller, Phys. Rev. 98 1407 (1955).

[10] J. Sorrels et al., Phys. Rev. 100 1457 (1955).

[11] Review of Particle Properties, Phys. Rev. D54 (1996).

[12] F.E. Close,An introduction to Quarks and Partons, Academic Press, London-New York York-san Fransisco (1979).

[13] L. Montanet et al., Phys. Rev. D50 (1994), Review of particles properties.

[14] W.-M Yao et al., J. Phys. G33, 1 (2006).

[15] N. Bianchi et al., Phys. Rev. C54 1688 (1996) .

[16] U.G. Meissner et al., Nucl. Phys. A430 670 (1984).

[17] C. Hajduk et al., Phys. Lett. B140 172 (1984).

[18] Kaiser et al., Phys. Lett. B362 23 (1995).

[19] M. Polyakov et al., Eur. Phys. J. A18, 691 (2003).

[20] A. Braghieri et al., Phys. Lett. B551, 46 (1995)

[21] Aachen-Berlin-Bonn-Hamburg-Heidelberg-München Collaboration, Phys. Rev. 175, 1669 (1968).

[22] W. Langgärtner et al., Phys. Rev. Lett. 87, 052001 (2001).

[23] M. Kotulla et al., Phys. Lett. B578 63 (2004).

[24] M. Fuchs et al. in preparation for Eur. Phys. J. A.

[25] Carbonara et al., Nuov. Cim. 36A, 219 (1976).

[26] V. Kleber et al., Eur. Phys. J. A9 1 (2000).

[27] F. Härter et al., Phys. Lett. B401, 229 (1997).

[28] A. Braghieri et al., Phys. Lett. B363, 46 (1995).

[29] M. Wolf et al., Eur. Phys. J. A9 5 (2000).

[30] Y. Assafiri et al., Phys. Rev. Lett. 90 222001 (2003).

[31] A. Fix et al., Eur.Phys.J. A25 115-135 (2005).

[32] U. Thomas et al., Preceding Letter.

[33] B. Krusche et al., Eur. Phys. J. A6 309 (1999).

[34] J.A. Gomez-Tejedor and E. Oset, Nucl. Phys. A600, 413 (1996).

[35] K. Ochi et al., nucl-th/9703058 (1997); M. Hirata et al., nucl-th/9711031 (1997).

[36] J.-M. Laget, L.Y. Murphy, shown in [30].

[37] V. Crede et al. [CB-ELSA], accepted by Phys. Re. Lett.

[38] B. Krusche et al. [TAPS], Phys. Rev. Lett. 74 3736 (1995).

[39] F. Renard et al. [GRAAL], Phys. Lett. B528 215 (2002).

[40] M. Dugger et al. [CLAS], Phys Rev. Lett. 89 222002 (2002).

[41] W.-T. Chiang et al., Nucl. Phys. A700 429 (2002).

[42] V. Shklyar et al., Phys. Lett. B650 172 (2007)

[43] J. Weiss et al., Eur. Phys. J. A16 275 (2003).

[44] V. Hejny et al., Eur. Phys. J. A6 83 (1999).

[45] Kaiser et al., Nucl. Phys. A612 297 (1997).

[46] B. Krusche et al., Phys. Lett. B358 40 (1995).

[47] P. Hoffmann-Rothe et al., Phys. Rev. Lett. 78 4697 (1997).

[48] J. Weiss et al., Eur. Phys. J. A11 371 (2001).

[49] V. Hejny et al., Eur. Phys. J. A13 493 (2002).

[50] M. Pfeiffer et al., Phys. Rev. Lett. 92 252001 (2004).

[51] D. Elsner, submitted to Eur. Phys. J. A.

[52] A.V. Anisovich et al., Eur. Phys. J A25 427 (2005).

[53] B. Saghai and Z. Li, Pittsburgh 2002, Physics of excited nucleons, 168-170, arXiv:nucl-th/0305004.

[54] G.Y. Chen et al., Nucl. Phys. A723 447 (2003).

[55] J. Ashman et al., Phys. Lett. B206, 364 (1988).

[56] G.M. Shore and G. Veneziano, Nucl. Phys. B381, 23 (1992).

[57] G.'t Hooft, Phys. Rev. Lett. 37, 8 (1976).

[58] E. Witten, Nucl. Phys. B156 269 (1979).

[59] G. Veneziano, Nucl. Phys. B159 213 (1979).

[60] G. Chirstos, Phys. Rep. 116 251 (1984).

[61] S. Okubo, Phys. Lett. 5 165 (1963); G. Zweig, CERN Report No. TH412, 1964; J. Iizuka, Prog. Theor. Phys. Suppl. 37-38 21 (1966).

[62] S. Capstick and P.R. Page, Phys. Rev. C66, 065204 (2002)

[63] T. Nakano et al., Phys. Rev. Lett. 91 012002 (2003).

[64] D. Diakonov and V. Petrov, Z. Phys. A359 305 (1997).

[65] V. Kuznetsov et al. [GRAAL], arXiv:hep-ex/0606065.

[66] A. Fix et al. Eur. Phys. J. A32 311 (2007).

[67] T.-S. H. Lee et al., J. Phys. G: Nucl. Part. Phys. 34 S83-S106 (2007)

[68] D. Drechsel et al., Nucl. Phys. A645 145 (1999)

[69] R. Walker, Phys. Rev. 182 1729 (1969)

[70] M. Guidal et al., Nucl. Phys. A627, 645 (1997).

[71] W.-T. Chiang et al., Phys.Rev. C68 045202 (2003), nucl-th/0212106

[72] T. Feuster et al., Phys. Rev. C58 457 (1998);T. Feuster et al., Phys. Rev. C59 460 (1999)

[73] G. Penner et al., Phys. Rev. C66 055211 (2002);G. Penner et al., Phys. Rev. C66 055212 (2002)

[74] V. Shklyar et al., Phys. Rev. C71 055206 (2005)

[75] V. Shklyar et al., Phys. Rev. C72 15210 (2005)

[76] S. Kamalov et al., Phys. Rev. Lett. 83 4494 (1999);S. Kamalov et al., Phys. Rev. C64 032201(R) (2001)

[77] I.S. Barker et al., Nucl. Phys. 95 347 (1975).

[78] G. Keaton et al., Phys. Rev. C53 1437 (1996)

[79] C.G. Fasano et al., Phys. Rev. C46 6 2430 (1992).

[80] W.T. Chiang et al., Phys. Rev. C55 2054 (1997).

[81] W.M. Kloet et al., Phys. Rev. C61 015501 (2000).

[82] B. Krusche et al., Prog. Part. Nucl. Phys. 51 399 (2003).

[83] G.F. Chew et al., Phys. Rev. 106 1345 (1957).

[84] G. Höhler, Pion-Nucleon Scattering, Landolt-Börnstein Vol. I/b2 (1983), ed. H. Schopper, Springer Verlag.

[85] A.J.G. Hey et R. L. Kelly, Phys. Reports 96, 71 (1983).

[86] J.M. Blatt and V. weisskopf, Theoretical Nuclear Physics (N.Y., Wiley and Sons, 1952).

[87] M.Lacombe et al., Phys. Lett. B101, 139 (1981).

[88] V.V. Anisovich et al.,Nucl. Phys. A544 747 (1992).

[89] P.Benz et al. Nucl. Phys. B65 158 (1973).

[90] Taber De Forest,Jr. Nucl. Phys. A392 232 (1983).

[91] B. Krusche et al. Phys. Lett. B358 40 (1995).

[92] J. Ajaka et al., Phys. Lett. B651 108 (2007).

[93] V. Shklyar et al., Phys. Rev. C71 055206 (2005).

[94] M. Dugger et al. [CLAS], , nucl-ex/0512019.

[95] K. Nakayama et al., nucl-th/0512074.

[96] D. Husmann et al., Phys. Bl. 44 40 (1988).

[97] E. Lohrmann et al., Hochenergiephysik, Teubner Studienbucher (1981).

[98] J.M. Jauch et al., The Theory of photons and electrons, Springer Verlag (1980).

[99] B. Rossi, High energy particles, Prentice Hall (1965).

[100] C.J.Y. Powrie et al., Phys. Rev. C64 034602 (2001).

[101] R. Burgwinkel, Aufbau un Test und Eichung des hochaufösenden Tagging-Systems TOPAS II am Bonner SAPHIR-Detektor, PhD thesis, university of Bonn (1996).

[102] B. Kopf, Untersuchung der photoinduzierten Reaktionen $\gamma p \rightarrow p\pi^o\pi^o$ und $\gamma p \rightarrow p\pi^o\eta$ an einen Flüssig-Wasserstoff-Target, PhD thesis, university of Dresden (2002).

[103] W. Schoyy, Das CsI(Tl) Kalorimeter des Crystal Barrel Detektors, PhD thesis, university of Karlsruhe (1989).

[104] E. Aker et al., The Crystal Barrel spectrometer at LEAR, Nucl. Instr. and Meth. A321 69 (1992).

[105] A. Fösel, Entwicklung und Bau eines Innendetectors für das Crystal Barrel Experiment an ELSA/Bonn, PhD thesis, university of Erlangen (2000).

[106] R. Novotny et al., The BaF_2 photon spectrometer TAPS, IEEE transactions on nuclear science 38 378 (1991).

[107] S. Jansen, Entwicklung eines neuen CPV-Systems für TAPS, Thesis, Justus Liebig university, Giessen (1998).

[108] C. Schmidt, Entwicklung eines neuen Datenakquisitionssystems für das CB-ELSA-Experiment, PhD thesis, university of Bonn (2004).

[109] R. Castelijns, Photoproduction of strange mesons and hyperons on the proton, PhD thesis, university of Groningen (2006).

[110] I. Horn, The decay of the γp system in the $p\pi^0\eta$ final state, PhD thesis, university of Bonn (2004).

[111] J. Junkersfeld, Kalibration des Crystal-Barrel-ELSA Detectors, mit Hilfe der Reaktion $\gamma p \to p\pi^0$, Thesis, university of Bonn (2000).

[112] L. Aphecetche et al.,Rosebud, http://www-subatech.in2p3.fr/ photons/taps/rosebud/1_library.shtml

[113] V. Hejny, Photoproduction van η-Mesonen an Helium 4, PhD thesis, Justus Liebig university, Giessen (1998).

[114] M. Hoefman, A study of Coherent Bremsstrahlung and Radiative Capture, PhD thesis, university of Groningen (1999).

[115] V. Credé et al., Crystal Barrel at ELSA (http://wwwnew.hiskp.uni-bonn.de).

[116] V. Wagner et al., Nucl. Instr. and Meth. A394 332 (1997).

[117] M. Kotulla, Neutronenansprechverhalten von TAPS Plastik-BaF_2-Phoswich-Detektormodule, Thesis, university of Giessen (1997).

[118] E. Schäfer, Pontecorvo-Reaktionen in Antiproton-Deuterium-Reaktionen im Fluge, PhF thesis, university of Mainz (1993).

[119] C. Zeitnitz et al., The GEANT-CALOR interface user's guide (2001) (http://www.staff.uni-mainz.de/zeitnitz/Gcalor/gcalor.html).

[120] Y.-S. Tsai, Pair production and bremsstrahlung of charged leptons, Rev. Mod. Phys. 46 815 (1974).

[121] D. Elsner et al., Bestimmung des Photonflusses (Determination of the photon flux) (2005) (http://wwwnew.hiskp.uni-bonn.de).

[122] A.R. Gabler et al., Response of TAPS to monochromatic photons with energies between 45 and 790 MeV NIM A346 168 (1994).

[123] Ripani et al., Nucl. Phys. A672 220 (2000); Ripani et al., Phys. Rev. Lett. 91 022002 (2003).

[124] U. Thomas et al., submitted to PRL.

[125] I. Horn, submitted to PRL.

[126] M.E. Röbig-Landau, Photoproduktion von $\eta-$Mesonen an komplexen Kernen, PhD thesis, university of Giessen (1995).

[127] A. Sarantsev et al., private communication.

[128] M. Kotulla et al., private commincation.

[129] P. Levi Sandri, Int. J. Mod. Phys. A22 341 (2007).

Data tables

Only the results of the $\eta-$meson photoproduction off the deuterium are final. The values of the $\pi^o\pi^o$ photoproduction off the deutrium and the $\eta^{'}$ photoproduction off the deuterium are preliminary therefore they will be completed and updated in the near futur.

$\pi^o\pi^o$ photoproduction off the deuterium

Invariant mass distribution

E_γ incident photon beam in MeV.
$m(\pi^o\pi^o)$ in MeV.
$m(N\pi^o)$ in MeV.
$d\sigma/dm$ differential cross section in nb/MeV.
sta. er. statistical error in nb/MeV.

E_γ	$m(\pi^o\pi^o)$	$d\sigma/dm(pn2\pi^o)$	sta. er.	$d\sigma/dm(p2\pi^o)$	sta. er.
448.512	260	1.446	0.05473	0.2779	0.152
448.512	300	11.57	0.1331	10.44	0.985
448.512	340	9.444	0.1022	4.709	0.2797
448.512	380	4.764	0.06566	1.886	0.1115
448.512	420	0.5759	0.02361	0.08388	0.01685
549.303	260	4.135	0.09303	4.073	0.5818
549.303	300	31.7	0.2371	40.87	1.837
549.303	340	34.83	0.2229	34	1.258
549.303	380	34.58	0.2017	22.22	0.5093
549.303	420	23.64	0.1561	11.97	0.2442
549.303	460	7.033	0.08208	3.051	0.09754
549.303	500	0.4298	0.01758	0.08027	0.01232
650.951	260	6.42	0.1287	2.018	0.2159
650.951	300	42.9	0.2752	41.16	1.117
650.951	340	52.82	0.281	43.48	0.9022
650.951	380	58.28	0.271	46.33	0.8029
650.951	420	59.29	0.2539	38.75	0.567
650.951	460	48.09	0.2144	27.86	0.3556
650.951	500	24.28	0.1485	13.29	0.1958
650.951	540	4.797	0.06491	2.217	0.07741
650.951	580	0.2884	0.01899	0.01148	0.003028
752.025	260	5.055	0.1134	1.982	0.2011
752.025	300	37.28	0.2722	25.68	0.9051
752.025	340	46.83	0.2765	26.17	0.5418
752.025	380	55.92	0.2783	31.15	0.5198
752.025	420	67.71	0.2907	38.71	0.5287
752.025	460	71.16	0.279	39.85	0.4799
752.025	500	67.79	0.2615	36.55	0.3846
752.025	540	42.51	0.1995	22.3	0.2432
752.025	580	14.71	0.1166	6.704	0.1111
752.025	620	2.07	0.04201	0.92	0.04726
752.025	660	0.03315	0.003679	0.001005	0.0003705

E_γ	$m(\pi^o\pi^o)$	$d\sigma/dm(pn2\pi^o)$	sta. er.	$d\sigma/dm(p2\pi^o)$	sta. er.
851.294	260	3.683	0.1039	1.712	0.1986
851.294	300	29.59	0.2623	14.42	0.5039
851.294	340	33.99	0.2503	14.91	0.3637
851.294	380	40.35	0.2571	19.11	0.4077
851.294	420	45.98	0.2554	23.1	0.3959
851.294	460	53.01	0.2593	26.25	0.3835
851.294	500	57.43	0.2592	28.37	0.3824
851.294	540	54.72	0.241	27.95	0.3422
851.294	580	42.01	0.2051	19.62	0.2378
851.294	620	21.57	0.1479	10.67	0.1537
851.294	660	5.291	0.07123	2.528	0.06948
851.294	700	0.4074	0.01614	0.04694	0.006251
950.755	260	3.211	0.09579	1.677	0.1563
950.755	300	25.54	0.2227	11.26	0.2978
950.755	340	32.64	0.2347	15.93	0.3497
950.755	380	36.37	0.2304	16.73	0.3102
950.755	420	39.86	0.2272	18.28	0.2921
950.755	460	42.72	0.2202	20.46	0.2971
950.755	500	45.6	0.2192	19.21	0.2567
950.755	540	46.68	0.2137	22.86	0.2933
950.755	580	44.25	0.2023	19.81	0.2534
950.755	620	37.46	0.1808	17.21	0.2071
950.755	660	25.09	0.1501	11.41	0.1432
950.755	700	10.07	0.09574	5.616	0.1014
950.755	740	1.809	0.03898	0.6764	0.03065
950.755	780	0.07981	0.006613	0.005824	0.001201
1051.66	260	2.189	0.07786	0.7482	0.08297
1051.66	300	28.85	0.2746	16.22	0.4427
1051.66	340	37.87	0.2804	25.26	0.5193
1051.66	380	40.96	0.2659	25.2	0.4495
1051.66	420	43.72	0.2561	24.42	0.3651
1051.66	460	45.56	0.2488	25.25	0.3606
1051.66	500	45.52	0.2341	24.45	0.3199
1051.66	540	46.22	0.2288	25.02	0.3253
1051.66	580	44.36	0.215	23.78	0.3082
1051.66	620	41.82	0.2048	22.73	0.2808
1051.66	660	37.96	0.1948	18.84	0.2309
1051.66	700	30.84	0.1818	18.06	0.2301
1051.66	740	16.04	0.1341	9.732	0.1423
1051.66	780	4.383	0.07006	3.04	0.1021
1051.66	820	0.3441	0.01719	0.01352	0.002854

E_γ	$m(\pi^o\pi^o)$	$d\sigma/dm(pn2\pi^o)$	sta. er.	$d\sigma/dm(p2\pi^o)$	sta. er.
1151.75	260	1.669	0.08099	0.3771	0.05091
1151.75	300	23.2	0.3073	12.15	0.3986
1151.75	340	29.44	0.2636	22.36	0.5432
1151.75	380	33.81	0.265	22.06	0.4121
1151.75	420	34.95	0.249	22.02	0.3625
1151.75	460	38.31	0.2537	26.8	0.4502
1151.75	500	36.87	0.2302	24.1	0.3633
1151.75	540	36.54	0.2184	21.71	0.3053
1151.75	580	37.59	0.2177	21.01	0.291
1151.75	620	35.16	0.2041	20.5	0.2963
1151.75	660	32.87	0.1966	19.63	0.2857
1151.75	700	28.85	0.182	15.35	0.2224
1151.75	740	25.46	0.1785	15.86	0.2472
1151.75	780	14.8	0.1389	8.817	0.1506
1151.75	820	4.405	0.07026	2.387	0.06633
1151.75	860	0.8606	0.03074	0.2223	0.01766
1151.75	900	0.02874	0.003905	0.0002246	0.0001769
1251.38	260	1.448	0.1317	0.117	0.03258
1251.38	300	13.96	0.2734	7.604	0.3542
1251.38	340	20.28	0.2738	15.58	0.5385
1251.38	380	21.99	0.2555	14.24	0.367
1251.38	420	23.73	0.2504	16.54	0.4051
1251.38	460	24.42	0.2383	14.05	0.3054
1251.38	500	26.08	0.2369	16.36	0.339
1251.38	540	26.06	0.2307	15.36	0.3049
1251.38	580	25.13	0.2138	14.09	0.2764
1251.38	620	25.46	0.2152	14.21	0.2787
1251.38	660	23.58	0.2041	16.2	0.3381
1251.38	700	22.05	0.1988	11.37	0.2528
1251.38	740	20.81	0.1971	11.11	0.2347
1251.38	780	16.9	0.1709	8.284	0.1787
1251.38	820	11.04	0.1386	7.15	0.1743
1251.38	860	4.375	0.08244	2.298	0.07405
1251.38	900	1.229	0.05404	0.3376	0.02694
1251.38	940	0.05309	0.006476	0.006907	0.002229
1251.38	980	0.00406	0.001263	0	0

E_γ	$m(\pi^o\pi^o)$	$d\sigma/dm(pn2\pi^o)$	sta. er.	$d\sigma/dm(p2\pi^o)$	sta. er.
1350.79	260	0.7187	0.06793	0.1731	0.04436
1350.79	300	10.48	0.2927	4.089	0.2528
1350.79	340	15.28	0.2782	10.69	0.4569
1350.79	380	17.47	0.2617	14.61	0.4982
1350.79	420	18.22	0.2455	14.62	0.4618
1350.79	460	19.34	0.2398	13.2	0.4783
1350.79	500	21.49	0.2427	15.24	0.3874
1350.79	540	21.18	0.229	12.93	0.3165
1350.79	580	20.44	0.2153	11.69	0.2733
1350.79	620	21.09	0.2181	12.07	0.2851
1350.79	660	20.13	0.2095	11.2	0.2693
1350.79	700	18.18	0.1994	10.75	0.2696
1350.79	740	17.63	0.2008	10.16	0.2688
1350.79	780	16.02	0.1847	8.324	0.2065
1350.79	820	13.91	0.1675	8.565	0.2149
1350.79	860	9.352	0.1325	6.094	0.162
1350.79	900	4.63	0.09804	3.008	0.1162
1350.79	940	1.17	0.0425	0.8494	0.0652
1350.79	980	0.2344	0.02199	0.02231	0.005301
1350.79	1020	0.005891	0.001194	0	0
1449.77	260	0.5669	0.07109	0.1086	0.03718
1449.77	300	8.443	0.269	3.503	0.261
1449.77	340	13.3	0.2693	9.854	0.4555
1449.77	380	15.42	0.2563	13.43	0.5473
1449.77	420	18.91	0.2808	14.1	0.4368
1449.77	460	18.52	0.2567	10.51	0.3233
1449.77	500	18.38	0.2353	11.15	0.3141
1449.77	540	18.81	0.2299	11.21	0.3064
1449.77	580	19.39	0.2273	12	0.2995
1449.77	620	18.92	0.214	11.35	0.308
1449.77	660	19.35	0.2177	11.51	0.2877
1449.77	700	17.7	0.2064	11.23	0.2971
1449.77	740	17.29	0.2052	10.13	0.2871
1449.77	780	15.48	0.1887	8.593	0.2467
1449.77	820	14.6	0.1775	7.578	0.2146
1449.77	860	12.23	0.1581	6.465	0.1809
1449.77	900	8.829	0.1332	5.424	0.1533
1449.77	940	4.549	0.09889	2.948	0.1337
1449.77	980	1.605	0.05821	1.05	0.07232
1449.77	1020	0.3432	0.02975	0.1027	0.01771
1449.77	1060	0.02034	0.004632	0.0006863	0.0005605
1449.77	1100	0.0004705	0.000359	0	0

E_γ	$m(\pi^o\pi^o)$	$d\sigma/dm(pn2\pi^o)$	sta. er.	$d\sigma/dm(p2\pi^o)$	sta. er.
1549.69	260	0.6724	0.08234	0.003697	0.00373
1549.69	300	7.59	0.2828	2.977	0.2484
1549.69	340	9.877	0.2351	6.025	0.3169
1549.69	380	12.7	0.2403	10.39	0.441
1549.69	420	13.46	0.2239	10.04	0.3949
1549.69	460	16.36	0.246	11.73	0.4858
1549.69	500	15.91	0.2202	9.767	0.3201
1549.69	540	16.2	0.2153	9.188	0.2782
1549.69	580	16.85	0.2087	8.689	0.2466
1549.69	620	18.21	0.2184	9.629	0.2729
1549.69	660	17.07	0.2034	9.763	0.2573
1549.69	700	17.41	0.2094	9.303	0.2514
1549.69	740	16.74	0.2063	9.909	0.3321
1549.69	780	15.61	0.1884	9	0.2425
1549.69	820	14.62	0.1779	7.817	0.2215
1549.69	860	12.99	0.1598	8.323	0.2236
1549.69	900	10.63	0.141	6.278	0.1717
1549.69	940	7.844	0.1238	4.28	0.1325
1549.69	980	4.637	0.09766	2.581	0.09484
1549.69	1020	1.627	0.05977	0.8736	0.05193
1549.69	1060	0.358	0.02467	0.1366	0.01703
1549.69	1100	0.02368	0.004544	0.004521	0.001374
1549.69	1140	0.0002546	0.0002616	0.0002688	0.0002688

E_γ	$m(\pi^o\pi^o)$	$d\sigma/dm(pn2\pi^o)$	sta. er.	$d\sigma/dm(p2\pi^o)$	sta. er.
1649.99	260	0.253	0.05315	0.06154	0.02583
1649.99	300	5.373	0.2154	2.677	0.2361
1649.99	340	9.515	0.3153	4.791	0.3185
1649.99	380	11.36	0.2687	9.146	0.5122
1649.99	420	12.8	0.262	8.819	0.4379
1649.99	460	12.87	0.2376	9.233	0.4247
1649.99	500	13.45	0.2295	7.704	0.3061
1649.99	540	14.09	0.2226	8.313	0.3124
1649.99	580	14.95	0.2264	7.852	0.2713
1649.99	620	15.7	0.2256	7.986	0.2811
1649.99	660	15.13	0.2162	8.632	0.2912
1649.99	700	15.74	0.2247	8.902	0.3024
1649.99	740	15.59	0.2208	10.55	0.5424
1649.99	780	16.1	0.2195	8.801	0.2762
1649.99	820	14.26	0.1977	7.414	0.2326
1649.99	860	13.19	0.1811	8.024	0.2641
1649.99	900	11.08	0.1616	6.58	0.2091
1649.99	940	9.571	0.1503	5.867	0.1963
1649.99	980	6.904	0.1304	4.479	0.1613
1649.99	1020	4.077	0.1025	2.392	0.1091
1649.99	1060	1.806	0.07599	1.561	0.1223
1649.99	1100	0.4463	0.03162	0.1203	0.01606
1649.99	1140	0.1048	0.0133	0.02213	0.005783
1649.99	1180	0.005601	0.002268	0.00123	0.0009062

E_γ	$m(\pi^o\pi^o)$	$d\sigma/dm(pn2\pi^o)$	sta. er.	$d\sigma/dm(p2\pi^o)$	sta. er.
1749.67	260	0.531	0.0894	0.007137	0.007333
1749.67	300	5.701	0.295	1.453	0.1801
1749.67	340	6.543	0.2263	4.234	0.3342
1749.67	380	8.256	0.2299	5.174	0.3549
1749.67	420	10.25	0.2472	7.895	0.4425
1749.67	460	10.7	0.2358	7.277	0.4566
1749.67	500	11.66	0.2318	7.419	0.3911
1749.67	540	12.3	0.2317	6.921	0.3318
1749.67	580	13.17	0.2348	8.535	0.3619
1749.67	620	13.13	0.2199	6.923	0.282
1749.67	660	13.63	0.2251	7.712	0.3151
1749.67	700	14.34	0.2331	7.89	0.2985
1749.67	740	13.88	0.2281	9.422	0.5042
1749.67	780	14.23	0.219	7.541	0.2659
1749.67	820	14.1	0.2103	8.522	0.2863
1749.67	860	13.32	0.198	6.817	0.2363
1749.67	900	12.14	0.1846	7.403	0.255
1749.67	940	10.47	0.1657	6.373	0.2168
1749.67	980	8.82	0.1527	5.068	0.1856
1749.67	1020	5.735	0.1233	3.869	0.1599
1749.67	1060	3.492	0.0969	2.056	0.1013
1749.67	1100	1.592	0.06818	1.076	0.0812
1749.67	1140	0.5258	0.03434	0.2996	0.03734
1749.67	1180	0.1269	0.01858	0.01232	0.004338
1749.67	1220	0.004272	0.001659	0	0
1749.67	1260	0.0007336	0.0005257	0	0

E_γ	$m(\pi^o\pi^o)$	$d\sigma/dm(pn2\pi^o)$	sta. er.	$d\sigma/dm(p2\pi^o)$	sta. er.
1849.84	260	0.3436	0.07084	0.04873	0.02453
1849.84	300	4.717	0.3167	1.277	0.1635
1849.84	340	6.293	0.2696	2.68	0.2466
1849.84	380	7.191	0.2309	4.418	0.3401
1849.84	420	8.287	0.2274	6.164	0.3893
1849.84	460	9.505	0.2271	8.352	0.4909
1849.84	500	11.38	0.2383	6.925	0.3501
1849.84	540	10.87	0.2243	6.577	0.3167
1849.84	580	11.94	0.2305	7.486	0.4364
1849.84	620	12.35	0.2214	7.201	0.3508
1849.84	660	13.21	0.2307	9.329	0.5278
1849.84	700	13.57	0.2333	7.48	0.2943
1849.84	740	13.19	0.231	7.57	0.3053
1849.84	780	13.4	0.2263	6.801	0.2734
1849.84	820	13.68	0.2182	7.484	0.2779
1849.84	860	13.2	0.2029	7.754	0.2759
1849.84	900	12.36	0.1927	7.025	0.2513
1849.84	940	11.57	0.1818	6.991	0.2455
1849.84	980	9.943	0.167	5.758	0.2027
1849.84	1020	7.871	0.1467	5.098	0.2113
1849.84	1060	5.494	0.1221	3.887	0.1686
1849.84	1100	3.493	0.09924	1.714	0.0919
1849.84	1140	1.971	0.07592	1.32	0.09285
1849.84	1180	0.6113	0.04406	0.2469	0.03024
1849.84	1220	0.1902	0.02422	0.04769	0.01125
1849.84	1260	0.03004	0.006956	0.0001921	0.0001956

E_γ	$m(\pi^o\pi^o)$	$d\sigma/dm(pn2\pi^o)$	sta. er.	$d\sigma/dm(p2\pi^o)$	sta. er.
1950.15	260	0.3377	0.08028	0	0
1950.15	300	3.431	0.2157	0.5457	0.09535
1950.15	340	5.475	0.2365	2.24	0.2304
1950.15	380	7.785	0.2684	4.641	0.3618
1950.15	420	7.422	0.2152	4.287	0.3153
1950.15	460	8.872	0.2241	6.16	0.3884
1950.15	500	10.05	0.2261	6.125	0.3188
1950.15	540	10.92	0.2326	8.166	0.5179
1950.15	580	11.96	0.2322	6.435	0.3591
1950.15	620	12.33	0.2287	6.986	0.3151
1950.15	660	12.54	0.2323	8.262	0.4719
1950.15	700	13.22	0.2388	6.638	0.2801
1950.15	740	13.2	0.2362	7.811	0.4009
1950.15	780	14.03	0.2342	7.104	0.338
1950.15	820	13.86	0.2223	7.777	0.293
1950.15	860	13.65	0.2121	8.176	0.276
1950.15	900	12.72	0.1992	6.583	0.2342
1950.15	940	12.25	0.1875	7.569	0.2474
1950.15	980	11.04	0.1786	6.654	0.2264
1950.15	1020	8.993	0.1601	6.058	0.2144
1950.15	1060	6.479	0.1313	4.176	0.1834
1950.15	1100	5.221	0.1199	3.059	0.1344
1950.15	1140	3.976	0.1097	2.345	0.1182
1950.15	1180	2.158	0.08041	1.409	0.09522
1950.15	1220	0.7785	0.04321	0.5484	0.05742
1950.15	1260	0.3004	0.02914	0.033	0.008601
1950.15	1300	0.01824	0.005201	0	0
1950.15	1340	0.0003551	0.0003793	0	0

E_γ	$m(\pi^o\pi^o)$	$d\sigma/dm(n2\pi^o)$	sta. er.
448.512	260	1.154	0.4394
448.512	300	21.37	1.846
448.512	340	7.881	0.5792
448.512	380	3.66	0.3354
448.512	420	0.1121	0.0432
549.303	260	1.795	0.4484
549.303	300	32.85	2.111
549.303	340	28.52	1.314
549.303	380	24.93	1.015
549.303	420	16.82	0.7083
549.303	460	4.419	0.366
549.303	500	0.008977	0.004046
650.951	260	1.942	0.3362
650.951	300	30.19	1.483
650.951	340	55.22	2.076
650.951	380	71.37	2.38
650.951	420	46.63	1.245
650.951	460	34.26	0.9346
650.951	500	15.25	0.5388
650.951	540	1.334	0.1295
650.951	580	0	0
752.025	260	0.7122	0.1524
752.025	300	21.43	1.201
752.025	340	44.5	1.8
752.025	380	56.19	1.961
752.025	420	62.77	1.883
752.025	460	54.15	1.289
752.025	500	51.85	1.166
752.025	540	43.57	1.278
752.025	580	9.135	0.4095
752.025	620	0.1552	0.02753
752.025	660	0.0004078	0.0002763

E_γ	$m(\pi^o\pi^o)$	$d\sigma/dm(n2\pi^o)$	sta. er.
851.294	260	0.5283	0.1417
851.294	300	15.37	1.03
851.294	340	20.13	1.086
851.294	380	33.64	1.384
851.294	420	30.03	0.924
851.294	460	42.88	1.237
851.294	500	40.95	0.9426
851.294	540	36.61	0.8337
851.294	580	36.02	1.014
851.294	620	15.36	0.5608
851.294	660	1.882	0.1581
851.294	700	0.007092	0.002755
950.755	260	0.01413	0.01809
950.755	300	10.01	0.6389
950.755	340	22.39	1.021
950.755	380	31.2	1.193
950.755	420	28.83	0.9978
950.755	460	29.84	0.8005
950.755	500	27.38	0.6753
950.755	540	31.12	0.7268
950.755	580	30.93	0.7541
950.755	620	24.87	0.6534
950.755	660	16.63	0.539
950.755	700	4.786	0.2415
950.755	740	0.1886	0.02959
950.755	780	0.0005148	0.0004055
1051.66	260	0.1176	0.04016
1051.66	300	5.001	0.3734
1051.66	340	12.82	0.6256
1051.66	380	20.34	0.7066
1051.66	420	25.61	0.8237
1051.66	460	26.44	0.8144
1051.66	500	29.84	0.8844
1051.66	540	35.64	1.039
1051.66	580	34.98	1.066
1051.66	620	24.49	0.7457
1051.66	660	19.07	0.6256
1051.66	700	17.4	0.6833
1051.66	740	6.15	0.3415
1051.66	780	0.2359	0.03753
1051.66	820	0.001632	0.0009837

E_γ	$m(\pi^o\pi^o)$	$d\sigma/dm(n2\pi^o)$	sta. er.
1151.75	260	0	0
1151.75	300	2.959	0.25
1151.75	340	10.55	0.5887
1151.75	380	18.74	0.7999
1151.75	420	16.08	0.6992
1151.75	460	24.34	0.8943
1151.75	500	26.5	0.9638
1151.75	540	19.73	0.7186
1151.75	580	21.92	0.6824
1151.75	620	24.49	0.8408
1151.75	660	16.28	0.5776
1151.75	700	14.36	0.6211
1151.75	740	11.81	0.5995
1151.75	780	3.652	0.2319
1151.75	820	0.6787	0.08254
1151.75	860	0.01808	0.005948
1151.75	900	0	0
1251.38	260	0.07443	0.03046
1251.38	300	1.299	0.1819
1251.38	340	7.236	0.5219
1251.38	380	11.03	0.673
1251.38	420	15.94	0.8604
1251.38	460	14.18	0.7606
1251.38	500	15.45	0.8063
1251.38	540	16.27	0.8187
1251.38	580	16.64	0.7643
1251.38	620	13.53	0.6865
1251.38	660	16.17	0.8042
1251.38	700	13.2	0.7247
1251.38	740	10.33	0.5857
1251.38	780	8.269	0.5519
1251.38	820	3.327	0.3169
1251.38	860	1.063	0.122
1251.38	900	0.03114	0.01106
1251.38	940	0.0001759	0.0001898
1251.38	980	0.0001975	0.0002011

E_γ	$m(\pi^o\pi^o)$	$d\sigma/dm(n2\pi^o)$	sta. er.
1350.79	260	0.0354	0.0196
1350.79	300	0.8721	0.1559
1350.79	340	2.541	0.3031
1350.79	380	5.687	0.4854
1350.79	420	7.55	0.5308
1350.79	460	10.31	0.6743
1350.79	500	11.9	0.7584
1350.79	540	12.69	0.7941
1350.79	580	13.14	0.7969
1350.79	620	13.49	0.6981
1350.79	660	11.44	0.7018
1350.79	700	8.48	0.5877
1350.79	740	10.42	0.7081
1350.79	780	9.505	0.6962
1350.79	820	6.158	0.5351
1350.79	860	3.252	0.3038
1350.79	900	1.45	0.1824
1350.79	940	0.08605	0.02411
1350.79	980	0.01315	0.005468
1350.79	1020	0	0
1449.77	260	0.008491	0.008491
1449.77	300	0.573	0.1219
1449.77	340	3.014	0.315
1449.77	380	5.018	0.485
1449.77	420	5.259	0.4827
1449.77	460	9.684	0.6956
1449.77	500	9.027	0.6139
1449.77	540	12.27	0.8064
1449.77	580	12.08	0.7998
1449.77	620	10.53	0.6512
1449.77	660	11.23	0.7037
1449.77	700	9.566	0.6123
1449.77	740	10.72	0.7023
1449.77	780	7.569	0.5374
1449.77	820	8.405	0.6265
1449.77	860	6.046	0.5044
1449.77	900	5.089	0.4026
1449.77	940	1.308	0.1622
1449.77	980	0.2346	0.04892
1449.77	1020	0.003229	0.002303
1449.77	1060	0	0
1449.77	1100	0	0

E_γ	$m(\pi^o\pi^o)$	$d\sigma/dm(n2\pi^o)$	sta. er.
1549.69	260	0	0
1549.69	300	0.3457	0.08394
1549.69	340	1.417	0.2113
1549.69	380	2.516	0.3053
1549.69	420	4.694	0.4452
1549.69	460	6.206	0.5096
1549.69	500	5.693	0.4689
1549.69	540	6.314	0.5108
1549.69	580	7.475	0.5074
1549.69	620	7.076	0.4522
1549.69	660	10.25	0.7074
1549.69	700	9.289	0.6281
1549.69	740	11.19	0.7055
1549.69	780	7.346	0.551
1549.69	820	6.414	0.4727
1549.69	860	7.493	0.5911
1549.69	900	5.364	0.4062
1549.69	940	4.153	0.3626
1549.69	980	2.059	0.2397
1549.69	1020	0.1387	0.0365
1549.69	1060	0.008081	0.004238
1549.69	1100	0	0
1549.69	1140	0	0

E_γ	$m(\pi^o\pi^o)$	$d\sigma/dm(n2\pi^o)$	sta. er.
1649.99	260	0	0
1649.99	300	0.1567	0.07176
1649.99	340	1.236	0.2005
1649.99	380	2.356	0.3071
1649.99	420	3.268	0.4091
1649.99	460	4.924	0.4857
1649.99	500	7.448	0.6471
1649.99	540	6.598	0.5523
1649.99	580	7.143	0.575
1649.99	620	8.354	0.6701
1649.99	660	7.43	0.5377
1649.99	700	10.95	0.8135
1649.99	740	5.797	0.4663
1649.99	780	7.575	0.5948
1649.99	820	8.114	0.62
1649.99	860	7.24	0.5676
1649.99	900	5.305	0.445
1649.99	940	5.475	0.5123
1649.99	980	3.027	0.3358
1649.99	1020	1.759	0.2362
1649.99	1060	0.07693	0.0256
1649.99	1100	0.03055	0.01111
1649.99	1140	0	0
1649.99	1180	0	0

E_γ	$m(\pi^o\pi^o)$	$d\sigma/dm(n2\pi^o)$	sta. er.
1749.67	260	0	0
1749.67	300	0.1163	0.05384
1749.67	340	0.566	0.1312
1749.67	380	1.896	0.2639
1749.67	420	1.97	0.279
1749.67	460	2.704	0.3318
1749.67	500	5.094	0.4941
1749.67	540	4.281	0.4813
1749.67	580	5.449	0.4954
1749.67	620	6.479	0.5377
1749.67	660	6.779	0.6237
1749.67	700	7.918	0.6737
1749.67	740	6.453	0.6249
1749.67	780	7.432	0.6264
1749.67	820	7.419	0.6376
1749.67	860	8.342	0.6852
1749.67	900	6.559	0.599
1749.67	940	3.733	0.3748
1749.67	980	4.147	0.422
1749.67	1020	1.627	0.2291
1749.67	1060	1.438	0.2087
1749.67	1100	0.3093	0.08165
1749.67	1140	0.01847	0.009175
1749.67	1180	0	0
1749.67	1220	0	0
1749.67	1260	0	0

E_γ	$m(\pi^o\pi^o)$	$d\sigma/dm(n2\pi^o)$	sta. er.
1849.84	260	0	0
1849.84	300	0.2794	0.1118
1849.84	340	0.9057	0.2161
1849.84	380	2.118	0.3742
1849.84	420	3.501	0.5131
1849.84	460	4.777	0.5428
1849.84	500	5.385	0.6356
1849.84	540	5.867	0.6226
1849.84	580	6.432	0.5994
1849.84	620	7.772	0.7418
1849.84	660	7.583	0.7011
1849.84	700	6.893	0.5992
1849.84	740	8.491	0.929
1849.84	780	4.61	0.4761
1849.84	820	8.24	0.6497
1849.84	860	10.81	0.8705
1849.84	900	6.759	0.6124
1849.84	940	6.576	0.6433
1849.84	980	6.479	0.5965
1849.84	1020	4.321	0.4898
1849.84	1060	3.917	0.4521
1849.84	1100	1.688	0.2235
1849.84	1140	1.377	0.2128
1849.84	1180	0.06696	0.02943
1849.84	1220	0	0
1849.84	1260	0	0

E_γ	$m(\pi^o\pi^o)$	$d\sigma/dm(n2\pi^o)$	sta. er.
1950.15	260	0	0
1950.15	300	0.3214	0.1131
1950.15	340	0.3027	0.1159
1950.15	380	2.755	0.437
1950.15	420	3.322	0.4625
1950.15	460	4.513	0.5934
1950.15	500	5.305	0.6325
1950.15	540	5.043	0.5899
1950.15	580	7.05	0.7071
1950.15	620	8.332	0.79
1950.15	660	6.194	0.5391
1950.15	700	7.79	0.7711
1950.15	740	5.755	0.5561
1950.15	780	8.934	0.8517
1950.15	820	10.11	0.9615
1950.15	860	8.226	0.6783
1950.15	900	8.334	0.7666
1950.15	940	7.435	0.6289
1950.15	980	7.501	0.6473
1950.15	1020	4.751	0.55
1950.15	1060	3.241	0.4381
1950.15	1100	3.38	0.4547
1950.15	1140	3.288	0.4144
1950.15	1180	0.9451	0.1813
1950.15	1220	0.2248	0.06508
1950.15	1260	0	0
1950.15	1300	0.0008103	0.0008103
1950.15	1340	0	0

E_γ	$m(N\pi^o)$	$d\sigma/dm(pn2\pi^o)$	sta. er.	$d\sigma/dm(p2\pi^o)$	sta. er.
448.512	1060	2.178	0.06553	3.214	0.3812
448.512	1100	23.99	0.1944	13.45	0.5474
448.512	1140	20.45	0.1514	9.436	0.3848
448.512	1180	8.212	0.09208	6.042	0.3485
448.512	1220	0.3835	0.02344	0.1751	0.05072
549.303	1060	3.66	0.08005	7.333	0.4632
549.303	1100	56.47	0.3084	44.97	0.8115
549.303	1140	78.46	0.3218	41.74	0.6578
549.303	1180	78.27	0.3074	45.42	0.693
549.303	1220	44.01	0.2263	32.83	0.634
549.303	1260	8.37	0.1043	9.287	0.5177
650.951	1060	2.915	0.06475	8.005	0.4981
650.951	1100	51.57	0.2808	48.88	0.7531
650.951	1140	104.8	0.364	68.51	0.6991
650.951	1180	161	0.4328	88.7	0.7326
650.951	1220	157.7	0.4213	87.98	0.7521
650.951	1260	79.37	0.2983	52.52	0.6662
650.951	1300	22.76	0.1622	16.62	0.4385
650.951	1340	2.294	0.05885	1.348	0.1681
752.025	1060	1.986	0.05014	3.405	0.195
752.025	1100	35.86	0.2357	28.02	0.466
752.025	1140	80.65	0.325	51.43	0.5377
752.025	1180	161.7	0.4426	93.79	0.6709
752.025	1220	234.5	0.5288	117.3	0.7335
752.025	1260	179.6	0.456	80.36	0.618
752.025	1300	86.92	0.3164	39.62	0.4554
752.025	1340	31.31	0.1913	15.15	0.3168
752.025	1380	6.963	0.09713	2.596	0.1403
752.025	1420	0.1424	0.0177	0.01064	0.008048
851.294	1060	1.54	0.04573	3.059	0.2179
851.294	1100	25.8	0.2055	21.16	0.4223
851.294	1140	55.66	0.2815	31.53	0.396
851.294	1180	101.7	0.3672	54.01	0.4903
851.294	1220	155.1	0.4464	76.12	0.5643
851.294	1260	166.9	0.4569	70.23	0.5364
851.294	1300	131.9	0.4029	53.33	0.4765
851.294	1340	81.59	0.318	33.93	0.3938
851.294	1380	38.12	0.2186	15.44	0.2798
851.294	1420	13.26	0.1347	5.541	0.1912
851.294	1460	1.654	0.05582	0.5415	0.06458

E_γ	$m(N\pi^o)$	$d\sigma/dm(pn2\pi^o)$	sta. er.	$d\sigma/dm(p2\pi^o)$	sta. er.
950.755	1060	1.77	0.04648	3.313	0.2101
950.755	1100	23.84	0.181	19.2	0.3383
950.755	1140	46.52	0.2359	27.75	0.3267
950.755	1180	76.87	0.2941	41.79	0.3786
950.755	1220	112.3	0.3557	50.72	0.4036
950.755	1260	119.5	0.3599	48.13	0.382
950.755	1300	116.6	0.3543	46.77	0.3818
950.755	1340	107.7	0.339	42.76	0.3656
950.755	1380	84.03	0.2993	35.57	0.347
950.755	1420	51.78	0.2357	23.07	0.2944
950.755	1460	22.61	0.1559	9.254	0.1834
950.755	1500	6.183	0.09159	2.927	0.1382
950.755	1540	0.09038	0.01936	0.02843	0.01687
1051.66	1060	1.562	0.039	2.394	0.1439
1051.66	1100	28.84	0.2126	28.93	0.4723
1051.66	1140	53.42	0.269	39.67	0.4284
1051.66	1180	81.5	0.3223	53.07	0.4678
1051.66	1220	107.6	0.3681	56.04	0.4435
1051.66	1260	104.6	0.3559	47.43	0.4003
1051.66	1300	97.08	0.3436	45.67	0.3916
1051.66	1340	96.41	0.3356	46.7	0.3936
1051.66	1380	102.8	0.3509	47.71	0.3972
1051.66	1420	94.36	0.333	46.62	0.4044
1051.66	1460	74.22	0.2989	40.54	0.4017
1051.66	1500	39.51	0.2164	22.43	0.3297
1051.66	1540	12.94	0.1318	6.104	0.1892
1051.66	1580	1.212	0.05507	0.4641	0.06009
1151.75	1060	1.439	0.04217	3.12	0.1923
1151.75	1100	23.82	0.2045	23.18	0.4006
1151.75	1140	43.8	0.2624	35.22	0.4321
1151.75	1180	68.64	0.3201	45.86	0.4407
1151.75	1220	85.5	0.3502	50.77	0.4527
1151.75	1260	81.28	0.335	39.4	0.388
1151.75	1300	66.28	0.3015	31.7	0.3406
1151.75	1340	58.93	0.2796	31.08	0.3369
1151.75	1380	66.36	0.2983	35.14	0.3573
1151.75	1420	76.11	0.3193	41.07	0.3902
1151.75	1460	82.42	0.3366	46.58	0.4272
1151.75	1500	72.98	0.318	42.87	0.4248
1151.75	1540	41.26	0.2377	24.19	0.3492
1151.75	1580	17.12	0.1599	8.006	0.2114
1151.75	1620	3.025	0.0809	0.8572	0.07017

E_γ	$m(N\pi^o)$	$d\sigma/dm(pn2\pi^o)$	sta. er.	$d\sigma/dm(p2\pi^o)$	sta. er.
1251.38	1060	1.261	0.05116	2.977	0.2277
1251.38	1100	17.23	0.2096	19.95	0.4913
1251.38	1140	30.29	0.2645	22.98	0.3971
1251.38	1180	45.22	0.3135	31.71	0.4437
1251.38	1220	56.08	0.3391	31.23	0.4037
1251.38	1260	56.56	0.3389	29.09	0.3995
1251.38	1300	44.5	0.2949	19.58	0.304
1251.38	1340	37.91	0.2742	17.91	0.2955
1251.38	1380	36.57	0.2658	18.74	0.3139
1251.38	1420	43.59	0.2926	22.61	0.3341
1251.38	1460	51.24	0.3155	27.52	0.3669
1251.38	1500	56.71	0.336	31.89	0.4112
1251.38	1540	49.04	0.3089	28.71	0.4085
1251.38	1580	34.49	0.2604	20.48	0.3471
1251.38	1620	18.93	0.2001	8.997	0.2414
1251.38	1660	5.355	0.1237	2.073	0.1409
1251.38	1700	0.1229	0.02901	0.00917	0.006572
1350.79	1060	0.7899	0.03727	1.722	0.1569
1350.79	1100	14.47	0.2046	18.76	0.5844
1350.79	1140	25.3	0.2644	22.35	0.4466
1350.79	1180	34.56	0.2973	25.9	0.4359
1350.79	1220	44.44	0.3372	27.44	0.4274
1350.79	1260	42.91	0.324	21.07	0.3568
1350.79	1300	34.98	0.2848	15.8	0.2936
1350.79	1340	30.31	0.2688	14.92	0.2921
1350.79	1380	27.46	0.254	14.26	0.2807
1350.79	1420	28.24	0.2536	15.52	0.2951
1350.79	1460	35.42	0.2888	19.27	0.3264
1350.79	1500	40.79	0.3095	23	0.3609
1350.79	1540	42.57	0.3217	24.02	0.4033
1350.79	1580	38.63	0.3052	23.5	0.4037
1350.79	1620	32.59	0.2792	21.25	0.3909
1350.79	1660	21.23	0.2283	11.4	0.3042
1350.79	1700	8.683	0.1636	3.929	0.2057
1350.79	1740	1.25	0.131	0.1244	0.04116

E_γ	$m(N\pi^o)$	$d\sigma/dm(pn2\pi^o)$	sta. er.	$d\sigma/dm(p2\pi^o)$	sta. er.
1449.77	1060	0.9264	0.04656	1.025	0.1224
1449.77	1100	15.23	0.2227	20.03	0.6451
1449.77	1140	23.76	0.2684	21.54	0.4561
1449.77	1180	31.19	0.294	22.47	0.4126
1449.77	1220	38.36	0.3243	23.14	0.4087
1449.77	1260	37.75	0.3143	18.23	0.3441
1449.77	1300	32.9	0.2891	15.32	0.3055
1449.77	1340	26.5	0.2556	12.81	0.2774
1449.77	1380	24.92	0.2495	12.78	0.2731
1449.77	1420	24.01	0.2425	13.34	0.2841
1449.77	1460	27.11	0.2569	15.16	0.3
1449.77	1500	33.12	0.2899	17.24	0.3164
1449.77	1540	35.4	0.2974	19.73	0.3595
1449.77	1580	35.75	0.3084	19.98	0.3774
1449.77	1620	37.06	0.3192	21.9	0.3984
1449.77	1660	34.48	0.3057	20.7	0.4253
1449.77	1700	23.07	0.2439	13.83	0.3363
1449.77	1740	11.03	0.1895	4.872	0.2499
1449.77	1780	2.187	0.1116	0.5867	0.08984
1549.69	1060	0.8369	0.04645	1.23	0.1607
1549.69	1100	12.79	0.199	16.56	0.6008
1549.69	1140	20.71	0.2521	16.03	0.3756
1549.69	1180	28.52	0.2817	18.63	0.3632
1549.69	1220	32.09	0.286	19.24	0.3541
1549.69	1260	34.21	0.2973	17.36	0.3336
1549.69	1300	29.36	0.2705	13.69	0.2868
1549.69	1340	24.23	0.2418	11.3	0.2524
1549.69	1380	21.63	0.2262	10.65	0.243
1549.69	1420	21.9	0.2282	10.89	0.2354
1549.69	1460	23.17	0.2327	12.58	0.2587
1549.69	1500	26.69	0.2514	13.97	0.2716
1549.69	1540	28.73	0.2619	15.3	0.293
1549.69	1580	29.75	0.2718	15.87	0.3113
1549.69	1620	32.01	0.2889	17.58	0.3419
1549.69	1660	33.1	0.2922	18.29	0.3449
1549.69	1700	30.16	0.2807	17.94	0.3835
1549.69	1740	22.67	0.2517	11.81	0.3175
1549.69	1780	11.9	0.1831	5.124	0.2358
1549.69	1820	3.567	0.1539	0.7465	0.09137

E_γ	$m(N\pi^o)$	$d\sigma/dm(pn2\pi^o)$	sta. er.	$d\sigma/dm(p2\pi^o)$	sta. er.
1649.99	1060	0.7267	0.04103	0.5041	0.06606
1649.99	1100	12.14	0.2195	13.99	0.5126
1649.99	1140	18.34	0.2611	17.02	0.4673
1649.99	1180	24.49	0.2852	20.33	0.4717
1649.99	1220	28.47	0.304	16.12	0.3614
1649.99	1260	29.3	0.3014	14.12	0.3224
1649.99	1300	25.72	0.2809	11.37	0.2889
1649.99	1340	22.67	0.262	10.48	0.2756
1649.99	1380	20.15	0.2414	9.533	0.253
1649.99	1420	18.68	0.2323	9.522	0.2513
1649.99	1460	20.86	0.2476	11.09	0.2726
1649.99	1500	22.33	0.2529	11.67	0.2787
1649.99	1540	23.63	0.2638	11.4	0.2697
1649.99	1580	23.79	0.2643	10.75	0.2629
1649.99	1620	27.49	0.2933	15.07	0.3415
1649.99	1660	30.67	0.3147	16.47	0.354
1649.99	1700	30.43	0.3176	16.74	0.3796
1649.99	1740	25.79	0.2888	14.72	0.3659
1649.99	1780	20.53	0.2637	12.18	0.4565
1649.99	1820	12.38	0.2098	5.925	0.2841
1649.99	1860	4.02	0.1597	1.048	0.1327

E_γ	$m(N\pi^o)$	$d\sigma/dm(pn2\pi^o)$	sta. er.	$d\sigma/dm(p2\pi^o)$	sta. er.
1749.67	1060	0.53	0.03617	0.4519	0.08216
1749.67	1100	10.32	0.2149	11.97	0.5199
1749.67	1140	15.24	0.2498	12.67	0.439
1749.67	1180	22.22	0.2955	16.49	0.4391
1749.67	1220	24.77	0.3021	14.99	0.4003
1749.67	1260	24.71	0.2919	13.14	0.3422
1749.67	1300	23.46	0.2863	11.05	0.3126
1749.67	1340	19.73	0.2574	9.771	0.2835
1749.67	1380	17.97	0.2448	8.371	0.2457
1749.67	1420	18.96	0.2524	9.977	0.2869
1749.67	1460	18.19	0.2405	9.678	0.2678
1749.67	1500	20.42	0.2613	11.04	0.2894
1749.67	1540	20.93	0.2626	11.59	0.3036
1749.67	1580	21.95	0.2696	11.78	0.3165
1749.67	1620	22.56	0.275	12.08	0.3127
1749.67	1660	24.75	0.2923	13.93	0.3517
1749.67	1700	25.81	0.3048	14.64	0.3768
1749.67	1740	24.23	0.296	13.28	0.3768
1749.67	1780	23.03	0.3041	12.04	0.3695
1749.67	1820	18.39	0.2686	11.06	0.5102
1749.67	1860	12.8	0.2232	7.603	0.4201
1749.67	1900	5.246	0.1618	1.815	0.1896
1749.67	1940	0.09929	0.0323	0	0

E_γ	$m(N\pi^o)$	$d\sigma/dm(pn2\pi^o)$	sta. er.	$d\sigma/dm(p2\pi^o)$	sta. er.
1849.84	1060	0.5048	0.03554	1.605	0.1915
1849.84	1100	9.128	0.1976	13.21	0.643
1849.84	1140	14	0.2441	12.18	0.4359
1849.84	1180	18.85	0.2728	15.26	0.4556
1849.84	1220	22.07	0.2907	14.02	0.3857
1849.84	1260	22.79	0.291	11.07	0.3211
1849.84	1300	23.12	0.2957	9.786	0.3101
1849.84	1340	19.27	0.2622	8.718	0.2659
1849.84	1380	18.06	0.2549	9.225	0.2803
1849.84	1420	17.96	0.2507	9.333	0.2811
1849.84	1460	19.09	0.2612	10.15	0.2833
1849.84	1500	20.15	0.2673	10.89	0.2967
1849.84	1540	20.99	0.2738	10.85	0.2937
1849.84	1580	20.59	0.2706	10.43	0.2862
1849.84	1620	21.76	0.2766	11.98	0.3198
1849.84	1660	22.85	0.2874	11.41	0.3095
1849.84	1700	24.17	0.2985	13.01	0.3525
1849.84	1740	23.78	0.3022	13.88	0.438
1849.84	1780	20.46	0.2781	11.07	0.3495
1849.84	1820	19.16	0.2749	9.7	0.3213
1849.84	1860	16.98	0.2629	8.849	0.3631
1849.84	1900	12.13	0.2205	8.142	0.4313
1849.84	1940	5.543	0.1605	2.72	0.2381
1849.84	1980	0.9625	0.136	0.08568	0.03496

E_γ	$m(N\pi^o)$	$d\sigma/dm(pn2\pi^o)$	sta. er.	$d\sigma/dm(p2\pi^o)$	sta. er.
1950.15	1060	0.5147	0.03495	0.8425	0.1263
1950.15	1100	8.736	0.1957	10.33	0.5209
1950.15	1140	13.5	0.251	13.59	0.496
1950.15	1180	17.24	0.2671	13.8	0.4502
1950.15	1220	20.96	0.2894	13.71	0.417
1950.15	1260	21.97	0.2877	11.38	0.3423
1950.15	1300	21.12	0.2815	9.768	0.3004
1950.15	1340	18.84	0.2613	8.998	0.2738
1950.15	1380	18.52	0.2574	9.159	0.2746
1950.15	1420	18.26	0.2538	10.15	0.2898
1950.15	1460	19.38	0.2614	11.31	0.3178
1950.15	1500	21.38	0.2781	10.89	0.292
1950.15	1540	21.74	0.2781	11.56	0.3011
1950.15	1580	20.77	0.273	10.92	0.2926
1950.15	1620	21.45	0.2755	10.69	0.2826
1950.15	1660	23.23	0.2885	12.62	0.3281
1950.15	1700	21.93	0.2791	11.56	0.3211
1950.15	1740	22.19	0.2884	12.7	0.3534
1950.15	1780	20.57	0.2771	10.73	0.3335
1950.15	1820	19.93	0.281	10.84	0.3537
1950.15	1860	18.9	0.2793	9.881	0.3809
1950.15	1900	16.03	0.2581	9.165	0.3988
1950.15	1940	12.41	0.2259	7.152	0.3985
1950.15	1980	6.778	0.1809	2.639	0.2164
1950.15	2020	1.013	0.1567	0.1411	0.03968

E_γ	$m(N\pi^o)$	$d\sigma/dm(n2\pi^o)$	sta. er.
448.512	1060	2.807	0.4338
448.512	1100	24.86	1.272
448.512	1140	20.39	1.044
448.512	1180	9.595	0.7775
448.512	1220	0.2568	0.1024
549.303	1060	2.962	0.3426
549.303	1100	41.15	1.392
549.303	1140	61.91	1.701
549.303	1180	59.35	1.587
549.303	1220	30.03	1.051
549.303	1260	6.46	0.5503
650.951	1060	1.502	0.1823
650.951	1100	44.74	1.309
650.951	1140	97.22	2.135
650.951	1180	123	1.968
650.951	1220	118.3	1.927
650.951	1260	56.67	1.324
650.951	1300	20.96	1.027
650.951	1340	0.6406	0.1551
752.025	1060	1.959	0.2182
752.025	1100	31.33	0.9494
752.025	1140	74.55	1.537
752.025	1180	156	3.54
752.025	1220	184.2	2.443
752.025	1260	131.2	1.952
752.025	1300	61.82	1.316
752.025	1340	30.13	1.21
752.025	1380	4.855	0.4371
752.025	1420	0.05591	0.0303
851.294	1060	0.926	0.1312
851.294	1100	18.93	0.6375
851.294	1140	52.41	1.226
851.294	1180	88.28	1.567
851.294	1220	118.8	1.983
851.294	1260	111.3	1.729
851.294	1300	93.75	1.617
851.294	1340	53.95	1.105
851.294	1380	24.05	0.7311
851.294	1420	8.318	0.5364
851.294	1460	0.6755	0.1322

E_γ	$m(N\pi^o)$	$d\sigma/dm(n2\pi^o)$	sta. er.
950.755	1060	0.9531	0.1022
950.755	1100	17.11	0.5306
950.755	1140	39.72	0.9215
950.755	1180	58.62	1.047
950.755	1220	79.43	1.324
950.755	1260	72.37	1.252
950.755	1300	72.3	1.305
950.755	1340	60.38	1.044
950.755	1380	55.34	0.9969
950.755	1420	34.6	0.7841
950.755	1460	15.19	0.5544
950.755	1500	3.817	0.3407
950.755	1540	0	0
1051.66	1060	0.6225	0.06566
1051.66	1100	18.18	0.6726
1051.66	1140	40.92	1.082
1051.66	1180	62.58	1.259
1051.66	1220	81.29	1.809
1051.66	1260	61.99	1.296
1051.66	1300	59.97	1.57
1051.66	1340	53.14	1.148
1051.66	1380	54.65	1.025
1051.66	1420	60.02	1.154
1051.66	1460	53.35	1.313
1051.66	1500	23.95	0.7182
1051.66	1540	7.183	0.4239
1051.66	1580	0.09909	0.03735
1151.75	1060	0.7591	0.1017
1151.75	1100	12.35	0.5012
1151.75	1140	27.24	0.8965
1151.75	1180	42.95	1.005
1151.75	1220	63.6	1.661
1151.75	1260	41.93	1.027
1151.75	1300	38.97	1.283
1151.75	1340	31.31	0.8905
1151.75	1380	36.29	0.9495
1151.75	1420	41.73	0.9605
1151.75	1460	50.08	1.099
1151.75	1500	35.99	0.8221
1151.75	1540	20.57	0.6262
1151.75	1580	8.502	0.4426
1151.75	1620	0.3977	0.07754

E_γ	$m(N\pi^o)$	$d\sigma/dm(n2\pi^o)$	sta. er.
1251.38	1060	0.4387	0.09396
1251.38	1100	9.588	0.5055
1251.38	1140	19.95	0.8735
1251.38	1180	35.38	1.477
1251.38	1220	38.86	1.368
1251.38	1260	27.39	0.9943
1251.38	1300	20.77	0.826
1251.38	1340	26.09	1.174
1251.38	1380	16.98	0.6839
1251.38	1420	24.89	0.8834
1251.38	1460	28.62	1.146
1251.38	1500	35.03	1.093
1251.38	1540	32.47	1.32
1251.38	1580	21.17	0.8808
1251.38	1620	10.57	0.633
1251.38	1660	0.8736	0.1592
1251.38	1700	0	0
1350.79	1060	0.2351	0.0462
1350.79	1100	9.573	0.6979
1350.79	1140	13.71	0.7713
1350.79	1180	24.43	1.075
1350.79	1220	28.78	1.274
1350.79	1260	22.86	1.06
1350.79	1300	20.04	1.179
1350.79	1340	16.79	1.01
1350.79	1380	19.07	1.02
1350.79	1420	19.2	1.011
1350.79	1460	18.17	0.8195
1350.79	1500	20.06	0.8718
1350.79	1540	21.03	0.8287
1350.79	1580	21.55	0.9709
1350.79	1620	18.03	0.8966
1350.79	1660	10.24	0.6351
1350.79	1700	3.732	0.3717
1350.79	1740	0	0

E_γ	$m(N\pi^o)$	$d\sigma/dm(n2\pi^o)$	sta. er.
1449.77	1060	0.2215	0.06832
1449.77	1100	8.728	0.5391
1449.77	1140	12.87	0.7477
1449.77	1180	18.7	0.9676
1449.77	1220	20	0.9865
1449.77	1260	19.19	0.9543
1449.77	1300	18.69	1.091
1449.77	1340	14.56	0.7797
1449.77	1380	18.39	1.189
1449.77	1420	17	0.8764
1449.77	1460	15.78	0.8362
1449.77	1500	19.12	0.9329
1449.77	1540	16.6	0.8323
1449.77	1580	20.64	0.9374
1449.77	1620	22.69	1.015
1449.77	1660	17.24	0.8405
1449.77	1700	12.24	0.7595
1449.77	1740	3.823	0.3618
1449.77	1780	0.0718	0.0382
1549.69	1060	0.1394	0.03592
1549.69	1100	6.309	0.4761
1549.69	1140	10.93	0.6545
1549.69	1180	15.23	0.7002
1549.69	1220	15.7	0.7428
1549.69	1260	16.65	0.8957
1549.69	1300	12.65	0.738
1549.69	1340	12.3	0.7156
1549.69	1380	13.19	0.9317
1549.69	1420	10.06	0.5712
1549.69	1460	13.57	0.6908
1549.69	1500	12.95	0.6375
1549.69	1540	13.25	0.6596
1549.69	1580	22.61	1.23
1549.69	1620	15.38	0.8208
1549.69	1660	15.39	0.7045
1549.69	1700	13.85	0.7052
1549.69	1740	10.05	0.6267
1549.69	1780	3.819	0.335
1549.69	1820	0.2774	0.08707

E_γ	$m(N\pi^o)$	$d\sigma/dm(n2\pi^o)$	sta. er.
1649.99	1060	0.03988	0.01752
1649.99	1100	6.623	0.5005
1649.99	1140	11.22	0.8099
1649.99	1180	15.84	1.012
1649.99	1220	19.12	1.222
1649.99	1260	16.77	1.086
1649.99	1300	14.31	0.9771
1649.99	1340	10.72	0.707
1649.99	1380	11.68	0.766
1649.99	1420	12.09	0.9804
1649.99	1460	15.25	1.027
1649.99	1500	14.48	0.8916
1649.99	1540	14.15	0.914
1649.99	1580	15.29	1.044
1649.99	1620	16.6	0.9151
1649.99	1660	18.76	1.12
1649.99	1700	15.67	0.9469
1649.99	1740	16.55	1.014
1649.99	1780	11.98	0.7993
1649.99	1820	4.254	0.4368
1649.99	1860	0.4116	0.1074

E_γ	$m(N\pi^o)$	$d\sigma/dm(n2\pi^o)$	sta. er.
1749.67	1060	0.07699	0.02427
1749.67	1100	4.123	0.3852
1749.67	1140	7.764	0.6145
1749.67	1180	11.19	0.8394
1749.67	1220	11.69	0.777
1749.67	1260	13.07	0.9693
1749.67	1300	11.68	0.9112
1749.67	1340	12.23	1.021
1749.67	1380	8.98	0.6615
1749.67	1420	10.28	0.7607
1749.67	1460	14.03	1
1749.67	1500	11.34	0.7929
1749.67	1540	12.01	0.8447
1749.67	1580	14.48	1.06
1749.67	1620	11.69	0.7947
1749.67	1660	15.59	1.062
1749.67	1700	14.3	0.9844
1749.67	1740	10.25	0.7418
1749.67	1780	13.5	0.9597
1749.67	1820	5.888	0.5108
1749.67	1860	5.917	0.5226
1749.67	1900	0.639	0.1264
1749.67	1940	0	0

E_γ	$m(N\pi^o)$	$d\sigma/dm(n2\pi^o)$	sta. er.
1849.84	1060	0.149	0.05242
1849.84	1100	4.261	0.4055
1849.84	1140	10.1	0.8458
1849.84	1180	10.55	0.8997
1849.84	1220	11.53	0.763
1849.84	1260	15.67	1.157
1849.84	1300	11.27	0.7631
1849.84	1340	8.793	0.6789
1849.84	1380	8.627	0.6615
1849.84	1420	9.294	0.6364
1849.84	1460	10.29	0.6793
1849.84	1500	9.401	0.6345
1849.84	1540	11.18	0.7389
1849.84	1580	12.46	0.7153
1849.84	1620	13.46	0.8939
1849.84	1660	10.19	0.6247
1849.84	1700	11.55	0.7135
1849.84	1740	11.07	0.743
1849.84	1780	9.689	0.7016
1849.84	1820	11.48	0.8533
1849.84	1860	11.31	0.9705
1849.84	1900	4.84	0.4731
1849.84	1940	2.072	0.3268
1849.84	1980	0	0

E_γ	$m(N\pi^o)$	$d\sigma/dm(n2\pi^o)$	sta. er.
1950.15	1060	0.2219	0.07005
1950.15	1100	4.702	0.5208
1950.15	1140	8.822	0.7928
1950.15	1180	12.38	0.8688
1950.15	1220	11.47	0.8151
1950.15	1260	10.5	0.7719
1950.15	1300	11.02	0.7398
1950.15	1340	8.564	0.6351
1950.15	1380	10.78	0.7584
1950.15	1420	10.42	0.7437
1950.15	1460	11.26	0.8609
1950.15	1500	10.74	0.7542
1950.15	1540	10.46	0.7284
1950.15	1580	11.12	0.7319
1950.15	1620	12.11	0.7617
1950.15	1660	9.582	0.6007
1950.15	1700	10.7	0.6831
1950.15	1740	12.52	0.9657
1950.15	1780	10.4	0.696
1950.15	1820	12.02	0.8392
1950.15	1860	10.08	0.9549
1950.15	1900	12.9	1.108
1950.15	1940	6.323	0.604
1950.15	1980	3.715	0.4668
1950.15	2020	0.03635	0.03701

Total cross section

E_γ incident photon beam in MeV.
σ total cross section in μb.
sta. er. statistical error in μb.

E_γ	$\sigma(pn2\pi^o)$	sta. er.	$\sigma(p2\pi^o)$	sta. er.	$\sigma(n2\pi^o)$	sta. er.
340	-0.004225	-0.0003486	0.004654	0.005165	0.06625	0.05266
361.5	0.07474	0.002269	0.02023	0.007844	0.466	0.06497
387.9	0.2028	0.005871	0.08214	0.0175	0.3297	0.05457
413.8	0.423	0.008237	0.159	0.01934	0.5124	0.05329
439.2	0.6912	0.01403	0.339	0.03257	0.5959	0.06701
464.1	1.145	0.0155	0.5531	0.03192	0.8824	0.06379
488.7	2.187	0.02751	1.112	0.05302	1.379	0.09548
512.6	3.519	0.03167	1.795	0.05663	1.722	0.09163
536.2	4.972	0.04565	2.619	0.07767	2.363	0.1244
559.3	6.636	0.04377	3.469	0.07006	3.524	0.1214
586.5	8.664	0.05223	4.669	0.07998	4.226	0.1336
613.1	10.5	0.0591	5.517	0.08486	5.689	0.154
639.1	11.87	0.05893	6.277	0.08111	6.063	0.1448
664.5	12.92	0.06111	6.766	0.0804	6.587	0.1461
689.4	15.96	0.07068	8.641	0.09122	8.091	0.1644
713.7	16.56	0.07235	8.587	0.08849	8.673	0.1672
737.5	17.8	0.07731	9.275	0.09209	8.782	0.1699
760.7	17.32	0.07768	9.179	0.09089	8.497	0.1669
787.2	17.45	0.06901	8.709	0.07622	9.298	0.1512
813	16.6	0.0808	8.106	0.08609	8.219	0.1672
838.2	16.05	0.06878	7.393	0.06959	8.173	0.1416
862.8	15.66	0.07916	7.32	0.07906	8.599	0.1763
886.7	14.11	0.06407	6.519	0.06245	8.001	0.1426
913.3	14.23	0.06352	6.569	0.06072	7.525	0.1341
939.3	14.47	0.06372	6.668	0.0598	7.976	0.135
964.4	15.35	0.06799	7.215	0.06346	8.153	0.1393
989	16.05	0.06998	7.786	0.06545	8.749	0.1432

E_γ	$\sigma(pn2\pi^o)$	sta. er.	$\sigma(p2\pi^o)$	sta. er.	$\sigma(n2\pi^o)$	sta. er.
1013	17.61	0.07521	8.898	0.0709	8.488	0.1429
1036	17.83	0.07659	9.109	0.07181	8.536	0.1433
1061	17.5	0.06922	9.087	0.0647	8.341	0.1277
1089	16.99	0.07542	9.287	0.07157	7.992	0.1366
1112	16.33	0.0778	8.976	0.07341	7.444	0.1374
1136	15.88	0.07056	8.813	0.06643	7.284	0.1239
1160	14.61	0.07597	8.144	0.07117	6.643	0.1317
1187	13.5	0.06832	7.587	0.06386	6.057	0.1167
1213	12.45	0.07959	6.965	0.07385	5.755	0.1371
1237	11.32	0.07235	6.302	0.06668	5.342	0.1252
1264	10.23	0.07024	5.679	0.06439	4.439	0.1159
1289	9.051	0.07072	5.117	0.06524	3.756	0.1135
1313	9.861	0.07647	5.615	0.07064	4.412	0.127
1337	9.657	0.07719	5.528	0.07137	4.381	0.1286
1374	9.044	0.05128	5.27	0.04774	3.815	0.08199
1426	8.895	0.05126	5.113	0.04733	3.962	0.08379
1475	8.978	0.05431	5.064	0.04964	4.058	0.0891
1550	8.298	0.0351	4.715	0.03219	3.551	0.05584
1650	7.717	0.03731	4.304	0.03391	3.506	0.06113
1750	7.352	0.0384	4.034	0.03467	3.37	0.06343
1850	7.272	0.03915	4.024	0.03561	3.394	0.06547
1950	7.555	0.0403	4.137	0.0363	3.328	0.06462

$\eta-$meson photoproduction off the deuterium

Angular distributions

E_γ incident photon beam in MeV
$cos(\theta_{cm})$ η angle in the cms
$d\sigma/d\Omega$ differential cross section in μb/sr.
sta. er. statistical error in μb/sr.

E_γ	$cos(\theta_{cm})$	$d\sigma/d\Omega(NNX\eta)$	sta. er.	$d\sigma/d\Omega(pn\eta)$	sta. er.
637.672	-0.9	0.1718	0.0112	0.1322	0.007975
637.672	-0.7	0.1017	0.007635	0.1313	0.008835
637.672	-0.5	0.06083	0.005546	0.09776	0.007407
637.672	-0.3	0.04009	0.004136	0.07061	0.00617
637.672	-0.1	0.02903	0.003114	0.03069	0.002614
637.672	0.1	0.01749	0.002104	0.01756	0.001697
637.672	0.3	0.01375	0.00164	0.006567	0.0005734
637.672	0.5	0.01047	0.001294	0	0.08435
637.672	0.7	0.01224	0.001321	0	0.08435
637.672	0.9	0.01801	0.001614	0.003731	0.0003672
661.95	-0.9	0.3979	0.01627	0.2751	0.01107
661.95	-0.7	0.2357	0.01096	0.192	0.008519
661.95	-0.5	0.1729	0.008637	0.1773	0.008324
661.95	-0.3	0.1394	0.00721	0.1598	0.007576
661.95	-0.1	0.1052	0.005803	0.1339	0.006554
661.95	0.1	0.06554	0.004223	0.08018	0.004635
661.95	0.3	0.06816	0.003969	0.1224	0.006524
661.95	0.5	0.05502	0.003306	0.07716	0.004104
661.95	0.7	0.03639	0.002524	0.06436	0.003526
661.95	0.9	0.02672	0.002071	0.04974	0.003147
688.582	-0.9	0.784	0.02068	0.5037	0.01289
688.582	-0.7	0.5966	0.01611	0.4521	0.01169
688.582	-0.5	0.5169	0.01369	0.5044	0.01265
688.582	-0.3	0.4045	0.01117	0.4062	0.01039
688.582	-0.1	0.3608	0.009788	0.3705	0.009473
688.582	0.1	0.3154	0.008538	0.3513	0.00889
688.582	0.3	0.2839	0.007611	0.3412	0.00844
688.582	0.5	0.231	0.006508	0.3054	0.007732
688.582	0.7	0.2167	0.006045	0.256	0.00672
688.582	0.9	0.1914	0.005533	0.2438	0.006467
714.707	-0.9	1.47	0.03161	0.9974	0.02122
714.707	-0.7	1.098	0.02378	0.8071	0.01723
714.707	-0.5	0.9469	0.0201	0.7956	0.0167
714.707	-0.3	0.8706	0.01787	0.771	0.01541
714.707	-0.1	0.8173	0.01618	0.7819	0.01518
714.707	0.1	0.7655	0.01469	0.8126	0.01497
714.707	0.3	0.7199	0.01344	0.7909	0.01429
714.707	0.5	0.6492	0.01211	0.7413	0.01315
714.707	0.7	0.607	0.01123	0.7217	0.01269
714.707	0.9	0.566	0.01055	0.6877	0.01195

E_γ	$cos(\theta_{cm})$	$d\sigma/d\Omega(NNX\eta)$	sta. er.	$d\sigma/d\Omega(pn\eta)$	sta. er.
737.573	-0.9	1.951	0.03881	1.487	0.02971
737.573	-0.7	1.606	0.03067	1.31	0.02509
737.573	-0.5	1.463	0.02647	1.274	0.02306
737.573	-0.3	1.336	0.02327	1.182	0.02025
737.573	-0.1	1.282	0.02116	1.258	0.02031
737.573	0.1	1.251	0.01953	1.298	0.0196
737.573	0.3	1.203	0.018	1.279	0.01853
737.573	0.5	1.147	0.01664	1.296	0.01813
737.573	0.7	1.091	0.01552	1.28	0.01741
737.573	0.9	1.051	0.01474	1.253	0.01665
760.016	-0.9	2.228	0.04322	1.766	0.03485
760.016	-0.7	1.869	0.03429	1.602	0.02984
760.016	-0.5	1.708	0.02938	1.501	0.02592
760.016	-0.3	1.544	0.02544	1.464	0.02374
760.016	-0.1	1.537	0.02336	1.487	0.02196
760.016	0.1	1.518	0.02153	1.529	0.02118
760.016	0.3	1.473	0.01982	1.516	0.0196
760.016	0.5	1.421	0.01835	1.529	0.01904
760.016	0.7	1.381	0.01723	1.536	0.0183
760.016	0.9	1.378	0.01659	1.645	0.01892
786.525	-0.9	2.299	0.03923	1.917	0.03323
786.525	-0.7	1.938	0.03075	1.689	0.0269
786.525	-0.5	1.79	0.02623	1.659	0.02405
786.525	-0.3	1.7	0.0231	1.599	0.02124
786.525	-0.1	1.664	0.02086	1.669	0.02023
786.525	0.1	1.633	0.01901	1.667	0.01875
786.525	0.3	1.687	0.01794	1.745	0.01793
786.525	0.5	1.613	0.01644	1.725	0.01685
786.525	0.7	1.597	0.01551	1.777	0.01649
786.525	0.9	1.559	0.01474	1.803	0.01626

E_γ	$cos(\theta_{cm})$	$d\sigma/d\Omega(NNX\eta)$	sta. er.	$d\sigma/d\Omega(pn\eta)$	sta. er.
812.518	-0.9	2.114	0.04741	1.882	0.04252
812.518	-0.7	1.822	0.03731	1.725	0.0354
812.518	-0.5	1.799	0.0327	1.633	0.02936
812.518	-0.3	1.769	0.0291	1.667	0.02721
812.518	-0.1	1.735	0.02613	1.701	0.02509
812.518	0.1	1.731	0.02386	1.765	0.0235
812.518	0.3	1.679	0.02168	1.786	0.02205
812.518	0.5	1.661	0.02011	1.83	0.02114
812.518	0.7	1.618	0.01875	1.823	0.02003
812.518	0.9	1.592	0.01785	1.929	0.02032
837.885	-0.9	1.924	0.04043	1.695	0.05191
837.885	-0.7	1.726	0.0325	1.544	0.04035
837.885	-0.5	1.703	0.02824	1.543	0.03489
837.885	-0.3	1.69	0.025	1.505	0.03027
837.885	-0.1	1.663	0.02227	1.548	0.02759
837.885	0.1	1.66	0.02018	1.554	0.02536
837.885	0.3	1.622	0.01831	1.585	0.02376
837.885	0.5	1.583	0.01682	1.703	0.02411
837.885	0.7	1.552	0.0157	1.739	0.02379
837.885	0.9	1.534	0.01498	1.897	0.02548
862.764	-0.9	1.922	0.05107	1.759	0.06913
862.764	-0.7	1.587	0.03862	1.389	0.04861
862.764	-0.5	1.591	0.03365	1.433	0.04213
862.764	-0.3	1.524	0.02911	1.458	0.03873
862.764	-0.1	1.528	0.02602	1.449	0.03427
862.764	0.1	1.52	0.02339	1.477	0.03098
862.764	0.3	1.479	0.02105	1.438	0.02786
862.764	0.5	1.414	0.01905	1.513	0.02792
862.764	0.7	1.39	0.01781	1.607	0.02824
862.764	0.9	1.315	0.01669	1.634	0.02947

E_γ	$cos(\theta_{cm})$	$d\sigma/d\Omega(NNX\eta)$	sta. er.	$d\sigma/d\Omega(pn\eta)$	sta. er.
887.05	-0.9	1.734	0.04191	1.37	0.0522
887.05	-0.7	1.504	0.0326	1.311	0.04245
887.05	-0.5	1.477	0.02797	1.197	0.03393
887.05	-0.3	1.474	0.02453	1.276	0.03058
887.05	-0.1	1.422	0.02136	1.241	0.02646
887.05	0.1	1.395	0.01899	1.307	0.02454
887.05	0.3	1.368	0.0171	1.239	0.02206
887.05	0.5	1.328	0.01559	1.36	0.02253
887.05	0.7	1.267	0.01438	1.311	0.02144
887.05	0.9	1.207	0.01358	1.286	0.02202
912.504	-0.9	1.464	0.04321	1.185	0.05784
912.504	-0.7	1.327	0.03409	1.166	0.0469
912.504	-0.5	1.307	0.02918	1.042	0.03687
912.504	-0.3	1.281	0.02526	1.021	0.03077
912.504	-0.1	1.295	0.0224	1.049	0.02725
912.504	0.1	1.24	0.01957	1.058	0.02449
912.504	0.3	1.181	0.01732	1.001	0.02191
912.504	0.5	1.166	0.01591	1.08	0.02161
912.504	0.7	1.146	0.01494	1.06	0.02118
912.504	0.9	1.008	0.01367	0.9422	0.02056
937.34	-0.9	1.228	0.03818	0.8986	0.04821
937.34	-0.7	1.209	0.03125	1.04	0.04323
937.34	-0.5	1.156	0.02615	0.9677	0.0349
937.34	-0.3	1.119	0.02233	0.9256	0.0282
937.34	-0.1	1.121	0.01962	0.954	0.02476
937.34	0.1	1.116	0.01742	0.9395	0.02165
937.34	0.3	1.077	0.0155	0.9623	0.01997
937.34	0.5	1.015	0.01392	0.964	0.01928
937.34	0.7	0.9605	0.01283	0.9454	0.01878
937.34	0.9	0.8316	0.01167	0.8094	0.01828

E_γ	$cos(\theta_{cm})$	$d\sigma/d\Omega(NNX\eta)$	sta. er.	$d\sigma/d\Omega(pn\eta)$	sta. er.
963.926	-0.9	1.195	0.03971	0.8953	0.05372
963.926	-0.7	1.067	0.03059	0.8268	0.04076
963.926	-0.5	1.055	0.02601	0.8333	0.03337
963.926	-0.3	1.097	0.023	0.9934	0.03331
963.926	-0.1	1.041	0.01961	0.869	0.02447
963.926	0.1	1.003	0.01707	0.9223	0.02283
963.926	0.3	0.9831	0.01527	0.968	0.02138
963.926	0.5	0.9175	0.01363	0.9286	0.01982
963.926	0.7	0.8581	0.01253	0.859	0.01877
963.926	0.9	0.7151	0.01128	0.7368	0.01881
989.864	-0.9	1.008	0.0363	0.793	0.05266
989.864	-0.7	0.9838	0.03007	0.8016	0.0416
989.864	-0.5	0.9908	0.02585	0.7645	0.03279
989.864	-0.3	0.968	0.02203	0.8093	0.02916
989.864	-0.1	0.9424	0.01892	0.7634	0.0238
989.864	0.1	0.9544	0.01684	0.8227	0.0216
989.864	0.3	0.8942	0.01471	0.7871	0.01899
989.864	0.5	0.8646	0.01339	0.8184	0.0186
989.864	0.7	0.7817	0.01214	0.748	0.01766
989.864	0.9	0.6375	0.01088	0.596	0.01717
1025.27	-0.9	0.7876	0.02409	0.6422	0.03926
1025.27	-0.7	0.8397	0.02089	0.6783	0.03086
1025.27	-0.5	0.8728	0.01839	0.687	0.02534
1025.27	-0.3	0.8667	0.01588	0.6955	0.02092
1025.27	-0.1	0.8606	0.01379	0.6915	0.01734
1025.27	0.1	0.871	0.01225	0.7688	0.01617
1025.27	0.3	0.8684	0.01102	0.7823	0.01459
1025.27	0.5	0.8315	0.009979	0.7863	0.01386
1025.27	0.7	0.7184	0.008871	0.7393	0.0137
1025.27	0.9	0.5501	0.007767	0.5284	0.01253

E_γ	$cos(\theta_{cm})$	$d\sigma/d\Omega(NNX\eta)$	sta. er.	$d\sigma/d\Omega(pn\eta)$	sta. er.
1074.13	-0.9	0.7226	0.02147	0.4737	0.03537
1074.13	-0.7	0.7289	0.01841	0.5041	0.02704
1074.13	-0.5	0.7373	0.016	0.5143	0.02141
1074.13	-0.3	0.819	0.01459	0.6273	0.01984
1074.13	-0.1	0.7856	0.01246	0.6551	0.01678
1074.13	0.1	0.8137	0.01123	0.7462	0.01533
1074.13	0.3	0.8211	0.0102	0.8005	0.01441
1074.13	0.5	0.804	0.009381	0.8319	0.01384
1074.13	0.7	0.6951	0.008386	0.7372	0.01345
1074.13	0.9	0.545	0.007475	0.5182	0.01226
1124.08	-0.9	0.6633	0.02054	0.2799	0.02817
1124.08	-0.7	0.6744	0.01768	0.3392	0.02455
1124.08	-0.5	0.6806	0.01557	0.4188	0.02091
1124.08	-0.3	0.7371	0.01421	0.5761	0.02083
1124.08	-0.1	0.759	0.01268	0.6308	0.01732
1124.08	0.1	0.7945	0.01153	0.6967	0.01599
1124.08	0.3	0.819	0.01062	0.7607	0.01477
1124.08	0.5	0.7954	0.009742	0.7659	0.01415
1124.08	0.7	0.7008	0.008821	0.6888	0.01387
1124.08	0.9	0.567	0.008059	0.4961	0.013
1174.51	-0.9	0.6215	0.01887	0.2675	0.03037
1174.51	-0.7	0.6362	0.01689	0.3372	0.02585
1174.51	-0.5	0.6348	0.01488	0.4033	0.02206
1174.51	-0.3	0.7133	0.01383	0.4986	0.01941
1174.51	-0.1	0.7095	0.01214	0.536	0.01621
1174.51	0.1	0.7801	0.01136	0.6478	0.01496
1174.51	0.3	0.8042	0.01052	0.706	0.01395
1174.51	0.5	0.7972	0.009815	0.6865	0.01312
1174.51	0.7	0.7102	0.009006	0.6664	0.0134
1174.51	0.9	0.5954	0.008439	0.4774	0.01281

E_γ	$cos(\theta_{cm})$	$d\sigma/d\Omega(NNX\eta)$	sta. er.	$d\sigma/d\Omega(pn\eta)$	sta. er.
1226.52	-0.9	0.6631	0.02123	0.1639	0.02852
1226.52	-0.7	0.6593	0.01855	0.297	0.02838
1226.52	-0.5	0.6592	0.01643	0.3282	0.02163
1226.52	-0.3	0.6594	0.01452	0.4247	0.02044
1226.52	-0.1	0.7175	0.01343	0.5013	0.01712
1226.52	0.1	0.7576	0.01238	0.6015	0.01626
1226.52	0.3	0.8042	0.01167	0.6912	0.01567
1226.52	0.5	0.7951	0.01091	0.688	0.01467
1226.52	0.7	0.726	0.01017	0.6356	0.01452
1226.52	0.9	0.6131	0.009635	0.5502	0.01573
1276.68	-0.9	0.5897	0.02084	0.1685	0.03154
1276.68	-0.7	0.6199	0.01869	0.2125	0.0256
1276.68	-0.5	0.6009	0.01628	0.276	0.02187
1276.68	-0.3	0.6364	0.01483	0.3495	0.01993
1276.68	-0.1	0.7004	0.01384	0.4613	0.0175
1276.68	0.1	0.7046	0.01249	0.5165	0.016
1276.68	0.3	0.7619	0.01193	0.5968	0.01523
1276.68	0.5	0.7621	0.01126	0.6298	0.01548
1276.68	0.7	0.6885	0.01047	0.5651	0.01506
1276.68	0.9	0.6003	0.0101	0.4822	0.01613
1325.1	-0.9	0.6147	0.02291	0.1851	0.03547
1325.1	-0.7	0.5844	0.01941	0.22	0.02698
1325.1	-0.5	0.5954	0.01742	0.265	0.02273
1325.1	-0.3	0.6176	0.0158	0.2982	0.01926
1325.1	-0.1	0.6481	0.01447	0.3465	0.01641
1325.1	0.1	0.7315	0.01389	0.4374	0.01525
1325.1	0.3	0.7694	0.01311	0.5031	0.01471
1325.1	0.5	0.7612	0.01234	0.4907	0.0142
1325.1	0.7	0.7141	0.01175	0.4781	0.01449
1325.1	0.9	0.6619	0.01181	0.444	0.01612

E_γ	$cos(\theta_{cm})$	$d\sigma/d\Omega(NNX\eta)$	sta. er.	$d\sigma/d\Omega(pn\eta)$	sta. er.
1374.25	-0.9	0.6387	0.02266	0.2789	0.04938
1374.25	-0.7	0.6082	0.01912	0.1812	0.02607
1374.25	-0.5	0.5896	0.01657	0.2242	0.02137
1374.25	-0.3	0.5572	0.01427	0.2517	0.0176
1374.25	-0.1	0.5935	0.01315	0.2867	0.01404
1374.25	0.1	0.6645	0.01262	0.3652	0.01344
1374.25	0.3	0.6953	0.01194	0.4295	0.01313
1374.25	0.5	0.7221	0.01157	0.4264	0.01258
1374.25	0.7	0.6899	0.01115	0.4349	0.01366
1374.25	0.9	0.6245	0.01107	0.4003	0.01549
1424.81	-0.9	0.6839	0.02476	0.1498	0.03795
1424.81	-0.7	0.6203	0.0206	0.1586	0.02634
1424.81	-0.5	0.5871	0.01748	0.1964	0.02123
1424.81	-0.3	0.5572	0.01495	0.212	0.01723
1424.81	-0.1	0.5921	0.01373	0.3082	0.01656
1424.81	0.1	0.6345	0.0129	0.3499	0.01416
1424.81	0.3	0.6847	0.01246	0.434	0.01459
1424.81	0.5	0.717	0.01219	0.4017	0.01363
1424.81	0.7	0.6749	0.01173	0.4051	0.01451
1424.81	0.9	0.6501	0.01206	0.4209	0.01789
1474.64	-0.9	0.6189	0.02356	0.1446	0.04423
1474.64	-0.7	0.5686	0.02008	0.121	0.02576
1474.64	-0.5	0.5285	0.0171	0.1037	0.01717
1474.64	-0.3	0.5378	0.01528	0.1653	0.01597
1474.64	-0.1	0.5452	0.01379	0.2233	0.01454
1474.64	0.1	0.6242	0.01346	0.3069	0.01418
1474.64	0.3	0.6888	0.0132	0.3783	0.01425
1474.64	0.5	0.7115	0.01287	0.4021	0.01436
1474.64	0.7	0.7446	0.01312	0.4213	0.01587
1474.64	0.9	0.721	0.01359	0.3863	0.01805

E_γ	$cos(\theta_{cm})$	$d\sigma/d\Omega(NNX\eta)$	sta. er.	$d\sigma/d\Omega(pn\eta)$	sta. er.
1524.44	-0.9	0.6029	0.02298	0.02131	0.02403
1524.44	-0.7	0.5594	0.01917	0.1072	0.02571
1524.44	-0.5	0.5033	0.01604	0.08457	0.01599
1524.44	-0.3	0.5063	0.01434	0.1272	0.01471
1524.44	-0.1	0.5332	0.01328	0.189	0.01381
1524.44	0.1	0.5931	0.01284	0.3107	0.01485
1524.44	0.3	0.683	0.01292	0.3457	0.01375
1524.44	0.5	0.72	0.01279	0.4024	0.01514
1524.44	0.7	0.7765	0.01331	0.4343	0.01662
1524.44	0.9	0.8286	0.01467	0.4986	0.02222
1574.72	-0.9	0.6111	0.02193	0.1569	0.04925
1574.72	-0.7	0.55	0.0181	0.1062	0.02886
1574.72	-0.5	0.4883	0.01502	0.09769	0.01733
1574.72	-0.3	0.4733	0.01317	0.1103	0.01321
1574.72	-0.1	0.5048	0.01227	0.1606	0.0115
1574.72	0.1	0.5684	0.01197	0.2311	0.01154
1574.72	0.3	0.6205	0.01175	0.2965	0.01216
1574.72	0.5	0.7075	0.01213	0.3076	0.01201
1574.72	0.7	0.7699	0.01273	0.3417	0.01373
1574.72	0.9	0.8448	0.01429	0.4648	0.01982
1624.57	-0.9	0.6451	0.02378	0.008643	0.01134
1624.57	-0.7	0.572	0.01978	0.1411	0.03294
1624.57	-0.5	0.475	0.01571	0.04583	0.01271
1624.57	-0.3	0.4585	0.01361	0.1006	0.01328
1624.57	-0.1	0.4776	0.01251	0.1937	0.01438
1624.57	0.1	0.5492	0.01238	0.2433	0.01345
1624.57	0.3	0.6727	0.01298	0.3187	0.01405
1624.57	0.5	0.7088	0.01301	0.3303	0.01434
1624.57	0.7	0.8049	0.01405	0.4012	0.01679
1624.57	0.9	0.9095	0.01602	0.5731	0.02547

E_γ	$cos(\theta_{cm})$	$d\sigma/d\Omega(NNX\eta)$	sta. er.	$d\sigma/d\Omega(pn\eta)$	sta. er.
1674.4	-0.9	0.5909	0.02337	0.09255	0.03775
1674.4	-0.7	0.5008	0.01842	0.07006	0.02689
1674.4	-0.5	0.4592	0.01552	0.06676	0.0158
1674.4	-0.3	0.425	0.01338	0.09687	0.01422
1674.4	-0.1	0.4672	0.01278	0.1558	0.01354
1674.4	0.1	0.558	0.01296	0.2229	0.01296
1674.4	0.3	0.6754	0.01353	0.2686	0.013
1674.4	0.5	0.7656	0.01406	0.3527	0.01527
1674.4	0.7	0.8505	0.01505	0.4198	0.0178
1674.4	0.9	0.9572	0.01731	0.5314	0.02498
1725.13	-0.9	0.6155	0.02344	0.07592	0.06458
1725.13	-0.7	0.5398	0.01915	0.1409	0.0459
1725.13	-0.5	0.4519	0.01541	0.02666	0.01039
1725.13	-0.3	0.4327	0.01349	0.08298	0.01385
1725.13	-0.1	0.4779	0.01292	0.1542	0.0141
1725.13	0.1	0.5285	0.01266	0.1802	0.01256
1725.13	0.3	0.6312	0.01322	0.2533	0.01362
1725.13	0.5	0.7373	0.01404	0.3196	0.01557
1725.13	0.7	0.8434	0.01536	0.4471	0.0196
1725.13	0.9	0.9154	0.01741	0.5012	0.02626
1775.3	-0.9	0.5661	0.02328	0.0304	0.02683
1775.3	-0.7	0.4965	0.01884	0.1278	0.04112
1775.3	-0.5	0.4263	0.01523	0.06385	0.01575
1775.3	-0.3	0.4235	0.01351	0.07048	0.01237
1775.3	-0.1	0.4544	0.01275	0.1197	0.01232
1775.3	0.1	0.576	0.01341	0.1687	0.01223
1775.3	0.3	0.6562	0.01372	0.2138	0.01253
1775.3	0.5	0.7577	0.01456	0.3051	0.01562
1775.3	0.7	0.8937	0.01624	0.4248	0.01926
1775.3	0.9	0.9725	0.01848	0.4806	0.02628

E_γ	$cos(\theta_{cm})$	$d\sigma/d\Omega(NNX\eta)$	sta. er.	$d\sigma/d\Omega(pn\eta)$	sta. er.
1825.16	-0.9	0.5958	0.02465	0.1756	0.06215
1825.16	-0.7	0.4845	0.01869	0.1138	0.04244
1825.16	-0.5	0.4357	0.01532	0.01556	0.008431
1825.16	-0.3	0.3973	0.01303	0.04148	0.009833
1825.16	-0.1	0.4581	0.01279	0.1333	0.01366
1825.16	0.1	0.5361	0.01299	0.134	0.01086
1825.16	0.3	0.653	0.01382	0.2445	0.0142
1825.16	0.5	0.7581	0.01479	0.2934	0.01544
1825.16	0.7	0.8986	0.01661	0.4433	0.02082
1825.16	0.9	0.9838	0.01899	0.5601	0.0302
1874.89	-0.9	0.6575	0.02543	0.02901	0.03945
1874.89	-0.7	0.55	0.0199	0.1579	0.07044
1874.89	-0.5	0.4594	0.01573	0.09982	0.02354
1874.89	-0.3	0.4308	0.01352	0.09216	0.01499
1874.89	-0.1	0.4478	0.0126	0.08115	0.01057
1874.89	0.1	0.4972	0.01249	0.1066	0.009816
1874.89	0.3	0.6116	0.01341	0.1857	0.01215
1874.89	0.5	0.7415	0.01474	0.2819	0.01565
1874.89	0.7	0.8821	0.01666	0.4351	0.02087
1874.89	0.9	0.9703	0.01915	0.4962	0.0271
1925.03	-0.9	0.6006	0.02427	0.03815	0.03417
1925.03	-0.7	0.4917	0.0186	0.1657	0.05248
1925.03	-0.5	0.4361	0.01509	0.02663	0.01154
1925.03	-0.3	0.3982	0.01281	0.03459	0.009638
1925.03	-0.1	0.4492	0.01246	0.08323	0.01061
1925.03	0.1	0.5244	0.01271	0.1384	0.01141
1925.03	0.3	0.6266	0.0135	0.1994	0.01287
1925.03	0.5	0.7589	0.01488	0.2955	0.01627
1925.03	0.7	0.8994	0.01685	0.4447	0.0218
1925.03	0.9	0.9848	0.01934	0.5748	0.03174

E_γ	$cos(\theta_{cm})$	$d\sigma/d\Omega(NNX\eta)$	sta. er.	$d\sigma/d\Omega(pn\eta)$	sta. er.
1975.19	-0.9	0.6318	0.02538	0.1914	0.3362
1975.19	-0.7	0.5349	0.01988	0.1425	0.07674
1975.19	-0.5	0.4083	0.01507	0.002384	0.004967
1975.19	-0.3	0.4247	0.01374	0.02137	0.00809
1975.19	-0.1	0.4494	0.01301	0.0633	0.009936
1975.19	0.1	0.5247	0.01332	0.09879	0.009968
1975.19	0.3	0.6125	0.01403	0.1852	0.01343
1975.19	0.5	0.7499	0.01561	0.3066	0.01799
1975.19	0.7	0.9417	0.01826	0.5639	0.02649
1975.19	0.9	1.024	0.021	0.5047	0.03127
2024.9	-0.9	0.561	0.02515	0	0.1234
2024.9	-0.7	0.4759	0.01968	0.06663	0.06664
2024.9	-0.5	0.4018	0.01576	0.007143	0.007677
2024.9	-0.3	0.4217	0.01453	0.01514	0.007455
2024.9	-0.1	0.4375	0.0137	0.0534	0.009403
2024.9	0.1	0.5367	0.01446	0.1047	0.01127
2024.9	0.3	0.6207	0.01522	0.1782	0.01398
2024.9	0.5	0.7409	0.01677	0.3114	0.01931
2024.9	0.7	0.8892	0.01923	0.4772	0.02611
2024.9	0.9	0.995	0.02246	0.4924	0.03269
2064.63	-0.9	0.6044	0.03296	0.05831	0.08723
2064.63	-0.7	0.4923	0.02407	0	0.1001
2064.63	-0.5	0.4357	0.01953	0.03436	0.02308
2064.63	-0.3	0.4305	0.01746	0.04463	0.01489
2064.63	-0.1	0.4544	0.01669	0.05771	0.01177
2064.63	0.1	0.524	0.01716	0.1082	0.013
2064.63	0.3	0.5889	0.01788	0.1332	0.0142
2064.63	0.5	0.7522	0.02045	0.2679	0.02063
2064.63	0.7	0.8883	0.02331	0.528	0.03262
2064.63	0.9	0.9371	0.02647	0.4429	0.03748

E_γ	$cos(\theta_{cm})$	$d\sigma/d\Omega(NNX\eta)$	sta. er.	$d\sigma/d\Omega(pn\eta)$	sta. er.
2125.01	-0.9	0.6625	0.03281	0.0131	0.04779
2125.01	-0.7	0.5116	0.02529	0.04177	0.03973
2125.01	-0.5	0.4153	0.01978	0.01022	0.01086
2125.01	-0.3	0.4022	0.01736	0.01603	0.00979
2125.01	-0.1	0.4177	0.01633	0.0682	0.01509
2125.01	0.1	0.4803	0.01673	0.07016	0.01317
2125.01	0.3	0.6102	0.01861	0.1742	0.02009
2125.01	0.5	0.6921	0.02021	0.2788	0.02636
2125.01	0.7	0.9235	0.02471	0.468	0.03672
2125.01	0.9	1.051	0.02916	0.4986	0.04839
2175.64	-0.9	0.6644	0.03734	0	0.1003
2175.64	-0.7	0.5138	0.02666	0.0614	0.08456
2175.64	-0.5	0.4036	0.02023	0.02208	0.01905
2175.64	-0.3	0.3879	0.01776	0.03713	0.01569
2175.64	-0.1	0.4104	0.01698	0.04468	0.01263
2175.64	0.1	0.4939	0.01788	0.06937	0.01344
2175.64	0.3	0.5933	0.01938	0.152	0.01863
2175.64	0.5	0.7035	0.02155	0.2699	0.02678
2175.64	0.7	0.8683	0.02537	0.3739	0.03437
2175.64	0.9	0.9627	0.02978	0.3917	0.04466
2250.42	-0.9	0.7079	0.02593	0.01861	0.02697
2250.42	-0.7	0.5156	0.01881	0.08983	0.0477
2250.42	-0.5	0.4184	0.01464	0.004555	0.005661
2250.42	-0.3	0.3902	0.01267	0.02899	0.01009
2250.42	-0.1	0.4252	0.0123	0.01946	0.006072
2250.42	0.1	0.457	0.01227	0.095	0.01176
2250.42	0.3	0.56	0.01351	0.1577	0.01457
2250.42	0.5	0.6598	0.01509	0.2378	0.01907
2250.42	0.7	0.8276	0.01803	0.5272	0.03159
2250.42	0.9	0.9661	0.02167	0.424	0.03703

E_γ	$cos(\theta_{cm})$	$d\sigma/d\Omega(NNX\eta)$	sta. er.	$d\sigma/d\Omega(pn\eta)$	sta. er.
2350.36	-0.9	0.631	0.024	0	0.12
2350.36	-0.7	0.4852	0.0177	-0.06633	0.0365
2350.36	-0.5	0.3895	0.01372	0	0.12
2350.36	-0.3	0.3693	0.01203	0.02254	0.01301
2350.36	-0.1	0.4086	0.01183	0.0383	0.01042
2350.36	0.1	0.4843	0.01248	0.08462	0.01222
2350.36	0.3	0.5691	0.01356	0.1266	0.01438
2350.36	0.5	0.6632	0.01515	0.2572	0.02113
2350.36	0.7	0.8715	0.01862	0.484	0.03219
2350.36	0.9	1.002	0.02218	0.4344	0.03882
2449.69	-0.9	0.6575	0.02675	0.01023	0.0109
2449.69	-0.7	0.5023	0.01996	-0.01467	0.01038
2449.69	-0.5	0.4629	0.01655	-0.00547	0.00709
2449.69	-0.3	0.4366	0.01442	0	0.1026
2449.69	-0.1	0.4334	0.01344	0.04648	0.01453
2449.69	0.1	0.5056	0.01408	0.06749	0.01202
2449.69	0.3	0.5671	0.01499	0.09988	0.01365
2449.69	0.5	0.6968	0.01733	0.1826	0.01877
2449.69	0.7	0.9105	0.02145	0.36	0.0286
2449.69	0.9	1.107	0.02658	0.3971	0.04158

E_γ	$cos(\theta_{cm})$	$d\sigma/d\Omega(p\eta)$	sta. er.	$d\sigma/d\Omega(n\eta)$	sta. er.
637.672	-0.9	0.07465	0.01056	0.0397	0.01451
637.672	-0.7	0.05256	0.01067	0	0.04742
637.672	-0.5	0.02942	0.005801	0	0.04715
637.672	-0.3	0.03011	0.006883	0.004052	0.002907
637.672	-0.1	0	0.0809	0.004034	0.002059
637.672	0.1	0	0.08838	0	0.04749
637.672	0.3	0	0.07954	0	0.04274
637.672	0.5	0	0.07728	0	0.04153
637.672	0.7	0	0.09257	0	0.04974
637.672	0.9	0	0.08186	0	0.04399
661.95	-0.9	0.09867	0.007554	0.08711	0.01697
661.95	-0.7	0.06519	0.005898	0.0699	0.01623
661.95	-0.5	0.06406	0.006109	0.06561	0.01692
661.95	-0.3	0.05535	0.007265	0.05872	0.01339
661.95	-0.1	0.04896	0.005774	0.0386	0.0115
661.95	0.1	0.03259	0.006406	0.008688	0.005446
661.95	0.3	0.1788	0.02457	0.05883	0.02202
661.95	0.5	0.07691	0.01364	0.001059	0.001689
661.95	0.7	0.1053	0.01591	0.01416	0.01376
661.95	0.9	0.02369	0.004289	0	0.04821
688.582	-0.9	0.2433	0.01023	0.2374	0.02655
688.582	-0.7	0.2003	0.008759	0.1851	0.02262
688.582	-0.5	0.2234	0.009746	0.2374	0.02764
688.582	-0.3	0.2118	0.009715	0.1532	0.01909
688.582	-0.1	0.1901	0.009312	0.1493	0.02041
688.582	0.1	0.1929	0.009636	0.1638	0.0233
688.582	0.3	0.2132	0.01091	0.1234	0.01947
688.582	0.5	0.1421	0.008913	0.1224	0.0192
688.582	0.7	0.1147	0.007275	0.1412	0.02303
688.582	0.9	0.1065	0.008079	0.03428	0.009554

E_γ	$cos(\theta_{cm})$	$d\sigma/d\Omega(p\eta)$	sta. er.	$d\sigma/d\Omega(n\eta)$	sta. er.
714.707	-0.9	0.5188	0.01768	0.5503	0.04204
714.707	-0.7	0.4414	0.01462	0.3756	0.03319
714.707	-0.5	0.4071	0.01313	0.3631	0.0308
714.707	-0.3	0.4673	0.01444	0.3427	0.0317
714.707	-0.1	0.4425	0.01415	0.3316	0.02915
714.707	0.1	0.4115	0.01338	0.3443	0.02973
714.707	0.3	0.4422	0.01469	0.2394	0.02466
714.707	0.5	0.4209	0.01482	0.3451	0.02978
714.707	0.7	0.3716	0.01407	0.3193	0.03035
714.707	0.9	0.2915	0.01267	0.2344	0.02646
737.573	-0.9	0.7559	0.02326	0.7321	0.05224
737.573	-0.7	0.7461	0.02055	0.5942	0.04222
737.573	-0.5	0.7345	0.01881	0.5582	0.03942
737.573	-0.3	0.7615	0.01905	0.5191	0.03687
737.573	-0.1	0.7522	0.0183	0.5224	0.0355
737.573	0.1	0.7663	0.01867	0.487	0.03414
737.573	0.3	0.6962	0.01756	0.5333	0.03505
737.573	0.5	0.6911	0.0178	0.52	0.03452
737.573	0.7	0.6245	0.01763	0.5066	0.03692
737.573	0.9	0.5454	0.01835	0.5044	0.03765
760.016	-0.9	0.9146	0.02786	0.8873	0.06375
760.016	-0.7	0.9094	0.02418	0.8135	0.05139
760.016	-0.5	0.926	0.02201	0.6649	0.04404
760.016	-0.3	0.9229	0.021	0.639	0.04056
760.016	-0.1	0.8811	0.01923	0.6394	0.03785
760.016	0.1	0.883	0.01917	0.6849	0.03919
760.016	0.3	0.8479	0.01821	0.5547	0.03229
760.016	0.5	0.7767	0.01744	0.541	0.0327
760.016	0.7	0.9184	0.02148	0.6604	0.03661
760.016	0.9	0.8677	0.02419	0.5383	0.03649

E_γ	$cos(\theta_{cm})$	$d\sigma/d\Omega(p\eta)$	sta. er.	$d\sigma/d\Omega(n\eta)$	sta. er.
786.525	-0.9	1.074	0.02804	0.8332	0.05034
786.525	-0.7	1.033	0.02265	0.8273	0.04466
786.525	-0.5	1.016	0.01991	0.6403	0.03641
786.525	-0.3	0.9882	0.01807	0.6584	0.03365
786.525	-0.1	1.015	0.01752	0.665	0.03198
786.525	0.1	0.9892	0.01689	0.6697	0.03106
786.525	0.3	1.033	0.01763	0.7448	0.03249
786.525	0.5	0.9087	0.01626	0.6393	0.02906
786.525	0.7	1.003	0.01875	0.6425	0.02959
786.525	0.9	0.9754	0.02179	0.6815	0.03357
812.518	-0.9	1.032	0.03539	0.9404	0.06694
812.518	-0.7	1.076	0.03007	0.7	0.04921
812.518	-0.5	0.9834	0.02389	0.7034	0.04303
812.518	-0.3	1.034	0.02269	0.6472	0.04055
812.518	-0.1	1.079	0.02183	0.6326	0.03668
812.518	0.1	1.079	0.021	0.6779	0.03692
812.518	0.3	1.133	0.02268	0.6662	0.0365
812.518	0.5	1.099	0.02373	0.6894	0.03571
812.518	0.7	1.038	0.02365	0.6747	0.03651
812.518	0.9	0.9937	0.0276	0.7781	0.04288
837.885	-0.9	0.9561	0.04089	0.9721	0.102
837.885	-0.7	0.8432	0.02945	0.9079	0.07776
837.885	-0.5	0.9599	0.02804	0.5245	0.04744
837.885	-0.3	0.894	0.02384	0.5168	0.04463
837.885	-0.1	0.9299	0.02278	0.5252	0.0408
837.885	0.1	0.936	0.0224	0.4808	0.03818
837.885	0.3	0.9727	0.02444	0.5071	0.03939
837.885	0.5	1.023	0.03061	0.6646	0.05036
837.885	0.7	0.9439	0.03449	0.5145	0.04216
837.885	0.9	1.109	0.05236	0.8937	0.07793

E_γ	$cos(\theta_{cm})$	$d\sigma/d\Omega(p\eta)$	sta. er.	$d\sigma/d\Omega(n\eta)$	sta. er.
862.764	-0.9	1.007	0.05593	0.9146	0.1152
862.764	-0.7	0.8781	0.03951	0.5606	0.07103
862.764	-0.5	0.8745	0.03314	0.5841	0.06357
862.764	-0.3	0.9417	0.03264	0.4226	0.05045
862.764	-0.1	0.9422	0.03049	0.4855	0.04839
862.764	0.1	0.9976	0.02989	0.4355	0.0446
862.764	0.3	0.9755	0.03126	0.5608	0.04943
862.764	0.5	0.9159	0.03703	0.4985	0.04805
862.764	0.7	0.6415	0.03283	0.4695	0.05033
862.764	0.9	0.7168	0.05597	0.6796	0.08171
887.05	-0.9	0.9839	0.05259	0.712	0.08887
887.05	-0.7	0.801	0.03412	0.5537	0.06224
887.05	-0.5	0.78	0.02879	0.5393	0.05755
887.05	-0.3	0.9066	0.02889	0.5229	0.04845
887.05	-0.1	0.8471	0.02458	0.3739	0.03823
887.05	0.1	0.8502	0.02297	0.5081	0.04159
887.05	0.3	0.8481	0.02436	0.3486	0.03148
887.05	0.5	0.813	0.02889	0.4675	0.04077
887.05	0.7	0.6235	0.03059	0.6001	0.05363
887.05	0.9	0.2993	0.02396	0.4616	0.05598
912.504	-0.9	0.7612	0.05092	0.7704	0.1147
912.504	-0.7	0.7432	0.03864	0.4844	0.06593
912.504	-0.5	0.6818	0.03166	0.392	0.04915
912.504	-0.3	0.646	0.02697	0.4226	0.04741
912.504	-0.1	0.7124	0.02571	0.278	0.03202
912.504	0.1	0.6771	0.02251	0.3452	0.03441
912.504	0.3	0.5837	0.02043	0.3922	0.0399
912.504	0.5	0.6	0.02425	0.4361	0.04277
912.504	0.7	0.5216	0.03375	0.3672	0.043
912.504	0.9	0.2817	0.03063	0.3289	0.05007

E_γ	$cos(\theta_{cm})$	$d\sigma/d\Omega(p\eta)$	sta. er.	$d\sigma/d\Omega(n\eta)$	sta. er.
937.34	-0.9	0.4891	0.03726	0.5034	0.08015
937.34	-0.7	0.5717	0.0324	0.5381	0.06543
937.34	-0.5	0.5359	0.02638	0.5088	0.0606
937.34	-0.3	0.5103	0.02174	0.3496	0.03846
937.34	-0.1	0.5259	0.01942	0.4393	0.04259
937.34	0.1	0.4818	0.01697	0.4259	0.03675
937.34	0.3	0.4794	0.01611	0.3908	0.03552
937.34	0.5	0.4652	0.01811	0.3955	0.037
937.34	0.7	0.5324	0.03557	0.3434	0.03447
937.34	0.9	0.3974	0.04835	0.6006	0.08165
963.926	-0.9	0.4374	0.03973	0.3922	0.06536
963.926	-0.7	0.4996	0.03453	0.4905	0.06353
963.926	-0.5	0.5106	0.02826	0.377	0.0488
963.926	-0.3	0.5554	0.02694	0.5114	0.05137
963.926	-0.1	0.4839	0.02019	0.4818	0.04462
963.926	0.1	0.449	0.01813	0.4457	0.03688
963.926	0.3	0.5451	0.01994	0.6838	0.05269
963.926	0.5	0.4797	0.02071	0.5717	0.04751
963.926	0.7	0.3071	0.0243	0.4597	0.04518
963.926	0.9	0.3315	0.05114	0.446	0.06943
989.864	-0.9	0.4193	0.04141	0.5346	0.1025
989.864	-0.7	0.3839	0.02978	0.5148	0.0769
989.864	-0.5	0.3095	0.02212	0.6256	0.06776
989.864	-0.3	0.391	0.02247	0.4021	0.04584
989.864	-0.1	0.3549	0.01697	0.3603	0.03711
989.864	0.1	0.3397	0.01484	0.4227	0.03767
989.864	0.3	0.3151	0.01339	0.5276	0.04215
989.864	0.5	0.3449	0.01628	0.48	0.04076
989.864	0.7	0.2388	0.02179	0.402	0.0402
989.864	0.9	0.1321	0.02448	0.414	0.06911

E_γ	$cos(\theta_{cm})$	$d\sigma/d\Omega(p\eta)$	sta. er.	$d\sigma/d\Omega(n\eta)$	sta. er.
1025.27	-0.9	0.2825	0.02792	0.3827	0.06498
1025.27	-0.7	0.3072	0.02039	0.495	0.05868
1025.27	-0.5	0.2844	0.01642	0.4796	0.04819
1025.27	-0.3	0.2999	0.01415	0.4323	0.0382
1025.27	-0.1	0.26	0.01081	0.4662	0.03502
1025.27	0.1	0.3024	0.01059	0.4194	0.02972
1025.27	0.3	0.2921	0.009637	0.4284	0.0296
1025.27	0.5	0.2809	0.01004	0.5137	0.03546
1025.27	0.7	0.2788	0.01751	0.3845	0.03614
1025.27	0.9	0.1986	0.03928	0.2514	0.04374
1074.13	-0.9	0.1888	0.02374	0.3231	0.07204
1074.13	-0.7	0.1993	0.01677	0.2926	0.04335
1074.13	-0.5	0.2054	0.0142	0.4187	0.04447
1074.13	-0.3	0.2761	0.01429	0.3976	0.03578
1074.13	-0.1	0.3003	0.01203	0.425	0.03183
1074.13	0.1	0.3252	0.01057	0.4215	0.02782
1074.13	0.3	0.3427	0.009931	0.3823	0.02641
1074.13	0.5	0.3376	0.0103	0.4547	0.03042
1074.13	0.7	0.2881	0.016	0.4663	0.03963
1074.13	0.9	0.1386	0.04537	0.3128	0.04787
1124.08	-0.9	0.1362	0.02064	0.249	0.05523
1124.08	-0.7	0.1512	0.01536	0.2459	0.0448
1124.08	-0.5	0.2027	0.01518	0.2514	0.03441
1124.08	-0.3	0.2711	0.01463	0.2621	0.03031
1124.08	-0.1	0.3146	0.01275	0.3502	0.03051
1124.08	0.1	0.3556	0.01185	0.347	0.02691
1124.08	0.3	0.3366	0.01018	0.3941	0.02721
1124.08	0.5	0.345	0.01089	0.2862	0.02483
1124.08	0.7	0.2475	0.01393	0.2698	0.03284
1124.08	0.9	0.0565	0.04403	0.3185	0.0507

E_γ	$cos(\theta_{cm})$	$d\sigma/d\Omega(p\eta)$	sta. er.	$d\sigma/d\Omega(n\eta)$	sta. er.
1174.51	-0.9	0.1093	0.01971	0.1641	0.05259
1174.51	-0.7	0.1606	0.01843	0.1691	0.03743
1174.51	-0.5	0.2038	0.0167	0.3087	0.04302
1174.51	-0.3	0.2647	0.01517	0.4142	0.04096
1174.51	-0.1	0.2559	0.01177	0.3087	0.02834
1174.51	0.1	0.3499	0.01176	0.3312	0.02491
1174.51	0.3	0.362	0.0106	0.3122	0.0225
1174.51	0.5	0.33	0.01009	0.3403	0.02588
1174.51	0.7	0.2444	0.01148	0.3555	0.03475
1174.51	0.9	0.07901	0.03983	0.3067	0.05138
1226.52	-0.9	0.05744	0.01793	0.01882	0.02966
1226.52	-0.7	0.1218	0.01874	0.1321	0.03692
1226.52	-0.5	0.1377	0.01526	0.2108	0.03667
1226.52	-0.3	0.2249	0.01505	0.1869	0.02971
1226.52	-0.1	0.2669	0.01309	0.2457	0.02857
1226.52	0.1	0.3226	0.01216	0.2917	0.02655
1226.52	0.3	0.3411	0.01107	0.3477	0.02778
1226.52	0.5	0.324	0.01074	0.3251	0.02874
1226.52	0.7	0.269	0.01299	0.3108	0.03643
1226.52	0.9	0.2106	0.04355	0.5247	0.09987
1276.68	-0.9	0.01221	0.009458	0.04495	0.03359
1276.68	-0.7	0.1324	0.02165	0.1328	0.04439
1276.68	-0.5	0.1279	0.01581	0.1584	0.03648
1276.68	-0.3	0.1889	0.01522	0.1843	0.0272
1276.68	-0.1	0.2166	0.01223	0.2234	0.02539
1276.68	0.1	0.255	0.01127	0.2735	0.02533
1276.68	0.3	0.2801	0.0105	0.3818	0.02776
1276.68	0.5	0.2805	0.01051	0.3963	0.03163
1276.68	0.7	0.2372	0.01234	0.3441	0.03753
1276.68	0.9	0.2185	0.05281	0.2853	0.06113

E_γ	$cos(\theta_{cm})$	$d\sigma/d\Omega(p\eta)$	sta. er.	$d\sigma/d\Omega(n\eta)$	sta. er.
1325.1	-0.9	0.05234	0.02347	0.06591	0.0746
1325.1	-0.7	0.04724	0.01362	0.1602	0.04994
1325.1	-0.5	0.197	0.02532	0.2124	0.04447
1325.1	-0.3	0.1696	0.01598	0.1683	0.03301
1325.1	-0.1	0.1842	0.01311	0.2597	0.03133
1325.1	0.1	0.2574	0.01274	0.2183	0.02444
1325.1	0.3	0.2659	0.01153	0.2787	0.02646
1325.1	0.5	0.2747	0.01204	0.3014	0.03134
1325.1	0.7	0.242	0.01384	0.2605	0.03829
1325.1	0.9	0.1372	0.03877	0.2354	0.06403
1374.25	-0.9	0	0.07599	0.07061	0.07292
1374.25	-0.7	0.04907	0.01513	0.1641	0.04911
1374.25	-0.5	0.08559	0.01482	0.241	0.04649
1374.25	-0.3	0.1389	0.01465	0.216	0.03447
1374.25	-0.1	0.1723	0.012	0.2005	0.02546
1374.25	0.1	0.2221	0.01113	0.1851	0.02071
1374.25	0.3	0.2532	0.01073	0.1841	0.01965
1374.25	0.5	0.2382	0.0103	0.2102	0.02263
1374.25	0.7	0.2576	0.01444	0.2125	0.03066
1374.25	0.9	0.1741	0.05347	0.1779	0.05031
1424.81	-0.9	0.05772	0.03365	0.05308	0.07302
1424.81	-0.7	0.04853	0.01651	0.08632	0.04176
1424.81	-0.5	0.1125	0.01804	0.08162	0.029
1424.81	-0.3	0.111	0.01336	0.1893	0.04031
1424.81	-0.1	0.1597	0.01243	0.2627	0.03803
1424.81	0.1	0.1582	0.00927	0.2816	0.03085
1424.81	0.3	0.2011	0.009554	0.2675	0.02869
1424.81	0.5	0.1922	0.009743	0.2238	0.02869
1424.81	0.7	0.2187	0.01364	0.2971	0.04737
1424.81	0.9	0.2926	0.05827	0.07849	0.04112

E_γ	$cos(\theta_{cm})$	$d\sigma/d\Omega(p\eta)$	sta. er.	$d\sigma/d\Omega(n\eta)$	sta. er.
1474.64	-0.9	0	0.07933	0.06023	0.09205
1474.64	-0.7	0.01522	0.00962	0.1248	0.05547
1474.64	-0.5	0.0308	0.01013	0.02383	0.01908
1474.64	-0.3	0.1129	0.0162	0.1116	0.0316
1474.64	-0.1	0.1633	0.01444	0.1298	0.0254
1474.64	0.1	0.2011	0.01198	0.1703	0.0252
1474.64	0.3	0.2052	0.01062	0.2352	0.02856
1474.64	0.5	0.2311	0.01179	0.2212	0.03055
1474.64	0.7	0.2722	0.01683	0.1761	0.03531
1474.64	0.9	0.207	0.04876	0.1098	0.05874
1524.44	-0.9	0	0.1096	0	0.08924
1524.44	-0.7	0.06681	0.02055	0.004044	0.01019
1524.44	-0.5	0.03674	0.01426	0.05824	0.02521
1524.44	-0.3	0.09239	0.01522	0.0982	0.03097
1524.44	-0.1	0.09562	0.01104	0.1556	0.0277
1524.44	0.1	0.1633	0.01069	0.1688	0.02436
1524.44	0.3	0.1532	0.008438	0.164	0.02233
1524.44	0.5	0.1998	0.0106	0.1978	0.0293
1524.44	0.7	0.2066	0.01256	0.2307	0.03771
1524.44	0.9	0.1862	0.0349	0.2237	0.08303
1574.72	-0.9	0.06857	0.04654	0	0.08528
1574.72	-0.7	0.03854	0.01902	0.03521	0.02862
1574.72	-0.5	0.06143	0.01512	0.03536	0.02282
1574.72	-0.3	0.05616	0.01078	0.09945	0.02908
1574.72	-0.1	0.1048	0.01018	0.08862	0.01895
1574.72	0.1	0.1313	0.008985	0.1374	0.02006
1574.72	0.3	0.1419	0.008398	0.2089	0.02398
1574.72	0.5	0.1528	0.008958	0.182	0.02461
1574.72	0.7	0.1776	0.01144	0.1772	0.03253
1574.72	0.9	0.2433	0.03562	0.2858	0.08025

E_γ	$cos(\theta_{cm})$	$d\sigma/d\Omega(p\eta)$	sta. er.	$d\sigma/d\Omega(n\eta)$	sta. er.
1624.57	-0.9	0.02572	0.05865	0	0.07641
1624.57	-0.7	0.03306	0.01556	0.1382	0.06114
1624.57	-0.5	0.05537	0.01834	0.08657	0.03542
1624.57	-0.3	0.08613	0.01514	0.04511	0.01863
1624.57	-0.1	0.1125	0.01196	0.1048	0.02198
1624.57	0.1	0.1136	0.008622	0.1456	0.02144
1624.57	0.3	0.1146	0.007345	0.221	0.02499
1624.57	0.5	0.1492	0.009128	0.1348	0.02133
1624.57	0.7	0.1838	0.01198	0.2065	0.03581
1624.57	0.9	0.3493	0.04717	0.2778	0.08381
1674.4	-0.9	0.1338	0.06374	0.0253	0.106
1674.4	-0.7	0.1184	0.04803	0.04311	0.05654
1674.4	-0.5	0.06351	0.01923	0.03772	0.02417
1674.4	-0.3	0.05435	0.01167	0.05941	0.02328
1674.4	-0.1	0.06934	0.00941	0.1175	0.0253
1674.4	0.1	0.1005	0.008072	0.1293	0.02068
1674.4	0.3	0.09431	0.006687	0.1214	0.01842
1674.4	0.5	0.1368	0.008618	0.1591	0.02444
1674.4	0.7	0.1817	0.01191	0.2039	0.03681
1674.4	0.9	0.1226	0.02014	0.19	0.07527
1725.13	-0.9	0.1043	0.1035	0.03278	0.09023
1725.13	-0.7	0.04954	0.02639	0.05994	0.0681
1725.13	-0.5	0.02882	0.01266	0	0.06533
1725.13	-0.3	0.04945	0.01117	0.05195	0.02881
1725.13	-0.1	0.07287	0.009771	0.08608	0.01952
1725.13	0.1	0.07558	0.007853	0.09444	0.01641
1725.13	0.3	0.1002	0.007747	0.103	0.01632
1725.13	0.5	0.1208	0.009257	0.1177	0.01917
1725.13	0.7	0.1843	0.01334	0.2288	0.03686
1725.13	0.9	0.2967	0.05048	0.2854	0.08136

E_γ	$cos(\theta_{cm})$	$d\sigma/d\Omega(p\eta)$	sta. er.	$d\sigma/d\Omega(n\eta)$	sta. er.
1775.3	-0.9	0	0.06675	0	0.07854
1775.3	-0.7	0.06681	0.04373	0.0956	0.08906
1775.3	-0.5	0.04655	0.0163	0.05994	0.03365
1775.3	-0.3	0.05054	0.01316	0.05833	0.02483
1775.3	-0.1	0.08626	0.01109	0.0567	0.01821
1775.3	0.1	0.07942	0.008061	0.1199	0.02072
1775.3	0.3	0.07874	0.007157	0.1119	0.018
1775.3	0.5	0.1042	0.00895	0.2321	0.03148
1775.3	0.7	0.1769	0.01379	0.203	0.03819
1775.3	0.9	0.2321	0.03847	0.1253	0.06044
1825.16	-0.9	0	0.07217	0.03408	0.08529
1825.16	-0.7	0.06618	0.05827	0.1472	0.07478
1825.16	-0.5	0.03913	0.02583	0.02768	0.02185
1825.16	-0.3	0.02384	0.009492	0.03823	0.01862
1825.16	-0.1	0.068	0.01039	0.0251	0.01053
1825.16	0.1	0.07166	0.008086	0.06287	0.01313
1825.16	0.3	0.1021	0.008733	0.1077	0.01741
1825.16	0.5	0.1328	0.01027	0.1539	0.02234
1825.16	0.7	0.1976	0.01525	0.2081	0.03512
1825.16	0.9	0.2684	0.04431	0.3656	0.1054
1874.89	-0.9	0	0.06922	0	0.06079
1874.89	-0.7	0.03274	0.04592	0	0.06079
1874.89	-0.5	0.04053	0.01991	0.04904	0.02784
1874.89	-0.3	0.07295	0.01669	0.07419	0.03818
1874.89	-0.1	0.05305	0.00976	0.03642	0.01228
1874.89	0.1	0.05497	0.006962	0.03959	0.01057
1874.89	0.3	0.0626	0.006512	0.08051	0.01427
1874.89	0.5	0.1116	0.009783	0.1327	0.02082
1874.89	0.7	0.1845	0.01447	0.2764	0.04244
1874.89	0.9	0.2841	0.03923	0.276	0.08038

E_γ	$cos(\theta_{cm})$	$d\sigma/d\Omega(p\eta)$	sta. er.	$d\sigma/d\Omega(n\eta)$	sta. er.
1925.03	-0.9	0.03543	0.0821	0.02925	0.1168
1925.03	-0.7	0.04482	0.06468	0.01003	0.02562
1925.03	-0.5	0.008524	0.01008	0.06263	0.04865
1925.03	-0.3	0.0134	0.008372	0.05799	0.02708
1925.03	-0.1	0.04307	0.009264	0.054	0.0177
1925.03	0.1	0.09032	0.01007	0.07746	0.01703
1925.03	0.3	0.105	0.009491	0.1594	0.02275
1925.03	0.5	0.1667	0.01292	0.1436	0.02206
1925.03	0.7	0.2453	0.01828	0.2413	0.03745
1925.03	0.9	0.3207	0.04128	0.2541	0.1118
1975.19	-0.9	0.005131	0.09644	0	0.09871
1975.19	-0.7	0.0247	0.09307	0	0.09871
1975.19	-0.5	0	0.09093	0	0.09871
1975.19	-0.3	0.01349	0.009547	0.03199	0.03422
1975.19	-0.1	0.05821	0.01176	0.01405	0.01088
1975.19	0.1	0.05813	0.008339	0.04736	0.01411
1975.19	0.3	0.09241	0.009844	0.1427	0.02445
1975.19	0.5	0.1646	0.01401	0.154	0.02977
1975.19	0.7	0.3198	0.02291	0.3491	0.05867
1975.19	0.9	0.282	0.04022	0.151	0.1034
2024.9	-0.9	0.03813	0.1297	0	0.08311
2024.9	-0.7	0	0.1087	0	0.08311
2024.9	-0.5	0.01166	0.01783	0.05102	0.05898
2024.9	-0.3	0.02681	0.0154	0	0.08311
2024.9	-0.1	0.02822	0.008858	0.04188	0.01674
2024.9	0.1	0.07598	0.01005	0.009329	0.00617
2024.9	0.3	0.09897	0.01019	0.07326	0.01595
2024.9	0.5	0.1523	0.01426	0.1227	0.02381
2024.9	0.7	0.2041	0.01716	0.2829	0.04737
2024.9	0.9	0.2009	0.02855	0.3083	0.1001

E_γ	$cos(\theta_{cm})$	$d\sigma/d\Omega(p\eta)$	sta. er.	$d\sigma/d\Omega(n\eta)$	sta. er.
2064.63	-0.9	0	0.08628	0	0.1093
2064.63	-0.7	0	0.08735	0	0.1093
2064.63	-0.5	0	0.08732	0	0.1093
2064.63	-0.3	0.05287	0.02438	0	0.1093
2064.63	-0.1	0.05796	0.01532	0.06885	0.03294
2064.63	0.1	0.07033	0.01058	0.02727	0.01666
2064.63	0.3	0.06978	0.009961	0.08489	0.02679
2064.63	0.5	0.1067	0.01285	0.2962	0.05664
2064.63	0.7	0.2994	0.02611	0.2816	0.07136
2064.63	0.9	0.3259	0.06355	0.1222	0.1119
2125.01	-0.9	0	0.1402	0	0.08431
2125.01	-0.7	0	0.1402	0.1791	0.1597
2125.01	-0.5	0	0.1402	0.04321	0.04321
2125.01	-0.3	0.02536	0.01905	0.02096	0.021
2125.01	-0.1	0.05859	0.01699	0.009435	0.009561
2125.01	0.1	0.06602	0.01405	0.005109	0.005431
2125.01	0.3	0.1324	0.01976	0.06384	0.01873
2125.01	0.5	0.1412	0.02111	0.1701	0.03499
2125.01	0.7	0.3159	0.03544	0.2087	0.05003
2125.01	0.9	0.7196	0.1018	0.2607	0.1194
2175.64	-0.9	0	0.1223	0	0.142
2175.64	-0.7	0	0.1223	0	0.142
2175.64	-0.5	0	0.1223	0	0.142
2175.64	-0.3	0.03839	0.02501	0	0.142
2175.64	-0.1	0.02653	0.01211	0	0.142
2175.64	0.1	0.04371	0.01161	0.05791	0.02392
2175.64	0.3	0.0938	0.01603	0.1083	0.03055
2175.64	0.5	0.134	0.02135	0.2829	0.05985
2175.64	0.7	0.2285	0.03077	0.3143	0.08042
2175.64	0.9	0.1437	0.04579	0.3172	0.1685

E_γ	$cos(\theta_{cm})$	$d\sigma/d\Omega(p\eta)$	sta. er.	$d\sigma/d\Omega(n\eta)$	sta. er.
2250.42	-0.9	0	0.1391	0	0.09558
2250.42	-0.7	0.04065	0.05133	0	0.09558
2250.42	-0.5	0	0.1391	0.03318	0.03544
2250.42	-0.3	0.0141	0.0115	0.04813	0.02828
2250.42	-0.1	0.01495	0.006676	0.02362	0.01225
2250.42	0.1	0.08483	0.01245	0.01274	0.006675
2250.42	0.3	0.1168	0.0136	0.04432	0.01198
2250.42	0.5	0.1414	0.01656	0.09236	0.02042
2250.42	0.7	0.3563	0.03194	0.2374	0.04218
2250.42	0.9	0.2504	0.04806	0.2864	0.09931
2350.36	-0.9	0	0.1403	0.07833	0.213
2350.36	-0.7	0	0.1403	0	0.1156
2350.36	-0.5	0	0.1403	0	0.1156
2350.36	-0.3	0.01473	0.01304	0.01981	0.02118
2350.36	-0.1	0.027	0.00974	0.02057	0.01241
2350.36	0.1	0.05349	0.01018	0.02335	0.009985
2350.36	0.3	0.0825	0.01206	0.04941	0.01387
2350.36	0.5	0.1373	0.01671	0.1494	0.02815
2350.36	0.7	0.3045	0.0301	0.2634	0.04894
2350.36	0.9	0.2618	0.04596	0.188	0.08348
2449.69	-0.9	0	0.1407	0.09313	0.1598
2449.69	-0.7	0	0.1407	0	0.111
2449.69	-0.5	0	0.1407	0	0.111
2449.69	-0.3	0	0.1407	0	0.111
2449.69	-0.1	0.03268	0.0116	0.01543	0.01102
2449.69	0.1	0.046	0.01069	0.03222	0.01232
2449.69	0.3	0.06734	0.01248	0.05247	0.01606
2449.69	0.5	0.08225	0.01354	0.1464	0.03215
2449.69	0.7	0.1951	0.022	0.1626	0.04268
2449.69	0.9	0.2236	0.03881	0.4892	0.1593

Total cross sections

E_γ incident photon beam in MeV.
σ total cross section in μb.
sta. er. statistical error in μb.

E_γ	$\sigma(NNX\eta)$	sta. er.	$\sigma(np\eta)$	sta. er.
637.672	0.5974	0.01595	0.5871	0.1203
661.95	1.637	0.0245	1.635	0.02163
688.582	4.902	0.03654	4.672	0.03094
714.707	10.69	0.05771	9.917	0.04898
737.573	16.82	0.07468	16.23	0.0671
760.016	20.18	0.08286	19.57	0.07557
786.525	21.97	0.07452	21.67	0.06899
812.518	22.02	0.09139	22.28	0.08713
837.885	20.93	0.07814	20.5	0.1011
862.764	19.19	0.0933	18.98	0.1256
887.05	17.81	0.07712	16.2	0.09927
912.504	15.6	0.07979	13.33	0.1049
937.34	13.61	0.07099	11.8	0.09352
963.926	12.48	0.0714	11.05	0.09719
989.864	11.34	0.0684	9.681	0.09368
1025.27	10.14	0.04803	8.799	0.06989
1074.13	9.39	0.04322	8.051	0.06388
1124.08	9.037	0.0427	7.08	0.06002
1174.51	8.799	0.04111	6.552	0.06042
1226.52	8.865	0.04539	6.106	0.06309
1276.68	8.375	0.04579	5.342	0.06361
1325.1	8.417	0.04959	4.603	0.06529
1374.25	8.022	0.04704	4.084	0.07085
1424.81	8.045	0.05008	3.786	0.06546
1474.64	7.903	0.05052	3.325	0.0676
1524.44	7.925	0.04922	3.126	0.05753
1574.72	7.714	0.0464	2.781	0.0698
1624.57	7.883	0.0499	2.805	0.05721
1674.4	7.854	0.05043	2.841	0.06553
1725.13	7.758	0.05073	2.552	0.09184
1775.3	7.82	0.05157	2.46	0.06764
1825.16	7.793	0.05234	2.47	0.089
1874.89	7.852	0.05319	2.415	0.09522
1925.03	7.754	0.05201	2.382	0.0794
1975.19	7.92	0.05493	2.31	0.09144
2024.9	7.641	0.05712	2.247	0.1494
2064.63	7.675	0.07005	2.165	0.1476
2125.01	7.749	0.07191	2.065	0.09626
2175.64	7.542	0.07621	1.895	0.1497
2250.42	7.449	0.05392	1.922	0.0791
2350.36	7.381	0.05263	1.68	0.1837
2449.69	7.891	0.06055	1.426	0.1194

E_γ	$\sigma(p\eta)$	sta. er.	$\sigma(n\eta)$	sta. er.
637.672	0.3424	0.2055	0.118	0.1221
661.95	0.7197	0.0363	0.4686	0.06465
688.582	2.279	0.02944	1.874	0.06837
714.707	5.277	0.04561	4.276	0.09835
737.573	8.878	0.0603	6.882	0.1227
760.016	11.1	0.0686	8.285	0.1343
786.525	12.59	0.06337	8.764	0.1135
812.518	13.23	0.08098	8.904	0.1374
837.885	11.96	0.1019	7.911	0.1891
862.764	10.98	0.1234	6.889	0.2078
887.05	9.667	0.0983	6.288	0.1711
912.504	7.756	0.1003	5.251	0.1793
937.34	6.272	0.09199	5.348	0.1718
963.926	5.694	0.0952	5.952	0.169
989.864	4.249	0.07498	5.803	0.189
1025.27	3.533	0.06275	5.31	0.1375
1074.13	3.303	0.06345	4.853	0.1327
1124.08	3.068	0.06135	3.646	0.1176
1174.51	2.961	0.05871	3.713	0.1189
1226.52	2.8	0.06127	3.088	0.1374
1276.68	2.374	0.06692	3.01	0.1156
1325.1	2.229	0.06277	2.726	0.1413
1374.25	2.036	0.09997	2.368	0.1286
1424.81	1.841	0.07692	2.146	0.1324
1474.64	1.762	0.1001	1.614	0.1437
1524.44	1.566	0.1211	1.545	0.1439
1574.72	1.376	0.06788	1.482	0.1375
1624.57	1.388	0.08349	1.503	0.1467
1674.4	1.368	0.08773	1.3	0.1568
1725.13	1.164	0.1213	1.323	0.1647
1775.3	1.094	0.09379	1.337	0.1518
1825.16	1.131	0.1091	1.386	0.1647
1874.89	1.13	0.09801	1.288	0.1371
1925.03	1.261	0.1165	1.334	0.1814
1975.19	1.307	0.1702	1.193	0.2153
2024.9	1.147	0.05161	1.073	0.09467
2064.63	1.205	0.0701	0.9159	0.1143
2125.01	1.207	0.07621	1.012	0.1318
2175.64	0.8723	0.06935	1.001	0.1318
2250.42	1.076	0.05634	0.8168	0.08875
2350.36	0.9143	0.05402	0.8571	0.09134
2449.69	0.8697	0.05956	0.8008	0.09799

E_γ	$d\sigma/d\Omega(p\eta)(E_\gamma)$	sta. er.	$d\sigma/d\Omega(p\eta)(E^*_\gamma)$	sta. er.
714.707	0.8397	0.02173	0.6717	0.02173
737.573	1.525	0.0343	1.551	0.0343
760.016	1.783	0.04255	2.356	0.04255
786.525	2.122	0.0374	2.486	0.0374
812.518	2.146	0.0485	2.712	0.0485
837.885	2.179	0.04165	2.52	0.04165
862.764	2.128	0.05468	2.697	0.05468
887.05	1.974	0.0434	2.229	0.0434
912.504	1.913	0.04593	1.992	0.04593
937.34	1.369	0.03308	1.198	0.03308
963.926	1.224	0.03138	1.015	0.03138
989.864	1.15	0.03078	0.873	0.03078
1025.27	0.9042	0.023	0.7883	0.023
1074.13	0.766	0.02054	0.6607	0.02054
1124.08	0.641	0.01701	0.4068	0.01701
1174.51	0.455	0.0176	0.4363	0.0176
1226.52	0.441	0.01863	0.3767	0.01863
1276.68	0.4073	0.0226	0.4268	0.0226
1325.1	0.3595	0.02772	0.4525	0.02772
1374.25	0.2965	0.02303	0.304	0.02303
1424.81	0.2888	0.02362	0.271	0.02362

E_γ	$d\sigma/d\Omega(n\eta)(E_\gamma)$	sta. er.	$d\sigma/d\Omega(n\eta)(E^*_\gamma)$	sta. er.
714.707	0.6352	0.03902	0.3915	0.03902
737.573	1.03	0.06832	1.095	0.06832
760.016	1.283	0.0884	1.769	0.0884
786.525	1.466	0.075	1.712	0.075
812.518	1.481	0.09527	1.812	0.09527
837.885	1.796	0.08135	1.726	0.08135
862.764	1.696	0.1093	2.039	0.1093
887.05	1.672	0.0841	1.663	0.0841
912.504	1.804	0.09362	1.701	0.09362
937.34	1.522	0.07623	1.312	0.07623
963.926	1.556	0.0793	1.231	0.0793
989.864	1.43	0.08375	1.321	0.08375
1025.27	1.372	0.06588	1.431	0.06588
1074.13	1.091	0.05738	1.232	0.05738
1124.08	0.9493	0.04448	0.7045	0.04448
1174.51	0.6567	0.04217	0.6677	0.04217
1226.52	0.6515	0.04097	0.5108	0.04097
1276.68	0.5202	0.04835	0.5703	0.04835
1325.1	0.5202	0.06298	0.6967	0.06298
1374.25	0.4225	0.0557	0.5295	0.0557
1424.81	0.574	0.06592	0.6062	0.06592

$\eta^{'}-$meson photoproduction off the deuterium

Angular distributions

E_γ incident photon beam in MeV
$cos(\theta_{cm})$ $\eta^{'}$ angle in the cms
$d\sigma/d\Omega$ differential cross section in μb/sr.
sta. er. statistical error in μb/sr.

E_γ	$cos(\theta_{cm})$	$d\sigma/d\Omega(NNX\eta^{'})$	sta. er.	$d\sigma/d\Omega(pn\eta^{'})$	sta. er.
1374.25	-0.9	0.05385	0.00754	0.03051	0.005085
1374.25	-0.7	0.04393	0.006078	0.03892	0.006111
1374.25	-0.5	0.03166	0.004814	0.02927	0.005137
1374.25	-0.3	0.02446	0.004025	0.02891	0.005192
1374.25	-0.1	0.01934	0.003436	0.02505	0.004936
1374.25	0.1	0.01354	0.002778	0.01931	0.004046
1374.25	0.3	0.009645	0.002285	0.01386	0.003504
1374.25	0.5	0.007873	0.002041	0.01496	0.003406
1374.25	0.7	0.00535	0.001705	0.008886	0.002484
1374.25	0.9	0.003634	0.001487	0.007775	0.002148
1424.81	-0.9	0.1124	0.01241	0.09075	0.01545
1424.81	-0.7	0.07869	0.009432	0.07808	0.01425
1424.81	-0.5	0.06983	0.008307	0.0729	0.01419
1424.81	-0.3	0.0612	0.007408	0.07324	0.01439
1424.81	-0.1	0.04137	0.005873	0.0515	0.01237
1424.81	0.1	0.0305	0.00491	0.04059	0.01077
1424.81	0.3	0.02256	0.004144	0.03178	0.009614
1424.81	0.5	0.02077	0.00393	0.02773	0.009629
1424.81	0.7	0.009753	0.002683	0.01674	0.007414
1424.81	0.9	0.005924	0.0021	0.0244	0.009214
1474.64	-0.9	0.1555	0.01492	0.08957	0.01374
1474.64	-0.7	0.1127	0.01147	0.08522	0.01362
1474.64	-0.5	0.09495	0.009879	0.09072	0.0136
1474.64	-0.3	0.08963	0.009188	0.1144	0.01602
1474.64	-0.1	0.06811	0.007747	0.1004	0.01463
1474.64	0.1	0.05261	0.006636	0.07962	0.01318
1474.64	0.3	0.04573	0.006071	0.08398	0.01388
1474.64	0.5	0.03902	0.005557	0.08705	0.01516
1474.64	0.7	0.03542	0.005325	0.05721	0.01209
1474.64	0.9	0.03045	0.005089	0.06724	0.01349

E_γ	$cos(\theta_{cm})$	$d\sigma/d\Omega(NNX\eta^{'})$	sta. er.	$d\sigma/d\Omega(pn\eta^{'})$	sta. er.
1524.44	-0.9	0.1378	0.01408	0.09365	0.01505
1524.44	-0.7	0.1193	0.01166	0.09579	0.01454
1524.44	-0.5	0.09643	0.009796	0.07215	0.0121
1524.44	-0.3	0.1012	0.009595	0.1222	0.01568
1524.44	-0.1	0.07869	0.008193	0.09646	0.01356
1524.44	0.1	0.08327	0.008228	0.1004	0.01415
1524.44	0.3	0.08734	0.008272	0.1017	0.01472
1524.44	0.5	0.09137	0.008363	0.1158	0.01658
1524.44	0.7	0.08791	0.008199	0.13	0.018
1524.44	0.9	0.07475	0.007689	0.1125	0.01807
1574.72	-0.9	0.09686	0.01216	0.09091	0.01489
1574.72	-0.7	0.09573	0.01091	0.09069	0.01402
1574.72	-0.5	0.1032	0.01064	0.1346	0.01576
1574.72	-0.3	0.1122	0.01065	0.1416	0.01606
1574.72	-0.1	0.1124	0.01033	0.1204	0.01471
1574.72	0.1	0.1214	0.01047	0.1245	0.01531
1574.72	0.3	0.1201	0.01021	0.1261	0.0154
1574.72	0.5	0.1222	0.0102	0.1416	0.01695
1574.72	0.7	0.1034	0.009415	0.09615	0.01387
1574.72	0.9	0.1097	0.009962	0.07859	0.01428
1624.57	-0.9	0.1184	0.01314	0.07183	0.01388
1624.57	-0.7	0.1061	0.01096	0.1055	0.01606
1624.57	-0.5	0.1144	0.01066	0.09589	0.01452
1624.57	-0.3	0.1145	0.01025	0.117	0.01503
1624.57	-0.1	0.127	0.0105	0.1046	0.0141
1624.57	0.1	0.1238	0.01013	0.1135	0.01517
1624.57	0.3	0.1454	0.01077	0.1686	0.019
1624.57	0.5	0.131	0.01009	0.1667	0.01919
1624.57	0.7	0.1397	0.01043	0.1478	0.01904
1624.57	0.9	0.1288	0.01025	0.1632	0.02291

E_γ	$cos(\theta_{cm})$	$d\sigma/d\Omega(NNX\eta^{'})$	sta. er.	$d\sigma/d\Omega(pn\eta^{'})$	sta. er.
1674.4	-0.9	0.1244	0.01499	0.1327	0.02157
1674.4	-0.7	0.1106	0.01242	0.1294	0.01919
1674.4	-0.5	0.1126	0.01171	0.1262	0.01715
1674.4	-0.3	0.1152	0.01137	0.1264	0.01697
1674.4	-0.1	0.1283	0.01167	0.1207	0.01657
1674.4	0.1	0.1418	0.01199	0.1217	0.01631
1674.4	0.3	0.1331	0.01141	0.1056	0.01525
1674.4	0.5	0.1369	0.01144	0.116	0.01687
1674.4	0.7	0.1384	0.01151	0.1192	0.01798
1674.4	0.9	0.1427	0.01197	0.1075	0.01927
1725.13	-0.9	0.07626	0.01191	0.06747	0.01776
1725.13	-0.7	0.09277	0.01184	0.06777	0.01567
1725.13	-0.5	0.0985	0.01145	0.0774	0.01483
1725.13	-0.3	0.1293	0.01257	0.09842	0.01611
1725.13	-0.1	0.1266	0.01206	0.101	0.01596
1725.13	0.1	0.1459	0.01266	0.1259	0.01795
1725.13	0.3	0.1494	0.01261	0.1218	0.0169
1725.13	0.5	0.1619	0.01303	0.1574	0.0201
1725.13	0.7	0.1429	0.0123	0.1302	0.01946
1725.13	0.9	0.1434	0.01261	0.1486	0.02411
1775.3	-0.9	0.09397	0.01247	0.01718	0.0089
1775.3	-0.7	0.1101	0.01224	0.05284	0.013
1775.3	-0.5	0.1214	0.01209	0.06263	0.01219
1775.3	-0.3	0.1283	0.01192	0.07153	0.01283
1775.3	-0.1	0.1401	0.01209	0.102	0.01455
1775.3	0.1	0.1417	0.0119	0.1098	0.015
1775.3	0.3	0.144	0.01183	0.146	0.01738
1775.3	0.5	0.1437	0.01175	0.1489	0.01772
1775.3	0.7	0.1393	0.01163	0.1715	0.02049
1775.3	0.9	0.1028	0.01022	0.1588	0.0219

E_γ	$cos(\theta_{cm})$	$d\sigma/d\Omega(NNX\eta^{'})$	sta. er.	$d\sigma/d\Omega(pn\eta^{'})$	sta. er.
1825.16	-0.9	0.03929	0.008342	0.006682	0.005948
1825.16	-0.7	0.07794	0.01081	0.03859	0.01221
1825.16	-0.5	0.1026	0.01165	0.04818	0.01165
1825.16	-0.3	0.1084	0.01144	0.07309	0.01386
1825.16	-0.1	0.1238	0.01184	0.06696	0.01231
1825.16	0.1	0.1491	0.01273	0.1402	0.01803
1825.16	0.3	0.1553	0.01287	0.1636	0.01862
1825.16	0.5	0.1932	0.01435	0.173	0.01983
1825.16	0.7	0.1897	0.01435	0.1876	0.02266
1825.16	0.9	0.1588	0.01335	0.1655	0.02318
1874.89	-0.9	0.08841	0.013	0.01537	0.0112
1874.89	-0.7	0.08545	0.0115	0.0361	0.01443
1874.89	-0.5	0.09194	0.01117	0.04431	0.01313
1874.89	-0.3	0.08972	0.01056	0.04326	0.01202
1874.89	-0.1	0.1086	0.01128	0.06871	0.01442
1874.89	0.1	0.1458	0.0128	0.1031	0.01742
1874.89	0.3	0.154	0.01301	0.1433	0.01997
1874.89	0.5	0.1907	0.01447	0.2129	0.02526
1874.89	0.7	0.1899	0.01462	0.2017	0.02667
1874.89	0.9	0.1989	0.01547	0.2241	0.03134
1925.03	-0.9	0.09639	0.01247	0.04716	0.02149
1925.03	-0.7	0.1012	0.01158	0.04486	0.0165
1925.03	-0.5	0.1007	0.0108	0.04523	0.01357
1925.03	-0.3	0.09118	0.009805	0.05379	0.01286
1925.03	-0.1	0.1052	0.01021	0.06595	0.01397
1925.03	0.1	0.1318	0.01122	0.09531	0.01612
1925.03	0.3	0.1518	0.01196	0.09326	0.01543
1925.03	0.5	0.1666	0.01257	0.179	0.02244
1925.03	0.7	0.2047	0.01412	0.2045	0.02595
1925.03	0.9	0.1797	0.01355	0.1826	0.02778

E_γ	$cos(\theta_{cm})$	$d\sigma/d\Omega(NNX\eta^{'})$	sta. er.	$d\sigma/d\Omega(pn\eta^{'})$	sta. er.
1975.19	-0.9	0.06497	0.01166	0.02104	0.01607
1975.19	-0.7	0.07439	0.01108	0.04716	0.02039
1975.19	-0.5	0.07772	0.01058	0.03561	0.01381
1975.19	-0.3	0.09552	0.01125	0.05664	0.01555
1975.19	-0.1	0.0971	0.01106	0.0411	0.01251
1975.19	0.1	0.1148	0.01186	0.06292	0.01463
1975.19	0.3	0.1607	0.01397	0.1047	0.01884
1975.19	0.5	0.1781	0.01477	0.1813	0.02497
1975.19	0.7	0.2414	0.01747	0.2763	0.03445
1975.19	0.9	0.2254	0.01746	0.1943	0.03128
2024.9	-0.9	0.07471	0.01272	0.008134	0.0108
2024.9	-0.7	0.07021	0.01123	0.03457	0.018
2024.9	-0.5	0.08652	0.01166	0.03812	0.01496
2024.9	-0.3	0.08006	0.01071	0.03192	0.01184
2024.9	-0.1	0.08597	0.01077	0.05848	0.01492
2024.9	0.1	0.109	0.01194	0.06646	0.01497
2024.9	0.3	0.1465	0.01379	0.1104	0.01871
2024.9	0.5	0.1795	0.01542	0.1635	0.02382
2024.9	0.7	0.2233	0.01761	0.2351	0.03233
2024.9	0.9	0.2529	0.01948	0.274	0.04036
2064.63	-0.9	0.1317	0.01943	0.001492	0.007054
2064.63	-0.7	0.08798	0.01446	0.04764	0.03071
2064.63	-0.5	0.09335	0.01399	0.05123	0.02369
2064.63	-0.3	0.08725	0.01296	0.09179	0.02815
2064.63	-0.1	0.08024	0.01211	0.05622	0.0201
2064.63	0.1	0.1009	0.01341	0.1246	0.0282
2064.63	0.3	0.1375	0.01564	0.1933	0.03534
2064.63	0.5	0.1619	0.01715	0.2007	0.03567
2064.63	0.7	0.1835	0.0187	0.2244	0.04364
2064.63	0.9	0.2201	0.02132	0.2009	0.04605

E_γ	$cos(\theta_{cm})$	$d\sigma/d\Omega(NNX\eta^{'})$	sta. er.	$d\sigma/d\Omega(pn\eta^{'})$	sta. er.
2125.01	-0.9	0.1376	0.02078	0.1782	0.0769
2125.01	-0.7	0.09175	0.01548	0.1019	0.04465
2125.01	-0.5	0.07722	0.01338	0.0669	0.02868
2125.01	-0.3	0.0694	0.0122	0.03477	0.01683
2125.01	-0.1	0.07504	0.01239	0.03761	0.01661
2125.01	0.1	0.08671	0.01316	0.043	0.01625
2125.01	0.3	0.1197	0.01544	0.05915	0.01874
2125.01	0.5	0.1616	0.01812	0.1066	0.02562
2125.01	0.7	0.2098	0.02117	0.1465	0.03415
2125.01	0.9	0.2557	0.02444	0.2023	0.04612
2175.64	-0.9	0.07681	0.01524	0.07592	0.04977
2175.64	-0.7	0.0815	0.01457	0.09529	0.04708
2175.64	-0.5	0.05894	0.01169	0.04162	0.02299
2175.64	-0.3	0.07757	0.01286	0.03301	0.01684
2175.64	-0.1	0.0796	0.01269	0.04588	0.01834
2175.64	0.1	0.1047	0.01441	0.03761	0.01531
2175.64	0.3	0.1363	0.0165	0.07214	0.02008
2175.64	0.5	0.1773	0.01917	0.1699	0.03283
2175.64	0.7	0.223	0.02218	0.2318	0.04158
2175.64	0.9	0.2496	0.02447	0.2879	0.05565
2250.42	-0.9	0.08439	0.01118	0.05464	0.03492
2250.42	-0.7	0.06645	0.009025	0.05713	0.02932
2250.42	-0.5	0.05673	0.007811	0.04564	0.01967
2250.42	-0.3	0.06233	0.007845	0.03956	0.0149
2250.42	-0.1	0.07094	0.008174	0.05164	0.01538
2250.42	0.1	0.08664	0.008977	0.07478	0.01676
2250.42	0.3	0.1095	0.01018	0.05884	0.01397
2250.42	0.5	0.1514	0.01224	0.1365	0.02191
2250.42	0.7	0.2116	0.01495	0.2414	0.03338
2250.42	0.9	0.2308	0.01626	0.1923	0.03498

E_γ	$cos(\theta_{cm})$	$d\sigma/d\Omega(NNX\eta^{'})$	sta. er.	$d\sigma/d\Omega(pn\eta^{'})$	sta. er.
2350.36	-0.9	0.02318	0.007013	0.06981	0.04989
2350.36	-0.7	0.03018	0.007245	0.02934	0.02799
2350.36	-0.5	0.0344	0.007295	0.02508	0.01778
2350.36	-0.3	0.04821	0.008343	0.01348	0.01096
2350.36	-0.1	0.05201	0.008514	0.02251	0.01173
2350.36	0.1	0.07491	0.01017	0.04216	0.01455
2350.36	0.3	0.108	0.0123	0.0527	0.01538
2350.36	0.5	0.1615	0.01535	0.09996	0.02135
2350.36	0.7	0.2265	0.0189	0.2063	0.03476
2350.36	0.9	0.2828	0.02253	0.1876	0.0389
2449.69	-0.9	0.1217	0.01568	0.05497	0.04455
2449.69	-0.7	0.08518	0.0119	0.07884	0.04629
2449.69	-0.5	0.07098	0.01022	0.0665	0.02953
2449.69	-0.3	0.06989	0.009772	0.04211	0.02011
2449.69	-0.1	0.06907	0.009554	0.04012	0.01538
2449.69	0.1	0.07987	0.01028	0.04022	0.01354
2449.69	0.3	0.1106	0.01229	0.05656	0.01503
2449.69	0.5	0.1493	0.0147	0.1037	0.02131
2449.69	0.7	0.2185	0.01854	0.1484	0.0291
2449.69	0.9	0.283	0.0222	0.1563	0.03554

E_γ	$cos(\theta_{cm})$	$d\sigma/d\Omega(p\eta^{'})$	sta. er.	$d\sigma/d\Omega(n\eta^{'})$	sta. er.
1374.25	-0.9	0.006933	0.00187	0	0
1374.25	-0.7	0.008024	0.001938	0	0
1374.25	-0.5	0.003302	0.001177	0	0
1374.25	-0.3	0.003357	0.001196	0	0
1374.25	-0.1	0.003067	0.001179	0	0
1374.25	0.1	0.001567	0.0007989	0	0
1374.25	0.3	0.001664	0.0008482	0	0
1374.25	0.5	0.0008156	0.0005657	0	0
1374.25	0.7	0.001442	0.0007403	0	0
1374.25	0.9	0.001569	0.0009233	0	0
1424.81	-0.9	0.03002	0.009405	0.02922	0.01446
1424.81	-0.7	0.03154	0.008485	0.02644	0.01289
1424.81	-0.5	0.0305	0.008368	0.02785	0.01318
1424.81	-0.3	0.03517	0.00907	0.01378	0.01002
1424.81	-0.1	0.03585	0.009415	0.01758	0.01031
1424.81	0.1	0.02683	0.008931	0.01134	0.008514
1424.81	0.3	0.02533	0.008069	0.009195	0.008647
1424.81	0.5	0.02616	0.009972	0.01089	0.01003
1424.81	0.7	0.001253	0.002021	0.006939	0.01137
1424.81	0.9	0.00236	0.003001	0.0818	0.0328
1474.64	-0.9	0.06943	0.01502	0.02812	0.01629
1474.64	-0.7	0.03798	0.009667	0.02589	0.01462
1474.64	-0.5	0.0507	0.01076	0.06213	0.02195
1474.64	-0.3	0.06653	0.01295	0.05572	0.02084
1474.64	-0.1	0.0663	0.01261	0.04882	0.01967
1474.64	0.1	0.04223	0.01028	0.06948	0.02517
1474.64	0.3	0.05208	0.01173	0.0344	0.01793
1474.64	0.5	0.03572	0.01062	0.05427	0.02345
1474.64	0.7	0.02144	0.008257	0.04814	0.02489
1474.64	0.9	0.01268	0.006956	0.05863	0.03007

E_γ	$cos(\theta_{cm})$	$d\sigma/d\Omega(p\eta^{'})$	sta. er.	$d\sigma/d\Omega(n\eta^{'})$	sta. er.
1524.44	-0.9	0.04424	0.01126	0.08718	0.02483
1524.44	-0.7	0.03097	0.007874	0.1033	0.02481
1524.44	-0.5	0.02298	0.006471	0.0512	0.017
1524.44	-0.3	0.06911	0.01116	0.05609	0.01775
1524.44	-0.1	0.0512	0.009363	0.04463	0.01573
1524.44	0.1	0.04725	0.00926	0.02984	0.01288
1524.44	0.3	0.06915	0.01172	0.02849	0.01359
1524.44	0.5	0.07015	0.01254	0.02103	0.01199
1524.44	0.7	0.08582	0.01449	0.05806	0.02212
1524.44	0.9	0.06416	0.01417	0.051	0.0241
1574.72	-0.9	0.06105	0.01299	0.07513	0.02406
1574.72	-0.7	0.03844	0.008698	0.07254	0.02175
1574.72	-0.5	0.059	0.009954	0.07509	0.02056
1574.72	-0.3	0.06849	0.01067	0.09218	0.02212
1574.72	-0.1	0.05553	0.009567	0.06133	0.01812
1574.72	0.1	0.0651	0.0107	0.0725	0.02041
1574.72	0.3	0.08061	0.01198	0.04031	0.01607
1574.72	0.5	0.09416	0.01371	0.05147	0.01894
1574.72	0.7	0.05412	0.01038	0.06321	0.02275
1574.72	0.9	0.06211	0.01322	0.0334	0.01865
1624.57	-0.9	0.03419	0.01065	0.0769	0.02803
1624.57	-0.7	0.03986	0.009871	0.06743	0.02264
1624.57	-0.5	0.03427	0.008703	0.02875	0.01455
1624.57	-0.3	0.07874	0.01241	0.0199	0.01163
1624.57	-0.1	0.06893	0.0116	0.008337	0.007649
1624.57	0.1	0.07492	0.01259	0.02	0.01209
1624.57	0.3	0.1088	0.01579	0.03295	0.01609
1624.57	0.5	0.07763	0.01372	0.0195	0.01368
1624.57	0.7	0.05868	0.01294	0.09011	0.03197
1624.57	0.9	0.04343	0.01308	0.2819	0.0647

E_γ	$cos(\theta_{cm})$	$d\sigma/d\Omega(p\eta^{'})$	sta. er.	$d\sigma/d\Omega(n\eta^{'})$	sta. er.
1674.4	-0.9	0.03842	0.01361	0.03069	0.01764
1674.4	-0.7	0.04481	0.01206	0.04365	0.01848
1674.4	-0.5	0.05106	0.01165	0.1151	0.02813
1674.4	-0.3	0.06668	0.01326	0.06058	0.0197
1674.4	-0.1	0.08256	0.01493	0.05924	0.01943
1674.4	0.1	0.0799	0.01457	0.0416	0.01732
1674.4	0.3	0.07175	0.01403	0.04298	0.01806
1674.4	0.5	0.1166	0.01932	0.02164	0.01409
1674.4	0.7	0.09668	0.01908	0.04066	0.02117
1674.4	0.9	0.04693	0.01531	0.04079	0.02418
1725.13	-0.9	0.03649	0.01363	0.07083	0.03389
1725.13	-0.7	0.03416	0.01055	0.04957	0.02327
1725.13	-0.5	0.04109	0.01027	0.05672	0.02252
1725.13	-0.3	0.05993	0.01207	0.04322	0.01909
1725.13	-0.1	0.0579	0.01168	0.06686	0.02432
1725.13	0.1	0.08371	0.01442	0.04939	0.02132
1725.13	0.3	0.08037	0.01394	0.04657	0.02049
1725.13	0.5	0.09695	0.01615	0.03611	0.01949
1725.13	0.7	0.06152	0.01426	0.01607	0.01522
1725.13	0.9	0.05119	0.0156	0.007914	0.01265
1775.3	-0.9	0.07372	0.01793	0.06248	0.02533
1775.3	-0.7	0.04923	0.0109	0.03032	0.01432
1775.3	-0.5	0.04499	0.009028	0.02969	0.01287
1775.3	-0.3	0.03742	0.008149	0.02779	0.01168
1775.3	-0.1	0.041	0.008295	0.04258	0.01457
1775.3	0.1	0.04351	0.008544	0.053	0.01628
1775.3	0.3	0.08448	0.01218	0.05297	0.01685
1775.3	0.5	0.05083	0.009786	0.06553	0.02004
1775.3	0.7	0.08604	0.01436	0.03894	0.01786
1775.3	0.9	0.1186	0.02042	0.06347	0.02775

E_γ	$cos(\theta_{cm})$	$d\sigma/d\Omega(p\eta^{'})$	sta. er.	$d\sigma/d\Omega(n\eta^{'})$	sta. er.
1825.16	-0.9	0.004365	0.005487	0.06436	0.03184
1825.16	-0.7	0.02372	0.009763	0.06692	0.02531
1825.16	-0.5	0.02083	0.007834	0.04381	0.01787
1825.16	-0.3	0.04517	0.01121	0.03969	0.01583
1825.16	-0.1	0.05368	0.01147	0.008169	0.007103
1825.16	0.1	0.1044	0.01649	0.02657	0.01313
1825.16	0.3	0.1089	0.01647	0.05326	0.01939
1825.16	0.5	0.09586	0.01616	0.03649	0.01679
1825.16	0.7	0.09778	0.01886	0.09999	0.03191
1825.16	0.9	0.06293	0.01892	0.08436	0.03612
1874.89	-0.9	0.005487	0.006701	0.03342	0.03037
1874.89	-0.7	0.02525	0.01065	0.106	0.04271
1874.89	-0.5	0.0337	0.01015	0.02127	0.01681
1874.89	-0.3	0.02497	0.008132	0.04474	0.02244
1874.89	-0.1	0.04591	0.01061	0.03657	0.01953
1874.89	0.1	0.07009	0.0132	0.04519	0.02192
1874.89	0.3	0.09943	0.01546	0.07889	0.02961
1874.89	0.5	0.1404	0.01928	0.08405	0.03301
1874.89	0.7	0.1232	0.02053	0.0872	0.03935
1874.89	0.9	0.1362	0.02936	0.0404	0.03419
1925.03	-0.9	0.01664	0.01536	0.1173	0.06012
1925.03	-0.7	0.01445	0.01041	0.01632	0.02266
1925.03	-0.5	0.02306	0.01017	0.0247	0.01732
1925.03	-0.3	0.02829	0.009821	0.02424	0.01519
1925.03	-0.1	0.02993	0.01006	0.0145	0.01139
1925.03	0.1	0.04128	0.01159	0.06913	0.02512
1925.03	0.3	0.05675	0.01313	0.06771	0.02561
1925.03	0.5	0.1288	0.02085	0.07868	0.02839
1925.03	0.7	0.1724	0.02714	0.06397	0.03042
1925.03	0.9	0.0773	0.02694	0.05749	0.04042

E_γ	$cos(\theta_{cm})$	$d\sigma/d\Omega(p\eta^{'})$	sta. er.	$d\sigma/d\Omega(n\eta^{'})$	sta. er.
1975.19	-0.9	0.02796	0.01801	0.1876	0.07484
1975.19	-0.7	0.0471	0.01692	0.07394	0.04811
1975.19	-0.5	0.01214	0.006694	0.03633	0.02031
1975.19	-0.3	0.0191	0.007573	0.05216	0.02124
1975.19	-0.1	0.01316	0.006011	0.007728	0.008054
1975.19	0.1	0.02605	0.008127	0.04037	0.01807
1975.19	0.3	0.04937	0.01109	0.03055	0.01577
1975.19	0.5	0.09764	0.01578	0.04957	0.02186
1975.19	0.7	0.1777	0.02462	0.04817	0.02437
1975.19	0.9	0.08278	0.02474	0.0342	0.02868
2024.9	-0.9	0.02454	0.02126	0.0911	0.05321
2024.9	-0.7	0.03693	0.01791	0.05606	0.03163
2024.9	-0.5	0.01759	0.009844	0.03101	0.01839
2024.9	-0.3	0.0186	0.008793	0.02525	0.02201
2024.9	-0.1	0.04546	0.01299	0.03874	0.01686
2024.9	0.1	0.03341	0.01059	0.04496	0.01838
2024.9	0.3	0.05361	0.01303	0.05414	0.0202
2024.9	0.5	0.08012	0.01661	0.07532	0.02532
2024.9	0.7	0.1088	0.02242	0.1161	0.03761
2024.9	0.9	0.1318	0.04197	0.1439	0.05775
2064.63	-0.9	0	0.07429	0.08376	0.07111
2064.63	-0.7	0.004033	0.00762	0.05269	0.04368
2064.63	-0.5	0.01606	0.0136	0.02887	0.02555
2064.63	-0.3	0.01743	0.01057	0.01964	0.01761
2064.63	-0.1	0.007212	0.006322	0.01058	0.01182
2064.63	0.1	0.03187	0.01266	0.04807	0.02527
2064.63	0.3	0.09921	0.02233	0.04101	0.02316
2064.63	0.5	0.1311	0.02524	0.08949	0.03686
2064.63	0.7	0.1381	0.03072	0.1545	0.0536
2064.63	0.9	0.1209	0.05027	0.05553	0.04977

E_γ	$cos(\theta_{cm})$	$d\sigma/d\Omega(p\eta^{'})$	sta. er.	$d\sigma/d\Omega(n\eta^{'})$	sta. er.
2125.01	-0.9	0.1406	0.06653	0.03664	0.04555
2125.01	-0.7	0.04635	0.02374	0.04758	0.03576
2125.01	-0.5	0.02541	0.01415	0.06264	0.0335
2125.01	-0.3	0.02011	0.01024	0.02335	0.01734
2125.01	-0.1	0.01367	0.008146	0.01813	0.01412
2125.01	0.1	0.01851	0.008712	0.01275	0.01159
2125.01	0.3	0.02856	0.01048	0.01474	0.01245
2125.01	0.5	0.04411	0.01324	0.02732	0.01789
2125.01	0.7	0.06331	0.01873	0.05707	0.0307
2125.01	0.9	0.1181	0.0442	0.09287	0.0558
2175.64	-0.9	0.02022	0.03186	0	0.3231
2175.64	-0.7	0.06524	0.03913	0.1247	0.1572
2175.64	-0.5	0.05405	0.02642	0.1033	0.1115
2175.64	-0.3	0.01494	0.01159	0.5182	0.2142
2175.64	-0.1	0.01593	0.01128	0.09105	0.07971
2175.64	0.1	0.01325	0.009431	0.05421	0.05845
2175.64	0.3	0.04053	0.0155	0	0.3231
2175.64	0.5	0.08034	0.02313	0	0.3231
2175.64	0.7	0.07572	0.02478	0	0.3231
2175.64	0.9	0.1399	0.05741	0	0.3231
2250.42	-0.9	0.06734	0.03682	0.06168	0.04769
2250.42	-0.7	0.03262	0.01645	0.06904	0.03296
2250.42	-0.5	0.01331	0.007927	0.02217	0.01491
2250.42	-0.3	0.01563	0.007015	0.02972	0.01471
2250.42	-0.1	0.02966	0.008877	0.009072	0.007254
2250.42	0.1	0.02101	0.006772	0.01536	0.008429
2250.42	0.3	0.0206	0.006242	0.01851	0.009361
2250.42	0.5	0.04467	0.009407	0.06116	0.01914
2250.42	0.7	0.08899	0.01546	0.09548	0.02839
2250.42	0.9	0.1108	0.02938	0.02829	0.02347

E_γ	$cos(\theta_{cm})$	$d\sigma/d\Omega(p\eta^{'})$	sta. er.	$d\sigma/d\Omega(n\eta^{'})$	sta. er.
2350.36	-0.9	0.02942	0.03372	0	0.07834
2350.36	-0.7	0.01194	0.01386	0.0007195	0.004949
2350.36	-0.5	0.02043	0.01249	0.005072	0.009698
2350.36	-0.3	0.005422	0.005438	0.001437	0.004386
2350.36	-0.1	0.01128	0.00658	0.005537	0.007641
2350.36	0.1	0.01145	0.006035	0.01611	0.01188
2350.36	0.3	0.02466	0.008318	0.01383	0.01047
2350.36	0.5	0.031	0.009309	0.04229	0.02033
2350.36	0.7	0.07865	0.01693	0.07936	0.03322
2350.36	0.9	0.08994	0.03061	0.1078	0.06358
2449.69	-0.9	0	0.09541	0.2621	0.1366
2449.69	-0.7	0.01579	0.02104	0.03498	0.03663
2449.69	-0.5	0.02088	0.01688	0	0.07399
2449.69	-0.3	0.01271	0.01138	0.03643	0.02415
2449.69	-0.1	0.01395	0.009416	0.0141	0.01338
2449.69	0.1	0.024	0.01087	0.03216	0.0182
2449.69	0.3	0.02171	0.009607	0.0384	0.01917
2449.69	0.5	0.06757	0.0177	0.03756	0.02109
2449.69	0.7	0.1038	0.02516	0.0716	0.03545
2449.69	0.9	0.1066	0.04252	0.2589	0.1127

Total cross sections

E_γ incident photon beam in MeV.
σ total cross section in μb.
sta. er. statistical error in μb.

E_γ	$\sigma(NNX\eta^{'})$	sta. er.	$\sigma(np\eta^{'})$	sta. er.
1374.25	0.268	0.01759	0.27	0.01631
1424.81	0.5693	0.02653	0.6339	0.04138
1474.64	0.91	0.03436	1.06	0.05331
1524.44	1.204	0.03831	1.29	0.05577
1574.72	1.379	0.03933	1.422	0.05548
1624.57	1.57	0.04448	1.556	0.06162
1674.4	1.613	0.0466	1.513	0.06427
1725.13	1.592	0.04725	1.368	0.06354
1775.3	1.59	0.04791	1.299	0.06315
1825.16	1.631	0.0488	1.303	0.06513
1874.89	1.688	0.05042	1.357	0.06959
1925.03	1.67	0.049	1.255	0.06642
1975.19	1.671	0.05176	1.211	0.07058
2024.9	1.645	0.05426	1.276	0.07813
2064.63	1.614	0.06991	1.414	0.1144
2125.01	1.614	0.07038	1.227	0.1143
2175.64	1.59	0.07217	1.359	0.1287
2250.42	1.421	0.04899	1.154	0.08686
2350.36	1.309	0.04683	0.9238	0.0804
2449.69	1.581	0.05716	0.9835	0.09579

E_γ	$\sigma(p\eta^{'})$	sta. er.	$\sigma(n\eta^{'})$	sta. er.
1374.25	0.03803	0.007219	0	0
1424.81	0.2747	0.02995	0.2449	0.0623
1474.64	0.543	0.04123	0.5799	0.09303
1524.44	0.6672	0.04277	0.6439	0.09183
1574.72	0.7745	0.04351	0.7776	0.09403
1624.57	0.7557	0.04597	0.6594	0.09017
1674.4	0.8479	0.05195	0.587	0.09134
1725.13	0.748	0.05101	0.5401	0.09077
1775.3	0.7616	0.05303	0.5597	0.09348
1825.16	0.7531	0.05421	0.6181	0.1001
1874.89	0.8688	0.06131	0.641	0.1052
1925.03	0.7013	0.0545	0.6092	0.1001
1975.19	0.6575	0.05689	0.6668	0.113
2024.9	0.6835	0.06238	0.8368	0.1358
2064.63	0.7257	0.08745	0.706	0.1644
2125.01	0.5777	0.08359	0.4921	0.1483
2175.64	0.6081	0.09149	0.6571	0.1757
2250.42	0.5015	0.06088	0.477	0.1106
2350.36	0.3805	0.05488	0.3275	0.09353
2449.69	0.5162	0.07354	0.6586	0.1513